Proceedings of 17th International Symposium on Performance Improvement of Concrete for Long life span Structure

Date
21-23 August. 2024

VENUE
Civil Engineering Research Institute for Cold Regions, conference hall

Organization
Muroran Institute of Technology, Japan
Hokkaido University, Japan

Organizing Committee

Advisory Committee

Prof. HAN Cheon Goo, Cheongju University, Korea
Prof. LI Baishou, Yanbian University, China
Prof. ZOU Chaoying, Harbin Institute of Technology, China
Prof. CUI Wenyi, Yanbian University, China
Dr. KIM Sung Wook, Korea Institute of Civil Engineering and Building Technology, Korea
Prof. MIZOGUCHI Mitsuo, Muroran Institute of Technology, Japan

Co-chairperson

Prof. HAMA Yukio, Muroran Institute of Technology / Hokkaido University, Japan
Prof. YAMADA Yoshitomo, The University of Ryukyus, Japan
Prof. YANG Yingzi, Harbin Institute of Technology, China
Prof. FANG Guangxiu, Yanbian University, China
Prof. LEE Gun Cheol, Korea National University of Transportation, Korea
Prof. HAN Min Cheol, Cheongju University, Korea

Executive Committee

Prof. HAMA Yukio, Muroran Institute of Technology / Hokkaido University, Japan
Prof. YAMADA Yoshitomo, The University of Ryukyus, Japan
Prof. TANIGUCHI Madoka, Muroran Institute of Technology, Japan
Prof. TAKASE Yuya, Muroran Institute of Technology, Japan
Assoc. Prof. KIM Jihoon, Muroran Institute of Technology, Japan
Prof. FUKASE Takayuki, Hokkaido University of Science, Japan
Mr. MIHARA Norihiro, Civil Engineering Research Institute for Cold Regions, Japan
Dr. NAKAMURA Takuro, Civil Engineering Research Institute for Cold Regions, Japan

SUPPORTED BY

ALC Association
Flowric Co., Ltd.
HAZAMA ANDO CORPORATION
HOKUDEN Integrated Consulting Service Co., Ltd.
Hokkaido Taiheiyo Ready-mixed CO., Ltd.
IWATA CHIZAKI INC.
Kett Electric Laboratory Co., Ltd.
KONOIKE CONSTRUCTION Co., Ltd.
NIPPON STEEL CEMENT Co., Ltd.
MINAMI-GUMI Corporation
SUMITOMO OSAKA CEMENT Co., Ltd.
TAIHEIYO CEMENT CORPORATION
TOYO CONSTRUCTION Co., Ltd.

Preface

On behalf of the PICLS 2024 Organizing Committee, I would like to extend my greetings. PICLS has been held annually as a conference for research exchange on concrete structures and materials among the three countries of China, Japan and Korea, sharing the family-like spirit of '和 (Harmony)' and the bonds of friendship that began in 2007 between Prof. HAN Cheon-Goo of Cheongju University, Korea, Prof. LI Baishou of Yanbian University, China, Prof. ZOU Chaoying of Harbin Institute of Technology and me.

In the meantime, although the 2020 event could not be held due to the Corona Disaster, this will be the 17th time the conference has been held. This will be the sixth time that the conference has been held in Japan, following Muroran (2008), Asahikawa (2011), Naha (2014), Muroran (2017) and Naha (2021: Online), and the first time in Sapporo, the central city of Hokkaido. Each time, we are grateful for the hospitality of the host country. This time, we hope that you will have an enjoyable and meaningful time in the northern city of Sapporo.

A total of 76 participants - 38 from Japan, 10 from China and 28 from Korea - are expected to attend PICLS 2024, where 2 special lectures and 21 general papers (7 from each country) are scheduled to be presented. The co-chair of this conference, Prof. YAMADA Yoshitomo of the University of the Ryukyus, has been awarded this year's AIJ Prize for Best Paper and Cement Association Prize, and a commemorative lecture is also planned.

In recent years, the summer heat has become increasingly severe worldwide, but we hope that the participants will be able to deepen the friendship between the three countries and have fruitful exchanges through discussions on the latest research results in Hokkaido, which is a little cooler than usual. Finally, we would like to thank the 13 companies that sponsored PICLS 2024.

21 Aug. 2024

PICLS2024 Co-Chairman (Japan)

Prof. HAMA Yukio, Dr. Eng.

Muroran Institute of Technology / Hokkaido University, Japan

Symposium Schedule

• DAY 1, Aug. 21, 2024

- 18:30 Welcome Party : *Hotel Sapporo Garden Palace*

• DAY 2, Aug. 22, 2024

- 09:00-09:15 Registration

- 09:15-09:30 Opening Address

Chair: TANIGUCHI Madoka (Muroran Institute of Technology, Japan)

◯ SHIMATA Akinori (Civil Engineering Research Institute for Cold Regions)

◯ HAMA Yukio (Muroran Institute of Technology, Japan)

Award commemorative lecture

Chair: TANIGUCHI Madoka (Muroran Institute of Technology, Japan)

9:30-9:50

Analytical Studies on Salt Damage of Reinforced Concrete Structures and Fluidity Evaluation of Fresh Concrete and Development to Machine Learning

Prof. YAMADA Yoshitomo (University of The Ryukyus, Japan)

Keynote speech

Chair: TANIGUCHI Madoka (Muroran Institute of Technology, Japan)

9:50-10:25

Water absorption and desorption characteristics of superabsorbent polymers and their concrete properties

Prof. GUAN Xinchun (Harbin Institute of Technology, China)

10:25-11:00

Applying thixotropy on cement-based materials with PVA and borax

Prof. Dongyeop HAN (Gyeongsang National University, Korea)

10:50-11:00 Break time

Session I: MATERIALS 1

Chair: Kim Jihoon (Muroran Institute of Technology, Japan)

11:00-12:30

001. Numerical analysis for the prediction of adhesion chloride in reinforced concrete structures considering rain exposure

*TOYODA Souta (University of the Ryukyus, Japan)

SAKIHARA Kohei (University of the Ryukyus, Japan)

KASAHARA Takumi (Prometech Software, Japan)

TAKADA Satoshi (Prometech Software, Japan)

002. CO_2 activation of cementitious materials based on the mineralization-desorption of amino acid salts absorbent

*TieFeng Chen (Harbin Institute of Technology, China)

Jingkai Xu (Harbin Institute of Technology, China)

003. Assessment of Physical Properties and Optimal Utilization of Cement-Free Precast Concrete Incorporating Industrial By-Products

*Sohee MOON (Kyungpook National University, Korea)

Youngwoong JUNG (Kyungpook National University, Korea)

Seongpyo KIM (Kyungpook National University, Korea)

Jayeon YUN (Kyungpook National University, Korea)

Kyungsu SHIN (Woosong University, Korea)

Hyeonggil CHOI (Kyungpook National University, Korea)

004. Chemical changes and CO_2 stability in carbonated hardened cement paste exposed to seawater

*FURUKAWA Ikuya (Shimane University, Japan)
Natsuki YOSHIDA (Shimane University, Japan)
Daiki ATARASHI (Shimane University, Japan)

005. Influence of cellulose nanocrystal on the hydration and microstructure of Portland cement paste

*Shuai Bai (Harbin Institute of Technology, China)
Xinchun Guan (Harbin Institute of Technology, China)

006. Development of Concrete Rheology Parameter Prediction Model Based on Concrete Slump Flow Using Machine Learning Algorithm

*Lee Yu-Jeong (Gyeongsang National University, Korea)
Lee Kang-Hyeok (Gyeongsang National University, Korea)
Kim In-Tae (Gyeongsang National University, Korea)
Lim Young-Ju (Gyeongsang National University, Korea)
Han, Dong-Yeop (Gyeongsang National University, Korea)

12:30-13:30 Lunch Time

Facility Tour (13:00-13:30)

Session II: MATERIALS 2

Chair: Kim Junho (Tokyo University of Science, Japan)

13:30-14:45

007. Improvement of Biochar on Activity of Carbonated Steel Slag

*Xiaojian Gao (Harbin Institute of Technology, China)
Linshan LI (Harbin Institute of Technology, China)

008. Simulation Analysis of Thermal-Mechanical Coupled Behavior in Viscoelastic Model for Lead Rubber Bearings

*ITO Yusaku (Hokkaido University, Japan)

ISHII Ken (Hokkaido University, Japan)

009. EXPERIMENTAL STUDY ON THE PERFORMANCE OF PC-CSA-CaO BLENDED SYSTEM IN SUB-ZERO TEMPERATURE

*Ge Zhang (Xi 'an University of Architecture and Technology, China)

Yijie Lei (Xi 'an University of Architecture and Technology, China)

Yixin Hao, (Xi 'an University of Architecture and Technology, China)

010. Evaluation of the Self-Sensing Properties of Reinforced Concrete Units Using Self-Sensing Mortar for Section Enlargement

*Jin Soep, Kim (Korea National University of Transportation, Korea)

Do Kyun, Kim (Korea National University of Transportation, Korea)

Geon Woo, Im (Korea National University of Transportation, Korea)

Young Min, Kim (Korea National University of Transportation, Korea)

Gun Choel, Lee (Korea National University of Transportation, Korea)

011. Heat-stored engineered cementitious composite containing phase change material

Huayang Sun (Harbin Institute of Technology, China)

Kunyang Yu (Harbin Institute of Technology, China)

Minjie Jia (Harbin Institute of Technology, China)

Yingzi Yang (Harbin Institute of Technology, China)

*Yushi Liu (Harbin Institute of Technology, China)

14:45-14:55 Break time

Session III: Structure/Construction

Chair：SAGAWA Takahiro (Maebashi Institute of Technology, Japan)

14:55-16:10

020. Machine Learning Model for RC Beam Subjected to Several Seismic Load and Crack Repair

*Miki Matusubayashi (Muroran Institute of Technology, Japan)
Sota Sugawara (Muroran Institute of Technology, Japan)
Mizuki Nakamura (Muroran Institute of Technology, Japan)
Yuya Takase (Muroran Institute of Technology, Japan)

021. Estimating the period of hot weather concreting in Republic of Korea and introducing caution periods

*Jiman JEONG (Cheongju University, Korea)
Han, Jun-Hui (Cheongju University, Korea)
Baek, Seong-Jin (Cheongju University, Korea)
Lim, Gun-Su (Cheongju University, Korea)
Kim, Jong (Cheongju University, Korea)
Han, Min-Cheol (Cheongju University, Korea)

022. Effect of Waste Clay Bricks on the Quality of Recycled Fine Aggregate

*Do Kyun, Kim (Korea National University of Transportation, Korea)
Jin Soep, Kim (Korea National University of Transportation, Korea)
Geon Woo, Im (Korea National University of Transportation, Korea)
Young Min, Kim (Korea National University of Transportation, Korea)
Gun Choel, Lee (Korea National University of Transportation, Korea)

023. Bond strength of adhesive post-installed anchor for rc cantilever beam damaged by shear load

*Taito Shiokoshi (Muroran Institute of Technology, Japan)
Atsuto Yasui (Muroran Institute of Technology, Japan)
Yuya Takase (Muroran Institute of Technology, Japan)

024. A Bonding Performance Evaluation of Super Retarding Concrete for Cold Joint Integration under Hot Weather Conditions

*Juntaek JEONG	(Cheongju University, Korea)
Jaewoong Park	(Cheongju University, Korea)
Gunsu Lim	(Cheongju University, Korea)
Jong Kim	(Cheongju University, Korea)
Mincheol Han	(Cheongju University, Korea)
Cheongoo Han	(Cheongju University, Korea)

16:10-16:20 Break time

Session IV: DURABILITY

Chair：SAKIHARA Kohei（University of the Ryukyus, Japan）

16:20-17:35

027. Study on the effect of suppressing frost damage deterioration of concrete with hydrophobic compounds

*Yasuda Reiko	(FLOWRIC CO.,LTD., Japan)
Nishi Hironobu	(FLOWRIC CO.,LTD., Japan)
Hama Yukio	(Muroran Institute of Technology, Japan)

028. C-S-H seeds used as accelerator for cold weather concreting

*Yingzi Yang	(Harbin Institute of Technology, China)
Sile Hu	(Harbin Institute of Technology, China)
Yi Jiang	(Harbin Institute of Technology, China)

029. A proposal for the mass concrete hydration heat reduction by applying proper mixing time and mixing methods

*Sungjin BAEK	(Cheongju University, Korea)
Gun-su Lim	(Cheongju University, Korea)
Jun-Hui, Han	(Cheongju University, Korea)
Jong, Kim	(Cheongju University, Korea)
Min-Cheol, Han	(Cheongju University, Korea)

030. Microstructural changes in blast-furnace cements with different replacement ratios under repeated drying and wetting cycles

*LUO XI (Muroran Institute of Technology, Japan)
Kim Jihoon (Muroran Institute of Technology, Japan)
Hama Yukio (Muroran Institute of Technology, Japan)

031. EFFECT OF CARBONATION CURING ON THE LOW TEMPERATURE SULFATE ATTACK PERFORMANCE OF CEMENT PASTE ADDED WITH AUTOCLAVED AERATED CONCRETE POWDER

*Ling Qin (Qingdao University of Technology, China)

17:40-17:55 Closing Remarks

◯ HAMA Yukio (Muroran Institute of Technology, Japan)

18:30-20:30 Banquet

Koropokkuru

DAY 3, Aug. 23, 2024

- 08:30- Depart from hotel
- 09:00-10:00 “Sapporo Olympic Museum”
- 10:30-11:10 “Shiroikoibito Park”
- 11:30-12:50 Lunch
- 13:40-15:30 Historical Village of Hokkaido “Kaitaku no mura”
- 16:30- Hotel sapporo garden palace

Contents

Award Commemorative Lecture

Report on the 2024 AIJ Award and the 2024 Cement Association Paper Award

Faculty of Engineering,
University of the Ryukyus.

Yoshitomo Yamada

Report on the Architectural Institute of Japan Award (Paper) for 2024

Analytical Studies on Salt Damage of Reinforced Concrete Structures and Fluidity Evaluation of Fresh Concrete and Development to Machine Learning

Together with other award winners in other fields

Background and objectives of the study

My research is being conducted to contribute to the following two backgrounds and objectives.

1. **Long life:** In building a recycling- based society, the long life of reinforced concrete structures is becoming more important. It is important to extend the service life of structures. However, in areas such as near the coast, damage caused by chloride ions is likely to occur. There is concern that it may deteriorate prematurely.
2. **Rationalization of design and construction:** The construction industry is facing a serious labor shortage. There is a demand for streamlining design and construction work at construction sites through the introduction of technology, and for improving labor productivity by reducing labor and manpower through automation.

Therefore, in this study, we have been working on the salt damage problem and the evaluation of the fluidity of fresh concrete using a numerical analysis approach and machine learning . The results of these studies are intended to contribute to the durability design of reinforced concrete structures and to the rationalization of concrete design of mix and construction.

Salt damage problem =>Use of numerical analysis and machine learning

$$\left(\frac{1}{2}[K]+\frac{1}{\Delta x}[C]\right)\{\phi(x+\Delta x)\}=\left(-\frac{1}{2}[K]+\frac{1}{\Delta x}[C]\right)\{\phi(x)\}+\{F\}$$

$$\left(\theta[K]+\frac{1}{\Delta t}[C]\right)\{\phi(t+\Delta t)\}=\left(-(1-\theta)[K]+\frac{1}{\Delta t}[C]\right)\{\phi(t)\}+\{F\}$$

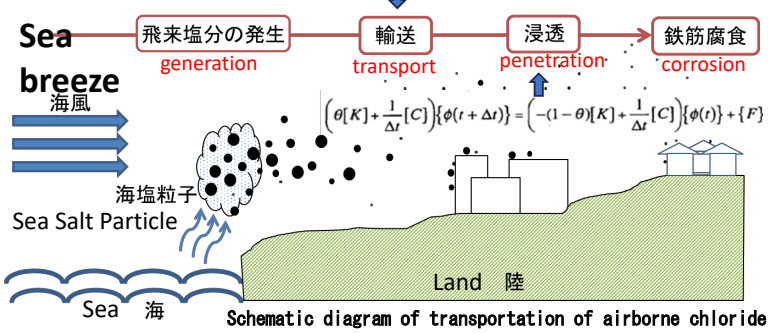

Schematic diagram of transportation of airborne chloride

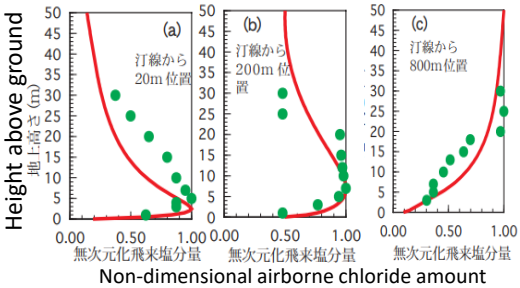

Airborne chloride transport analysis by FEM

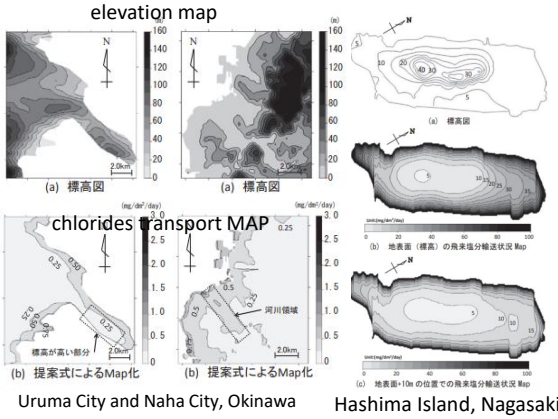

GIS-based MAP of airborne chloride transport conditions

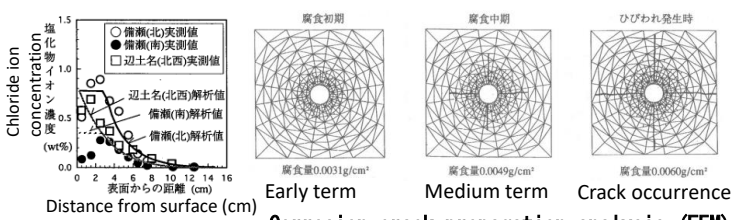

Corrosion crack propagation analysis (FEM)

Chloride ions penetration analysis using FEM

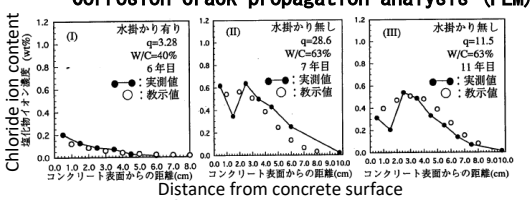

Prediction results of chloride ions penetration by machine learning (NN)

Fluidity Evaluation => Use of numerical analysis and machine learning

Rotational Viscometer

Flow constitutive equation:

$$\dot{\varepsilon}_{ij}^{vp} = \gamma\langle\phi(F)\rangle\frac{\partial Q}{\partial \tau_{ij}}$$

Equation of motion :

$$\rho\frac{Dv_i}{Dt} = \rho K_i - \frac{\partial p}{\partial x_i} + (\eta + \Lambda)\Delta v_i + 2e_{ij}\frac{\partial \Lambda}{\partial x_i}$$

$$\therefore \Lambda = \tau_y \Big/ \sqrt{2\left(e_{11}^2 + e_{22}^2 + e_{33}^2\right) + 4\left(e_{12}^2 + e_{23}^2 + e_{31}^2\right)}$$

Flow constitutive equation and equation of motion based on overstress theory (Bingham model)

Model of mortar movement when a pressure gradient occurs

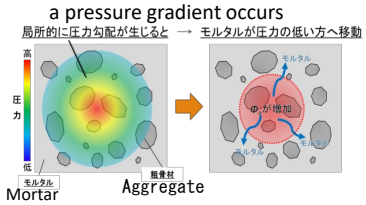

Mortar Aggregate

Coarse aggregate segregation model

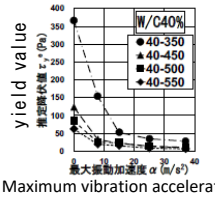

Maximum vibration acceleration

Rheological constant change due to vibration

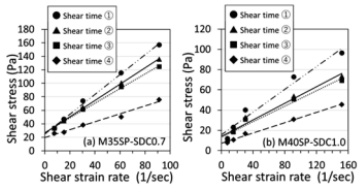

Flow curve of paste considering thixotropy

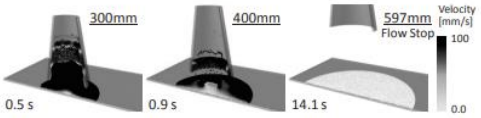

Slump analysis by MPS method

Prediction of fresh concrete properties using machine learning (RF)

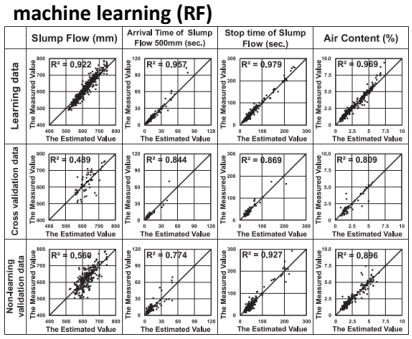

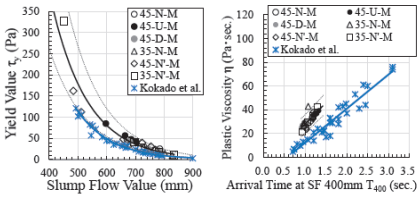

Estimation of rheological constants by slump flow test

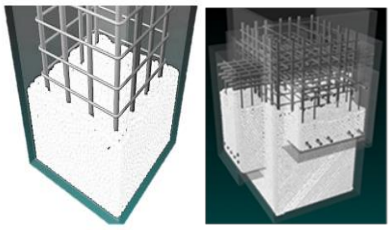

Filling analysis using BIM and MPS methods

Report on the 2024 Cement Association Paper Award

Machine learning-assisted determination of visual material segregation and prediction of rheological constants of high fluidity concrete

This award was jointly received by myself and my students.

[Research Background]

- **Visual material segregation determination of high fluidity concrete**
- **Estimation of rheological constants of high fluidity concrete**

It is necessary to actually mix the high-fluidity concrete and conduct a slump flow test.

Slump flow test

*** Preparation and testing take time and effort.**

[Research Objectives]

By using machine learning, we will develop a labor-saving method to visually determine the segregation of materials and predict rheological constants of high fluidity concrete without conducting slump flow tests.

[Visual material segregation judgment]

Prepare multiple datasets and perform machine learning.
(543 sets in this study)

Information on materials and mixes used for high flow concrete

Visual material segregation judgment

Machine Learning Predictions

Confusion matrix and evaluation indexs
(precision rate, Recall, specificity, Total Evaluation is MCC Evaluation)

Confusion matrix

		Prediction Results	
		segregation	non segregation
Experimental Results	segregation	TN (True Negative)	FP (False Positive)
	non segregation	FN (False Negative)	TP (True Positive)

[Machine Learning]
MCC : 0.56 to 0.66
Precision rate: 0.88 - 0.91
Recall: 0.80 - 0.84
Specificity: 0.78 to 0.83

Formulation using logistic regression analysis

Formulation using highly important features

$$y = \frac{1}{1 + e^{-a}}$$

$$a = \sum_{k=1}^{n} w_k x_k + w_0$$

$w_1 \sim w_n$…*Regression coefficients for each explanatory variable*、
$x_1 \ldots x_n$ each explanatory variable ,
w_0… constant term

[Proposal formula]
MCC : 0.33
Precision rate: 0.84
Recall: 0.57
Specificity: 0.78

[Prediction of rheological constants]

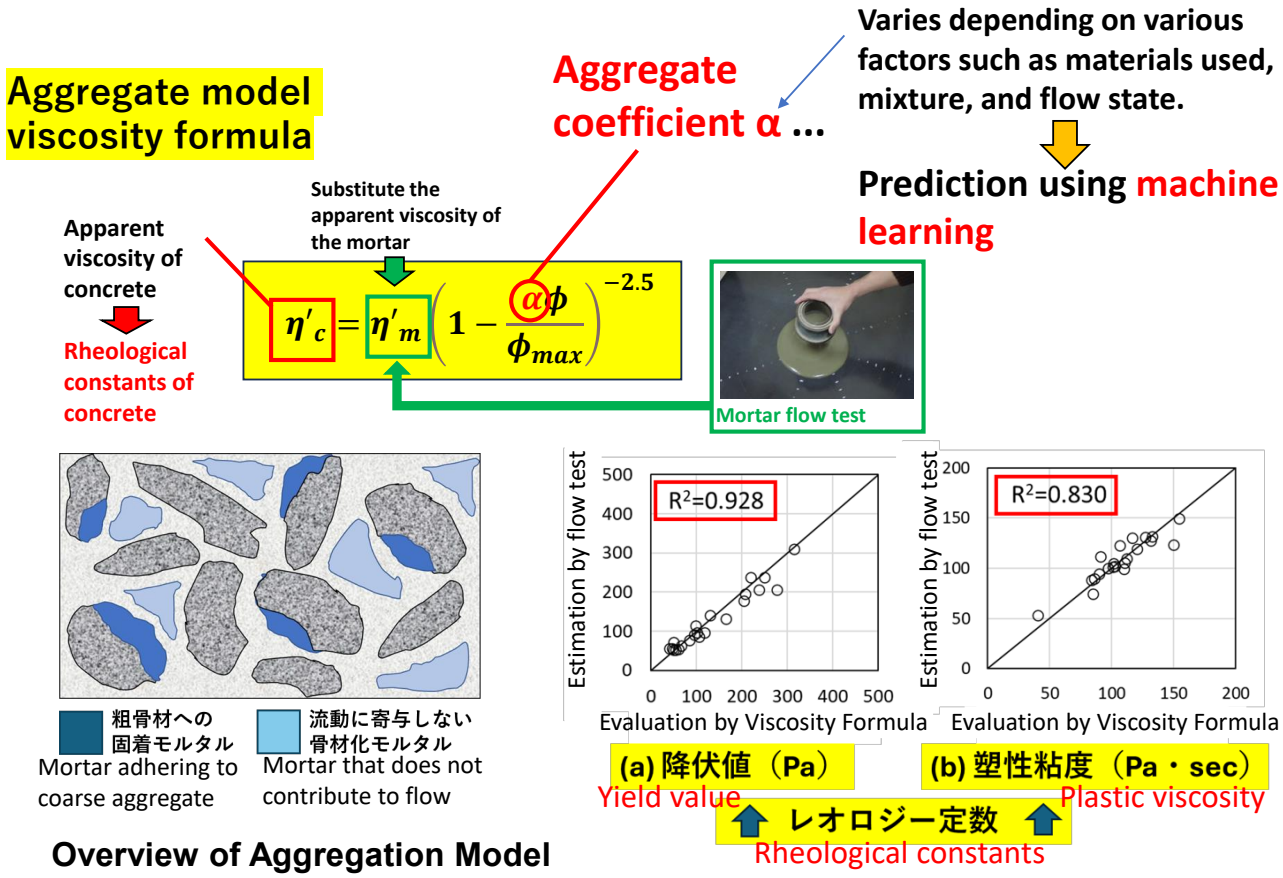

Acknowledgements

In conducting this research, I am grateful for the guidance of my **former teacher**, the advice of my **collaborators**, and the cooperation of past **graduates of the Building Materials Laboratory** of the University of the Ryukyus. Without their support, this research would not have been possible. **I appreciate everyone.**

Architectural Institute of Japan Award

Sement Association Paper Award

Thank you for your attention

Keynote Speech

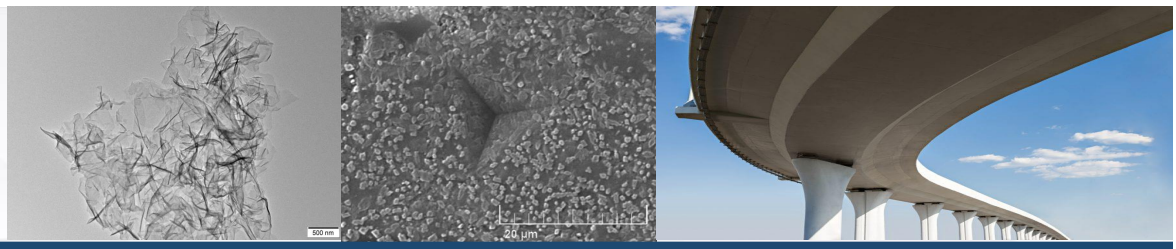

Water absorption and desorption characteristics of superabsorbent polymers and their concrete properties

Xinchun Guan

Harbin Institute of Technology

Research background

- **Superabsorbent polymer (SAP)** is a functional polymer material that exhibit swelling upon contact with water, allowing them to absorb water to **a level hundreds to thousands of times** their own weight.

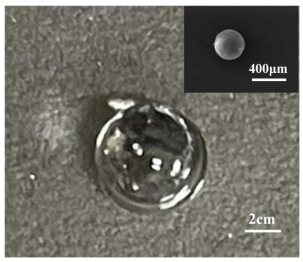

Dry SAP particles

Swelling SAP gels

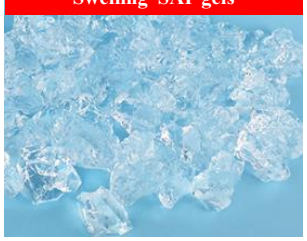

Research background

- The **hydrophilic groups** of SAPs are the key source of its water absorption capacity. When SAP absorbs water, its hydrophilic groups bind to water molecules through **hydrogen bonding**, allowing water molecules to begin entering the network. The dissociated cations increase the osmotic pressure of the solution within the network, driving the further expansion of SAP's network in the solution until dynamic equilibrium is reached.

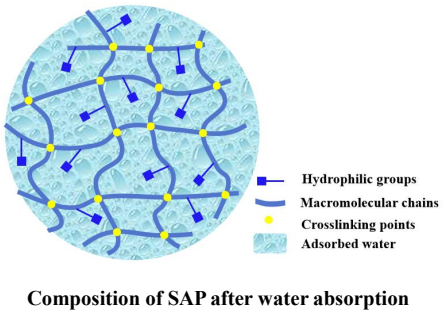

Composition of SAP after water absorption

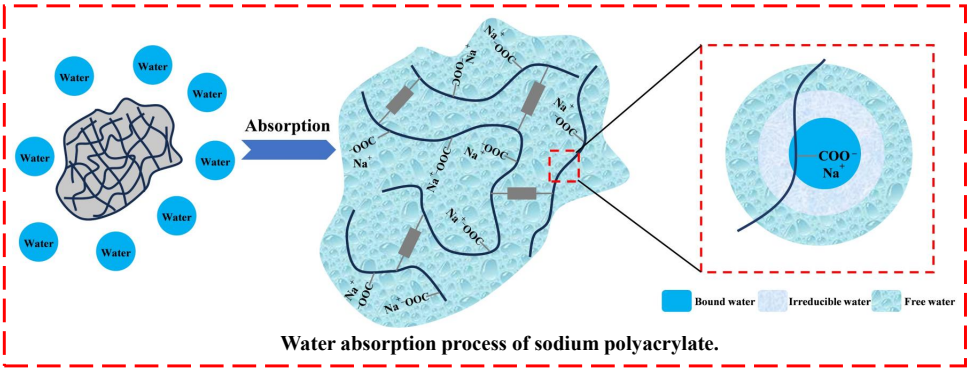

Water absorption process of sodium polyacrylate.

Research background

1920

Fiber-based water absorbing materials; (< 11g/g)

2018

The cross-linked acrylic homopolymers (sodium neutralized) taking up the largest share of the SAP market.

1960

USDA developed the first SAPs for water conservation in soil; (> 400g/g)

2007

RELEM establishes TC-SAP chapter

2005

Radiation synthesis of SAPs based on natural polymers (cellulose)

1978

The worldwide first commercial production of SAP for femine napkins (in Japan)

1982

The first production of SAPs for baby in Europe

1990

Global production of SAPs was more than 10,000,00 tons

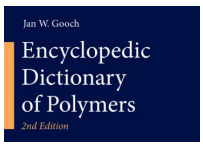

J C. B, et al. Superabsorbent Polymers.. Progress in Polymer Science (2021).

Research background

- The hygiene products are **the largest application** area of SAPs, accounting for the vast majority of the market share. The proportion of SAPs in agriculture and **construction** is gradually **increasing**.
- The research on SAPs or hydrogels is **growing**. The development of **biodegradable SAPs** will play an increasingly important role in industry and academia.

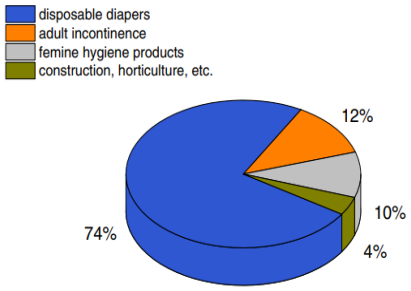

Global SAP consumption in 2014

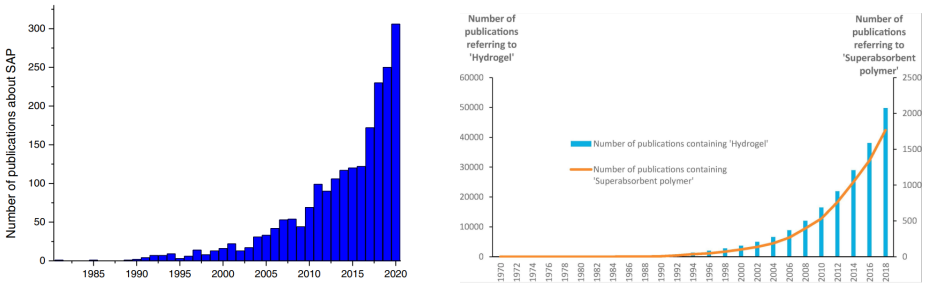

Number of publications containing the words 'hydrogel' or 'SAP'

J C. B, et al., 2021; Ma and Wen, 2020;

Research background

- At the beginning of the 21st century, SAPs were used as **internal curing agents** due to their excellent **water retention capacity** to reduce the loss of internal moisture in concrete and achieve the goal of **reducing autogenous shrinkage.**

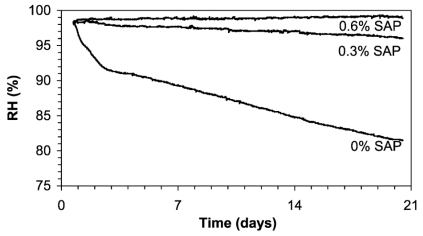

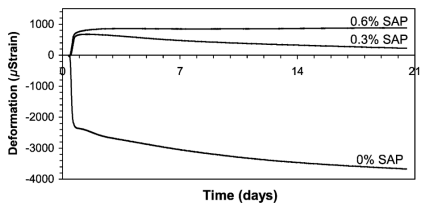

Internal humidity and autogenous shrinkage of cement paste with or without SAPs

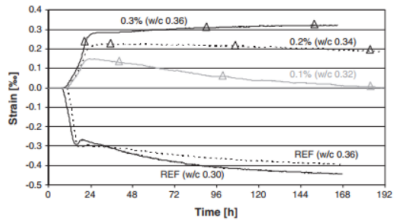

SAPs with additional water on the autogenous shrinkage of cement mortar

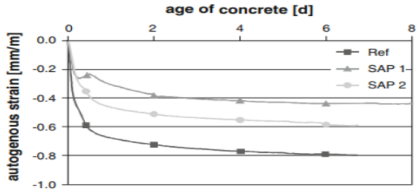

The autogenous shrinkage of cement mortar with different types of SAPs

Jensen O M, 2001;Soliman A M,2011;Mechtcherine, 2014

Research background

- Around 2010, the addition of SAPs to **improve the frost resistance** of concrete gradually attracted the attention of many researchers.
- To explain the improvement of concrete frost resistance by SAPs, many scholars have begun to pay attention to the **voids system** introduced by SAPs in concrete

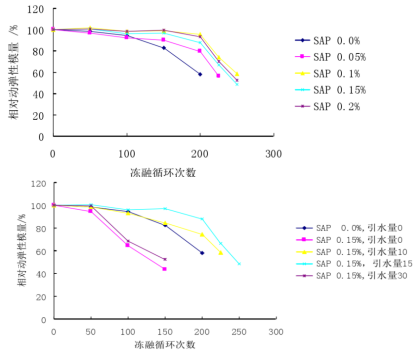

The frost resistance of concrete with different amount of extra-entrained water and different dosage of SAPs (in Chinese)

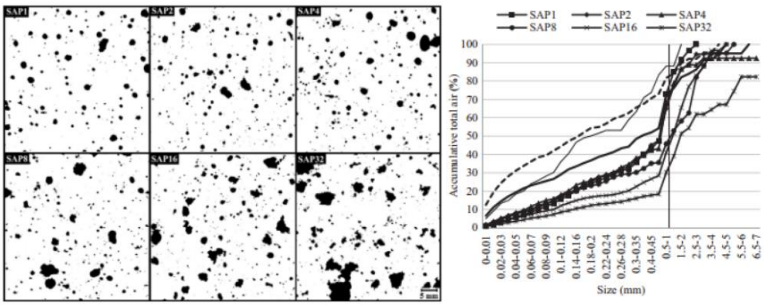

Analysis of Voids System introduced by SAPs in Cement paste

Lu D F, 2013 (in Chinese); Riyazi S, 2017

Research background

- **As early as 2010, Lee et al. already found that the addition of SAP can effectively reduce the water permeability of mortar with cracks, and the addition of SAP also contributes to the healing of cracks**

◆ Self-sealing of concrete

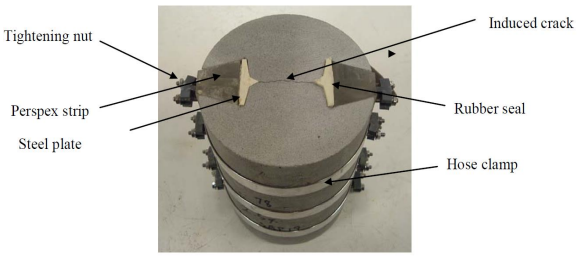

Conference Paper in Cement and Concrete Research · August2010
Hai Xiang Dennis Lee, Hong Seong Wong , Nick Buenfeld

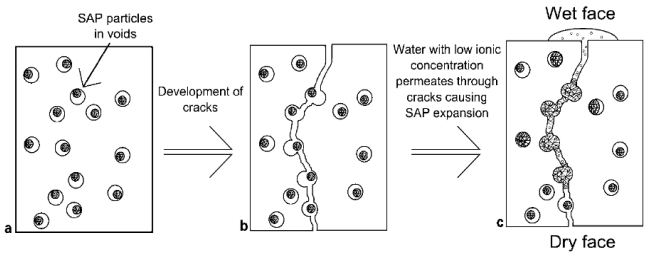

Lee, H. X. D., H. S. Wong, and N. R. Buenfeld. "Potential of superabsorbent polymer for self-sealing cracks in concrete." Advances in Applied Ceramics 109.5 (2010): 296-302.

Research background

- **Subsequently, Snoeck et al. studied the effect of the addition of SAP on the self-healing of ECC cracks, and found that SAP can also improve the self-healing effect of cracks in low humidity environment**

  - **Self-healing of concrete**

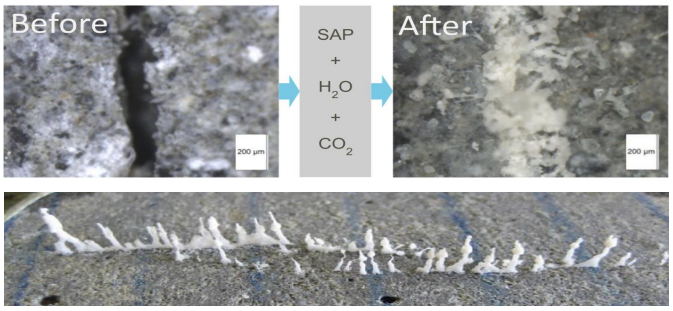

Snoeck D (2015) Self-healing and microstructure of cementitious materials with microfibres and superabsorbent polymers. PhD thesis, Ghent University

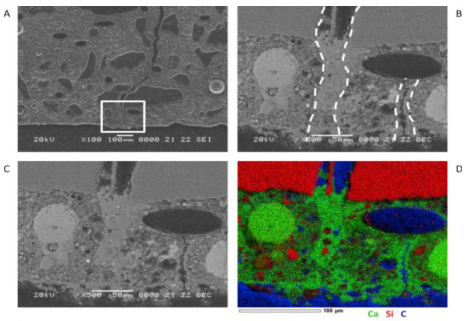

Snoeck, Didier, et al. Cement and Concrete Composites 65 (2016): 83-93.

Research background

- **Recently, the addition of SAP has attracted attention to the transmission performance of cement-based materials**

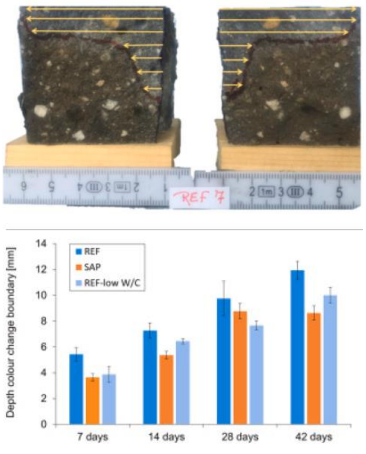

Depth of the $AgNO_3$ colour change boundary for uncracked specimens after 7, 14, 28 and 42d in a chloride solution

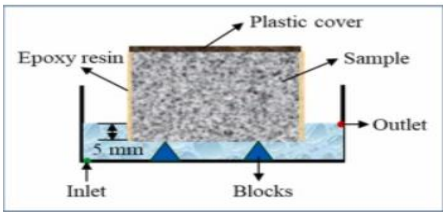

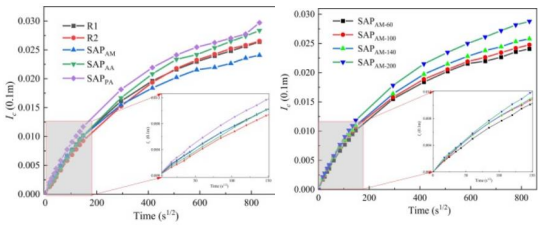

Cumulative water absorption amount of concrete with SAP

Mullem T V, 2024; Zheng S N, 2024

Research contents

01 **Effect of SAP on compressive strength of concrete**

02 **Effect of SAP on the frost resistance of concrete**

03 **Effect of SAP on self-healing properties of cement**

04 **Bio-based SAP synthesis for concrete field**

Research background

Strength

☐ SAP affects strength in opposite ways

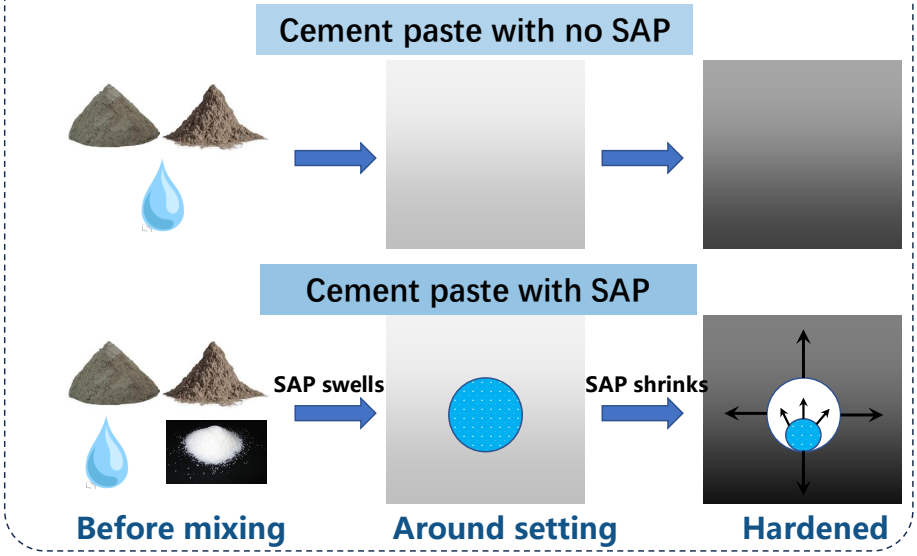

☐ The overall effect is in dispute

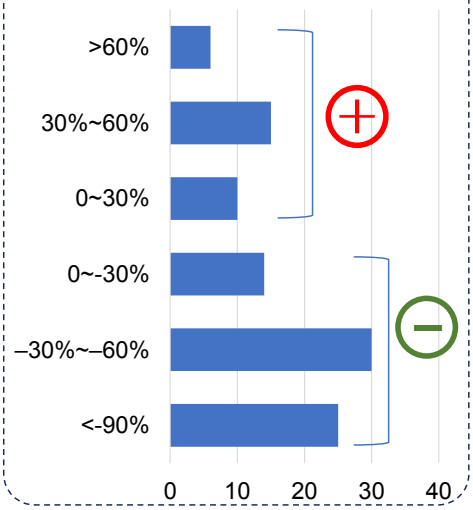

☐ We need a unified theory to foresee the overall effect and design concrete with SAP

Research contents

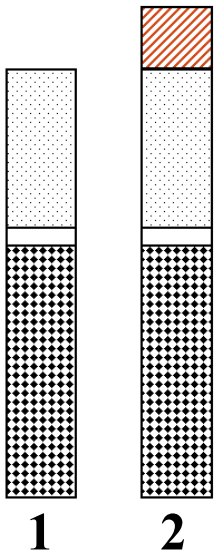

$$F_1 = C \cdot f_1^{\,m} \cdot r^{-a_1}$$
$$F_2 = C \cdot f_2^{\,m} \cdot r^{-a_2}$$

$$\frac{F_2}{F_1} = \left(\frac{f_2}{f_1}\right)^m \cdot \frac{r^{-a_2}}{r^{-a_1}}$$

$$Q = \frac{Q_I}{Q_{II}}$$

- 圣婴，这块太抽象了。不太好讲。片子可以多一些，重点将我们公式的思想讲清楚。特别重要的符号内涵也得标上。
- 另外，还是采取下图上字的形式。我需要一两行字，一方面，利于我来讲，另一方面，也利于别人听和理解

13

- We use *Q* to indicate the overall effect of SAP: positive (*Q*>1) or negative (*Q*<1)

Research contents

- How do we calculate Q_I and Q_{II}?

Q_I—The effect of internal curing

$$Q_I = (f_2 / f_1)^m$$

$$Q_I = (X_2 / X_1)^{3m}$$

$$f = f_0 X^3$$

$$X = \frac{V_{gel}(\alpha)}{V_{space}(\alpha)}$$

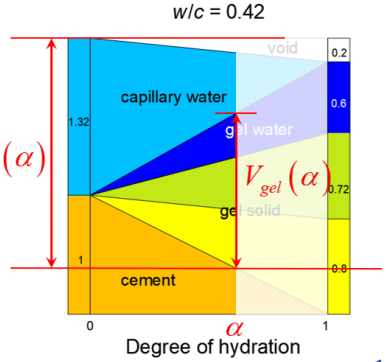

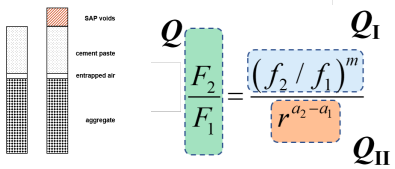

$$Q = \frac{Q_I}{Q_{II}} = \frac{F_2}{F_1} = \frac{(f_2/f_1)^m}{r^{a_2-a_1}}$$

Q_{II}—The effect of air voids

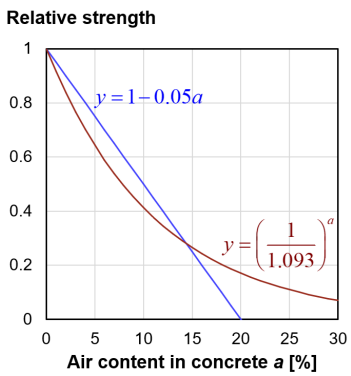

Popovics S, Ujhelyi J. (2008) J Mater Civ Eng. 20(7):459-463.

14

Research contents

☐ How well does our model work?

Source		Assmann (2008)				Justs et al. (2015)			Kang et al. (2017)		
Type		Mortar				Mortar			Mortar		
Measured	Age [d]	91	91	91	91	365	365	365	28	28	28
	F [MPa]	117.2	109.8	96.8	97.4	215	186	174	186	178	166
	Q [%]	100	93.7	82.6	83.1	100	86.5	80.9	100	95.7	89.2
Calculated	Q [%]	100	90.8	82.8	82.8	100	92.5	83.1	100	96.9	92.9
	Q_I [%]	100	121.0	136.6	136.6	100	128.9	136.6	100	129.2	142.0
	Q_{II} [%]	100	133.3	165.0	165.0	100	139.3	164.4	100	133.2	152.9

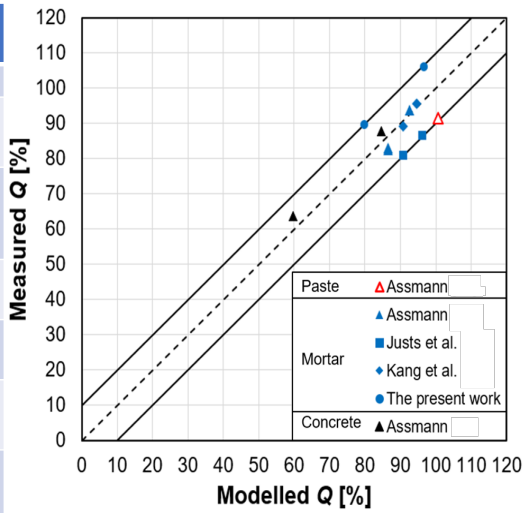

☐ All of the data points lie between the +/- 10% error lines.

Research contents

☐ What does our model imply?

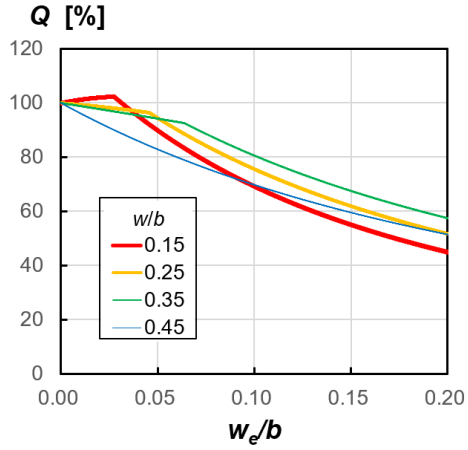

Paste content = 70%

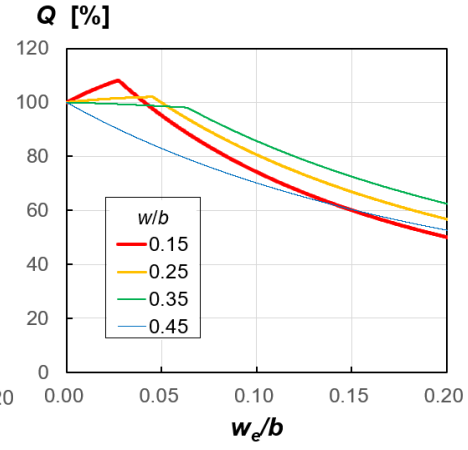

Paste content = 90%

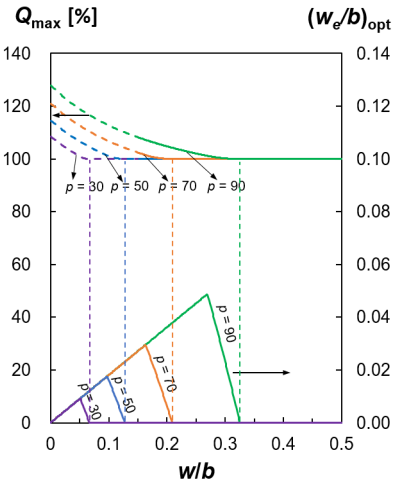

Research contents

01 **Effect of SAP on compressive strength of concrete**

02 **Effect of SAP on the frost resistance of concrete**

03 **Effect of SAP on self-healing properties of cement**

04 **Bio-based SAP synthesis for concrete field**

Research content

☐ Introducing **Voids** is an effective means to reduce freeze-thaw damage:

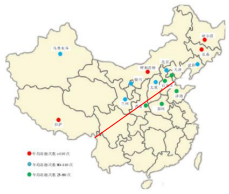

- More than **50%** of regions in China will suffer from freeze-thaw damage

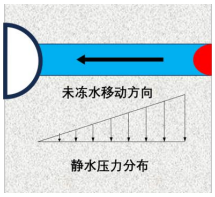

- Water freezes and **expands** by **9%** in volume
- Unfozen water flowing outside the pore generates **static water pressure**

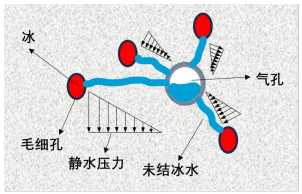

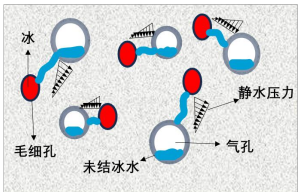

- Introducing voids can reduce the distance of unfrozen water movement and thus **lower hydrostatic pressure**

☐ SAP can **stably** introduce voids

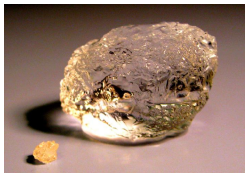

- SAP can absorb water **hundred times** its own weight

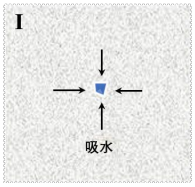

I:Water absorption under the **ion concentration difference**

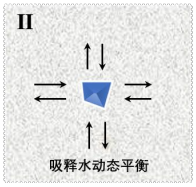

II:Water absorption **balance**

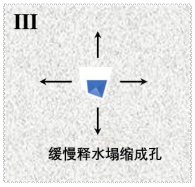

III:Release water under the **humidity difference**

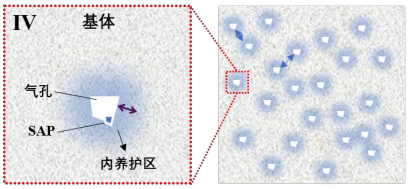

IV： SAP completely **collapses** to form **void**

Research content

- Reflecting the **volume fraction of swelling SAP** by the **void area fraction**

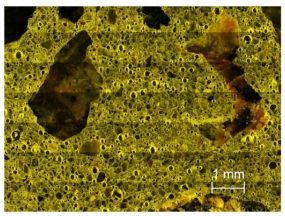

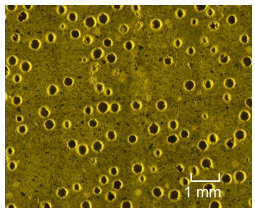

$$k = 1 + \frac{\rho_{SAP}}{\rho_w}\chi$$

k —Volume expansion ratio
ρ_{SAP} —The density of SAP
ρ_w —The density of water
χ —The water absorption capacity of SAP

- The **air content** obtained by using the **voids analysis technology** of hardened cement paste can determine the water absorption capacity of SAP in cement paste

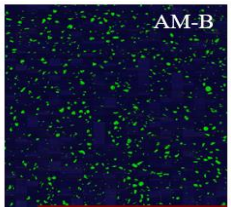

$$AC = \frac{\rho_w \cdot \left(V_c \frac{T_v}{T_t} V_{SAP}\right)}{m_{SAP}} \quad (4)$$

Vc is the volume of cement paste; ρ_w is the density of water; m_{SAP} and V_{SAP} are the mass and volume of dry SAP; T_v/T_t is the air content of cement paste. Due to the cement paste mixed with SAP used in the void analysis experiment was prepared by vacuum pumping, the air content in the test results is the void content (T_v/T_t), which is created by SAP.

Air content	The water absorption capacity of SAP
5.92%	13.3g/g

Research content

- A **more concise and rapid** method——^{1}H low-field NMR was used to determine the water absorption capacity of SAP in cement paste, and the void system was estimated
- The **voids system** closely related to the frost resistance of concrete was **estimated** based on the water absorption capacity of SAP.

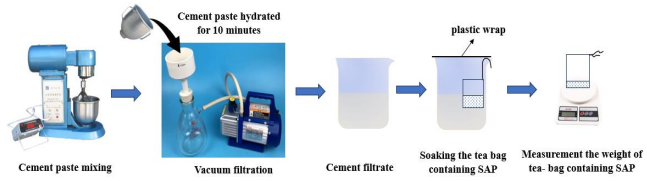

Tea-bag method

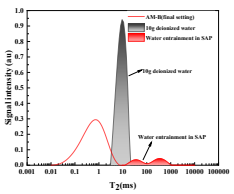

$$\frac{W}{W_f} = \frac{S_w}{S_{wf}} \quad (3)$$

W is the mass of deionized water(g); W_f is the free water content in the cement paste(g); S_w is the signal intensity of deionized water at this mass(au); S_{wf} is the signal strength of the free water content in the cement paste(au).

^{1}H low-field NMR

	AM (40-80μm)	AM (120-160μm)	AM (200-300μm)	AA (120-160μm)	
Tea-bag method	27g/g	27g/g	27g/g	11.5g/g	→ Inaccurate
Voids system analysis	6.7g/g	17.2g/g	25.25g/g	1.14g/g	→ Time-consuming
^{1}H low-field NMR	8.8g/g	16.3g/g	21.32g/g	0.87g/g	

Comparison of results

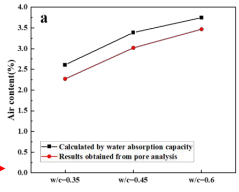

Pre design a voids system and validate it using void analysis based on the SAP water absorption capacity results obtained from ^{1}H low-field NMR

Research contents

- When the total water-cement ratio is the same, the addition of SAP increases the frost resistance of concrete. And SAP with stronger water absorption capacity is more conducive to increasing the frost resistance of concrete. **This is due to SAP absorbing water, resulting in a decrease in the actual water-cement ratio.**
- The addition of SAP can also increase the frost resistance of concrete when the basic water cement ratio is the same. But smaller particle size SAP is more pronounced. This is because there are more SAP particles, **which further reduces the void spacing coefficient**.

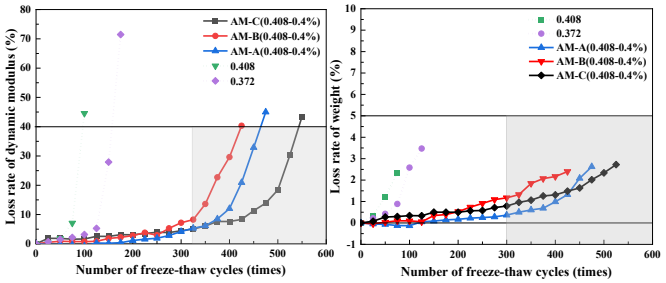

The **total water-cement ratio** is the same

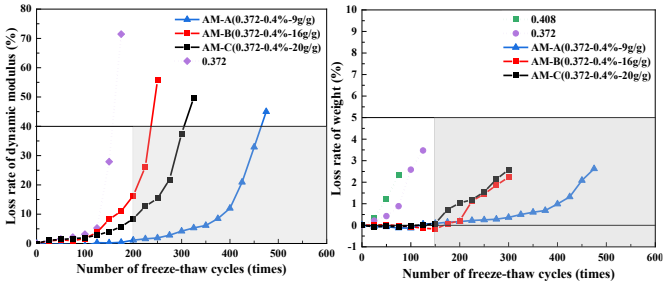

The **basic water-cement ratio** is the same

Research contents

- When the total air content is the same, the smaller the particle size of SAP, the better the frost resistance of concrete, because small particle size SAP is more conducive to **reducing the void spacing coefficient.**
- SAP(AA), which **does not absorb water** in the cement paste environment, cannot form pores and therefore **cannot improve the frost resistance of concrete**
- Due to the water absorption effect of SAP, it is difficult to determine the degree of concrete freeze-thaw damage through **quality loss.**

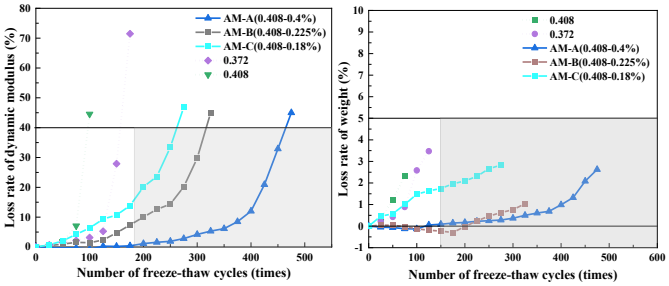

The **air content** is the same

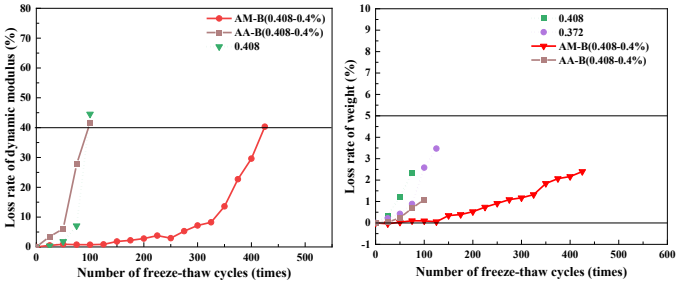

SAP has **different water absorption capabilities**

Research contents

01 Effect of SAP on compressive strength of concrete

02 Effect of SAP on the frost resistance of concrete

03 Effect of SAP on self-healing properties of cement

04 Bio-based SAP synthesis for concrete field

Effect of SAP on self-healing properties of cement method

Raw materials

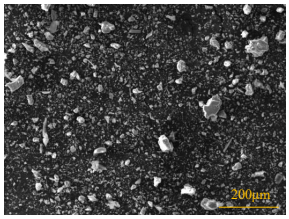

Cement

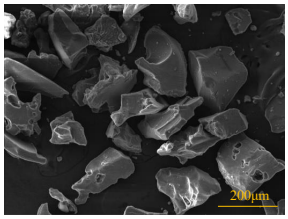

Sodium Polyacrylate-AA

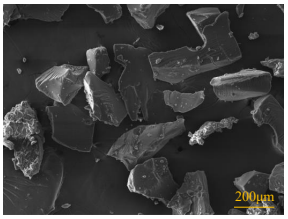

Sodium polyacrylate acrylamide copolymer-AM

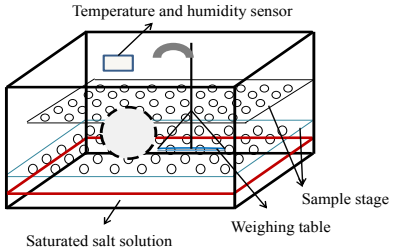

Temperature and humidity box

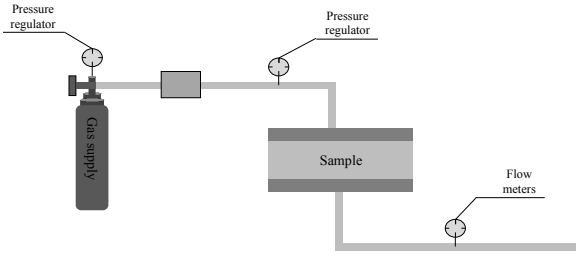

Air permeability test device diagram

Effect of SAP on self-healing properties of cement

- After 56 days in different humidity environment, AA and AM can absorb 37.0% and 34.0% of water vapor at 59% RH, and 98.5% and 72.5% of water vapor at 86% RH. At 97% RH, it can absorb 233.2% and 210.5% of water vapor.
- With the increase of relative humidity, the hygroscopic capacity of SAP increased gradually. The equilibrium moisture absorption of AA was higher than that of AM.
- After 12 days in the environment of 33% relative humidity, desorption basically reached equilibrium. The desorption rates of AA and AM reached 46.67% and 59.14%, 64.17% and 70.33%, 83.32% and 90.51%, respectively, when the relative humidity was 59%, 86% and 97%. It was found that the desorption rate of AA was slower than that of AM.

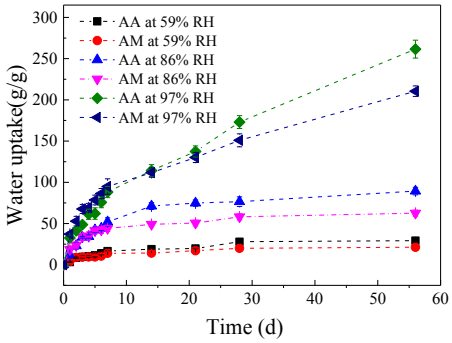

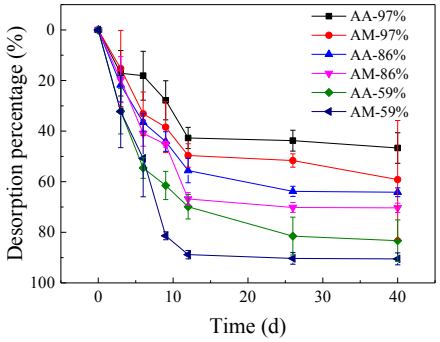

Effect of SAP on self-healing properties of cement

- The addition of SAP can improve the hydration degree of cement.
- At 97% RH, AA can increase the hydration degree of cement by 53.58%, and AM can increase the hydration degree of cement by 20.13%.

Cement TG

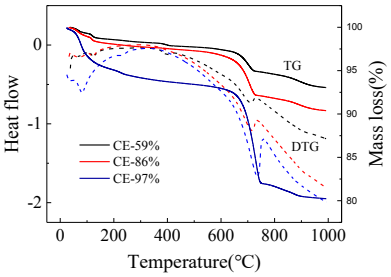

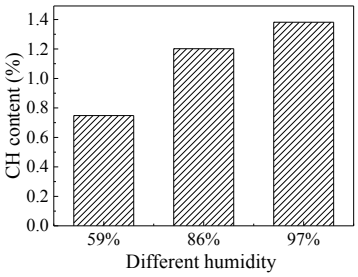

Cement with SAP

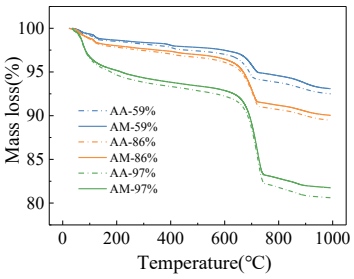

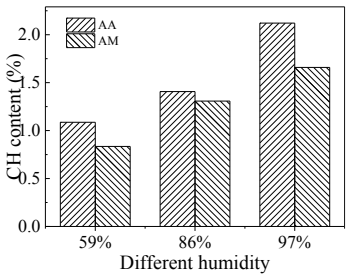

Effect of SAP on self-healing properties of cement

- **With the increase of the number of dry wet cycles, the swelling properties of the two types of SAP showed a downward trend.**
- **After six dry-et cycles, AA and am can maintain 68.45% and 61.90% of the initial swelling properties in deionized aqueous solution.**
- **In the cement filtrate, the swelling properties of AA and am are 38.40% and 52.43% of the initial swelling after one cycle, and can reach 7.30% and 26.26% after six dry-et cycles.**

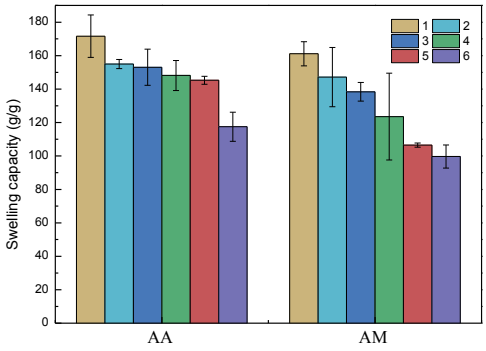

Deionized Water
DW

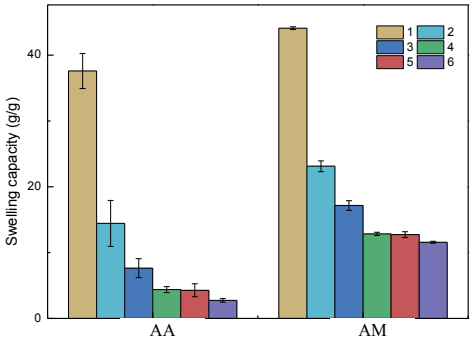

Cement filtrate
CF

unpublished data

Effect of SAP on self-healing properties of cement

- **After soaking in cement filtrate and then in ionic water, the repeated swelling performance of SAP increased first and then decreased.**
- **After six cycles, the swelling properties of AA and am can reach 57.66% and 56.23% of the initial equilibrium of raw materials.**

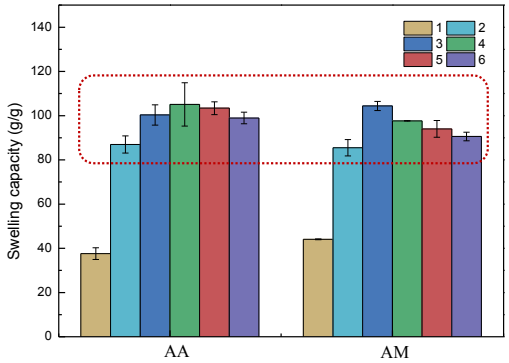

Cement filtrate+Deionized water
C+D

unpublished data

Effect of SAP on self-healing properties of cement

- With the increase of drying and wetting cycles, the water release rate and water release of SAP increased gradually at the same time.
- The water release rate and quantity of AM were higher than AA.
- AA was soaked in CF and then repeatedly absorbed water in aqueous solution, and its water release and water release rate were higher than that of AM.

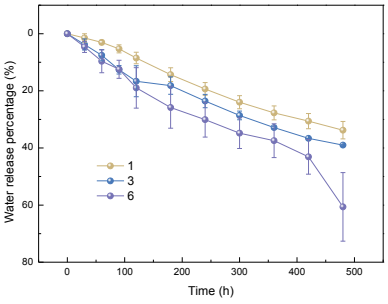

AA-DW

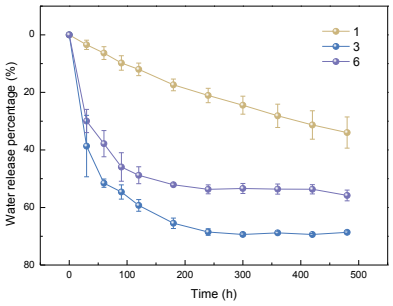

AA-CF

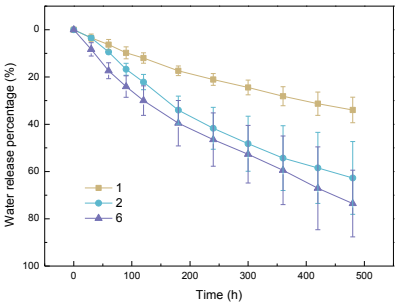

AA-C+D

unpublished data

Effect of SAP on self-healing properties of cement

- SAP improves the crack healing rate.
- The order of self-healing effect was E3>E2>E1.

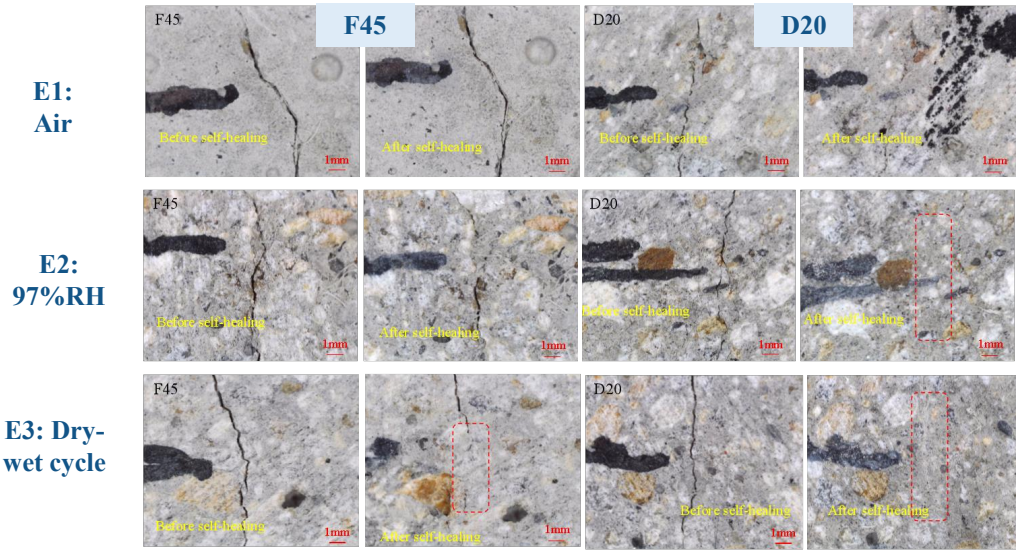

unpublished data

Effect of SAP on self-healing properties of cement

- **In the air, the specimens in the control group almost did not have much crack healing, and the recovery rate of gas relative permeability coefficient was only 7.55%, while the healing rate of D20 could reach 18.90%.**
- **At 97% RH, the specimens in the control group also showed certain internal crack healing, and the recovery rate of the relative permeability coefficient of gas could reach 17.02%, while the maximum recovery rate of the specimens mixed with SAP mortar could reach 81.92%.**
- **The self-healing effect was the best in E3 environment, followed by E2 and E1.**

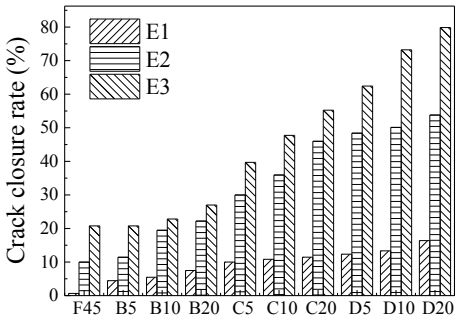

Surface crack healing rate

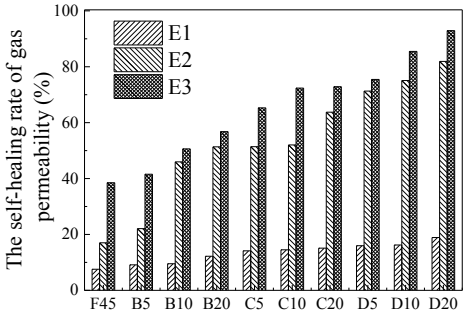

Recovery of gas relative permeability coefficient

unpublished data

Effect of SAP on self-healing properties of cement

- **In E2 environment, the volume ratio of healing products in F45 matrix and C10 specimen was 0.85% and 1.85%, respectively.**

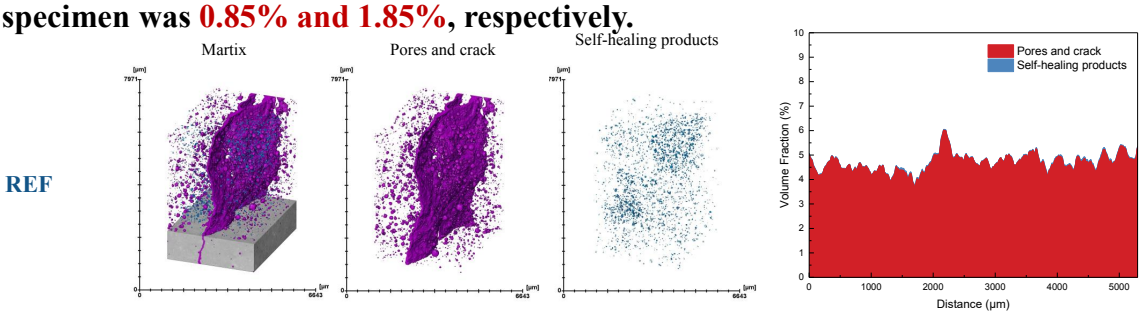

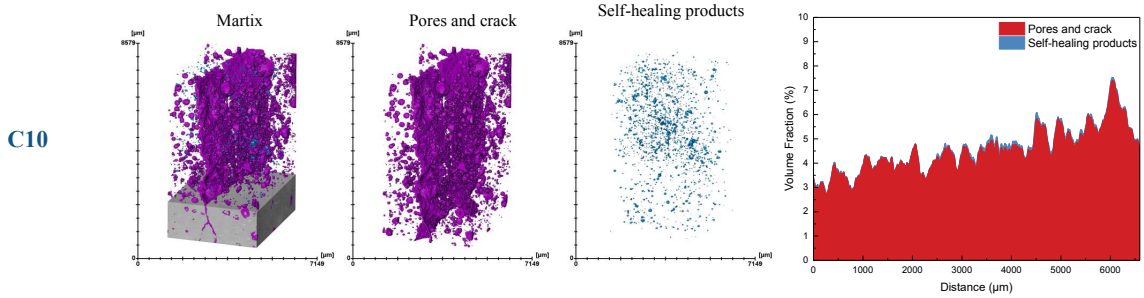

unpublished data

Effect of SAP on self-healing properties of cement

- **In E3 environment, the volume ratio of healing products in F45 matrix and C10 specimen was 11.35% and 47.94%, respectively.**

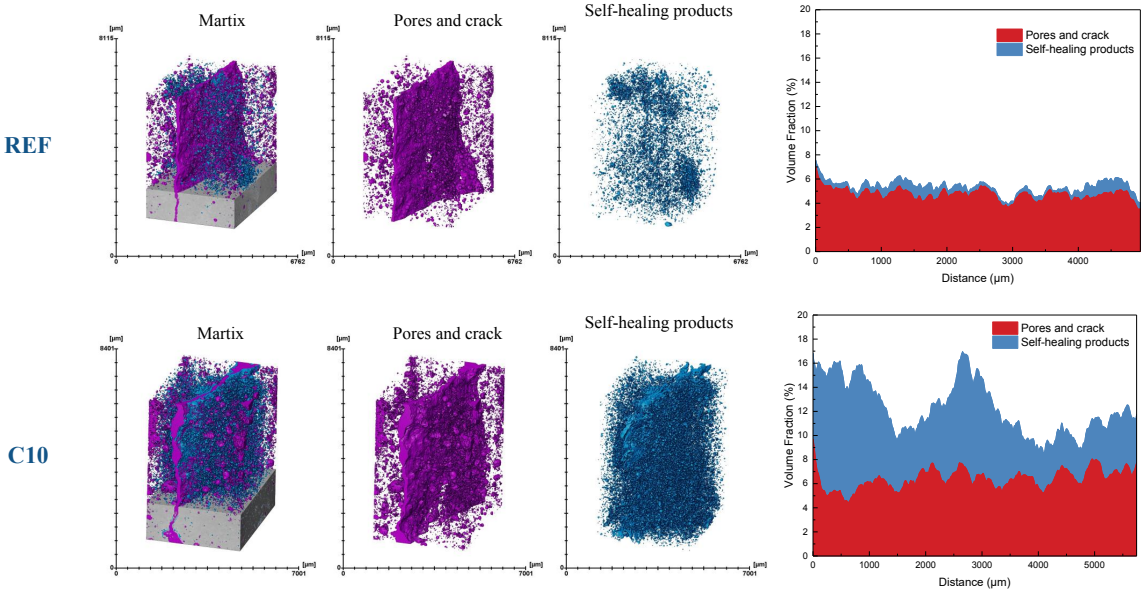

unpublished data

Effect of SAP on self-healing properties of cement

- **The addition of SAP did not change the type of hydration products.**
- **The healing products at the crack are mainly calcite and a small amount of calcium hydroxide.**

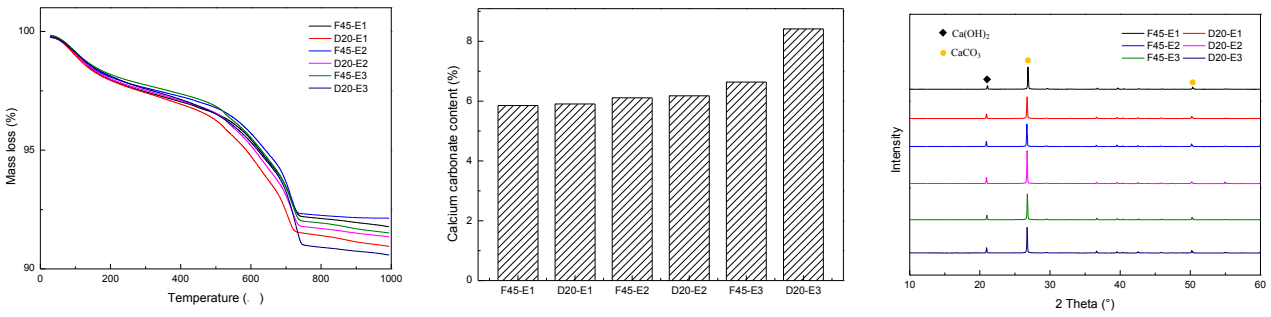

TG | **Calcium carbonate content** | **XRD**

unpublished data

Effect of SAP on self-healing properties of cement

- **Needle like products and calcite exist in the cracks.**
- **Compared with the control group, more calcium carbonate can be observed in the cracks of the specimens mixed with SAP mortar.**

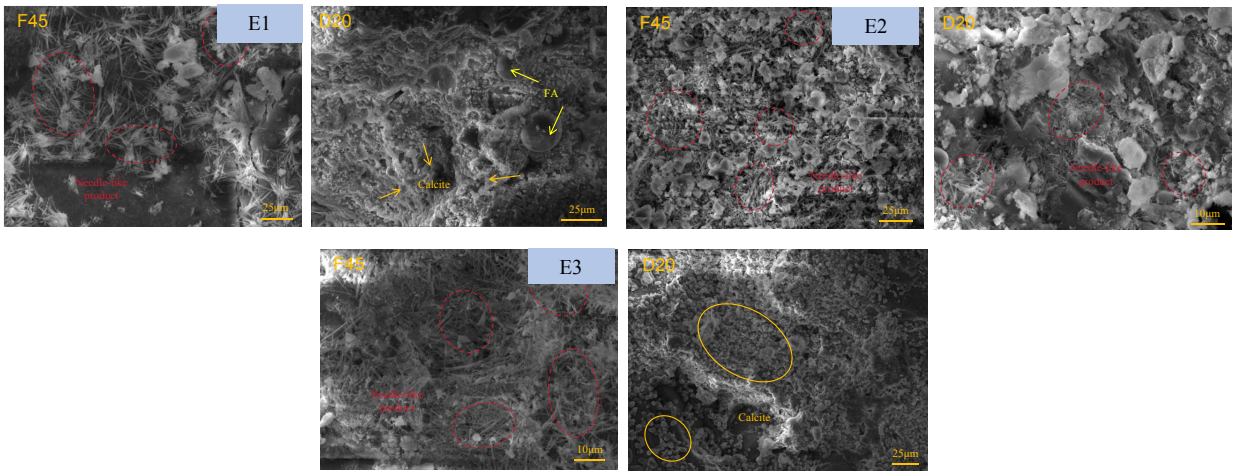

unpublished data

Research contents

01 Effect of SAP on compressive strength of concrete

02 Effect of SAP on the frost resistance of concrete

03 Effect of SAP on self-healing properties of cement

04 Bio-based SAP synthesis for concrete field

Bio-based SAP synthesis for concrete field

- The **main drawbacks** of using SAP in the field of concrete are as follows:

Raw materials are mostly derived from petroleum.

Premature water release leads to bleeding

Poor salt resistance

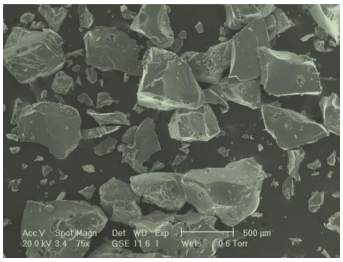

Mostly irregular particles

Bio-based SAP synthesis for concrete field

- Corn starch is a **natural, renewable resource** that is widely **available** and **inexpensive**. Additionally, it has **good biodegradability**, reducing **environmental pollution**.
- Based on the compositions of SAPs, **a starch-based superabsorbent polymer** was synthesized by aqueous solution polymerization.

Hydrophilic Monomers

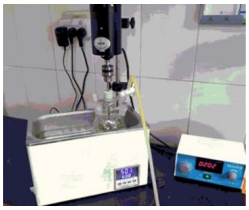

Aqueous solution polymerization

Starch-based SAP

Guan X C, et al., Synthesis and characterization of a starch-based superabsorbent polymer…, Construction and Building Materials. 2024;415.

Bio-based SAP synthesis for concrete field

- By using starch as the main chain and grafting stronger hydrophilic -SO_3H and non-ionic -$CONH_2$ groups, a starch-based SAP with high water-absorption and salt-resistant was synthesised.

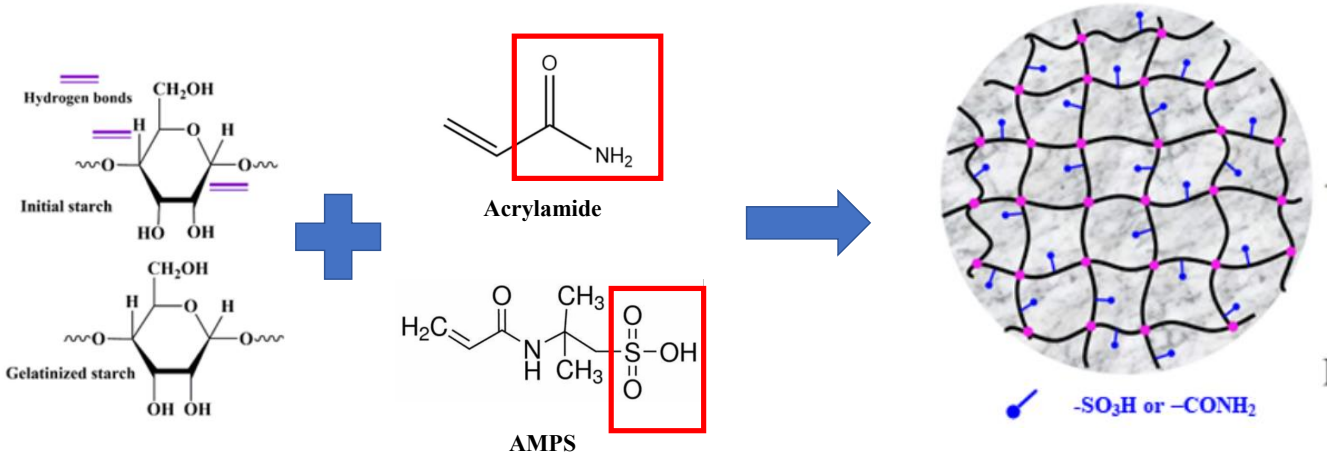

Guan X C, et al., Synthesis and characterization of a starch-based superabsorbent polymer…, Construction and Building Materials. 2024;415.

Bio-based SAP synthesis for concrete field

- The -SO_3H and -$CONH_2$ groups were grafted onto the starch chain. Starch-based SAP has lower crystallinity.
- Starch-based SAP shows the better thermal stability compared to other SAPs.

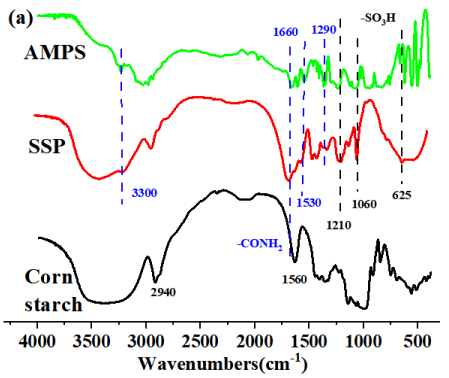

FT-IR

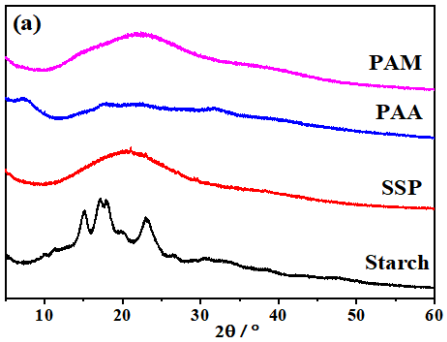

XRD

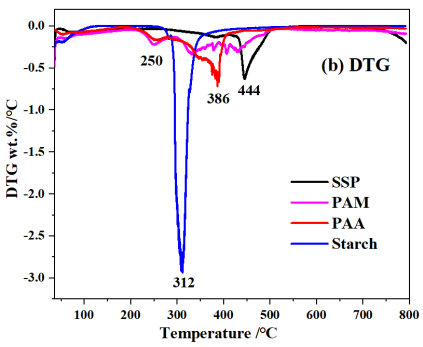

TGA

Bio-based SAP synthesis for concrete field

☐ **The starch-based SAP has a porous surface, can utilize gel films to form a network structure, and has more space.**

Conventional SAP

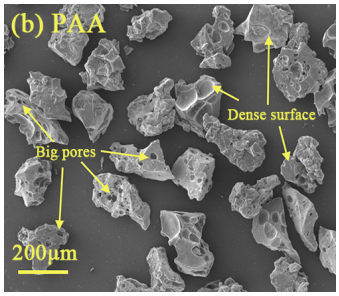

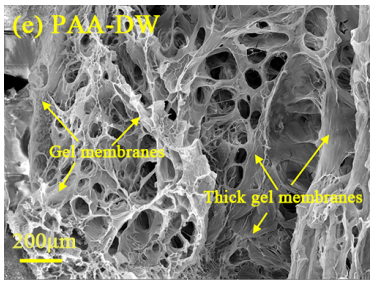

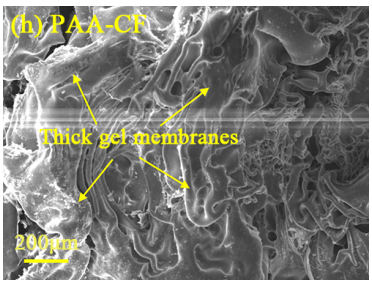

Starch-based SAP

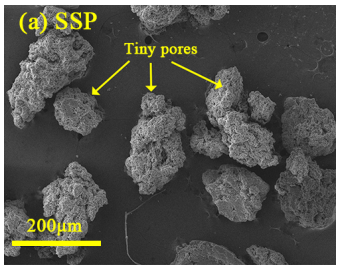

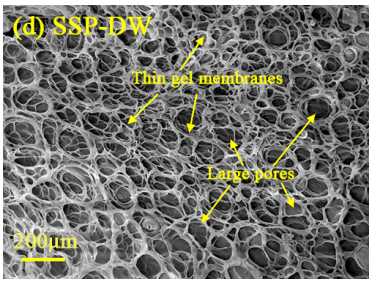

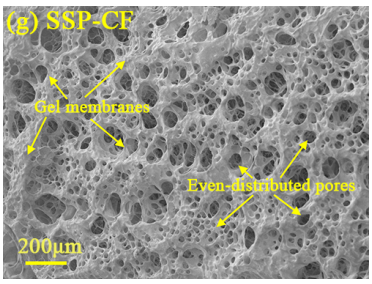

Bio-based SAP synthesis for concrete field

☐ **Compared to traditional SAP, the starch-based SAP has a higher water absorption, longer water desorption time, and lower ion sensitivity.**

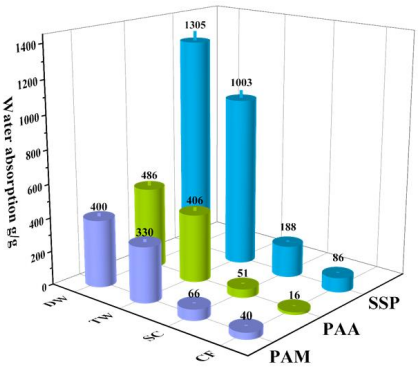

Water absorption of SAPs

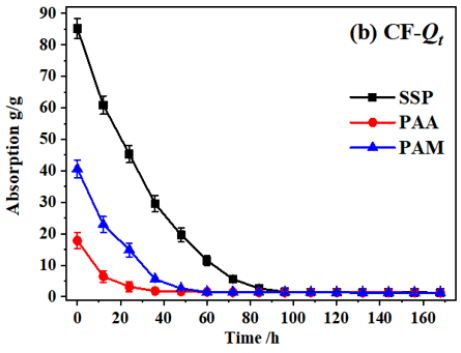

Desorption progress of SAP gels

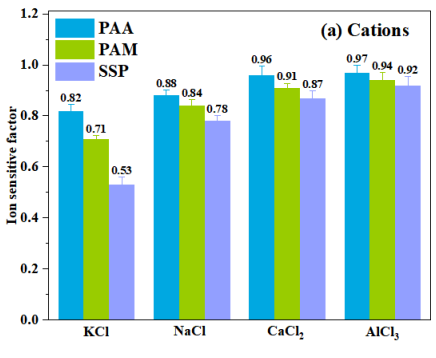

Ion sensitivity of SAPs

Bio-based SAP synthesis for concrete field

- **Compared to traditional SAP, the starch-based SAP significantly reduces autogenous shrinkage of cement paste, has minimal impact on compressive strength, and offers better overall performance.**

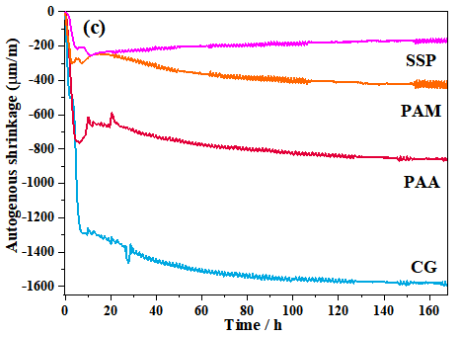

Autogenous shrinkage

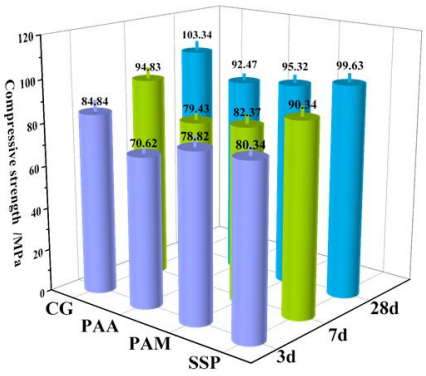

Compressive strength

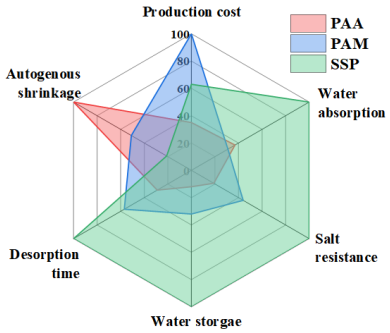

Comprehensive comparison

Bio-based SAP synthesis for concrete field

- **A spherical starch-based SAP with salt (alkaline) resistance was synthesized using corn starch via inverse suspension polymerization.**

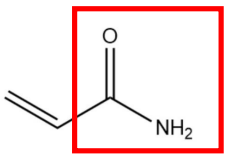

Acrylamide

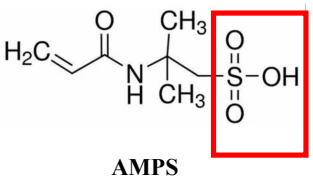

AMPS

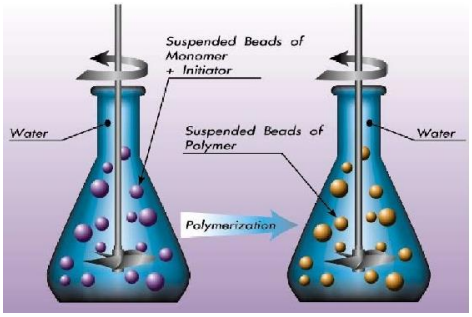

Inverse suspension polymerization

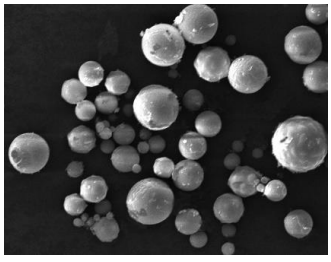

Spherical starch-based SAP

Bio-based SAP synthesis for concrete field

- By using corn starch as the raw material, two different solutions (oil phase and aqueous phase) are pre-configured to synthesize a spherical starch-based SAP by stirring and other operations.

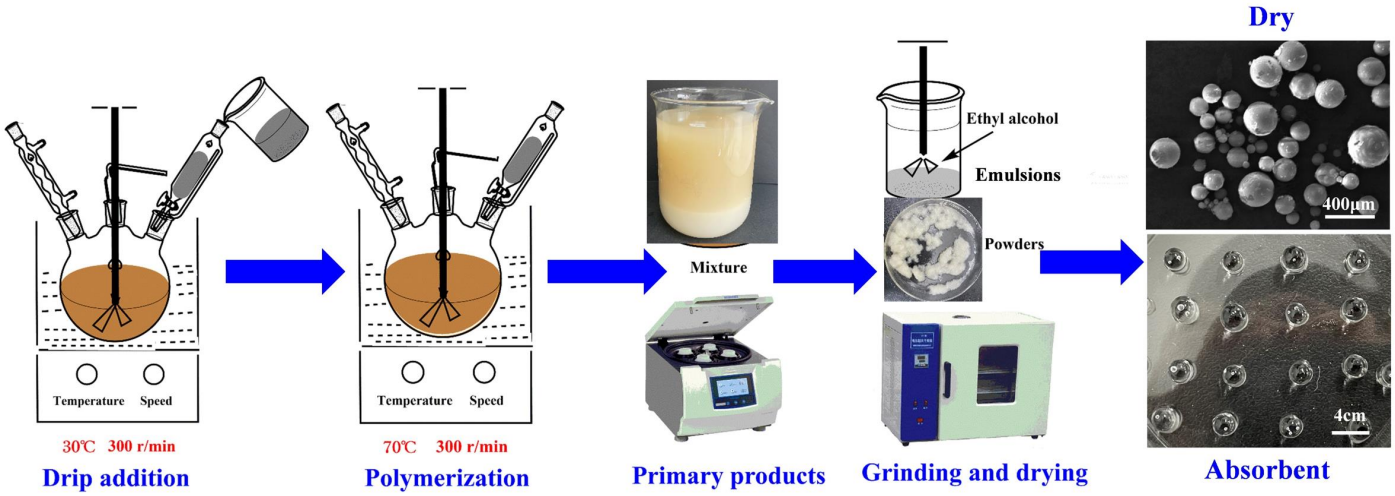

Bio-based SAP synthesis for concrete field

- We have established a characterization method that can quantitatively characterize the sphericity of particles, which is beneficial for optimizing the synthesis process."

SAP	PAA	PAM	SSP	SSSP
Particle size /um	250 ~ 425	212 ~ 425	300 ~ 500	212 ~ 425
Sphericity (*s*)	0.49 ± 0.03	0.48 ± 0.04	0.51 ± 0.04	0.96 ± 0.02

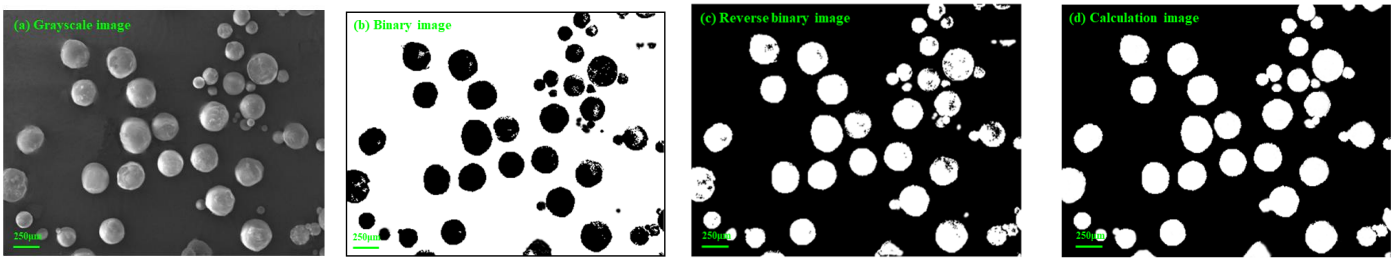

Image processing of SAP particles.

Bio-based SAP synthesis for concrete field

- The synthesis scheme was optimized based on the sphericity of the particles, and the optimal synthesis conditions were determined.
- The main factors affecting the water absorption of spherical starch-based SAP are the proportion of acrylamide, initiator, and cross-linker, with their optimal contents being 0.7, 1.2%, and 0.12% of the monomer mass, respectively.

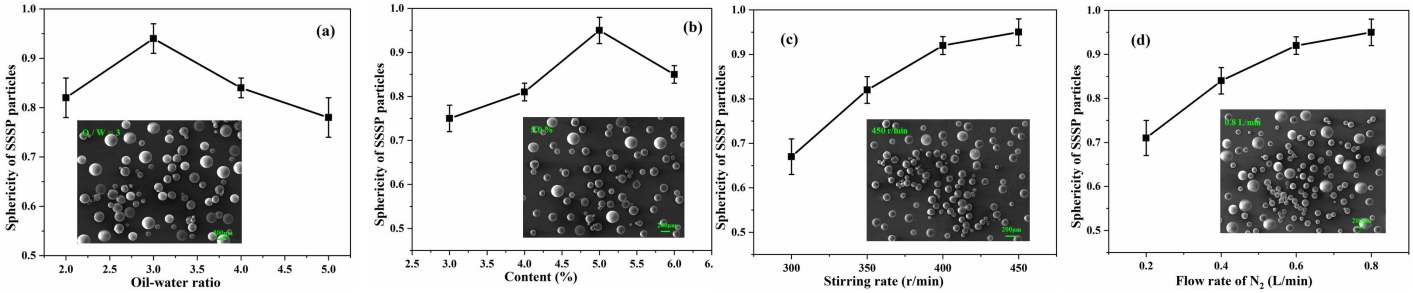

Influencing factors of sphericity (a) mass ratio of organic phase to aqueous phase (b) dispersing agent (c) stirring speed (d) N_2 flow rate.

Bio-based SAP synthesis for concrete field

- The performance of spherical starch-based SAP was improved by grafting with stronger hydrophilic -SO_3H and non-ionic -$CONH_2$ groups onto starch, with AMPS being more readily involved in graft copolymerization.

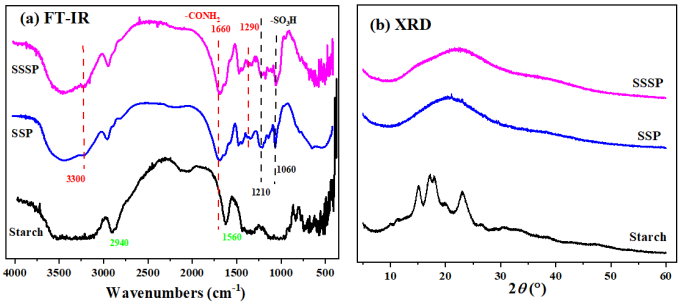

FT-IR XRD

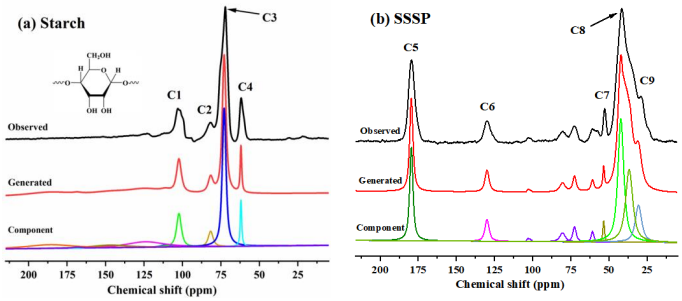

SSNMR

Bio-based SAP synthesis for concrete field

- The surface of spherical starch-based SAP particles is smooth, with a uniform size distribution. The absorbent particles of spherical starch-based SAP are spherical gels, capable of forming gel membranes and pores, which facilitate water entry into the network structure.

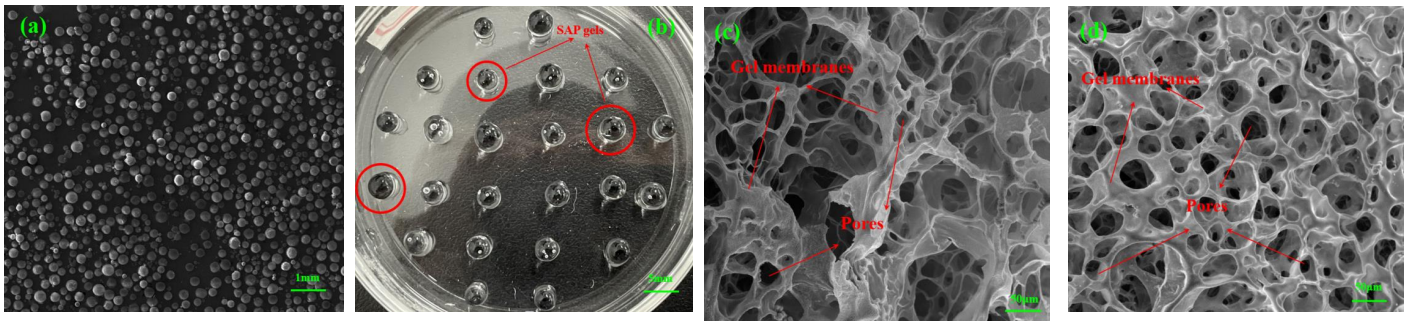

Morphology of spherical starch-based SAP (a) dry particles (b) absorbent particles (c)(d) microstructure of gels in deionized water and cement slurry filtrate.

Bio-based SAP synthesis for concrete field

- The water absorption, water storage, and salt (alkaline) resistance of starch-based SAP are higher than those of petroleum-based SAP.
- The spherical starch-based SAP exhibits a longer water desorption time.

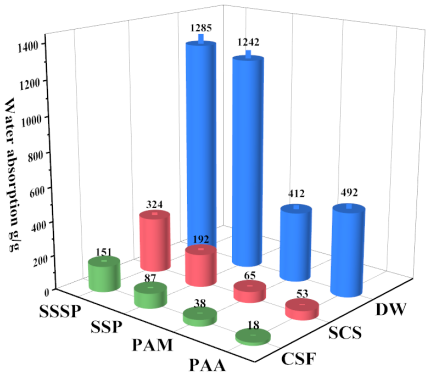

Water absorption of SAPs

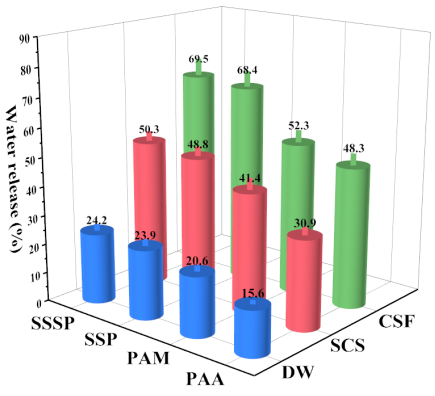

Water storage of SAP gels.

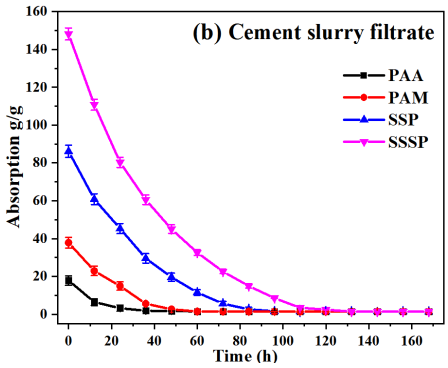

Desorption progress of SAP gels

Bio-based SAP synthesis for concrete field

☐ **Compared to traditional SAPs, the spherical starch-based SAP significantly reduces autogenous shrinkage, has minimal impact on compressive strength, and the voids left after desorption are spherical.**

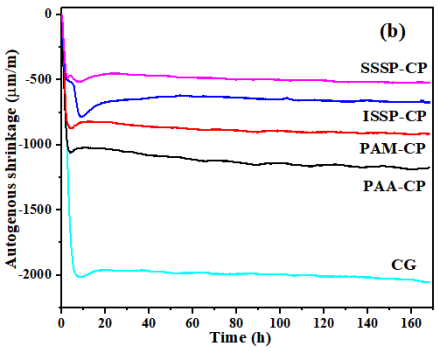

Autogenous shrinkage

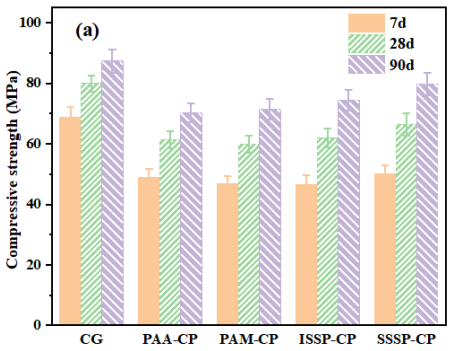

Compressive strength

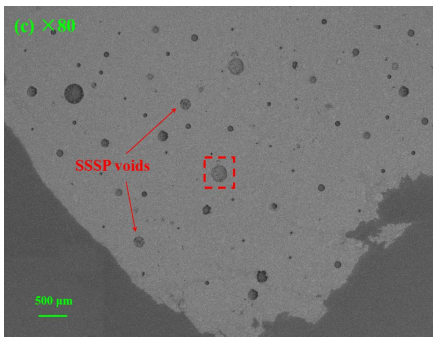

Voids left by the water desorption of spherical starch-based SAP.

Summary

☐ **Effect of SAP on compressive strength of concrete**

The addition of SAP and entrained water can either improve or impair the compressive strength of concrete. The impact of SAP and entrained water on compressive strength is influenced by at least three key factors: **paste content**, **water-to-binder (w/b) ratio**, and **the ratio of entrained water to binder**.

☐ **Effect of SAP on the frost resistance of concrete**

SAP has the ability to significantly **improve the frost resistance of concrete**. The effect of **large particle size SAP** is most pronounced when the total water-cement ratio is consistent. Conversely, the effect of **small particle size SAP** is most pronounced when the base water-cement ratio or air content is consistent. Additionally, due to its **superior void-forming ability**, AM demonstrates a more significant improvement in the frost resistance of concrete compared to AA.

Summary

☐ Effect of SAP on self-healing properties of cement

AA has the ability to **obtain water from the external environment**. When the relative humidity is 97%, sodium polyacrylate and polyacrylic acid acrylamide copolymer can absorb 233.2% and 210.5% of water vapor, respectively. **With the increase of relative humidity, the hygroscopic capacity of SAP increased gradually.** Sodium polyacrylate and polyacrylic acid acrylamide copolymer can increase the hydration degree of cement by 53.58% and 20.13%, respectively. With the **increase of AA particle size and content**, the **crack closure rate** and the **recovery rate of relative coefficient of gas permeability** gradually increase

☐ Bio-based SAP synthesis for concrete field

Two types of **starch-based SAP** were prepared using the **aqueous solution polymerization** and the **inverse suspension polymerization**. Compared to traditional SAP, the starch-based SAP prepared in this study have **higher water absorption** and **stronger salt resistance**, effectively mitigating the autogenous shrinkage of hardened cement paste while having a smaller impact on strength.

哈爾濱工業大學
HARBIN INSTITUTE OF TECHNOLOGY

Think you!

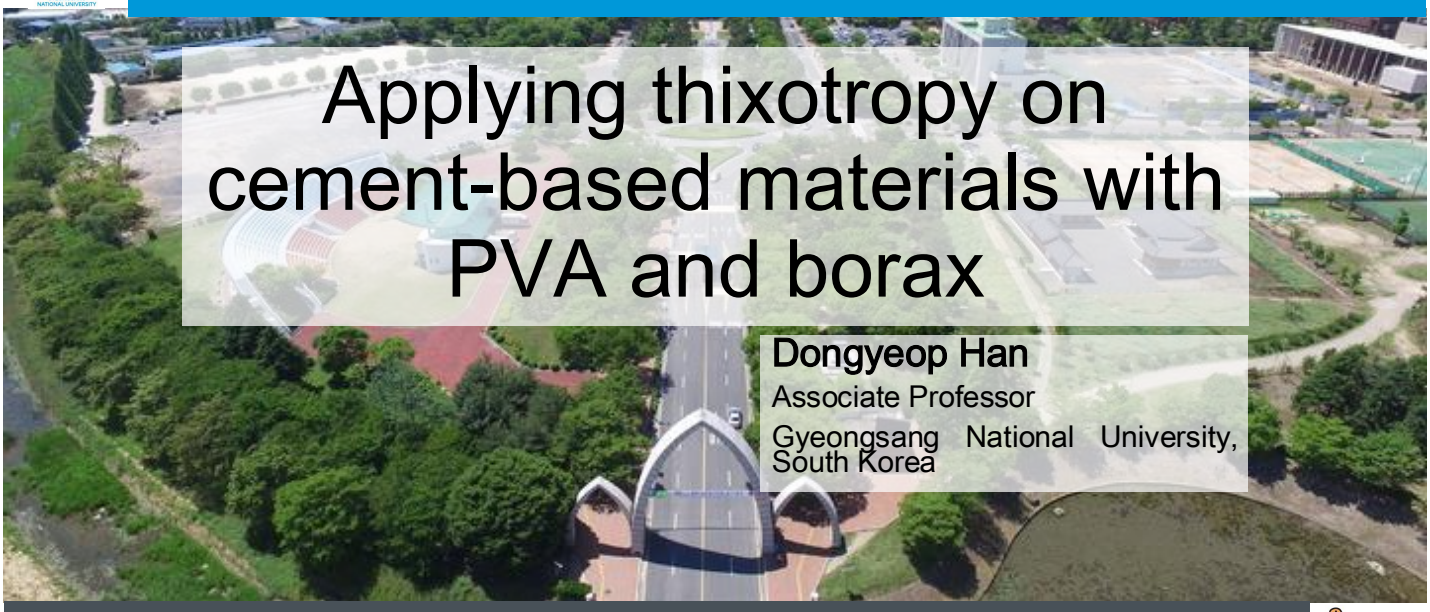

Applying thixotropy on cement-based materials with PVA and borax

Dongyeop Han
Associate Professor
Gyeongsang National University, South Korea

Introducing where I am

Introducing where I am

National flagship University of gyeongsannam-do

Gyeongsan National University

慶尙國立大學校

Background

Thixotropy

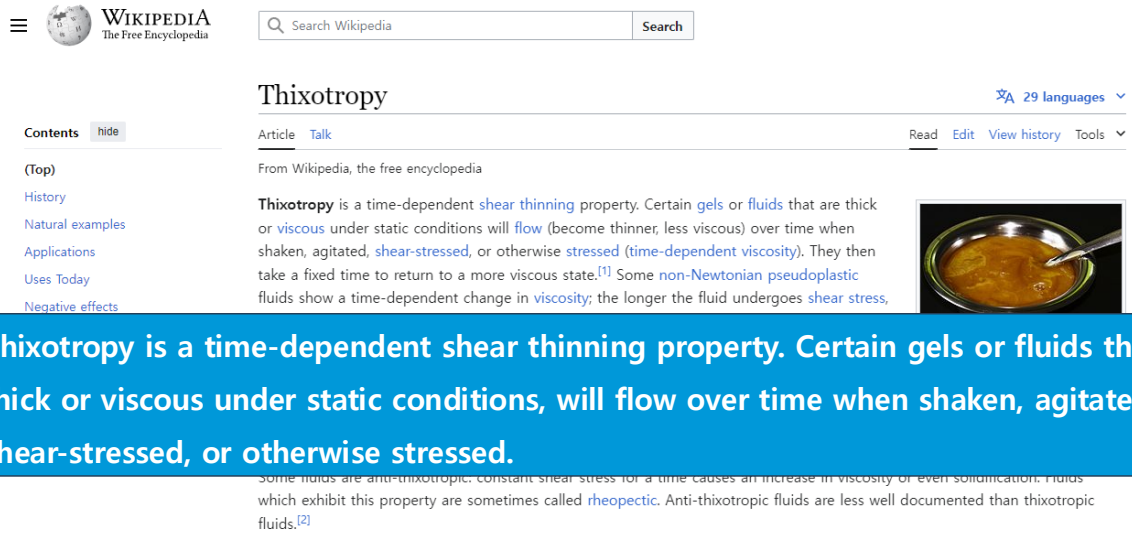

Thixotropy is a time-dependent shear thinning property. Certain gels or fluids that are thick or viscous under static conditions, will flow over time when shaken, agitated, shear-stressed, or otherwise stressed.

Background

Thixotropy

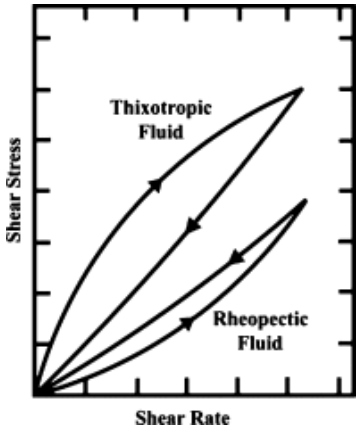

Background

Why does thixotropy occur (in cementitious materials)?

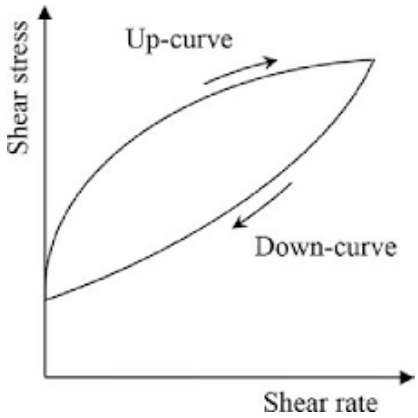

Up-curve with higher shear stress: breaking aggregation of particles

Down-curve with lower shear stress: already broken aggregated particles

Space between up-curve and down-curve: stress of breaking particles: **thixotropy**

Thixotropy: reversable aggregation of particles

Background

Two aggregations of cement particles

Reversible aggregation: colloidal forces

Irreversible aggregation: hydration

Background

Two aggregations of cement particles

Reversible aggregation: colloidal forces

Irreversible aggregation: hydration

BUT

Thixotropy of cement paste is too weak to be a beneficial property.

Construction Materials Research Lab

Background

Thixotropy and cement-based materials constructions

Flowing to settling

Background

Thixotropy and cement-based materials constructions

Background

Thixotropy and cement-based materials constructions

Background

Other methods of providing thixotropic behaviors

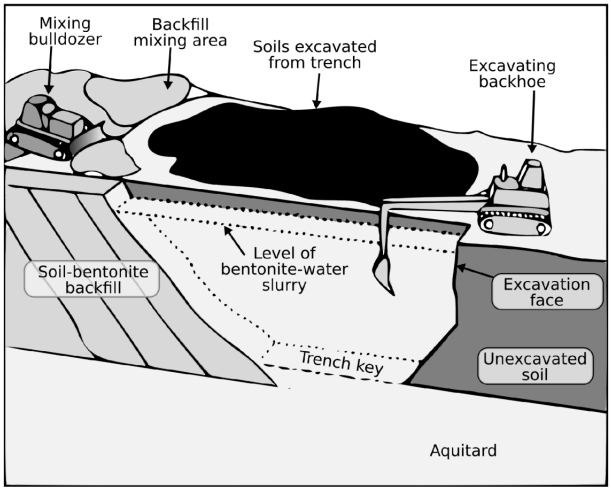

Bentonite slurry: the thixotropic nature allows to decrease in viscosity under shear stress, facilitating easy pumping and injection. When the shear stress is removed, the viscosity increases, providing solid support and sealing effects.

Background

Other methods of providing thixotropic behaviors

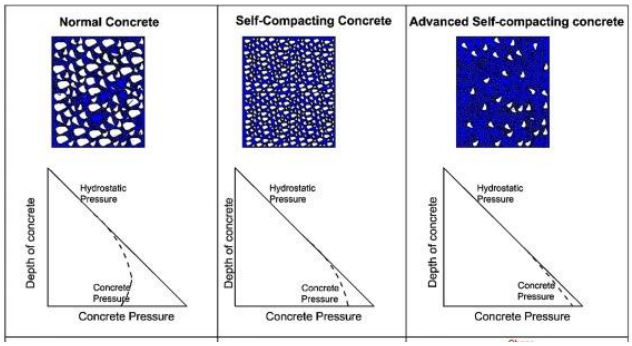

Pulverized clays (e.g. metakaolinite): Metakaolin-enhanced SCC exhibits significant thixotropic behavior, meaning it can undergo structural rebuilding after being disturbed by shear forces (such as during mixing or pouring). This ability helps in reducing the lateral pressure exerted on the formwork once the concrete is placed.

Research objective

Providing thixotropy on cement-based materials and reducing leaking materials through the formwork gap

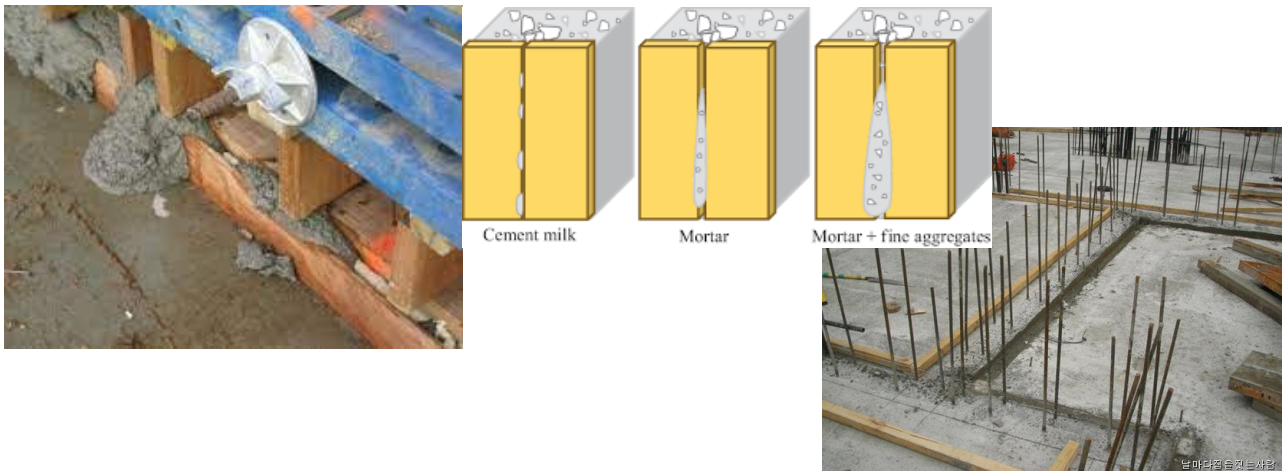

Research objective

Providing thixotropy on cement-based materials and reducing leaking materials through the formwork gap

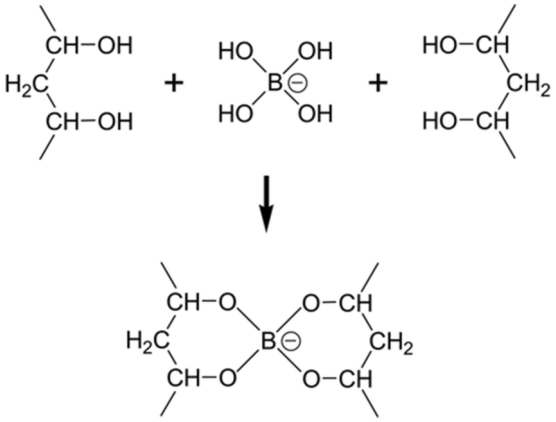

Research 1. Providing thixotropy

Table 1. Experimental plan

	Mixture conditions		Test
Phase 1	w/c	0.3, 0.4	·Table flow (with and without dropping) ·Flow curve (yield stress, and viscosity) ·Compressive strength (3, 7, and 28 days)
	Dosage of PVA solution (g)*	0, 10, 20, 30, 50, 100, 150, 180, 200	
	Dosage of Borax solution (g)**	0, 10, 20, 30, 50, 100, 150, 200, 250, 300	
Phase 2	w/c	0.3	·Table flow (with and without dropping) ·Flow curve (yield stress, viscosity, and thixotropy) ·Compressive strength (3, 7, and 28 days) ·Setting time (Vicat needle)
	Dosage of PVA solution and Borax solution ($_{\text{Mass cement}}$ %)***	0, 1, 2, 3, 4, 5	

* PVA solution was 4% and the dosage of Borax solution was fixed 200g for dosage of PVA solution assessment
** Borax solution was 4% and the dosage of Borax solution was fixed 100g for dosage of PVA solution assessment
*** For PVA solution and Borax solution, the dosages were 4%, and 5%, respectively.

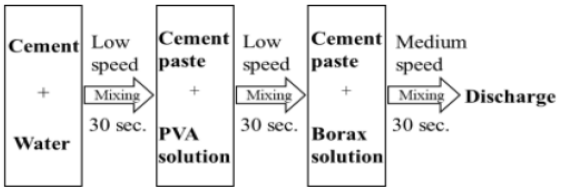

Figure 1. Mixing protocol for cement paste

Research 1. Providing thixotropy

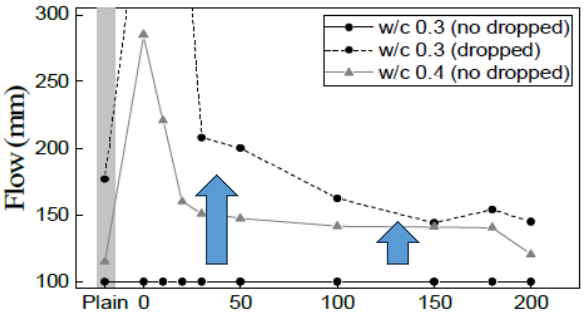

(a) Influence of PVA solution
(The borax solution was added 200g for every case.)

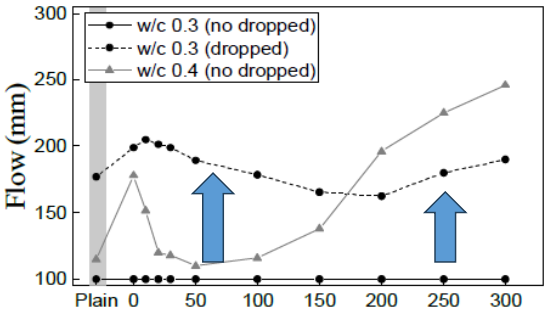

(b) Influence of borax solution
(The PVA solution was added 100g for every case.)

Increased flow with dropping the drop table

Construction Materials Research Lab

Research 1. Providing thixotropy

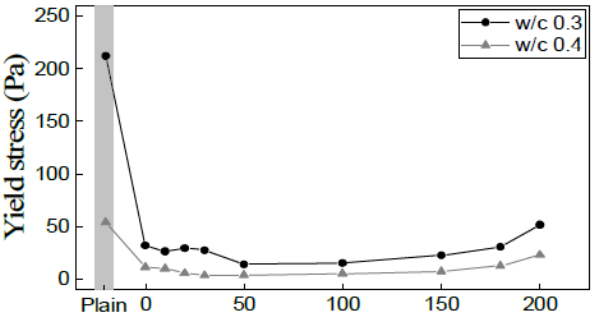

(a) Influence of PVA solution

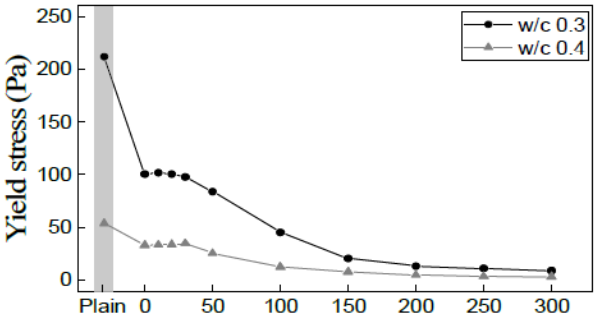

(b) Influence of borax solution

Yield stresses were measured low because the values were obtained by flow curve analysis with flowing status although the flow values without dropping were 100 ('0').

Construction Materials Research Lab

Research 1. Providing thixotropy

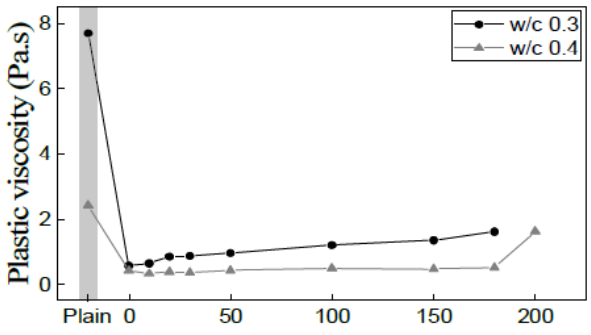

(a) Influence of PVA solution

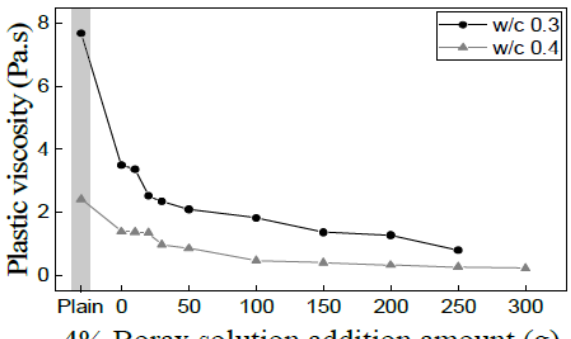

(b) Influence of borax solution

Viscosities were measured low because the values were obtained by flow curve analysis with flowing status

Research 1. Providing thixotropy

w/c: 0.3 cement paste

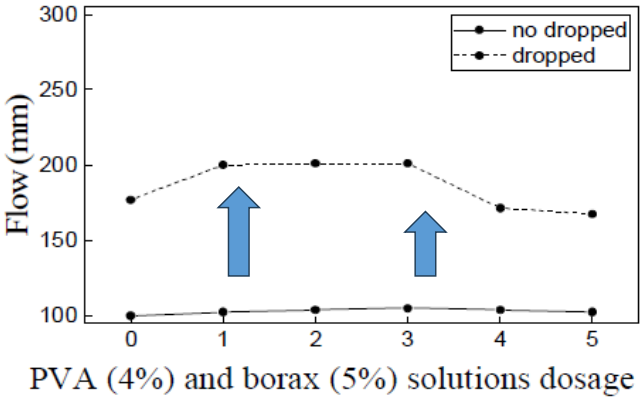

Increased flow with dropping the drop table

Research 1. Providing thixotropy

w/c: 0.3 cement paste

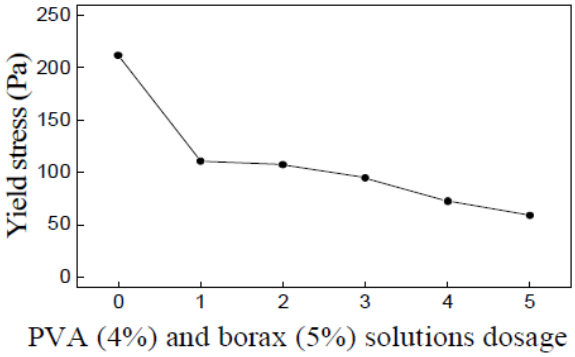

Figure 9. Influence of PVA and borax solutions on yield stress (by adding percentage)

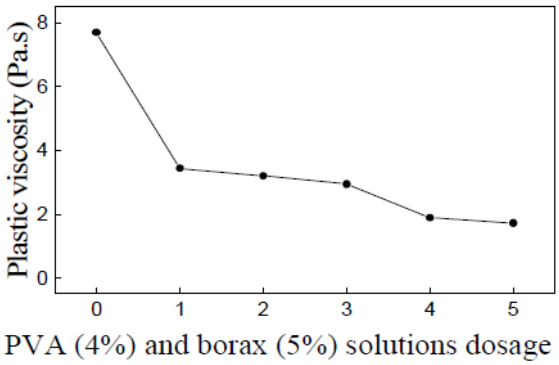

Figure 10. Influence of PVA and borax solutions on viscosity (by adding percentage)

Research 1. Providing thixotropy

w/c: 0.3 cement paste

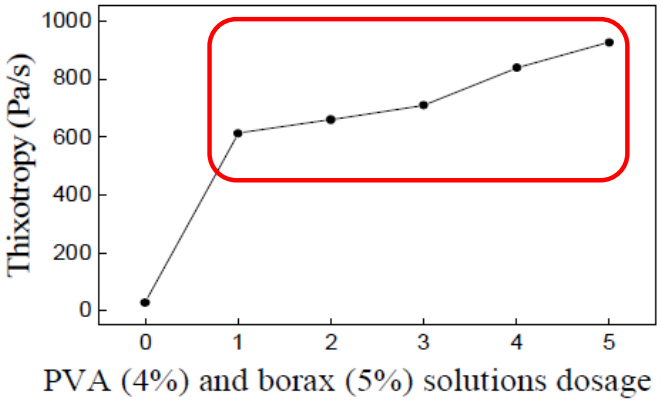

Figure 11. Influence of PVA and borax solutions on thixotropy (by adding percentage)

Research 1. Providing thixotropy

Conclusions

✓ PVA and borax can provide thixotropic properties into the cement paste (cement-based materials).

Research 2. Providing thixotropy on mortar and reducing leakage

Table 1. Experimental plan

	Mixture conditions			Test	
Phase 1		w/c*	0.35, 0.40 0.45		Same SP dosage
		Cement : Sand	1 : 1		
		Gap(mm)	3, 5, 7, 9		
	Superplasticizer	Type	General Superplasticizer	- Table flow(with and without dropping) - Thixotropy - Leaking weight and length - Compressive strength @ 28 days	
		Dosage(% cement mass)	0.3		
	PVA**	Type	suspension		
		Dosage(% cement mass)	0, 2, 4, 6, 8		
	Borax***	Type	suspension		
		Dosage(% of PVA mass)	50		
Phase 2		w/c*	0.35, 0.40, 0.45		Same fluidity
		Cement : Sand	1 : 1		
		Gap(mm)	3, 5, 7, 9		
	Superplasticizer	Type	General Superplasticizer	- Table flow(with and without dropping) - Thixotropy - Leaking weight and length	
		Dosage(% cement mass)	0.4, 0.55, 0.7 for each w/c case		
	PVA**	Type	suspension		
		Dosage(% cement mass)	0, 2, 4, 6, 8		
	Borax***	Type	suspension		
		Dosage(% of PVA mass)	50		

* Water-to-cement ratio
** 7% PVA suspension
*** 5% Borax suspension

Research 2. Providing thixotropy on mortar and reducing leakage

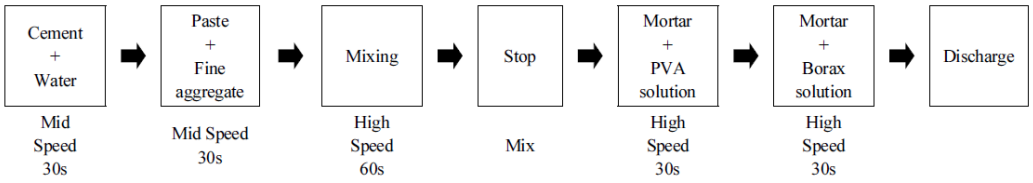

Figure 2. Mortar mixing protocol

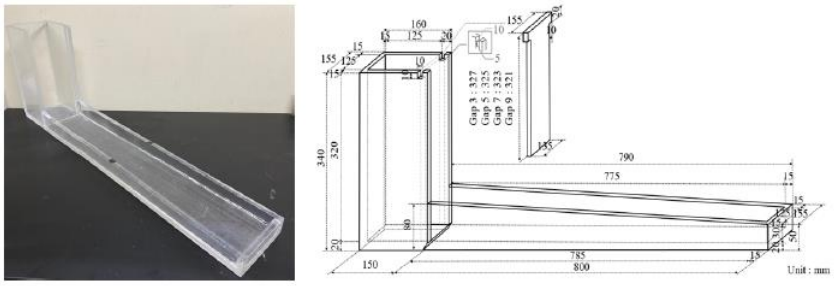

Figure 4. Formwork Leakage test set-up

Research 2. Providing thixotropy on mortar and reducing leakage

Same SP dosage

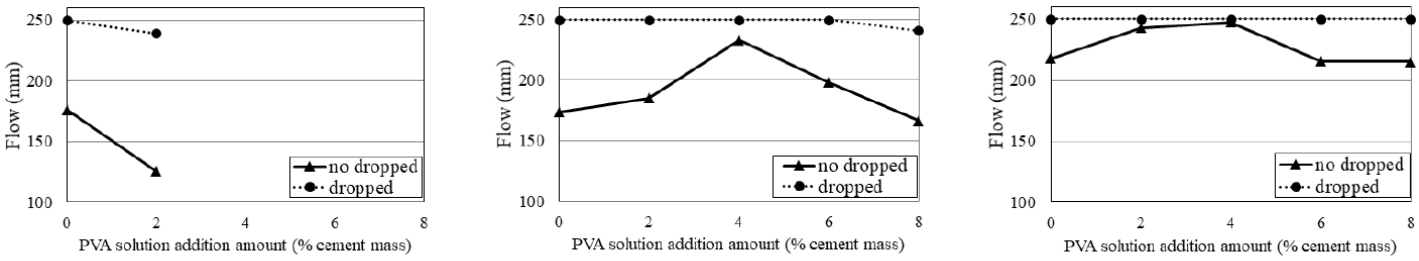

(a) w/c 0.35 (b) w/c 0.40 (c) w/c 0.45

couldn't be mixed at w/c 0.35 with higher than 4% PVA

Research 2. Providing thixotropy on mortar and reducing leakage

Same SP dosage

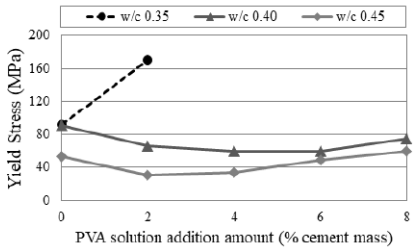

Figure 6. Influence of PVA and Borax solution on Yield stress depending on water-to-cement ratio

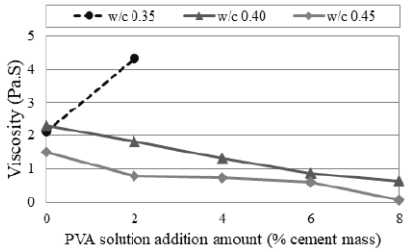

Figure 7. Influence of PVA and Borax solution on Viscosity depending on water-to-cement ratio

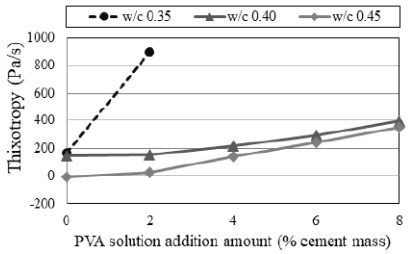

Figure 8. Influence of PVA and Borax solution on Thixotropy depending on water-to-cement ratio

couldn't be mixed at w/c 0.35 with higher than 4% PVA

Research 2. Providing thixotropy on mortar and reducing leakage

Same SP dosage

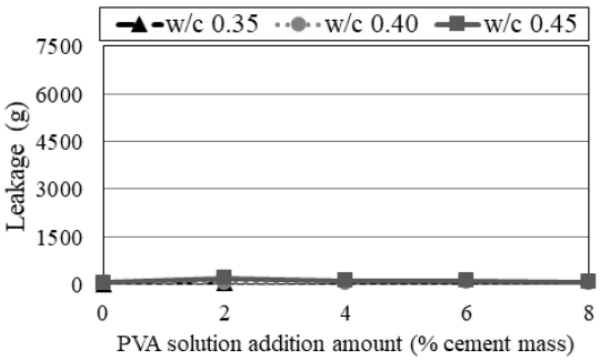

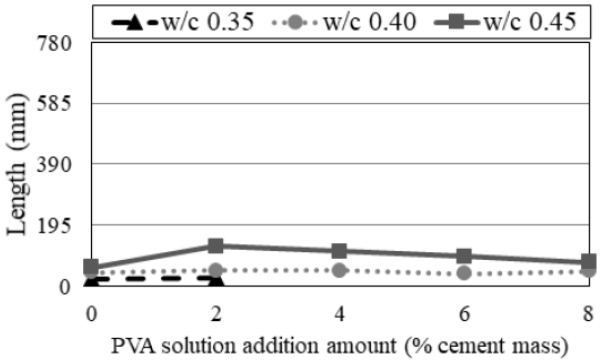

(a) 3mm

Construction Materials Research Lab

Research 2. Providing thixotropy on mortar and reducing leakage

Same SP dosage

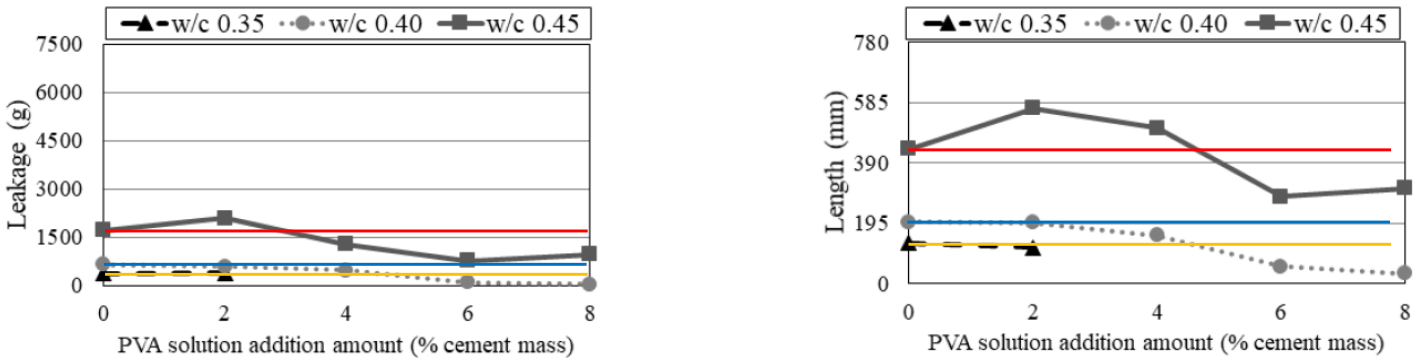

(b) 5mm

Research 2. Providing thixotropy on mortar and reducing leakage

Same SP dosage

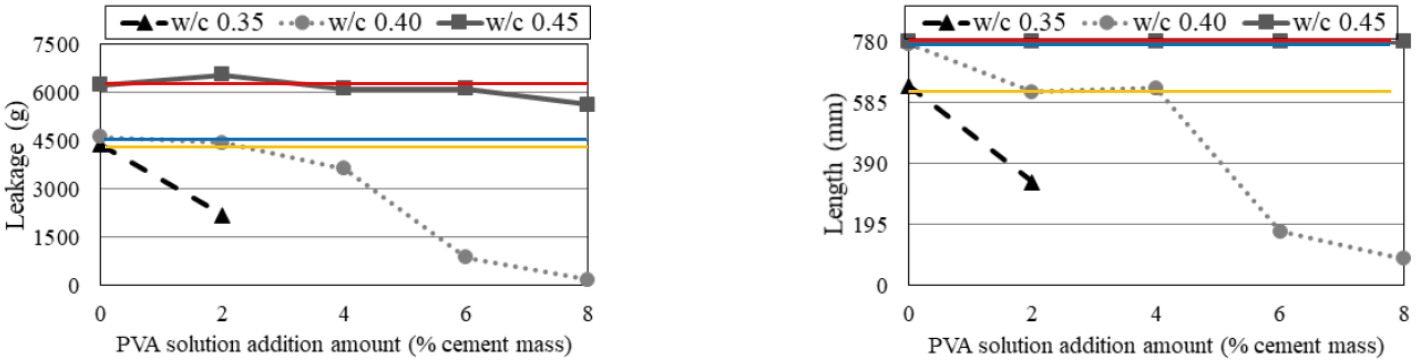

(c) 7mm

Research 2. Providing thixotropy on mortar and reducing leakage

Same SP dosage

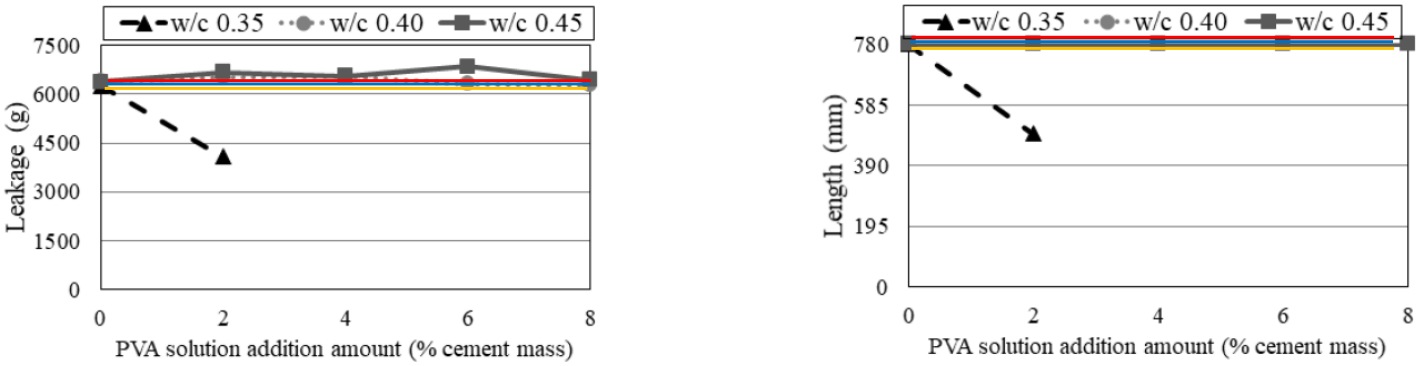

(d) 9mm

Research 2. Providing thixotropy on mortar and reducing leakage

Same fluidity

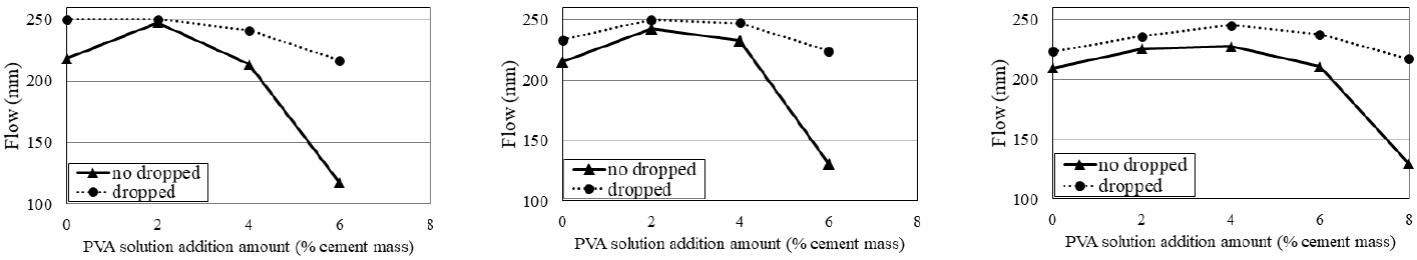

(a) w/c 0.35 (b) w/c 0.40 (c) w/c 0.45

Research 2. Providing thixotropy on mortar and reducing leakage

Same fluidity

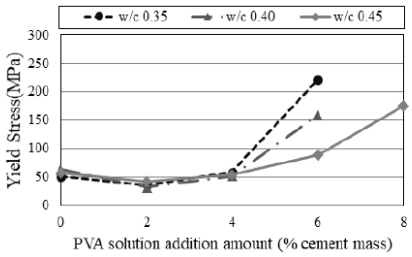

Figure 12. Influence of PVA and Borax solution on Yield stress depending on water-to-cement ratio

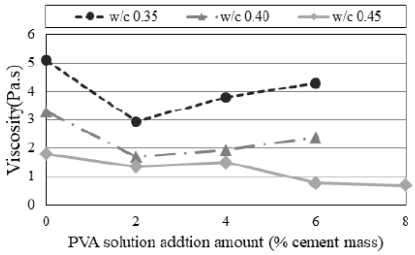

Figure 13. Influence of PVA and Borax solution on Viscosity depending on water-to-cement ratio

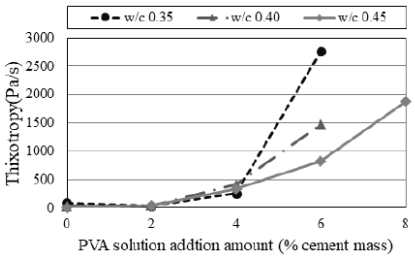

Figure 14. Influence of PVA and Borax solution on Thixotropy depending on water-to-cement ratio

Research 2. Providing thixotropy on mortar and reducing leakage

Same fluidity

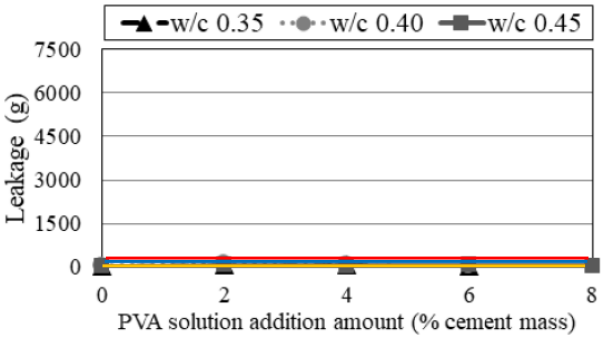

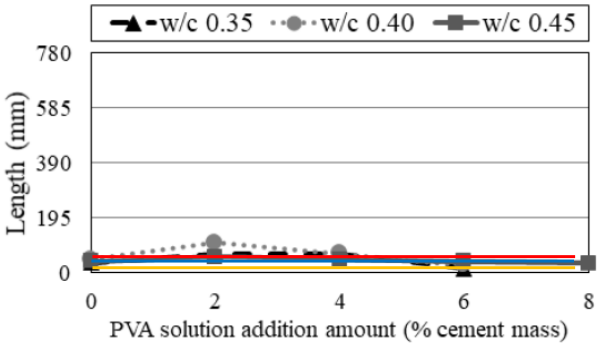

(a) 3mm

Construction Materials Research Lab

Research 2. Providing thixotropy on mortar and reducing leakage

Same fluidity

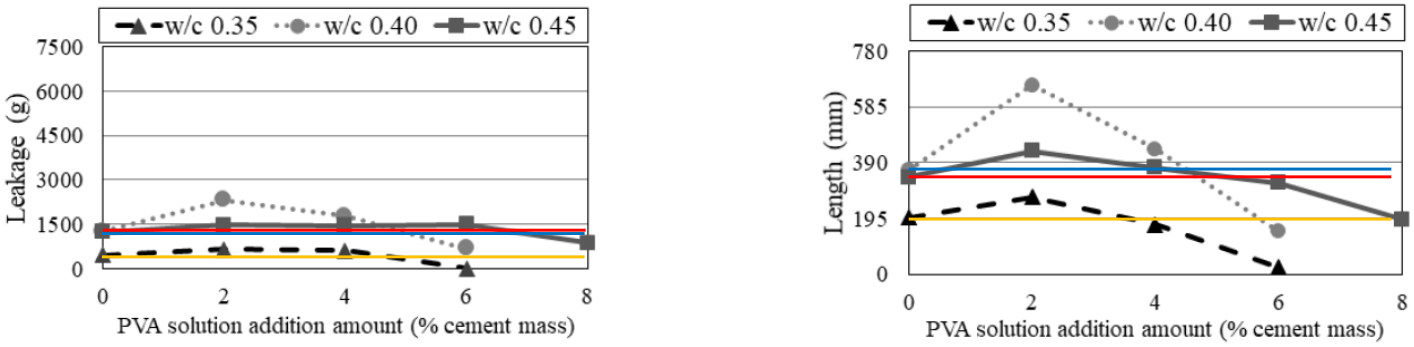

(b) 5mm

Research 2. Providing thixotropy on mortar and reducing leakage

Same fluidity

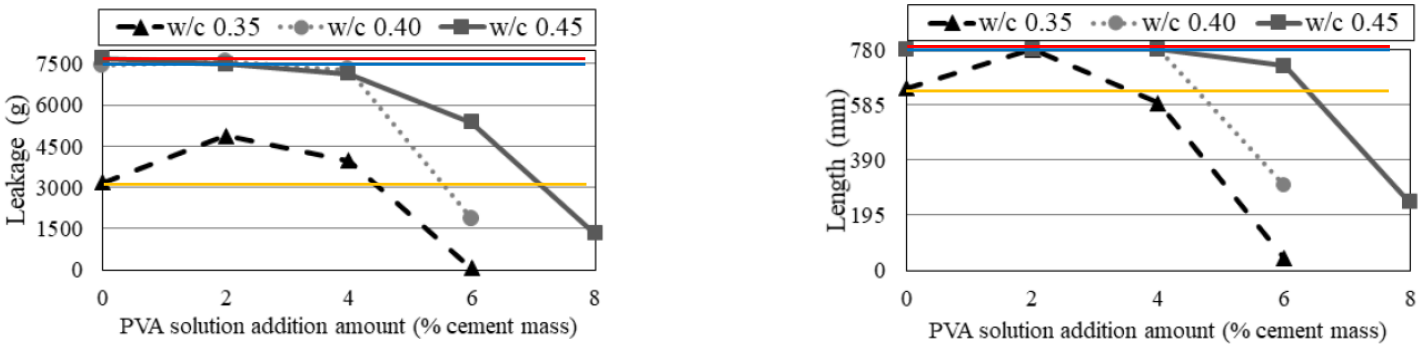

(c) 7mm

Construction Materials Research Lab

Research 2. Providing thixotropy on mortar and reducing leakage

Same fluidity

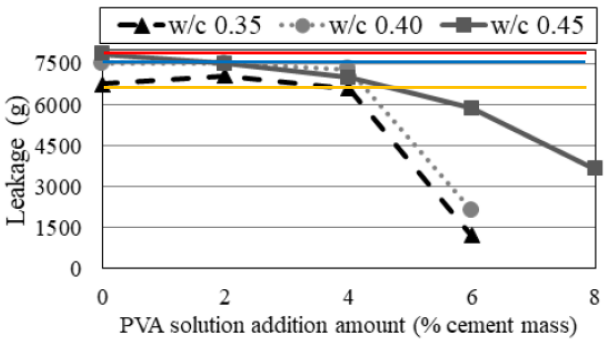

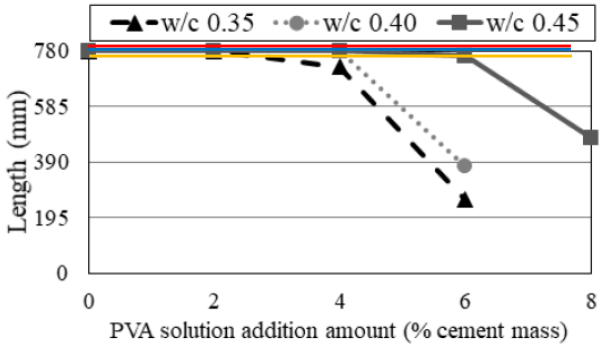

(d) 9mm

Research 2. Providing thixotropy on mortar and reducing leakage

Conclusions

- ✓ PVA and borax can provide thixotropic properties into the mortar.
- ✓ Thixotropy provided by PVA and borax can reduce the leakage of cement-based materials.

Construction Materials Research Lab

Research 3. Providing thixotropy on concrete and reducing leakage

Table 1. Experimental framework

Mixture conditions			Test
W/C*		0.55	
Unit water content (kg/m^3)		Fixed 185, Variable 185****	**Adding PVA and borax** **Replacing PVA and borax**
S/a		0.45	
SP**	Type	Polycarboxylate	- Slump and Slump flow - EIS(using data from slump and slump flow) - Rheology(yield stress, plastic viscosity, thixotropy) - Setting time(vicat needle) - Leakage weight and length(before and after compaction)
	Dosage (% cement mass)	0.5	
PVA***	Type	Diluted solution(6.53 %)	
	Dosage (% cement mass)	0, 3, 4, 5, 6, 7	
Borax	Type	Diluted solution(5 %)	
	Dosage (% PVA mass)	50	

*Water-to-cement ratio
**Super plasticizer
***Polyvinyl alcohol
****Subtract water mass of the PVA and borax solutions from unit water content to keep the same unit water content

Research 3. Providing thixotropy on concrete and reducing leakage

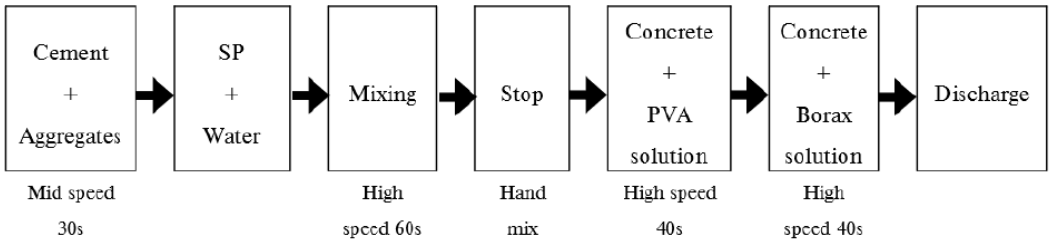

Figure 1. Concrete mixing procedure

Construction Materials Research Lab

Research 3. Providing thixotropy on concrete and reducing leakage

Table 4. Mixture proportions of high fluidity concrete for thixotropy

No.	Application of PVA and borax		Unit weight(kg/m^3)						
			W	OPC	S	G	PVA	Borax	SP
1	Plain(No PVA and borax)		185	336	770	868	0	0	17
2	AD	3%	185	336	770	868	10	5	17
3		4%	185	336	770	868	13	7	17
4		5%	185	336	770	868	17	8	17
5		6%	185	336	770	868	20	10	17
6		7%	185	336	770	868	24	12	17
7	RP	3%	171	336	770	868	10	5	17
8		4%	166	336	770	868	13	7	17
9		5%	161	336	770	868	17	8	17
10		6%	156	336	770	868	20	10	17
11		7%	152	336	770	868	24	12	17

Research 3. Providing thixotropy on concrete and reducing leakage

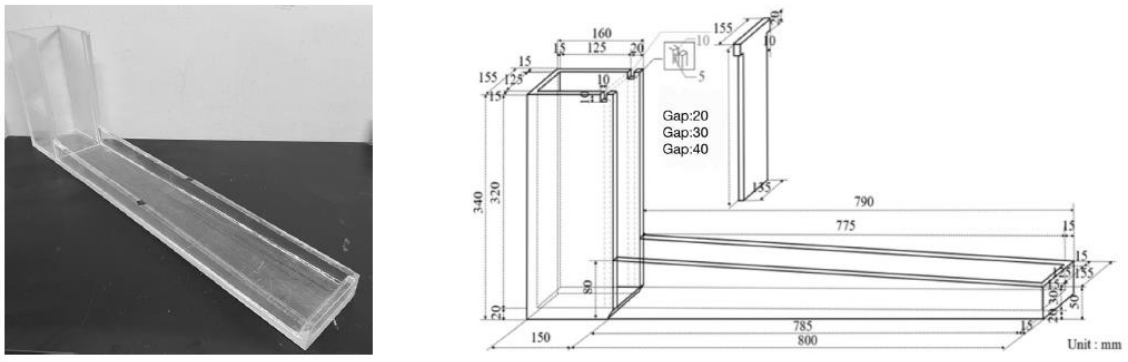

Figure 4. Formwork seepage test set-up

Construction Materials Research Lab

Research 3. Providing thixotropy on concrete and reducing leakage

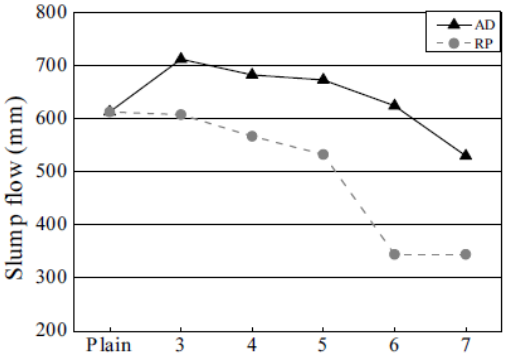

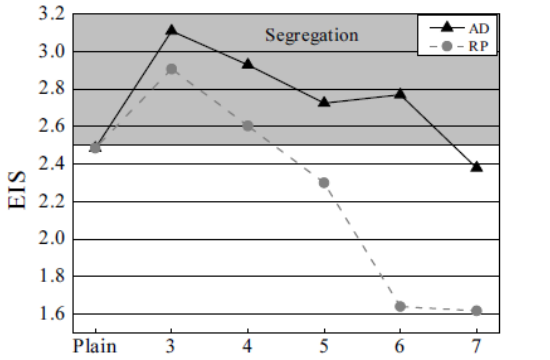

Adding PVA and borax solutions can cause segregation of concrete mixtures.

Research 3. Providing thixotropy on concrete and reducing leakage

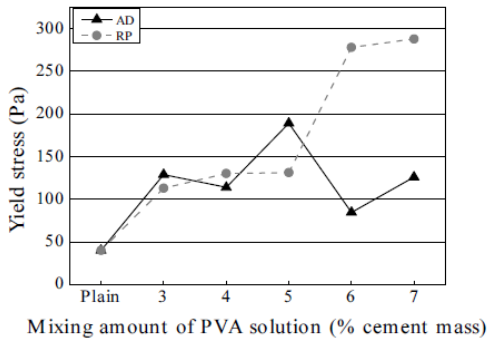

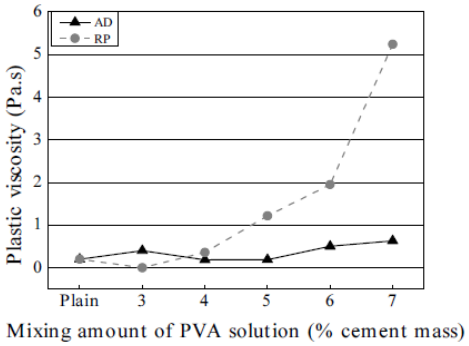

Construction Materials Research Lab

Research 3. Providing thixotropy on concrete and reducing leakage

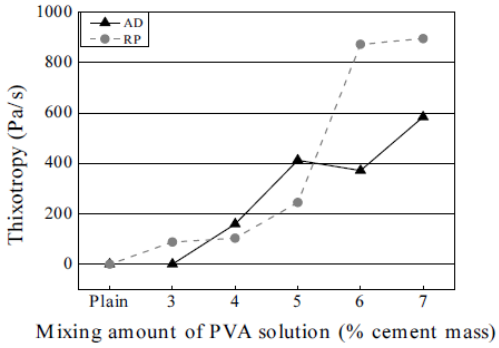

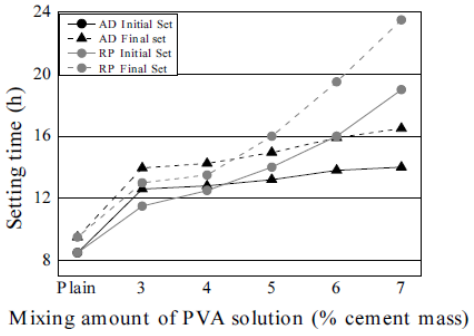

Research 3. Providing thixotropy on concrete and reducing leakage

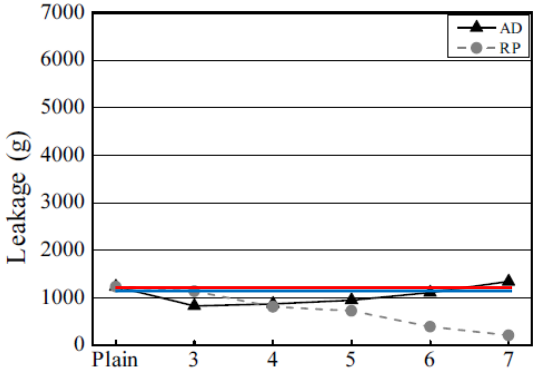

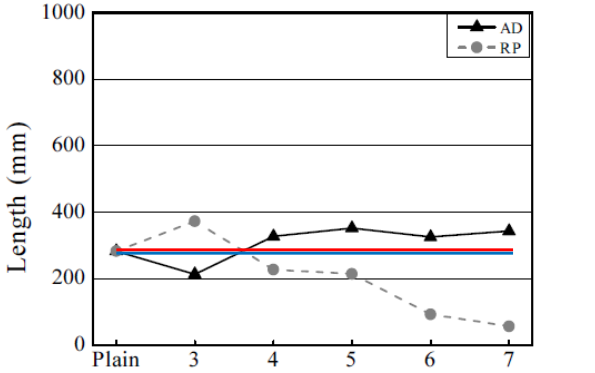

(a) Gap 20mm

Construction Materials Research Lab

Research 3. Providing thixotropy on concrete and reducing leakage

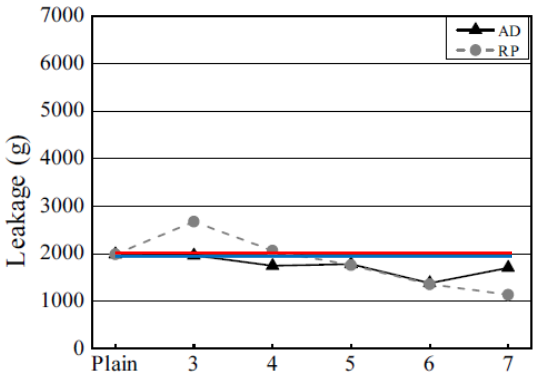

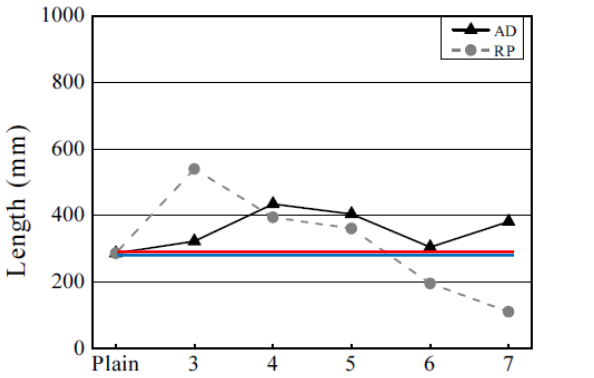

(b) Gap 30mm

Research 3. Providing thixotropy on concrete and reducing leakage

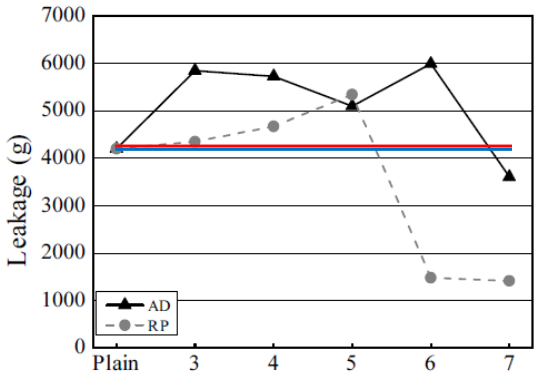

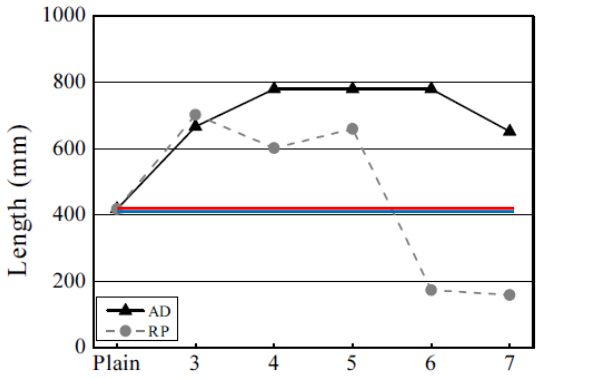

(c) Gap 40mm

Construction Materials Research Lab

Research 3. Providing thixotropy on concrete and reducing leakage

Conclusions

- ✓ PVA and borax can provide thixotropic properties into the concrete and reduce the leakage of cement-based materials.
- ✓ When PVA and borax were replaced, thixotropy and leakage reducing performances were enhanced rather than they were added.
- ✓ The suggestable dosage of PVA for reducing mixtures leakage, 6% of PVA solution (with 50 % borax solution to PVA solution) replacement.
- ✓ Because of borax, setting time of the mixtures is delayed.

Research 4. Solving the delaying setting time of high thixotropic mixtures with borax

Research 4. Solving the delaying setting time of high thixotropic mixtures with borax

Reason of delayed setting time

Cement and Concrete Research 84 (2016) 62–75

Contents lists available at ScienceDirect

Cement and Concrete Research

journal homepage: www.elsevier.com/locate/cemconres

Effect of retarders on the early hydration of calcium-sulpho-aluminate (CSA) type cements

Maciej Zajac, Jan Skocek, Frank Bullerj

Heidelberg Technology Center GmbH, Rohrbacher Str. 95, 69181 Le

ARTICLE INFO

Article history:
Received 5 December 2014
Accepted 25 February 2016
Available online 29 March 2016

Keywords:
Sulphoaluminate (D)
Pore solution (B)
Retardation (A)
SEM (B)
X-ray diffraction (B)

ABSTRACT

The retardation of calcium-sulpho-aluminate (CSA) type cements by three common retarders—sodium gluconate, sodium–potassium tartrate and borax is investigated at a 2% addition rate. Each of the retarders has a different effect on the early-age hydrate assemblage, as shown by quantitative X-ray diffraction, thermogravimetric analysis, scanning electron microscopy and pore solution analysis. Regardless of the retarder used, the hydration starts with mainly the dissolution of ready soluble (calcium) alkali sulphates and ye'elimite, followed by the formation of ettringite and aluminium hydroxide, whereby the specific clinker mineral dissolution as well as ettringite-forming reaction is delayed in different ways depending on the retarder used. The results showed that the retardation is mainly caused by preventing hydrates formation in the case of tartrate and gluconate. Contrary, borax retards the hydration by preventing to a certain extent the dissolution of ye'elimite and lowers the initial pH. Furthermore, the morphology of ettringite is altered depending on the type of the retarder used.

Research 4. Solving the delaying setting time of high thixotropic mixtures with borax

Strategy for compensating delayed setting time caused by borax

Reason: decreased pH → **Increase pH by adding alkali solution**

Phenomenon: delayed setting time → **adding accelerator**

Construction Materials Research Lab

Research 4. Solving the delaying setting time of high thixotropic mixtures with borax

Conclusions

- ✓ PVA and borax can provide thixotropic property on the cement-based materials such as cement paste, mortar, and concrete.
- ✓ Thanks to the thixotropic properties, the leakage of cement-based materials caused by gap of formwork can be decreased.
- ✓ Because of borax, setting time of the mixtures is delayed. To compensate the delaying of setting time, alkali solutions and accelerator were used, but the results were not satisfied so far.


Q&A

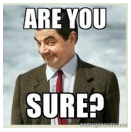
ARE YOU
SURE?

Part1 :

Materials

NUMERICAL ANALYSIS FOR THE PREDICTION OF ADHESION CHLORIDE IN REINFORCED CONCRETE STRUCTURES CONSIDERING RAIN EXPOSURE

Souta TOYODA
Technical Staff, University of the Ryukyus, Okinawa, Japan

Kohei SAKIHARA
Associate Professor, Faculty of Engineering, University of the Ryukyus, Okinawa, Japan

Takumi KASAHARA
General Manager, Quality Assurance Dept., Prometech Software, Inc., Tokyo, Japan

Satoshi TAKADA
Simulation Technology Dept., Prometech Software, Inc., Tokyo, Japan

ABSTRACT:
This study aims to quantitatively assess the adherence of chloride to pillar members considering rainfall. First, airborne chloride concentrations were measured on each pillar of a reinforced concrete structure located in a coastal region. Additionally, rain exposure tests were conducted using water-sensitive paper. Analysis of the diffusion and adhesion of airborne chloride particles was performed, considering the rainfall, wind conditions, and topography surrounding the reinforced concrete structures. A model for the chloride adherence on each pillar surface, factoring in rainfall, was developed. The outcomes of these analyses were compared and discussed in relation to the results from the exposure tests. The analytical results generally reflect the trends observed in the exposure test results. It was also found that the analysis was more stable when the minimum grid spacing of the wind velocity field was reduced.
Keywords: Chloride attack, Airborne chlorine, Thin mortar specimen. Water-sensitive paper, Numerical analysis, Lattice Boltzmann method, Moving Particle Semi-implicit method, Rain exposure

1. INTRODUCTION

In coastal regions, airborne chloride-induced salt damage is a primary factor in the deterioration of reinforced concrete structures. This is particularly true in Okinawa Prefecture, where many structures feature pilotis, raising concerns regarding diminished durability due to chloride attack on the concrete pillars. The amount of airborne chloride adhering to each structural component varies with weather conditions, surrounding topography, and structural geometry. The Standard Specification and Commentary for Building Works JASS 5 Reinforced Concrete Construction 2022 [1], updated in November 2022, defines deterioration environment categories for each component. Given these considerations, the need for detailed and quantitative assessment of external environmental forces and degradation rates for each component is anticipated to grow.

Building on previous research, the authors measured airborne chloride deposition on the surface of various structural components using thin mortar specimens in the coastal areas of Okinawa Prefecture, employing the random walk method [2] to predict deposition rates [3][4]. However, these measurements did not correlate appropriately with exposure test results, possibly due to the variable washing-out effects of rainfall on different components.

This study involved measuring airborne chloride using these specimens and conducting rain exposure tests with water-sensitive paper on pillars in coastal structures. Numerical analyses were performed to examine chloride diffusion and deposition, considering the structure's geometry and surrounding topography. These analyses aimed to model chloride deposition on each pillar surface and to compare and discuss the results with those of the exposure tests. Additionally, the study explored the impact of the analytical model, the grid spacing of the wind velocity field, and the density of airborne chloride particles around the structure on the chloride deposition on pillars.

2. EXPOSURE TEST

2.1 EXPOSURE TEST OVERVIEW

In this study, measurements were conducted using a specimen (see Fig. 2) for a structure situated along the coast of the East China Sea in Benoki, Kunigami Village, northern mainland Okinawa Prefecture, as illustrated in Fig. 1. The specimens were composed of ordinary Portland cement and standard sand used for cement strength tests as the fine aggregate, with a water/cement ratio of 60%. The dimensions of the specimens were 40 × 40 × 10 mm, and they were covered with aluminum tape on all sides except for the exposed surface. The location of the specimen and the

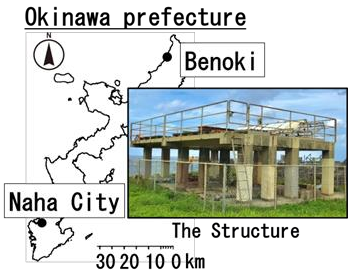

Fig. 1 Location of the structure

Fig. 2 Thin mortar specimen

Table 1 Exposure test period

Period	Detail
1st period	2021.10-2021.12
2nd period	2022.1-2022.3
3rd period	2022.10-1022.12
4th period	2023.1-2023.3

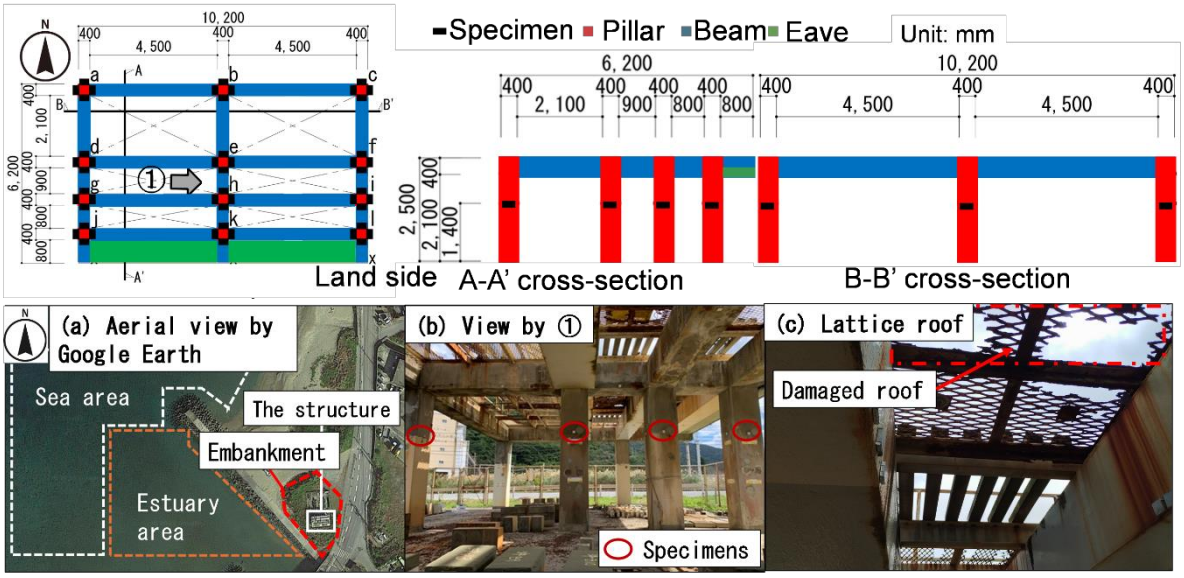

Fig. 3 Plan of the structure and surrounding environment

structure's surrounding environment are depicted in Fig. 3, which indicates a sea area to the north-west and an estuarine area extending from the south-west to the south. Additionally, the structure is surrounded by approximately 2 m of fill. The exposure periods, spanning four seasons from winter to spring, are detailed in Table 1. The upper part of the structure features a steel lattice roof, partially missing due to corrosion, as shown in Fig. 3(c).

2.2 WIND CONDITIONS IN EXPOSURE TESTS

During the exposure tests with the specimens, wind conditions were systematically recorded and are presented in Fig. 4. The average wind speed was calculated by averaging the wind speeds measured every 15 min for each wind direction. The wind direction ratio was determined by classifying the wind directions, recorded every 15 min, into 16 categories and subsequently dividing the number of measurements in each category by the total number of data points.

The analysis of average wind speeds reveals that the north-west and north-north-west directions predominated, as shown in Fig. 4(a). This pattern is likely influenced by the monsoon during the winter and spring seasons. Regarding the wind direction ratio, the north-northwest and southeast directions were notably significant (Fig. 4(b)). These findings suggest that

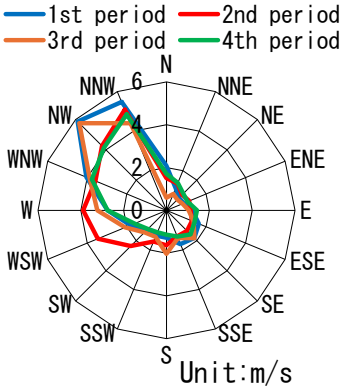

(a) Wind speed

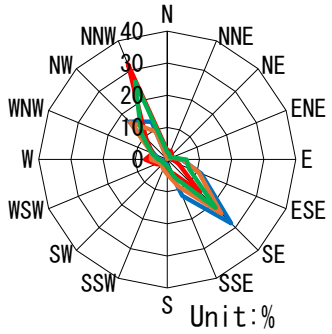

(b)Wind direction

Fig. 4 Wind condition

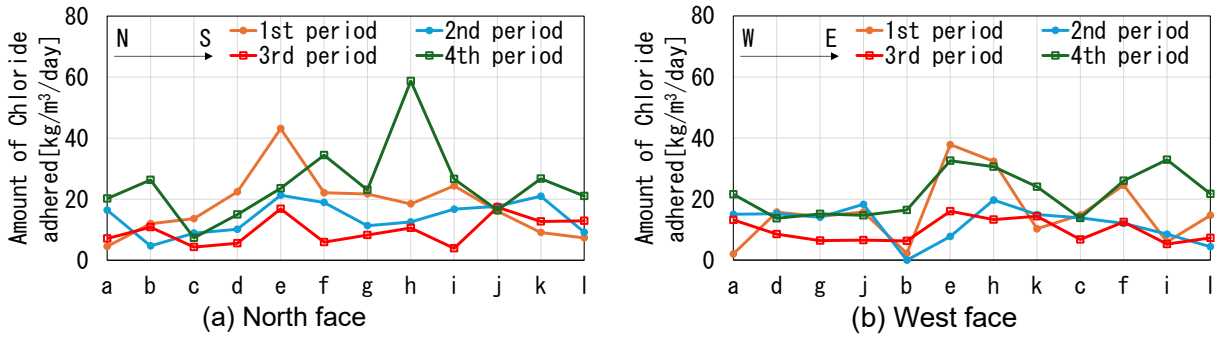

(a) North face (b) West face

Fig. 5 Chloride deposition of pillar

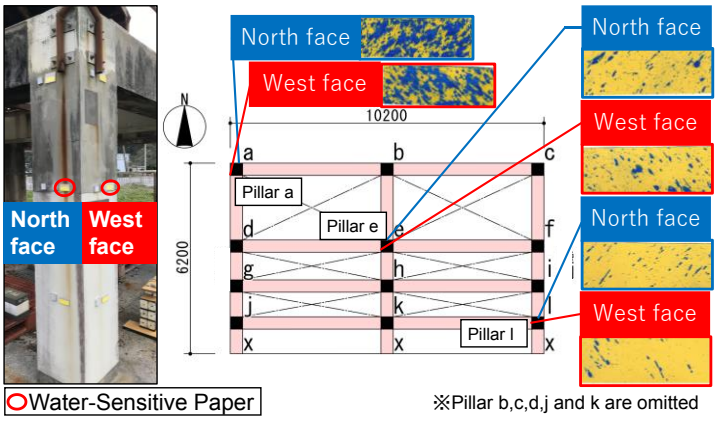

Fig. 6 Some results of water-sensitive paper tests

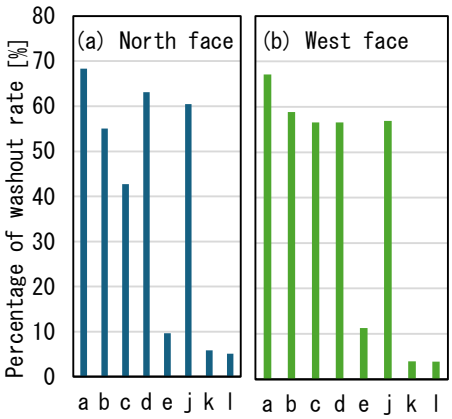

Fig. 7 Percentage of washout rate

during the study's exposure period, the dominant wind direction was north-west, characterized by the highest wind speed and wind direction ratio, facilitating significant transport of airborne chloride from the sea area located to the north-west of the structure. However, the substantial southeast wind directional fraction also indicates the presence of sea salt particles in the coastal zone, highlighting the significant influence of southeast winds on the transport of airborne chloride.

2.3 EXPOSURE TEST RESULTS

In this study, specimens were affixed to four orientations of pillars and exposure tests were conducted. The sea area extends to the northwest of the structure, and airborne chloride adhered to the structure originates from and is transported by the sea area. Therefore, more airborne chloride is expected to adhere to the north and west faces of the structure's pillars than to the south and east faces. In fact, the specimens on the north and west faces of the pillars adhered more airborne chloride than those on the south and east faces. In this study, we will discuss the results of exposure tests on the north and west faces, where airborne chloride adhered more heavily.

Analyzing the results for the northern face of the structure shown in Fig. 5(a), a consistent trend was observed across all four periods, although Pillar e in Period 1 and Pillar h in Period 4 exhibited relatively high values. Pillars located to the north of the structure would be expected to have the highest amount of adhered chloride because they are closest to the sea area where airborne chloride is supplied. However, Pillars a, b, and c, positioned at the northernmost part of the structure, registered lower levels of attached chloride compared with those in the central part. A possible reason for these results is that these pillars, located at the outermost perimeter of the structure, were more exposed to rain and had a greater washing effect, resulting in less chloride adhesion.

Turning to the west face of the structure, depicted in Fig. 5(b), a similar pattern emerges, with exceptions noted in certain pillars. Based on these observations, variations in rainfall by pillar location must be considered when forecasting the amount of salt deposited on them. Consequently, the subsequent section describes rain exposure tests conducted using water-sensitive paper to quantitatively assess the variation in rain exposure across different pillars.

2.4 RAIN EXPOSURE TEST USING WATER-SENSITIVE PAPER

In this study, the impact of pillar position within a structure on rainfall capture was quantified using a water-sensitive paper. The water-sensitive paper used in this study was a commercial product. This water-sensitive paper turns into dark blue color when exposed to droplets. In this study, the area of this dark blue coloration was marked as the area washed away by rainfall. Fig. 6 and 7 display a few of the test results and the percentage of wash-off, respectively.

The washout percentage represents the portion of the water-sensitive paper's total area that was colored dark blue due to droplet exposure. According to Fig. 7,

Pillars a, b, c, d, and j on the north and west sides experienced 40–70% rainwater exposure. In contrast, Pillar e in the central area received approximately 10% exposure, while Pillars k and l on the south and east sides registered less than 6%. These findings indicate that the pillars located on the north and west sides of the building were subjected to the highest levels of rainfall, whereas those on the south and east sides received the least. Based on the above, this study analyzed the rain exposure of the structure and compared the results of the analysis with the results of rain exposure tests using water-sensitive paper in order to take into account the washout effect of rain exposure when conducting the analysis of airborne chloride.

3. OVERVIEW OF NUMERICAL ANALYSIS

In this study, numerical analysis was employed to simulate rain exposure conditions and the diffusion and deposition of airborne chloride. The lattice Boltzmann method was utilized to calculate the wind velocity field surrounding the structure, while the particle method was used to determine the diffusion and deposition behavior of rainfall and airborne chloride on the pillars. Subsequent sections provide a detailed description of the numerical methods implemented in this research. Additionally, the data derived from the numerical analysis informed the formulation of the deposited chloride amounts, factoring in rain exposure.

3.1 ANALYSIS MODEL AND ANALYSIS CONDITIONS

The analysis model reproduced the structure, including the embankment, within a 30 × 30 × 15 m square space area, as shown in Fig. 8. As detailed in Section 2.1, an embankment is formed around the structure, and it is possible that this topography influences the wind flow, including airborne chloride. In addition, the upper part of the structure is covered by a lattice roof. To assess the impact of the lattice roof on rain exposure, two models were utilized: one with the lattice roof and another without it, as illustrated in Fig. 9.

3.2 WIND VELOCITY FIELD ANALYSIS VIA THE LATTICE BOLTZMANN METHOD

The lattice Boltzmann method (LBM) [5] is a numerical fluid analysis technique that reproduces macroscopic fluid behavior by statistically treating the microscopic behavior of fluid particles. This method is favored for its ease of parallel computation, straightforward boundary condition settings, and its capability to model complex fluid phenomena relatively easily. Consequently, LBM is now extensively utilized across various fields, not only in engineering.

In wind field analysis using LBM, employing smaller lattice spacing tends to stabilize the analysis. However, in three-dimensional analysis, smaller lattice spacings require significantly more computational time, rendering larger lattice spacings preferable after verifying the accuracy and stability of the analysis.

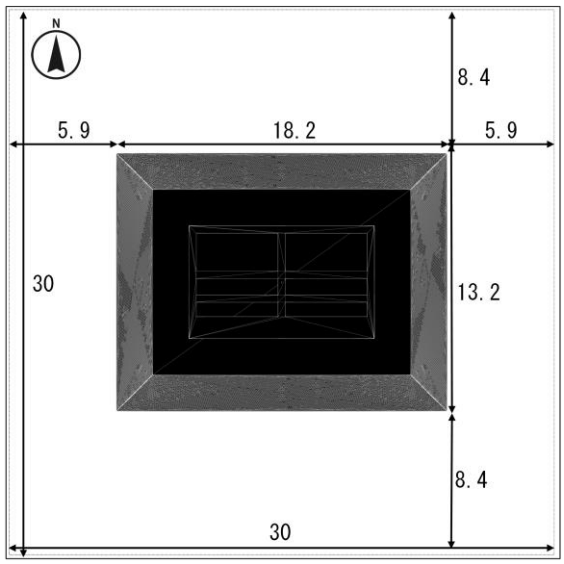

(a) Ground plan

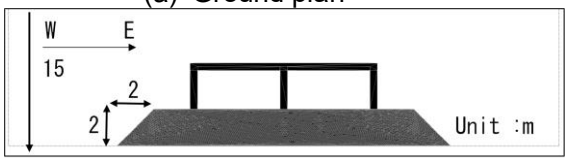

(b) Elevation view

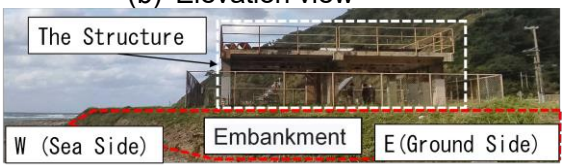

(c) Topography around the structure

Fig. 8 Analysis area

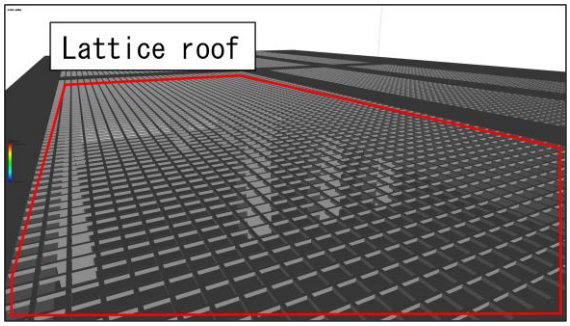

(a) Roofed model

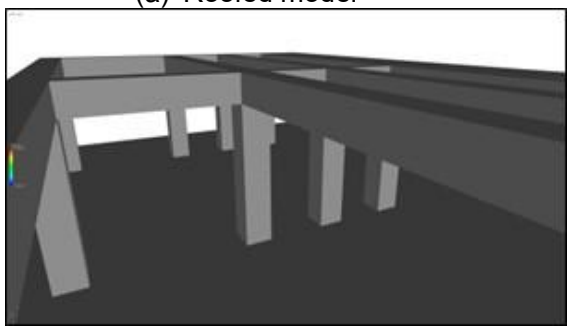

(b) Roofless model

Fig. 9 Differences between models

As depicted in Fig. 10, this study evaluated the impact of two different lattice spacings (referred to as minimum lattice spacing of 25 mm and 50 mm, respectively) on the analysis results; 50 mm is equivalent to the lattice spacing of a fenestrated roof, and a larger lattice spacing would affect the wind analysis of a lattice roof would not be properly evaluated. Therefore, the maximum minimum lattice spacing for the wind analysis in this study was set at 50 mm, and a half size, 25 mm, was used for comparison.

As discussed in Section 2.2, airborne chloride particles around the structure could influence wind velocity, potentially causing chloride deposition from directions other than those from which the wind originates from the coastal area. Therefore, wind field analysis in this study was conducted for all 16 directional patterns, using the average wind speed recorded during the exposure period as a constant inflow from the side of the analysis space. The lower surface of the analysis space and the surface of the structure were set to non-slip conditions, whereas the sides and top of the analysis space were set to free-slip conditions.

3.3 RAIN COVER ANALYSIS BY PARTICLE METHOD

For rain exposure analysis, the MPS method, a particle method, was used. An overview of the MPS method is given below.

For the rain exposure analysis in this study, the moving particle semi-implicit (MPS) method [6], a particle-based numerical analysis technique, was employed. The MPS method models fluid behavior by simulating the fluid as individual particles and tracking their motion. This method has advantages over lattice-based approaches, such as easier preprocessing and the ability to manage phenomena such as the coalescence and breakup of droplets. It is widely applied across various fields for its flexibility and capability in handling complex fluid dynamics.

The wind velocity field necessary for the MPS-based rain exposure analysis was determined via LBM, considering the meteorological conditions recorded during the specimen exposure test period. The boundary conditions set for the rainfall simulation were as follows: rainfall intensity of 10 mm/h, raindrop diameter of 2 mm, and an inflow velocity of 6 m/s. The particles representing the rain were introduced from the upper surface of the analysis space, allowing for a comprehensive simulation of rain exposure under controlled and variable conditions.

3.4 AIRBORNE CHLORIDE ANALYSIS USING PARTICLE METHOD

In the airborne chloride analysis conducted in this study, the particle method, comparable to that used in the rain exposure analysis, was employed. The influence of the number of airborne chloride particles on the analysis outcomes was examined by analyzing two different particle rates: 20,000 particles per second (20k particles/s) and 60,000 particles per second (60k particles/s). This variation allowed for an assessment

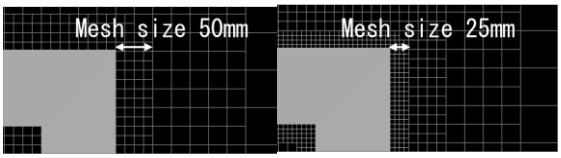

(a) 50mm (b) 25mm

Fig. 10 Minimum mesh size

Table 2 Analytical condition

Name	Face	Mesh size [mm]	Particles [Pcs/s]
N-25mm-20k	N	25	20,000
N-50mm-20k	N	50	20,000
N-25mm-60k	N	25	60,000
N-50mm-60k	N	50	60,000
W-25mm-20k	W	25	20,000
W-50mm-20k	W	50	20,000
W-25mm-60k	W	25	60,000
W-50mm-60k	W	50	60,000

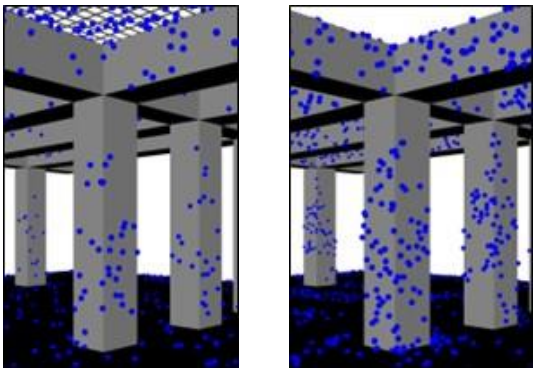

(a) Roofed model (b) Roofless model

Fig. 11 Rain exposure condition of the pillar

of how the quantity of particles impacts the results of the analysis. Aside from the number of particles, other analysis conditions were standardized: the particle diameter was set at 0.6 mm, matching the dimension used in the rain exposure analysis. The particle inflow velocity was aligned with the wind inflow velocity determined in the wind velocity field analysis.

3.5 FORMULATION OF THE AMOUNT OF DEPOSITED CHLORIDE CONSIDERING RAIN DROP

In the analysis of airborne chloride in this study, to incorporate the effect of washout by rain exposure, the results from the airborne chloride analysis were adjusted. This adjustment used a correction equation

derived from the rain exposure analysis results presented in Section 3.3. The purpose of this adjustment was to calculate the deposited salt while factoring in the effects of rain exposure.

$$CD = PD/A \times \{1 - RF(a) \times RP/RP(a)\} \quad (1)$$

CD : Number of adhered chloride particles per unit area, considering rain exposure [particles/m^2]
PD : Number of adhered chloride particles obtained from diffusion and adhesion analysis of airborne chloride [particles]
A : Area of each pillar member [m^2]
$RF(a)$: a obtained from the rain exposure test.
$RP(a)$: Normalized rain drop particle counts for pillars a obtained from rain exposure analysis [particles]
RP : Normalized rain drop particle counts for each pillars obtained from rain exposure analysis [particles]

4. ANALYSIS RESULTS AND DISCUSSION

In this study, eight distinct analyses, as detailed in Table 2, were conducted to investigate the effects of minimum lattice spacing and the number of inflow particles on the analytical results.

4.1 COMPARISON OF ANALYTICAL MODELS

Fig. 11 illustrates the rain exposure of the pillars as determined through numerical analysis. In Fig. 11(a), which depicts the model with a roof, rainfall particles predominantly strike the roof grid, resulting in fewer rainfall particles impacting the walls of the pillars compared with the roofless model shown in Fig. 11(b). Fig. 12 presents both the rain exposure test results and the numerical analysis results for the models with and without roofs. The results in Fig. 12 were normalized by dividing each by the respective maximum value. Fig. 12 reveals that for Pillars e, k, and l, located southeast of the center of the structure, the rain exposure in the roofed model is less than that in the unroofed model, aligning more closely with the rain exposure test results. However, Fig. 12(a) indicates that the analytical results for Pillars b and c on the north side exceed the experimental results, while those for Pillars d and j on the west side fall below the experimental results. This discrepancy could be attributed to the prevailing wind conditions during the rain exposure test, which were more westerly than the average wind speed utilized in the analysis. In conclusion, employing an analytical model that more closely mirrors the actual structure enables a more accurate replication of the rain exposure conditions.

4.2 COMPARISON WITH AND WITHOUT CONSIDERATION OF RAINDROPS

Fig. 13 displays the results of the airborne chloride analysis, considering both the scenarios with and without the effects of rain exposure. This figure also compares these analytical results to those obtained from exposure tests conducted on the specimens. The analysis was based on a model equipped with a roof, employing a 25 mm grid and utilizing 20k particles in the wind velocity field analysis. In Fig. 13, 14, and 15 (presented in the subsequent section), the exposure test results are averaged over four periods, and each set of analysis and exposure test results is normalized by dividing by the maximum value.
In Fig. 13(a), for Pillars a, b, and c on the north side, the analytical results that do not consider the washout effect of rain exposure are significantly higher than the exposure test results. In contrast, the results that account for rain exposure closely align with the exposure test results. However, for Pillars k and l on the south side, the analytical results, whether considering rain exposure or not, consistently exceed the exposure test results. This discrepancy could be due to the indirect washout effects of rain on the roof and beams, which subsequently affect the pillars. Similarly, on the west face as shown in Fig. 13(b), accounting for rain exposure yields satisfactory results for Pillars a, d, g, and j on the west side.

4.3 Comparison by minimum grid spacing and number of airborne chloride particles

Fig. 14 shows the results of the analysis using 50 mm and 25 mm grid spacings. Focusing on the north face in Fig. 14(a), the results using the 50 mm grid are consistently satisfactory. However, for the 25 mm grid, deviations from the exposure test results, particularly for pillars k and l on the south side, are noted. On the west face, shown in Fig. 14(b), the discrepancies with the exposure test results tend to be greater than those for the north face, with significant deviations noted in

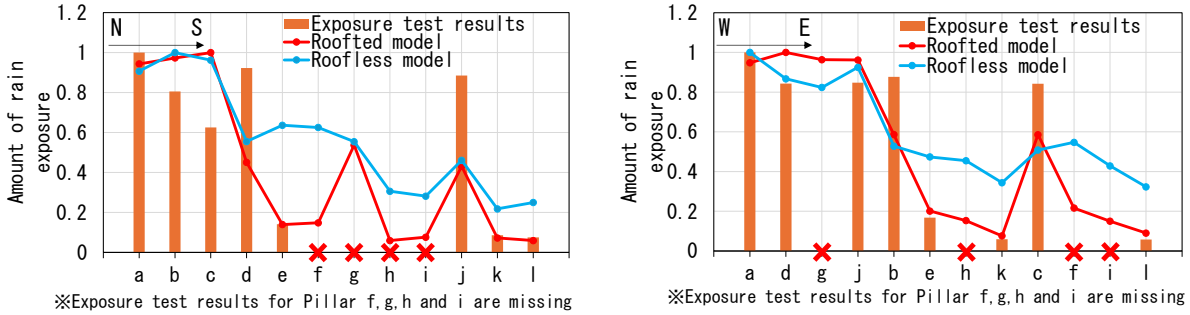

(a) North face (b)West face

Fig. 12 Analysis results and rain exposure test result

the analytical results for the 50 mm grid, particularly for pillars b, h, and c.

Fig. 15 examines the results for 20k and 60k particles, revealing minimal differences between the results for the north and west faces. This indicates that, within the scope of this study, a particle inflow rate of approximately 20,000 particles per second is sufficient from a computational speed perspective.

Fig. 16 shows the results of the wind velocity field analysis across eight patterns, varying in minimum grid spacing and number of inflow particles, alongside a scatter plot of the exposure test results. The figure also includes the root-mean-square-error (RMSE). The analysis for the north face shows less variation with the 50 mm grid compared with the 25 mm grid, regardless of the number of airborne chloride particles. Conversely, the 25 mm grid exhibits smaller scatter on the west face. In terms of RMSE, the 25 mm grid achieves a smaller error range (0.16–0.20) compared with the 50 mm grid (0.09–0.25), suggesting that a 25 mm minimum grid spacing offers greater stability.

In conclusion, the analysis in this study indicates that 25mm grid spacing is more stable than 50mm grid spacing. However, a minimum lattice spacing smaller than 25 mm has not been studied. Therefore, the optimal value of the minimum lattice spacing in this analysis will be studied in the future. In addition, the model of the structure and surrounding topography used in this study is simplified, and it is necessary to study the influence on the analysis results by improving the reproducibility of the model.

Future plans include further study of the analytical model and conditions to improve the accuracy and stability of the results.

5. CONCLUSIONS

The key findings of this study are summarized as follows:

(1) The trends in adhered chloride observed on the north and west faces of the structure during each period of exposure tests displayed similar patterns,

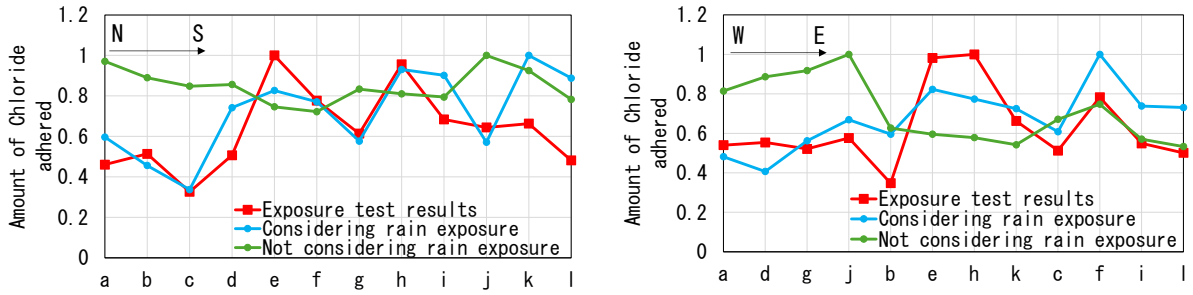

(a) North face (b) West face

Fig. 13 Differences in analysis results due to the consideration of rain exposure

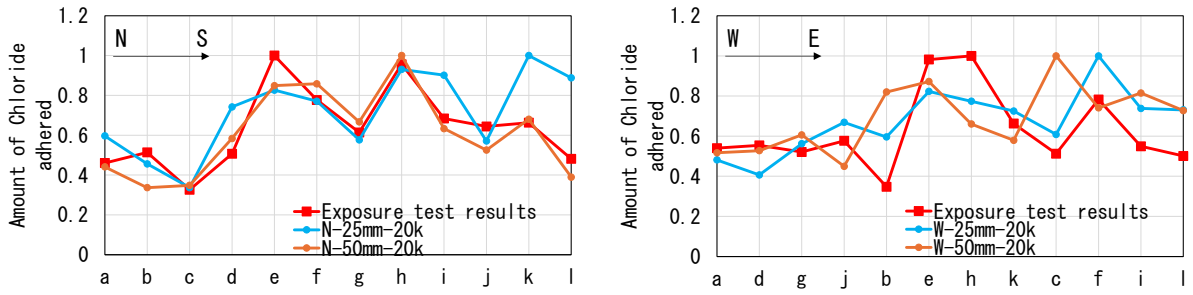

(a) North face (b) West face

Fig. 14 Differences in analysis results depending on the number of particles

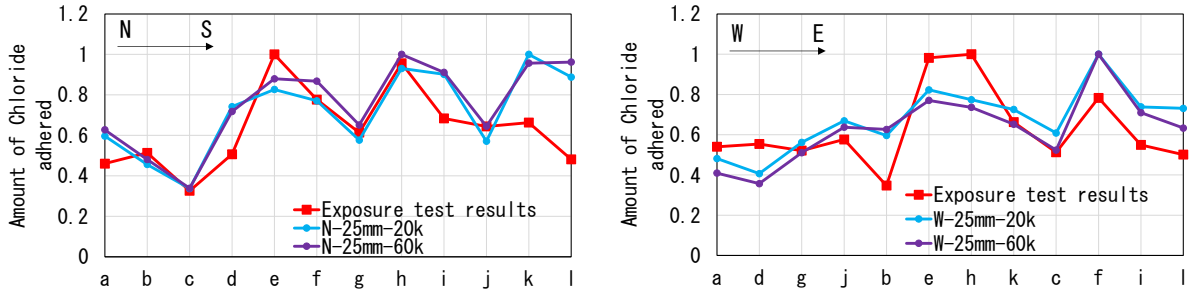

(a) North face (b) West face

Fig. 15 Differences in analysis results depending on the number of particles

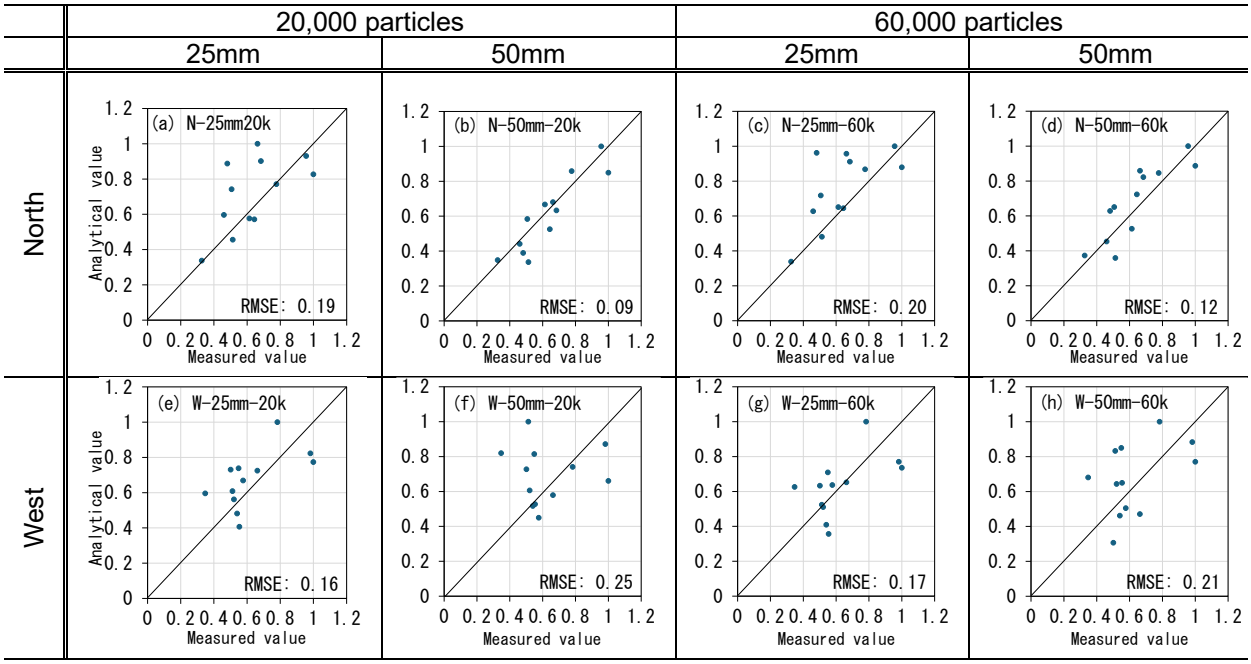

Fig. 16 Comparison of the results of each analysis

although certain variations were noted.

(2) Rain exposure tests utilizing water-sensitive paper revealed that rain exposure conditions varied depending on the location of the pillars and the prevailing wind conditions. The rain exposure analysis further confirmed that the model with a roof more accurately captured the trend of the exposure test results compared with the model without a roof.

(3) In the analysis of airborne chloride, considering the wind direction ratio and rain exposure, the results were more consistent with the exposure test results when rain exposure was considered. The optimal number of inflow particles for airborne chloride should be approximately 20,000 particles per second.

(4) Regarding the minimum grid spacing in the wind field analysis, the 50 mm grid performed best for the north direction but was the least accurate for the west direction. In contrast, the 25 mm grid demonstrated stable analysis results with minimal variation in both the north and west directions.

Future research will focus on refining the analytical model and conditions to enhance both the accuracy and stability of the results.

ACKNOWLEDGEMENTS

This research was supported by a Grant-in-Aid for Scientific Research (C) from the Japan Society for the Promotion of Science, “Salt Damage Environment Assessment by AI with Digital Twin” (PI: Kohei Sakihara, Project No. 24K07756), a FY2023 research grant from the Japan Concrete Institute (PI: Kohei Sakihara), and a FY2024 technical development support project from Okinawa Shimatate Association. The research was conducted as a part of the Okinawa Shimatate Association’s 2024 Technical Development Support Project (Principal Investigator: Kohei Sakihara). We hereby express our gratitude to them.

REFERENCES

1) Architectural Institute of Japan, “Standard Specifications for Building Construction and its Commentary JASS 5 Reinforced Concrete Construction 2022,” 2022.

2) LEY,A.J.,: A random walk model of two dimensional diffusion in the neutral surface layer, Atmospheric Environment, No.16, pp.2799-2808, 1982

3) Toyoda, S. and Sakihara, K., “Numerical Analysis of Adhered Chloride on Each Member of Reinforced Concrete Structures in Coastal Areas,” Proceedings of the Japan Concrete Institute, Vol. 45, No. 1, 2023, pp. 514–519.

4) Toyoda, S. and Sakihara, K., “Simulation of Diffusion and Deposition of Airborne Chlorides on Reinforced Concrete Structures in Coastal Areas Considering Environmental Factors,” Proceedings of Repair, Reinforcement and Upgrading of Concrete Structures, Vol. 23, 2023, pp. 407–412.

5) Chen, S. and Doolen, G.D., “Lattice Boltzmann Method for Fluid Flows,” Annual Review of Fluid Mechanics, Vol. 30, 1998, pp. 329–364.

6) Koshizuka, S. and Oka, Y., “Moving Particle Semi-implicit Method for Fragmentation of Incompressible Fluid,” Nuclear Science and Engineering, Vol. 123, 1996, pp. 421–434.

CO_2 Activation of Cementitious Materials Based on the Mineralization-desorption of Amino Acid Salts Absorbent

Tiefeng Chen
Lecturer/Ph.D, Harbin Institute of Technology, China

Jingkai Xu
Master student, Harbin Institute of Technology, China

ABSTRACT:
This study presents a new CCUS method, which uses potassium glycine (KG) solution to capture CO_2 derived from industrial flue gases and sequesters the CO_2 in wollastonite by mineralization-desorption, thus achieving the cyclic regeneration of KG absorbent and the activation of wollastonite. The results confirm the favorable absorption capacity and desorption efficiency of this method, with the CO_2 cyclic capacity of KG absorbent up to 0.47 mol/mol. The presence of CO_2-rich KG significantly improved the activity of carbonated wollastonite, resulting in decreased critical and median pore diameters and a 25—30% increase in compressive strength of cement paste. Two mechanism were proposed: The metastable $CaCO_3$ in wollastonite enhance the microstructure of cement matrix; The carbamate in CO_2-rich KG induced the formation of inorganic-organic composites with better mechanical performance.

Keywords: wollastonite, potassium glycine, mineralization, calcium carbonate, cement paste.

1. INTRODUCTION

It is generally believed that excessive emissions of greenhouse gases, represented by carbon dioxide (CO_2), are contributing to the growing concern about global warming. The increase in atmospheric carbon dioxide concentration of about 48% since the industrial revolution has led to a global average temperature rise of 0.95—1.2 °C [1]. The CO_2 absorbent is one of the most effective CCUS methods that can be installed in the industrial plants to eliminate or reduce CO_2 in flue gas. Amine-based absorbents, such as mono-ethanolamine (MEA), are widely utilized for this purpose [2]. However, though possessing the advantages of low cost and ideal absorption capacity, these alkanolamines still have crucial problems such as the corrosivity, volatility and toxicity, especially during their oxidative degradation process occurring in flue gas [3]. In contrast to MEA, amino acid salts have better environmental impact, lower volatility, higher oxygen stability, and similar CO_2 absorption capacity.

Another concern with amine-based absorbents is the energy consumption during the desorption process. Thermal desorption is the most common method used to regenerate amine-based absorbents. The CO_2-rich solution is pumped into a desorber at temperatures above 80 °C to release the CO_2 so that it can be reused for CO_2 capture. This is the most energy-intensive step in CO_2 capture, accounting for about 70-80% of the total energy consumption, and the high temperature accelerates the oxidative degradation of the absorbent. In consequence, mineralization-desorption was proposed for both amine-based and amino acid salt-based absorbents. In this method, calcium or magnesium minerals were utilized to introduce Ca^{2+} and Mg^{2+} into the CO_2-rich solution, causing calcium and magnesium carbonates to precipitate. The absorbent is thus regenerated chemically instead of thermally [4]. This technology has a great potential as an approach for the disposal of industrial solid wastes containing calcium and magnesium oxides, including cement kiln dust, steel slag, and high-calcium fly ash [5].

Wollastonite, theoretically composed of $CaO\text{-}SiO_2$ (CS), is a natural white-colored mineral that is abundantly available in China, India, Kazakhstan, the US, Mexico, and other countries. In the last decade, wollastonite has been utilized as a mineral admixture in concrete. Taking advantage of the carbonate precipitation process, the non-hydraulic wollastonite can be used as a low-carbon binder in concrete via CO_2 mineralization reactions.

2. EXPERIMENTS

2.1 RAW MATERIALS

The Portland Cement (P.I. 42.5) used had a density of 3.15 g/cm3 and a specific surface area of 330.1 m2/kg. Wollastonite purchased from Yanxi Mineral Products Company in Hubei Province of China was used. The superplasticizer used was polycarboxylate-based with a water reduction rate of 35%. Glycine and potassium hydroxide (KOH) were purchased from J&K Scientific Ltd. The KG (NH_2CH_2COOK) solution was prepared with equimolar amounts of glycine and KOH in deionized water.

2.2 ABSORPTION AND MINERALIZATION

The absorption and mineralization-desorption tests were conducted in the reaction vessel shown in Fig. 1. The reaction gas is a heated gas mixture containing 20% CO_2 in N_2. The reaction gas was pumped through aqueous KG solution (3 mol/L) at a flow rate of 0.5 L/min. The temperature of the reaction vessel was maintained at 40 °C by a water bath. The CO_2 concentration at the

outlet was monitored every 10 s using a Gasboard-3100P gas analyzer. The pumping of the reaction gas was terminated when the CO_2 concentration of outlet and inlet was equal. During CO_2 absorption, the solution samples were extracted at selected times. Hydrochloric acid titration was used to determine the quantity of CO_2 uptake by the KG solution as a function of absorption duration.

For the mineralization-desorption experiment, wollastonite was added in the KG solution that had absorbed CO_2 with a liquid-solid ratio of 6 mL/g and continuously mixed by the stirrer. Then, the solid and liquid phases were separated using a vacuum filter. In addition, as a comparison, the conventional carbonated wollastonite was also prepared: wollastonite aqueous solution at a liquid-solid ratio of 0.1 mL/g was spread into a very thin layer and placed in a carbonation chamber to be CO_2 exposed for 24 h. The CO_2 concentration was kept at 20%. More details of the conventional carbonation regime can be found in previous works [6].

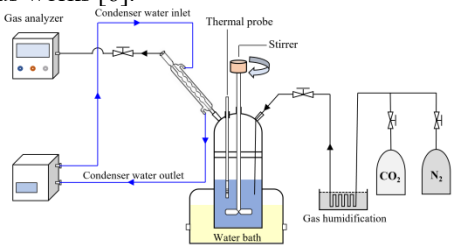

Fig. 1 Schematic diagram of CO_2 absorption

2.3 SPECIMENS PREPARATION

The cement paste specimens were prepared in three groups, including the control group, the group incorporating conventional carbonated wollastonite (PC-WC), and the group incorporating KG-carbonated wollastonite (PC-WKC). The mix proportions are shown in Table 1. The pastes were molded into the 40×40×160 mm3 molds and then cured at 20 ° C for 24 hours. Afterwards, the specimens were demolded and cured at standard curing environment (20±1 ° C, RH＞95%).

Table 1 Mix proportion of cement paste

Mixture	PC (%)	W_C (%)	W_{KC} (%)	Water/Binder
Control group	100	0	0	0.35
PC-W_C	80	20	0	
PC-W_{KC}	80	0	20	

2.3 TESTING METHODS

The ^{13}C NMR of the KG solution was performed using an Advance III NMR spectrometer (Bruker). The sample solutions were spiked with 5 vol% D_2O in quartz tubes to obtain a signal lock. The NMR spectra were collected at the frequency of 100.62 MHz for ^{13}C, with the pulse program of zgig30. The acquisition time and the relaxation delay were 1.36 s and 50 s, respectively.

The FTIR tests of wollastonite samples adopted wave number ranges of 4000–500 cm-1 with the resolution of 2 cm-1. An averaging 64 scans for each measurement was adopted. The wollastonite samples were collected after different durations of mineralization-desorption in KG solution.

The XRD test samples were scanned using the a Bruker D8 Advanced X-ray diffractometer in the 2θ angle range of 5°– 60° with Cu-Kα radiation. The scan speed and step were 5°/min and 0.02°, respectively. 10 wt% of corundum as an internal standard was mixed with the dried wollastonite samples. Peak functions based on XRD patterns and the crystal structure parameters were used to identify the contents of different crystals. 67

TG test was conducted to determine the CO_2 uptake and mineralization efficiency of wollastonite using a TA Discovery SDT 650 simultaneous thermal analyzer under nitrogen atmosphere. The resolution and the heating rate were 0.1 μg and 10 °C/min, respectively. For a portion of samples, a NETZSCH STA 449 F3 Jupiter Synchro Thermal Analyzer was used to combine the TG with a mass spectrometer (MS).

The pore structure of paste samples was measured with a mercury intrusion porosimeter (AutoPore IV 9510). The pressures ranged from 0 to 60,000 psi. 3 to 5 mm-size granular samples were cored from the center of the cement paste specimens and soaked in pure ethanol.

Flexural and compressive strength tests were determined in accordance with ASTM C78 and ASTM C109. Three prism specimens were prepared for three-point bending test at a loading rate of 1.2 MPa/min and the average value was recorded. Compressive strength was measured on six samples produced from the fractured flexural specimens at a loading rate of 1.8 kN/s and the average value was recorded.

3. RESULTS

3.1 ABSORPTION AND DESORPTION BEHAVIOR OF KG SOLUTION

The concentration of dissolved CO_2 in the KG solution versus pH value is shown in Fig. 2. The initial equilibrium in the aqueous KG solution can be described by Eq. (1). At this point, the pH of the KG solution is equal to 13.8. As the introduction of CO_2, the pH decreases, whereas the CO_2 absorbed in solution increases rapidly during the first 30 min. Then, the absorption rate starts to slow down. Eventually, the equilibrium is reached at a CO_2 concentration of 0.76 mol/mol and the pH value of 10.88. It can be concluded that the solubility of CO_2 in KG solution is close to the current major amine-based CO_2 absorbents, such as MEA [7].

$$NH_2CH_2COOK+H_2O \longleftrightarrow NH_3^+CH_2COOK+OH^- \quad (1)$$

During the mineralization-desorption experiment, the introduction of wollastonite lead to a decrease of CO_2 absorbed in the KG solution. The CO_3^{2-} and HCO_3^- in CO_2-rich KG solution react with Ca^{2+} dissolved from wollastonite to form $CaCO_3$. The mineralization-desorption process reaches equilibrium at a CO_2 concentration of 0.29 mol/mol and the pH of 10.88. The CO_2 cyclic capacity, i.e. the difference in CO_2 loading before and after desorption, is equal to 0.47 mol/mol.

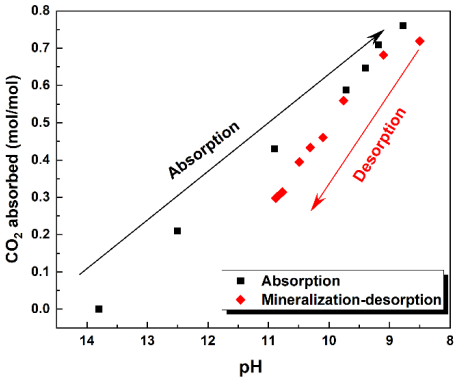

Fig. 2 CO_2 uptake versus pH value for absorption and mineralization-desorption process

The state of carbon nuclei in the KG solution during CO_2 absorption and mineralization-desorption is quantitatively measured by ^{13}C NMR spectroscopy. In CO_2-rich KG solution, three chemical species can be recognized by ^{13}C NMR, including KG/KGH^+ (corresponding to NH_2CH_2COOK and $NH_3^+CH_2COOK$), carbamate ($NHCO_2^-CH_2COOK$), and carbonate/bicarbonate (CO_3^{2-} and HCO_3^-). The peaks C_1, C_3, and C_5 correspond to different carbon signals of the carbamate, so they should have the same integration area in theory. The same applies to the peaks C_2 and C_6 (corresponding to the carbon signals of KG/KGH^+). Based on stoichiometry, the sum of C_1 and C_2 is equal to the initial content of KG, and we can obtain the relative content of the following chemical species (mol/mol KG):

$$\text{Carbamate content}=C_1/(C_1+C_2) \quad (2)$$

$$CO_3^{2-}/HCO_3^- \text{ content}=C_4/(C_1+C_2) \quad (3)$$

Combined with the absorbed CO_2 measured by the titration, the relative contents of carbamate and CO_3^{2-} / HCO_3^- during the mineralization-desorption process can be calculated, as shown in Fig. 3. At the beginning of mineralization-desorption, carbamate and CO_3^{2-}/HCO_3^- coexist in the CO_2-rich KG solution with the concentrations of 0.36 mol/mol and 0.4 mol/mol, respectively. With the introduction of wollastonite, the content of CO_3^{2-}/HCO_3^- decreases significantly, while the content of carbamate increases in the first 30 min. Then, with a continuous increase in pH, the decrease in content of CO_3^{2-}/HCO_3^- slows down, while the carbamate reaches the maximum and then begins to decrease. After about 120 min of mineralization-desorption, the content of CO_3^{2-}/HCO_3^- decreases to almost zero, and the content of carbamate gradually stabilizes at about 0.29 mol/mol.

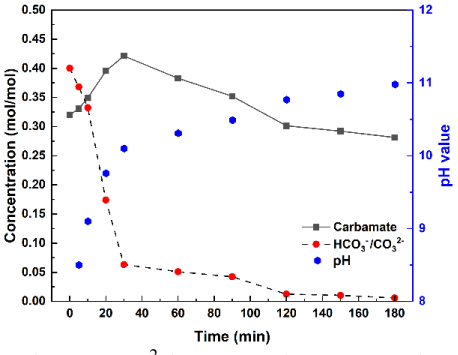

Fig. 3 Carbamate, CO_3^{2-}/HCO_3^-, and pH versus time during mineralization desorption

The reaction mechanics of CO_2-rich amino acid salt absorbents and calcium ions has been discussed in several literatures. The mineralization-desorption process is characterized by three stages. First, Stage I corresponds to the first 30 min during which the pH value increases from 8.5 to 10.1. The introduction of wollastonite leads to a significant reduction of CO_3^{2-}/HCO_3^- as a result of the following reactions:

$$CaSiO_3+CO_3^{2-}+H_2O \longrightarrow CaCO_3+SiO_2\cdot xH_2O+OH^- \quad (4)$$

$$HCO_3^-+OH^- \longrightarrow CO_3^{2-}+H_2O \quad (5)$$

At the same time, the content of carbamate increases. Li et al. [8] proposed a mechanism to explain this phenomenon:

$$NH_3^+CH_2COOK+HCO_3^-+OH^- \rightarrow NHCOO^-CH_2COOK+H_2O \quad (6)$$

The decrease in CO_3^{2-}/HCO_3^- is about three times of the increase in carbamate. It indicates that about two-thirds of CO_3^{2-} / HCO_3^- consumed in this stage reacts with wollastonite to form $CaCO_3$, while the other third is involved in the formation of carbamate.

Stage II is corresponding to 30—120 min, during which the pH increases from 10.1 to 10.77. The CO_3^{2-}/HCO_3^- concentration continues to decline, but apparently at a slower rate. The carbamate concentration also begins to decrease after reaching the maximum value. During this period, the reaction mechanism in Eq (6) stopped. Due to the increase in pH, the following reaction begins to take place in the system. The reduction of carbamate can be attributed to its reaction with Ca^{2+} to form the same moles of KG and $CaCO_3$.

$$KO_2CCH_2NHCOO^-+Ca^{2+}+OH^- \rightarrow KO_2CCH_2NH_2+CaCO_3 \quad (7)$$

In stage III, the pH increases from 10.77 to 10.98. The CO_3^{2-}/HCO_3^- concentration becomes stabilized and the reduction of carbamate slows down. After 180 min of mineralization-desorption, the final concentrations of CO_3^{2-}/HCO_3^- and carbamate are 0.01 mol/mol and 0.28 mol/mol, respectively. It indicates that the CO_2 absorbed in CO_3^{2-} / HCO_3^- is more easily released than that in carbamate. The CO_2 cyclic capacity of the KG solution is dominated by the reduction of CO_3^{2-}/HCO_3^-.

3.2 CARBONATION BEHAVIOR OF WOLLASTONITE

FTIR tests were conducted to determine the polycrystalline of the calcite carbonates generated in the KG-carbonated wollastonite composites. As seen

in the FTIR spectra of KG-carbonated wollastonite with different mineralization-desorption durations in Fig. 4, in which aragonite, vaterite and calcite, are abbreviated as, A, V and C, respectively. The asymmetrical stretching vibration of the Si-O bond (v_3) appears as a broad absorption band between 900 cm^{-1} and 1100 cm^{-1} [9]. The medium intensity band around 800 cm^{-1} responds to the symmetric stretching vibrations of Si-O bond (v_2 and v_4), and the signal at about 960 cm^{-1} is attributed to stretching vibrations of the Si-OH group [10]. As mineralization-desorption progresses, the intensity of the v_3 increases and shifts to a higher wavenumber, indicating that the progressive decalcification of wollastonite facilitates the polymerization of silicate. The absorption bands of $CaCO_3$ are as follow: The symmetric stretching (v_1) of carbonate at around 1080 cm^{-1}, the in-plane and out-plane bending (v_2 and v_4) at around 870 cm^{-1} and 720 cm^{-1}, and the stretching vibration (v_3) located at around 1450 cm^{-1}.

It can be observed from Fig. 4 that the v_4 peak at 712 cm^{-1} is absent or minimal during the first 20 min. This characteristic in-plane bending for calcite appears after 30 min of mineralization-desorption. The presence of the peak at 876 cm^{-1} is an indicative of vaterite formation in the system from the beginning of desorption. The split peak at around 1420—1480 cm^{-1} indicates the presence of ACC. This split v_3 peak is arise from the lack of symmetry around the carbonates. The presence of the aragonite characteristic peak is not significant in the spectra throughout the desorption process. Therefore, it can be concluded that vaterite and ACC are the primary $CaCO_3$ polymorphs in the KG-wollastonite system during the early stage. After 30 min of desorption, the characteristic calcite peak at 712 cm^{-1} begins to increase significantly. A number of literatures prove that in the absence of amino acid salts, either in gas-solid or liquid-solid systems, the polymorphs $CaCO_3$ produced by calcium silicates and CO_2 are primarily calcite. KG resulted in a reduction of the calcite content and stabilize the metastable vaterite and ACC, especially in the early stage.

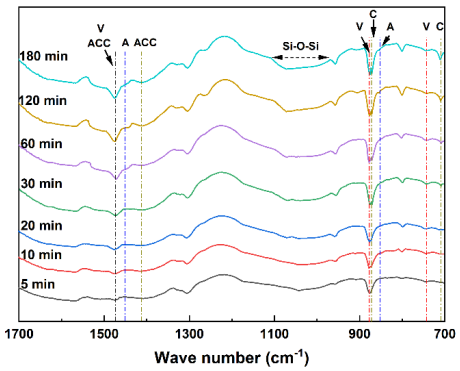

Fig. 4 FTIR spectra of wollastonite undergone different duration of mineralization-desorption

XRD patterns of KG-carbonated wollastonite are shown in Fig. 5 (a). XRD patterns present similar phenomena to FTIR, that is, the calcite content is relatively low in the early mineralization-desorption. The presence of vaterite in the system is also verified. XRD Rietveld refinement is conducted to determine the quantitative proportion of different $CaCO_3$ polymorphs, as seen in Fig. 5 (b). In addition to unreacted wollastonite, the calcite, aragonite, vaterite, and some amorphous phases are detected. The amorphous phases mainly contain C-S-H, silica gel, and ACC. During the first 30 min of mineralization desorption, the proportion of vaterite is significantly higher than the other two crystalline $CaCO_3$ polymorphs, reaching 10.3%. At this moment, the content of calcite is just 4.9%. After 30 min, the rate of vaterite formation declined, meanwhile, the content of calcite keeps increasing. At the end of the desorption, the calcite content outweighs the vaterite, being 14.5% and 12.7%, respectively. The content of aragonite is consistently kept at a low level, less than 5%, which is also consistent with the FTIR results. In such a KG-wollastonite system, more than 60% of wollastonite is consumed within 180 min.

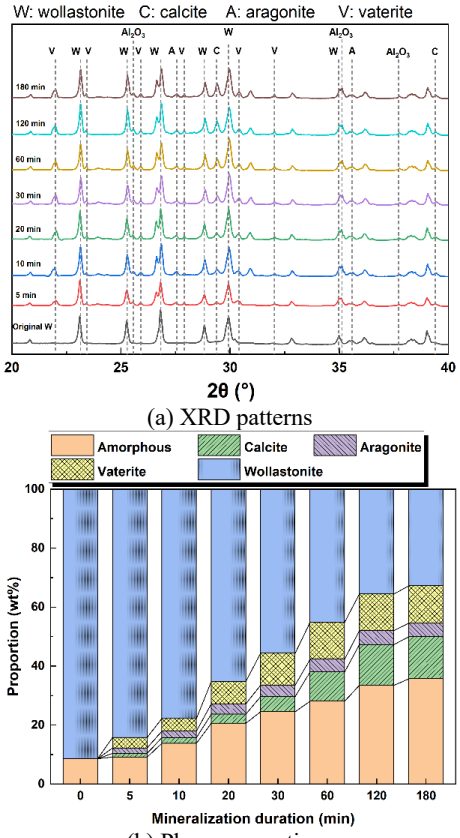

(a) XRD patterns

(b) Phase proportions

Fig. 5 XRD patterns and phase proportions of wollastonite

The derivative weight loss curves of wollastonite after different durations of KG-carbonation are presented in Fig. 6. There are three apparent peaks in the ranges of 220—400 °C, 640—720 °C, and 800—950 °C, respectively. Among them, the peak at 640—720 °C can be observed commonly in the derivative weight loss curve of carbonated calcium silicate minerals, corresponding to the calcite. However, the other two peaks are less common in the carbonation of cementitious materials. TG equipped mass spectrometry (MS) is applied to 20 min KG-carbonated wollastonite as shown at the bottom of Fig. 6. The MS result indicates that the weight loss in the range from 220 °C to 400 °C

is mainly due to the decomposition of chemically bound water. Generally, the C-S-H or Ca-modified silica gel without aluminum would remove the bound water below 200 °C. Therefore, we surmise this peak of bound water is induced by dehydration of ACC. It has been reported that water is clearly involved in most of the stable phases of ACC [11]. The presence of water in ACC located in the coordination sphere round calcium ions prevents the reorganization into stable crystalline anhydrous phases. In addition, this weight loss between 220 °C and 400 °C may also be partly due to the decomposition of residual organics [12]. The decomposition of CO_2 causes a gradual decline and two sharp decline of weight, located at 400—600 °C, 600—700 °C, and 850—950 °C. The gradual weight loss between 400—600 °C can be identified as decomposition of ACC and vaterite, because these CaCO3 polymorphs are less crystalline. The first sharp weight loss peak between 600—700 °C can be attributed to the decomposition of recrystallized calcite. The less than perfect crystalline state and higher dispersion of this kind of the calcite make it less thermally stable. [13]. The second sharp weight loss occurs between 850—950 °C, with peaking at approximately 900 °C, which is corresponding to well-crystallized calcite decomposing. In previous studies on the production of calcite by carbonation of various calcium silicates without amino acid salt, the decomposition temperatures of calcite were mostly around 800 °C [14], which is much lower than the findings in this research. On the one hand, it may be due to the fact that the presence of the organic compounds modifies the crystal structure of calcite, resulting in better thermostability. Kim et al. [15] have proved that polar amino acids can participate the precipitation of calcite to form an inorganic-organic composite biomineral-like mineral, possessing significantly enhanced hardness and covalent bonds strength. On the other hand, with the presence of KG, significantly more CO_2 is dissolved in the solid-liquid reaction system compared to pure water, which may accelerate the carbonation rate of wollastonite and improve the crystal structure.

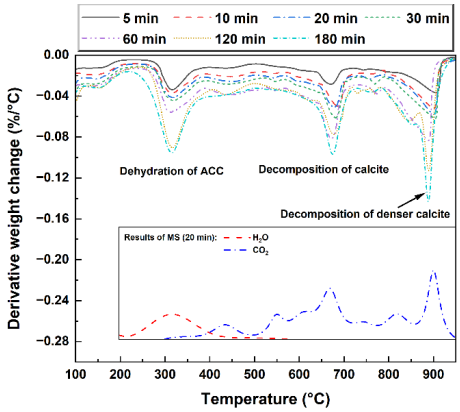

Fig. 6 Derivative weight loss curves of wollastonite after different durations of desorption

3.3 PORE STRUCTURE AND STRENGTH OF CEMENT PASTE CONTAINING WOLLASTONITE

The MIP results shows the pore structure of the cement paste samples, as seen in Fig. 7. The porosity of PC-WC increases by 5.74% compared to the control group. The proportion of large capillary pores, the critical pore diameter, and the median pore diameter of PC-WC are also higher. As for the cement paste containing 20% KG-carbonated wollastonite, the porosity increases by 2.68% compared to the control group, but the critical pore diameter and the median pore diameter are close to the control group. The fraction of large pores is even slightly lower.

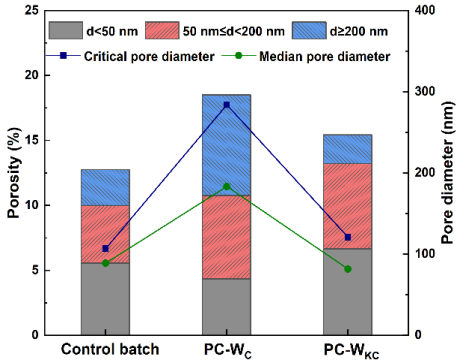

Fig. 7 Pore structure of cement paste containing carbonated wollastonite

The flexural and compressive strengths of the control group, PC-WC, and PC-WKC are shown in Fig. 8. As shown in Fig. 8 (a), addition of WC reduces the compressive strength of the cement paste at all ages, in contrast to the control group. This reduction varies from 23% to 12.4% with increasing age. The 3-d compressive strength of PC-WKC is lowest of the three groups, decreasing by 26.1% compared to the control group. However, the compressive strength of PC-WKC specimens increases more rapidly after 3 d. The 7 d compressive strength of PC-WKC ¬is significantly higher than PC-WC and is similar to the control group. At 28 d and 56 d, the compressive strength of PC-WKC becomes the highest of the three groups, being 9.2% and 10.7% higher than the control group. For the flexural strength of the specimens shown in Fig. 8 (b), the scenario is somewhat similar. At the early age, the PC-WC and the PC-WKC have comparable flexural strengths, both lower than the control group. When the age exceeds 7 d, the flexural strength of PC-WKC becomes higher than that of PC-WC, though still lower than that of the control group.

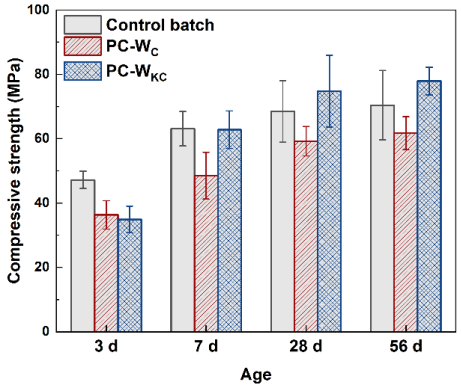

(a) Compressive strength

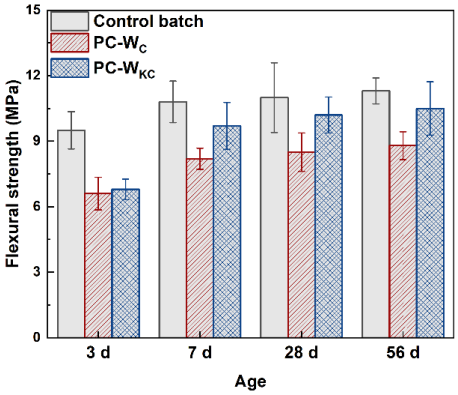

(b) Flexural strength

Fig. 8 The compressive and flexural strengths of cement paste specimens

4. DISSCUSION

As can be seen in Section 3, the KG-carbonated wollastonite contains considerable amounts of metastable $CaCO_3$, mainly in the forms of ACC and vaterite. The formation of these metastable $CaCO_3$ polymorphs has similarities to the biomineralization process. Amino acids can be bound to the nucleus surface by interactions between their negatively-charged carboxyl groups and Ca^{2+} ions, thereby retarding the crystallization kinetics of calcite. [16]. In the KG-wollastonite system, this role of calcite inhibitor is taken over by the carbamate ($NHCO_2^-CH_2COOK$). It is indicated in Fig.3, nearly half of the CO_2 is immobilized in the form of carboxyl group in carbamate during the CO_2 absorption process. As mentioned above in Eq. (8), the mineralization of carbamate with Ca^{2+} requires the participation of OH^-. In the early stage of desorption, because of the relatively low pH of the solution, this mineralization reaction between carbamate and Ca^{2+} would not occur. Instead, carbamate is adsorbed onto the surface of these metastable $CaCO_3$ polymorphs, retarding the dissolution-recrystallization of metastable $CaCO_3$ into calcite [17], as shown in Fig. 9 (a). As mineralization-desorption progresses, the pH value increases from 8.5 to 10.1. The carbamate content reaches its maximum through the mechanism in Eq. (7) while the CO_3^{2-}/HCO_3^- content decreases dramatically. After that, the carbamate begins to react with calcium ions and the inhibition of calcite precipitation decreases, resulting in a rapid increase in calcite content.

Compared to the conventional carbonated wollastonite, the addition of KG-carbonated wollastonite results in higher strength and improved pore structure of cement paste. Two possible reasons are proposed for this phenomenon. Firstly, higher pH of the cement paste may lead to further consumption of the carbamate adsorbed on the surface of the metastable $CaCO_3$, so that the metastable $CaCO_3$ begins to transform into calcite. This process may have filling and binding effects on the defects in cement matrix, as shown in Fig. 9 (b). Secondly, the inorganic-organic nanocomposites possess remarkable mechanical performance [18]. The hardness of the inorganic-organic nanocomposites is almost twice that of pure calcite, which consequently increases the strength of the cement paste.

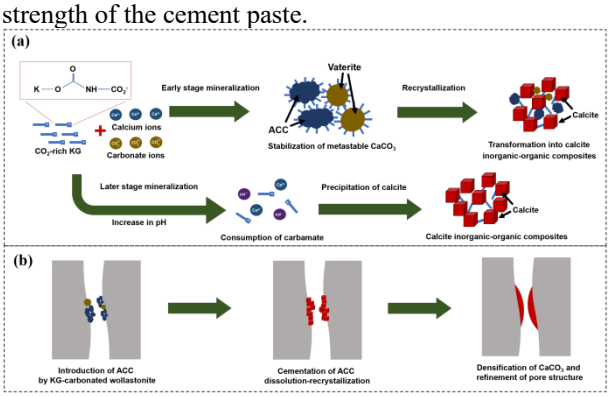

Fig. 9 Mechanism of (a) Formation and transformation of $CaCO_3$ polymorphs in different stages, and (b) Pore structure improvement via dissolution-recrystallization of $CaCO_3$

5. CONCLUSION

In this study, the wollastonite was used for the mineralization-desorption of potassium glycine (KG) CO_2 absorbent and also as a mineral admixture capable of sequestering CO_2. According to the results of this research, the conclusions can be derived as follows:

(1) 3 mol/L KG as the CO_2 absorbent possesses the equilibrium CO_2 concentration of 0.76 mol/mol, including 0.4 mol/mol in carbonate/bicarbonate and 0.36 mol/mol in carbamate. At atmospheric pressure and 40 °C, the CO_2 cyclic capacity of the KG absorbent is up to 0.47 mol/mol. It is comparable to the absorption and desorption efficiencies of the widely used MEA absorbent combined with thermal desorption.

(2) Carbonation of wollastonite in CO_2-rich KG solution results in the stabilization of metastable $CaCO_3$ in the early stage, generating amorphous calcium carbonate (ACC) and vaterite. In the later stage of mineralization-desorption, calcite is no longer inhibited to precipitate and its content increases rapidly.

(3) The KG-carbonated wollastonite contains a portion of calcite with higher thermal stability, with the decomposition temperature of 850—950 °C. It may be attributed to the improvement of the calcite crystal structure by CO_2-rich KG solution, forming an inorganic-organic composite mineral with higher thermal stability and favorable mechanical properties.

(4) As a result of the presence of wollastonite, the porosity of the cement paste increases. But KG-carbonated wollastonite can also decrease the critical and median pore sizes as well as reduce the fraction of large pores.

(5) Addition of KG-carbonated wollastonite decreases 3 d compressive and flexural strengths of the cement paste. However, the strength of cement paste incorporating KG-carbonated wollastonite exceeds or approaches that of the plain cement paste after 7 d. It may be due to the dissolution-recrystallization of the metastable $CaCO_3$ occurs in cement paste, filling and repairing the defects.

In conclusion, this study demonstrated through experimental results that KG absorbent combined with mineralization-desorption using wollastonite can be a potential method for CO_2 capture and storage, and the

KG-carbonated wollastonite can be an ideal mineral admixture. Nevertheless, further studies are needed to further elaborate on the mechanism of stabilization of metastable $CaCO_3$ and its enhancement on strength and pore structure.

REFERENCE

1. World Meteorlogical Organization, “WMO Statement on the Status of the Global Climate in 2019”, 2020.
2. Ooo, Z.L., Tan, P., Tan, S., et al. "Amine-based solvent for CO2 absorption and its impact on carbon steel corrosion: A perspective review", Chin J Chem Eng. Vol. 28, 2020.
3. Hook, R.J., "An Investigation of Some Sterically Hindered Amines as Potential Carbon Dioxide Scrubbing Compounds", Ind Eng Chem Res., Vol. 36, 1997.
4. Gadikota, G., "Multiphase carbon mineralization for the reactive separation of CO_2 and directed synthesis of H_2", Nat Rev Chem, Vol. 4, 2020.
5. Yu, B., Li, K., Ji, L., et al., "Coupling a sterically hindered amine-based absorption and coal fly ash triggered amine regeneration: A high energy-saving process for CO2 absorption and sequestration", International Journal of Greenhouse Gas Control, Vol. 87, 2019.
6. L. Li, T. Chen, X. Gao, Effects of superimposed carbonation synergy on BOFS cement-based materials, Cem Concr Compos. 138 (2023) 105008. https://doi.org/10.1016/J.CEMCONCOMP.2023.105008.
7. Portugal, A.F., Sousa, J.M., Magalhães, F.D., et al., "Solubility of carbon dioxide in aqueous solutions of amino acid salts", Chem Eng Sci, Vol. 64, 2009.
8. Li, Y., Duan, X., Song, W., et al., "Reaction mechanisms of carbon dioxide capture by amino acid salt and desorption by heat or mineralization", Chemical Engineering Journal, Vol. 405, 2021.
9. Sáez Del Bosque, I.F., Martínez-Ramírez, S., Blanco-Varela, M.T., "FTIR study of the effect of temperature and nanosilica on the nano structure of C-S-H gel formed by hydrating tricalcium silicate", Constr Build Mater., Vol. 52, 2014.
10. Ugliengo, P., Saunders, V., Garrone, E., "Silanol as a model for the free hydroxyl of amorphous silica: Ab initio calculations of the interaction with water", Journal of Physical Chemistry, Vo. 94, 1990.
11. Levi-Kalisman, Y., Raz, S., Weiner, S., et al., "Structural differences between biogenic amorphous calcium carbonate phases using X-ray absorption spectroscopy", Adv Funct Mater., Vol. 12, 2002.
12. Weiss, I.M., Muth, C., Drumm, R., et al., "Thermal decomposition of the amino acids glycine, cysteine, aspartic acid, asparagine, glutamic acid, glutamine, arginine and histidine", BMC Biophys, Vol. 11, 2018.
13. Šauman, Z., "Carbonization of porous concrete and its main binding components", Cem Concr Res., Vol. 1, 1971.
14. Baffoe, E., Ghahremaninezhad, A., "Effect of proteins on the mineralization, microstructure and mechanical properties of carbonation cured calcium silicate", Cem Concr Compos., Vol. 141, 2023.
15. Kim, Y.Y., Carloni, J.D., Demarchi, B., et al., "Meldrum, Tuning hardness in calcite by incorporation of amino acids", Nat Mater., Vol. 15, 2016.
16. Tong, H., Ma, W., Wang, L., et al., "Control over the crystal phase, shape, size and aggregation of calcium carbonate via a L-aspartic acid inducing process", Biomaterials, Vol. 25, 2004.
17. Khan, R.I., Ashraf, W., Olek, J., "Amino acids as performance-controlling additives in carbonation-activated cementitious materials", Cem Concr Res., Vol. 147, 2021.
18. Cantaert, B., Kuo, D., Matsumura, S., et al., "Use of Amorphous Calcium Carbonate for the Design of New Materials", Chempluschem, Vol. 82, 2017.

ASSESSMENT OF PHYSICAL PROPERTIES AND OPTIMAL UTILIZATION OF CEMENT-FREE PRECAST CONCRETE INCORPORATING INDUSTRIAL BY-PRODUCTS

Sohee MOON
Master's Student, School of Architectural, Civil, Environmental, and Energy Engineering, Kyungpook National University, Daegu, Republic of Korea

Youngwoong JUNG
Bachelor-Master Integrated Student, School of Architectural, Civil, Environmental, and Energy Engineering, Kyungpook National University, Daegu, Republic of Korea

Seongpyo KIM
Bachelor-Master Integrated Student, School of Architectural, Civil, Environmental, and Energy Engineering, Kyungpook National University, Daegu, Republic of Korea

Jayeon YUN
Bachelor-Master Integrated Student, School of Architectural, Civil, Environmental, and Energy Engineering, Kyungpook National University, Daegu, Republic of Korea

Kyungsu SHIN
Adjunct Professor, Department of Architectural Engineering, Woosong University, Daejeon, Republic of Korea

Hyeonggil CHOI
Associate Professor, School of Architecture, Kyungpook National University, Daegu, Republic of Korea

ABSTRACT:
The objective of this study was to evaluate the physical properties of precast concrete using stainless steel slag, combined heat and power plant fly ash, and return dust, which are industrial by-products. Furthermore, the optimal utilization of these industrial by-products within the context of this study was evaluated based on the results of physical characteristics. The strength development at an early age was found to be particularly noteworthy at 10% of the amount of industrial by-products utilized. XRD and SEM analysis indicate that the incorporation of industrial by-products facilitates the generation of hydration products that affect concrete strength through steam curing. Consequently, in consideration of the characteristics and workability of precast concrete, which necessitates rapid strength development, the optimal usage of industrial by-products is believed to be approximately 10%.
Keywords: industrial by-product, precast concrete, physical properties, optimal usage

1. INTRODUCTION

In recent years, the carbon neutrality movement has been actively implemented worldwide with the objective of reducing carbon dioxide (CO_2) emissions, which constitute the primary cause of global warming [1]. In South Korea, considerable efforts have been made to reduce greenhouse gas (GHG) emissions, including an increase in the 2030 Nationally Determined Contribution (NDC) to 30% [2,3]. GHG reduction is a response to climate change. However, the impact and damage of climate change caused by GHG emissions in the past are expected to last for the next 50–200 years [4]. In particular, the construction industry, which accounts for approximately 40% of all CO_2 gas emissions, is closely related to climate change, including global warming [5]. Consequently, GHG reduction is anticipated to assume a pivotal role in the future of the construction industry [6–10]. It has been reported that carbon dioxide emissions from the production and manufacture of Ordinary Portland Cement, the main component of concrete, account for approximately 5% of global carbon dioxide emissions. At present, the reduction of carbon dioxide emissions from the production and manufacture of cement is a matter of urgent priority. This is a matter of significant concern within the construction industry [11].

As part of a plan to reduce carbon dioxide emissions, research is being conducted on the use of industrial by-products as substitutes for cement. These by-products include ground granulated blast furnace slag and fly ash, and their application to actual sites is achieving significant results in reducing carbon dioxide emissions. The annual volume of blast furnace slag is about

Table 1. Mix proportion

W/B (%)	S/a (%)	AD[a)] (%)	Unit weight (kg/m^3)					Binder (wt%)			
			W	B	S	G	Gypsum	GGBFS[b)]	STS slag[c)]	CHPPA[d)]	Return dust
35.0	46.5	0.9	147	420	845	983	40.0	60	-	-	-
								50	10	-	-
									-	10	-
									-	-	10
								40	20	-	-
									-	20	-
									-	-	20

a) Polycarbonate superplasticizer, b) Ground granulated blast furnace slag
c) Stainless steel slag, d) Combined heat power plant ash

12 million tons, while the annual volume of fly ash is approximately 8 million tons. Given the considerable quantity of materials generated, numerous related studies have been conducted. However, the industrial by-products to be utilized in this study are not materials that have received significant attention in the literature.

It is generally understood that the production of one ton of stainless steel products generates one ton of Combined heat power plant ash has an annual production volume of approximately 600,000 to 1 million tons, representing approximately 8 to 15% of fly ash production. Return dust is an industrial byproduct generated during the manufacturing process of cement-based products. The amount generated is relatively small, which has resulted in a shortage of refining facilities. Consequently, most of them are disposed of through subcontractors, which has led to disposal problems such as illegal disposal. Therefore, it is imperative to prepare alternatives.

Furthermore, a considerable quantity of carbon dioxide is produced not only during the production of cement but also throughout the process of constructing and demolishing buildings. It has been reported that approximately 14% of carbon dioxide is generated during the installation and dismantling of formwork for pouring concrete. Consequently, the generation of carbon dioxide emissions in the field is also regarded as a significant concern that cannot be disregarded [12]. Consequently, the manufacturing of concrete components, such as columns, beams, slabs, and walls, in advance at a factory and subsequent transportation to the construction site, followed by assembly and installation, is attracting attention. The use of precast concrete has the advantage of reducing the construction period and associated costs when compared to the existing method of manufacturing formwork on site, pouring concrete, and then curing it. The research and development of precast concrete is currently being actively pursued due to the potential for reducing the environmental impact of the construction process. This can be achieved by reducing on-site waste and carbon dioxide emissions.

The objective of this study is to utilize industrial by-products as a cement substitute to address the aforementioned issues. Accordingly, we present basic data on the application of industrial by-products, specifically the optimal usage amount of STS slag, combined heat power plant ash, and return dust in cementless precast concrete based on ground granulated blast furnace slag and natural gypsum. In order to achieve this objective, the physical properties of precast concrete were evaluated according to changes in the mixing ratio of each material (stainless steel slag, combined heat power plant ash, and return dust) in order to ascertain the optimal usage amount.

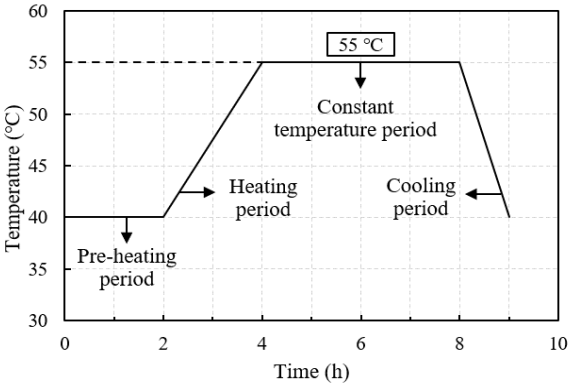

Figure 1. Steam curing process

2. EXPERIMENTAL PLAN AND MATERIALS

2.1 MIX PROPORTION

Table 1 presents the mix proportion table of this study. Following several mixing experiments and an analysis of existing research, the water/binder ratio (W/B) was set at 35.0% and the fine aggregate ratio (S/a) was set at 46.5% [13-14]. The ratio of natural gypsum was set at 40% for the binder, with the amounts of stainless steel slag, combined heat power plant ash, and return dust set at 0%, 10%, and 20%, respectively. The ratio of ground granulated blast furnace slag was then adjusted accordingly.

2.2 CURING CONDITIONS

Following the casting process, all specimens were subjected to steam curing in accordance with the conditions depicted in Figure 1. The specimen was cured at 40°C for 2 hours, and the temperature gradually increased at a rate of 5~10°C/h. The specimens were kept at a constant temperature of 55°C for 4 hours. The specimens were then cooled at a rate of

Table 2. Chemical compositions and physical properties of the used materials

Type	Chemical compositions (%)								Density (g/cm^3)	Blaine (cm^2/g)
	CaO	SiO_2	Al_2O_3	MgO	SO_3	MnO	F	Fe_2O_3		
STS slag[a)]	57.5	29.0	1.99	4.73	0.33	0.93	2.43	-	3.06	2261
CHPPA[b)]	28.2	27.0	14.0	4.98	9.42	0.19	-	13.3	2.75	5651
Return dust	63.8	22.1	6.76	0.92	4.33	-	0.59	0.36	2.67	6824

a) Stainless steel slag, b) Combined heat power plant ash

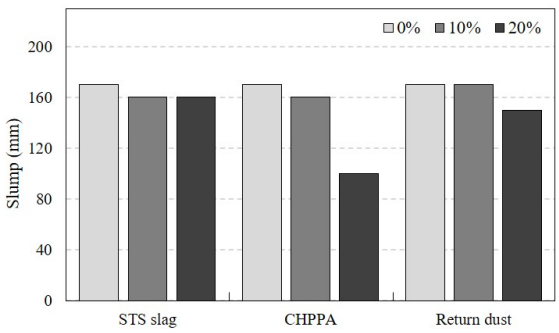

Figure 2. Slump test

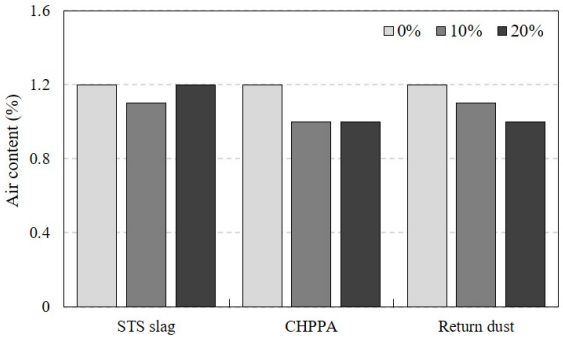

Figure 3. Air content test

15°C/h. Following demolding, the specimens were subjected to standard curing conditions (20 ± 2°C, RH 95%) for 1, 7, and 14 days.

2.3 MATERIALS USED

The density and fineness of the stainless steel slag, combined heat power plant ash, and return dust utilized in the experiment are presented in Table 2. Additionally, the XRF (X-ray fluorescence analysis) analysis outcomes are displayed. As a consequence of the chemical composition analysis of stainless steel slag, the CaO content was identified to be higher than that of the commonly utilized ground granulated blast furnace slag. Consequently, difficulties have been reported in using concrete due to volume expansion problems [15-17]. The combined heat power plant ash was found to have a higher CaO content than the chemical composition of commonly used fly ash. According to existing research, it is known that the CaO content is high due to the desulfurization reaction. Furthermore, it has been reported that the SiO_2 content is relatively low compared to that of fly ash, indicating both latent hydraulic and pozzolanic reactivity [18-19]. The return dust was found to have a significantly higher CaO content. Consequently, it can be reasonably assumed that reactivity with SO_3 can be expected. The industrial by-products contain chemical components that constitute cement, including SiO_2, Al_2O_3, and Fe_2O_3. Consequently, they are anticipated to function as a binder that can substitute for cement. Consequently, in this study, ground granulated blast furnace slag and natural gypsum, in conjunction with the aforementioned industrial by-products, were employed as binders. The aggregate was free of dust, dirt, and impurities, and contained 0.9% of a polycarboxylate superplasticizer. The experiment was conducted using purified water that was free of oil, acid, alkali, and other organic impurities.

2.4 TEST METHOD

The basic properties of concrete were evaluated by measuring slump and air content, in accordance with the specifications of KS F 2402 and KS F 2421, respectively. The target slump was set at 170mm, and the target air content was set at 1.0% on the assumption that no air-entraining agent was used in the concrete.

Compressive strength was measured according to KS F 2405. The size of the specimen was Ø 100 mm × 200 mm. Given the characteristics of precast concrete, which is manufactured in a factory and requires rapid strength development at an early age, measurements were taken at 1, 7, and 14 days of age.

In addition, given the importance of early strength development, scanning electron microscopy (SEM) and X-ray diffraction (XRD) were performed at 1 and 7 days of age for microstructural analysis. The objective was to examine the hydration products of STS slag, combined heat power plant ash, and return dust, as well as to assess the strength development characteristics in relation to the amount of usage.

3. EXPERIMENTAL RESULTS AND DISCUSSION

3.1 SLUMP

Figure 2 presents the results of the slump test conducted with the incorporation of stainless steel slag, combined heat power plant ash, and return dust. The slump test result of a mixture of blast furnace slag and natural gypsum alone was 170mm. Both 10% and 20% stainless steel slag usage were found to be 160mm. The combined heat power plant ash was found to have a slump value of 160mm and 100mm at 10% and 20% usage, respectively. The return dust usage of 10% and 20% was measured at 170mm and 150mm, respectively. With the exception of stainless steel slag, the slump exhibited a downward trend as the usage of other

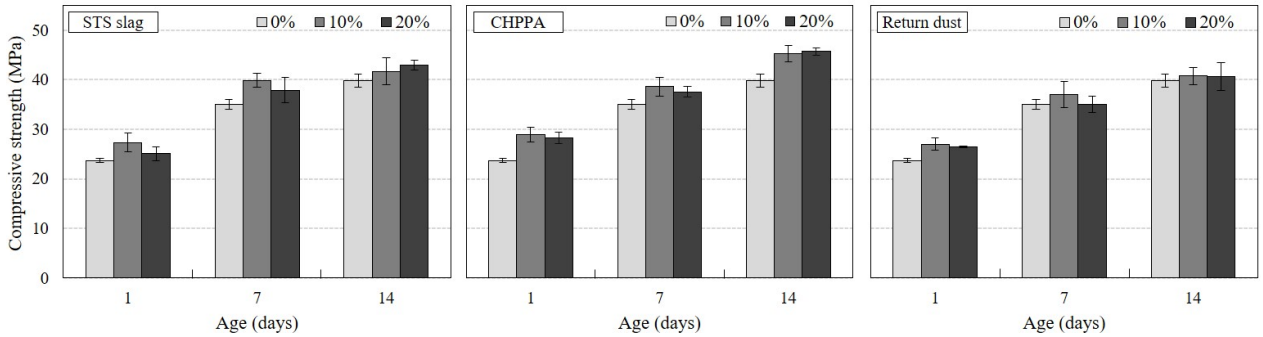

Figure 4. Compressive strength

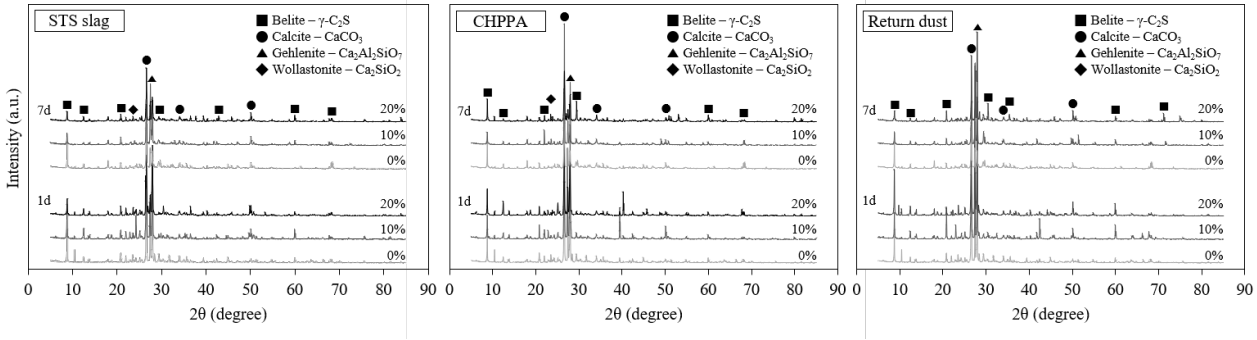

Figure 5. XRD analysis

industrial by-products increased. Nevertheless, the observed difference is not deemed to be significant. In the case of combined heat power plant ash, a reduction in slump of over 40% was observed at a usage level of 20%. Previous research suggests that this phenomenon may be attributed to the observed increase in viscosity and material separation resistance as the quantity of combined heat power plant ash utilized in the mixture is augmented [18]. Through this, it is judged that 10% usage is the most appropriate regardless of the type of industrial by-product.

3.2 AIR CONTENT

Figure 3 depicts the results of the air content test, stratified according to the utilization of stainless steel slag, combined heat power plant ash, and return dust. The air content of the mixture comprising solely blast furnace slag and natural gypsum was found to be within the target range of 1.0%. The air content was found to be 1.1% and 1.2% at 10% and 20% usage of stainless steel slag, respectively. The combined heat power plant ash was found to be 1.0% at both 10% and 20% usage. The return dust was measured at 1.1% and 1.0% at usage rates of 10% and 20%, respectively. No significant differences were observed in the air content in relation to the quantity of stainless steel slag, combined heat power plant ash, and return dust utilized. The air content when industrial by-products were applied was found to be generally lower than the air content measurement results obtained when mixing only existing blast furnace slag and natural gypsum. It is postulated that the fine powder of the industrial by-products in question, which have an elevated Blaine value, absorbs entrained air, thus reducing the air content.

3.3 COMPREESIVE STRENGTH

Figure 4 presents the compressive strength test results according to the usage amount and age of the materials in question: stainless steel slag, combined heat power plant ash, and return dust. The compressive strength measurement results indicated that the strength exhibited a tendency to increase as the aging period increased. It was demonstrated that the compressive strength of the specimen produced by the addition of industrial by-products was superior to that of the existing blast furnace slag and natural gypsum-based specimens. Regardless of the type of industrial by-product, the intensity at 1 and 7 days of age was found to be relatively high at a usage of 10%. However, at 14 days of age, it was found to have slightly better strength development performance in the range of stainless steel slag and combined heat power plant ash usage of 20%, although no significant difference was observed. Regardless of the type of industrial by-product, a usage rate of 10% is deemed appropriate, exhibiting a slight decline in slump and remarkable strength development performance regardless of age.

Accordingly, within the scope of this study, it is determined that the most appropriate amount of industrial by-products is 10%, taking into account workability and the characteristics of precast concrete that must be manufactured in a factory and rapidly develop strength.

3.4 XRD(X-Ray Diffraction)

X-ray diffraction (XRD) analysis was conducted to validate the hydration products generated within the manufactured specimen. The XRD analysis results at 1 day and 7 days of age are presented in Figure 5. Regardless of the industrial by-product utilized,

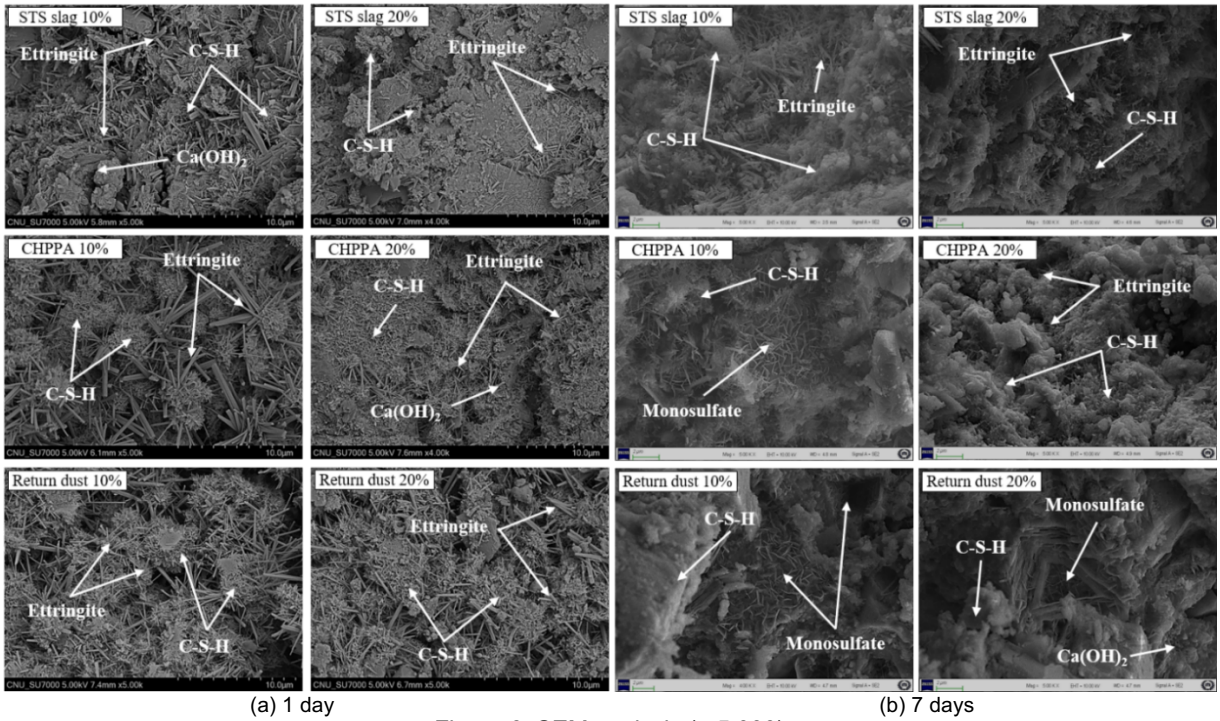

(a) 1 day (b) 7 days

Figure 6. SEM analysis (× 5,000)

components such as belite (γ-C_2S), calcite ($CaCO_3$), and gehlenite ($Ca_2Al_2SiO_7$) were observed to be prominent peaks in all specimens. As evidenced by existing studies, gehlenite ($Ca_2Al_2SiO_7$) plays a pivotal role in the generation of hydration products, including C-S-H gel, which is instrumental in the development of concrete strength. This process involves the utilization of industrial by-products, such as stainless steel slag, combined heat power plant ash, and return dust, which were previously difficult to employ as a concrete binder due to issues such as volume expansion. These by-products undergo steam curing to produce C-S-H gel, Belite (γ-C_2S), and Calcite ($CaCO_3$). It is believed that hydration products, such as gehlenite ($Ca_2Al_2SiO_7$), could be generated as a result of this process. Consequently, it is postulated that the generation of hydration products that affect the strength of concrete more efficiently has led to the achievement of excellent results in strength development performance. However, for a more quantitative evaluation, it is recommended that additional QXRD analysis, such as Rietveld analysis, be conducted.

3.5 SEM(Scanning Electron Microscope)

Figure 6 presents the results of the scanning electron microscopy (SEM) analysis of the samples of stainless steel slag, combined heat and power plant ash, and return dust at the ages of one and seven days. In the case of stainless steel slag, it contained a considerable quantity of calcium oxide, which renders it unsuitable for use in concrete due to the potential for volume changes. However, when applied to precast concrete manufactured in a factory through steam curing, it is believed to have contributed to the development of early-age strength by efficiently generating hydration products at an early age. It is postulated that the replacement of stainless steel slag in concrete will result in a reduction of strength due to the generation of voids resulting from the excessive production of calcium carbonate and ettringite, expansive hydrates. In the case of combined heat power plant ash, it is hypothesized that the use of natural gypsum as a binder through steam curing served to stimulate the destruction of the passive film of blast furnace slag and combined heat power plant ash. Consequently, it is postulated that the internal hydration reaction was facilitated, resulting in the production of hydrates such as C-S-H and ettringite. Given that combined heat power plant ash is known to exhibit both latent hydraulic reactivity and pozzolanic reactivity, it is postulated that the silicate material produced by the pozzolanic reaction acts as a catalyst, facilitating the bonding of combined heat power plant ash and thereby promoting high strength development performance. In the case of return dust, the calcium oxide content is notably elevated, approaching that of stainless steel slag. Consequently, it is postulated that when applied to precast concrete undergoing steam curing, it facilitates the hydration reaction and generates hydration products with greater efficiency. It is postulated that the material has contributed to the intensity of the initial age by suppressing volume expansion.

4. CONCLUSIONS

The objective of this study was to assess the potential of incorporating stainless steel slag, combined heat and power plant ash, and return dust into cement-free precast concrete based on blast furnace slag and natural gypsum. To this end, we sought to evaluate the optimal usage amount of each industrial by-product through analysis of physical properties and microstructure. The conclusion is as follows.

(1) The results of the slump and air content tests demonstrated excellent performance at 10% usage, regardless of the type of industrial byproduct. The compressive strength test results indicated that the initial aging strength was relatively high at 10% usage.

(2) The XRD analysis revealed that industrial by-products exhibited high strength development performance, resulting in the generation of hydration products that affect the strength of concrete, including C-S-H gel and C2S, through steam curing.

(3) The results of the SEM analysis indicated that the hydration products formed through steam curing of stainless steel slag and return dust resolved the volume expansion issue and contributed to the strength development performance at an early age. The combined heat and power plant ash has been demonstrated to exhibit high strength development performance, which is believed to be a consequence of its ability to promote the creation of hydrates in conjunction with natural gypsum, which acts as a stimulant.

Accordingly, within the scope of this study, it is deemed appropriate to utilize a 10% proportion of industrial by-products in order to facilitate workability and strength development performance at an early age. Should further data be accumulated through additional experiments under various conditions in the future, it is anticipated that this data will serve as the basis for determining the applicability of industrial by-products to precast concrete.

ACKNOWLEDGEMENT

This research was supported by the National Research Foundation of Korea (NRF) grant funded by the Korea government (MSIT) (NRF-2021R1C1C1011347).

REFERENCES

1. Jeong, Y.S.; Cho, S.; Mun, S.H.; Ji, C. Scenario to Reduce Greenhouse Gas Emissions in Building Sector towards the goal of Carbon Neutrality by 2050. J. Archit. Inst. Korea 2021, 37, 189–197.
2. The Government of the Republic of Korea. 2050 Carbon Neutral Strategy; The Government of the Republic of Korea: Seoul, Korea, 2020.
3. Ministry of Environment. Road Map for the Achievement of National INDC, KOREA; Ministry of Environment: Seoul, Korea, 2014.
4. IPCC. 2001: Climate Change; IPCC: Geneva, Switzerland, 2001.
5. Cheng, C.C.; Pouffary, S.; Svenningsen, N.; Callaway, J.M. The Kyoto Protocol, The Clean Development Mechanism and the Building and Construction Sector: A Report for the UNEP Sustainable Buildings and Construction Initiative; UNEP SBCI: Paris, France, 2008.
6. Gartner, E. Industrially Interesting Approaches to "Low-CO2" Cements. Cem. Concr. Res. 2004, 34, 1489–1498.
7. Lee, S.H.; Kim, S.K. CO_2 Reduction in the Cement Industry, Concrete and Environment; Kimoondang: Seoul, Korea, 2011; pp. 16–30.
8. Yang, K.H., Moon, J.H. Design of Supplementary Cementitious Materials and Unit Content of Binder for Reducing CO_2 Emission of Concrete. J. Korea Concr. Inst. 2012, 24, 597–604.
9. Schneider, M. Process technology for efficient and sustainable cement production. Cem. Concr. Res. 2015, 78, 14–23.
10. Lee, M.H. Fundamental properties of mortar and concrete using high-calcium fly ash. J. Korean Recycl. Constr. Resour. Inst. 2016, 4, 284–291.
11. Cho, J. W. (2011). CO_2 Reduction Cement Technologies. Magazine of the Korea Concrete Institute, 23(6), 32-35.
12. Kang, S. H., Ahn, H. J., Lee, C. S., Lee, D., Cho, H., & Kang, K. I. (2019). Assessment of CO_2 Emissions of Eco-friendly Lightweight Form in the Construction Process. In Proceedings of the Korean Institute of Building Construction Conference (pp. 10-11). The Korean Institute of Building Construction.
13. Nam, H. K., Lim, J. G., & Lee, S. S. (2015). Engineering Properties of the Non-Cement Mortar Using the Fly Ash From Combined Heat Power Plant and Recycled Fine Aggregate. Journal of the Korea Institute of Building Construction, 15(6), 553-559.
14. Kim, T. H., Jang, S. Y., & Kwon, S. J. (2019). Durability Characteristics in Concrete with Ternary Blended Concrete and Low Fineness GGBFS. Journal of the Korean Recycled Construction Resources Institute, 7(4), 287-294.
15. Cho, B. S. (2014). Study on Stable Use of Stainless EAF Oxidizing Slag as Fine Aggregate of Concrete. Journal of the Korea institute for structural maintenance and inspection, 18(3), 133-142.
16. Choi, S. W., Kim, J. S., Jeun, J. Y., Kim, E. K., & Ryu, D. H. (2008). The Experimental Study on the Properties on Concrete to use the Electric Arc Furnance Slag as Fine Aggregate. In Proceedings of the Korea Concrete Institute Conference (pp. 389-392). Korea Concrete Institute.
17. Hwang, C. S., Park, K. T., & Choi, Y. C. (2018). Pore Characteristics of Stainless Steel Slag AOD Blended Cement Pastes by Carbonation Curing. Journal of the Korea institute for structural maintenance and inspection, 22(3), 90-96.
18. Lee, S. S., Back, M. J., Won, C., Ahn, J. H., & Park, C. L. (1995). THE QUALITY PROPERTIES FOR FLY ASH OF COMBINED HEAT POWER PLAINT AND MECHANANICAL PROPERTIES IN CONCRETE. In Proceedings of the Korea Concrete Institute Conference (pp. 69-74). Korea Concrete Institute.
19. Min, K., Lee, J., Lee, D., Kim, J., & Jung, C. (2017). Analysis of Physical and Chemical Properties of CFBC Fly Ash in Vietnam for Solidification. The Journal of Engineering Geology, 27(3), 245-253.

CHEMICAL CHANGES AND CO_2 STABILITY IN CARBONATED HARDENED CEMENT PASTE EXPOSED TO SEAWATER

FURUKAWA, Ikuya
Graduate student, Shimane University, Japan

YOSHIDA, Natsuki
Specially appointed associate professor, Osaka University, Japan

ATARASHI, Daiki
Professor, Shimane University, Japan

ABSTRACT: In this study, the effect of seawater on hardened cement pastes subjected to enforced carbonation was investigated. The results showed that Friedel's salt (F-salt) was clearly observed in the non-carbonated specimens after seawater immersion, but it was only slightly observed in the carbonated specimens.The reason for this difference is the formation of F-salt in the non-carbonated sample due to ion exchange between monosulfate (Ms) and Cl^- in seawater. In the carbonated samples, on the other hand, carbonation decomposed Ms into $CaCO_3$ and Al_2O_3 gels. As a result, no F-salt was formed by ion exchange with Cl^-. The $CaCO_3$ crystalline phases observed in the carbonated samples were calcite and vaterite, which remained stable after seawater immersion. Furthermore, the CO_2 fixation rate did not change and no CO_3^{2-} release was observed after seawater immersion.
Keywords: carbonation, seawater immersion, effects of seawater, friedel's salt, brucite, monocarboaluminate

1. INTRODUCTION

Global warming caused by greenhouse gases has become a worldwide environmental issue, prompting various industries globally to make efforts in greenhouse gas reduction [1]. In 2020, the Japanese government set a goal to achieve "carbon neutrality" by 2050, aiming to reduce overall greenhouse gas emissions to zero [2]. Since then, numerous Japanese industries have been actively researching methods to achieve carbon neutrality.

The cement industry alone emits 40 million tons of CO_2 annually, accounting for 4% of Japan's total CO_2 emissions [3]. Reducing CO_2 emissions in the cement sector is thus an urgent priority in achieving carbon neutrality, driving ongoing research into CO_2 reduction strategies. One approach involves reducing clinker usage by substituting it with blended materials such as finely ground blast furnace slag and limestone. Moreover, technologies have been developed to enable concrete to absorb and fix CO_2 [4].

In this study, our focus was on technologies capable of absorbing and immobilizing CO_2. CO_2 immobilized in cement is fixed through chemical reactions with cement hydrates. One issue with immobilizing CO_2 in cement is that it lowers the pH of the cement, leading to neutralization. However, since unreinforced precast products have no steel bars, deterioration due to steel bar corrosion will not occur despite neutralization. This makes them promising candidates for innovative carbon-negative concrete, and carbonation of precast products is under consideration.

Among precast products, enforced carbonation products are being considered for use in wave-dissipating blocks in marine environments [5]. When cementitious materials are used in marine environments, cement hydrates are known to be chemically affected by ions derived from seawater (Na^+, Mg^{2+}, Cl^-, SO_4^{2-}, etc.) [6]. There is insufficient understanding regarding the chemical stability of immobilized CO_2 and its impact on concrete durability when subjected to enforced carbonation in a marine environment.

In this study, we immersed enforced carbonated paste specimens in seawater to investigate the effect of seawater on the chemical alterations of constituent compounds.

2. EXPERIMENTAL METHOD

2.1 Materials

Ordinary Portland cement (OPC) was used to produce thin hardened cement sheets (20 mm × 20 mm × 3 mm) with a water to powder ratio of 0.50. Table 1 presents the chemical composition of OPC. The sheets were cured for 14 days in water followed by 7 days of drying in small desiccators maintained at 11% relative humidity (RH).

Table 1 Chemical composition of OPC

Chemical composition (%)					
SiO_2	Al_2O_3	Fe_2O_3	CaO	MgO	SO_3
21.41	4.81	3.20	65.01	1.08	2.02

Subsequently, the cured material was transferred to a small desiccator set to 95% RH, where enforced carbonation was conducted by introducing 100% CO_2 gas at a flow rate of 200 mL/min for 30 minutes per day (referred to as OPC_Carbo).
Two additional samples were also prepared for comparison: one without enforced carbonation (OPC_Non-Carbo), using the same cement as OPC_Carbo, and the other without enforced carbonation but incorporating 30% limestone powder (LSP) as a replacement for OPC (OPC+LSP_Non-Carbo). OPC+LSP_Non-Carbo represents a typical low-carbon cement characterized by the pre-existence of CO_3^{2-} in the system.
For each condition, 6 hardened specimens were immersed in seawater (1 L) at 20°C for specified durations (7, 14, 56, and 91 days). The seawater used for immersion was collected from the coast of Matsue City, Shimane Prefecture, facing the Sea of Japan.

Table 2 Chemical composition of LSP

Chemical composition (%)			
Al_2O_3	Fe_2O_3	CaO	MgO
0.03	0.02	56.01	0.2

2.2 Analysis method

(1) Analysis by TG-DTA

Calcium hydroxide ($Ca(OH)_2$, CH) in cement paste and brucite ($Mg(OH)_2$, MH), formed by the reaction of CH in cement with Mg^{2+} in seawater, were determined by TG-DTA (Thermo Gravimetry-Differential Thermal Analysis). The quantities of CH and MH in the cement were calculated based on the amount of water decomposed from CH and MH. The water content was determined using a thermogravimetric differential thermal analyzer (TG-DTA, NETZSCH STA2500) with a temperature increase rate of 10°C/min. The dehydration temperature range for CH was 450-500°C [7], and for MH it was 340-410°C [8]. The onset and completion temperatures of mass loss were identified. The amount of water decomposed from CH was calculated from the mass loss observed between the onset and completion temperatures on the TG curve. Using these values, the contents of CH and MH were calculated according to equations (1) and (2).

$$M_{CH} = \frac{\Delta m_{CH}}{m_0 - m_{1000}} \times \frac{56.08}{18.02} \times 100 \quad (1)$$

M_{CH}: Reaction rate of CH (%)
Δm_{CH}: Amount of water produced by the decomposition of CH (mg)
m_0: Amount of sample for measurement (mg)
m_{1000}: Amount of sample heated to 1000°C (mg)
56.08: Material amount of CaO
18.02: Amount of H_2O

$$M_{MH} = \frac{\Delta m_{MH}}{m_0 - m_{1000}} \times \frac{40.30}{18.02} \times 100 \quad (2)$$

M_{MH}: Reaction rate of CH (%)
Δm_{MH}: Amount of water produced by the decomposition of CH (mg)
m_0: Amount of sample for measurement (mg)
m_{1000}: Amount of sample heated to 1000°C (mg)
40.30: Material amount of MgO
18.02: Amount of H_2O

(2) Analysis by IC

A TOC (Total Organic Carbon) meter (Shimadzu Corporation, TOC-L and SSM-5000A models) equipped with a solid sample fuel apparatus was used to measure CO2 liberated by adding phosphoric acid to the sample to make it acidic (pH 3 or lower) and heating it at 200°C. The CO_2 fixation rate was calculated from the amount of carbon obtained by the measurement using the non-dispersive infrared absorption. The CO_2 fixation rate was calculated from the amount of carbon obtained from the measurements using Equation (3).

$$\alpha = \frac{X \times \frac{1}{1000} \times \frac{1}{M_C}}{\frac{100 - L}{100} \times \frac{A}{100} \times \frac{1}{M_{CaO}}} \times 100 \quad (3)$$

α : Carbon oxidation rate (%)
X: Amount of carbon (mg/g)
M_C: Molecular weight of carbon (C)
A: Percentage of CaO in the sample (%)
M_{CaO}: Molecular weight of calcium oxide (CaO)
L: Loss on intense heat when sample is held at 1000°C (%)

(3) Analysis by XRD

XRD (X-Ray Diffraction) (Bluker, D2, PHASER tube Cu, source: CuKα, tube voltage 30 kV, current 10 mA) was used to analyze the hydration products.

(4) Analysis by FT-IR

FT-IR (Fourier Transform Infrared Spectroscopy) measurements were performed using the KBr method with an infrared spectrophotometer (FT/IR-4600 model manufactured by Japan Spectroscopic Corporation). The measurement conditions included 64 scans and a spectral range from 400 to 4000 cm^{-1}.

3. RESULTS AND DISCUSSION

3.1 Analysis of OPC before and after carbonation

The XRD analysis result, the FT-IR anarysis results and the TG-DTA results of OPC_Non-Carbo and OPC_Carbo are shown in Fig. 1, Fig. 2 and Fig. 3, respectively. As shown in Fig. 1, monosulfate (Ms), which was identified in OPC_Non-Carbo, was not detected in OPC_Carbo after enforced carbonation. This absence is attributed to the decomposition of Ms into $CaCO_3$ and Al_2O_3 gels during enforced carbonation [9], leading to the disappearance of AFm in OPC_Carbo. Calcite and vaterite are the crystalline phase carbonation

Ett:ettringite,Ms:monosulfate,Mc:monocarboaluminate,C_4AF:ferrite,Vat:vaterite,Cal:calcite

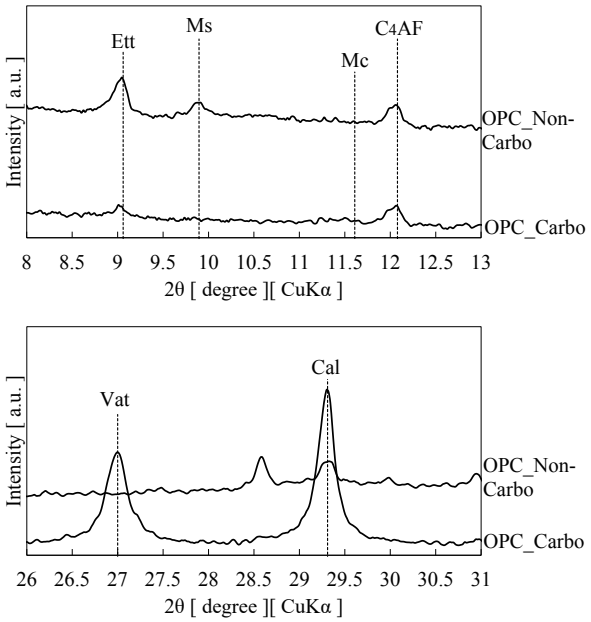

Fig.1 XRD pattern
(OPC_Non-Carbo & OPC_Carbo)

products formed during this process.

As shown in Fig. 2, the absorption band around 970 cm^{-1} attributed to the stretching vibration of the Si-O bond in C-S-H, observed in OPC_Non-Carbo [10], was absent in OPC_Carbo after enforced carbonation. Instead, absorption bands at 875 cm^{-1}, corresponding to the inverse symmetric external angular vibration of CO_3^{2-} in $CaCO_3$ [11], and at 1080 cm^{-1}, associated with the stretching vibration of the Si-O bond in silica gel [10], were detected in this sample. These findings indicate that C-S-H decomposes into $CaCO_3$ and SiO_2 gel under enforced carbonation.

As shown in Fig. 3, in OPC_Non-Carbo, the CH pyrolysis reaction occurred at 450°C and 500°C. In OPC_Carbo, a less pronounced pyrolysis reaction was observed, and a small amount of CH was detected. This is thought to be due to the reaction of the CH in the cement reacted with CO_2 through forced carbonation to form $CaCO_3$, which formed a protective layer. This layer inhibits the diffusion of CO_2 and prevents the complete reaction [12].

3.2 Analysis results of OPC+LSP_Non-Carbo

Fig. 4 shows the XRD analysis results before and after seawater immersion for OPC+LSP_Non-Carbo.

In general, it is known that in cement exposed to seawater, Cl^- ions from seawater undergo ion exchange with anions in the AFm interlayer to produce Friedel's salt [13].

In OPC+LSP_Non-Carbo, as shown in Fig. 4, monocarbonate (Mc) forms, and during seawater immersion, CO_3^{2-} is released from the interlayer and exchanges ions with Cl^-, resulting in the formation of Friedel's salt. The peak ettringite content increased after immersion due to the reaction of SO_4^{2-} in seawater with

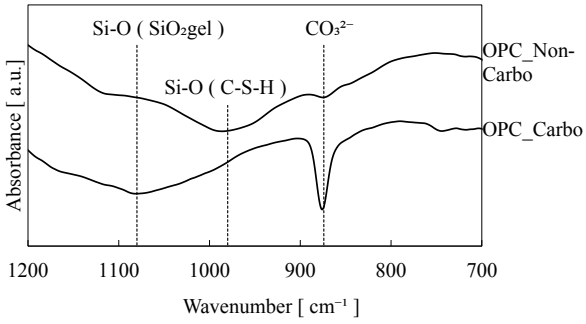

Fig. 2 FT-IR [cm^{-1}=700~1200]
(OPC_Non-Carbo & OPC_Carbo)

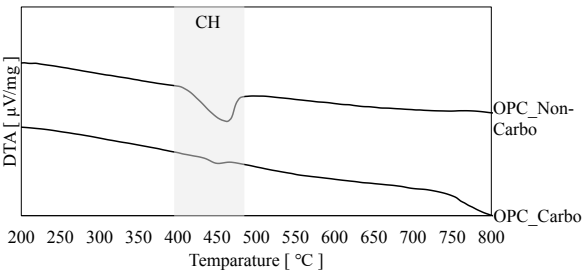

Fig. 3 Pyrolysis reaction of CH by DTA
(OPC_Non-Carbo & OPC_Carbo)

Ett:ettringite,Mc:monocarboaluminate,
C_4AF:ferrite,F:friedel's salt

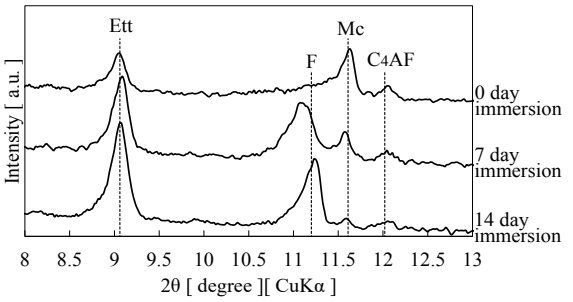

Fig. 4 XRD pattern
(OPC+LSP_Non-Carobo)

the calcium aluminate components of the solid-liquid phase in the cement. This finding is consistent with previous reports [14].

3.3. Analysis results of OPC_ Non-Carbo samples after seawater immersion

(1) Changes in the AFm phase after seawater immersion

Fig. 5 shows the results of the XRD analysis of the OPC_ Non-Carbo sample.

AFm (monosulfate (Ms)) was observed in the sample before seawater immersion. However, after immersion in seawater, Cl^- ions from seawater and SO_4^{2-} ions from Ms underwent ion exchange, resulting in the formation of Friedel's salt.

Additionally, an increase in the ettringite (Ett) peak and a gypsum ($CaSO_4 \cdot 2H_2O$) peak were observed after seawater immersion. This is because the sulfates in seawater (Na_2SO_4, $CaSO_4$, $MgSO_4$) reacted with the calcium aluminate hydrates in the solid-liquid phase of

the cement, leading to an increase in the Ett peak. Additionally, the sulfates in seawater react with calcium hydroxide in cement to form gypsum [6].

(2) Changes in CH after seawater immersion

Fig. 6 shows the results of DTA analysis before and after seawater immersion, and Fig. 7 shows the results of hydroxide content in cement before and after seawater immersion calculated from the TG analysis results.

As shown in Fig. 6, before seawater immersion, the pyrolysis reaction of calcium hydroxide (CH) was observed at 450-500°C. At 7 and 14 days of seawater immersion, pyrolysis reactions were observed at 450-500°C and 340-410°C. At 56 and 91 days of seawater immersion, only the pyrolysis reaction at 450-500°C was observed. This can be attributed to the reaction of magnesium salts ($MgSO_4$, $MgCl_2$) in seawater with CH in cement, forming magnesium hydroxide (MH) [15]. The weight loss observed at 340-410°C is due to brucite. However, as shown in Fig. 7, not all CH reacts to form MH. It is hypothesized that this occurs because some CH dissolves into the seawater after immersion.

Ett:ettringite,Ms:monosulfate,gyp:gypsum
C$_4$AF:ferrite,F:friedel's salt

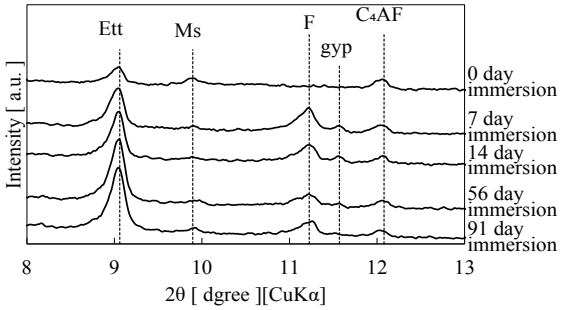

Fig. 5 XRD patterns before and after seawater immersion (OPC_Non-Carbo)

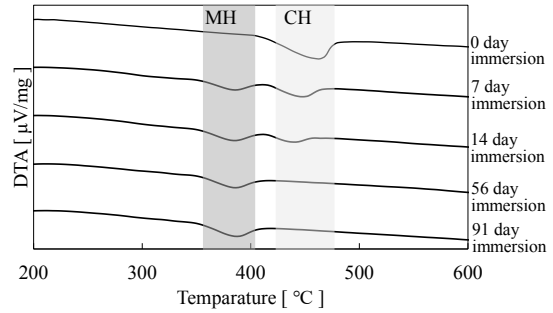

Fig. 6 Qualitative determination of hydroxides by DTA (OPC_Non-Carbo)

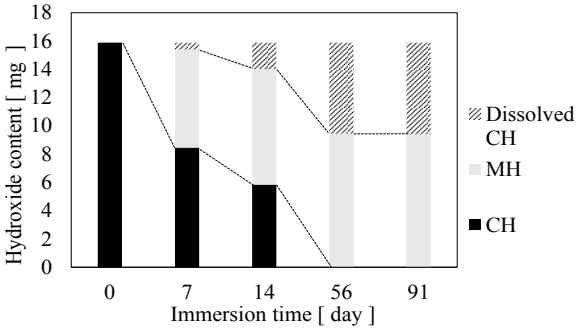

Fig. 7 Amount of hydroxide and type of hydroxide in cement (OPC_Non-Carbo)

3.4 Analysis results of OPC_ Carbo samples after seawater immersion

(1) Changes in AFm phase after seawater immersion

Fig. 8 shows the results of XRD analysis of OPC_Carbo. A trace amount of Friedel's salt was observed on day 7 of seawater immersion. However, due to the decomposition of monosulfate (Ms) by enforced carbonation in the OPC_Carbo sample, it was inferred that Friedel's salt formation was not due to ion exchange between Ms and Cl^- in seawater. Instead, it was formed through the reaction between calcium aluminate hydrate and Cl^- in seawater.

No gypsum was observed after seawater immersion. The reason for this is assumed to be that the CH in the cement reacted with CO_2 to form $CaCO_3$ through enforced carbonation, and the remaining unreacted CH was covered by $CaCO_3$ by the protective layer, which acted as a barrier and did not react with the sulfate in the seawater [12].

In addition, ettringite formation was observed at very low amounts compared with the OPC_Non-Carbo sample. We speculated that this was due to a decrease in calcium aluminate hydrate reacting with CO_2 by carbonation.

(2) Changes in CH after seawater immersion

Fig. 9 shows the results of DTA analysis before and after seawater immersion, and Fig. 10 shows the results of hydroxide content in cement before and after seawater immersion calculated by TG analysis results.

Fig. 9 shows that even though the pyrolysis reaction of CH was observed at 450-500°C before seawater immersion and at 7, 14, and 56 days of seawater immersion, no MH was observed. The reason that MH was not observed was inferred to be that magnesium salts in seawater did not react due to the barrier function of the protective layer on the surface of CH as well as the reason that gypsum was not formed.

As depicted in Fig. 10, no calcium hydroxide (CH) was observed after 91 days of seawater immersion. It was concluded that all CH present after enforced carbonation had dissolved into the seawater.

(3) Stability of $CaCO_3$ produced by enforced carbonation

Fig. 11 shows the results of XRD analysis of OPC_Carbo of $CaCO_3$ after immersion in seawater.

Vaterite and calcite remained stable after seawater immersion, and no significant change in peak intensity was observed. The $CaCO_3$ covering CH as a protective layer is thought to have leached into seawater after seawater immersion, but since the amount of CH is small, the amount of $CaCO_3$ covering CH is also considered to be small, and no significant change in peak intensity was observed.

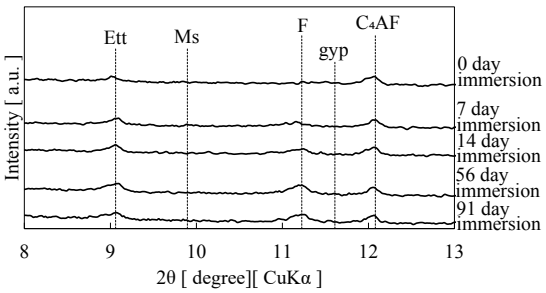

Fig. 8 XRD patterns before and after seawater immersion (OPC_Carbo)

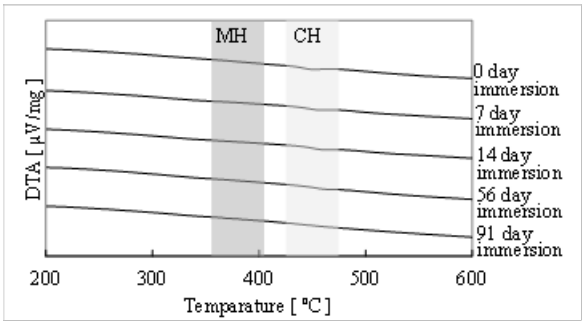

Fig. 9 Qualitative determination of hydroxides by DTA (OPC_Carbo)

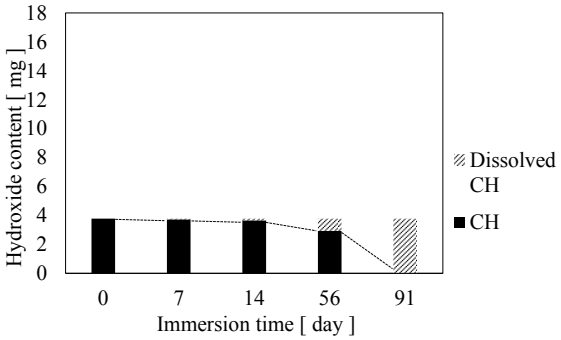

Fig. 10 Amount of hydroxide and type of hydroxide in cement (OPC_Carbo)

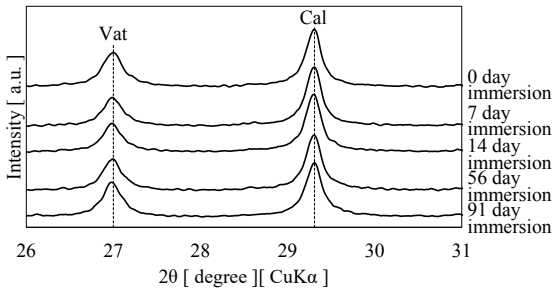

Fig. 11 XRD pattern before and after seawater immersion ($CaCO_3$)

(4) CO_2 fixation rates before and after seawater immersion

Fig. 12 shows the results of CO_2 fixation rates before and after seawater immersion in OPC_Carbo samples.

No significant change in CO_2 fixation rate was observed from before seawater immersion to 91 days of seawater immersion. This may be due to the fact that no Mc was formed in the enforced carbonation sample in the AFm phase, no release of carbonate ions by ion exchange between Cl^- and CO_3^{2-} occurred, and the physical dissolution of the protective layer ($CaCO_3$) due to CH dissolution was only a trace amount.

These results suggest that the immobilized CO_2 remained stable during the initial stages of seawater immersion, and there was no substantial leaching of carbonate ions.

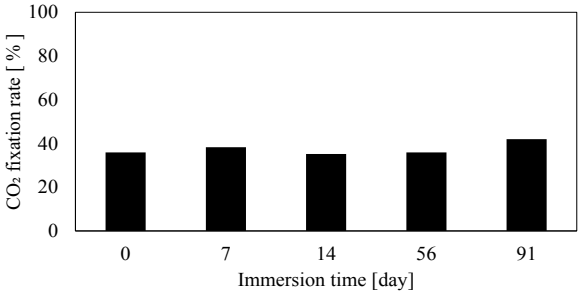

Fig. 12 CO_2 fixation rate calculated by IC (OPC_Carbo)

4. CONCLUSIONS

In this study, enforced carbonated OPC was immersed in seawater for 91 days, and the following results were obtained.

(1) The enforced carbonation of OPC did not produce monocarboaluminate, which resulted in no leaching of CO_3^{2-} by AFm ion exchange after seawater immersion.

(2) In the non-carbonated sample, CH in the cement reacted with the ions in seawater after seawater immersion, producing gypsum and brucite. However, in the carbonated samples soaked in seawater, CH was covered by $CaCO_3$ and did not react with the ions present in seawater, and neither gypsum nor brucite was observed.

(3) Calcite and vaterite formed by enforced carbonation remained stable after 91 days of seawater immersion.

(4) After 91 days of seawater immersion, CO_2 immobilized by enforced carbonation was stable and no significant leaching of CO_3^{2-} was observed.

Future studies will include sulfate degradation [16] due to the formation of thaumasite in the presence of carbonate ions and the formation of M-S-H [17] due to magnesium salts in seawater. Additionally, we intend to continue long-term immersion in seawater to clarify the stability and chemical changes of immobilized CO_2.

REFERENCE

1. F.Sano,“Evaluations on the Japan’s Greenhouse Gas Emission Reduction Target for 2030” ,Journal of Japan Society of Energy and Resources,Vol.37,No.1,2015
2. S.Sakamoto,“Emission Reductions and Carbon Dioxide Removals in Japan’s Carbon

Neutrality in 2050",Environmental Intelligence Science Academic Research Paper Series,Vol.37,2023
3. T.Nishida, Development of mixed cement with low environmental impact using limestone powder",Cement Science and Concrete Technology, Vol.66, 2012
4. K.Miyazaki,"Interaction of hydrates and gas diffusion on the progress of neutralization of hardened cement", Proceedings of the Japan Concrete Institute,Vol.42, No.1, 2020
5. T.torichigai,"Development of Materials, Manufacturing Methods, and a Quality Control for Innovative Carbon Negative Concrete-Progress in 2023- -CUCO:Carbon Utilized COncrete-",Concrete Journal, Vol.62, No.4, pp300~307, Apr.2024
6. T.Yamaji"Study on a Deterioration and Deterioration Indicator of Concrete under Marine Enviroments "Vol.66, No.1, pp.21-37, 2010.2
7. T.Sato,"Recent problems in the thermal decomposition of calcium and magnesium hydroxides", Gypsum&Lime No.146, pp.25-31,1977
8. T.Hirose,"Magnesium Hydroxide Technology Trend", Journal of the Rubber Industry Association of Japan, Vol.75, No8, pp.327-329,2002
9. E.suzuki, "Thermal Decomposition and Carbonation of Teracalcium Aluminate Monosulfate", Journal of the Society of Inorganic Materials,Vol.8, No.290, pp17-25, 2001
10. S.Kondo"Studies on Synthesis of Highly Reactive β-C_2S Bylow-temperature Heating of Carbonated C-S-H With Ca/Si＝2.0 and Utilization of Carbonation Reaction", Cement Science and Concrete Technology, Vol.74, pp.365-372
11. Ping.Yu, "Structure of Calcium Silicate Hydrate (C-S-H):Near-, Mid-, and Far-Infrared Spectroscopy" Journal of the American Ceramic Society, Vol.82, Issue 3, pp742-748, 1999
12. I.Garan, "Assessment of the protective effect of carbonation on portlandite crystals", Cement and Concrete Research, Vol.74 pp68-77, 2015
13. E.Sakai, "Morphology control of calcium aluminide hydrates", Inorganic Materials, Vol.2, No.258, pp.375-382, 1995
14. T.Iyoda,"Comparison of Salt Immobilization on Immersion Test in Different Salt Concentration of Various Admixtures",Cement Science and Concrete Technology, Vol.69, No.1, pp.470-447, 2015
15. N.Yoshida, "Deterioration phenomena of various mortars immersed in $MgSO_4$ and Na_2SO_4 solutions", Proceedings of the Japan Concrete Institute, Vol.37, No.1, pp709-714,2015
16. N.Yoshida "Thaumasite Form of Sulfate Attack－A Review of the Deterioration Mechanism and the Evaluating Method of Risk－" Concrete Journal, Vol.43, No.6, pp.20-27, Jun. 2005
17. K. De Weerdt, "The effect of sea water on the phase assemblage of hydrated cement paste", Cement & Concrete Composites, Vol.55, pp215-222, 2015

Influence of cellulose nanocrystal on the hydration and microstructure of Portland cement paste

Shuai Bai
Lecturer, School of Civil Engineering, Harbin Institute of Technology, Harbin, China.

Xinchun Guan
Professor, School of Civil Engineering, Harbin Institute of Technology, Harbin, China

ABSTRACT:
The early hydration and microstructure of cement paste with nanocellulose (CNC) was investigated coupled with isothermal calorimetry (IC), scanning electron microscopy (SEM), and X-ray diffraction (XRD). IC results showed that at both water-cement ratios, CNC prolonged the ending time of the induction period and acceleration period and reduced the main exothermic peak to inhibit early hydration. The inhibition effect became more significant with the increase of CNC dosage. XRD results showed that CNC inhibited the formation of ettringite and portlandite, and SEM images also confirmed that CNC delayed the formation and deposition of early hydration products. In the presence of CNC, porous microstructures were formed later, and the appearance of needle-like C-S-H gels was also delayed. After 24 h of hydrating, the needle-like C-S-H gels appeared first in CNC-cement paste, and the early-formed structure was also denser than pure cement paste.

Keywords: nanocellulose; cement; early hydration; microstructure

1. INTRODUCTION

Nanocellulose, as a new type of nanomaterial extracted from natural plants, can generally be divided into three categories: bacterial nanocellulose (BNC), cellulose nanofibril (CNF), and cellulose nanocrystal (CNC) [9]. Compared with other nanomaterials, it has the advantages of high mechanical properties, lightweight, and large specific surface area. The elastic modulus and crystallinity of nanocellulose can reach 220 GPa [10] and 84~89% [11], respectively. It makes nanocellulose comparable to existing nanomaterials in improving the properties of cement and concrete materials. Academics have found that lightweight and tough nanocellulose can limit cracking in cement-based material, effectively enhance mechanical properties such as compressive strength [12], flexural strength [13,14], elastic modulus [15,16] and toughness [17,18], and improve the durability such as autogenous shrinkage [19], sulfate corrosion [20], carbonation [21,22,23] and freeze-thaw [24,25]. It is not difficult to see that nanocellulose has shown great potential in improving the performance of concrete. In addition, nanocellulose derived from wood or plants is intrinsically green, renewable, and sustainable. The large-scale application of nanocellulose in cement and concrete materials will be valuable and meaningful for environmental, energy, and resource conservation [9,26].

In order to maximize the utilization of nanocellulose to regulate the properties of concrete, it is necessary to focus on the micro-mechanism of nanocellulose, especially cement hydration. Fu et al. [27] studied the influence of CNC on cement hydration by isothermal calorimetry and thermogravimetric analysis. They found that CNC delayed early-age hydration but increased the 7-day and 28-day total heat release and Ca(OH)2 content. Cao et al. [28] believed that two mechanisms could explain the acceleration effect of CNC on cement hydration. First, the steric stabilization between CNCs and cement particles is similar to the dispersion mechanism of superplasticizers, and second, CNCs provide the paths for water diffusion through the hydration product shell to the unhydrated cement particles. Flores et al. [29] noted that CNC delayed early hydration due to its adsorption onto cement particle surfaces. However, the steric stabilization between CNC and cement particles could promote later hydration. The study by Vanin et al. [30] indicated that CNC effectively improved the 7-day hydration degree of cement paste with the increase of CNC dosage from 0% to 1.0%. Furthermore, Lee and Kim [31] also reported that in the presence of CNC, the amount of C-S-H of fiber-reinforced ECC increased by up to 18%, and the hydration of unhydrated areas in the cement was enhanced. Although the positive effect of CNC on cement hydration has been confirmed, relevant studies are still in the initial stage. For example, the influence of dosage and dispersibility and the influence of CNC at different water-cement ratios and hydration temperatures still need to be further studied.

Therefore, this paper investigated the early hydration of cement paste with CNC at low and high water-cement ratios, and the influence of CNC dosage and water-cement ratio was highlighted. Isothermal calorimetry, SEM, and XRD analysis were carried out to study the hydration heat evolution, hydration products, and microstructure of cement paste containing CNC. Based on the above analysis results, the influence mechanism of CNC on the early hydration process was explained.

2. EXPERIMENTS

2.1 Raw materials

Portland cement (P·O 42.5) contains 21.14% SiO_2,

5.72% Al_2O_3, 3.62% Fe_2O_3, 64.84% CaO, 1.53% MgO, 0.45% Na_2O_{eq}, and 1.33% f-CaO, which conforms to the Chinese standard GB175-2007. The cellulose nanocrystal (CNC) was purchased by Guilin Qihong Technology Co., Ltd., and the properties of CNC are given in Table 1.

Table 1. Properties of cellulose nanocrystal.

Type	OD /(nm)	Length /(nm)	Purity /(%)	Functional group	Zeta potential (mV)	State
CNC	4-10	100-500	> 99.6	-COONa/-OH	-17.7	Powder

2.2 Sample preparation

Cellulose nanocrystal (CNC) was added to Portland cement as additive incorporation. The water-cement ratios of 0.3 and 0.5 was chosen. To minimize possible agglomeration of CNC in fresh paste, CNC powders were dispersed into water ultrasonically for 30 min in advance. All cement pastes with and without CNC were prepared according to the Chinese standard GB/T 17671-1999 [32] and cured at 25℃ for different hydration ages.

3. RESULTS

3.1 Hydration exotherm and hydration kinetics of CNC-cement paste

Cumulative exothermic curves of CNC-cement pastes are displayed in Fig. 3. At a water-cement ratio of 0.3, cumulative exothermic curves of cement pastes containing different dosages of CNC are lower than that of pure cement paste, especially at 0.4% CNC. At a water-cement ratio of 0.5, cumulative exothermic curves of CNC-cement pastes can be divided into two stages of hydration. In the first stage, cumulative exothermic curves of cement pastes containing different dosages of CNC are lower than that of pure cement paste, while the opposite phenomenon occurs in the second stage. From 0.05% to 0.4% CNC dosages, the turning points of the first and second stages are 50h, 45h, 55h, and 80h, respectively. The above results show that at a higher water-cement ratio, CNC can have a pronounced acceleration effect at least after hydration for 45h, and excessive CNC dosage results in a significant extension of the required hydration time. Moreover, exothermic rate curves of CNC-cement pastes are also displayed in Fig. 4. Unlike the cumulative exotherm, the changing trend of the exothermic rate is the same at both water-cement ratios. All curves move toward the X-axis's positive direction and the Y-axis's negative direction with increasing CNC dosage.

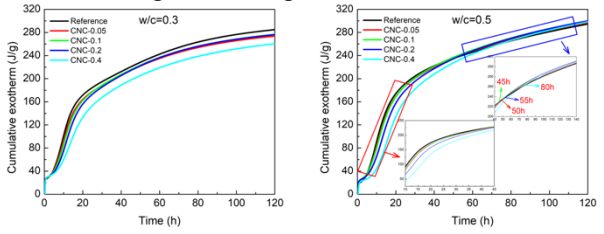

Fig. 3. Cumulative exothermic curves of CNC-cement pastes at water-cement ratios of 0.3 and 0.5.

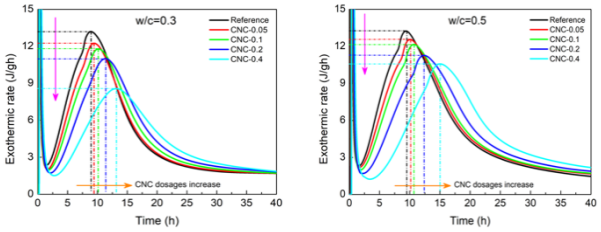

Fig. 4. Exothermic rate curves of CNC-cement pastes at water-cement ratios of 0.3 and 0.5.

3.2 Induction period and acceleration period of CNC-cement paste

Referring to the method (Fig. 5) in the literature [33], the ending time of the induction period (T1), the ending time of the acceleration period (T2), and the acceleration period duration (T2-T1) were determined and further shown in Fig. 6. At both water-cement ratios, the addition of CNC leads to a longer induction ending time and the T1 value gradually increases with CNC dosage increasing. The ending time of the acceleration period and acceleration period duration also increase with the increase of CNC dosage. Differently, after incorporating the CNC, the cumulative exotherm of the acceleration period increases at a water-cement ratio of 0.3, while the cumulative exotherm of the acceleration period decreases at a water-cement ratio of 0.5 (shown in Fig. 6). Moreover, the main exothermic peak value decreases with the increase of CNC dosage. The above results indicate that CNC prolongs the ending time of the induction period and inhibits the main exothermic peak. Although CNC prolongs the acceleration period, it still inhibits the cumulative exotherm during the acceleration period in case of a low water-cement ratio (0.3).

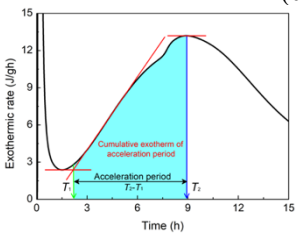

Fig. 5. Typical schematic representation of critical points (T1 and T2) for cement hydration.

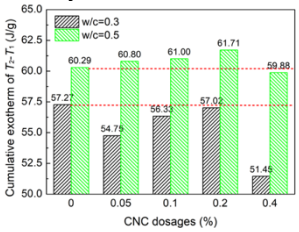

Fig. 6. Cumulative exotherm of acceleration period of CNC-cement pastes at water-cement ratios of 0.3 and 0.5.

The hydration parameters of CNC-cement pastes are shown in Fig. 7. Overall, the parameter values under the water-cement ratio of 0.5 are higher than those under the water-cement ratio of 0.3. For the induction ending time (Fig. 7a), the T1 values of both water-cement ratios are relatively close at CNC dosages of 0%~0.2%. As the CNC dosage is up to 0.4%, the gap between T1 values of both water-cement ratios increases suddenly. For the acceleration ending time (Fig. 7b), there is an apparent gap between the T2 values of both water-cement ratios,

and this gap increases with the increase of CNC dosage. For the acceleration period duration (Fig. 7c), the gap between the T2-T1 values of both water-cement ratios is relatively stable. For the main exothermic peak (Fig. 7d), the gap between peak values of both water-cement ratios is large at a CNC dosage of 0.4%. The above results indicate that the conditions of high CNC dosage and low water-cement ratio aggravate the retarding effect of CNC on early hydration.

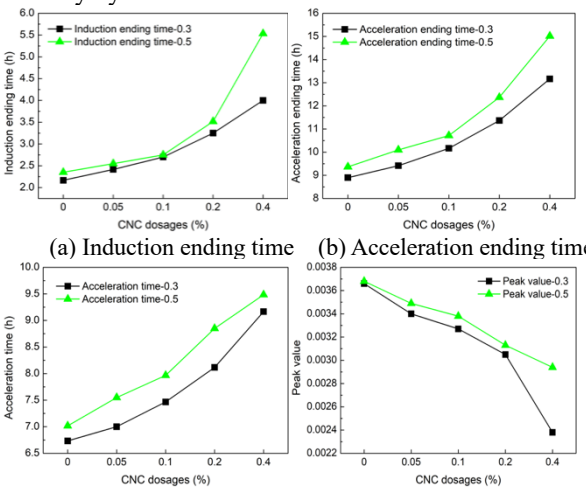

(a) Induction ending time (b) Acceleration ending time

(c) Acceleration period durati (d) Exothermic peak

Fig. 7. Hydration parameters of CNC-cement pastes at water-cement ratios of 0.3 and 0.5.

3.3 Phase evolution and microstructure of CNC-cement paste

The pure cement pastes (Reference) and 0.2% CNC-cement pastes (CNC-0.2) with a water-cement ratio of 0.5 were selected for XRD analysis to investigate the effect of CNC on partial hydration products in the early hydration stage. The evolution of various mineral phases involved in hydrating cement pastes is marked in Fig. 8. For ettringite [34], a significant peak (~9.07 nm) for ettringite can be observed after 10h, and the peak intensity of pure cement paste is higher than that of CNC-cement paste, even up to 24h. For portlandite [35], it is observed that the prominent peak intensities of pure cement paste are much higher than those of CNC-cement pastes after 5.5h. As the hydration proceeds to 24h, the prominent peak intensities of both cement pastes gradually approached. For C3S and C2S [36], it is seen that the peak intensities of pure cement pastes are consistently lower than those of CNC-cement pastes. The above observation indicates that the presence of CNC slows down the depletion of C3S and C2S and simultaneously retards the formation of ettringite and portlandite, which also confirms the retarding effect of CNC on early cement hydration.

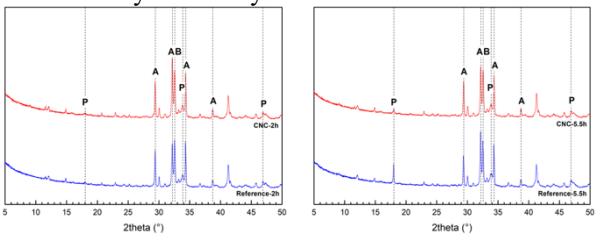

(a) 2h (b) 5.5h

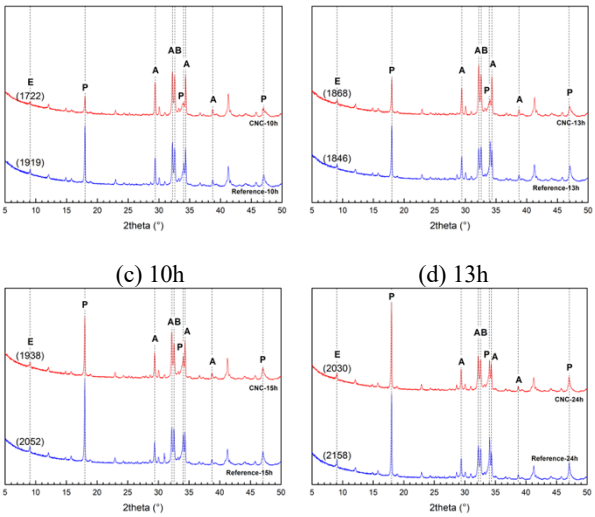

(c) 10h (d) 13h

(e) 15h (f) 24h

Fig. 8. XRD patterns of pure cement pastes and 0.2% CNC-cement pastes at a water-cement ratio of 0.5. (A: C3S, B: C2S, E: ettringite, and P: portlandite)

Moreover, the SEM images of pure cement pastes (Reference) and 0.2% CNC-cement pastes (CNC-0.2) at different hydration ages are displayed in Fig. 9. After 2h of hydration, it is found that hydration degrees of both pastes are extremely low, mainly composed of unhydrated cement particles. However, obvious hydration products can be observed on the surface of cement particles in pure cement paste but not on the surface of CNC-cement paste. As the hydration reaction proceeds to 5.5h, hydration products are gradually formed and accumulated. Comparing Figs. 9c and 9d, it is observed that hydration products generated on the surface of the cement particles in pure cement paste are significantly more than those of CNC-cement paste. It was further found that when the hydration reaction lasted for 10h, cement particles were basically completely covered by hydration products in pure cement paste, while only a tiny part of hydration products were deposited on the surface of cement particles in CNC-cement paste. The above observation suggests that the incorporation of CNC inhibits early hydration, which is consistent with the results of early hydration heat evolution. After 24h of hydration, it is observed that a large number of needle-like C-S-H gels appeared in CNC-cement paste, and the early formed structure was also denser compared with pure cement paste. This phenomenon shows that the positive effect of CNC on cement hydration gradually appears as the hydration reaction continues.

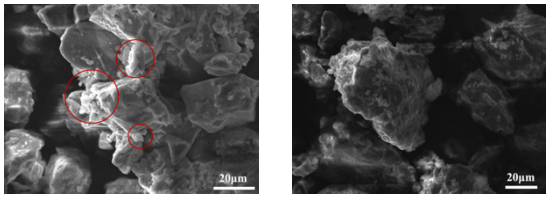

(a) Reference-2h (b) CNC-0.2-2h

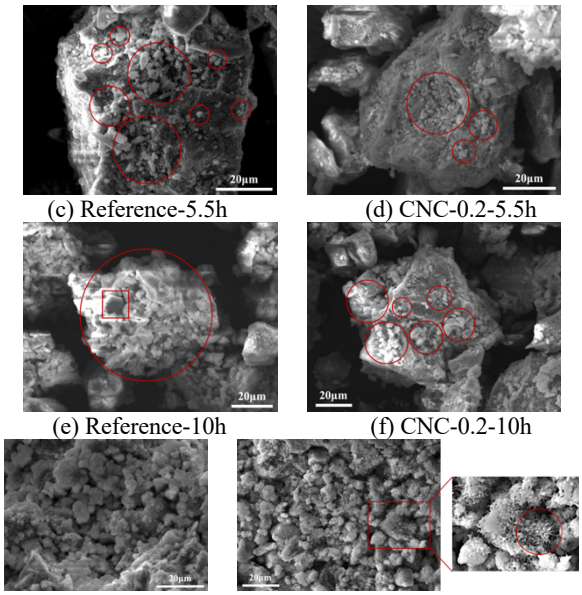

(c) Reference-5.5h (d) CNC-0.2-5.5h

(e) Reference-10h (f) CNC-0.2-10h

(g) Reference-24h (g) C NC-0.2-24h

Fig. 9. SEM images of pure cement pastes and 0.2% CNC-cement pastes at a water-cement ratio of 0.5.

4. CONCLUSIONS

Early hydration of cement paste with different dosages of CNC at low and high water-cement ratios was investigated, and the mechanism of CNC on early hydration was attempted to be explained. The following conclusions can be drawn:

(1) CNC had an inhibition effect on the early hydration of cement, mainly including the delay of the ending time of the induction period and acceleration period and the decrease of the main exothermic peak. However, the effects of CNC at low and high water-cement ratios were not the same. At a water-cement ratio of 0.3, the cumulative exotherms of CNC-cement pastes were inhibited before 120 h. At a water-cement ratio of 0.5, the cumulative exotherms of CNC-cement pastes were inhibited at the initial stage, but the inhibition effect of CNC gradually disappeared with the increase of hydration time (as early as 45h).

(2) In the presence of CNC, the formation of ettringite and portlandite was significantly inhibited before 24 h of hydrating. SEM images also prove that CNC inhibited the formation and deposition of early hydration products. After 24 h of hydrating, the needle-like C-S-H gels were first observed in the CNC-cement paste, and hydration products were smaller in size and more uniform in distribution.

(3) The mechanism of CNC on early hydration was different under high and low water-cement ratios. At a high water-cement ratio (0.5), CNC with a negative charge could adsorb on the surface of C3A with a positive charge, thereby reducing the contact area between C3A and free water to inhibit the hydration reaction. Meanwhile, the hydrophilic CNC also provided free water transport channels for internal unhydrated clinkers, effectively promoting cement hydration. Therefore, the cumulative exothermic curve of CNC-cement paste showed the evolution characteristics of low first and then high. At a low water-cement ratio (0.3), the low free water content, together with the water absorption and charge absorption of CNC, resulted in the decrease of free water reacting with clinkers, which aggravated the inhibition of early hydration. Thus, the CNC-cement paste exhibited a lower cumulative exothermic curve.

REFERENCES

[1] M.M. Norhasri, M. Hamidah, A.M. Fadzil. Applications of using nano material in concrete: A review. Construction and Building Materials, 133(2017), 91-97.

[2] P. Dong, A. Allahverdi, C.M. Andrei, N.D. Bassim.. The effects of nano-silica on early-age hydration reactions of nano Portland cement. Cement and Concrete Composites, 133(2022), 104698.

[3] H. Chen, P. Hou, X. Zhou, L. Black, S. Adu-Amankwah, P. Feng, N. Cui, M.A. Glinicki, Y. Cai, S. Zhang, P. Zhao, Q. Li, X. Cheng. Toward performance improvement of supersulfated cement by nano silica: Asynchronous regulation on the hydration kinetics of silicate and aluminate. Cement and Concrete Research, 167(2023), 107117.

[4] O. Benkirane, S. Haruna, M. Fall. Strength and microstructure of cemented paste backfill modified with nano-silica particles and cured under non-isothermal conditions. Powder Technology, 419(2023), 118311.

[5] J. Jiang, X. Dong, H. Wang, F. Wang, Y. Li, Z. Lu. Enhanced mechanical and photocatalytic performance of cement mortar reinforced by nano-TiO2 hydrosol-coated sand. Cement and Concrete Composites, 137(2023), 104906.

[6] L. Zhang, G. Lin, X. Qian, D. Yan, K. Qian, S. Ruan. Unveil the role of nano-CaCO3 in early shrinkage and tensile properties of cement paste: From experimental work to modeling. Composites Part B: Engineering, 243(2022), 110185.

[7] X. Ming, Q. Liu, M. Wang, Y. Cai, B. Chen, Z. Li. Improved chloride binding capacity and corrosion protection of cement-based materials by incorporating alumina nano particles. Cement and Concrete Composites, 136(2023), 104898.

[8] L. Raki, J. Beaudoin, R. Alizadeh, J. Makar, T. Sato. Cement and concrete nanoscience and nanotechnology. Materials, 3(2)(2010), 918-942.

[9] R.F. Santos, J.C.L. Ribeiro, J.M. Franco de Carvalho, W.L.E. Magalhães, L.G. Pedroti, G.H. Nalon, G.E.S.D. Lima. Nanofibrillated cellulose and its applications in cement-based composites: A review. Construction and Building Materials, 288(2021), 123122.

[10] R.J. Moon, A. Martini, J. Nairn, J. Simonsen, J. Youngblood. Cellulose nanomaterials review: structure, properties and nanocomposites. Chemical Society Reviews, 40(7)(2011), 3941-3994.

[11] W. Czaja, D. Romanovicz, R.M. Brown. Structural investigations of microbial cellulose produced in stationary and agitated culture. Cellulose, 11(2004), 403-411.

[12] R. Mejdoub, H. Hammi, J.J. Suñol, M. Khitouni, A. M'nif, S. Boufi. Nanofibrillated cellulose as nanoreinforcement in Portland cement: Thermal, mechanical and microstructural properties. Journal of Composite Materials, 51(17)(2017), 2491-2503.

[13] O. Onuaguluchi, D.K. Panesar, M. Sain. Properties of nanofibre reinforced cement composites. Construction and Building Materials, 63(2014), 119-124.

[14] R. Reixach, J. Claramunt, M.À. Chamorro, J. Llorens, M.M. Pareta, Q. Tarrés, P. Mutjé. On the Path to a New Generation of Cement-Based Composites through the Use of Lignocellulosic Micro/Nanofibers. Materials, 12(10)(2019), 1584.

[15] J. Claramunt, H. Ventura, R.D. Toledo Filho, M. Ardanuy. Effect of nanocelluloses on the microstructure and mechanical performance of CAC cementitious matrices. Cement and Concrete Research, 119(2019), 64-76.

[16] F. Mohammadkazemi, K. Doosthoseini, E. Ganjian, M.

Azin. Manufacturing of bacterial nano-cellulose reinforced fiber−cement composites. Construction and Building Materials, 101(2015), 958-964.
[17] C.S. Fonseca, M.F. Silva, R.F. Mendes, P.R.G. Hein, A.L. Zangiacomo, H. Savastano Jr, G.H.D. Tonoli. Jute fibers and micro/nanofibrils as reinforcement in extruded fiber-cement composites. Construction and Building Materials, 211(2019), 517-527.
[18] S.J. Peters, T.S. Rushing, E.N. Landis, T.K. Cummins. Nanocellulose and microcellulose fibers for concrete. Transportation Research Record: Journal of the Transportation Research Board, 2142(2018), 25-28.
[19] O.A. Hisseine, N.A. Soliman, B. Tolnai, A. Tagnit-Hamou. Nano-engineered ultra-high performance concrete for controlled autogenous shrinkage using nanocellulose. Cement and Concrete Research, 137(2020), 106217.
[20] J. Goncalves, M. El-Bakkari, Y. Boluk, V. Bindiganavile. Cellulose nanofibres (CNF) for sulphate resistance in cement based systems. Cement and Concrete Composites, 99(2019), 100-111.
[21] Z. Zhang, U. Angst. Microstructure and moisture transport in carbonated cement-based materials incorporating cellulose nanofibrils. Cement and Concrete Research, 162(2022), 106990.
[22] V. Pizzol, L. Mendes, L. Frezzatti, H. Savastano Jr, G. Tonoli. Effect of accelerated carbonation on the microstructure and physical properties of hybrid fiber-cement composites. Minerals Engineering, 59(2014), 101-106.
[23] S.F. Santos, R. Schmidt, A.E. Almeida, G.H. Tonoli, H. Savastano. Supercritical carbonation treatment on extruded fibre–cement reinforced with vegetable fibres. Cement and Concrete Composites, 56(2015), 84-94.
[24] D. Barnat-Hunek, M. Szymańska-Chargot, M. Jarosz-Hadam, G. Łagód. Effect of cellulose nanofibrils and nanocrystals on physical properties of concrete. Construction and Building Materials, 223(2019), 1-11.
[25] H. Lee, W. Kim. Long-term durability evaluation of fiber-reinforced ECC using wood-based cellulose nanocrystals. Construction and Building Materials, 238(2020), 117754
[26] A. Barhoum, K. Deshmukh, M. García-Betancourt, S. Alibakhshi, S.M. Mousavi, A. Meftahi, M.S.K. Sabery, P. Samyn. Nanocelluloses as sustainable membrane materials for separation and filtration technologies: Principles, opportunities, and challenges. Carbohydrate Polymers, 317(2023), 121057.
[27] T. Fu, F. Montes, P. Suraneni, J. Youngblood, J. Weiss. The influence of cellulose nanocrystals on the hydration and flexural strength of Portland cement pastes. Polymers, 9(9)(2017), 424.
[28] Y. Cao, P. Zavaterri, J. Youngblood, R. Moon, J. Weiss. The influence of cellulose nanocrystal additions on the performance of cement paste. Cement and Concrete Composites, 56(2015), 73-83.
[29] J. Flores, M. Kamali, A. Ghahremaninezhad. An investigation into the properties and microstructure of cement mixtures modified with cellulose nanocrystal. Materials, 10(5)(2017), 498.
[30] D.V.F. Vanin, V.D. Andrade, T.A. Fiorentin, D.O.D.S. Recouvreux, H.A. Al-Qureshi. Cement pastes modified by cellulose nanocrystals: a dynamic moduli evolution assessment by the impulse excitation technique. Materials Chemistry and Physics, 239(2019), 122038.
[31] H. Lee, W. Kim. Long-term durability evaluation of fiber-reinforced ECC using wood-based cellulose nanocrystals. Construction and Building Materials, 238(2020), 117754.
[32] GB/T 17671-1999, Method of Testing Cements: Determination of Strength, 1999. Beijing.
[33] M.M. Costoya Fernández. Effect of particle size on the hydration kinetics and microstructural development of tricalcium silicate (No. THESIS). (2008) EPFL.
[34] I. Kirchberger, F. Goetz-Neunhoeffer, J. Neubauer. Enhancing the aluminate reaction during OPC hydration by combining increased sulfate content, triethanolamine and tartaric acid. Cement and Concrete Research, 170(2023), 107188.
[35] K. Xue, C. Wan, Y. Xu, Y. Jiang, Y. Cheng. Effect of pre-hydration age on phase assemblage, microstructure and compressive strength of CO2 cured cement mortar. Construction and Building Materials, 325(2022), 126760.
[36] J. Chen, A. Akono. Influence of multi-walled carbon nanotubes on the hydration products of ordinary Portland cement paste. Cement and Concrete Research, 137(2020), 106197.
[37] Yuan R. Cementitious Material Science (in Chinese). 2nd ed. Wuhan: Wuhan University of Technology Press, (1996), 86-91.
[38] H.F. Taylor. Cement chemistry. 2nd ed. London: Thomas Telford, (1997), 193-194.
[39] I. Kirchberger, F. Goetz-Neunhoeffer, J. Neubauer. Enhancing the aluminate reaction during OPC hydration by combining increased sulfate content, triethanolamine and tartaric acid. Cement and Concrete Research, 170(2023), 107188.
[40] K. Scrivener, A. Ouzia, P. Juilland, A. Kunhi Mohamed. Advances in understanding cement hydration mechanisms. Cement and Concrete Research, 124(2019), 105823.

DEVELOPMENT OF CONCRETE RHEOLOGY PARAMETER PREDICTION MODEL BASED ON CONCRETE SLUMP FLOW USING MACHINE LEARNING ALGORITHM

LEE, Yu-Jeong
Ph.D Candidate, Department of Architectural Engineering, Gyeongsang National University, Jinju, 52828, Korea

LEE, Kang-Hyeok
Master student, Department of Architectural Engineering, Gyeongsang National University, Jinju, 52828, Korea

KIM, In-Tae
Master student, Department of Architectural Engineering, Gyeongsang National University, Jinju, 52828, Korea

LIM, Young-Ju
Master student, Department of Architectural Engineering, Gyeongsang National University, Jinju, 52828, Korea

HAN, Dong-Yeop
Associate Professor, Department of Architectural Engineering, and Engineering Research Institute, Gyeongsang National University, Jinju, 52828, Korea

ABSTRACT:
The Concrete is a complex mixture composed of various materials, and its fluidity is treated as an important physical property because it has a high relationship with other properties of concrete.The slump flow test is commonly used to evaluate the fluidity of concrete. However, due to the limitations of being qualitative and subjective, a quantitative and scientific method for assessing the fluidity of concrete using rheological constants was proposed. Therefore this study aims to develop a predicting model for concrete rheological parameters based on the conventional test results of concrete slump flow using a machine learning algorithm. In this study, to achieve the research purpose, the prediction model's performance was analyzed according to the preprocessing, quality, and number of training data. As a result of the analysis, data preprocessing using both data cleaning and normalization was effective. The higher the quality and more extensive the number of training data, the better the performance of the prediction model. This study can contribute to developing a rheology parameters prediction model based on fresh concrete slump flow data.
Keywords: concrete, rheology, machine learning, artificial neural network, slump flow

1. INTRODUCTION

Concrete is a complex mixture composed of various materials and exhibits different physical properties depending on the material ratios and interactions of the binders that constitute it[1.2]. Among these properties, the fluidity of fresh concrete is known to be related to other characteristics such as ease of construction, resistance to material separation, and pumpability, making it one of the critical physical properties of concrete. Typically, methods such as slump and slump flow measurements are used to evaluate the fluidity of concrete at construction sites[3,4]. These methods are widely used due to their ease and simplicity; however, the results can vary based on the experience and skill of the experimenter. Additionally, there are limitations in accurately assessing the fluidity of concrete through these methods[5,6]. In this context, the need for a method to quantitatively and scientifically evaluate the fluidity of fresh concrete has emerged, leading to the proposal of a method using rheology to meet these technical requirements[7,8,9].

Rheology is the study of the flow and deformation of materials, focusing on the behavior of suspensions and other substances with both solid and fluid properties [9]. Fresh concrete can be viewed as a suspension where coarse aggregates are mixed with mortar, or aggregates are mixed with cement paste[10]. The fluidity of this cement-based suspension is assumed to behave as a non-Newtonian fluid and is often described using the Bingham model[8,11,12,13]. Concrete, considered as a Bingham fluid, can have its fluidity quantitatively assessed by measuring rheological constants such as yield stress and plastic viscosity using a rheometer

[14,15,16]. However, while the measurement of rheological constants can quantitatively and scientifically define and evaluate the flow performance of concrete, it requires expensive equipment and large quantities of concrete samples. Additionally, the complex testing methods make it challenging to apply directly on construction sites [17,18,19]. Consequently, much research has been conducted to investigate the correlation between qualitative fluidity evaluation methods like slump and slump flow tests and the quantitative evaluation provided by rheological constants. It has been established that the yield stress, a rheological constant, is related to the results of slump and slump flow tests of concrete [20,21,22,23].

As the construction industry recently entered the era of the Fourth Industrial Revolution, efforts are being made to adopt and apply new technologies. With the advent of the Fourth Industrial Revolution, the construction industry can enhance productivity through advanced technologies such as the Internet of Things (IoT), AI (Artificial Intelligence), 3D printing, and BIM (Building Information Modeling). These technologies enable effective project management, ensuring high quality and safety[24]. Among these advancements, research is being conducted to efficiently manage and evaluate the quality of concrete by predicting its physical properties using various artificial intelligence techniques such as machine learning and artificial neural networks (ANN).

Machine learning, a subset of artificial intelligence, involves using algorithms to endow computers with human-like learning capabilities. It analyzes data based on artificial intelligence neural networks and includes methodologies like deep learning, which involves self-learning from analysis results to make judgments or predictions[25,26,27]. However, current studies related to predicting the physical properties of concrete using artificial intelligence techniques primarily focus on hardened concrete [28,29,30,31,32]. Research on predicting the physical properties of fresh concrete based on machine learning is relatively scarce.

The most widely used machine learning algorithm aims to automate the decision-making process by creating a generalized model learned from known cases[33,34]. When the user provides the model with the desired input and output values, the algorithm learns to produce the desired output. This learned algorithm can then generate appropriate output when given new input values. The algorithm learned in this way can produce appropriate output when given new input values. What is important when trying to predict data based on a machine learning algorithm is that a large amount of data is needed for sufficient learning and that it is necessary to analyze whether the various learning parameters of the prediction model are suitable for the data used.

Therefore, in order to more easily and efficiently utilize rheological constants, a scientific and quantitative fluidity evaluation method for fresh concrete based on a machine learning algorithm, rheology analysis was conducted using concrete slump flow data, a conventional method of fluidity evaluation data. The goal was to predict integers, and we would like to analyze the impact of the data preprocessing process and the number and quality of data used for learning on the performance of the prediction model. The development of this prediction model is expected to contribute to the quantitative fluidity evaluation of fresh concrete without direct rheological constant measurement at future construction sites.

2. THEORETICAL CONSIDERATIONS

2.1 MACHINE LEARNING

Machine Learning is shown as schematized in Figure 1, it is a field of artificial intelligence that develops systems that allow computers to improve and solve problems by learning from data without the user being explicitly programmed. Machines learn data, identify patterns, and carry out the corresponding learning. It is an artificial intelligence technology that aims to make predictions or decisions based on artificial intelligence [42]. Machine learning can be applied to solve various problems by converting large amounts of data into data with meaningful information, so many algorithms are used in various fields such as image and voice recognition, natural language processing, recommendation systems, and predictive analysis. This machine learning process largely progresses through data collection, appropriate model parameter selection, model learning and testing, and performance evaluation. Data collection and appropriate model parameter selection are steps that greatly affect the performance of the machine learning algorithm. Looking at existing studies related to machine learning, it is known that when trying to solve a problem using machine learning technology, the performance of the machine learning model improves when the problem has a lot of data and various input variables[43]. Therefore, when using machine learning technology, collecting large amounts of data and appropriate data preprocessing can have a significant impact on improving machine learning performance [44].

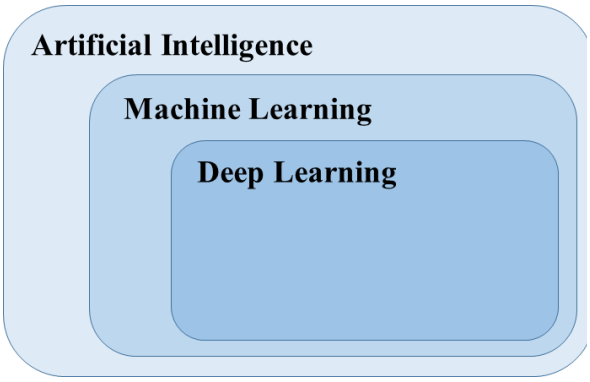

Figure 1. Diagram of Artificial Intelligence

2.2 DATA PREPROCESSING METHODS

Data preprocessing refers to the process of converting collected data into data suitable for application to machine learning algorithms to improve model learning results [45,46]. Data preprocessing methods include data cleaning, which excludes missing values or outliers that are judged to be incorrect values, contradictions that are

data that do not match the unit or type of the input data, and inconsistent data, taking into account the characteristics of the input data, and processing duplicate data. Data Integration: When learning data that can have a wide range, such as numeric data, tasks such as summarization, normalization, standardization, and aggregation are performed to narrow the range or dimension of the data. There are the same Data Transformation, Data Reduction and Data Balancing, which reduce large amounts of data to time units [47]. In this study, considering the characteristics of concrete slump flow data and rheological constant data, a data cleaning method was used to remove data outliers that may occur due to material separation, etc., and the data characteristics of the data with a relatively wide distribution range of the overall data were considered. A data transformation method was used to reduce the range, and among the data transformation methods, a method of reducing the distribution range of the data by multiplying the input data by a certain decimal number (0.001) and data normalization were used. We sought to determine the impact of the data preprocessing process on the performance of the model by analyzing how the performance of the rheological constant prediction model through concrete slump flow data based on a machine learning algorithm changes depending on the presence or absence of data preprocessing.

2.3 MODEL PERFORMANCE EVALUATION

In this study, to evaluate the performance of a prediction model using a machine learning algorithm, the coefficient of determination (R-Squared), mean square error (MSE), and mean absolute error (MAE) were used as evaluation indices.

The coefficient of determination is mainly used to evaluate the goodness of fit of a regression model and indicates how much variability the dependent variable has from given data. The coefficient of determination can be calculated through equation (2), where Y_i is the actual value, $\hat{Y}$ is the predicted value, $\overline{Y}$ is the mean of the actual values, and the closer it is to 1, the better the model can be considered to explain the data.

$$R^2 = 1 - \frac{\sum(Y_i - \hat{Y}_i)^2}{\sum(Y_i - \overline{Y})^2} \quad (1)$$

There is no absolute evaluation standard for the coefficient of determination, but in the engineering field, a coefficient of determination of 0.7 or more means high explanatory power, so the standard for evaluating prediction performance is a coefficient of determination of 0.7 or more [48].

MSE is an indicator to evaluate whether the model's output value was correctly predicted and is one of the indicators commonly used as a loss function. This is the average value obtained by squaring the difference between the actual value and the value predicted by the model. Unlike MAE, the difference between the actual value and the predicted value is squared, so Fig. As shown in Figure 2, it can be said to be equal to the average of the area of the difference between the predicted value derived from the model and the actual value. If there are outliers in the input data, the MSE value may increase.

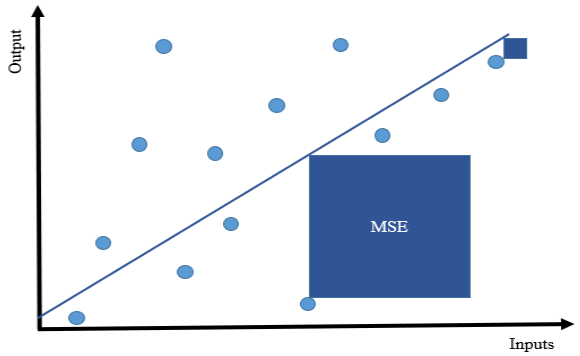

Figure 2. Concept of MSE:The Average of Differential Area between Predicted Data and Actual Data

MAE refers to the difference between the actual value and the predicted value converted to an absolute value, divided by the number of data, and averaged. Because the absolute value of the error is taken, the size of the error can be directly reflected, and it is a performance evaluation indicator suitable for use when the loss due to the error increases linearly or when there are many outliers.

MAE and MSE are indicators that express the size of the error. The smaller the value, the better the model's performance. Each performance indicator can be calculated through equations (2) and (3). In equations (2) and (3), n is the number of data, Y_i is the value of the input data (actual value), and $\hat{Y}$ is the value predicted by the model.

$$MAE = \frac{\sum_{i=1}^{n}|Y_i - \hat{Y}_i|}{n} \quad (2)$$

$$MSE = \frac{1}{n}\sum_{i=1}^{n}(Y_i - \hat{Y}_i)^2 \quad (3)$$

In this study, we attempted to evaluate the performance of the prediction model through the coefficient of determination derived using actual rheological constant data and rheological constant prediction values derived from the prediction model. In addition, in order to analyze whether the prediction model can predict with a certain level of performance, the rheological constant prediction using concrete slump flow data according to the data preprocessing process was repeated 20 times, and the minimum values of the model performance indicators MAE and MSE were derived; The maximum and average values were compared.

3. ANALYSIS PLAN

3.1 DATA SET

The training data for the prediction model to predict the rheological constant of concrete based on the slump flow data of concrete is two types: the fluidity evaluation data of fresh concrete obtained through experiment and the data predicted by machine learning algorithm are used

again as training data. It was collected through several methods. The experimental plan for creating the prediction model is shown in Table 1. The experimental plan for collecting slump flow test data and rheological constant data, which are fluidity evaluation data for fresh concrete, was conducted in the mixing range of normal strength concrete, and the number of data used to learn the prediction model was 667. In addition, the performance of the learned prediction model is affected by the number of data to be learned. According to the characteristics of the machine learning algorithm, in order to secure a large amount of learning data, the rheological constant data predicted by learning the slump flow data collected through experiments is reused. Using it as training data, we analyzed how the number of training data affects prediction performance. Table shows the number of training data used to analyze the performance of the prediction model according to data preprocessing and the quality and number of training data. Same as Table 2. 70% of the total data input for learning a prediction model based on a machine learning algorithm was used in the Train Set for learning the model, and 30% was used in the Test Set to evaluate the model's performance. To test the model, 20% of the Test Set, which was divided by 30% of the total training data, was used as a validation set to periodically evaluate the model's performance and select the optimal model during training of the prediction model. The ratio of these data sets is same as Figure 3. The training data entered into the prediction model was randomly selected according to a specified ratio and divided into Train Set, Test Set, and Validation Set.

Table. 1 Experiment Plan for Data Collection

W^* (kg/m^3)	W/C^{**}	S/a^{***}	SP^{****}(%)	Elapsed Time (m)
175 180 185 190	0.35 0.40 0.45 0.50 0.55 0.60	0.40 0.45 0.50	0 0.25 0.50 0.75 1.00	0 15 30 45 60

* Unit Water
** Water-to-cement ratio
*** Fine Aggregate Ratio
**** Superplasticizer (/cement mass %)

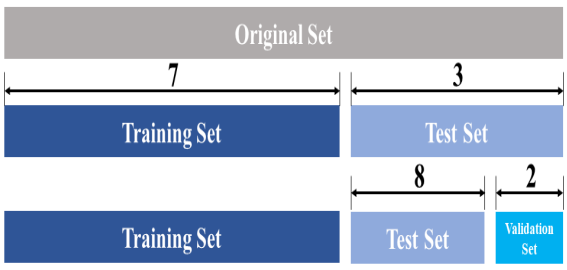

Figure 3. Dataset Split Ratio

Table. 2 Number of Data Used to Learn Rheology Constant Prediction Model

Prediction Performance Analysis according to Data Preprocessing of Training Data	
Non Preprocessing	667
Data Cleaning	625
Summarization	
Normalization	
DC * + S	
DC + N **	
DC + N + S ***	

Prediction Performance Analysis according to Quality of Training Data	
Non **** (R^2 0.29)	667
DC (R^2 0.53)	625
R^2 0.60	584
R^2 0.65	560
R^2 0.70	522
R^2 0.75	488
R^2 0.80	443
R^2 0.85	378

Prediction Performance Analysis of Models Using Predicted Data by Models with Different R-Squared of Training Data	
R^2 0.60	1640
R^2 0.65	1735
R^2 0.70	1620
R^2 0.75	1665
R^2 0.80	1507
R^2 0.85	1405

3.2 PREDICTIVE MODEL ALGORITHM

The machine learning algorithm used in this study to predict rheological constants based on slump flow data of concrete is the Multilayer Perceptron (MLP), a type of Artificial Neural Network (ANN). A multilayer neural network refers to an artificial neural network structure composed of multiple hidden layers. Multilayer neural networks are mainly used in the fields of machine learning and deep learning, and the deeper the neural network is constructed, the more complex problems it can handle and can also affect the performance of the machine learning model (Seong et al. 2022).

The detailed conditions of the multilayer neural network model used in this study are listed in Table 3. In this study, to learn an efficient model using input data, we applied a stochastic gradient descent method that divides the entire training data into 16 batches and trained them, and the optimizer was set to Adam. The error function used was MAPE (Mean Absolute Percentage Error Rate). The number of learning epochs for the entire data was set to 1000, and the number of nodes in each layer was reduced to 512, 256, 128, 64, 32, and 1. Dropout was used to randomly deactivate 50% of neurons to prevent overfitting of the model.

Table. 3 Detailed Conditions of Multilayer Perceptron Model

Activation Function	ELU
Optimizer	Adam
Hidden Layer	4
Batch Size	16
Epochs	1000

4. RESULTS ANALYSIS

4.1 ANALYSIS OF EXPERIMENTAL RESULTS

To collect data for creating a rheological constant prediction model based on slump flow data of concrete, the experiment described in Table 1 was performed. The obtained data is shown in Figures 4 and 5.

First, as shown in Figure 4, the concrete slump flow test results indicate that the overall slump flow increases as the unit water quantity, water-cement ratio, and the amount of water-reducing agent added increase.

Looking at the static yield stress measurement results among the rheological constants of concrete shown in Figure 5, it can be observed that, similar to the slump flow test results, the yield stress decreased as the unit water quantity, water-cement ratio, and the amount of water-reducing agent added increased. However, it can be seen that when the amount of water reducer added increases in a concrete mix with a high unit quantity and water-cement ratio, the yield stress increases rather than decreases. This result is attributed to the material separation boundary or segregation of the concrete, which could not be determined with the naked eye. It is believed that this is a result of the inability to measure normal rheology (Lee et al., 2020).

Through these experiments, slump flow data and rheological constant data of fresh concrete were collected. Among the 667 collected data points, those determined to be at the material separation boundary or exhibiting segregation were identified through EIS, mixing elements, slump flow, and rheological constant change trends. These data points were excluded through data cleaning, a preprocessing process.

4.2 IMPACT OF DATA PREPROCESSING ON PREDICTION MODEL

To analyze the impact of the data preprocessing process on the performance of the prediction model based on the

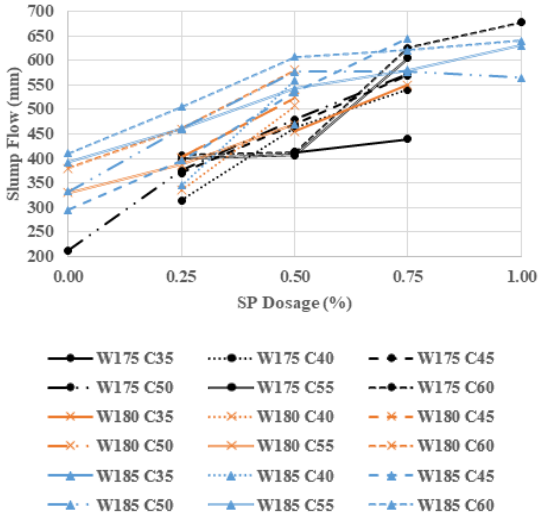

Figure 4. Slump Flow Test Results according to Mixing Factors

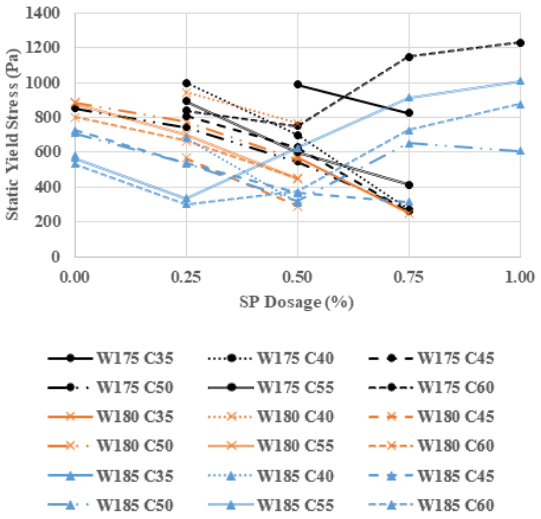

Figure 5. Static Yield Stress according to Mixing Factors

machine learning algorithm, the performance of the rheological constant prediction model through concrete slump flow data was compared and analyzed according to different preprocessing processes. The classification of the model according to the preprocessing process is shown in Table 4.

Table. 4 Classification of Predictive Models about Data Preprocessing

	Data Cleaning	Summarization	Normalization
Case 1	X	X	X
Case 2	O	X	X
Case 3	X	O	X
Case 4	X	X	O
Case 5	O	O	X
Case 6	O	X	O
Case 7	O	O	O

Figure 6 illustrates the results of evaluating the performance of the model predicting the rheological constant of fresh concrete according to data preprocessing using the MAE (Mean Absolute Error) index. When comparing Case 1 and Case 2, it is observed that the model's prediction performance slightly improves as the data cleaning process progresses. Notably, among the data preprocessing techniques, there was a significant difference in the MAE index depending on the presence or absence of Data Transformation preprocessing. In Cases 3, 4, 5, 6, and 7, where both the Data Transformation technique and Data Cleaning technique were applied, the model performance significantly improved. Among these, Case 6, which applied both the Data Normalization technique and the Data Cleaning technique, was judged to have the best performance. In the model where both data preprocessing techniques were applied together, the difference between the minimum, maximum, and average values of the MAE index decreased. This indicates that an appropriate data preprocessing process contributes to the production of uniform results by the prediction model. However, when all three preprocessing techniques (Data Cleaning, Summarization, and Normalization) were applied, the model's performance slightly decreased.

Figure 7 shows the results of evaluating the performance of the model predicting the rheological constant of fresh concrete according to data preprocessing using the MSE (Mean Squared Error) index. The performance evaluation of the model through the MSE indicator also shows similar results. As a result of evaluating the performance of the model using the MSE index, the performance of the prediction model greatly improved depending on the presence or absence of Data Transformation preprocessing. The performance improvement effect of the prediction model was significant when both the Data Transformation technique and Data Cleaning technique were applied together. Among them, Case 6, which applied both Normalization and Data Cleaning, was evaluated as having the best performance.

Figure 8 shows the prediction results of the model predicting the rheological constant of fresh concrete according to data preprocessing. It illustrates the coefficient of determination between the rheological constant data of actual fresh concrete and the rheological constant data predicted by the model, and schematizes the relationship between the predicted and actual values of the model. It was determined that the larger the coefficient of determination between the actual concrete rheological constant data and the predicted data, the more accurately the model predicted.

The performance evaluation results of the model through the coefficient of determination showed different results from those evaluated through MAE and MSE. In Case 1, the MAE and MSE indicators had very large values, but the coefficient of determination had a relatively high value. Large values of MAE and MSE mean that the model does not make accurate predictions, resulting in a large error between the actual and predicted values, which reduces prediction accuracy.

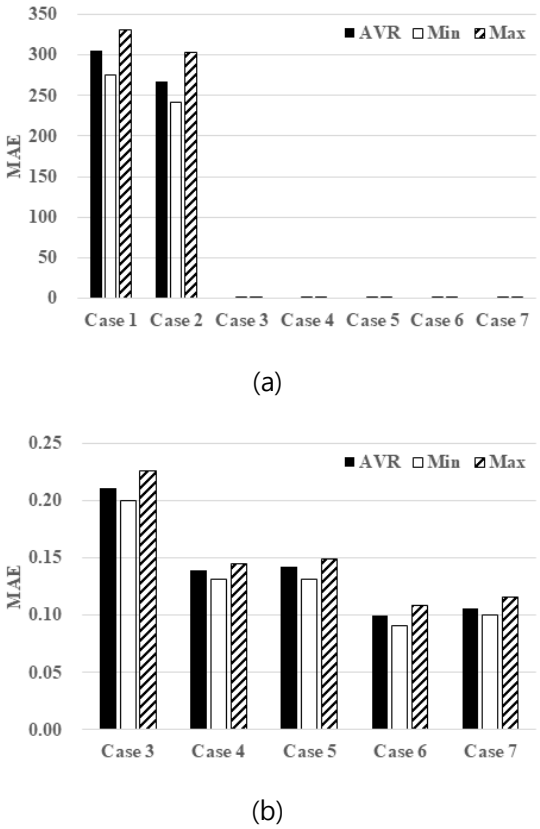

Figure 6. Model Performance Evaluation by MAE according to Data Preprocessing

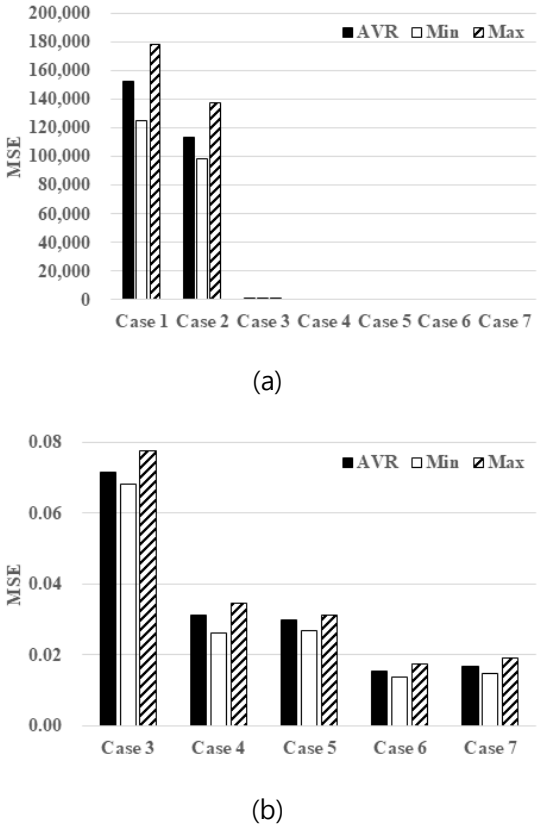

Figure 7. Model Performance Evaluation by MSE according to Data Preprocessing

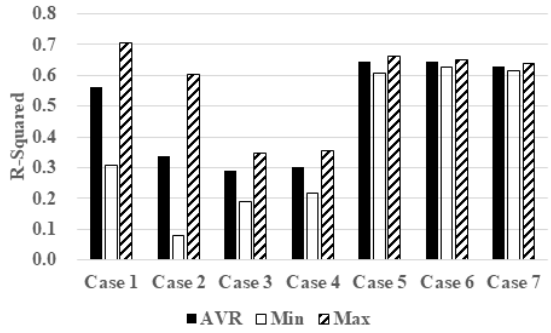

(a) R-Squared according to data Preprocessing

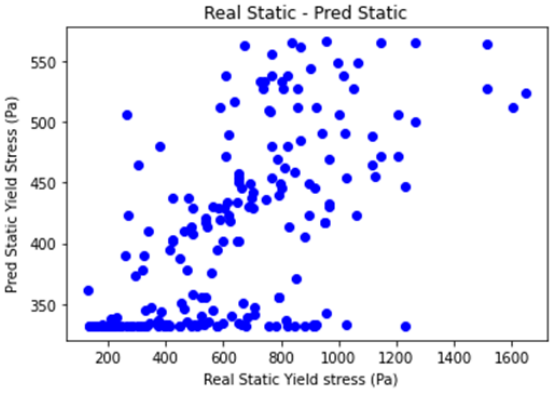

(b) Case 1 (Non Preprocessing)

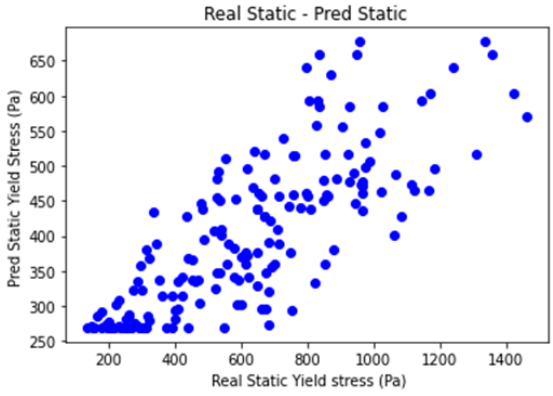

(c) Case 2 (Data Cleaning)

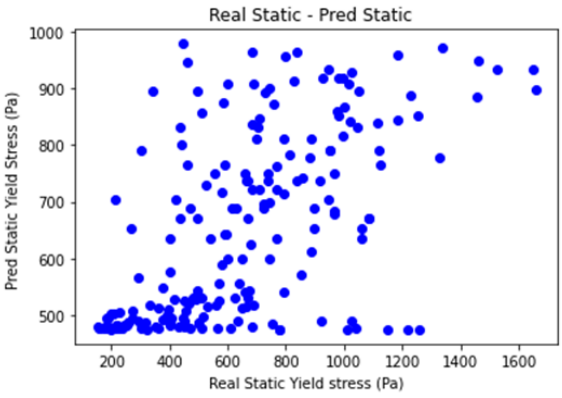

(d) Case 3 (Data Summarization)

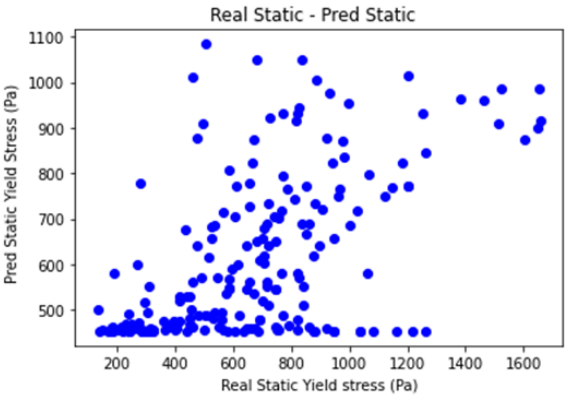

(d) Case 4 (Data Normalization)

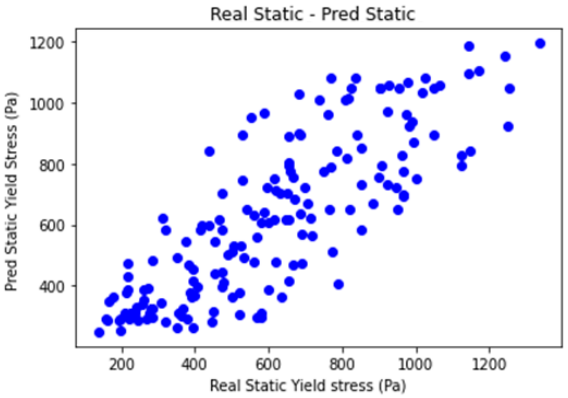

(e) Case 5 (Data Cleaning + Summarization)

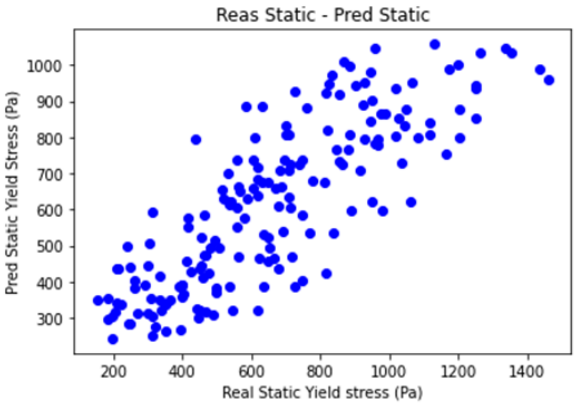

(f) Case 6 (Data Cleaning + Normalization)

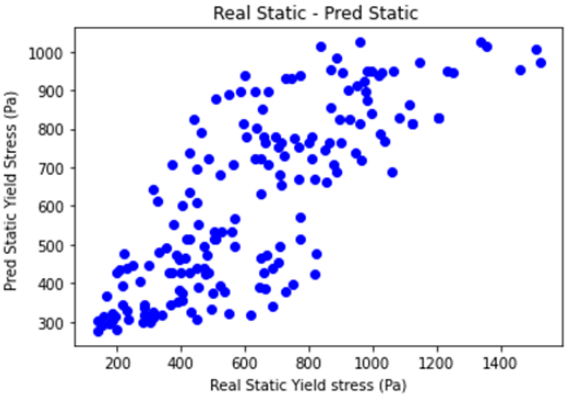

(g) Case 7 (DC + S + N)

Figure 8. Model Performance Evaluation by R-Squared and Prediction Results about Data Preprocessing

On the other hand, the coefficient of determination is an indicator of how well the model explains the volatility of the dependent variable. A larger value means that the model explains the data better. However, even if the coefficient of determination is high as in Case 1, if the MAE and MSE are large, it can be judged that the model is not predicting accurately. Additionally, in Case 1, there is a large difference between the minimum, maximum, and average values of the coefficient of determination, which means that the prediction performance changes every time the model is repeatedly trained. Case 1 is a case in which no preprocessing was performed, and it is believed that the data used for learning contained many outliers.

Similar to Case 1, in Case 2, the MAE and MSE values are large, the coefficient of determination is relatively high, and there is a significant difference in the minimum, maximum, and average values of the coefficient of determination. The performance evaluation through MAE and MSE showed significant improvement when data transformation processing was applied and outliers were removed through data cleaning. However, the coefficient of determination is believed to have decreased because the distribution of the data used for learning is relatively large.

Figure 9 shows the error according to the number of learning repetitions in Case 2. In Case 2, as learning is repeated, the error of the training data decreases, but the error of the test data initially decreases and then increases again, eventually becoming larger than the error of the training data. These results indicate that overfitting has occurred. When overfitting occurs, accurate predictions are possible with the training data, but prediction performance deteriorates when new data (Test Dataset) is input. It is known that overfitting can be improved by appropriately processing the learning data input to the model, such as using regularization techniques.

In Cases 5, 6, and 7, where Data Transformation was applied together with other preprocessing techniques, the increase in the coefficient of determination and the decrease in the difference between the minimum, maximum, and average values of the coefficient of determination are believed to be the result of improved prediction performance of the model through the processing of input data.

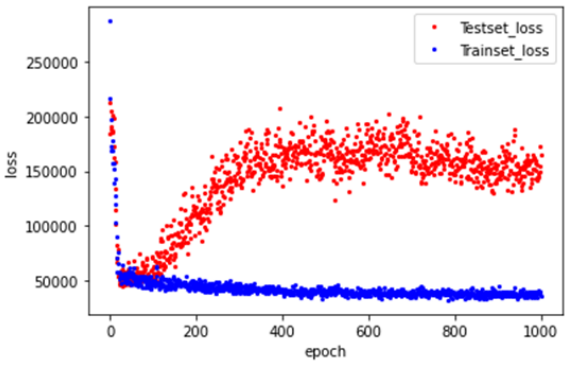

Figure 9. Loss according to Epoch in Case 2 (Data Cleaning)

In Case 3 and Case 4, it is observed that both MSE and MAE decreased, but the coefficient of determination also decreased. Small MAE and MSE indicate that the error between the model's predicted values and the actual values is small. However, a small coefficient of determination means that the model's explanatory power over the data is low, indicating that the model's predictions are inaccurate or do not explain the data well. Therefore, in Cases 3 and 4, where the MAE and MSE are small but the coefficient of determination is small, the model's performance is still judged to be insufficient.

In Case 5, 6, and 7, where both Data Transformation and Data Cleaning were applied together, it is evident that MSE and MAE decreased and the coefficient of determination increased. Additionally, when diagramming the model's predicted values and actual values, it can be seen that the data error has decreased and the data distribution has narrowed. This implies that data preprocessing has a significant impact on the performance of prediction models based on machine learning algorithms. It is believed that model performance can be improved when outlier removal and appropriate data processing are performed together.

4.3 IMPACT OF TRAINING DATA ON PREDICTION

When we previously analyzed the impact of data preprocessing on the performance of the prediction model, it was determined that outlier removal and data processing helped improve the prediction performance of the model. Accordingly, to analyze the impact of learning data on the performance of a prediction model based on a machine learning algorithm, prediction results were analyzed according to the coefficient of determination of the learning data.

Figure 10 shows the learning data with outliers removed based on the coefficient of determination. There is no absolute evaluation standard for the coefficient of determination, but in the engineering field, a coefficient of determination of 0.7 or more means high explanatory power (Cohen, 1988; Kim et al., 2022). We attempted to analyze the prediction performance when using data with an increased coefficient of determination by narrowing the distribution of data from training data from which outliers due to material separation were removed. To judge and remove outlier data, we identified data that was out of the range of the overall data distribution as shown in Figure 8(a). If the distribution of each data point was out of range due to material separation or similar issues, and if the resulting value differed significantly from other data of the mixture, it was judged to be an experimental error and was removed.

The performance evaluation results of the prediction model according to the coefficient of determination of the learning data input to the prediction model are shown in Figure 11. It was found that as the coefficient of determination of the learning data increases, the performance index of the prediction model also improves. As the coefficient of determination increases, the MAE and MSE indicators decrease, and the coefficient of determination between the predicted value

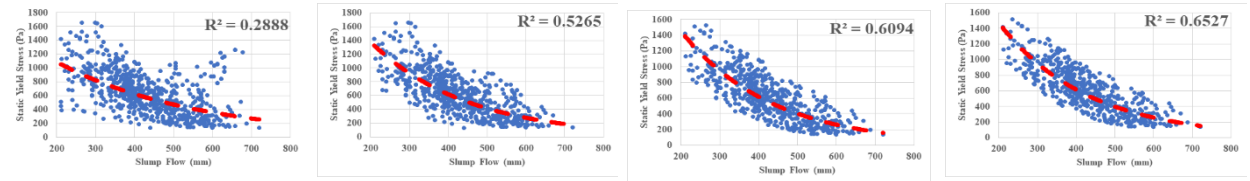

(a) Non Preprocessing (b) Data Cleaning (c) R-Squared 0.60 (d) R-Squared 0.65

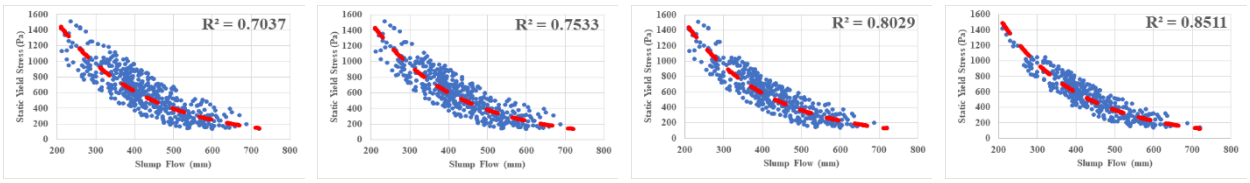

(e) R-Squared 0.70 (f) R-Squared 0.75 (g) R-Squared 0.80 (h) R-Squared 0.85

Figure 10. Training Data according to R-Squared

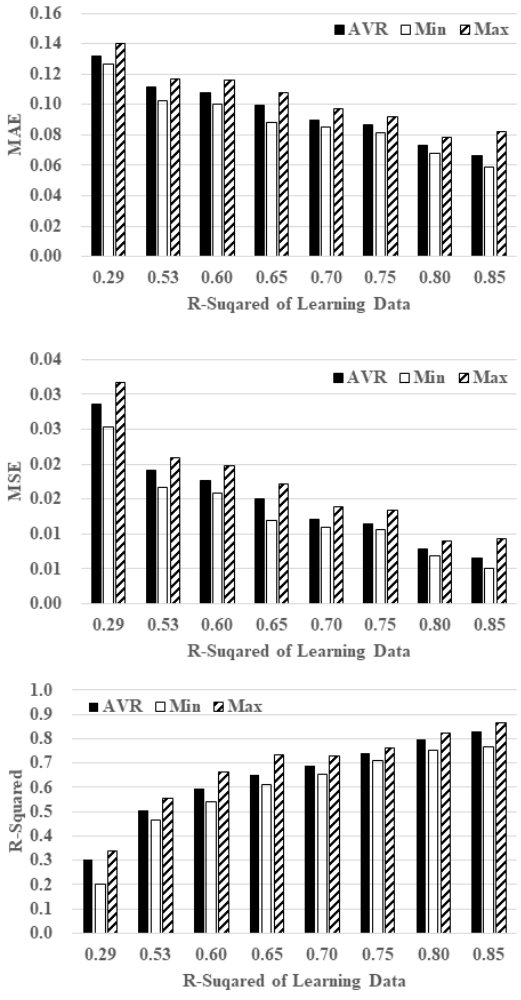

Fig. 11 Performance evaluation results of the prediction model according to R-Squared of the learning data

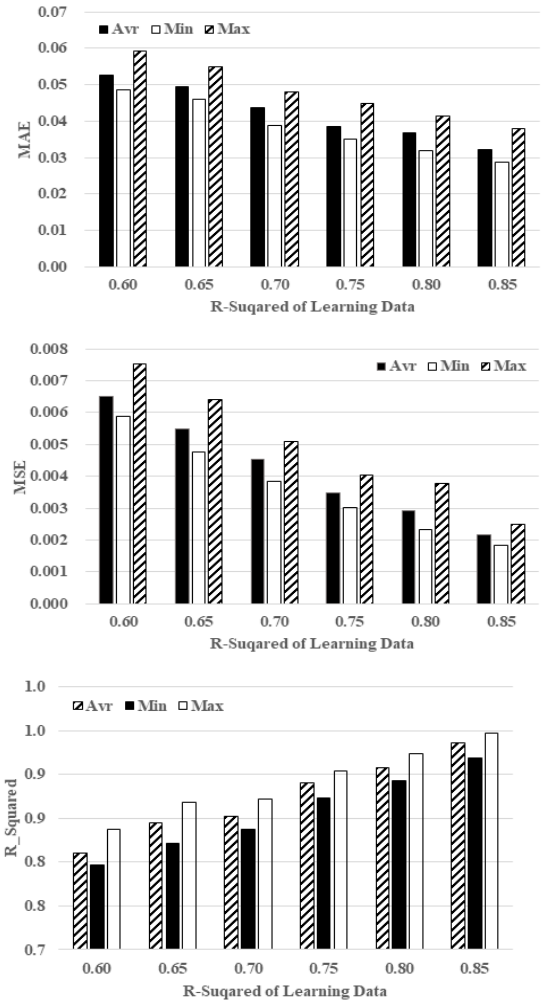

Fig. 12 Predictive performance evaluation results of the model learned using the model's predicted data

by the model and the actual value increases. This indicates that the quality of the training data affects the prediction performance of the model.

However, when the coefficient of determination of the learning data is 0.85, the difference between the minimum, maximum, and average values of the performance indicators of the prediction model decreases and then increases again. This suggests that excessively deleting data to increase the coefficient of determination of the learning data can have a detrimental effect on model performance.

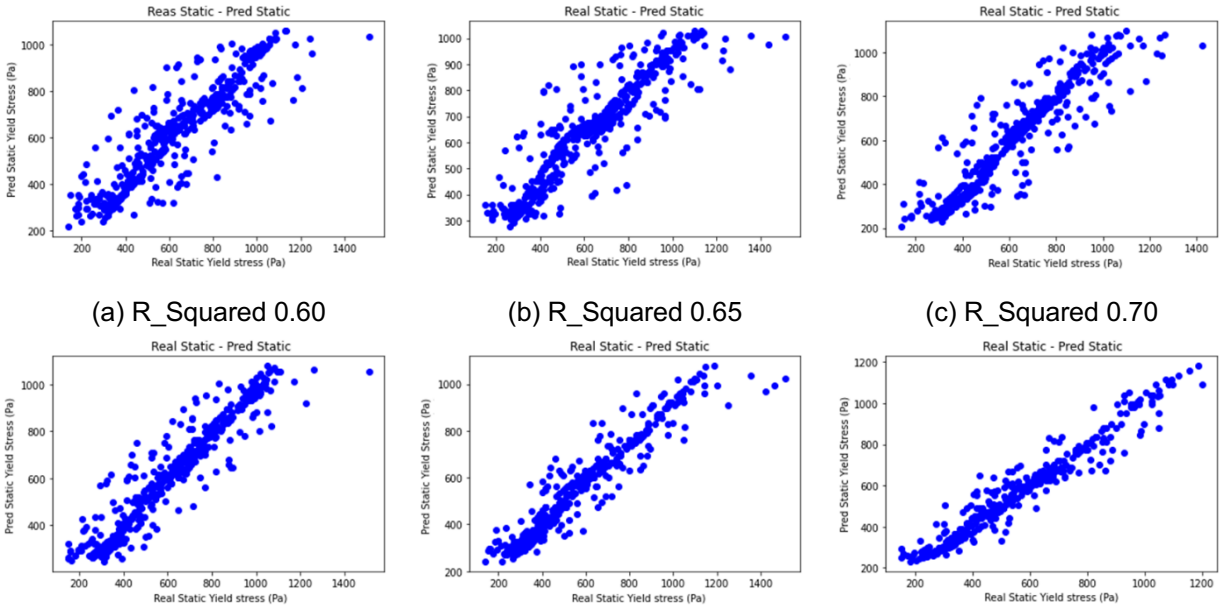

(a) R_Squared 0.60 (b) R_Squared 0.65 (c) R_Squared 0.70

(d) R_Squared 0.75 (e) R_Squared 0.80 (f) R_Squared 0.85

Figure. 13 Prediction results when the data predicted by the model is used as training data

Figure 12 shows the results of evaluating the performance of the prediction model when the R-Squared of the input data is varied through MAE, MSE, and the coefficient of determination between the predicted value by the model and the actual value. Comparing these results to those in Figure 11, it was found that the prediction performance of the model that used the values predicted by the prediction model as learning data was evaluated higher. This improvement is believed to be influenced by the increase in the number of training data, and the accuracy of the model's predicted values was high enough that, even when provided as training data again, performance improved rather than deteriorated.

Figure 13 illustrates the performance evaluation results of the prediction model when the result value predicted by the model is used again as learning data. It shows MAE, MSE, and the coefficient of determination between the predicted value by the model and the actual value. When compared to Figure 10, it was found that the prediction performance of the model that used the values predicted by the prediction model as learning data was evaluated higher. This is believed to be due to the increase in the number of training data, and since the accuracy of the model's predicted values was high, performance did not deteriorate but improved even though it was provided as training data again.

Figure 12 demonstrates that when the result value predicted by the model is used again as learning data, the higher the coefficient of determination of the data used to train the model, the higher the prediction accuracy. Comparing Figures 8 and 12, it was confirmed that as the coefficient of determination of the learning data increases and the number of learning data increases, the distribution of the values predicted by the model narrows. Through the above analysis results, it was concluded that in the rheological constant prediction model of fresh concrete based on a machine learning algorithm, appropriate preprocessing and processing of the learning data and the quality of the learning data have a significant impact on the prediction performance of the model.

5. CONCLUSION

In this study, a concrete rheological constant prediction model was developed through concrete slump flow using a machine learning algorithm. The preprocessing process of the learning data, as well as the impact of the quality and quantity of learning data on the performance of the prediction model, were analyzed.

The study found that the data preprocessing process has a significant impact on the performance of prediction models based on machine learning algorithms. Among the data preprocessing methods, data normalization, which converts input data into a form suitable for modeling, was judged to be particularly effective in improving the performance of prediction models. Additionally, even when the data normalization method is applied, the performance of the prediction model is further improved when a data cleaning process that removes error values such as missing values or outliers is applied. It is important to remove error values through this process to facilitate accurate learning of the model.

However, when comparing the predicted rheological constants derived from the prediction model and the actual rheological constants, there was a tendency for accuracy to improve, but it was difficult to say that the data distribution was aligned on the same straight line. It was confirmed that the prediction performance of the model, which was difficult to improve through data preprocessing alone, could be enhanced by increasing the quality and quantity of learning data.

It was observed that the higher the coefficient of determination between the data input to the model, the better the model's prediction performance. Furthermore,

the prediction accuracy increased even when the predicted values obtained through training data with a high coefficient of determination were re-entered as training data. These findings can contribute to the development of a rheological constant prediction model based on slump flow data of fresh concrete.

References

1. Ferraris, C. F., Obla, K. H., and Hill, R. (2001) The Influence of Mineral Admixtures on the Rheology of Cement Paste and Concrete. *Cement and Concrete Research* 31(2), 245-255
2. Seo, I., Lee, H. S., Park, H. G., and Kim, W. J. (2009) An Experimental Study on Correlation between Rheological Parameter of Picked Mortar and Fluidity of Concrete from 30 to 150MPa. *Journal of the Architectural Institute of Korea Structure & Construction* 25(9), 93-100. (In Korean)
3. Mindess, S. and Young, J. F. (2002) Concrete-second edition. Prentice Hall
4. Gambhir, M. L. (2004) Concrete Technology. Tata McGraw-Hill
5. Kwon, S. H., Kim, Y. J., Lee, G. C., and Choi, Y. W. (2013) Measurements and Applications of Concrete Rheology. *Magazine of the Korea Concrete Institute* 25(3), 24-28. (In Korean)
6. Tsong Yen. (1999) Flow behavior of high strength high-performance concrete. cement & concrete composites
7. Tattersall, G. H. (1991) Workability and Quality Control of Concrete. London, CRC Press
8. Powers, T. C. (1968) The Properties of Fresh Concrete. New York, John Wiley & Sons
9. Tattersall, G. H. and Banfill, P.F.G. (1983) The Rheology of Fresh Concrete. London, Pitman Books
10. Ferraris, C. F. and deLarrard, F. (1998) Testing and modeling of fresh concrete rheology. Marryland: Building and Fire Research Laboratory National Institute of Standards and Technology Gaithersburg
11. Rouseel, N. and Roy, R. L. (2005) The Marsh Cone as a Viscometer : Theoretical Analysis and Practical Limits. *Materials and Structures* 38, 25-30
12. Rouseel, N. (2005) From mini-cone test to Abrams cone test: measurement of cement-based materials yield stress using slump test. *Cement and Concrete Research* 45, 817-822
13. Banfill, P. F. G. (1991) Rheology of Fresh Cement and Concrete. London, E&FN Spon
14. Brower, L. and Ferraris, C. (2003) Comparison of Concrete Rheometers. *Concrete International* 25(8), 41-47
15. Gram, A. and Silfwerbrand, J. (2014) Obtaining Rheological Parameters from Flow Test – Analytical, Computational and Lab Test Approach. *Cement and Concrete Research* 63, 29-34
16. Roussel, N. (2007) The LCPC BOX: A Cheap and Simple Technique for Yield Stress Measurements of SCC. *Materials and Structures* 40(9), 889-896
17. Roussel, N. (2006) Correlation between Yield Stress and Slump: Comparison between Numerical Simulations and Concrete Rheometers Results. *Materials and Structures* 39, 501-509
18. Saak, A. W., Jennings, H. M. and Shah, S. P. (2004) A Generalized Approach for the Determination of Yield Stress by Slump and Slump Flow. Ce*ment and Concrete Research* 34(3), 363-371
19. Shin, T. Y., Kim, J. H. and Han, S. H. (2017) Rheological Porperties Considering the Effect of Aggregates on Concrete Slump Flow. *Materials and Structures* 50, 239
20. Hu, C. (1995) Rheologie des betons fluides. *Etudes et Recherches des Laboratoires des Ponts et Chaussees* OA16
21. Morinaga, S. (1973) Pumpability of Concrete and Pumping Pressure in Pipelines, Fresh concrete: Important Properties and their Measurement. *Proceedings of a RILEM Conference*, Leeds, England
22. Chidiac. (2000) Controlling the Quality of Fresh Concrete-A New Approach. *Magazine of Concrete Research*
23. Chidiac. (2006) Slump and Slump Flow for Characterizing Yield Stress of Fresh Concrete. *ACI Materials Journal*
24. Kim, T. W., Park, S. H., Choi, B. J., Kang, Y. C., Park, K. M., Jeong, W. S. and Koo, C. W. (2022) A Survey of Perception Differences Among University Students, Professors, and Practitioners on the Consturction Technologies in the Fourth Industrial Revolution. *Korean Journal of Construction Engineering and Management* 23(3), 95-103. (In Korean)
25. Samuel, A. L. (1959). Some Studies in Machine Learning Using the Game of Checkers. *IBM Journal of Research and Development* 3(3), 210-229
26. Bengio. Y. A. (2013) Representation Learning: A Review and New Perspectives. *IEEE Transactions on Pattern Analysis and Machine Intelligence* 35(8), 1798-1828
27. Jurgen, S. (2014) Deep Learning in Neural Networks: An Overview. *Neural Networks* 61, 85-117

28. Kim, I. S., Lee, J. H., Yang, D. S., and Park, S. K. (2002) Prediction on Mix Proportion Factor and Strength of Concrete Using Neural Network. *Journal of the Korea Concrete Institute* 14(4), 457-466. (In Korean)
29. Jeon, J. S., Kim, H. S., and Kim, C. H. (2021) Study on Prediction of Compressive Strength of Concrrete based on Aggregate Shape Features and Artificial Neural Network. *Journal of the Korea Institute for Structural Maintenance and Inspection* 25(5), 135-140. (In Korean)
30. Wassim, B. C., Majdi, F. and Moncef, L. N. (2020) Machine Learning Prediction of Mechanical Properties of Concrete: Critical Review. *Construction and Building Materials* 260.
31. Hosein, N., Amir, H. R. and Pouyan, F. (2018) Compressive Strength Prediction of Environmentally Freindly Concrete Using Artificial Neural Networks. *Journal of Building Engineering* 16, 213-219.
32. Ali, B., Venous, B., Mahsa, M. G. and Kursat, E. A. (2017) Prediction of the Compressive Strength of Normal and High-Performance Concretes Using M5P Model Tree Algorithm. Construction and Building Materials 142, 199-207.
33. Maulud, D. P and Abdulazeez, A. M. (2020) A Review on Linear Regression Comprehensive in Machine Learning. *Journal of Applied Science and Technology Trends* 1(4), 140-147
34. Shalev, S. S. and Ben, D. S. (2014) Understanding Machine Learning: From Theroy to Algorithms. *Cambridge University Press*
35. Attia, P. M., Grover, A., Jin, N. et al. (2020) Closed-loop Optimization of fast-charging protocols for batteries with machine learning. *Nature* 578, 397-402
36. Li, Y., Zhong, Q. and Shi, K. (2019) Lithium-Ion Battery State of Health Monitoring Based on Ensemble Learning. *IEEE Access* 7, 8754-8762
37. Weng, C., Cui, Y., Sun, J. and Peng, H. (2013) On-board State of Health Monitoring of Lithium-Ion Batteries Using Incremental Capacity Analysis with Support Vector Regression. *Journal of Power Sources* 234, 36-44
38. Darius. R., Saurabh. S., Valentin. R., Michael. P., David. F. (2021) Machine Learning Pipeline for Battery State of Health Estimation. *Nature Machine Intelligence* 3(5), 1-10
39. Bishop, C. M. (2006). Pattern Recognition and Machine Learning. Springer.
40. Mowla, N. I., Tran, N. H., Han, Z., and Hong, C. S. (2019). A Comprehensive Review on Machine Learning for Networking: Evolution, Applications and Research Opportunities. *Journal of Network and Computer Applications* 143, 1-25. https://doi.org/10.1016/j.jnca.2019.05.005
41. Huang, Y., Cheng, Y., Bapna, A., Firat, O., Chen, M. X., Chen, D., Lee, H. J., Ngiam, J., Le, Q. V., Wu, Y., and Chen, Z. (2019) GPipe: Efficient Trainning of Giant Neural Networks Using Pipeline Parallelism. Proceedings of the 33rd International Conference on Neural Information Processing Systems. Curran Associates Inc., Red Hook, NY, USA, Article 10, 103-112
42. Francois, C. (2022) Deep Learning with Python. Seoul, Gilbut
43. Hinton, G. E., Osindero, S. and Teh, Y. W. (2006) A Fast Learning Algorithm for Deep Belief Nets. Neural Compu 18(7), 1527-1554
44. Humphrey, G. B., Gibbs, M. S., Dandy, G. C. and Maier, H. R. (2016) A Hybrid Approach to Monthly Streamflow Forecasting: Intergrating Hydrological Model Ouputs into a Bayesian Artificail Neural Network. *Journal of Hydrology* 540, 623-640
45. Joo, D. S., Choi, D. J. and Park, H. (2000) The Effects of Data Preprocessing in the Determination of Coagulant Dosing Rate. *Water Resarch* 34(13), 3295-3302. (In Korean)
46. Seong, N. C. and Hong, G. P. (2022) An Analysis of the Effect of the Data Preprocess on the Performance of Building Load Prediction Model Using Multilayer Neural Networks. *Journal of the Korean Institute of Architectural Sustainable Environment and Building Systems* 16(4), 273-284. (In Korean)
47. Garcia, S., Ramirez-Gallego, S., Luengo, J., Benitez, J. M. and Herrera, F. (2016) Big Data Preprocessing: Methods and Prospects. *Big Data Analysis* 1(1), 1-22
48. Cohen, J. (1988) Statistical power analysis for the behavioral sciences (2nd ed.). New York, NY: Routledge.

Improvement of Biochar on Activity of Carbonated Steel Slag

Xiaojian GAO
Professor, School of Civil Engineering, Harbin Institute of Technology, Harbin 150006, China.

Linshan LI
PhD student, School of Civil Engineering, Harbin Institute of Technology, Harbin 150006, China.

ABSTRACT

Steel slag is widely acknowledged as an effective material for capturing CO_2. However, the formation of a dense $CaCO_3$ layer on the surface of carbonated steel slag inhibits both CO_2 sequestration and the hydration reactions of the slag. The addition of porous biochar to an aqueous carbonated steel slag slurry creates numerous additional nucleation sites, promoting the crystallization of nano-$CaCO_3$ and preventing the formation of the $CaCO_3$ layer. This results in an increase in CO_2 sequestration from 10.2% to 14.0% and reduces $CaCO_3$ deposition on the steel slag surface. Incorporating biochar into cement specimens using the active mineral slurry leads to a 45.4% increase in 3-d strength. Although biochar negatively affects pore structure and delays cement hydration, when combined with carbonated steel slag, these drawbacks are mitigated, enhancing the benefits of carbonated slag. Different types of biochar, such as rice straw, reed straw, and bamboo biochar, play unique roles in the process.

Keywords: Biochar; Steel slag; Aqueous carbonation; $CaCO_3$ layer.

1. INTRODUCTION

Steel slag (SS) is a solid waste discharged from steelmaking processes, with an emission amount of approximately 15% to 20% of crude steel production [1, 2]. As of 2023, China's annual crude steel production exceeds 1 billion tons, accounting for more than half of global production [3, 4]. A large amount of SS is accumulating, occupying significant land area and causing water pollution, posing a serious threat to the quality of life for local residents. Developed countries such as the United States, Japan, and Europe have SS utilization rates exceeding 80%, but China, a major steel-producing country, the utilization rate is less than 30% [5, 6]. Despite numerous methods for utilizing SS, many are not practically recognized in engineering due to cost or technological limitations [7, 8]. Therefore, there is a vast research prospect for the resource utilization of SS in China. Due to the high demand in the construction industry for cement products, the annual average growth rate of global cement production continues to rise. The production of Portland cement clinker not only consumes significant resources and energy but also results in a large amount of CO_2 emissions. Using SS as a substitute for cement clinker can effectively alleviate the tight demand for Portland cement.

The main chemical components of SS are calcium, magnesium, silicon, iron, aluminum, manganese oxides, with major mineral phases including dicalcium silicate, tricalcium silicate, calcium-magnesium olivine, and metal oxide phases, along with small amounts of free metallic iron and calcium oxides [9, 10]. Mineral of SS is identical to that of Portland cement, and its cementitious activity makes it an excellent alternative for cement. However, the volume expansion caused by f-CaO limits its utilization [11]. Carbonation treatment is considered one of the best technologies to address this issue [12]. Besides f-CaO, other minerals in SS, including dicalcium silicate, and tricalcium silicate, are ideal components for CO_2 reactions, making SS one of the most ideal materials for CO_2 capture.

In recent years, carbonated SS have gained attention for their ability to sequester CO_2 and enhance concrete performance. However, high carbonation degree can reduce the hydration activity of SS, leading to a predominant barrier layer of calcite that inhibits calcium leaching and suppresses CO_2 reactivity [13]. The thickness of the barrier layer is influenced by CO_2 conditions, SS composition, and particle size. Addition of highly carbonated SS can decrease cement strength and cumulative heat release compared to uncarbonated SS [14, 15]. Traditionally, methods such as grinding, porous treatment, stirring, ultrasonic treatment, high gravity carbonation process, and addition of organic acids or ammonium salts have been used to enhance the activity of carbonated SS [16, 17]. However, the widespread adoption of these technologies is limited by complex processes and high energy consumption. The porous structure and functional groups of biochar make it an excellent material for capturing CO_2. Biochar has nanometer-sized pores with many active sites, which facilitate $CaCO_3$ crystallization. Biochar with a large specific surface area can also increase the strength of concrete and reduce carbonation shrinkage.

Currently, there is limited research on the synergistic use of biochar and SS in carbonation treatment, and little attention has been given to the types of biochar. Highly active mineral slurries were prepared by combining biochar and SS in aqueous carbonation. These slurries were used as replacements for water and cementitious materials. The compressive strength and pore structure of cement specimens, as well as the CO_2 sequestration and microstructure of mineral slurries, were evaluated.

2. MATERIALS AND METHODS

2.1 RAW MATERIALS

This study utilized P.I. 42.5 Portland cement (PC) provided by Chinese Academy of Building Materials Science and SS (Basic oxygen furnace slag) provided by Wuhan Weishen Co., Ltd. The SS was stored in powder form in waterproof sealed bags to prevent weathering by CO_2. The common plant residues - rice straw, reed straw, and bamboo - were selected for biochar preparation. The process involved removing surface adhesion, air-drying, crushing in a high-temperature furnace at a rate of 8°C/min, and heating under low oxygen conditions for 2.5 h to convert organic matter into charcoal and water vapor. After cooling to 25°C, biochar particles underwent crushing and sieving. Details can be found in Table 1. The prepared biochar was vacuum-packed to prevent contamination.

Table.1 Details of biochar preparation

Sample Code	Raw Materials	Heating Rate	Burning Temperature	Burning Time	Screening Requirements
Ri	Rice straw	8°C/min	500°C	2.5 h	<150 μm
Re	Reed straw	8°C/min	500°C	2.5 h	<150 μm
Bb	Bamboo	8°C/min	750°C	2.5 h	<50 μm

Particle size distributions of PC, SS, and biochar were analyzed with a laser particle size analyzer (Mastersizer 2000, Malvern), as depicted in Fig.1. Rice straw biochar and reed straw biochar exhibited larger particle sizes, whereas bamboo biochar had the smallest particles, likely due to differences in pyrolysis temperature. Table.2 shows the chemical compositions of PC, SS, and biochar. Element composition and basic information of biochar are shown in Table.3. Mineral composition of biochar was analyzed using an X-ray diffractometer, as shown in Fig.2. The pore size distribution of biochar was determined using a BET analyzer (Micromeritics ASAP 2460) with N_2 as the adsorption gas, degassing at 250°C for 7 hours, results are shown in Fig.3. Thermal analysis of biochar revealed weight loss between 50-1000°C, as shown in Fig.4. It is essential to adjust the real CO_2 sequestration in mineral slurries based on the amount of biochar added. In Fig.5, SEM shows that all biochar has a porous structure, with varying pore sizes and porosity.

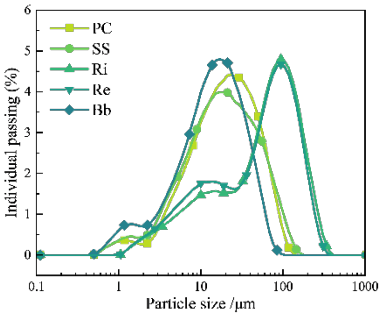

Fig.1 Particle size distribution of raw materials

Table.2 Chemical composition (wt.%)

	CaO	SiO_2	Al_2O_3	Fe_2O_3	MgO	SO_3	K_2O	Others
PC	62.1	20.4	4.5	3.2	2.8	2.1	0.1	4.8
SS	36.7	16.9	3.8	29.6	5.4	0.5	-	7.1
Ri	0.8	91.4	0.6	0.2	1.6	0.5	2.6	2.3
Re	4.4	68.0	2.4	0.7	6.3	3.0	4.8	10.4
Bb	2.6	61.0	15.1	3.0	3.5	1.6	9.2	4.0

Table.3 Elemental composition of biochar

Sample	N (%)	C (%)	H (%)	S (%)	O (%)	O/C	H/C	PH Value
Ri	0.4	45.9	0.8	0.1	6.5	0.1	0.02	10.2
Re	0.5	56.7	1.4	0.1	9.1	0.2	0.02	9.7
Bb	1.0	63.2	1.6	0.3	8.9	0.1	0.03	8.5

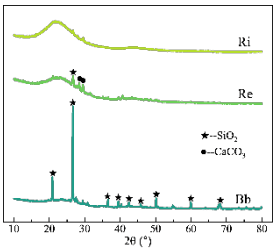

Fig.2 XRD patterns

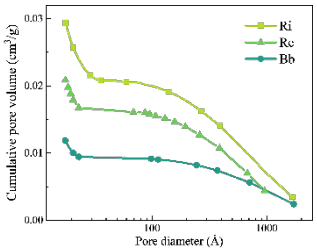

Fig.3 Cumulative pore volume

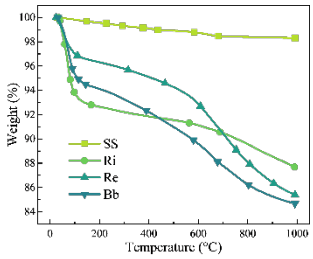

Fig.4 TG curves of biochar

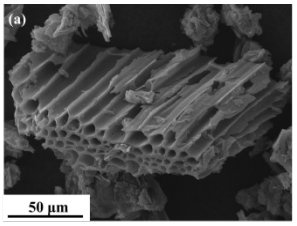

(a) Ri

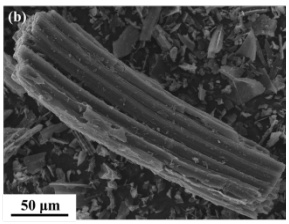

(b) Re

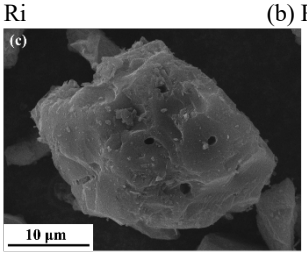

(c) Bb

Fig.5 SEM images of biochar

2.2 PREPARATION OF MINERAL SLURRIES AND CEMENT SPECIMENS

1% biochar and 15% SS were weighed and mixed with water at a 2.5 water-to-slag ratio. The slurry was then poured into a high-pressure vessel with CO_2 gas introduced until the pressure reached 2.5 MPa. Stirring at 250 r/min continued for 2 h. Various mineral slurries were prepared and stored in sealed bottles. Cement specimens were made with different slurries at a water-to-cement ratio of 0.4, mixed with PC at a weight ratio of 1:1.5. Specimens were named based on the added slurries, as recorded in Table.4. In this work, the slurry

prepared by the synergistic action of biochar and carbonated SS is referred to as active mineral slurry. The other three types of slurries, including slurry containing only SS (SP), slurry containing only carbonated SS (CSP), and slurry containing only biochar and SS (RiSP/ReSP/BbSP), are collectively referred to as mineral slurry.

Table.4 Naming and proportioning of mineral slurry

Sample code	Ri (wt.%)	Re (wt.%)	Bb (wt.%)	SS (wt.%)	PC (wt.%)	Carbonation duration (h)
CRiSP	1	-	-	15	84	2
RiSP	1	-	-	15	84	0
CReSP	-	1	-	15	84	2
ReSP		1	-	15	84	0
CBbSP	-	-	1	15	84	2
BbSP	-	-	1	15	84	0
CSP	-	-	-	16	84	2
SP	-	-	-	16	84	0

2.3 TESTS AND CHARACTERIZATION

The microstructure of the mineral slurry was analyzed using a scanning electron microscope (SEM) Zeiss Gemini 560. The compressive strength of cement specimens was tested at various time points including 3, 7, 28, 56, and 72 days. The pore size distribution of the 28-day specimen was determined using a mercury porosimeter AutoPore IV 9500. ^{29}Si nuclear magnetic resonance (NMR) spectra of the 28-day specimen were acquired using an AVANCE III HD apparatus with a pulse duration of 4.0 μs and a spinning speed of 79.5 Hz. An eight-channel isothermal calorimeter (TAM air) was utilized to measure the heat release over a 200-hour period of freshly mixed mineral slurry with PC, following the same mixing ratio as the cement specimens. Thermal gravimetric (TG) analysis was employed to calculate the CO_2 sequestration of the mineral slurry, with the thermal analyzer (SDT650) heating from 50°C to 1000°C at a rate of 10°C/min.

3. RESULTS

3.1 SEM

SEM images of SS and biochar before and after carbonation treatment are shown in Fig.6. Uncarbonated SS exhibits clear edges and corners, with a smooth and flat surface. After carbonation treatment, the SS surface is covered with numerous fine carbonation products, including rod-shaped calcite and flaky portlandite. The calcite morphology is unique, with a cauliflower-like appearance formed through the growth, extension, aggregation, and fusion of micrometer-sized rod-shaped calcite crystals. This "cauliflower-like" calcite inhibits the hydration activity and CO_2 reactivity of SS due to the formation of a barrier layer. In Fig.7, images of rice straw biochar, reed straw biochar, and bamboo biochar in active mineral slurry are presented. Despite their differing shapes and porosities, all three types of biochar contain embedded clusters of calcite. The morphology of calcite on biochar is similar to that on carbonated SS, with particle-like and rod-like structures growing in various directions. The porosity of each type of biochar affects the growth and arrangement of calcite clusters, with rice straw biochar providing the largest space for growth and bamboo biochar having the smallest space. The porous structure of biochar allows for more $CaCO_3$ precipitation and facilitates nano-$CaCO_3$ crystallization, reducing the thickness of barrier layer, thus, enhancing the hydration activity and CO_2 reactivity of carbonated SS.

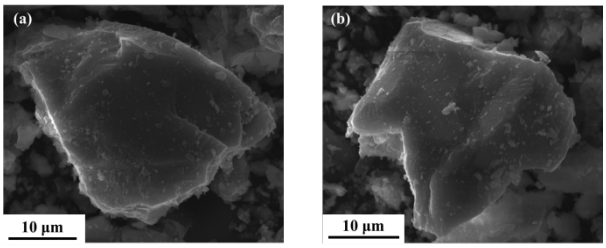

(a) Uncarbonated SS particles

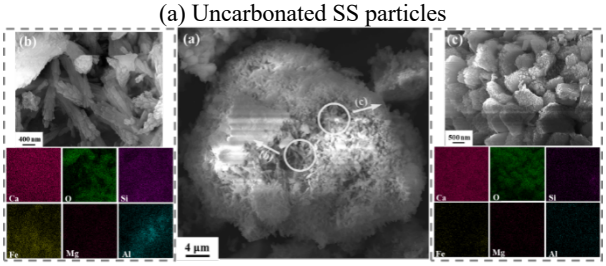

(b) Carbonated SS particles

Fig.6 Images of SS particles

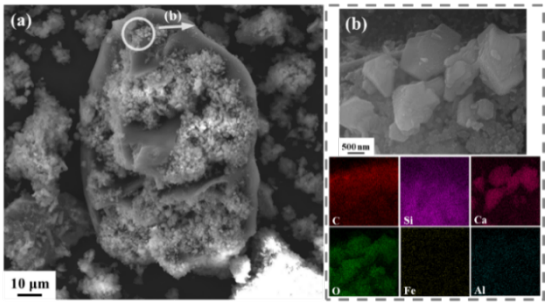

(a) Rice straw biochar in active mineral slurry

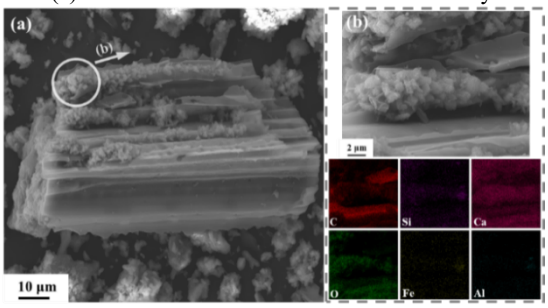

(b) Reed straw biochar in active mineral slurry

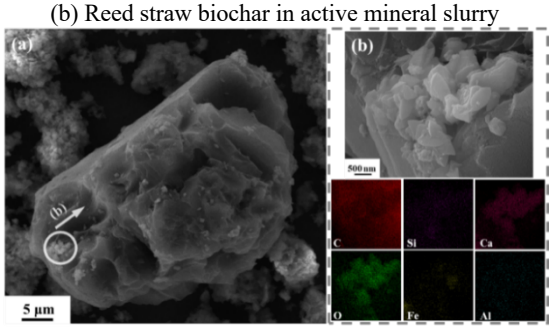

(c) Bamboo biochar in active mineral slurry

Fig.7 Images of biochar in active mineral slurry

3.2 COMPRESSIVE STRENGTH

The compressive strength of specimens with active mineral slurries were compared to those with uncarbonated slurries, as shown in Fig.8. Compressive strength is a key method to assess the suitability of mineral slurry for preparing cement specimens and can also indicate the activity of mineral slurry. Although replacing SS with biochar led to a slight decrease in strength, this was resolved after carbonation treatment. On 3 d, specimens with CSP, CRiSP, CReSP, and CBbSP showed strength increases of 23.0%, 36.3%, 79.1%, and 20.7% compared to corresponding uncarbonated slurries. On 7 d, specimens with CSP, CRiSP, CReSP, and CBbSP showed strength increases of 23.6%, 70.9%, 32.6%, and 48.7% compared to corresponding uncarbonated slurries. The synergistic effect of biochar and carbonation treatment maximized the activity of carbonated SS. However, the strength enhancement by active mineral slurries decreased over time. On 72 d, specimens with CSP, CRiSP, CReSP, and CBbSP showed strength increases of 5.3%, 20.0%, 26.5%, and -0.4% compared to corresponding uncarbonated slurries, indicating that the strength advantage of active mineral slurries was more pronounced in the early stages. Among 3 types of biochar, rice straw biochar and reed straw biochar had a stronger effect on strength enhancement. In CBbSP, bamboo biochar acted as a filler and nucleation agent in cement hydration. The presence of $CaCO_3$ in active mineral slurries filled pores in specimens and provided nucleation sites for hydration products, leading to strength enhancement. However, the inert $CaCO_3$ barrier layer somewhat inhibited SS activity. Biochar reduced the thickness of the $CaCO_3$ layer, allowing for better utilization of nucleation and filling effects, confirming SEM image findings.

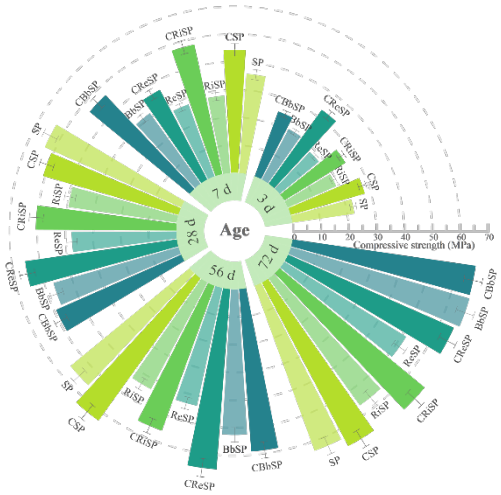

Fig.8 Compressive strength of cement specimens

3.3 MIP

Fig.9 presents data on median pore diameter, average pore diameter, most probable pore diameter, and porosity. Fig.10 displays the statistics of pore size distribution. Specimens with active mineral slurry exhibited significantly lower porosity compared to those with uncarbonated slurry, due to the filling effect of $CaCO_3$. This trend was also evident in the statistics of median pore diameter, most probable diameter, and porosity, which correlated with compressive strength. The addition of biochar increased porosity and enlarged pore size, although these values decreased following carbonation treatment. Specimens containing biochar displayed a notable increase in the number of pores at 10-50 nm after carbonation, comprising almost half of all pores, while pores < 10 nm increased and 50-100 nm pores decreased. Interestingly, after carbonation treatment, mineral slurry containing only SS exhibited decreased porosity, but increased median pore diameter and most probable pore diameter. The pores that were initially smaller than 10 nm mainly transitioned to pores within the range of 10 to 50 nm. This shift may be attributed to uneven $CaCO_3$ distribution leading to pore structure degradation. Biochar effectively prevented pore size escalation by promoting more uniform $CaCO_3$ precipitation, resulting in a refined pore structure. However, the presence of large pores in biochar, despite $CaCO_3$ filling some of them, resulted in specimens with biochar retaining greater characteristic pore size compared to those without biochar. Among the biochar types studied, reed straw biochar had the most pronounced impact on refining pore structure.

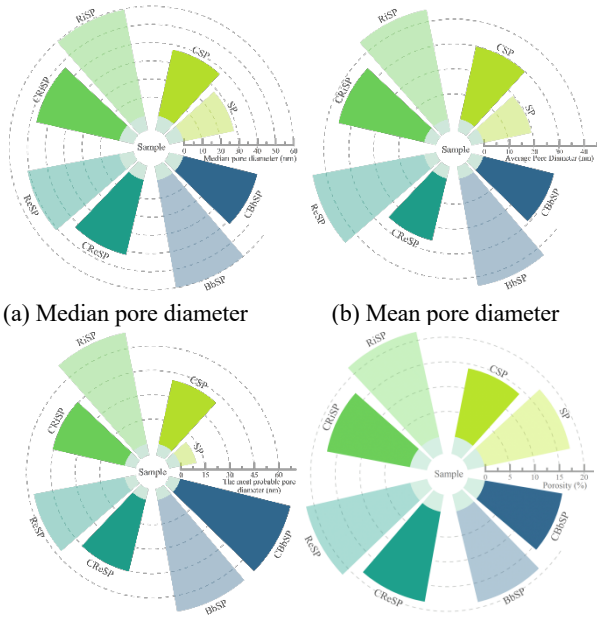

(a) Median pore diameter (b) Mean pore diameter

(c) The most probable diameter (d) Porosity

Fig.9 Pore structure of cement specimens

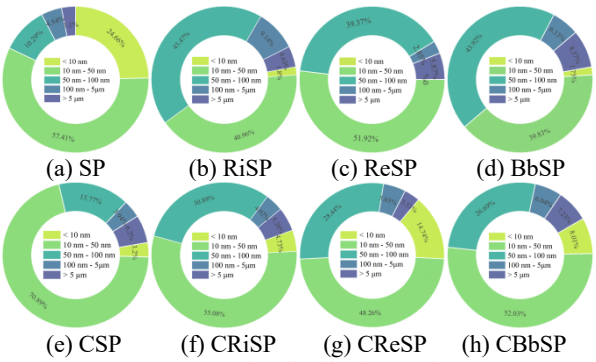

(a) SP (b) RiSP (c) ReSP (d) BbSP

(e) CSP (f) CRiSP (g) CReSP (h) CBbSP

Fig.10 Pore size distribution statistics

3.4 ^{29}SI NMR

Cement specimens with SS and reed straw biochar were tested using ^{29}Si NMR to study the impact of active mineral slurry on C-S-H gel, as shown in Fig.11. Si in C-S-H gel exists as silicon-oxygen tetrahedra (Q^n), with n indicating bridging oxygen atoms. Deconvolution analysis showed proportions of Q^n, with only Q^0, Q^1, and Q^2 observed in the spectra, as shown in Fig.12. Samples with SS showed reduced Q^1 and increased Q^2 after carbonation treatment, affecting Ca/Si ratio and chain length insignificantly. Reed straw biochar delayed hydration, with ReSP having highest Ca/Si and shortest chain length, correlating with strength and pore structure. Activating biochar into mineral slurry significantly improved C-S-H gel polymerization. CReSP had the highest hydration degree, enhancing carbonated SS activity despite pore structure deterioration, attributed to high polymerization degree of C-S-H gel supporting strength.

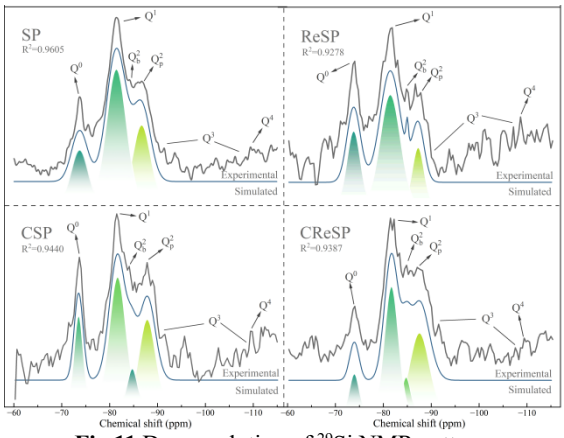

Fig.11 Deconvolution of ^{29}Si NMR patterns

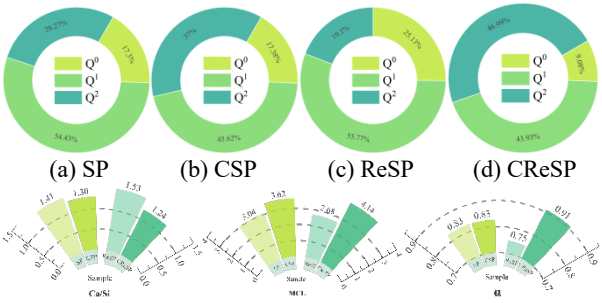

(a) SP (b) CSP (c) ReSP (d) CReSP

(e) Ca/Si (f) MCL (g) Hydration degree

Fig.12 Hydration degree statistics

3.5 HYDRATION HEAT EVOLUTION

The hydration heat evolution of mineral slurries was recorded, as shown in Fig.13. The more heat released by the slurry, the higher the activity. Overall, hydration heat evolution between slurries is consistent, but when local details are magnified, difference still can be captured. In the initial period (0-0.3 h), the 8 slurries clearly divided into two camps, with the active mineral slurries uniformly taking the advantage over the uncarbonated slurries. The rough surface of carbonated SS absorbed more water firstly, the hydration heat release was also more intense at this stage. Difference between the two camps can also be clearly seen from the cumulative heat release chart for the same period. No significant differences were found in the induction period (0.3-5 h) and the acceleration period (5-12 h), but differences gradually emerged in the deceleration period (12-50 h) and the stable period (< 50 h). The longer the hydration age, the more pronounced the differences. From cumulative heat flow, the hydration activity of the mineral slurry is highest for CSP, followed by CBbSP, CRiSP, CReSP, SP, ReSP, BbSP, and RiSP. Activity mineral slurries always exhibit a greater activity, but non-hydrated biochar substitution for SS will slightly inhibit the hydration process, without masking the advantages brought by carbonation treatment. Differences between biochar are not significant, with CBbSP exhibiting slightly higher hydration heat, indicating it is the most active mineral slurry, possibly due to its tiny particle. Generally, the finer the particle size, the higher the slurry activity.

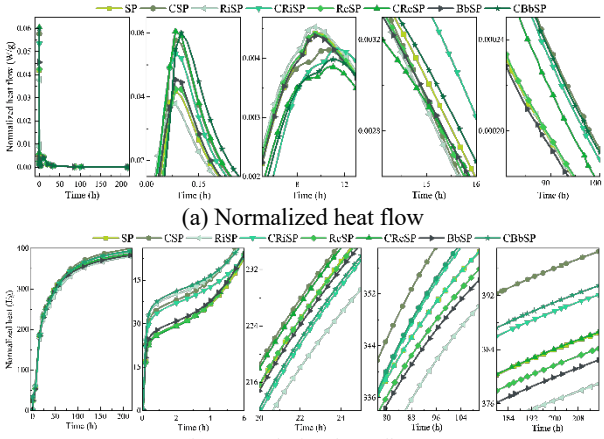

(a) Normalized heat flow

(b) Cumulative heat flow

Fig.13 Hydration heat evolution of mineral slurries

3.6 CO_2 SEQUESTRATION OF MINERAL SLURRY

TG was used to calculate the CO_2 sequestration, as shown in Fig.14. Rice straw biochar with large pore being more effective in capturing CO_2 than reed straw biochar and bamboo biochar, and the lowest carbonation efficiency observed in SP. Therefore, it is certainly feasible to improve the CO_2-capture efficiency by adding biochar, especially the biochar with high porosity. Based on $CaCO_3$ content, the CO_2 sequestration was determined to be 1.0% for SP, 10.2% for CSP, 2.0% for RiSP, and 14.0% for CRiSP. The porous structure of biochar facilitates $CaCO_3$ crystallization. After the barrier layer thins, minerals inside SS may participate more actively in hydration and CO_2 reactions. Similar trends were observed in specimens with uncarbonated slurries.

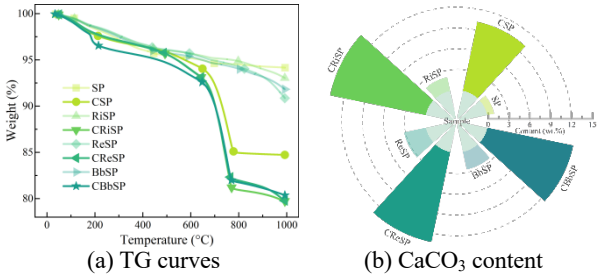

(a) TG curves (b) $CaCO_3$ content

Fig.14 TG results

4. CONCLUSIONS

This study aimed to address the issue of the inert barrier layer formed on carbonated steel slag, which inhibits internal carbonation and suppresses steel slag reactivity. By adding different porous biochar to carbonated steel slag, high activity mineral slurries were prepared. The effects of mineral slurries on cement specimen strength, pore structure, hydration heat, and C-S-H gel were investigated. Biochar's dual enhancement mechanism on hydration activity and CO_2 reactivity of steel slag was identified.

(1) SEM showed carbonated steel slag coated with calcite barrier layer, obstructing mineral reactions. Biochar added more locations for calcite clusters, reducing buildup. Rice straw biochar with highest porosity grew most calcite clusters.

(2) Active mineral slurries improved strength, particularly in early stages. Reed straw biochar slurry increased strength by 45.4% on 3 d. Slurries slightly affected pore structure but enhanced hydration of C-S-H gel. Biochar allowed for better nucleation of $CaCO_3$.

(3) Biochar delayed hydration heat release, but carbonation treatment compensated. Bamboo biochar had highest activity, with highest heat release. Rice straw biochar excelled in CO_2 sequestration, increasing from 10.2% to 14.0%.

With the development of green recycling in the steel industry, the application field of steel slag is constantly adjusting. The synergistic effect of steel slag and biochar in construction fields will highlight the characteristics of high quality and environmental protection, and move towards the direction of large-scale, multi-path, and high value-added utilization.

ACKNOWLEDGMENTS:

This research was supported by China Postdoctoral Science Foundation (No. 2022M710971), and National Natural Science Foundation of China (No.52108202), and Natural Science Foundation of Heilongjiang Province of China (No. LH2021E110).

REFERENCE:

[1] W. Gao, W. Zhou, X. Lyu, X. Liu, H. Su, C. Li, H. Wang, Comprehensive utilization of steel slag: A review, Powder Technology, 422 (2023) 118449.
[2] L. Zhu, Influence of waste residue treatment in metallurgical iron and steel plant on environmental protection, China Metal Bull., (2020) 191-192.
[3] C.S.Y. Nbsc, National Bureau of Statistics of China (NBSC), China Statistics Press, Beijing, 2016.
[4] L. Paliu-Popa, A.G. Babucea, C.I. Răbonţu, A. Bălăcescu, The impact of the economic and financial crisis on the evolutionary trend of world crude steel production, Metalurgija, 54 (2015) 721-724.
[5] D.-m. Yan, H.-f. Jiang, J. Yang, Research status of comprehensive utilization of iron from red mud, SPIE, pp. 126-132.
[6] H. Motz, J. Geiseler, Products of steel slags an opportunity to save natural resources, Waste management, 21 (2001) 285-293.
[7] P.S. Humbert, J. Castro-Gomes, CO2 activated steel slag-based materials: A review, Journal of Cleaner Production, 208 (2019) 448-457.
[8] Eurostat, Municipal Waste Statistics—Statistics Explained, (2020).
[9] J. Waligora, D. Bulteel, P. Degrugilliers, D. Damidot, J.L. Potdevin, M. Measson, Chemical and mineralogical characterizations of LD converter steel slags: A multi-analytical techniques approach, Materials characterization, 61 (2010) 39-48.
[10] M.P.d. Luxán, R. Sotolongo, F. Dorrego, E. Herrero, Characteristics of the slags produced in the fusion of scrap steel by electric arc furnace, Cement and concrete research, 30 (2000) 517-519.
[11] P. Librandi, P. Nielsen, G. Costa, R. Snellings, M. Quaghebeur, R. Baciocchi, Mechanical and environmental properties of carbonated steel slag compacts as a function of mineralogy and CO2 uptake, Journal of CO2 Utilization, 33 (2019) 201-214.
[12] X. Huang, J. Zhang, L. Zhang, Accelerated carbonation of steel slag: A review of methods, mechanisms and influencing factors, Construction and Building Materials, 411 (2024) 134603.
[13] S. Srivastava, M. Cerutti, H. Nguyen, V. Carvelli, P. Kinnunen, M. Illikainen, Carbonated steel slags as supplementary cementitious materials: Reaction kinetics and phase evolution, Cement and Concrete Composites, 142 (2023) 105213.
[14] L. Li, T. Chen, X. Gao, Synergistic effect of CO2-mineralized steel slag and carbonation curing on cement paste, Cement and Concrete Composites, 145 (2024) 105357.
[15] L. Li, T. Chen, X. Gao, Effects of superimposed carbonation synergy on BOFS cement-based materials, Cement and Concrete Composites, 138 (2023) 105008.
[16] M.A. Gómez-Casero, L. Pérez-Villarejo, E. Castro, D. Eliche-Quesada, Effect of steel slag and curing temperature on the improvement in technological properties of biomass bottom ash based alkali-activated materials, Construction and Building Materials, 302 (2021) 124205.
[17] S. Yuan, Y.-h. Qin, Y.-p. Jin, Y.-j. Li, Suspension roasting process of vanadium-bearing stone coal: Characterization, kinetics and thermodynamics, Transactions of Nonferrous Metals Society of China, 32 (2022) 3767-3779.

SIMULATION ANALYSIS OF THERMAL-MECHANICAL COUPLED BEHAVIOR IN VISCOELASTIC MODEL FOR LEAD RUBBER BEARINGS

Yusaku ITO
Graduate Student, Hokkaido University, Sapporo, Japan

Ken ISHII
Assistant Professor, Hokkaido University, Sapporo, Japan

ABSTRACT:
Recently, amid concerns about giant earthquake such as Nankai Trough Earthquake, seismic isolators have been adopted for high-rise buildings. Wind loads are also being considered as a major load for high-rise buildings, but no measures have been taken against the simultaneous occurrence of seismic and wind disasters. The objective of our research is to achieve simulation analysis using any model that can represent the behavior of seismic isolators for both earthquake and wind loads in a unified manner. This paper presents thermal-mechanical coupled behavior analysis using viscoelastic model for lead rubber bearings that can represent both behaviors in a unified manner.

Keywords: seismic isolation, lead rubber bearing, wind load, creep behavior, viscoelastic model, thermal-mechanical coupled behavior

1. INTRODUCTION

In recent years, amid concerns about giant earthquakes such as Nankai Trough Earthquake, seismic isolators have been adopted for high-rise buildings. On the other hand, there is concern that natural disasters such as the worrisome giant earthquakes may compound the risk of other disasters. Currently, measures are being taken for high-rise buildings to take into account wind load as a major load in addition to seismic motion, but it is not assumed that earthquakes and typhoons and other disasters occur simultaneously, and there is concern about what to expect when they do occur at the same time. Therefore, the objective of my research is to achieve simulation analysis using any model that can represent the behavior of seismic isolators for both earthquake and wind loads in a unified manner, so that the behavior can be assumed in time history even when earthquake and wind disasters occur simultaneously.
We have studied a viscoelastic model that can represent both behaviors of lead rubber bearings. We have conducted simulation analysis of lead rubber bearing using viscoelastic model and confirmed that both wind and seismic responses can be represented. However, the following issues remain.

A) Simulation analysis has not been performed for the heat generated by lead plugs of the lead rubber bearings due to repeated deformation.
B) The accuracy of the simulation analysis for the experimental lead rubber bearing behavior is low.

This paper addresses the issue A) and attempts to simulate the behavior with heat generation at lead plugs by conducting thermal-mechanical coupled behavior analysis with the viscoelastic model that has been studied in the past. The issue B) is addressed in the future.

2. WIND LOADING TESTS

This section describes the wind loading tests [1] that are the subject of simulations in this paper.
In the following, lead rubber bearing is referred to as LRB.

2.1 TEST SPECIMEN

The test subject is a square type LRB with a rubber outer side length of 400 mm, a total rubber thickness of 79.2 mm, and four lead plugs of 40 mm in diameter. The intercept load Q_d at 100% shear strain is 44 kN.

2.2 TEST CONDITION

Assuming wind loading, a constant load Q_s to the positive side as the average component and a variable load $\pm\Delta Q$ with equal amplitude to both the positive and negative sides as the variable component were loaded horizontally to the LRB. The ratio of the magnitude of the constant load Q_s to the variable load $\pm Q$ was 1:1, and the tests were conducted in the range where the ratio to the intercept load Q_d was 0.2~1.2 (9 kN ± 9 kN ~ 52 kN ± 52 kN), respectively. The period of the variable load was 3 seconds, and a test was conducted for a total of 7200 seconds. The vertical load was assumed to be equivalent to a surface pressure of 15 MPa.

2.3 CREEP BEHAVIOR

In the test results, horizontal vibration of the LRB was observed during the 2-hour test, but as time passed, the center position of the vibration shifted to the positive side. In this paper, this behavior is referred to as creep behavior. As an example of creep behavior, the load-

deformation relationship of one of the test results is shown in Figure 1.

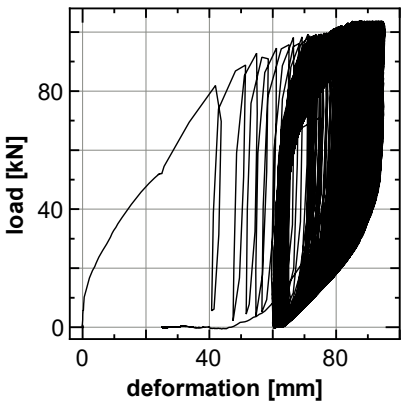

Figure 1 load-deformation relationship
(52 kN ± 52 kN)

Figure 1 shows the load-deformation relationship when a load of 52 kN ± 52 kN was loaded, and it shows that the creep progresses in the horizontal direction during the 2-hour excitation, but the width of the creep progression seems to gradually decrease. It can also be seen that the hysteresis loop become larger as the creep progresses.

3. SIMULATION ANALYSIS WITH VISCOELASTIC MODEL

In this section, we describe the results of the previous simulation analysis in order to compare them with the results of the thermal-mechanical coupled behavior analysis performed in this paper and explain the viscoelastic model for representing both wind and seismic responses.

3.1 VISCOELASTIC MODEL

A viscoelastic model, as shown in Figure 2, is constructed to reproduce the creep behavior of LRB in response to wind loads.

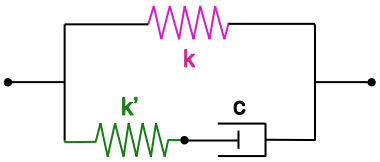

Figure 2 Viscoelastic Analysis Model
k: elastic spring (rubber part)
k': elastoplastic spring (plug part)
c: viscous dashpot

For each part of Figure 2, k is an elastic element representing the restoring force of the rubber part of the LRB, k' is an elastoplastic element representing the characteristic of the plug part, and C is a viscous dashpot, a viscous damping element introduced to represent creep behavior. With this model, the behavior of the viscoelastic model for wind loading is expected to be consistent with the creep behavior of LRBs described in Section 2.

Let us assume that the restoring force characteristics of LRB are represented by a modified bilinear model with maximum strain dependence; using the LRB specifications, the bilinear restoring force characteristics are calculated by the following equation.

$$\text{Intercept load: } Q_d = \tau_p \cdot A_p \quad (1)$$

$$\text{Secondary Stiffness: } K_d = \frac{G_r \cdot A_r}{H_r} + \frac{\alpha \cdot A_p}{H_r} \quad (2)$$

$$\text{Primary Stiffness: } K_1 = \beta \cdot K_d \quad (3)$$

In equations (1) ~ (3), τ_p is plug yield stress, A_p is plug cross-sectional area, G_r is rubber shear stiffness, A_r is rubber cross-sectional area, H_r is total rubber thickness, α is plug apparent stiffness, and β is pre-yield stiffness ratio.
Both k and k' are represented by a modified bilinear model, where k has an intercept load of 0 and k' has a secondary stiffness of 0. The parameters in Table 1 allow us to decompose the characteristic of the LRB into the rubber part k and the lead plug part k', paying attention to the ratio of primary to secondary stiffness.

Table 1 Specification of modified bilinear model

Specifications	LRB	Rubber part	Plug part
Rubber Area [m^2]	A_r: 151773×10^{-6}	A_r	+0
Total rubber thickness [m]	H_r: 79.2×10^{-3}	H_r	H_r
Shear stiffness[N/m^2]	G_r: 0.392×10^6	G_r	+0
Plug Area [m^2]	A_p: 5027×10^{-6}	+0	$\mathbf{A_p}$
Yield stress [N/m^2]	τ_p: 8.33×10^6	+0	$\boldsymbol{\tau_p}$
Apparent stiffness[N/m^2]	α: 0.588×10^6	+0	$\boldsymbol{\alpha}$
Stiffness ratio	β: 13	1 + 0	※below

※ $\beta + (\beta - 1)(G_r \cdot A_r)/(\alpha \cdot A_p)$

3.2 SIMULATION ANALYSIS OF WIND LOADING TESTS WITH VISCOELASTIC MODEL

The simulation analysis is performed up to 100 seconds from the start of test, when the creep behavior of LRB is noticeable and the effect of the temperature rise of the specimen is negligible.
The characteristics of the dashpot in Figure 2 are assumed to be linear viscous damping, and the reproducibility of the test results is checked by varying the damping coefficient C within the range shown in Table 2.
In this study, simulation analysis for viscoelastic models is performed using OpenSees [2], an open system for earthquake engineering simulation, which is a finite element analysis framework.
Figure 3 shows an example of the analysis results.

Different creep behaviors are obtained depending on the damping coefficient of the viscoelastic model for each. Table 2 shows the values of the damping coefficients that reproduce well the experimental results for each load amplitude, shaded. In the range where the maximum load is less than the yield load, there is an amplitude dependence of the damping coefficient that is optimal. In the range where the maximum load is greater than the yield load, $C = 3 \times 10^7$[N/(m/s)] is the optimum value.

Table 2 Setting and optimum values of coefficient

Load Amplitude	viscous damping coefficient			
$0.2Q_d \pm 0.2Q_d$	5×10^6		5×10^7	5×10^8
$0.33Q_d \pm 0.33Q_d$	5×10^6		5×10^7	5×10^8
$0.4Q_d \pm 0.4Q_d$	5×10^6		5×10^7	5×10^8
$0.5Q_d \pm 0.5Q_d$	5×10^6	3×10^7	5×10^7	5×10^8
$0.67Q_d \pm 0.67Q_d$	5×10^6	3×10^7	5×10^7	5×10^8
$1.0Q_d \pm 1.0Q_d$	5×10^6	3×10^7	5×10^7	5×10^8
$1.1Q_d \pm 1.1Q_d$	5×10^6	3×10^7	5×10^7	5×10^8
$1.2Q_d \pm 1.2Q_d$	5×10^6	3×10^7	5×10^7	5×10^8

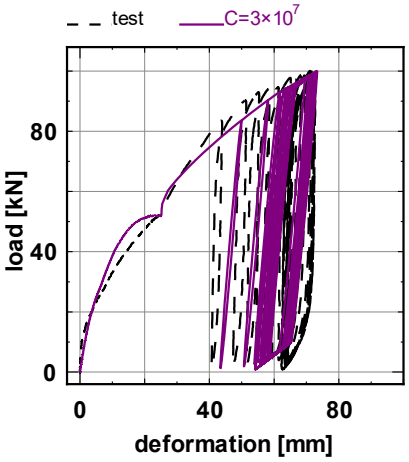

Figure 3 load-deformation relationship (for 100 seconds, 52 kN ± 52 kN)

3.3 SEISMIC RESPONCE ANALYSIS WITH VISCOELASTIC MODEL

In this section, we will examine the effects of the large and small damping coefficients verified in Section 3.2 on seismic response and consider whether the viscoelastic model studied can be used for seismic response analysis as well. The viscoelastic model in Figure 2 is given a mass point equivalent to a surface pressure of 15 MPa, and the El Centro wave is input. For the damping coefficients, set C=5×10^6, 5×10^7, 5×10^8, and 5×10^9 [N/(m/s)] to include parameters that reproduce test results well. Response displacement waveforms are shown in Figure 4. Figure 4 shows that the seismic response remains almost unchanged when the parameter C is varied in the range of 1000 times. The viscous damping coefficient was introduced to reproduce the wind response, but if it is of the same order of magnitude as the value identified from the wind loading test, its effect on the seismic response is limited.

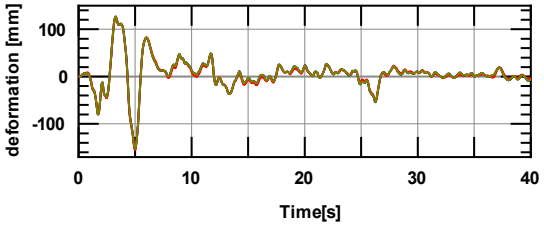

Figure 4 Seismic response displacement of viscoelastic model

4. THERMAL-MECHANICAL COUPLED BEHAVIOR ANALYSIS

As mentioned in Introduction, simulation analysis has been performed using a viscoelastic model. However, the simulation in Section 3 did not take temperature rise into account, and thus could not represent changes in the behavior of LRB due to hysteresis absorption at lead plugs.

The goal of this section is to improve the reproducibility of wind-loading test by performing thermal-mechanical coupled behavior analysis on the previous models to account for the temperature rise due to hysteresis absorption of the plug. Figure 5 shows the analysis flow in thermal-mechanical coupled behavior analysis.

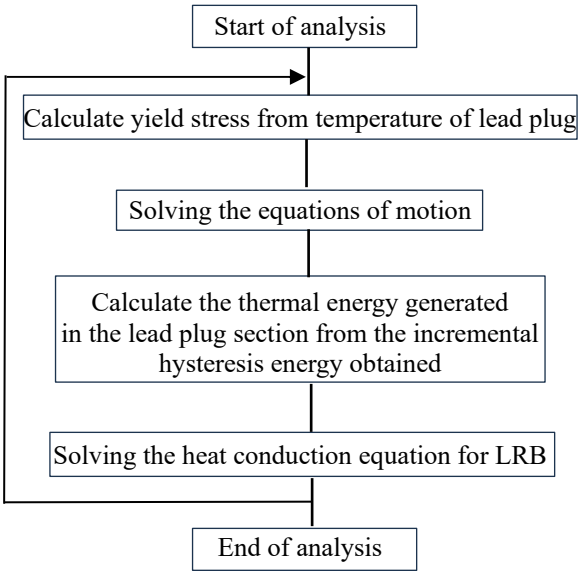

Figure 5 Analysis Flow

4.1 SIMPLIFICATION OF THERMAL-MECHANICAL COUPLED BEHAVIOR ANALYSIS

In this paper, a square LRB with four lead plugs is the subject of analysis, but heat conduction analysis requires analysis in three dimensions, which takes a great deal of analysis time. In this section, the square LRB with four lead plugs used in this report is simplified to a single round LRB to reduce analysis time. The simplification method has been developed by Takizawa et al. [3]. The reason for the difference in analysis time between a square LRB with four lead plugs and a round LRB with

one lead plug is the difference in analysis range. Due to symmetry, round LRB with a single lead plug can be analyzed in two dimensions, but square LRB with four lead plugs requires a three-dimensional analysis. For the above reasons, a square LRB with four lead plugs is approximated and simplified to a round LRB with a single lead plug, as shown in Figure 5. A square LRB with four lead plugs is divided into four parts and approximated to a square LRB with one lead plug so that the cross-sectional area of the rubber part becomes 1/4, then approximated to a round LRB with one lead plug without changing the cross-sectional area of the rubber part.

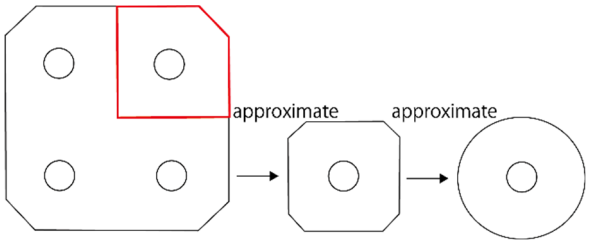

Figure 5 Simplified method

Takizawa et al. proved that the load-deformation relationship between this simplified LRB and the LRB before simplification was almost the same. Therefore, in this paper, we use this method to simplify the analytical calculation. With the simplification, the size of the analytical model in this paper becomes as shown in Table 3.

Table 3 Specification of analytical model of LRB

specification	Square with 4 plug	Square with 1 plug	Round with 1 plug
Side length[mm]	400	200	223.4
Plug diameter[mm] ×number	40	40	40
Rubber thickness[mm] ×number	2.4×33	2.4×33	2.4×33
Steel plate thickness[mm] ×number	2.2×32	2.2×32	2.2×32

4.2 THERMAL-MECHANICAL COUPLED BEHAVIOR ANALYSIS WITH VISCOELASTIC MODEL (C=3×10^7)

In section 3, we analyzed the viscoelastic model, but could not properly evaluate the effect of the lead plug temperature rise. Therefore, in this section, thermal-mechanical coupled behavior analysis is used to simulate in the load region where the maximum load exceeds the yield load (22 kN ± 22 kN ~ 52 kN ± 52 kN), where heat is generated in the lead plug. By doing so, we expect to be able to simulate a 2-hour wind loading test with a high degree of reproducibility. Heat generation at lead plugs occurs because lead plugs are elastoplastic and therefore absorb historical energy when yielding. In section 4.2, the simulations was performed by substituting the viscous damping coefficient $C = 3 \times 10^7$ [N/(m/s)], which was shown to be appropriate in section 3. Figure 6.1 shows a comparison between the simulation using the thermal-mechanical coupled behavior analysis (TCA) that takes into account the temperature rise of the lead plug, compared to the wind loading test and the simulation (without TCA) analyzed in Section 3 (52 kN ± 52 kN). The load-deformation relationships at $C = 3 \times 10^7$ [N/(m/s)] are shown for 7200 seconds, respectively. Figure 7.1 shows the load-deformation relationship (52 kN ± 52 kN) due to each property of the viscoelastic model with thermal-mechanical coupled behavior analysis. Referring to Figure 2 of the viscoelastic model described in Section 3, the respective properties in Figure 7.1 are k for elastic spring, k' for elastoplastic spring, and C for viscous dashpot.

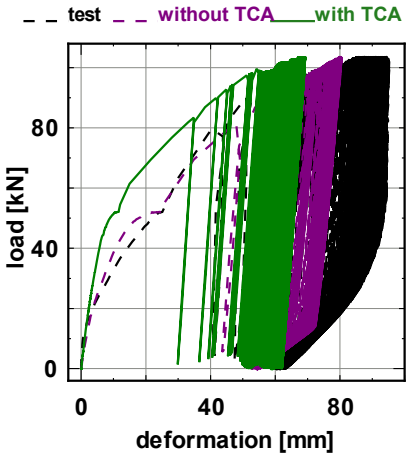

Figure 6.1 Differences with and without TCA ($C = 3 \times 10^7$, 52 kN ± 52 kN)

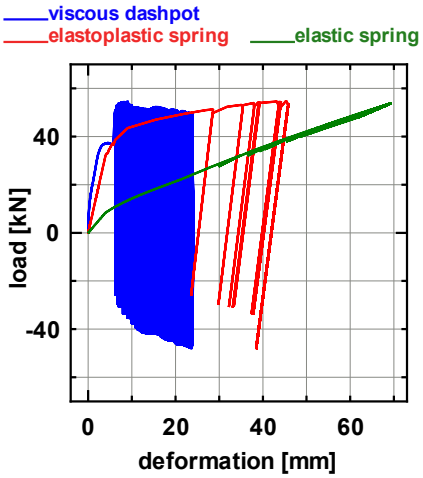

Figure 7.1 Load-deformation relationship for each property ($C = 3 \times 10^7$, 52 kN ± 52 kN)

Figure 6, shows that the simulation using the thermal-mechanical coupled behavior analysis appears to have a smaller amount of creep than the simulation not using it. Figure 7.1 also show that the graph of elastoplastic spring does not appear to absorb any energy in the

hysteresis loop. Any graph that absorbs hysteresis energy draws a loop for each cycle and has area. This means that no heat is being generated at the lead plug.
Figure 8 shows the load-deformation relationship for each cycle of the 52 kN ± 52 kN simulation at C=3e7. Since a load with a cycle of 3 seconds was applied in the wind loading test, the graph of the 7200-second test draws loops of 2400 cycles. One cycle of the test draws a loop, whereas one cycle of the simulation draws a line. Also, one cycle of the test creeps as time passes from 100 cycles, to 1000 cycles, to 2400 cycles, whereas one cycle of the simulation seems no horizontal movement over time. Each cycle shows that it does not draw a loop.

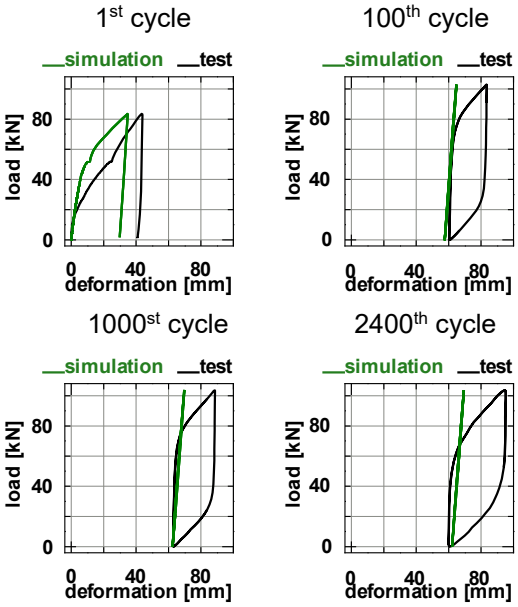

Figure 8.1 Load-deformation relationship by each cycle ($C = 3 \times 10^7$, 52 kN ± 52 kN)

4.3 THERMAL-MECHANICAL COUPLED BEHAVIOR ANALYSIS WITH VISCOELASTIC MODEL (C=5×10⁶, 1×10⁶)

In section 4.2, we compared the reproducibility of the simulation with TCA, but the difference in the amount of creep from the experimental results was larger than in the simulation without TCA, at $C = 3 \times 10^7$ [N/(m/s)]. Therefore, in Section 4.3, we compared the results by giving a smaller value of the viscous damping coefficient than $C = 3 \times 10^7$ [N/(m/s)]. Figures 6.2, 7.2, and 8.2 show the simulations of Figures 6.1 and 7.1 with the viscous damping coefficient changed from $C = 3 \times 10^7$ to $C = 5 \times 10^6$ [N/(m/s)]. Figures 6.3, 7.3, and 8.3 show the simulations of Figures 6.1 and 7.1 with the viscous damping coefficient changed from $C = 3 \times 10^7$ to $C = 1 \times 10^6$ [N/(m/s)]. At $C = 5 \times 10^6$, the behavior of the first cycle is fairly accurate to the test results; at $C = 1 \times 10^6$, the first cycle loops and approaches the test results. From the above, we can say that it seems possible to accurately simulate the creep progression by changing the viscous damping coefficient. Figure 7.3 also shows that changing the viscous damping coefficient also changes the behavior of the elastoplastic spring.

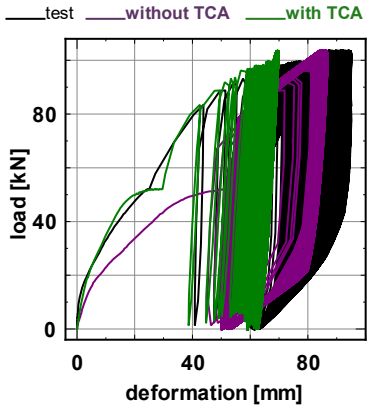

Figure 6.2 ($C = 5 \times 10^6$)

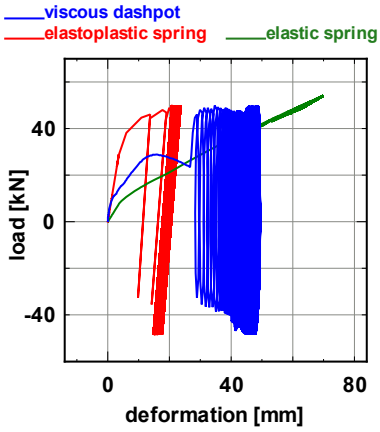

Figure 7.2 ($C = 5 \times 10^6$)

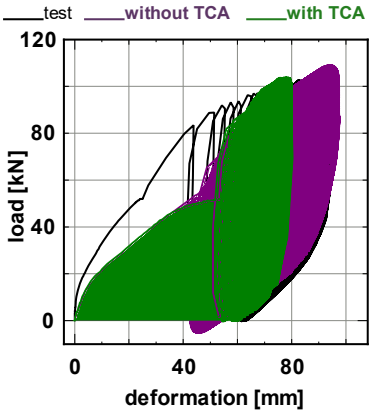

Figure 6.3 ($C = 1 \times 10^6$)

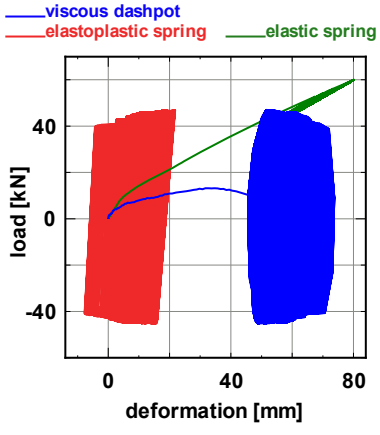

Figure 7.3 ($C = 1 \times 10^6$)

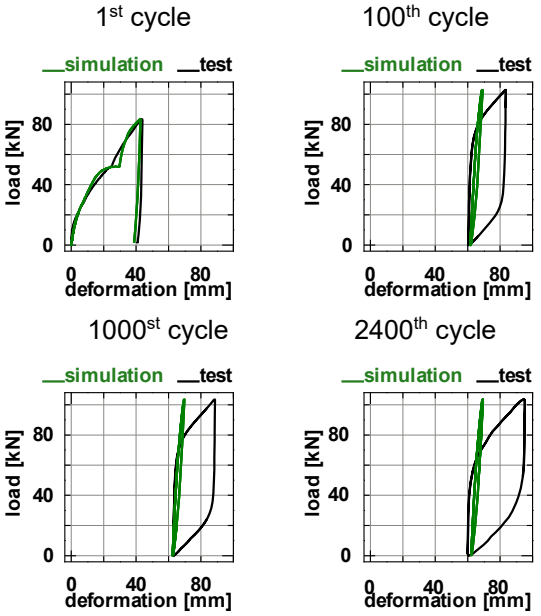

Figure 8.2 ($C = 5 \times 10^6$)

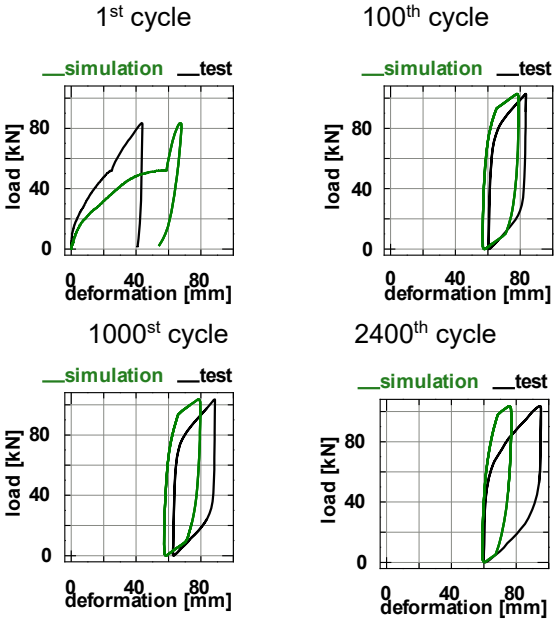

Figure 8.3 ($C = 1 \times 10^6$)

5. CONCLUSIONS

In the introduction to this paper, the purpose of this study was to simulate the lead plugs in LRB for the loading region where heat generation was observed. In this paper, simulations were performed using thermal-mechanical coupled behavior analysis on the viscoelastic model constructed. The results obtained in this paper are as follows.

・The viscoelastic model, which can reproduce both wind and seismic responses, was simulated for a 2-hour wind loading test using thermal-mechanical coupled behavior analysis.

・It is possible to reproduce the creep of LRBs more accurately by changing the viscous damping coefficient in accordance with the progress of repeated excitation.

On the other hand, there are two current issues in simulating viscoelastic models using thermomechanical coupled behavior analysis, which will be addressed in future research as follows.

・There is room for further study on the appropriateness of the viscous damping coefficient.

・The effect of changing the viscoelastic model on the elastoplastic hysteresis loop of the lead plug by changing the viscous damping coefficient has not been analyzed.

REFERENCES

1. Ishii Ken, Kikuchi Masaru, Wake Tomotaka, Nagahiro Kenta, “Wind Loading Tests of Square type Lead Rubber Bearing (Part3)”, AIJ Journal, 2023, pp.611-612
2. Pacific Earthquake Engineering Research Center, The Open System for Earthquake Engineering Simulation, http://opensees.berkeley.edu
3. Takizawa Isamu, Wake Tomotaka, Kikuchi Masaru, Ishii Ken, “Improved thermo-dynamic behavior of lead-rubber bearings due to distributed lead-core configurations”, AIJ Journal, 2019, pp.147-148

EXPERIMENTAL STUDY ON THE PERFORMANCE OF PC-CSA-CaO BLENDED SYSTEM IN SUB-ZERO TEMPERATURE

Ge Zhang
Dr., College of Material Science and Technology, Xi'an University of Architecture & Technology, Xi'an, China.

Yijie Lei
Mr., College of Material Science and Technology, Xi'an University of Architecture & Technology, Xi'an, China.

Yixin Hao
Mrs., College of Material Science and Technology, Xi'an University of Architecture & Technology, Xi'an, China.

ABSTRACT:
In order to reduce the risk of early frost damage of concrete at sub-zero temperature, calcium oxide (CaO) and sulfoaluminate cement (CSA) were added to Portland cement (PC) to form a novel PC-CSA-CaO blended system. In this study, the strength, setting time, fluidity, deformation, temperature curve and the hydration products of PC-CSA-CaO blended system were studied. The results showed that the flexural strength and compressive strength of PC at -10℃ were slightly enhanced when CaO and CSA were added separately, while those were significantly increased when CaO and CSA were added simultaneously. The setting time and fluidity were obviously decreased by the presence of CaO because the fast and violent reaction and water consumption. Additionally, frost heave deformation could be effectively decreased by the addition of CaO and CSA. It was not only due to the heat release of CaO, but also attributed to the faster hydration by adding CaO and CSA.

Keywords: PC-CSA-CaO, Hydration, strength, setting time, fluidity, deformation

1. INTRODUCTION

Concrete, as the most widely used building material in recent years, played an important role in construction in cold regions [1-2]. However, adverse weather conditions had a significant negative impact on the early performance development of concrete [3-4]. Firstly, the decrease in temperature would affect the hydration rate of cement, seriously hindering the development of concrete strength [3]. Secondly, when the ambient temperature dropped below freezing point, the ice expansion pressure caused by the freezing of water in concrete would cause irreversible damage to the concrete structure [4].

In order to solve this problem, two methods were usually adopted: one was using insulation methods (warm shed method, heat storage method, electric heating method) to keep the concrete at a suitable temperature and promote the hydration of cement [5]. However, this method consumed a lot of manpower and energy sources, which contradicted the goal of green and low-carbon. The second was adding chemical admixtures [6]. However, the excessive addition of inorganic salt additives would cause a serious negative effect, such as steel corrosion, salt crystallization, and sulfate corrosion [7]. Therefore, it is necessary to seek a green, harmless, low-carbon and environmentally friendly method to solve the problem.

Calcium oxide (CaO), as a common heating and water absorbing material, could react with water to generate CH and rapidly release a large amount of heat, accompanied by a certain volume expansion [8]. If CaO can be reasonably used as a heat source in the cement system to provide heat for early hydration of cement in a negative temperature environment, it could promote cement hydration, delay the time before freezing, increase the early hydration time of cement, and be beneficial to the development of early structure of the cement. Li [9] firstly added CaO as a self-heating material to CSA under the negative temperature of -5℃. The results showed that the temperature of the system increased from 0℃ to 6℃ in 130 min.

In addition, sulphoaluminate cement (CSA) had some favorable properties such as fast hardening, early strength and good frost resistance. Recently, some scholars have proposed to add CSA to Portland cement (PC) to obtain the composite system with a better performance [10-12]. The combination of CSA and PC could have both high early strength and stable late strength [13, 14]. It mainly due to that in the composite system, $C_4A_3\bar{S}$ in CSA firstly rapidly hydrated and then C_3S in PC subsequently hydrated [15, 16].

In this study, CaO and CSA were added to PC to form a novel PC-CSA-CaO blended system. The effects of CaO and CSA on the performance and hydration of PC at -10℃ environment were studied. The flexural strength, compressive strength, setting time, fluidity, deformation,

temperature curve and the hydration products of PC-CSA-CaO blended system were studied.

2. MATERIALS AND METHODS

2.1 MATERIALS

The chemical compositions of PC, CaO and CSA clinker used in this study were shown in Table 1~3, respectively. The CSA was composed of 75% CSA clinker and 25% gypsum. The purity of gypsum was ≥99%. To obtain the suitable fluidity, polycarboxylate superplasticizer was used.

Three composite systems were set up: (1) PC-CaO, composed of 95% PC and 5% CaO; (2) PC-CSA, composed of 90% PC and 10% CSA; (3) PC-CSA-CaO, composed of 85.5% PC, 9.5% CSA and 5% CaO.

The w/c was 0.26 and the ratio of binder to sand was 1:1. The dosage of polycarboxylate superplasticizer was 0.3%.

2.2 METHODS

(1) Strength

After preparing the mortar according to the mix proportion, mortar was poured into a 40 mm × 40 mm × 160 mm steel mould. Then, it was covered with polyethylene film and was immediately placed in a negative temperature curing chamber for curing at a temperature of -10℃. After being cured to the specified age (1d, 7d, 28d), flexural strength and compressive strength was tested according to "Method for Testing the Strength of Cement Mortar (ISO Method)" (GB/T 17671-2021).

(2) Setting Time

Cement paste was prepared to test the setting time. The determination was carried out in accordance with the standard "Method for testing water consumption, setting time, and stability of cement standard consistency" (GB/T 1346-2011). The experimental instrument was the Vicat apparatus.

(3) Fluidity

Mortar was prepared to test the fluidity. The determination was carried out in accordance with the "Method for determining the fluidity of cement mortar" (GB/T 2419-2005).

(4) Deformation

The determination of the deformation was based on the standard "Concrete expansion agent" (GB/T 23439-2017). The size of the mould used was 40 mm × 40 mm × 160 mm, and a longitudinal limiter was applied. After 24 h, sample was demoulded and the initial length was immediately measured. Subsequently, the specimens were cured at the temperature of -10℃. The deformation of sample was the length change compared with the initial.

(5) Temperature curve

The temperature change curve of samples was tested by using the temperature recorder, as shown in Fig. 1. Mortar was prepared and poured into a 100 mm × 100 mm × 100 mm mould. Simultaneously, a thermocouple was put into the center of the sample. The initial temperature was 20℃, and the sample was quickly put into the environment of -10℃.

Table 1. Chemical compositions of PC (%)

SiO_2	Al_2O_3	Fe_2O_3	CaO	MgO	SO_3	NaO	f-CaO	Loss	Cl^-
20.82	4.40	3.27	63.34	2.88	2.42	0.59	0.87	1.54	0.02

Table 2. Chemical compositions of CaO (%)

CaO	MgO	Fe	P	S	SiO_2	HCl(insolubility)
98.2	0.79	0.033	0.0046	0.02	0.17	≤0.03

Table 3. Chemical compositions of CSA clinker (%)

SiO_2	Al_2O_3	Fe_2O_3	CaO	MgO	SO_3	TiO_2
8.2	34.3	2.5	41.8	3.2	8.5	1.0

Fig.1 Diagram of temperature recorder.

(6) Hydration products

Hydration products of the samples were analyzed by using XRD. The hydration was stopped by isopropyl alcohol. Before test, 10 wt. % CaF_2 was blended as the internal standard substance. The scanning angle range 2θ was 5～70°, step size was 0.02°, and divergence slit was 1°. After testing, XRD Rietveld analysis was used to calculate the content of the hydration products.

3. RESULTS AND DISCUSSIONS

3.1 STRENGTH

The flexural strength of PC, PC-CaO, PC-CSA and PC-

CSA-CaO system under -10℃ was shown in Fig. 2. The flexural strength of PC at 1d, 7d, and 28d was only 0.3, 2.1 and 4.1 MPa, respectively. It was indicating that the negative temperature significantly affected the hydration of cement. The addition of CaO and CSA respectively enhanced the flexural strength to a different extent. When adding CaO, the flexural strength of PC-CaO could up to 6.2 MPa at 28d, while that of adding CSA was 4.4 MPa. When the CaO and CSA was added simultaneously, the early flexural strength and the late flexural strength were enhanced more significantly. It was 2.2 and 6.5 MPa at 1d and 28d respectively. It could be concluded that there is a synergistic effect between CaO and CSA. The reaction of CaO provided early heat and the addition of CSA accelerated the hydration of the system.

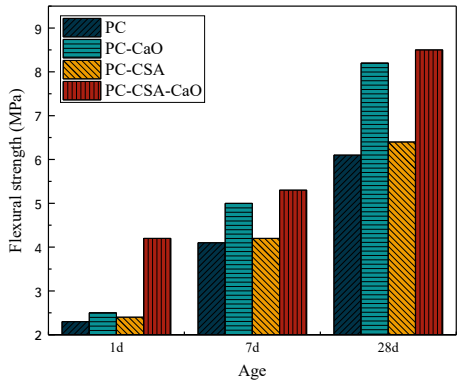

Fig.2 Flexural strength of samples at different ages

The compressive strength of PC, PC-CaO, PC-CSA and PC-CSA-CaO system under -10℃ was shown in Fig. 3.

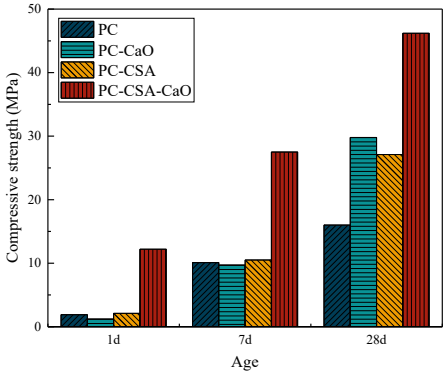

Fig.3 Compressive strength of samples at different ages

From Fig. 3, the development of compressive strength for PC was slow. It was only 1.9, 10.1 and 16.0 MPa at 1d, 7d and 28d. When adding CaO and CSA respectively, the early compressive strength at 1d and 7d was hardly increased, while that of at 28d was obviously increased to 29.8 and 27.1 MPa, respectively. In addition, the combination of CaO and CSA enhanced the compressive strength at each stage. It was 12.2, 27.5 and 46.2 MPa at 1d, 7d and 28d, respectively.

When adding CaO, the reaction of it released amount of heat, which would accelerate the hydration of cement at the low temperature [9]. However, the formation of CH may hinder the dissolution of C_3S, which further hindered the hydration at early stage.

When adding CSA, $C_4A_3\bar{S}$ was hydrated in the first few minutes to form ettringite (AFt), which was a needle-like crystal [15]. It was benefit for the formation of early structures. Subsequently, C_3S in PC hydrated to form gel-like C-S-H, which could fill in the AFt skeleton to form a denser microstructure [16]. However, in the low temperature, this process was hindered.

The combination of CaO and CSA accelerated the hydration from different aspects. Once there was enough heat, the acceleration by CSA acted. Therefore, the compressive strength of samples was enhanced by the combination of CaO and CSA at each stage.

3.2 SETTING TIME

The setting time of samples was shown in Fig. 4. The initial and finial setting time of PC was 163 and 218 min. The addition of CaO significantly shortened the setting time. It was only 7 and 21 min for initial and finial setting time. The reaction of CaO was rapid and drastic. Simultaneously, a large amount water was consumed to accelerate the setting. In addition, the hydration of cement was accelerated by the released heat. When adding CSA, the setting time was also shortened. It was 75 and 87 min for initial and finial setting time. The hydration of $C_4A_3\bar{S}$ and formation of AFt also consumed water. Additionally, the hydration of the blended system was faster than that of PC. With the combination of CaO and CSA, the initial and finial setting time was decreased to 20 and 29 min, respectively. Because the heat release of CaO and the acceleration of hydration by CSA, the hydration of the blended system was fast and the water consumed rapidly.

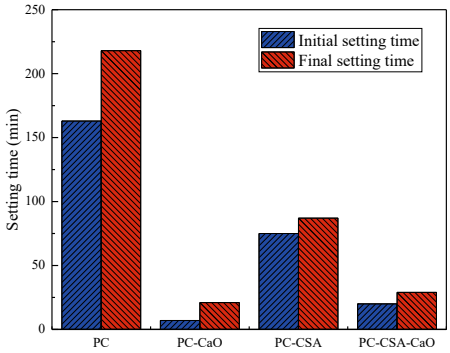

Fig.4 Setting time of different systems

3.3 FLUIDITY

The fluidity of different systems was shown in Fig. 5. Similar to setting time, PC had the largest fluidity, which was 300 mm. The adding of CaO obviously decreased the fluidity, which was 175 mm. It related to the rapid consumption of free water because the reaction of CaO.

The addition of CSA also decreased the fluidity of PC. It mainly because of the faster formation of AFt, which consumed a large amount of free water. Besides, the blended system hydrated faster than PC, and simultaneously large amount of hydration products formed, which decreased the fluidity. When adding CaO and CSA simultaneously, the fluidity was further decreased. In the action of CaO and CSA, the free water was consumed faster and the hydration of the blended system was also accelerated. Therefore, it was only 165 mm for PC-CSA-CaO system.

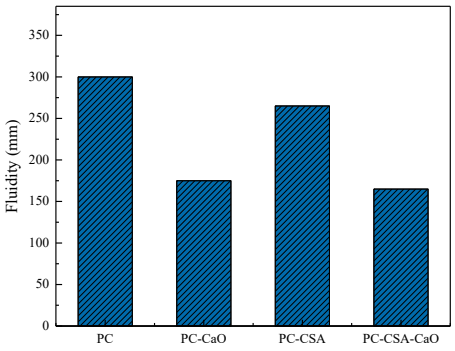

Fig.5 Fluidity of different systems

3.4 DEFORMATION

The deformation of different systems at -10℃ was shown in Fig. 6. From Fig. 6, the expansion rate of PC rapidly increased to 0.11% at early stage, and then tended to be gentle. This may be due to insufficient hydration of cement at an early stage. The system contained a lot of free water. The temperature of the system decreased continuously under the action of negative temperature environment. When it dropped below freezing point, the free water in the system frozen, forming ice crystals, which caused about 9% volume expansion.

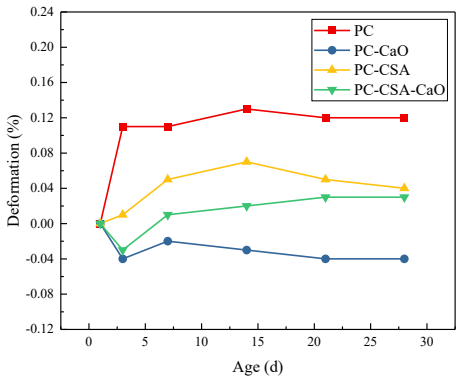

Fig.6 The deformation of different systems

When adding CaO, the expansion rate of PC-CaO rapidly decreased below 0 at early age, indicating that it was shrinkage at initial. For PC-CaO system, the rapid reaction of CaO released large amount of heat, which delayed the freezing of the sample. In addition, a lot of free water was consumed by the reaction of CaO, which significantly reduced the frost heave deformation. In addition, although the reaction of CaO and formation of CH was a process of increasing volume, this process occurred at the early stage due to its faster reaction rate. Therefore, the expansion efficiency brought by CaO cannot be well played. Thus, the frost heave deformation and expansion brought by CaO was small enough to be offset by the shrinkage of the cement paste.

After adding CSA, the rapid hydration consumed some free water, which decreased volume expansion caused by the transformation of free water to ice to a certain extent. Therefore, the expansion rate of PC-CSA system was lower than that of PC at each stage. However, at the low temperature of -10℃, the remaining free water that did not participate in the reaction was frozen. Therefore, the expansion rate was increased with age before 14d. Due to the slow hydration process, some free water melted and participated in the hydration, which reduced the expansion rate at late stage.

When with the CaO and CSA addition simultaneously, the volume of PC-CSA-CaO system firstly shrunk to -0.03% at the early age of 3d, and then slightly expanded to 0.3% at late stage of 28d. The presence of CaO not only released amount of heat to prevent frost damage, but also consumed a lot of free water. It effectively prevented early freezing damage of system, which significantly reduced the volume expansion caused by the transformation of free water to ice. In addition, the initial heat provided favorable conditions for early hydration of CSA. The faster hydration of the blended system also decreased the early freezing damage. Under the continuous hydration, more and more hydration products filled the pores, resulting in a small expansion at a later stage.

3.5 TEMPERATURE CURVE

The temperature curve of different systems was shown in Fig. 7. From Fig. 7, the temperature of PC system firstly increased to 22.1℃ and then rapidly reduced in the -10℃ environment. At the low temperature, only a few cement particles hydrated and released the hydration heat. At the time of 65 min, PC system went into the negative temperature.

After adding CaO, the temperature of PC-CaO system rapidly increased to 30.1℃, mainly due to that the reaction of CaO to release a lot of heat. Under this effect, the cement also had more opportunity to hydrate, and the time above negative temperature had been extended to 90 minutes, which was 38.5% longer than the PC system. It could be proved that CaO can effectively act as an early heat source in cement.

After adding CSA, the temperature of PC-CSA system was also rapidly increased to 26.7℃. The early hydration of the system was accelerated by the presence of $C_4A_3\bar{S}$ in CSA. It hydrated rapidly to form amount of needle-like AFt crystals. Simultaneously, a large amount of heat released. Under this effect, the time above negative temperature extended to 85 minutes, which was 30.7% longer than the PC system. It suggested that the promotion of early hydration was also beneficial to the

maintenance of early temperature

When adding CaO and CSA simultaneously, the temperature of PC-CSA-CaO system could rapidly up to 33.3℃, indicating there was a synergistic effect between CaO and CSA. In this blended system, CaO acted as the internal heat source and CSA acted as a mineral accelerator. The heat released by CaO and hydration heat accelerated by CSA further enhanced the early temperature of samples. Further, the time above negative temperature was extended to 101 minutes, which was 55.4% longer than the PC system.

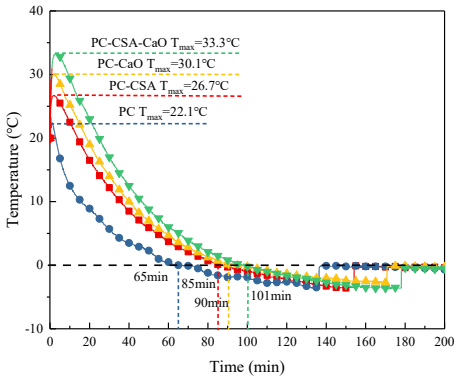

Fig.7 The temperature curve of different systems

3.6 HYRATION PRODUCTS

The XRD patterns of different systems at 28d was shown in Fig. 8. From Fig. 8, it could be seen that the types of the crystal hydration products of samples in different systems were similar, indicating that the addition of CaO and CSA did not change the hydration products type. However, the patterns intensity of AFt and CH changed by the addition of CaO and CSA. In order to analyze accurately, XRD Rietveld was used to calculate the contents of AFt and CH, as shown in Fig. 9.

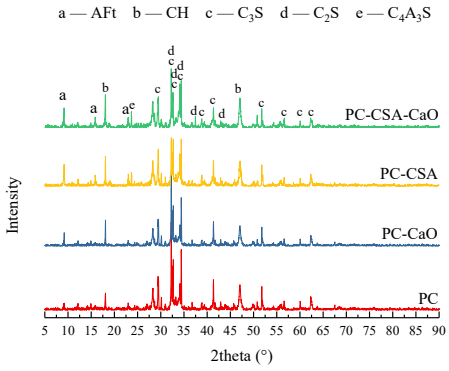

Fig.8 The XRD patterns of different systems at 28d

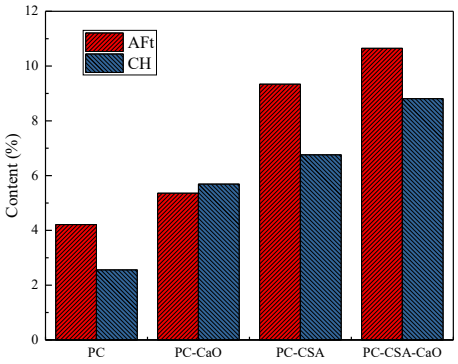

Fig.9 The content of AFt and CH in different systems

From Fig. 9, the content of AFt and CH in PC system was low because the hydration was hindered by the low temperature of -10℃. Besides, due to the early frost heave damage, the microstructure of the matrix was destroyed, thus obtaining a lower strength.

The adding of CaO effectively improved the AFt and CH content of PC. On the one hand, the reaction of CaO led to a large amount of CH formation. Besides, the higher temperature and more time above negative temperature was also beneficial to the hydration of cement particles. However, the formation of CH caused by CaO may be not beneficial to the hydration of C_3S. Therefore, although this system could effectively avoid frost heave damage, it was still not high in strength.

The addition of CSA further increased the content of AFt and CH. Firstly, AFt was the one of the main hydration products of $C_4A_3\overline{S}$. It hydrated fast in the PC-CSA system to form large amount of AFt. Besides, the presence of CSA was beneficial to the hydration of the whole system by increasing the early temperature and longer time before negative temperature. Thus, the hydration of silicate phase was also accelerated and the amount of CH was also increased. However, combined with the result of deformation, the system would still suffer from freezing damage, so the strength was still not high.

When CaO and CSA added simultaneously, the content of AFt and CH was further increased. On the one hand, the reaction of CaO itself would generate a large amount of CH. On the other hand, as the internal heat source, CaO released a large amount of heat, which was beneficial to the hydration of the system. Furthermore, in the presence of CSA, the hydration of the system was further accelerated, which was beneficial to increase of hydration products. When heat was provided and hydration was accelerated, the PC-CSA-CaO blended system reduced the risk of early freezing damage and was able to hydrate to produce a large number of hydration products, resulting in a denser microstructure and thus a higher strength at the low temperature of -10℃.

4. CONCLUSIONS

In this study, CaO and CSA were added to PC to reduce the risk of early frost damage of concrete at sub-zero temperature. The stength, setting time, fluidity,

deformation, temperature curve and the hydration products of PC, PC-CaO, PC-CSA and PC-CSA-CaO system were studied. On the basis of the results above, the following conclusion can be drawn:

(1) When CaO and CSA were added separately, the flexural strength and compressive strength of PC were slightly increased at -10℃, while the flexural strength and compressive strength of PC were significantly increased when CaO and CSA were added simultaneously.
(2) The presence of CaO greatly shortened the setting time and fluidity due to the fast and violent reaction induced by CaO and the large amount of water consumed.
(3) The frost heave deformation of PC was reduced to varying degrees by the addition of CaO and CSA. In the presence of CaO, a large amount of free water was consumed, significantly reducing the risk of frost heave damage.
(4) CaO could be effectively used as an early heat source in cement. Under the early high heat excitation, CSA further promoted the hydration of cement and released a large amount of hydration heat.
(5) When CaO and CSA were added at the same time, the contents of AFt and CH were significantly increased, which was conducive to the increase of microstructure density of the matrix and strength.

ACKNOWLEDGEMENT:

The National Natural Science Foundation of China (No. 5220081915) for current research are gratefully acknowledged.

REFERENCES：

1.G. Zhang, Y. Yang, H. Yang, H. Li, "Calcium sulphoaluminate cement used as mineral accelerator to improve the property of Portland cement at sub-zero temperature", Cement and Concrete Composites, Vol. 106, 2020, pp. 103452.
2.Demirboga, R., Karagol, F., Polat, R., Kaygusuz, M. A., "The effects of urea on strength gaining of fresh concrete under the cold weather conditions", Constr Build Mater, Vol. 64, 2014, pp. 114-20.
3.Lei X., "Discuss the safety management measures of oil - field surface engineering construction in winter", China Petroleum and Chemical Standards and Quality, Vol. 42, No. 7, 2022, pp. 47-49.
4.Ba H., Yang Y., Feng Q., "Research on frost resistance of concrete working in minus temperature", Architecture Technology, Vol. 10, 2002, pp. 734-735.
5.Wang L., "Research on winter construction technology of tunnels in high altitude and cold regions", Value Engineering, Vol. 42, No. 14, 2023, pp. 94-96.
6.Rixom, M. R., Mailvaganam, N., "Chemical admixture for concrete", London, 1999.
7.Juenger, M. C., Monteiro, P. J., Gartner, E. M., Denbeaux, G. P., "A soft X-ray microscope investigation into the effects of calcium chloride on tricalcium silicate hydration", Cement and Concrete Research, Vol. 35, No. 1, 2005, pp. 19-25.
8.Liu C., Xue Y., Wei W., "Research progress of food self-heating technology", Journal of Chinese Institute of Food Science and Technology, Vol. 20, No. 11, 2020, pp. 351-356.
9.Haohao Li, "Experimental study on spontaneous heating mix ratio of prestressed passage grouting material in plateau area", Hunan University of Science and Technology, 2019, pp. 46-59.
11.Xiaowan Xu, "The experimental study on properties of Portland cement-Sulphoaluminate cement blended system", Shenyang Jianzhu University, 2018, pp. 41-46.
12.G. Le Saout, B. Lothenbach, A. Hori, et al., "Hydration of Portland cement with additions of calcium sulfoaluminates", Cement and Concrete Research, Vol. 43, 2013, pp. 81-94.
13.G. Li, Q. Liu, M. Niu, et al., "Characteristic of silica nanoparticles on mechanical performance and microstructure of sulphoaluminate cement/ordinary Portland cement binary blends", Vol. 242, 2020, pp. 118158.
14.G. Ji, H. A. Ali, K. Sun, et al., "Volume deformation and hydration behavior of ordinary Portland Cement/Calcium Sulfoaluminate cement blends", Vol. 16, No. 7, 2023, pp. 2652.
15.G. Le Saout, B. Lothenbach, A. Hori, et al., "Hydration of Portland cement with additions of calcium sulfoaluminates", Cement and Concrete Research, Vol. 43, 2013, pp. 81-94.
16.R. Tr Ba H auchessec, J. M. Mechling, A. Lecomte, et al., "Hydration of ordinary Portland cement and calcium sulfoaluminate cement blends", Cement and Concrete Research, Vol. 56, 2015, pp. 106-114.

Evaluation of the Self-Sensing Properties of Reinforced Concrete Units Using Self-Sensing Mortar for Section Enlargement

Jinseob KIM
Master course, Dept. of Architectural Engineering, Korea National University of Transportation, South Korea.

Dokyun KIM
Master course, Dept. of Architectural Engineering, Korea National University of Transportation, South Korea.

Geonwoo IM
Master course, Dept. of Architectural Engineering, Korea National University of Transportation, South Korea

Youngmin KIM
Doctor course, Dept. of Architectural Engineering, Korea National University of Transportation, South Korea.

Guncheol LEE
Professor, Dept. of Architectural Engineering, Korea National University of Transportation, South Korea.

ABSTRACT
This study examined the relationship between compressive strength and self-sensing capability of concrete sections enlarged with self-sensing mortar. Based on these findings, a mock-up test was performed using reinforced concrete structural unit members. Experimental results indicated that concrete with section enlargement using self-sensing mortar exhibited increased compressive strength compared to plain concrete. Furthermore, a high correlation (R^2 = 0.9) was observed between the fractional change in resistance (FCR) and compressive stress. The mock-up test of reinforced concrete structural unit members also demonstrated a strong correlation between FCR and strain. These findings confirmed the potential of using self-sensing mortar for structural health monitoring of section-enlarged members.

Keywords: section enlargement, self-sensing mortar, reinforced concrete, unit members, carbon nanotubes

1. INTRODUCTION

The advent of the Fourth Industrial Revolution has led to the implementation of big data, AI, nanotechnology, and other advancements across various industries, including construction. Significant research is being conducted to leverage these technologies actively within the construction sector[1)].

A prominent area of research in the construction industry, particularly regarding concrete, is the development of smart concrete, characterized by self-sensing capabilities. Self-sensing technology utilizes the piezoresistive properties of conductive materials to monitor the health of concrete structures by evaluating their deformation and damage. This is achieved by incorporating conductive materials, such as metal powders and carbon nanotubes, into the otherwise non-conductive concrete, thereby imparting conductivity. [2)]

Implementing self-sensing technology enables immediate and continuous monitoring of a building's state, providing a significant advantage over traditional techniques that rely on visual inspection, core sampling, and changes in chemical properties to assess the degradation of a building's performance. Numerous studies have analyzed self-sensing properties of concrete in response to different types of stress, highlighting its potential for health monitoring. However, most of these studies have been limited to specimen-level or unit structural members, such as beams and columns. There are few cases where self-sensing technology has been applied to, and evaluated in, actual structures with complex assemblies of structural members.

Additionally, since self-sensing technology is primarily examined at the level of individual concrete members, its current application is limited to newly constructed buildings. Therefore, there is a pressing need to develop methods for health monitoring of existing buildings using self-sensing technology. With the recent increases in aging buildings and approvals for their vertical extensions, the reinforcement of structural members in existing building has become more common. However, there are currently no available methods to evaluate post-reinforcement stress distribution, deformation, and damage.

To address this, this study aimed to apply health monitoring using self-sensing technology to existing structural members requiring reinforcement. We used compression test specimens reinforced with self-sensing mortar through section enlargement. By evaluating the relationship between the fractional change in resistance (FCR), stress, and strain under stress, we confirmed their self-sensing performance. Additionally, in the mock-up

test using reinforced concrete structural unit members, we aimed to propose an equation that can predict the strain of reinforced concrete members based on the relationship between stress and the FCR.

2. EXPERIMENTAL PLAN AND METHOD

2.1 Experimental design

The experimental plan is outlined in Table 1, and the mix proportions of the self-sensing mortar are detailed in Table 2. The study was conducted in two series: Series I and Series II. In Series I, specimens with sections enlarged using self-sensing mortar were tested to examine the relationship between their mechanical properties and the FCR. Series II involved a mock-up test based on results from Series I to evaluate the performance of self-sensing mortar for section enlargement applied to reinforced concrete structural members, including columns and beams. This was done by measuring FCR and strain under applied stress until failure.

Table 1. Experimental Plan

Series	Specimen Type	Experimental Details
Series I	Compression test specimens using self-sensing mortar for section enlargement	·Compressive Strength (28 days) and Fractional Change in Resistance (28 days)
Series II	Reinforced concrete unit members	· Fractional Change in Resistance and Stain

Table 2. Self-Sensing Mortar Mix Proportions

W/B (%)	Unit Material Quantity (kg/m³)				High-Performance Admixture (%)
	Cement	Polymer	Silica Sand	CCPM	
34	902	38	855	85	1.5

CCPM : Carbon composite porous material

Table 3. Concrete Mix Proportions for the Mock-up Test

W/C (%)	FAR (%)	Unit Material Quantity (kg/m³)			AE (%)
		Cement	Fine Aggregate	Coarse Aggregate	
53.0	43	315	764	1 032	0.7

FAR : Fine Aggregate Ratio

2.2 Experimental method

2.2.1 Compressive strength

Specimens for measuring the compressive strengths of self-sensing mortar and baseline concrete were fabricated to a size of Φ100×200 mm in accordance with KS F 2405 (Test Method for Compressive Strength of Concrete)[3]. The compression test specimens for section enlargement were produced with a size of Φ80×200 mm, as shown in Figure 1. These specimens were initially cured underwater at 20±2°C for 28 days. After section enlargement with a thickness of 10 mm using self-sensing mortar, the specimens were again cured underwater for an additional 28 days. Compressive strengths and FCR until failure were measured along with strain.

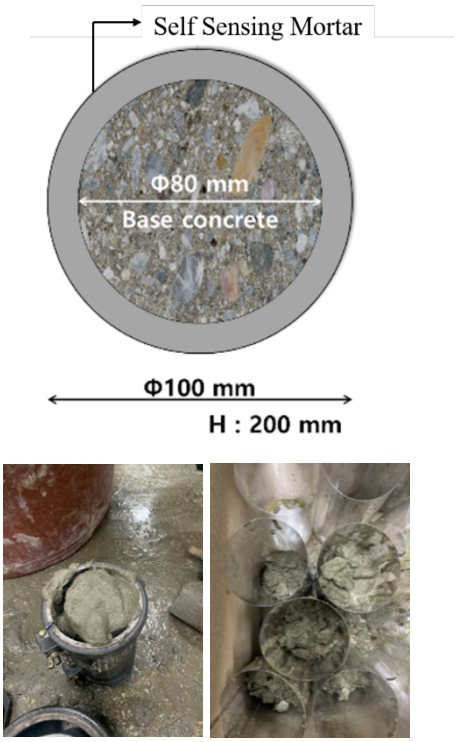

Figure 1. Section enlargement of Compression Test Specimen

2.2.2 Mock-up Test of Reinforced Concrete Structural Unit Members

To evaluate the self-sensing performance of reinforced concrete structural unit members with section enlargement using self-sensing mortar, a physical model was constructed as shown in Figure 2. The lower foundation was made to a size of 1900 (width) × 500 (depth) × 300 (height) mm, while the columns were sized at 100 (width) × 100 (depth) × 1000 (height) mm, and the beams were sized at 2600 (width) × 100 (depth) × 100 (height) mm. Before concrete pouring, each member was reinforced with strained steel bars of yield strength (fy) 400 MPa and a diameter of 6 mm, with a cover thickness of 10 mm.

Furthermore, during the construction of the formwork for the physical model, foam boards of size 250 (width) × 100 (depth) × 30 (height) mm were attached to the

areas where the section enlargement with self-sensing mortar was to occur. After constructing the physical model with section enlargement using self-sensing mortar, its self-sensing performance was evaluated by applying stress using a three-point loading method at the center of the beam, with a loading rate of 23 N/s until failure.

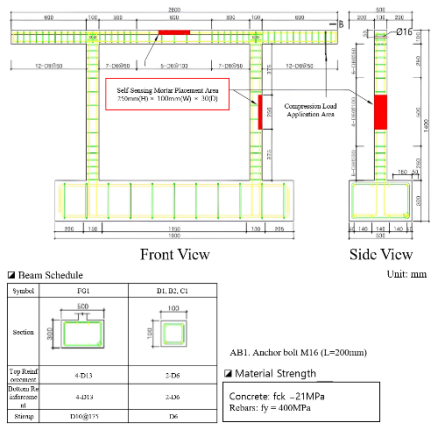

Figure 2. Reinforced Concrete Structural Unit Member Drawings

2.2.3 Measurement of Electrical Resistance and Strain

To analyze the relationship between electrical resistance, strain, and stress in concrete with section enlargement using self-sensing mortar, the following procedures were performed, as illustrated in Figure 3:

Compression test specimens were equipped with strain gauges at the center of the specimen. Electrical resistance electrodes (copper wires) were applied with silver paste at 50 mm intervals above and below the centerline of the specimen. Additionally, electrodes for electrical supply were attached at 30 mm intervals on the outside of electrodes for resistance measurement.

Data on electrical resistance, stress, and strain were collected using a data logger (DAQ 970A) at 1-second intervals until failure of the compression test specimens and the physical model specimens. The collected data were then used to determine the correlations.

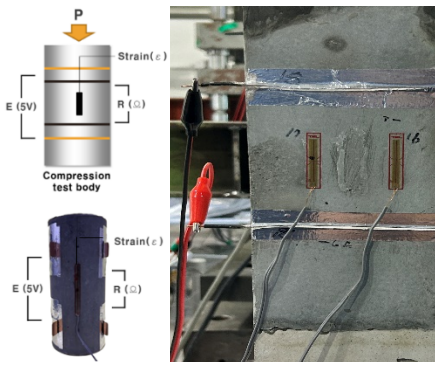

Figure 3. Measurement of Electrical Resistance and Strain by Specimen Type

3. Experimental results and analysis

3.1 Compressive strength characteristics after section enlargement

Figure 4 shows the results of measuring the compressive strengths of self-sensing mortar and section-enlarged concrete at 28 days. First, the compressive strength of the baseline concrete was measured at 26.4 MPa at 28 days, meeting the target of 27 MPa. The compressive strength of the self-sensing mortar at 28 days was 49.4 MPa, and the compressive strength after section enlargement was 37.3 MPa, an improvement of 10 MPa (40%) compared to the section enlargement rate of 36%.

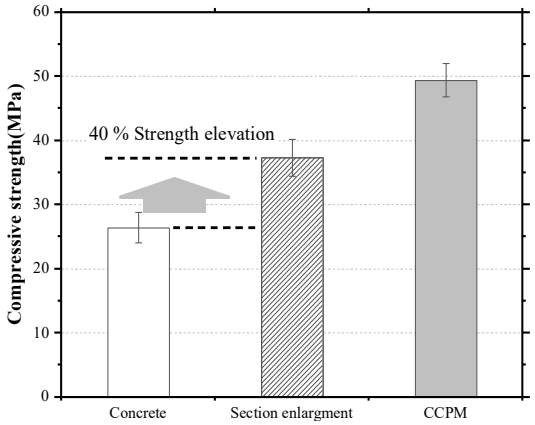

Figure 4. Compressive Strength Measurement Results Before and After Section Enlargement

3.2 Electrical properties of compressive strength test specimens

Figure 5 shows the relationships between the fractional change in resistance (FCR) and stress, as well as FCR and strain, under compressive stress conditions until failure for self-sensing mortar. Figure 6 presents these relationships for section-enlarged concrete under the same compressive stress conditions until failure.

For both self-sensing mortar and section-enlarged concrete, FCR generally decreased until compressive failure. This trend is attributed to the closer spacing of carbon nanotube networks within the specimens under compressive stress, which enhances electrical conductivity4). The same trend was observed in the relationships between FCR and strain, and FCR and stress. Additionally, for self-sensing mortar, there was no significant change in FCR up to 30% of stress and strain, which is likely because no substantial deformation or cracking occurred up to this point. The coefficients of determination (R^2) for FCR versus stress and for FCR and strain were similar at 0.931 and 0.934, respectively. After section enlargement, the FCR exhibited a decreasing trend under compressive stress conditions. Unlike the self-sensing mortar, no large changes in FCR were observed, indicating that the immediate deformation occurred due to the thinner 10 mm section enlargement. This aligns with Jung et al.5)'s findings that sensors with a smaller cross-sectional area and larger aspect ratio exhibit superior sensing performance. Consequently, the R^2 values for FCR versus stress and FCR versus strain were 0.967 and 0.995, respectively,

indicating high accuracy. It is suggested that evaluating self-sensing performance on a relatively thin section after section enlargement provides greater accuracy compared to measuring self-sensing performance over the entire cross-section using compressive resistance.

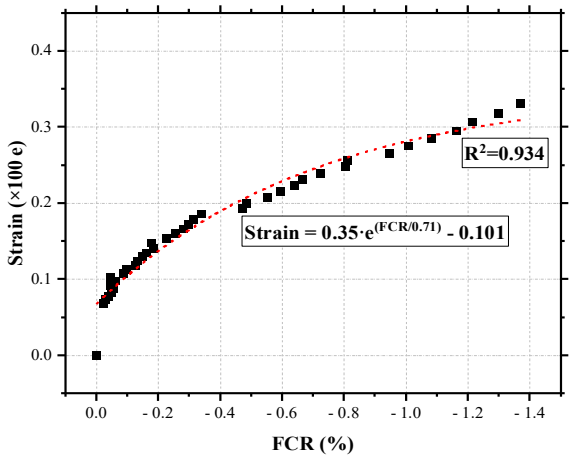

a) FCR - Strain

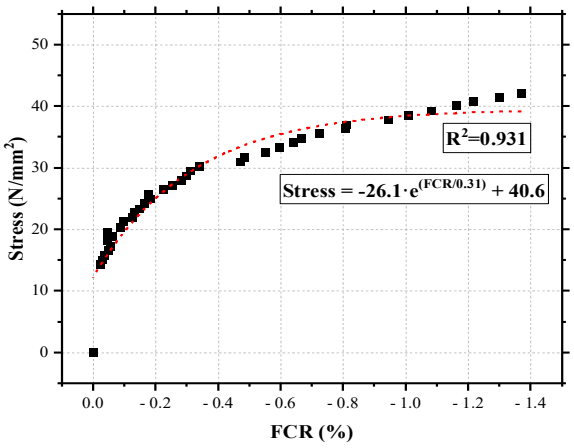

b) FCR- Stress

Figure 5. Electrical properties of self-sensing mortar under compressive stress conditions

Category	Compression Test Specimen
Self-Sensing Mortar	• FCR – Stress(f) (R^2 = 0.934) $f = 40.6\text{-}26.1 \cdot e^{(FCR/0.31)}$ • FCR – Strain(ε) (R^2= 0.931) $\varepsilon = -0.101+0.35 \cdot e^{(FCR/0.71)}$
Section-Enlarged Concrete	• FCR – Stress(f) (R^2 = 0.995) $f = 46.5\text{-}49.1 \cdot e^{(FCR/0.35)}$ • FCR – Strain(ε) (R^2= 0.967) $\varepsilon = 0.24+0.25 \cdot e^{(FCR/0.73)}$

Table 4. Self-sensing correlations of section-enlarged specimens

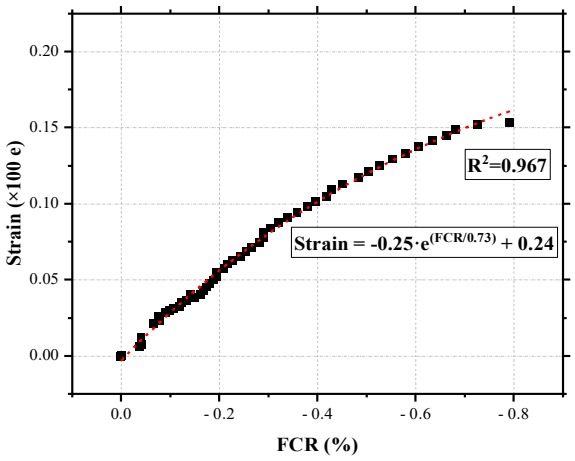

a) FCR - Strain

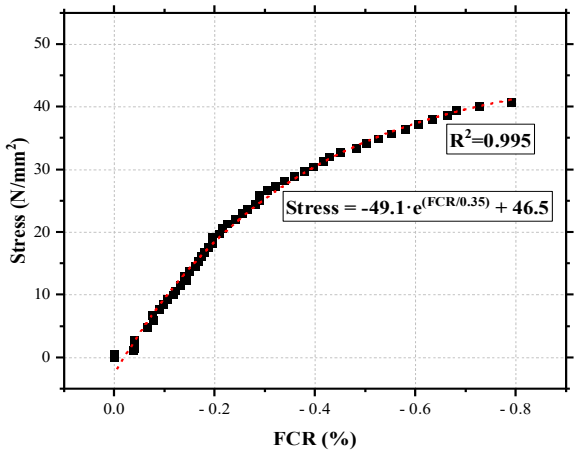

b) FCR – Stress

Figure 6. Electrical properties of section-enlarged specimens under compressive stress conditions

3.3 Electrical properties of Mock-up specimens

The results of analyzing the self-sensing properties of a physical model of reinforced concrete with section enlargement using self-sensing mortar are shown in Figure 7 and Figure 8. Firstly, in the beam with section enlargement at the upper part, when compressive stress is applied, the spacing between the conductive nanomaterial network becomes closer (Tunnel effect). As shown in Figure 7-a), this leads to improved conductivity and a decrease in electrical resistance, with a fractional change in resistance (FCR) of approximately -6.5%. Additionally, strain tends to contract due to compressive stress. However, in the section-enlarged column, both electrical resistance and strain increased as shown in Figure 7-b). This result is attributed to the fact that the column, constrained by the deflection of the beam, experiences compressive stress inwardly, while tensile stress acts on the enlarged outer part. The relationship between the FCR and strain for both the section-enlarged beam and column appears to be proportional. The analysis of the correlation is shown in Table 5 and Figure 8. It is possible to derive a formula to predict the strain of members from the FCR.

The coefficient of determination (R^2) for the columns and beams is 0.999, indicating a strong correlation, suggesting the potential of using for health monitoring of section-enlarged members.

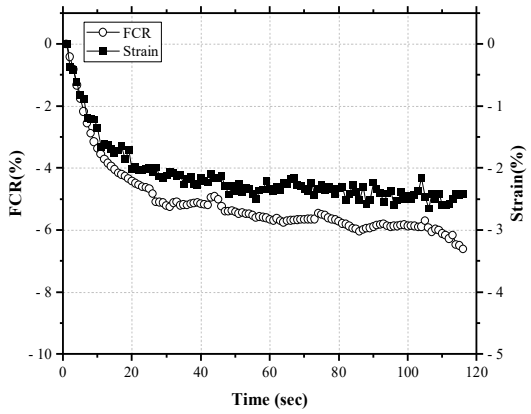

a) Beam with section enlargement

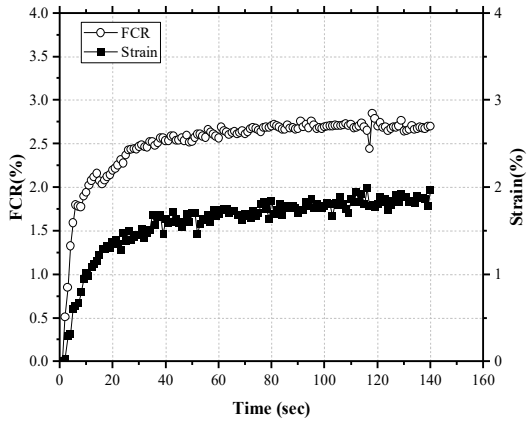

b) Column with section enlargement

Figure 7. FCR and Strain under Load in the Physical Model

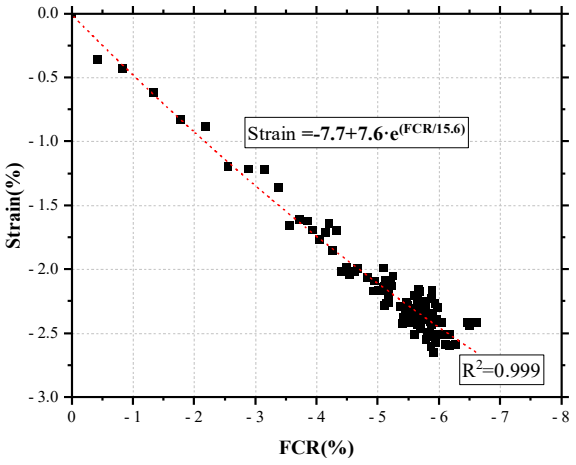

a) Beam with section enlargement

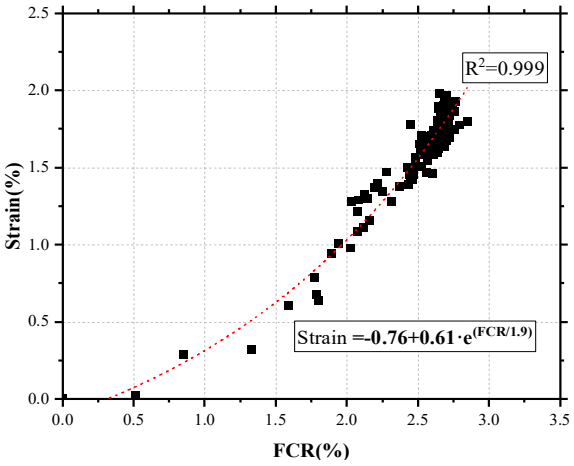

b) Column with section enlargement

Figure 8. Correlation between FCR and Strain in the Physical Model

Category	Correlation	Coefficient of Determination (R^2)
Beam	• FCR – Strain(ε) (R^2= 0.999) $\varepsilon = -7.7+7.6\cdot e^{(FCR/15.6)}$	0.999
Column	• FCR – Strain(ε) (R^2= 0.999) $\varepsilon = -0.76+0.61\cdot e^{(FCR/1.9)}$	0.999

Table 5. Self-Sensing Correlations of Section-Enlarged Members in the Physical Model

4. Conclusion

This study evaluated the self-sensing properties of reinforced concrete structural unit members with cross-sectional reinforcement using self-sensing mortar. The results can be summarized as follows:

1) **Effect of Self-Sensing Mortar on Compression Test Specimens:** For compression test specimens reinforced with section enlargement using self-sensing mortar, the electrical resistance decreased due to the tunneling effect of carbon nanotubes when stress was applied. Additionally, the deformation of the compression test specimens also decreased, and the relationships between electrical resistance and strain, as well as between electrical resistance and stress, were similar. The coefficients of determination for these relationships were above 0.9, indicating high accuracy.

2) **Self-Sensing Mortar in Reinforced Concrete Unit Members**: In reinforced concrete structural unit members, measurements of electrical resistance and strain from the central parts of columns and beams, after reinforcement with self-sensing mortar and applying stress until failure, showed that electrical

resistance decreased at the top of the beam under compressive stress. Conversely, electrical resistance increased in the columns constrained by the beam where bending strain occurred.

3) **Prediction of Strain Using FCR**: In tests of reinforced concrete structural unit members, an equation was proposed to predict strain using the FCR, with the same exponential function used for compression test specimens. The coefficients of determination for both were above 0.9, demonstrating high accuracy.

The results of this study confirmed both self-sensing performance in reinforced concrete structural unit members and the potential of using self-sensing technology for health monitoring in actual buildings.

ACKNOWLEDGEMENT
This research was supported by the Mid-career Researcher Program through the National Research Foundation of Korea (NRF) funded by the Ministry of Education (No. 2023R1A2C2006400).

References

1. Na, S., Heo, S., Choi, W., Kim, C., & Whang, S.W. (2023). Artificial Intelligence (AI)-Based Technology Adoption in the Construction Industry: A Cross National Perspective Using the Technology Acceptance Model. *Buildings*, 13(10), 2518.

2. Lee SH, Han SJ, Jan BS, Kim kw, Seo SY. Evaluation of Self-Sensing Performance of UHPC with Carbon Nanotube. Journal of the Korea Concrete Institute; 2020 Oct 19;32(6):505-12.

3. "Polymer Cement Mortar for Repair of Concrete Structures," Korean Standards Association, KS F 4042, 2002

4. Jang AY, Yun HD, Hong SW, Lee GC, Seo SY, Park WS. Effect of Multi-Walled Carbon Nanotubes (MWCNTs) Addition on Repeated Compressive Strain-Sensing Properties of Hybrid Steel and Polyethylene Fibers Reinforced Strain-Hardening Cement Composite (Hy-SHCC). Journal of the Korea Concrete Institute Vol. 34, No. 2, pp.

5. Jung JH, Yoon JH, Kim I, Shim SE. "Piezoresistive Effect of Rubber Composites," Journal of the Korean Rubber Society, 2013, Vol. 48, No. 1, pp. 76-84

6. Lee SY, Kim MK, Kim DJ. Effect of Loading Rate on Self-stress Sensing Capacity of the Smart UHPC, Journal of the Korea Academia-Industrial.2021May;22(5):88-8.

7. Lee GC, Kim YM, Kwon HW. Fundamental properties of repair mortar using CNT impregnated in porous material, Journal of the Korea Institute of Building Construction. 2021 Nov ;22(2):67-8

Heat-stored engineered cementitious composite containing phase change material

Huayang Sun
Doctoral student
State Key Laboratory of Silicate Materials for Architectures, Wuhan University of Technology, Wuhan 430070, PR China.
School of Civil Engineering, Harbin Institute of Technology, Harbin, China.

Kunyang Yu*
Associate professor
School of Water Conservancy and Civil Engineering, Northeast Agricultural University, Harbin, 150030, China.
School of Civil Engineering, Harbin Institute of Technology, Harbin, China.

Minjie Jia
Doctoral student, School of Civil Engineering, Harbin Institute of Technology, Harbin, China.

Yingzi Yang
Professor, School of Civil Engineering, Harbin Institute of Technology, Harbin, China.

Yushi Liu*
Associate professor
School of Civil Engineering, Harbin Institute of Technology, Harbin, China.
State Key Laboratory of Silicate Materials for Architectures, Wuhan University of Technology, Wuhan 430070, PR China

ABSTRACT:

This study developed a kind of heat-stored Engineered Cementitious Composite (ECC) by replacing micro silica sand with varying proportions of microencapsulated n-octadecane/fly ash cenosphere (ODE/FAC) phase change material (PCM), in order to enhance the tensile and thermal properties. The increased incorporation content of ODE/FAC reduced the compressive strength, flexural strength, and tensile cracking strength of the ECC specimens, while concurrently enhancing their tensile strength and tensile strain capacity. Furthermore, the inclusion of ODE/FAC composites endowed ECC specimens with heat storage capacity. The prepared novel heat-stored ECC showed significant potentials in green building applications by integrating load-bearing capabilities with indoor temperature control in structural concrete elements.

Keywords: Phase change materials; Engineered cementitious composites; Tensile strength.

1. INTRODUCTION

In recent years, energy utilization and efficiency of buildings have become a trending topic in the world. This is due to the fact that as one of the major energy-consuming sectors, the building industry plays a crucial role in energy conservation and emission reduction[1]. It is worth noting that throughout the life cycle of a building, most of the energy consumption is used to maintain the thermal comfort of the dwelling[2]. Therefore, developing thermal energy storage systems in building is important

for reducing energy consumption and efficient energy utilization.

The excellent thermal energy storage capacity of building envelope usually is required in order to absorb indoor waste heat, thus tailoring the thermal comfort. Presently, the common ways accompanied by a complex heat storage system. In contrast, latent heat storage system with phase change materials (PCMs) has the advantages of excellent heat storage capacity, simplicity of application, and good architectural compatibility[6,7]. PCMs can be considered as superior heat storage materials because they can absorb and discharge a large amount of latent heat at a nearly constant temperature by phase change process. The indoor temperature fluctuations can be mitigated when PCMs are used in building structures such as wall, floor, ceiling, etc., thereby achieving energy saving and emission reduction performance in buildings[8–10].

Previous studies have demonstrated that the incorporation of PCMs can endow cement-based materials with latent heat storage capacity, forming heat-stored functionalized building materials. However, the addition of PCM into cement-based materials can cause several problems. One of the main problems is the effect on the mechanical properties of cement-based materials[11,12]. Research results have shown that even low doses of PCM can significantly reduce compressive strength, flexural strength, and other mechanical properties of concrete.

Researchers have explored using strain-hardening cementitious composites (ECCs) as a potential solution to address these challenges[13,14]. ECCs are known for their excellent ductility and crack width control[15], which are critical for maintaining the structural integrity of concrete under stress. ECCs designed according to the principles of fracture mechanics typically exhibit strain-hardening behavior and form a succession of small cracks[16,17]. Unlike ordinary concrete, the tensile properties of ECCs are influenced by the synergies of matrix strength to enhance thermal storage in buildings can be broadly divided into three categories: latent heat storage, sensible heat storage, and chemical energy storage[3–5]. Sensible heat storage has a smaller unit volume of heat storage capacity. Thermochemical energy storage is usually
and bridging behavior of fibers. According to the micromechanical modeling of ECC, too high matrix strength prevents the formation of multiple cracks, which reduces the strain capacity of the composite. Therefore, adding PCMs to ECCs may reduce the tensile and flexural strength of cementitious materials, while the incorporation of fibers could counteract this adverse effect. By integrating PCM into ECC, the loss of strength can be offset by strain-hardening behavior while also benefiting from the thermal properties of PCM. For example, it has been shown that while mechanical strength may decrease with increasing PCM content, tensile strain capacity can be enhanced[18–20], offering potential benefits for applications requiring high flexibility and deformability. PCM-infused ECCs offer a viable approach to developing multifunctional materials capable of load-bearing and thermal management.

Furthermore, using microencapsulation techniques has improved the stability and compatibility of PCMs within the cement matrix, thereby mitigating the adverse effects on mechanical properties. The encapsulation process ensures that the PCMs remain uniformly distributed and effectively contained within the concrete, preventing leakage and enhancing durability. This study aims to systematically investigate the effects of different n-octadecane/fly ash cenosphere (ODE/FAC) PCM ratios on the mechanical properties of ECC.

2. EXPERIMENTAL SECTION

2.1 N-OCTADECANE/FLY ASH CENOSPHERE (ODE/FAC) FORM-STABLE PCM

The preparation process of ODE/FAC form-stable PCM was as follows. Firstly, the FAC was perforated by NaOH solution, the specific process can be referred by the literature[21]. Then, the melted ODE was immersed into the cavity of FAC via vacuum impregnation method. Lastly, ODE/FAC can be obtained after suction filtration.

2.2 RAW MATERIALS AND MIXED PROPORTION OF ECC

The ordinary Portland cement (P.O.42.5) from Yatai Group Harbin Cement Company, fly ash (FA) was provided by a local power station, and silica fume (SF) was obtained from Elkem Asia. The chemical composition of the cement, FA, and SF are presented in Table 1. Shanghai Sunrise Polymer Material Co., Ltd supplied polycarboxylate ether superplasticizer (SP, 40wt%). The particle size of silica sand was 60-150 μm. PE fibers were chosen, and their properties are detailed in Table 2. The mix proportions for ECC are presented in Table 3.

2.3 SPECIMEN PREPARATION

The cement, fly ash, silica fume, silica sand, and phase change materials were mixed in a mixer for 1 minute. After the solid components were mixed well, the water and superplasticizer mixture was added slowly while mixing at low speed until the mixture showed a flow pattern, and then PE fibers were added slowly. The mixing was done continuously at a slow speed for 4 minutes from the start of water addition to fiber addition and then switched to fast speed for 6-7 minutes to prevent fiber agglomeration, which could affect the test results. The freshly mixed paste was molded, and the specimens were covered with cling film to prevent moisture loss. After 24 hours of curing at room temperature of 20 ± 2 °C and with a relative humidity greater than 95%, the specimens were removed from the molds and placed in a steam oven at 60°C for three days. At the end of the curing period, all the specimens are removed and left in the laboratory for one day to prepare them for measurement.

Table 1
Chemical composition of cement, silica fume, and FA (wt. %).

Ingredients	SiO_2	Al_2O_3	CaO	Fe_2O_3	K_2O	MgO	Na_2O	SO_3
SAC	21.4	5.45	64.48	3.5	0.23	1.46	0.22	2.64
FA	49.22	27.8	3.14	1.29	1.06	0.86	0.92	0.16
SF	95.1	0.5	0.6	0.45	4.12	0.7	1.31	0.50

Table 2
Physical and mechanical properties of PE fiber.

Type of fiber	Diameter (μm)	Length (mm)	Tensile Strength (MPa)	Elastic modulus (GPa)	Density (g/cm^3)
PE	20	18	3800	113	0.97

Table 3
Mix proportions of ECC in this study (kg/m^3).

Mix ID	Cement	Fly ash	Silica fume	Water	Aggregate	SP	PCM	PE fiber (vol 1.5%)
P0	533.2	733.15	66.65	359.91	479.88	5	0	14.7
P5	533.2	733.15	66.65	359.91	455.89	5	8.81	14.7
P10	533.2	733.15	66.65	359.91	431.59	5	17.63	14.7
P20	533.2	733.15	66.65	359.91	383.90	5	35.25	14.7

2.4 TEST METHODS

For the flexural and compressive strength test of specimens, three and six specimens were respectively used and tested using a microcomputer automatic cement compression and bending tester (YAW-300) at loading rates of 50 N/s and 2.4 kN/s, respectively, according to Chinese National Standard GB/T 1346-2011. The dimensions of the flexural test specimens were 40 mm (W) × 40 mm (H) × 160 mm (L), and the dimensions of the compressive test specimens were cubes with a side length of 40 mm[22].

The uniaxial tensile test of ECC specimens was carried out based on the dumbbell-type specimen recommended by JSCE[23]. The specimen dimensions and test setup are shown in Fig. 1. The test was carried out on a universal material testing machine, and the loading mode was displacement loading with a loading rate of 0.5 mm/min. During the test, the system automatically recorded the tensile load, and the strain in the tensile zone of the specimen was collected by two linear variable differential transducers (LVDTs) fixed on the specimen. For each group, four specimens were tested.

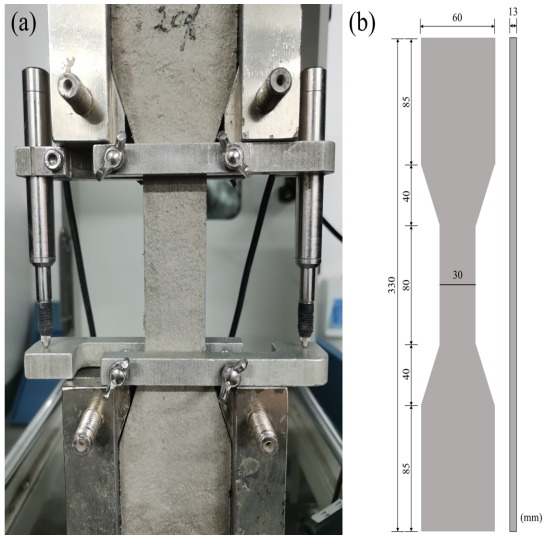

Fig. 1. Uniaxial tensile test: (a) the device and (b) the specimen dimensions.

The modulus of elasticity and fracture toughness of the matrix was assessed by three-point bending tests, as shown in Fig. 2 (a). The specimen was a 40 mm (W) × 40 mm (H) × 160 mm (L) notched beam with a pre-notch cut at mid-span to a depth of 16 mm, as shown in Fig. 2 (b). A hydraulic universal machine was used to load at a loading rate of 0.05 mm/s, and a clip extensometer recorded the crack mouth opening displacement (CMOD). The tests were performed according to the standard method for fracture testing (ASTM E399)[24].

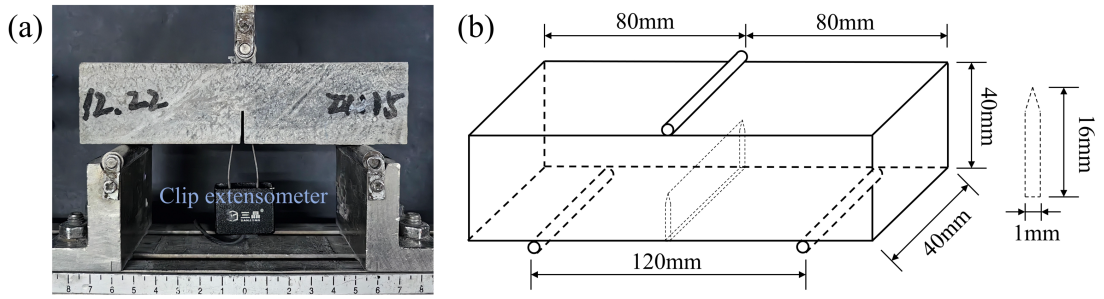

Fig. 2. Fracture toughness test: (a) the device and (b) the specimen size.

The single fiber pull-out test obtained the frictional bond strength at the fiber-matrix interface. The mixing ratio of the specimens did not contain fibers, and the rest of the components were the same as the corresponding ECC. Fig. 3(a) shows the mold used to prepare the single fiber pull-out specimens. During preparation, long PE fibers were first glued onto the interlayer at equal intervals with double-sided adhesive. After fixing the fibers, a freshly mixed cement mortar matrix without fibers was poured into the molds. The specimens were taken out of the molds after 24 h and transferred to a steam oven at 60°C for 3 days. The cured specimens were cut using a precision cutter, as shown in Fig. 3(b). The embedding depth of the fibers is controlled to about 5 mm, and the embedding depth of the fibers in the specimen was equal to the thickness of the specimen. The cut specimens were tested using the device shown in Fig. 3(c). The test procedure starts with gluing the specimen to the lower fixture fixed on the X-Y table. The free end of the fiber needs to be glued with high-strength glue to an aluminum plate fixed on the upper fixture, which was fixed on top of a transducer with a range of 10N and an accuracy of 0.001N. The test was conducted in displacement loading mode with a 0.5 mm/min loading speed.

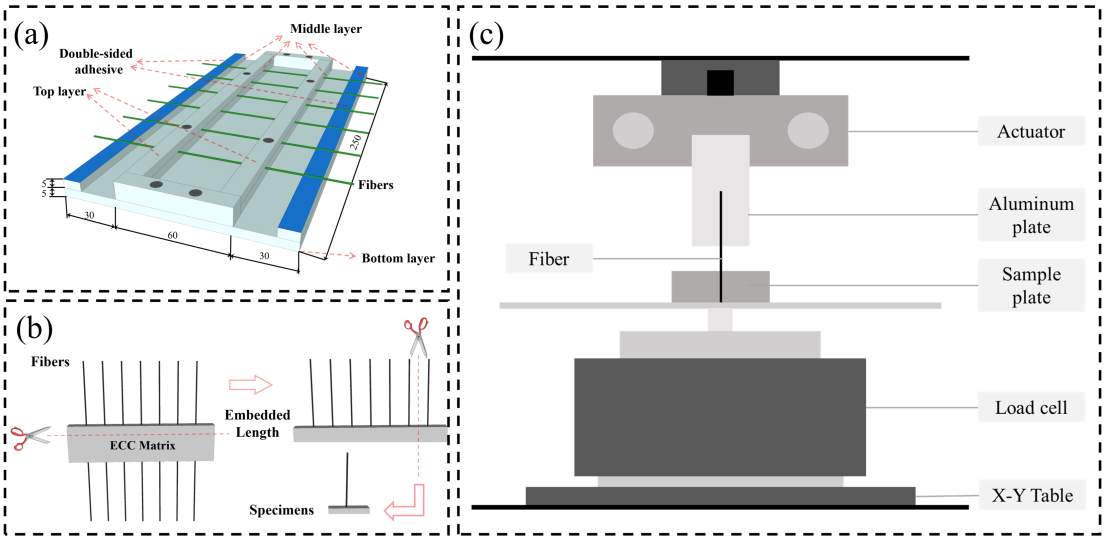

Fig. 3. Single fiber pullout test: (a) the mold, (b) the specimens, and (c) the device.

3. RESULTS AND DISCUSSION

3.1 FLEXURAL STRENGTH AND COMPRESSIVE STRENGTH

Flexural and compressive strength tests were performed at room temperature to evaluate the influence of ODE/FAC form-stable PCM on the mechanical properties of heat-stored ECCs. As shown in Fig. 4, the compressive strength of ECC in the control group decreased continuously with increasing addition of ODE/FAC form-stable PCM. Compared with the control group, the compressive strengths of ECC with 5%, 10%, and 20% ODE/FAC form-stable PCM were decreased from 64.56 MPa to 61.06 MPa, 59.28 MPa, and 57.59 MPa, respectively. In contrast to the continuous decrease in compressive strength, the flexural strength of the ECC materials also decreased with the increase in the amount of ODE/FAC form-stable PCM. The flexural strengths of ECC specimens with different ODE/FAC form-stable PCM dosages were 18.88 MPa, 18.23 MPa, and 18.08 MPa, respectively, as compared to 22.56 MPa of the control group. This contradicts the traditional view that there is

always a greater loss of mechanical properties when ODE/FAC form-stable PCM is added to cement-based materials. The main reasons for the large loss of mechanical properties of conventional cement materials are the following two: 1) microencapsulated PCMs usually exhibit low strength; 2) microencapsulated PCMs act as matrix material around the particles at the microscopic scale, provide resistance under tensile strain by load transfer in adjacent fibers, and increase fiber bridging along cracks, resulting in a triaxial compression state[18]. This results in a significant compensation for the loss of compressive strength with the addition of ODE/FAC form-stable PCM. In addition, an increase in ODE/FAC form-stable PCM content leaded to a decrease in matrix strength and an increase in friction at the fiber-matrix interface, both of which may counteract each other, thus leading to a smaller range of fluctuations in flexural strength with increasing ODE/FAC form-stable PCM yield. As elaborated in the subsequent section.

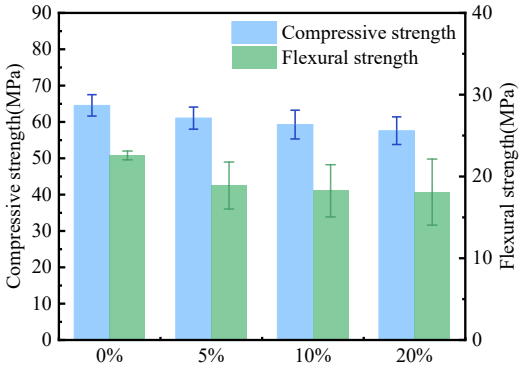

Fig. 4. Influence of n-octadecane/FAC content on the flexural strength and compressive strength of ECC.

3.2 UNIAXIAL TENSILE PROPERTIES

The uniaxial tensile stress-strain curves of ECC specimens with different contents of n-octadecane/FAC are shown in Fig. 5. The curves are consisted of three main stages. The first stage is the elasticity stage, in which the stress of the tensile specimen increases sharply with the increase of strain, and the stress-strain curve is linear until the specimen produces the first crack when it ends and enters the next stage. The second stage is the strain-hardening stage. The first crack appears on the surface of the specimen. The stress-strain curve shows a decreasing trend for the first time and then rises again, at which time the stress value is the initial cracking strength. After the bridging fiber is subjected to an external load, the number of cracks in the specimen increases with the increase of external load, the crack spacing decreases gradually, and the stress-strain curve shows a high-frequency fluctuation curve. Until the external load exceeds the maximum load the bridging fiber can withstand, the maximum stress value is the ultimate tensile strength, and the corresponding strain value is the ultimate tensile strain. The third stage is the strain-softening stage. The external load exceeds the maximum load the fiber can bear, and the specimen no longer produces new cracks. With the increase of tensile strain, the worst cracking surface of the bridging fiber bearing capacity continues to open; the fiber is constantly pulled out of the stress and continues to fall, judging the specimen damage. All the specimens in the test exhibited the complete four stages, indicating that all the ECC specimens showed tensile strain hardening behavior and the damage mode of multi-seam cracking.

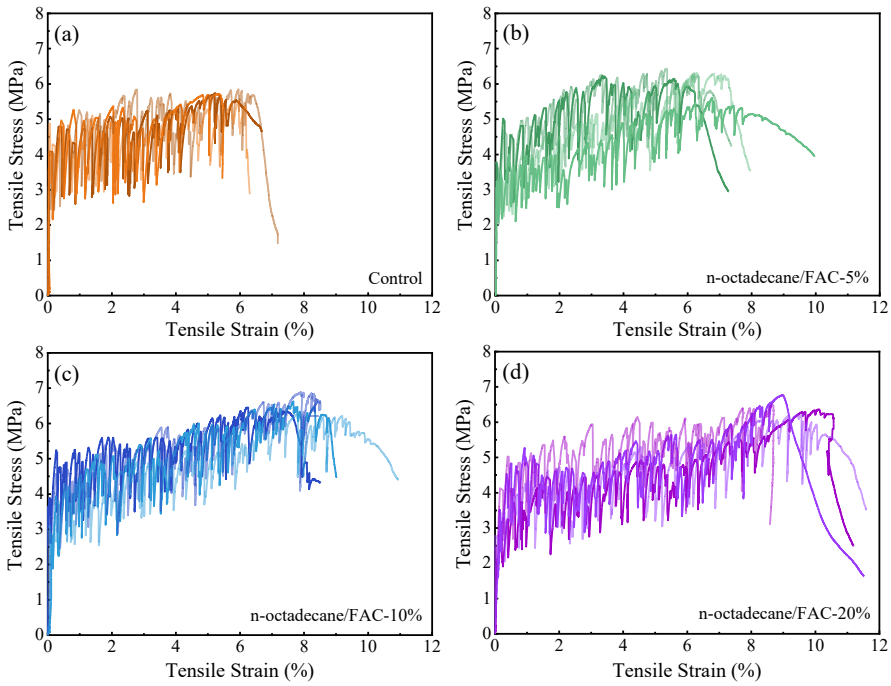

Fig. 5. Tensile stress-strain curves of ECC with different contents of n-octadecane/FAC: (a) 0%, (b) 5%, (c) 10%, and (d) 20%

From the results of uniaxial tensile tests in Table 4, it can be seen that the cracking strength of ECC specimens decreases with the increase of PCM content. The cracking strength of specimen P0 was 4.24 MPa, while specimens P5 and P20 were 3.28 MPa and 2.69 MPa, with decreases of 22.64% and 36.56%, respectively. The tensile strength of the specimens increased with the increase in the dosage of PCM. The tensile strength of specimen P0 was 5.70 MPa, whereas the tensile strength of specimens P5 and P20 were 6.08 MPa and 6.46 MPa, with an increase of 6.67% and 13.33%, respectively. The tensile strain of the specimens increased significantly with the increase of PCM content. The tensile strain of the specimen without PCM was 5.62% and reached a maximum value of 9.34% when the PCM content was 20%. The tensile strain of the specimen was affected by the number of cracks and crack width of the material. The number of cracks in the material increases significantly with the increase in PCM content, which was the main reason for the increase in strain of the specimen. As shown in Fig. 6, the number of cracks increased significantly with the increase of PCM content, the crack spacing decreases significantly, and the crack width also became considerably smaller.

Table 4
Uniaxial tensile of ECC.

Mixture ID	First cracking strength (MPa)	Tensile strength (MPa)	Ultimate strain (%)	Crack numbers	Average crack spacing (mm)	Residual crack width (μm)
P0	4.24±0.63	5.70±0.21	5.62±0.48	21.50±4.50	3.72	209.12

P5	3.28±0.50	6.08±0.48	6.44±0.86	27.25±4.25	2.94	189.06
P10	3.23±0.47	6.53±0.35	7.64±0.49	33.25±3.25	2.48	183.82
P20	2.69±0.84	6.46±0.32	9.34±1.03	41.00±5.00	1.95	182.24

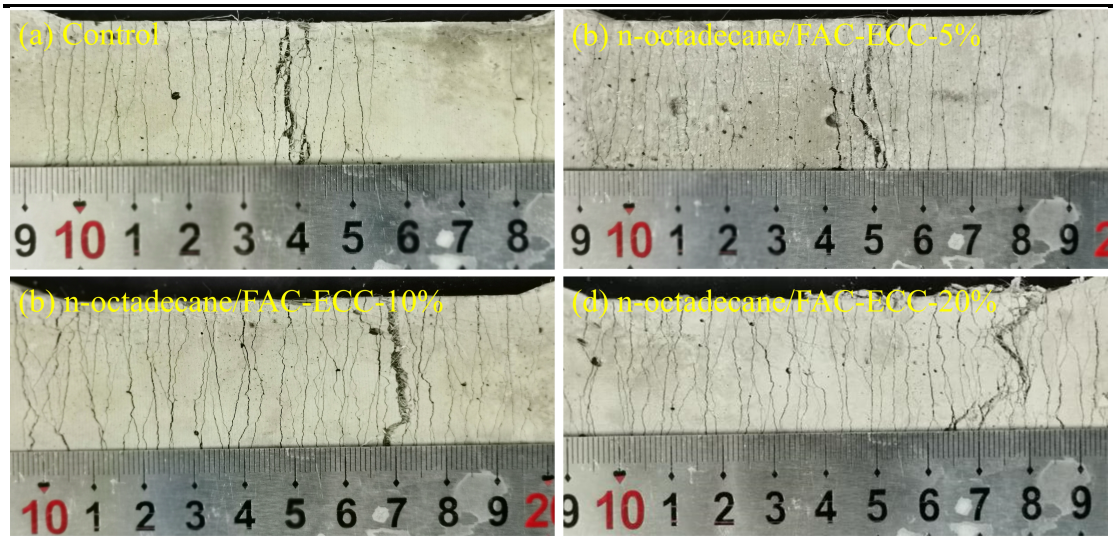

Fig. 6. Cracking morphology of ECC specimens with different contents of n-octadecane/FAC: (a) 0%, (b) 5%, (c) 10%, and (d) 20%

3.3 MICROMECHANICAL ANALYSIS

Three-point bending tests on prismatic specimens with notches measured the modulus of elasticity and fracture toughness of the matrix. According to ASTM E399-19[24], the modulus of elasticity E_m and fracture toughness K_m of the matrix can be calculated by the following equations:

$$K_m = \frac{1.5P_{max}S\sqrt{a_0}}{th^2} \cdot \frac{1.99-\left(\frac{a_0}{h}\right)\left(1-\frac{a_0}{h}\right)\left[2.15-3.93\frac{a_0}{h}+2.7\left(\frac{a_0}{h}\right)^2\right]}{\left(1+2\frac{a_0}{h}\right)\left(1-\frac{a_0}{h}\right)^{3/2}} \quad (1)$$

$$E_m = \frac{1}{tc_i}[3.70+32.60tan^2(\frac{\pi}{2}\cdot\frac{a_0+h_0}{h+h_0})] \quad (2)$$

$$c_i = \frac{V_i}{F_i} \quad (3)$$

where P_{max} represents the peak load, S is the span of the notched specimen, t is the thickness of the specimen, h is the height of the specimen, h_0 is the thickness of the thin steel plate at the knife edge of the clip extensometer, and a_0 is the crack length. C_i represents the slope of the elastic phase of the test line. Calculated from any point in the straight line segment of the ascending section of the test curve of the specimen, V_i and F_i are the crack width and load values at that point, respectively.

The results of calculating the fracture toughness and modulus of elasticity are demonstrated in Fig. 7. The fracture toughness and Young's matrix modulus decreased with the increase of PCM content. the fracture toughness and Young's modulus of the matrix decreased by 18.68% and 20.73%, respectively, when the PCM content was increased from 0% to 20%. This is similar to the results for compressive strength.

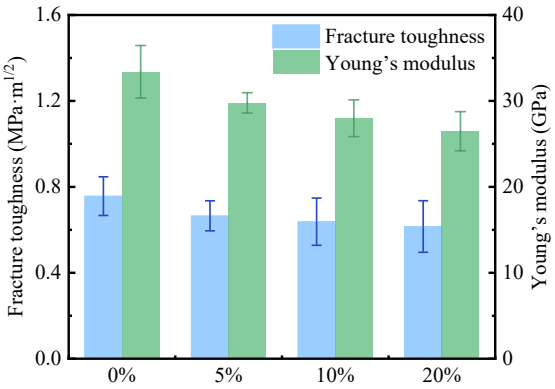

Fig. 7. Fracture toughness and Young's modulus of specimens with different content of n-octadecane/FAC.

The effect of PCM content on the interfacial properties of PE fibers and cement matrix was analyzed by monofilament pull-out tests, the results are shown in Fig 8. Fig 8 shows that the load of fibers at similar burial depths increases with the increase of PCM content, which indicates that the friction at the interface is increasing. According to Eq. 4[25], the interfacial frictional bond strength between the fibers and the matrix can be calculated.

$$\tau_0 = P_{\max} / \pi d_f L_e \quad (4)$$

where τ_0 is the fiber/matrix interface frictional bond strength, *Pmax* is the peak load, Le is the embedded length of the fiber, and *df* is the diameter of the fiber.

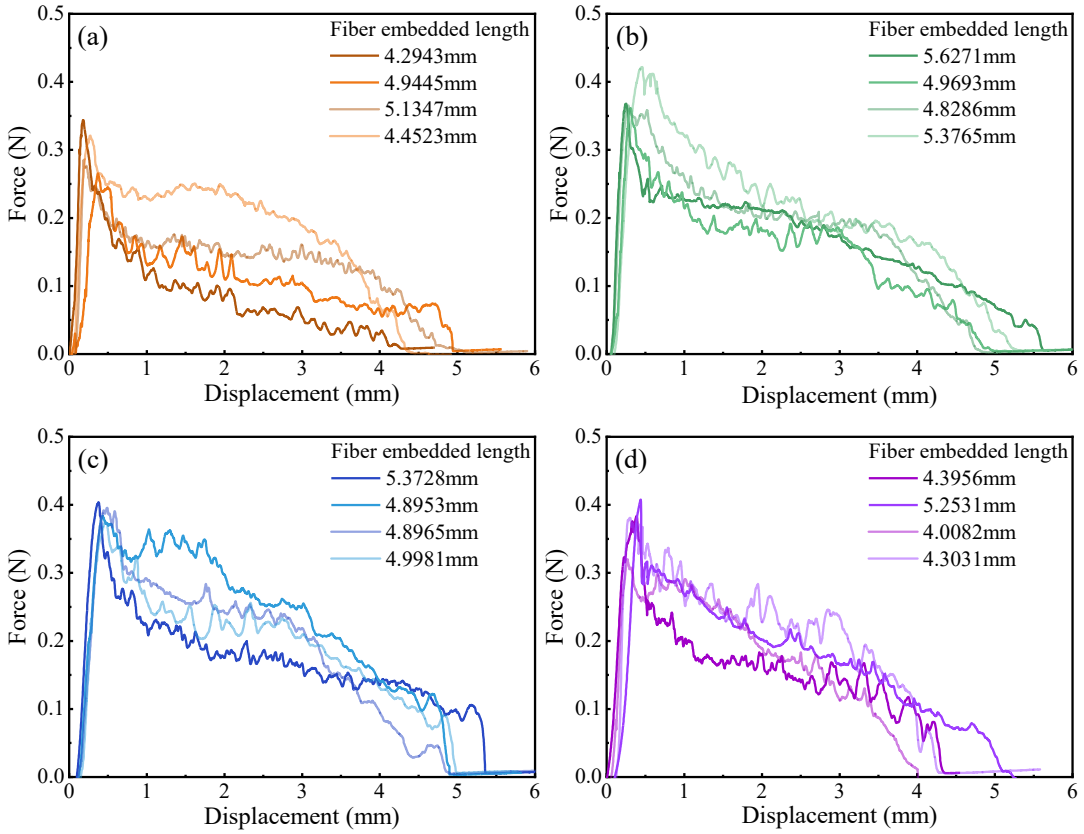

Fig. 8. Single fiber pull-out curve of ECC with different contents of n-octadecane/FAC: (a) 0%, (b) 5%, (c) 10%, and (d) 20%

The interfacial friction in the monofilament pull-out tests with different PCM content levels is calculated in Table 5. From the table, it can be seen that PCM significantly improved the interfacial friction between fiber and cement matrix; the friction coefficient between matrix and fiber without PCM addition was 1.098 MPa, while the interfacial friction coefficient between matrix and fiber with 5% PCM content was 1.199 MPa, which was improved by 9.20%. The interfacial friction was 1.385 MPa when the PCM content was 20%, which was improved by 26.02% compared to the specimen without PCM content. This is due to the micro-filler effect of ODE/FAC, which fills the pores and cracks in the transition zone, resulting in fewer gaps and cracks in the transition zone between the fibers and the matrix and improving the densification degree of the interfacial transition zone and, thus increases the interfacial friction.

Table 5
The fiber/matrix interface frictional bond strength.

Mixture ID	P0	P5	P10	P20
τ_0(MPa)	1.098±0.212	1.199±0.115	1.289±0.162	1.385±0.291

The micromechanical parameters used as inputs in modeling the σ-δ relationship are given in Table 6, including matrix, fiber, and interface parameters. According to the experimental results, the interfacial friction, matrix cracking strength, and modulus of elasticity vary with the n-octadecane/FAC content. Whereas, according to previous literature all other parameters are shown to be unaffected and hence were considered as constants. Using the obtained K_m and τ_0 and the other parameters listed in Table 6, the stress-crack opening (σ-δ) relation of the ECC can be calculated by considering the random distribution of the fibers and the bi-directional pull-out of the fibers, as shown in Fig. 9. The fiber crack bridging behavior depends on the interaction between the fiber, matrix, and interface properties. Considering the same fibers prepared, the shape of the σ-δ curve is mainly influenced by the matrix and interface properties. From the curves in Fig. 10, it can be seen that with the increase of n-octadecane/FAC content, there was a tendency for the crack opening displacement to decrease under the compound effect of increased interfacial bonding and weakened matrix while the bridging stress increases.

Table 6
Micromechanical parameters.

Micromechanical parameters		P0	P5	P10	P20
Fiber	Fiber length, L_f (mm)	18[a]	18[a]	18[a]	18[a]
	Fiber diameter, d_f (μm)	20[a]	20[a]	20[a]	20[a]
	Fiber elastic modulus, E_f (GPa)	113[a]	113[a]	113[a]	113[a]
	Fiber strength, σ_{fu} (MPa)	3800[a]	3800[a]	3800[a]	3800[a]
	Fiber strength reduction factor, f'	0.33[b]	0.33[b]	0.33[b]	0.33[b]
Interface	Interfacial chemical bond, G_d (J/m^2)	0[b]	0[b]	0[b]	0[b]
	Interfacial frictional bond, τ_0 (MPa)	1.098[c]	1.199[c]	1.289[c]	1.385[c]
	Slip-hardening coefficient, β	0[b]	0[b]	0[b]	0[b]
	Subbing coefficient, f	0.59[b]	0.59[b]	0.59[b]	0.59[b]
Matrix	Elastic modulus, E_m (MPa)	33.39[c]	29.77[c]	27.99[c]	26.47[c]
	Cracking strength, σ_{fc} (MPa)	4.24[c]	3.28[c]	3.23[c]	2.69[c]

Note: [a] Nominal properties from Table 2.

[b] These values were assumed according to Refs[26,27].

[c] Test results in this study.

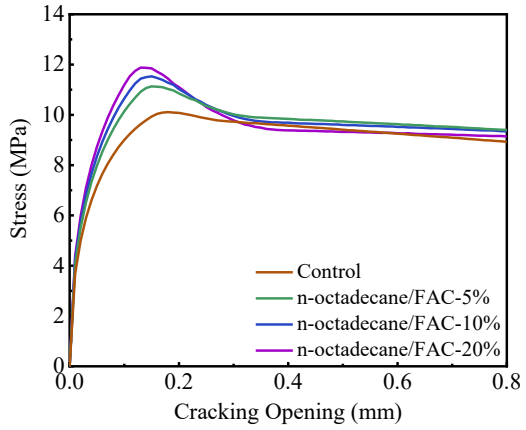

Fig. 9. Simulated σ-δ curves for ECC with different contents of n-octadecane/FAC

Based on the ECC micromechanical design model[28,29], the ability of ECC to achieve multi-seam cracking and strain hardening behavior required the satisfaction of a strength criterion and an energy criterion, as shown in Eqs. (5), (6), and (7). These are the strength criterion that requires the initial crack strength σ_{fc} to be less than the maximum bridge stress σ_0 that can be provided by the bridging fibers and the energy criterion that requires the required complementary energy J'_b to be greater than the fracture toughness of the crack tip J_{tip}, respectively. Based on the basis of the design criterion, two pseudo-strain hardening (PSH) indices were defined to describe the potential for strain hardening of the specimen quantitatively, $PSH_{strength}$ and PSH_{energy}, as shown in Eqs. (8) and (9)[30]. Thus, these two criteria quantitatively evaluated the strain-hardening potential of ECCs at different PCM content.

$$\sigma_0 > \sigma_{fc} \tag{5}$$

$$J_b' \equiv \sigma_0\delta_0 - \int_0^{\delta_0}\sigma(\delta)d\delta > J_{tip} \tag{6}$$

$$J_{tip} = \frac{K_m^2}{E_m} \tag{7}$$

$$PSH_{strength} = \sigma_0/\sigma_{fc} \tag{8}$$

$$PSH_{energy} = J_b'/J_{tip} \tag{9}$$

where δ_0 is the crack opening at the maximum bridging stress σ_0.

Based on the above model, the calculated maximum bridge stress, initial crack strength, crack tip fracture toughness, compensatory energy, and PSH index of the obtained ECC specimens are shown in Table 7. The strain-hardening index was greater than 1, which was the critical condition for the ability of materials to produce strain-hardening. The essential values of $PSH_{strength}$ and PSH_{energy} for PE-ECC to be able to saturate cracking were 1.2 and 3[31], respectively. The values in this experiment were much larger than this value, so all the specimens were able to show saturated multi-seam cracking mode. The results show that the increase in PCM content can significantly increase the value of the PSH index. When the content of PCM was gradually increased from 0% to 20%, the $PSH_{strength}$ was gradually increased from 2.38 to 4.42, and the value of the PSH_{energy} was gradually increased from 22.46 to 31.71. Therefore, the possibility of saturation cracking of ECC materials increased with increasing PCM contents, corresponding to an increase in tensile strain capacity.

Table 7

Uniaxial tensile of ECC.

Mixture ID	σ_{fc} (MPa)	σ_0 (MPa)	$PSH_{strength}$	Jb' (J/m^2)	$Jtip$ (J/m^2)	PSH_{energy}
P0	4.24	10.11	2.38	385.10	17.15	22.46
P5	3.28	11.13	3.39	432.89	14.86	29.13
P10	3.23	11.53	3.57	446.47	14.54	30.71
P20	2.69	11.88	4.42	453.70	14.31	31.71

4. CONCLUSION

ODE/FAC form-stable PCM developed in this study was used as an ultrafine aggregate to replace silica sand to produce ECC with higher mechanical properties. Based on the testing of mechanical properties such as flexural strength, compressive strength, and tensile properties. The increase of ODE/FAC form-stable PCM content reduced the compressive strength, flexural strength and tensile cracking strength of ECC, the tensile strength and tensile strain showed an increase. The addition of ODE/FAC form-stable PCM also increased the number of cracks and reduced the crack width of ECC in the uniaxial tensile test. The overall performance of ECC was still better than that of the low-content group, although the dispersion was higher when the ODE/FAC form-stable PCM dosage reached 20% due to uneven distribution. Adding ODE/FAC form-stable PCM increased the interfacial friction between the fibers and the cement matrix, and the specimen with 20% PCM content increased the interfacial friction by 26.02% as compared to the specimen without ODE/FAC form-stable PCM. The micromechanical model analysis showed that the strength PSH index and energy PSH index of the ECC specimens increased with increasing the amount of ODE/FAC form-stable PCM. This indicated that adding ODE/FAC form-stable PCM can improve the steady-state cracking and tensile strain hardening ability of specimens with multiple cracks.

5. ACKNOWLEDGEMENT

The financial supports from State Key Laboratory of Silicate Materials for Architectures (Wuhan University of Technology) and National Natural Science Foundation of China (No. 51902068).

REFERENCE

[1] D. Ürge-Vorsatz, L.F. Cabeza, S. Serrano, C. Barreneche, K. Petrichenko, Heating and cooling energy trends and drivers in buildings, Renew. Sustain. Energy Rev. 41 (2015) 85–98.

[2] A. Yousefi, W. Tang, M. Khavarian, C. Fang, Development of novel form-stable phase change material (PCM) composite using recycled expanded glass for thermal energy storage in cementitious composite, Renew. Energy 175 (2021) 14–28.

[3] R. Baetens, B.P. Jelle, A. Gustavsen, Phase change materials for building applications: A state-of-the-art review, Energy Build. 42 (2010) 1361–1368.

[4] S. Álvarez, L.F. Cabeza, A. Ruiz-Pardo, A. Castell, J.A. Tenorio, Building integration of PCM for natural cooling of buildings, Appl. Energy 109 (2013) 514–522.

[5] C. Barreneche, M.E. Navarro, A.I. Fernández, L.F. Cabeza, Improvement of the thermal inertia of building materials incorporating PCM. Evaluation in the macroscale, Appl. Energy 109 (2013) 428–432.

[6] Y. Zhao, X. Min, Z. Huang, Y. Liu, X. Wu, M. Fang, Honeycomb-like structured biological porous carbon encapsulating PEG: A shape-stable phase change material with enhanced thermal conductivity for thermal energy storage, Energy Build. 158 (2018) 1049–1062.

[7] F. Cheng, X. Zhang, R. Wen, Z. Huang, M. Fang, Y. Liu, X. Wu, X. Min, Thermal conductivity enhancement of form-stable tetradecanol/expanded perlite composite phase change materials by adding Cu powder and carbon fiber for thermal energy storage, Appl. Therm. Eng. 156 (2019) 653–659.

[8] T. Salgueiro, A. Samagaio, M. Gonçalves, A. Figueiredo, J. Labrincha, L. Silva, Incorporation of phase change materials in an expanded clay containing mortar for indoor thermal regulation of buildings, J. Energy Storage 36 (2021) 102385.

[9] S. Ben Romdhane, A. Amamou, R. Ben

Khalifa, N.M. Saïd, Z. Younsi, A. Jemni, A review on thermal energy storage using phase change materials in passive building applications, J. Build. Eng. 32 (2020) 101563.

[10] K. Faraj, M. Khaled, J. Faraj, F. Hachem, C. Castelain, A review on phase change materials for thermal energy storage in buildings: Heating and hybrid applications, J. Energy Storage 33 (2021) 101913.

[11] M. Hunger, A.G. Entrop, I. Mandilaras, H.J.H. Brouwers, M. Founti, The behavior of self-compacting concrete containing micro-encapsulated Phase Change Materials, Cem. Concr. Compos. 31 (2009) 731–743.

[12] B. Xu, Z. Li, Paraffin/diatomite composite phase change material incorporated cement-based composite for thermal energy storage, Appl. Energy 105 (2013) 229–237.

[13] S. Erdem, E. Gürbüz, Influence of microencapsulated phase change materials on the flexural behavior and micromechanical impact damage of hybrid fibre reinforced engineered cementitious composites, Compos. Part B Eng. 166 (2019) 633–644.

[14] D. Desai, M. Miller, J.P. Lynch, V.C. Li, Development of thermally adaptive Engineered Cementitious Composite for passive heat storage, Constr. Build. Mater. 67 (2014) 366–372.

[15] M. Şahmaran, V.C. Li, Durability of mechanically loaded engineered cementitious composites under highly alkaline environments, Cem. Concr. Compos. 30 (2008) 72–81.

[16] V.C. Li, On Engineered Cementitious Composites (ECC)- A Review of the Material and its Applications, Transp. Res. Rec. J. Transp. Res. Board 2164 (2003) 1–8.

[17] V.C. Li, From micromechanics to structural engineering-the design of cementitous composites for civil engineering applications, Struct. Eng. Eng. 10 (1994) 1–34 (n.d.).

[18] E. Gürbüz, S. Erdem, Development and thermo-mechanical analysis of high-performance hybrid fibre engineered cementitious composites with microencapsulated phase change materials, Constr. Build. Mater. 263 (2020) 120139.

[19] Z. Lu, C. Lu, C.K.Y. Leung, Z. Li, Graphene oxide modified Strain Hardening Cementitious Composites with enhanced mechanical and thermal properties by incorporating ultra-fine phase change materials, Cem. Concr. Compos. 98 (2019) 83–94.

[20] B. Xu, Z. Li, Performance of novel thermal energy storage engineered cementitious composites incorporating a paraffin/diatomite composite phase change material, Appl. Energy 121 (2014) 114–122.

[21] K. Yu, Y. Liu, M. Jia, C. Wang, Y. Yang, Thermal energy storage cement mortar containing encapsulated hydrated salt/fly ash cenosphere phase change material: Thermo-mechanical properties and energy saving analysis, J. Energy Storage 51 (2022) 104388.

[22] ASTM C109/C109M, Standard Test Method for Compressive Strength of Hydraulic Cement Mortars, ASTM International, West Conshohocken, PA, 2013, (n.d.).

[23] Japan Society of Civil Engineers, Recommendations for Design and Construction of High performance fiber reinforced cement composites with multiple fine cracks (HPFRCC), Concrete Engineering Series No, 2008, p. 82., (n.d.).

[24] A. International, E399: Standard Test Method for Plane-Strain Fracture Toughness of Metallic Materials, vol. 1, 2009., (n.d.).

[25] T. Liu, R. Bai, Z. Chen, Y. Li, Y. Yang, Tailoring of polyethylene fiber surface by coating silane coupling agent for strain hardening cementitious composite, Constr. Build. Mater. 278 (2021) 122263.

[26] R. Ranade, V. Li, M.D. Stults, T. Rushing, J. Roth, W. Heard, Micromechanics of High-Strength, High-Ductility Concrete, ACI Mater. J. 110 (2013) 375–384.

[27] E.-H. Yang, S. Wang, Y. Yang, V.C. Li, Fiber-Bridging Constitutive Law of Engineered Cementitious Composites, J. Adv. Concr. Technol. 6 (2008) 181–193.

[28] V.C. Li, C.K.Y. Leung, Steady-State and Multiple Cracking of Short Random Fiber Composites, J. Eng. Mech. 118 (1992) 2246–2264.

[29] V.C. Li, D.K. Mishra, H.C. Wu, Matrix design for pseudo-strain-hardening fibre reinforced cementitious composites, Mater. Struct. 28 (1995) 586–595., (n.d.).

[30] K. Tetsushi, V.C. Li, Multiple Cracking Sequence and Saturation in Fiber Reinforced Cementitious Composites, Concrete Research and Technology, vol. 9, Japan Concrete Institute, 1998, pp. 19–33., (n.d.).

[31] T. Liu, Y. Yang, Z. Chen, Y. Li, R. Bai, Optimization of fiber volume fraction to enhance reinforcing efficiency in hybrid fiber reinforced strain hardening cementitious composite, Cem. Concr. Compos. 113 (2020) 103704.

IMPACT OF ANHYDRITE AND BLAINE SPECIFIC SURFACE AREA ON THE REACTIVITY OF LOW-BASICITY BLAST FURNACE SLAG

KONO, Hiroto
Graduate student, Shimane University, Japan

YOSHIDA, Natsuki
Specially appointed associate professor, Osaka University, Japan

NITO, Nobukazu
DC Co., LTD., Technical Center , Kawasaki-shi, Japan

ATARASHI, Daiki
Professor, Shimane University, Japan

ABSTRACT:
In this study, the impacts of changes in blaine specific surface area (blaine value) and anhydrite ($C\bar{S}$) addition on the reactivity of blast furnace slag fine powder (BFS) were investigated in a blast furnace cement type B system (BB). BFS had a lower basicity compared to the BFS typically used in ordinary cements were used in this study. It was found that the reactivity of BFS with low basicity at 7 days of curing could be improved to the reactivity of the ordinary BFS by controlling both the particle size and the amount of $C\bar{S}$ addition.
On the other hand, the strength development of blast-furnace cement with $C\bar{S}$ added to low-basicity BFS was equal to that of blast-furnace cement with ordinary BFS (basicity of 1.8), even if the reactivity of BFS was not increased to the ordinary BFS reactivity.
KEY WORDS: blast furnace slag, low basicity, anhydrite, blaine specific surface area, ettringite, activity index

1. INTRODUCTION

Currently, the cement and concrete industry in Japan emits approximately 40 million tonnes of CO_2 annually, constituting about 4% of the country's total industrial output. Reducing CO_2 emissions is crucial to reduce environmental impact. As a measure, there's a proposal to replace part of the clinker with supplementary cementitious materials (SCMs). In particular, increasing the use of blast furnace cement incorporating blast furnace slag fine powder (BFS), an industrial by-product from steel plants, is being considered.
The reactivity of BFS is important for the strength development of blast-furnace cement, with basicity ($(CaO+MgO+Al_2O_3)/SiO_2$) typically serving as an indicator [1]. According to JIS standards, BFS is specified to have a basicity of 1.60 or higher. However, in Japan, BFS with a basicity of approximately 1.8 is commonly used to ensure adequate reactivity. Recently, BFS with lower basicity has been discharged due to operational issues in blast furnaces. However, blast furnace cements utilizing BFS with lower basicity exhibit reduced initial strength development due to BFS's lower initial reactivity [2]. Therefore, methods to improve the reactivity of BFS with lower basicity need to be established.
One method to improve the reactivity of BFS is to use BFS with a high blaine value specific surface area (blaine value value) or to utilize additives [3]. However, Iyoda et al. [4] reported that the higher blaine value of BFS in concrete made with blast furnace cement, the greater the amount of autogenous shrinkage, which can cause cracking. Anhydrite ($C\bar{S}$) is one of the stimulants of BFS, but Anzai et al. [5] reported that excessive addition of $C\bar{S}$ causes a reduction in the medium and long-term reaction rate of BFS, so its addition should be kept to a minimum.
In this study, the impacts of changes in blaine value specific surface area and anhydrite ($C\bar{S}$) addition on the reactivity of blast furnace slag fine powder (BFS) were investigated in a blast furnace cement type B system (BB). The impact of the change in reactivity of BFS with varying powder content and $C\bar{S}$ addition on the strength development of the mortar specimens was also investigated.

2. EXPERIMENTAL METHOD

2.1 Materials

In this study, five types of BFS (blast furnace slag) were used: BFS I (blaine value 4640, basicity 1.85), BFS II (blaine value 4500, basicity 1.73), BFS III (blaine value 4930, basicity 1.73), BFS IV (blaine value 5490, basicity 1.73), and BFS V (blaine value 6500, basicity 1.73). The basicity of BFS II~BFS V is lower than that of BFS I (the ordinary basicity). Ordinary portland cement (OPC) was used as the cementitious material. OPC characteristics are presented in Table 1, while Table 2 outlines the chemical properties of BFS I to BFS V.

2.2 Preparation of paste specimens

Table 3 presents details of the prepared specimens and their mixing conditions. Five types of BB paste

Table 1 Mineral and Chemical composition of OPC

	Chemical composition (%)							Blaine (cm^3/g)
OPC	SiO_2	Al_2O_3	CaO	MgO	SO_3	Fe_2O_3	ig.loss	
	21.41	4.84	65.01	1.08	2.02	3.20	0.97	3260

Table 2 Chemical composition, Blaine value and Basicity of BFS

	Chemical composition (%)									Basicity	Blaine (cm^2/g)
	SiO_2	Al_2O_3	CaO	MgO	K_2O	TiO_2	Na_2O	Fe_2O_3	MnO		
BFS I	34.21	14.66	42.33	6.14	0.40	0.53	0.22	0.31	0.18	1.85	4640
BFS II	35.60	13.67	41.14	6.86	0.43	0.54	0.23	0.27	0.25	1.73	4500
BFS III	35.61	13.66	41.14	6.84	0.42	0.54	0.23	0.28	0.25	1.73	4930
BFS IV	35.60	13.67	41.14	6.86	0.43	0.54	0.23	0.27	0.25	1.73	5490
BFS V	35.60	13.67	41.14	6.86	0.43	0.54	0.23	0.27	0.25	1.73	6500

Table 3 Mix proportions of cement pastes

Name of specimens	Ratio of Binder(%)			SO_3(%)
	OPC	BFS	$C\bar{S}$	
BB I	55.0	45.0	0.0	1.1
BB II				
BB II-$C\bar{S}$2.0		43.0	2.0	2.3
BB II-$C\bar{S}$3.5		41.5	3.5	3.2
BB II-$C\bar{S}$5.0		40.0	5.0	4.0
BB II-$C\bar{S}$7.0		38.0	7.0	5.2
BB III		45.0	0.0	1.1
BB III-$C\bar{S}$2.0		43.0	2.0	2.3
BB III-$C\bar{S}$3.5		41.5	3.5	3.2
BB IV		45.0	0.0	1.1
BB V				

specimens were prepared using BFS I to BFS V, each comprising BFS at 45% of OPC (BB I, BB II, BB III, BB IV, and BB V). Additionally, complete BB were prepared using BFS II, and specimens with CS added at 2.0%, 3.5%, 5.0%, and 7.0% of BFS were prepared (BB II-$C\bar{S}$2.0, BB II-$C\bar{S}$3.5, BB II-$C\bar{S}$5.0, and BB II- $C\bar{S}$7.0). Similarly, specimens were prepared with 2.0% and 3.5% $C\bar{S}$ added to BFS III (BB III-$C\bar{S}$2.0 and BB III-$C\bar{S}$3.5). The amount of SO_3 (sulfate) in the cement is detailed in Table 3, where the system without $C\bar{S}$ shows 1.1% SO_3 derived from OPC. Notably, only BB II- $C\bar{S}$7.0 exceeds the JIS standard range for SO_3 content. These specimens were combined with a water-to-powder ratio of 0.5, then sealed and cured for a designated period. After that, hydration of these samples was stopped.

2.3 Analysis method

(1) Calculation of portlandite (CH) volume for TG-DTA

The amount of CH produced in the cement paste was calculated from the amount of H_2O decomposed from CH. The amount of H_2O decomposed from CH measured using a thermogravimetric differential thermal analyzer (TG-DTA, NETZSCH STA2500, rise rate of temperature is 10°C/min^{-1}). The temperature range of dehydration of CH was determined to be 350~550°C, and the start and end temperatures of mass loss were determined in the range. The amount of H_2O decomposed from CH was calculated from the mass loss from the start temperature to the end temperature on TG curve. Those values were used to calculate the CH content from (1).

$$M_{CH}=\frac{\Delta m_{CH}}{m_0-m_{1000}}\times\frac{56.08}{18.02}\times 100 \qquad (1)$$

M_{CH}: Portlandite (CH) content ratio (%)
Δm_{CH}: Amount of water produced by decomposition of portlandite(CH) (mg)
m_0: Amount of sample for measurement (mg)
m_{1000}: Amount of sample heated up to 1000°C (mg)
56.08: molecular weight of CaO
18.02: molecular weight of H_2O

(2) Ig. Loss

Samples were heated at 700°C for 2 hours using an electric furnace. The difference between the mass loss rate observed at each curing time and the rate of mass loss before hydration was used to calculate the amount of bound water, representing the mass loss due to dehydration of bound water.

(3) X-ray diffractometer (XRD)

Hydration products (crystalline phase) were analyzed by the internal standard method (standard material: MgO) using a powder X-ray diffractometer (Bluker D2 PHASER tube Cu, source: CuKα tube voltage 30kV, current 10mA).

(4) Analysis of BFS reaction rates

After grinding samples, the reaction rate of BFS was calculated by quantifying the amount of unreacted BFS by the salicylic acid-acetone-methanol selective dissolution method [6].

2.4 Analysis of mortar specimens

The activity index was determined as the ratio of the compressive strength of the test mortar (OPC mixed with 50% BFS) to the reference mortar (OPC only) at 7 days

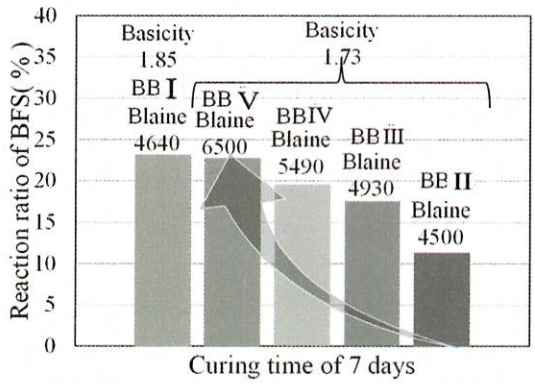

Fig. 1 Impact of blaine specific surface area on BFS reaction rate

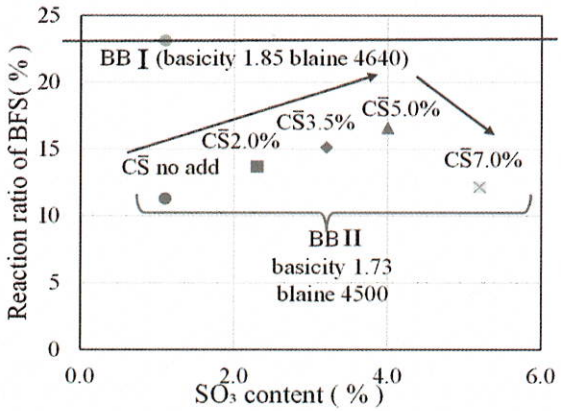

Fig. 2 Impact of SO_3 on BFS reaction rate

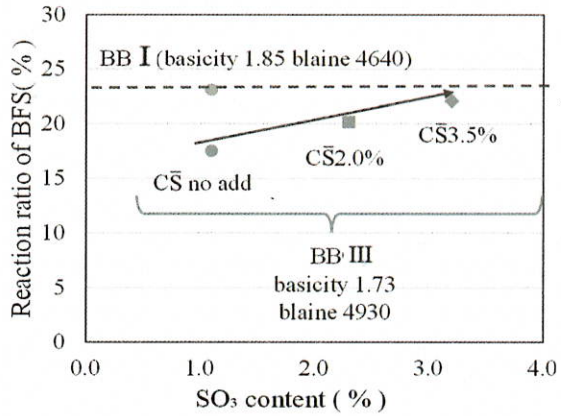

Fig. 3 Impact of blaine specific surface area and SO_3 on BFS reaction rate

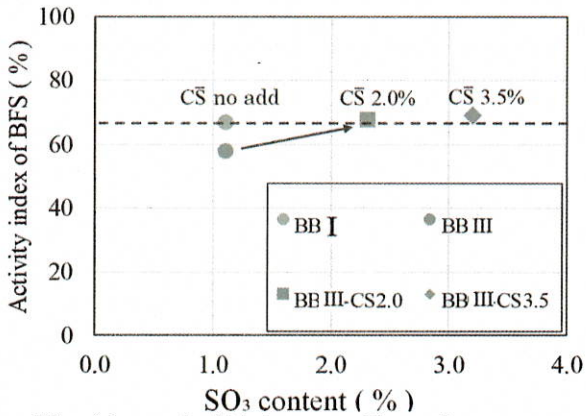

Fig. 4 Impact of blaine specific surface area and SO_3 on activity index of BFS

of age, following JIS A 6202 "Blast furnace slag fine powder for concrete". CS̄ was added uniformly to the cement in proportion to BFS. Compressive strength testing of the mortar was conducted in accordance with JIS R 5201 "Physical Test Methods for Cement".

3. RESULTS AND DISCUSSION

3.1 Investigation of the reactivity of BFS in blast furnace cement type B system

(1) Impact of blaine specific surface area (blaine value) on reactivity of BFS

Fig. 1 shows the BFS reaction rates of BB I to BB V at 7 days of curing time. Comparing BB I (basicity 1.85, blaine value 4640) and BB II (basicity 1.73, blaine value 4500), which , BB I showed higher BFS reactivity than BB II, with reactivity decreasing as basicity decreased. Comparing BB II to BB V, the BFS reaction rate increased with higher fineness of BFS, indicating that increased fineness promoted BFS reaction. Moreover, comparing BB V (basicity 1.73, blaine value 6500) to BB I, BFS reactivity in BB V was similar to BB I, showing that increasing BFS fineness from 4500 to 6500 enhanced reactivity even for BFS with lower basicity. However, previous studies by Iyoda et al. noted rapid autogenous shrinkage in mortar specimens using BFS with a fineness around 6000 at very early stages of maturation [4], suggesting the need to explore methods other than increasing fineness to improve BFS reactivity. Therefore, the next section examines the impact of varying CS̄ addition on the reactivity of BFS with low basicity.

(2) Impact of CS̄ on reactivity of BFS

Fig. 2 shows the relationship between the reactivity of BFS from BB II, which has lower basicity, and the amount of SO_3. For BB II (basicity 1.73, blaine value 4500), the reactivity of BFS increases with the increase in SO_3 content in the cement when the CS̄ addition rate ranges from 2.0% to 5.0%. However, the reactivity of BFS from BB II does not reach that of BFS from BB I, which has higher basicity, when used as a blending material. Furthermore, in BB- CS̄7.0, where the SO_3 content exceeded the JIS standard range [7], the addition of CS̄ did not improve BFS reactivity. According to a previous study [8] [9], impact of anhydrite on the hydration reaction of BFS in the presence of calcium hydroxide (CH) was noted to involve the formation of colloidal ettringite (Ett), creating a dense hydration product layer on unreacted BFS surfaces that hinders mass transfer. Thus, it is inferred that BB III- CS̄7.0

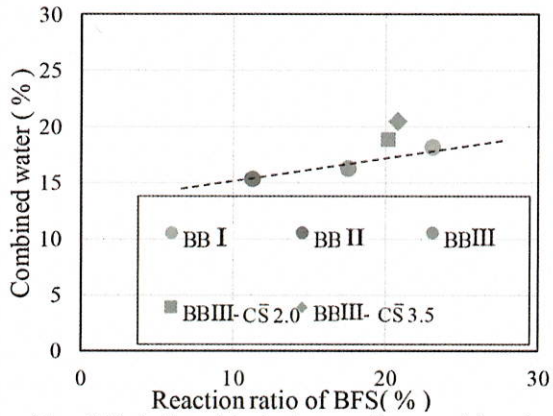

Fig. 5 Relationship between the combined water and reaction ratio of BFS at 7 days

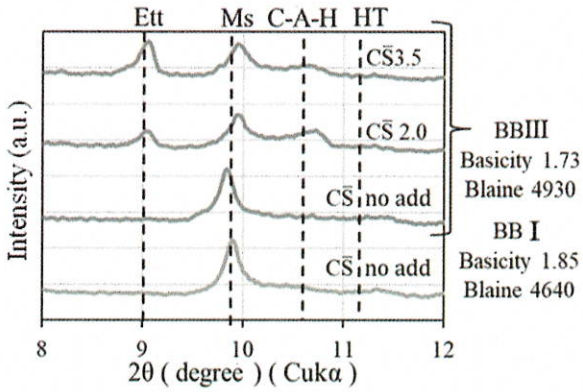

Fig. 6 XRD pattern of BB

experienced excessive C S̄ addition resulting in significant colloidal Ett formation on unreacted BFS surfaces at 7 days of curing time. As a result, the reaction of BFS is inhibited.

From the above, it is evident that the reactivity of BFS in BB using low-basicity BFS as a mixture material cannot simply be improved by controlling the CS̄ addition rate alone.

(3) Impact of CS̄ and blaine value on reactivity of BFS

Fig. 3 shows the relationship between BFS reactivity and SO_3 content in BB III, which has a higher blaine value compared to BB II. In BB III (basicity 1.73, blaine value 4930), the reactivity of BFS Improved with an increase in SO_3 content in the cement. When 3.5% CS̄ is added, the reactivity of BFS in BB III approaches that of BFS from BB I, which uses BFS with higher basicity as a mix material, reaching nearly the same level. This suggests that the reactivity of low-basicity BFS at 7 days can be nearly matched to that of high-basicity BFS by setting the blaine value to 4930 and controlling CS̄ addition at 3.5%.

In summary, the reactivity of BB with low-basicity BFS at 7 days is inferior to those with high-basicity BFS when controlling only blaine value or C S̄ addition. However, by controlling both blaine value or C S̄ addition, the reactivity of BB with high-basicity BFS can be improved that of BB with current low-basicity BFS at 7 days.

3.2 Impact of C S̄ and blaine value on strength development of mortar

Next, the Impacts of CS̄ and blaine value on the strength development of mortar specimens were investigated. Fig. 4 shows the relationship among the activity index, blaine value, and SO_3 content of each BFS.

According to the standard specified in JIS A 6206 for BFS4000, which related to "Blast furnace slag fine powder for concrete," the blaine value of BFS should range between 3500 cm^2/g and 5000 cm^2/g, and the activity index should exceed 55 at 7 days of material age. All BFS samples met these JIS standards.

The activity index of low-basicity BFS III (basicity 1.73, blaine value 4930) equaled or exceeded that of high-basicity BFS I when 2.0% and 3.5% of CS̄ were added. This suggests that incorporating CS into blast-furnace cement using BFS III, which has lower basicity, can achieve strength development equal to or better than that of blast-furnace cement using BFS I, which has higher basicity.

On the other hand, Fig 3 indicates that the reactivity of BFS in BB III- CS̄2.0, where 2.0% CS̄ is added to blast-furnace cement using low-basicity BFS III, is lower compared to that of blast-furnace cement with high-basicity BFS I.

Therefore, the reason for the comparable or superior strength development of blast-furnace cement with low-basicity BFS III compared to that of blast-furnace cement with high-basicity BFS I may cause not only from BFS reactivity but also from the characteristics of cement hydrates in blast-furnace cement.

Therefore, cement hydrates are discussed in the next section.

3.3 Investigation of hydration products in blast furnace cement type B

Fig. 5 shows the relationship between BFS reaction rate in each BB and the bound water content at 7 days of age. In contrast, within the CS̄-added system, the plotted points showing the relationship between BFS reaction rate and bound water content at 7 days was out from a linear trend. This suggests that the CS̄-added system produces hydrates with higher bound water content compared to the system without CS̄.

Fig. 6 shows XRD patterns of BB I, BB III, BB III- CS̄2.0, and BB III- CS̄3.5 at 7 days of curing time. The principal hydration products (crystalline phases) in the CS̄-added system include ettringite (Ett), monosulfate (Ms), and calcium aluminate hydrate (CAH), BB I and BB III without CS̄ primarily shows peaks of Ms and hydrotalcite (HT), with no Ett or CAH peaks observed. Thus, the reason why the activity indices of BFS in BB III- CS̄2.0 and BB III- CS̄3.5, with CS̄ addition, were equal to or higher than those in BB I with high-basicity BFS as the mixture material, is presumably due to the formation of Ett, which contains higher binding water content, facilitated by CS̄ addition.

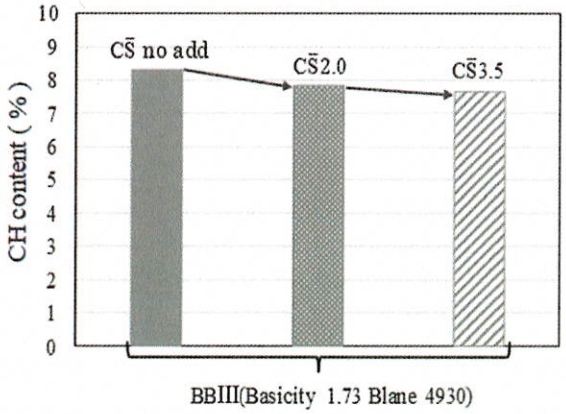

Fig. 7 CH content of BB paste

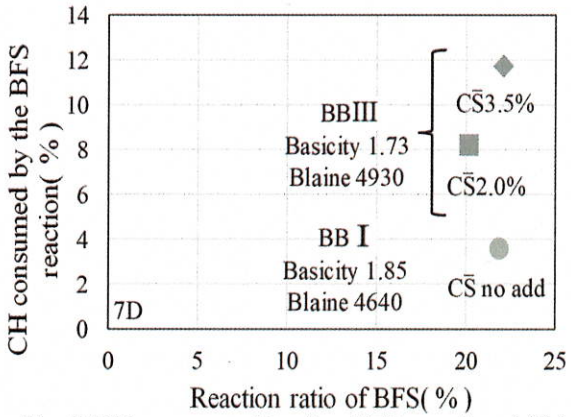

Fig. 8 CH consumed by the BFS reaction (%)

Therefore, while Section 3.1 focused on enhancing BFS reactivity, for evaluating the strength development of mortar specimens using BFS, it is crucial to design materials that not only improve BFS reactivity but also generate hydrates with significant binding water content, such as Ett.

Comparing BB I (basicity 1.85, blaine value 4640) and BB III (basicity 1.73, blaine value 4930), there was no difference observed in the peak size of calcium aluminate hydrates. However, BB I exhibited a larger amount of bound water compared to BB III. This reason could be attributed to the influence of low-crystallinity hydration products, such as calcium silicate hydrate.

3.4 CH content in blast furnace cement type B

Fig. 7 shows the amount of CH in each BB at 7 days of curing time, and the amount of CH in the BB paste decreased as the addition rate of $C\bar{S}$ increased in BB III (basicity 1.73, blaine value 4930). Fig. 8 shows the relationship between the BFS reaction rate of each BB and the amount of CH consumed by BFS in each BB paste at 7 days of curing time. The calculation of the amount of CH consumed by BFS in each BB paste is as shown in Equation (2) below.

$$Y=(((X_a\times0.55)-X_b)/(X_a\times0.55))\times100 \quad (2)$$

Y: Amount of CH consumed by BFS (%)
Xa: Amount of CH in OPC at 7 days of curing time (%)
Xb: Amount of CH in BB at 7 days of curing time (%)

Comparing BB III- $C\bar{S}$2.0 and BB III- $C\bar{S}$3.5, which have been supplemented with CS, with BB I lacking $C\bar{S}$ addition, it becomes evident that BFS consumes more CH as $C\bar{S}$ dosage increases. Previous studies have reported that in systems where BFS coexists with $C\bar{S}$ and CH, Al_2O_3 in BFS react with CH and $C\bar{S}$ to form ettringite (Ett). [10].

In this study, the reason for the decrease in CH content in BB paste as the $C\bar{S}$ addition rate increases can be attributed to the consumption of CH in the formation of Ett through BFS reaction. Additionally, previous reports indicate that a reduction in CH content in cement leads to advancing neutralization, making it difficult to ensure durability[11].

Therefore, in future research aiming to optimize the addition of $C\bar{S}$ to BFS, it is also important to consider the content of calcium hydroxide (CH) in blast-furnace cement.

4. CONCLUSIONS

In this study, the impacts of changes in blaine specific surface area and anhydrite ($C\bar{S}$) addition on the reactivity of blast furnace slag fine powder (BFS) were investigated in a blast furnace cement type B system (BB). The impact of the change in reactivity of BFS with varying powder content and $C\bar{S}$addition on the strength development of the mortar specimens was also investigated.

As a result, the following findings were obtained.

(1) It was found that the reactivity of BFS with low basicity at 7 days of curing could be improved to the reactivity of the ordinary BFS by controlling both the particle size and the amount of $C\bar{S}$ addition.

(2) the strength development of blast-furnace cement with $C\bar{S}$ added to low-basicity BFS was equal to that of blast-furnace cement with ordinary BFS, even if the reactivity of BFS was not increased to the ordinary BFS reactivity. We can considered that the hydration products of blast-furnace cement with $C\bar{S}$ has higher binding water content, compared with that of blast-furnace cement without $C\bar{S}$

(3) the amount of CH in the BB paste decreased with increasing $C\bar{S}$ addition rates. It is considered that the amount of CH consumed by the BFS increased by $C\bar{S}$ addition.

REFERENCE

1. Japanese Industrial Standard: JIS R 5211 (2019)
2. J. Adachi et al., "Effect of Expansion Additives as Stimulant on Hydration of Blast Furnace

Slag and Blast Furnace Cement", Cement Science and Concrete Technology, Vol. 74, 2020, pp. 51-58
3. N. Nito et al., "Influences of Chemical Compositions And Finess of Blast Furnace Slag on Strength and Hydration of High Volume Blast Furnace Slag Cement", Cement Science and Concrete Technology, Vol. 74, 2020, pp. 15-21
4. T. Iyoda et al., "Effect of Blaine value and Amount of BFS and Gypsum for Hydration Heat and Autogenous Shrinkage", Proceedings of the Japan Concrete Institute, Vol. 29, No. 1, 2007, pp. 99-104
5. T. Ansai et al., "Long-Term Hydration Reaction of High Blast-Furnace Slag Cement", Cement Science and Concrete Technology, Vol. 64, 2010, pp. 48-53
6. R. Kondo et al.," Studies on a Method to Determine the Amount of Granulated Rlastfurna,ce Slag and the Rate of Hydration of Slag in Cements", Yogyo-Kyokai-Shi, Vol.77, 1969, pp.39-46
7. Japanese Industrial Standard: JIS R 6206 (2013)
8. P.K Mehta : Mechanism of Expansion Associated with Eteringite Formation,Cement and Concreate Reserch, Vol. 3, 1973, pp. 1-6
9. R. Kondo et al., "The Latent Hydraulic Property of Granulated Blast Furnace Slag by Various Activators", Iron and Steel, No. 65, 1979, pp. 1825-1829
10. R. Kondo. "Effect of various particles size of calcium carbonate powders on the hydration of Portland cement", Gypsum and Lime, No.147 ,1977 ,pp.13- 21
11. T. Yonezawa et al., "Energy-CO_2-Minimum (ECM) Cement・Concrete System", Concrete Engineering, Vol .48, 2009, pp. 69-73

EFFECTS OF TRIISOPROPANOLAMINE ON HYDRATION REACTION OF CEMENT MIXED WITH LIMESTONE POWDER AND BLAST FURNACE SLAG POWDER

KANAGA, Syuya
Graduate student, Shimane University, Japan

YOSHIDA, Natsuki
Specially appointed associate professor, Osaka University, Japan

ATARASHI, Daiki
Professor, Shimane University, Japan

ABSTRACT:
In this study, we investigated the effects of triisopropanolamine (TIPA) on the compressive strength and hydration reaction of ordinary Portland cement (OPC) mixed with limestone powder (LSP) and blast furnace slag powder (BFS). The compressive strength of cement mixed with 10% LSP and 10% BFS at 28 days of age was improved to the same level as that of OPC. Furthermore, the compressive strength of cement containing TIPA was higher than that of OPC. The reactivity of aluminate (C_3A), ferrite (C_4AF), and $CaCO_3$ were accelerated by adding TIPA, and production of monocarboaluminate (Mc) and hemicarboaluminate (Hc) increased accordingly.
Therefore, the increase in compressive strength in this study is presumably due to the increase in the amount of hydration products in the pore phase such as Mc and Hc.
Keywords: compressive strength, limestone powder, blast furnace slag powder, amine additives, portland cement, hydration reaction

1. INTRODUCTION

In recent years, the world has been actively working to reduce CO_2, a greenhouse gas that causes global warming. On the other hand, the cement industry emitted approximately 40 million tons of CO_2 in FY2020, making it the fourth largest source of CO_2 emissions in the industrial sector of Japan [1]. Therefore, reducing and curbing CO_2emissions from the cement industry are essential for building a low-carbon society. One of the solutions to this issue is expected to be the reduction of the clinker ratio using cement with increased minor additional constituents.
The current JIS 5210 allows only 5% of the minor additional constituents. that can be substituted for ordinary Portland cement (OPC). Therefore, efforts to increase the amount of small-volume mixed components for revising JIS standards are active toward the establishment of a low-carbon society [2]. In addition, it is expected that the clinker ratio will be 0.8 by 2050, when a carbon-neutral society is expected to be established [1], so efforts should be made to increase the minor additional constituents. in the formula to 20% or more. The use of limestone powder (LSP) is also assumed as minor additional constituents of the clinker mixture, because LSP is relatively easy to obtain and achieves 100% domestic self-sufficiency in Japan. However, it has been reported that the compressive strength of cements with LSP as minor additional constituents as the amount of LSP mixed increases [3]. Therefore, it is necessary to improve the compressive strength reduction.
Triisopropanolamine (TIPA), an amine-based additive, is being investigated to improve strength reduction. Ichikawa et al. reported that TIPA greatly enhances the reaction in the interstitial phase, resulting in an increase in compressive strength [4]. Uno et al. also reported that the addition of TIPA to cement mixed with LSP improved the reactivity of LSP and C_4AF and enhanced the compressive strength [5]. In other words, the addition of TIPA is effective in increasing the mixing volume of LSP.
On the other hand, combined use of LSP and BFS to improve strength reduction is also under investigation. Kuga et al. reported that the strength reduction improves in systems that use LSP and BFS [6]. Therefore, it is expected that the combination of LSP and BFS will increase the ratio of a small amount of the mixed component, and furthermore, the addition of TIPA will improve the strength reduction of the cement with the addition of a small amount of the mixed component.
In this study, mortar specimens were prepared by adding LSP, BFS, and TIPA to OPC, and the compressive strength of each specimen was compared with that of OPC to evaluate strength development. In addition, hydration reaction analysis was performed for the cement minerals and mixtures in the paste samples.

2. EXPERIMENTAL METHOD

Table 1 Mineral composition of OPC

Mineral composition (wt%) (Bogue)				Chemical composition (wt%)
C_3S	C_2S	C_3A	C_4AF	SO_3
59	17	7	10	2.02

Table 2 Chemical composition of LSP and BFS

Mixed material	Chemical composition (wt%)					
	CaO	SiO_2	Al_2O_3	Fe_2O_3	MgO	Ig.Loss
LSP	56.01	-	0.03	0.02	0.2	43.23
BFS	41.79	34.12	14.18	-	7.02	0.5

Table 3 Mix proportions of cement pastes and mortar specimens

Name of binder	Proportions of binder (wt%)			
	OPC	LSP	BFS	TIPA
OPC	100	–	–	–
L20	80	20	–	–
B20	80	–	20	–
L10B10	80	10	10	–
L10B10T	80	10	10	0.03

2.1 Materials

In this study, OPC (Blaine specific surface area 3260cm^2/g), LSP (Blaine specific surface area 5000 cm^2/g), BFS (Blaine specific surface area 4340 cm^2/g), TIPA, and standard sand (according to JIS R 5201) were used as materials. The mineral composition of OPC calculated using the Bogue equation is shown in Table 1. Table 2 shows the chemical compositions of LSP and BFS, respectively. Table 3 shows the formulations of the mortar specimen and cement paste samples prepared using OPC, LSP, BFS, and TIPA. Hereafter, each formulation is denoted by its name in Table 3. Distilled water was used as mixing water. In the system containing TIPA, the amount of added TIPA was 0.03 mass% of the total powder.

2.2 Analysis method of mortar samples

(1) Compressive strength test

Mortar specimens were prepared with the following mass ratios: cement 1 (formulation in Table 1), standard sand 3, and water 0.5. The specimens were subjected to compressive strength tests in accordance with JIS R 5201. The age of the specimens was 28 days.

2.3 Analysis method of cement paste samples

(1) X-ray diffractometer (XRD)

Cement paste samples were prepared using the formulations listed in Table 3 and sealed and cured in a constant temperature room at 20°C until the specified age of the material (1, 3, 7, and 28 days). The water to powder ratio (W/P) was set to 0.4 to prevent material separation. After curing for the prescribed number of days, the cement paste samples were crushed and free water was removed using acetone. Then, decompression drying using an aspirator (0.02MPa) was performed for 1 day.

The reaction rate of cement minerals and LSP were determined by the internal standard method (standard: 10 mass% MgO added internally) using powder X-ray diffraction (Bluker, D2 PHASER tube sphere Cu, source: CuKα, tube voltage 30kV, current 10mA) on the samples after decompression drying using equation (1) was calculated from the peak area [7].

$$\alpha_i(t) = 100 - \frac{\frac{S_i(t)}{S_{MgO}(t)} \times \frac{100}{100 - Ig.loss(t)}}{\frac{S_i(0)}{S_{MgO}(0)} \times \frac{100}{100 - Ig.loss(0)}} \times 100 \qquad (1)$$

t: Hydration time

$\alpha_i(t)$: Reaction ratio (%) of the sample hydrated for t hours

$S_i(t)$: Peak area of XRD pattern of the sample hydrated for t hours.

$Ig.loss(t)$: Intense thermal loss of the sample hydrated for t hours at 1000 ℃ (%)

The following diffraction peaks (2θ) were also used for quantification.

Alite(C_3S)(2θ =51.7° and 51.9°), aluminate (C_3A)(2θ = 33.2)°, ferrite (C_4AF)(2θ =12.2°), $CaCO_3$ (2θ =48.5°), MgO (2θ= 42.9°)

TOPAS (Bruker-AXS) was used for Rietveld analysis. In addition to periclase (internal standard), gypsum, semi-aqueous gypsum, portlandite (CH), ettringite (Ett), monosulfate (Ms), monocarboaluminate (Mc), and hemicarboaluminate (Hc) were set according to the phase contained in the sample, and the content of each

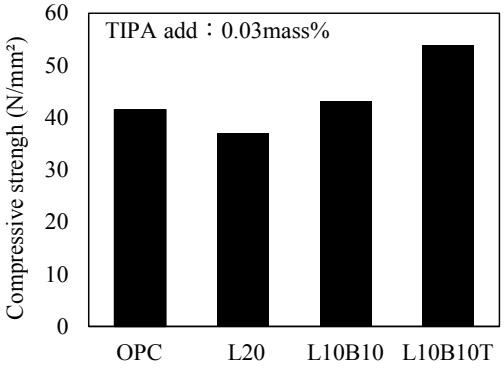

Fig. 1 Compressive strength of each system at 28 days

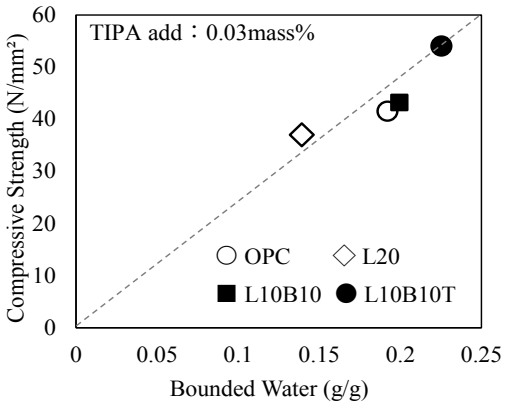

Fig. 2 Relationship between compressive strength and ignition loss

mineral phase was determined the content of each mineral phase was determined.

(2) Calculation of the reaction rate of BFS

The residual amount of unreacted BFS was determined for cement paste samples mixed with BFS using the salicylic acid-acetone-methanol selective dissolution method [8], and the reaction rate of BFS was calculated. The correction term was calculated in advance by determining the amount of BFS dissolved in a single phase of BFS using the same method, and the correction was based on strong thermal loss (1000°C). However, BFS is accompanied by an increase in mass above 800°C a correction for the mass increase was made [9]. Also, the LSP did not dissolve using the selective dissolution method, and the amount of LSP remaining was corrected.

(3) Bound water content

One gram of the sample was heated in an electric furnace, and the amount of bound water was determined from the weight loss at 1000°C. Because the weight loss in this case includes the loss due to calcination of LSP and the loss due to dehydration of the crystalline water of gypsum, these losses were corrected in the calculation. The weight loss due to LSP and gypsum was determined from the ignition loss (1000°C) of the unhydrated cement.

3.EXPERIMENTAL RESULTS AND DISCUSSION

3.1 Effect of TIPA on the compressive strength of mortar with LSP and BFS

Fig. 1 shows the compressive strength of OPC, L20 (20% LSP), L10B10 (10% LSP and 10% BFS), and L10B10T (L10B10 with 0.03 mass% TIPA) at 28 days of age. As previously reported, the compressive strength of L20 was lower than that of and OPC at 28 days of age [5].

On the other hand, as shown by Kuga, the compressive strength of L10B10 mixed with LSP and BFS at 28 days of age improved to the same level as that of OPC [7].

Furthermore, L10B10T, TIPA was added to L10B10, showed improved compressive strength, was higher than that of OPC and L10B10.

These results suggest that the addition of TIPA to a system in which LSP and BFS are mixed may increase the minor additional constituents to 20% or more, and that the LSP+BFS+TIPA system is effective for increasing the minor additional constituents.

3.2 Effect of TIPA on the amount of bound water in cement combined with LSP and BFS

Fig. 2 shows the relationship between compressive strength and ignition loss at 28 days of age in L20, L10B10, and L10B10T. In this study, a correlation between compressive strength and binding water content was obtained [10].

L20 showed a lower value of binding water content than OPC. On the other hand, L10B10 showed a binding water content equivalent to that of OPC, and L10B10T with TIPA showed a binding water content higher than that of OPC.

Therefore, it is considered that the strength improved to the same level as that of OPC by the combined mixing of LSP and BFS, and the strength above that of OPC by the addition of TIPA was due to the increase in the amount of hydration products.

3.3 Effect of TIPA on hydration products of cement with LSP and BFS

Fig. 3 shows the XRD patterns of L20, L10B10, and L10B10T at 28 days of age, and the formation peaks of ettringite (Ett) and monocarboaluminate (Mc) were observed in L20. On the other hand, hemi-carboaluminate (Hc) was also identified in L10B10 and L10B10T. Furthermore, the addition of TIPA to L10B10 increased the peak areas of Mc and Hc. This may be attributed to the increased reactivity of cement minerals and LSP due to the addition of TIPA.

3.4 Effect of TIPA on the reaction of cement minerals and mixtures of cement mixed with LSP and BFS.

(1) C_3A reaction ratio

Fig. 4 shows the C_3A reaction rates of L20, B20, L10B10, and L10B10T. The addition of TIPA accelerated the initial reaction of C_3A more than other formulations.The accelerated reaction of C_3A by the addition of TIPA has been reported in previous studies, and it is assumed that the reaction of the Al gel, which inhibits the reaction of C_3A, with TIPA results in the formation of an Al-TIPA complex [11].

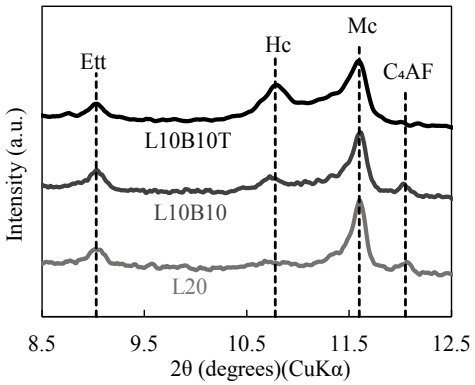

Fig. 3 XRD pattern of each system

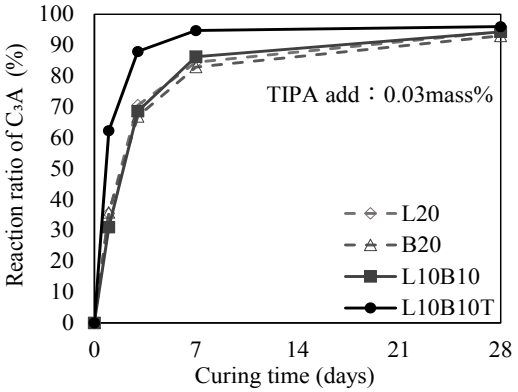

Fig. 4 C_3A reaction ratio for each system

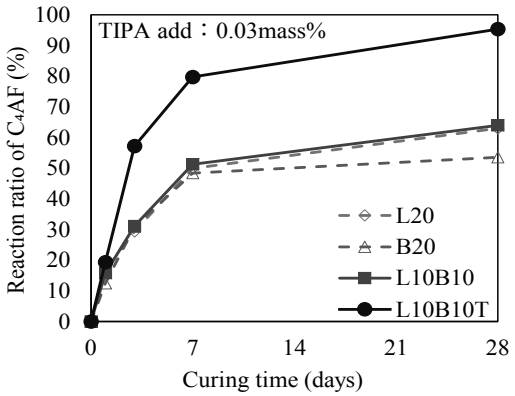

Fig. 5 C_4AF reaction ratio for each system

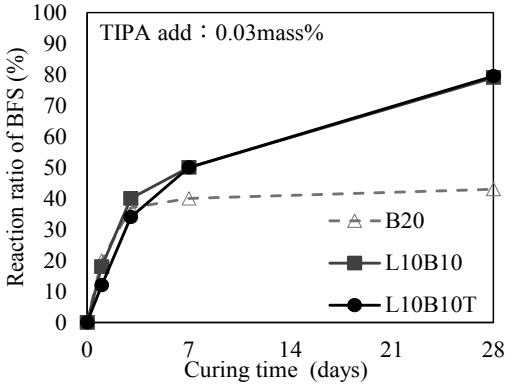

Fig. 6 BFS reaction ratio for each system

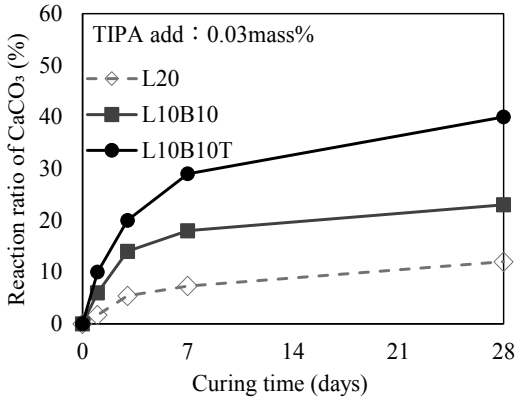

Fig. 7 $CaCO_3$ reaction ratio for each system

(2) C_4AF reaction ratio

Fig. 5 shows the C_4AF reactivity of L20, B20, L10B10, and L10B10T. L10B10T, in which TIPA was added to L10B10, showed much higher C_4AF reactivity than the other systems.

It is known that in the process of hydration of C_4AF, Fe-rich gel hydrates (Fe gel) are formed from the surface of C_4AF to the interior, leading to a rate-limiting mass transfer and inhibiting the reaction [12].

However, the addition of TIPA enhanced the reactivity of C_4AF because the Fe gel and TIPA, which inhibit the hydration of C_4AF, formed an Fe-TIPA complex and the solubility of the Fe gel was enhanced [4].

(3) BFS reaction ratio

Fig. 6 shows the BFS reactivity of B20, L10B10, and L10B10T. L10B10 showed improved BFS reactivity compared to B20. On the other hand, L10B10T showed no significant change in BFS reactivity compared to L10B10, suggesting that the addition of TIPA to the combined LSP and BFS system does not significantly influence the reactivity of BFS.

(4) $CaCO_3$ reaction ratio

Fig. 7 shows the $CaCO_3$ reaction rates in L20, L10B10, and L10B10T. L10B10 showed slightly better $CaCO_3$reactivity compared to L20.

On the other hand, L10B10T, in which TIPA was added to L10B10, showed a significant improvement in $CaCO_3$ reactivity at each age compared with L10B10 and L20. Amines such as TIPA are used as CO_2 absorbent solutions, and previous studies have reported that the solubility and reactivity of $CO_2$is improved in amine solutions [13].

Therefore, it was possible that the addition of TIPA increased the solubility of CO_3^{2-} in this study as well, which may have improved the reactivity of $CaCO_3$.

In a previous study, Li et al. reported that the reaction of Al^{3+} and Fe^{3+} in the liquid phase of cement mixed with LSP with LSP-derived CO_3^{2-} produced Hc:$3CaO\text{-}Al_2O_3\text{-}1/2Ca(OH)_2\text{-}11H_2O$ and Mc:$3CaO\text{-}Al_2O_3\text{-}CaCO_3\text{-}12H_2O$ are reported to be formed [14].

On the other hand, the increase in the production of Hc and Mc by adding TIPA to the mixed system of LSP and BFS was due to the enhanced reactivity of C_3A and C_4AF, as shown in Figs. 4 and 5, and from Fig. 7, the enhanced reactivity of $CaCO_3$, which may have led to the formation of more Al^{3+}, Fe^{3+}, and CO_3^{2-} in the liquid

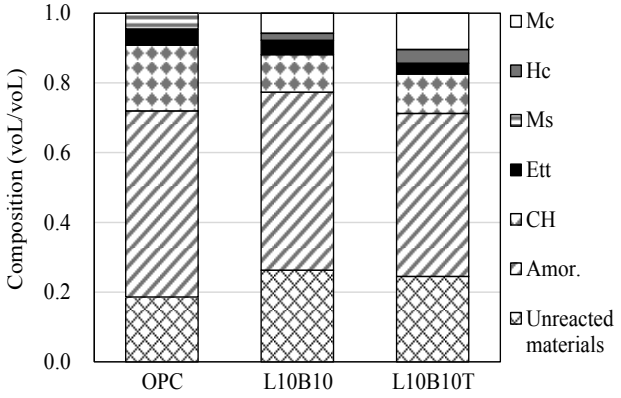

Fig. 8 Composition of each cement

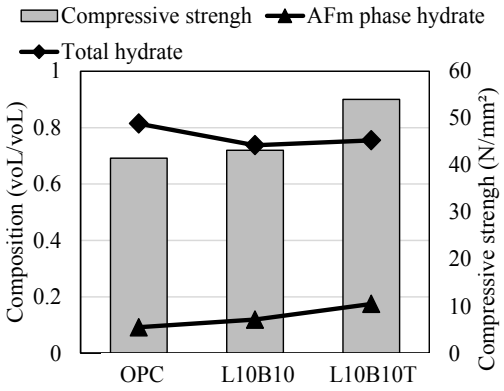

Fig. 9 Relationship between hydration products

phase, facilitating the formation of Hc and Mc.

3.5 Effect of TIPA on phase composition of cement mixed with LSP and BFS

Fig. 8 shows the phase composition of the paste samples of OPC, L10B10, and L10B10T at 28 days of age; L10B10 and L10B10T showed increased hydration products in the pore phase compared to OPC. This result was attributed to the increased reactivity of C_3A and C_4AF due to the combination of BFS and the addition of TIPA.

L10B10 and L10B10T also showed lower total hydration product content compared to OPC; it is speculated that this is due to L10B10 and L10B10T having a 20% lower clinker ratio than OPC. Furthermore, L10B10 and L10B10T showed much lower CH contents than OPC. This may be because L10B10 and L10B10T have a lower clinker ratio than OPC, as well as the fact that they are mixed with BFS; thus, CH is consumed by the latent hydraulicity of BFS.

Fig. 9 shows the relationship between the hydration product content and compressive strength of OPC, L10B10, and L10B10T. No correlation was observed between the total hydration product content and compressive strength for each system.

On the other hand, there was a correlation between the amount of hydration products in the pore phase and compressive strength in each system. Therefore, the increase in compressive strength in this study can be attributed to the increase in the amount of hydration products (Mc, Hc) and the filling of voids in the mortar [15]. It is also reported that the volume per unit mass of Hc is larger than that of other hydration products [16], suggesting that Hc has a greater pore filling effect than Mc.

4.CONCLUSIONS

In this study, mortar and cement paste specimens were prepared by mixing ordinary Portland cement (OPC) with limestone powder (LSP), blast furnace slag powder (BFS) and triisopropanolamine (TIPA), and compressive strength measurements and hydration reaction analysis were conducted at 28 days of age for each system.

The following conclusions were obtained.

(1) Compressive strength at 28 days of age was improved to the same level as that of OPC when LSP and BFS were used together. The compressive strength at 28 days of age of the lumber improved to a value equal to or greater than OPC by adding TIPA to the combined system of LSP and BFS. In other words, the system combining LSP, BFS and TIPA was effective in increasing the amount of small volume mixed components, suggesting the possibility of adding more than 20% of small volume mixed components.

(2) The addition of TIPA to the system containing LSP and BFS increased the reactivity of aluminate (C_3A), ferrite (C_4AF), and $CaCO_3$compared to the system containing LSP and BFS. On the other hand, no change was observed in BFS reactivity, indicating that TIPA has little effect on BFS reactivity.

(3) Addition of TIPA to the combined system of LSP and BFS increased the amount of monocarboaluminate (Mc) and hemicarboaluminate (Hc) formed. This was attributed to the increase in reactivity of C_3A, C_4AF, and $CaCO_3$ by the addition of TIPA, which supplied more Al^{3+}, Fe^{3+}, and CO_3^{2-} in the system.

(4) The number of crystalline hydration products in the pore phase increased in the system combining LSP and BFS or adding TIPA to it, compared to OPC. It is suggested that the compressive strength may have increased accordingly.

ACKNOWLEDGEMENT

This research was supported in part by a research grant from the Cement Association of Japan. We would like to express our deepest gratitude to them.

REFERENCE

1. Japan Cement Association: Long-term vision of the cement industry toward carbon neutrality, 2022
2. Japan Cement Association: Business Plan for FY2024, 2024
3. S. Hiramoto, Y. Ueki, Y. Otsuka: “Durability of blast furnace cement concrete with increasing limestone powder replacement ratio in

Portland cement", Proceedings of the Japan Concrete Institute, Vol.36, No.1, 2014
4. M. Ichikawa, S. Sano, Y. Komukai: "Relation between cement characters and strength enhancement with Triisopropanolamine", Cement Science and Concrete Technology, No.50, pp.110-115, 1996
5. K. Uno et al., "The effect of amine on physical properties and hydration reaction of various Portland cements containing limestone powder", Cement Concrete, Transactions of the Japan Concrete Institute, Vol.77, pp.96-104, 2023
6. R. Kuga et al., "Effect of blast furnace slag powder and limestone powder on strength improvement of cements with different Al_2O_3 content", JSCE 64th Annual Conference, Vol.64, pp. 901-902, 2009
7. H. Imoto, E. Sakai, M. Daimon: "Quantitative analysis for the hydration of limestone filler cement, Cement Science and Concrete Technology", No.56, pp.42-49, 2002
8. R. Kondo, E. Osawa: "Studies on a method to determination the amount of granulated blast furnace slag and rate of hydration of slag in cement", Journal of Ceramic Association of Japan, Vol.77, pp.39-46, 1969
9. Japan Cement Association: A book to understand cement standards -JIS cement manual-, p.200,1997
10. H. Yamazaki: "Basic study on the effect of mineral powder on the strength of concrete", Journal of JSCE, Vol.85, pp.24-53, 1962
11. E. Gartner, D. Myers: "Influence of tertiary alkanolamines on Portland cement hydration", J American Ceramic Society 76(6), pp.1521-1530, 1993
12. M. Fukuhara et al., "Behavior of Fe component in the hydration of tetracalcium-aluminoferrite with gypsum during ettringite forming period", Journal of Ceramic Association, Vol.88, No.1020, pp.435-440, 1980
13. K. Teranishi, A. Ishikawa, H. Nakai: "Computational chemistry studies on CO_2 chemical absorption technique: Challenge on energy and environmental issues", Society of Computer Chemistry, Vol.15, No.2, pp. A15-A29, 2016
14. S. Lee et al., "Effects of gypsum dihydrate on hydration of $3C_3A \cdot CaCO_3$-$CaSO_4 \cdot 2H_2O$-$CaCO_3$ system", Journal of the Society of Inorganic Materials, No.51, pp.38-48, 1997
15. E. Sakai et al., "Filler cement, Easy-to-understand cement science", Japan Cement Association, pp. 54-62, 1993
16. M. Balonis, F. P. Glasser: "The density of cement phases", Cement and Concrete Research, Vol.39, pp.733-739, 2009

INFLUENCE OF HIGH TEMPERATURE CURING AND SPECIFIC SURFACE AREA OF LIMESTONE POWDER ON HYDRATION REACTION OF ORDINARY PORTLAND CEMENT MIXED WITH LIMESTONE POWDER

SAKAMOTO, Wataru
Graduate student, Shimane University, Japan

YOSHIDA, Natsuki
Specially appointed associate professor, Shimane University, Japan

TAKATSUKA, Ryo
Graduate student, Shimane University, Japan

ATARASHI, Daiki
Professor, Shimane University, Japan

ABSTRACT:
In this study, the influence of high-temperature (40 °C) curing and differences in the blaine specific surface area (5000 cm^2/g and 9000 cm^2/g) of LSP on the hydration reaction of OPC mixed with LSP were investigated. In the study of high-temperature curing, 40 °C curing inhibited the reaction of LSP ($CaCO_3$) and promoted the hydration reaction of C_4AF compared with 20 °C curing. And LSP of 9000 cm^2/g in OPC was more reactive than LSP of 5000 cm^2/g. Furthermore, the initial hydration reaction of C_3S in OPC mixed with LSP of 9000 cm^2/g was greatly accelerated compared to C_3S in OPC mixed with LSP of 5000 cm^2/g. As a result, a large amount of hydrates such as CH were formed during the initial hydration of OPC mixed with LSP of 9000 cm^2/g.
Keywords: limestone powder, high-temperature curing, blaine specific surface area, monocarboaluminate

1. INTRODUCTION

Global warming has been progressing rapidly in recent years, and efforts to reduce the emission of CO_2 are underway around the world. The cement and concrete industry in Japan emits approximately 40 million tons of CO_2 annually (equivalent to about 3-4% of the amount of CO_2 emitted from Japan) [1]. Thus, this industry emits a large amount of CO_2. Therefore, the cement and concrete industry has been also working to reduce CO_2.
Most of the CO_2 emitted by the cement and concrete industry comes from production of clinker, material of ordinary Portland cement (OPC). The reduction of CO_2 emitted from clinker production are achieved by reducing the percentage of clinker in the cement. As one of the examples, cement with a portion of clinker replaced with limestone powder (LSP) is considered. Unlike blast furnace slag and fly ash, which are frequently used as supplementary cementitious materials, LSP emits almost no CO_2 during its manufacturing process. Therefore, increasing the use of the cement mixed with LSP will significantly contribute to reducing CO_2 from the cement industry. As fundamental studies to increase the opportunities to use OPC mixed with LSP, the two factors that may influence the hydration reaction of OPC mixed with LSP were investigated.
The first factor is the hydration reaction under high temperature conditions, assuming the climate of Southeast Asia, where the demand for cement is expected to increase in the future.
The second factor is the influence of the specific surface area of LSP on the hydration reaction of OPC. The specific surface area of LSP is not precisely defined. The research committee of LSP in Japan Concrete Institute proposed that the specific surface area of LSP should be at least 2500 cm^2/g, which is rough definition [2], [3]. Therefore, LSP with various specific surface areas are expected to be produced.
In this study, the influence of high-temperature (40 °C) curing and differences in the blaine specific surface area (5000 cm^2/g and 9000 cm^2/g) of LSP on the hydration reaction of OPC mixed with LSP were investigated.

2. EXPERIMENTAL METHOD

2.1 Sample preparation

(1) Materials

Ordinary Portland cement (N) and LSP of blaine specific surface area of 5000 cm^2/g and 9000 cm^2/g were used as materials. The mineral compositions of N were calculated by using the Bogue formula and are shown in Table 1. The chemical compositions of LSP are shown in Table 2.

(2) Experiment I: the influence of high-temperature (40 °C) curing

Table 1 Mineral and Chemical composition of OPC (N)

	Mineral composition (wt%) (Bogue)				Chemical composition (wt%)
N	C_3S	C_2S	C_3A	C_4AF	SO_3
	59	17	7	10	2.02

Table 2 Chemical composition of LSP

	Chemical composition (wt%)							
LSP	SiO_2	Al_2O_3	Fe_2O_3	CaO	MgO	SO_3	Na_2O	K_2O
	0.00	0.03	0.02	56.01	0.20	0.00	0.00	0.00

N and LSP of 5000 cm^2/g were mixed at a ratio of 90:10 wt%. The cement paste was mixed with 0.5 water/powder. Sealing and curing (1,3,7,14,28 day) were performed under 20 °C and 40 °C (20-N-LSP and 40-N-LSP, respectively). After that, samples whose hydration was stopped with acetone was used for analysis.

(3) Experiment II: the influence of differences in the blaine specific surface area

N and LSP (5000 cm^2/g and 9000 cm^2/g) were mixed at a ratio of 90:10 wt%. OPC mixed with LSP of 5000 cm^2/g are named "N-LSP5000" and OPC mixed with LSP of 9000 cm^2/g are named "N-LSP9000". These cement pastes were mixed with 0.5 water/powder. Sealing and curing (1, 3, 7, 14, 28 day) were performed under 20 ℃. After that, samples whose hydration was stopped with acetone was used for analysis.

2.2 Analysis method

(1) Content ratio of portlandite (CH)

The amount of CH produced in the cement paste of Experiment II was calculated from the amount of H_2O decomposed from CH. The amount of H_2O decomposed from CH measured using a thermogravimetric differential thermal analyzer (TG-DTA, NETZSCH STA2500, rise rate of temperature is 10℃/min^{-1}). The amount of H_2O decomposed from CH was calculated from the decrease in weight from the start temperature to the end temperature on TG curve. The temperature range of the decrease in weight by the dehydration of CH was determined from endothermic peak on DTA curve. Those values were used to calculate the CH content ratio from (1).

$$M_{CH}=\frac{\Delta m_{CH}}{m_0-m_{1000}}\times\frac{56.08}{18.02}\times100 \quad (1)$$

M_{CH}: CH content ratio (%)
Δm_{CH}: Amount of water produced by decomposition of CH (mg)
m_0: Amount of sample for measurement (mg)
m_{1000}: Amount of sample after heating at 1000 °C (mg)
56.08: molecular weight of CaO
18.02: molecular weight of H_2O

(2) Ig. Loss

Samples of Experiment II were heated in electric furnace, and the Ignition loss (Ig.loss) was calculated from the decrease in weight at 1000°C. Since the decrease in weight up to 1000 °C includes the loss in weight due to the decarbonation of LSP, the decrease in weight up to 1000 °C was calculated excluding the loss in weight due to the decarbonation of LSP.

(3) X-ray diffractometer (XRD)

XRD measurements were performed on the samples from Experiment I and Experiment II.XRD (Bluker, D2, PHASER tube sphere Cu, source: CuKα, tube voltage 30kV, current 10mA) was used for analysis of hydration products and calculation of reaction ratio of cement minerals.

It was calculated from the peak area using the same formula as in a previous paper [4] (Equation (2)).

$$\alpha_i(t)=100-\frac{\frac{S_i(t)}{S_{MgO}(t)}\times\frac{100}{100-Ig.loss(t)}}{\frac{S_i(0)}{S_{MgO}(0)}\times\frac{100}{100-Ig.loss(0)}}\times100 \quad (2)$$

t: Hydration time
$\alpha_i(t)$: Reaction ratio (%) of the sample hydrated for t hours
$S_i(t)$: Peak area of XRD pattern of the sample hydrated for t hours.
Ig.loss(t): Intense thermal loss of the sample hydrated for t hours at 1000 °C (%)

C_3S (2θ = 51.7° and 51.9°), C_4AF (2θ = 12.2°), C_3A (2θ = 33.2°), LSP (Calcite) (2θ = 48.5°) and MgO (2θ = 42.9°) were quantified.

3. RESULTS AND DISCUSSION

3.1 Experiment I

(1) Reaction ratio of C_4AF

Fig. 1 shows the influence of high-temperature (40 °C) curing on the reaction of C_4AF. In 40-N-LSP, the

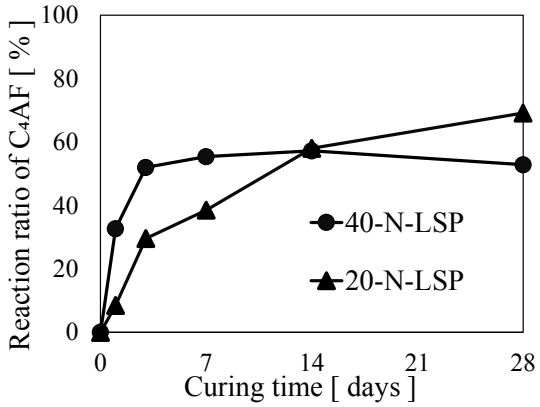

Fig. 1 Reaction ratio of C_4AF in 20-N-LSP and 40-N-LSP

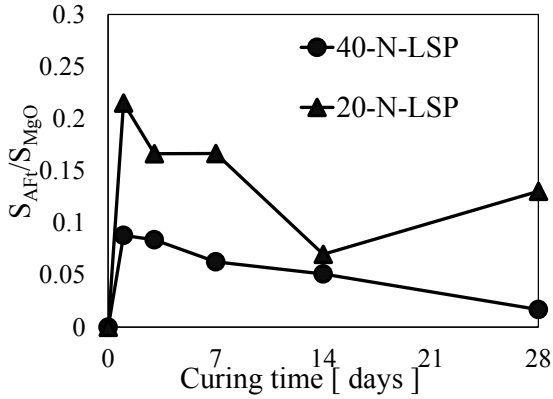

Fig. 3 The ratio of the peak area of AFt to the peak area of MgO (S_{AFt}/S_{MgO})

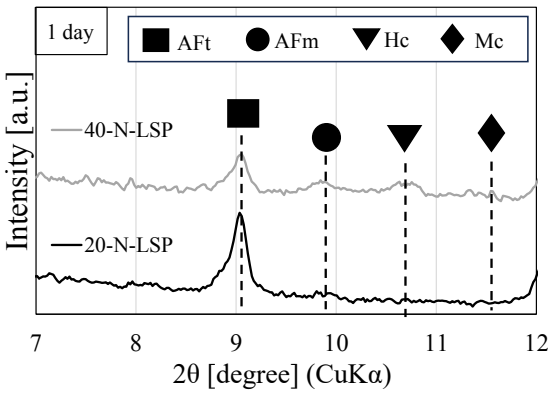

Fig. 2 XRD patterns of 20-N-LSP and 40-N-LSP at 1 day

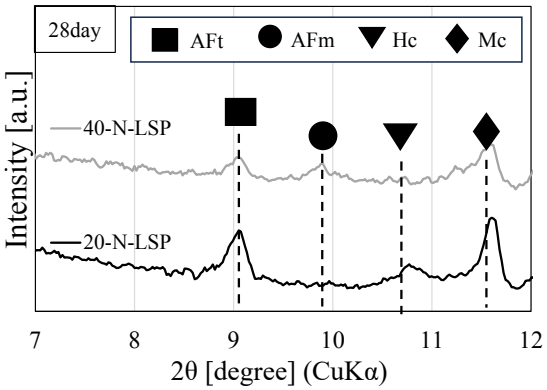

Fig. 4 XRD patterns of 20-N-LSP and 40-N-LSP at 28 days

hydration reaction of C_4AF up to 7 days was accelerated compared with 20-N-LSP. However, at 40°C curing, the reaction of C_4AF after 7 days was inhibited compared with that at 20°C. It has been reported that the hydration reaction is accelerated at higher temperatures in the initial stages of curing, but that the hydration reaction slows down at higher temperatures as the curing time increases [5]. A large amount of hydrate generated by the high-temperature hydration reaction envelop the cement minerals in the early stage and inhibit the hydration reaction inside the particles [5].

(2) Hydration products

XRD patterns of 20-N-LSP and 40-N-LSP at 1 day are shown in Fig. 2. The size of a peak on the XRD pattern is considered to depend on the amount of the component of that peak [6]. It was confirmed that the peak of ettringite (AFt) (Chemical composition : $3CaO \cdot Al_2O_3 \cdot 3CaSO_4 \cdot 32H_2O$) in 40-N-LSP was smaller than that in 20-N-LSP.

The ratio of the peak area of AFt to the peak area of MgO (S_{AFt}/S_{MgO}) is shown in Fig. 3. S_{AFt}/S_{MgO} up to 28 days at curing temperature 40 °C was smaller than that at 20 °C. As shown in Fig. 2, the XRD pattern at 1 day showed no peak of dihydrate gypsum ($CaSO_4 \cdot 2H_2O$) in either curing temperature, suggesting that the dissolution of $CaSO_4 \cdot 2H_2O$ ($CaSO_4 \cdot 2H_2O \rightarrow Ca^{2+} + SO_4^{2-} + 2H_2O$) was already complete within 1 day. On the other hand, the reaction ratio of C_4AF at 40 °C up to 1 day was larger than that at 20 °C (Fig. 1). This result indicates that Al^{3+} dissolved from C_4AF at 40°C was also larger than that at 20°C. Therefore, the amount of SO_4^{2-} relative to Al^{3+} (SO_3/Al_2O_3) in the liquid phase after 1 day in 40-N-LSP was lower than that in 20-N-LSP. The higher SO_3/Al_2O_3 in the liquid phase, the more stable the AFt [7]. So, the amount of AFt in 40-N-LSP was probably lower than that in 20-N-LSP. At a curing temperature of 20 °C, S_{AFt}/S_{MgO} increased again from 14 to 28 days. This suggests that the amount of AFt increased again between 14 and 28 days in 20-N-LSP. On the other hand, no increase in S_{AFt}/S_{MgO} was observed between 14 and 28 days in 40-N-LSP. In a previous study [3] , the reaction between LSP and monosulfate (AFm) produces monocarboaluminate (Mc). The SO_4^{2-} released from AFm reacts with calcium aluminate hydrates such as AFm, leading to a delayed increase in AFt. (DEF: Delayed Ettringite Formation). In this study, it is suggested that DEF may have occurred by this mechanism, but more detailed studies are needed in the future.

XRD patterns of 20-N-LSP and 40-N-LSP at 28 days are shown in Fig. 4. The peak of AFm was observed in 40-N-LSP, while it was not observed in 20-N-LSP. In addition, it was confirmed that the peak of Mc in 40-N-LSP was smaller than that in 20-N-LSP. In addition, the peak of hemicarboaluminate (Hc) confirmed in 20-N-

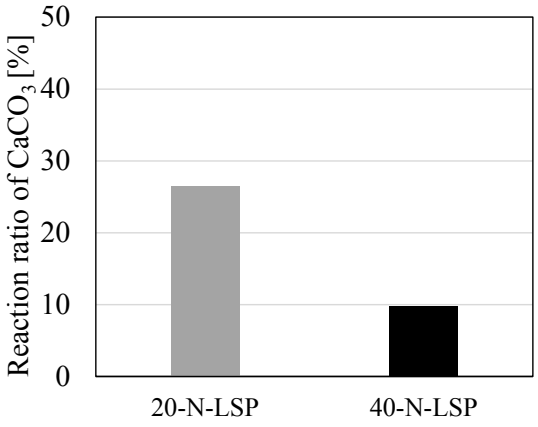

Fig. 5 Reaction ratio of $CaCO_3$ (LSP) at 28 days

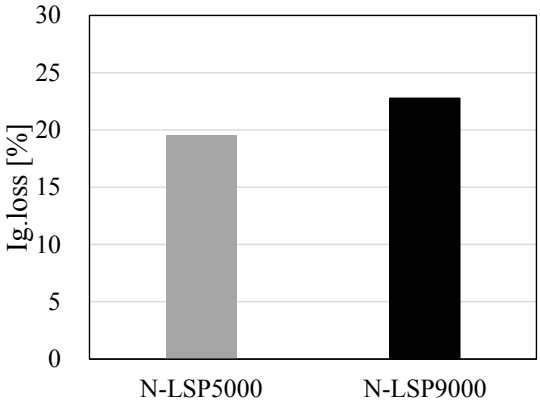

Fig. 7 Ig.loss after 7 days of curing

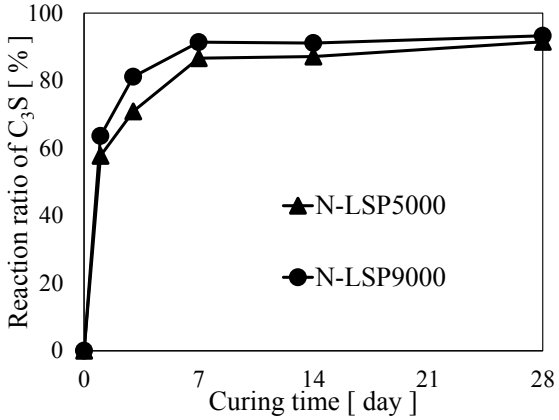

Fig. 6 Reaction ratio of C_3S in N-LSP5000 and N-LSP9000

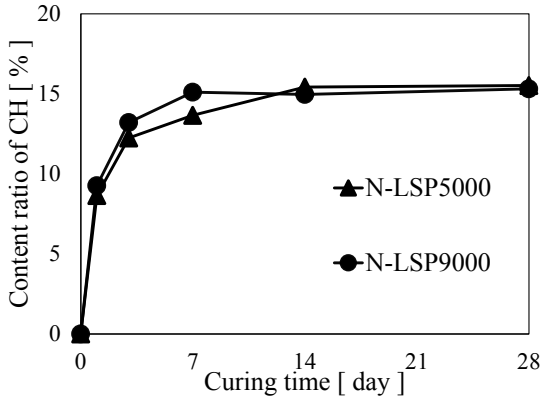

Fig. 8 Content ratio of CH in N-LSP5000 and N-LSP9000

LSP was not confirmed in 40-N-LSP. From the above, it is considered that the amount of Mc and Hc decrease as the curing temperature increases.

(3) Influence of high temperature curing on the reaction of $CaCO_3$

Fig. 5 shows the influence of curing temperature on the reaction ratio of LSP at 28 days. The reaction ratio of LSP in 40-N-LSP was lower than that in 20-N-LSP. Previous studies have shown that calcite solubility decreases with increasing temperature [8]. Therefore, this study suggests that the solubility of LSP decreased with increasing temperature. Hc and Mc are formed by the reaction of calcium aluminate phase (C_4AF and C_3A) and the CO_3^{2-} from LSP [9]. The reaction ratio of LSP decreased as the curing temperature increased, which likely caused 40-N-LSP to have lower amounts of Mc and Hc than 20-N-LSP (Fig. 4).

3.2 Experiment II

(1) Influence of blaine specific surface area of LSP on hydration reaction of C_3S

One of the effects of LSP on the hydration reaction of OPC is “the fine powder effect” that accelerates the initial hydration reaction of alite (C_3S), which constitute about 60 wt% of the mineral of OPC [9]. Most of the hydrates produced by hydration reaction of C_3S are formed on the surface of C_3S. The layer of hydrate formed on the surface of C_3S inhibits the hydration reaction of C_3S. A model has been proposed as the mechanism for the fine powder effect by LSP, in which hydrates of C_3S are deposited not only on the surface of C_3S but also on the surface of LSP particle [9]. As a result, the thickness of the hydrate layer on the surface of C_3S temporarily decreases, and the hydration reaction of C_3S is thought to proceed more easily [10]. The thickness of the hydrate layer on the surface of LSP is considered equivalent to the thickness of the hydrate layer deposited on the surface of C_3S [9].

Fig. 6 shows the reaction ratio of C_3S. The reaction ratio of C_3S in N-LSP9000 in the early stage (1~7 days) of hydration reaction is higher than that of C_3S in N-LSP5000. With the increase in the blaine specific surface area of LSP, the surface area of LSP on which hydrates of C_3S are deposited also increases. Therefore, the increase in the blaine specific surface area of LSP is expected to precipitate a large amount of hydrates on the surface of LSP surrounding C_3S. For these reasons, the fine powder effect is thought to have been greater due to the increase in specific surface area of LSP.

Ig.loss at 7 days is shown in Fig. 7. Ig.loss indicates the amount of bound water in a sample. Ig.loss at 7 days in N-LSP9000 was more than that in N-LSP5000. The main reason for this may be that the initial hydration reaction of C_3S was accelerated in N-LSP9000, resulting in an

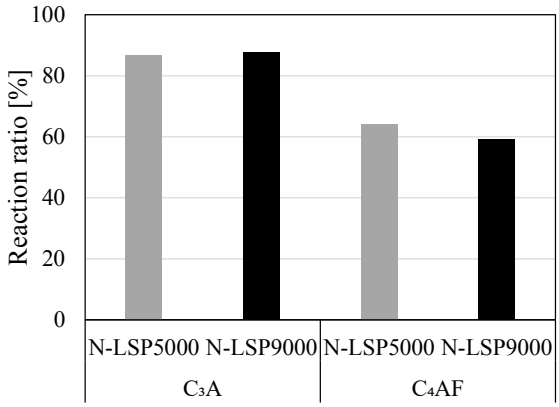

Fig. 9 Reaction ration of C_3A and C_4AF after 28 days of curing

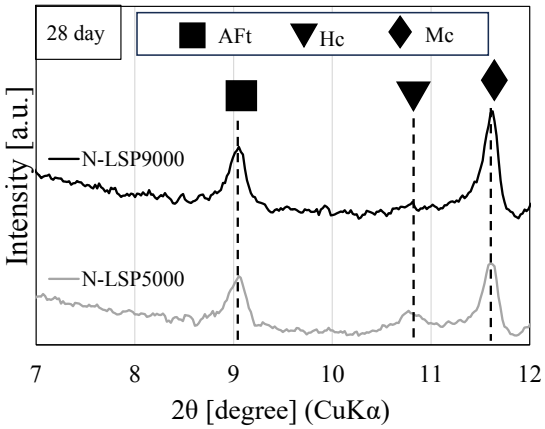

Fig. 10 XRD pattern of calcium aluminate hydrates after 28 days of curing

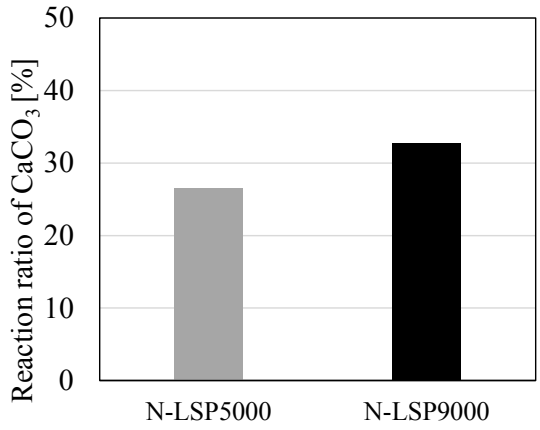

Fig. 11 Reaction ratio of $CaCO_3$ (LSP) at 28 days

increase in CH and C-S-H produced by the hydration of C_3S in the early stages of curing.

The content ratio of CH, one of the hydrates produced by the C_3S hydration reaction, is shown in Fig. 8. The content ratio of CH in N-LSP9000 in the initial stage of curing (1~7 days) is higher than in N-LSP5000. This result could be attributed to the result (Fig. 6) that the reaction rate of C_3S in N-LSP9000 during the early stages of curing was higher than that of C_3S in N-LSP5000.

(2) Influence of blaine specific surface area of LSP on hydration reaction of C_3A and C_4AF

C_3A and C_4AF form calcium aluminate hydrates from their calcium and aluminum components by their hydration reaction. The reaction ratios of C_3A and C_4AF at 28 days are shown in Fig. 9. The reaction ratios of C_3A and C_4AF were almost the same for N-LSP5000 and N-LSP9000. This result indicates that the total amount of calcium and aluminum components contributing to the formation of calcium aluminate hydrates such as AFt, AFm, Mc and Hc at 28 days is similar in N-LSP5000 and N-LSP9000.

(3) Influence of blaine specific surface area of LSP on the formation behavior of calcium aluminate hydrates

Fig. 10 shows the XRD patterns at 28 days of the range where the peak of calcium aluminate hydrate appears. There is no significant difference in the peak size of AFt between N-LSP9000 and N-LSP5000. On the other hand, the peak size of Hc is slightly larger in N-LSP5000 than in N-LSP9000, while the peak size of Mc is larger in N-LSP9000 than in N-LSP5000. Hc and Mc are formed by the reaction of C_3A and C_4AF with LSP ($CaCO_3$) [9], [11], [12]. The chemical compositions of Hc and Mc are $3CaO \cdot Al_2O_3 \cdot 1/2CaCO_3 \cdot 1/2Ca(OH)_2 \cdot 12H_2O$ and $3CaO \cdot Al_2O_3 \cdot CaCO_3 \cdot 12H_2O$, respectively. The amount of $CaCO_3$ in Mc is twice as large as in Hc. So, the formation of Mc requires more $CaCO_3$ than Hc. Since the amount of Mc in N-LSP9000 was larger than that in N-LSP5000, LSP of 9000 cm^2/g was expected to be more reactive than LSP of 5000 cm^2/g.

(4) Influence of blaine specific surface area of LSP on the reactivity of LSP

Fig. 11 shows the reaction ratio of LSP ($CaCO_3$) at 28 days. The reaction ratio of $CaCO_3$ in N-LSP9000 was higher than that in N-LSP5000. This is likely due to the increase in the specific surface area of LSP, which results in a larger contact area with reactants such as calcium and aluminum from C_3A and C_4AF.

4. CONCLUSIONS

In this study, the influence of high-temperature (40 °C) curing (Experiment I) and differences in the blaine specific surface area (5000 cm^2/g and 9000 cm^2/g) of LSP (Experiment II) on the hydration reaction of OPC mixed with LSP were investigated. Knowledge from this study are presented below.

・Experiment I

(1) The reaction ratio of C_4AF was higher in 40 °C curing than in 20 °C curing up to 7 days, but lower than in 20 °C curing after 7 days. It was considered that the microstructure generated by the accelerated reaction at high temperature enveloped the cement minerals in early stage and inhibited the hydration reaction after 7 days inside the particles.

(2) It was estimated that during the initial stage (1-7 days) of 40 °C curing, the reaction ratio of C_4AF

decreased, leading to a reduction in SO_4^{2-}/Al_2O_3 in the liquid phase and and resulting in a higher amount of AFt compared to 20 °C curing.

(3) The reaction ratio of LSP in 40 °C was lower than that in 20 °C. This result was thought to be caused by the low solubility of calcium carbonate in high temperature curing.

(4) It was assumed that the lower reaction ratio of LSP at 40 °C resulted in lower amounts of Mc and Hc.

・Experiment II

(1) The hydration reaction of C_3S in the initial stage (1-7 days) was faster in OPC mixed with LSP of 9000 cm^2/g (N-LSP9000) compared to OPC mixed with LSP of 5000 cm^2/g (N-LSP5000). Consequently, the amount of hydrate, such as CH, was larger in initial curing of N-LSP9000.

(2) The reaction ratio of C_3A and C_4AF at 28 days were not significantly different despite the differences in the blaine specific surface area of LSP.

(3) At 28 days, the amount of ettringite was almost the same in both N-LSP9000 and N-LSP5000. However, the amount of hemicarboalminate was slightly larger in N-LSP5000, while the amount of monocarboaluminate was larger in N-LSP9000.

(4) At 28 days, the greater amount of monocarboaluminate in N-LSP9000 than in N-LSP5000 was assumed to be due to the increased reaction of LSP ($CaCO_3$) resulting from its higher specific surface area.

REFERENCE

1. D. Atarashi, “New View of Neutralization / Carbonation; Consideration for Environment”, Concrete Engineering, Vol. 61, No. 9, 2023, pp. 769-773
2. M. Daimon et al., “Report by Research Committee of Limestone Powder”, Proceedings of the Japan Concrete Institute, Vol. 20, No. 1, 1998, pp. 49-58
3. E. Sakai et al., “Characteristics and Utilization of Limestone Powder and its Application”, Concrete Engineering, Vol. 36, No. 6, 1998, pp. 3-9
4. H. Imoto et al., “Quantitative analysis for the hydration of limestone filler cement”, Cement Science and Concrete Technology, Vol.56, 2022, pp.42-49
5. Architectural Institute of Japan, “Guidelines for Construction of Concrete in Hot Weather and Commentary”, Architectural Institute of Japan, 2019, pp. 15-44,
6. M. Kato, “Ceramics Basic Course 3: X-ray Diffraction Analysis”, UCHIDA ROKAKUHO PUBLISHING CO, 1990, p.210
7. M. Daimon, “Science of Cement – Production and Hardening of Portland Cement –”, UCHIDA ROKAKUHO PUBLISHING CO, 1995, pp47-63
8. Li Yiman, “Calcite scaling potential of kangding geothermal field”, UNU-GTP, 2017, Num. 16.
9. M. Morioka, “Limestone Powder”, Concrete Engineering, Vol. 51, No. 5, 2014, pp. 405-408
10. H. Imoto et al., “Hydration Reaction Analysis of Mixed Cement”, Proceedings of the Japan Concrete Institute, Vol. 25, No. 1, 2003, pp. 41-46
11. E. Sakai et al., “Influence of Limestone Powder on the Hydration of Various Calcium Aluminates”, Inorganic Materials, Vol. 4, 1997, pp. 126-131
12. K. Hajime, “Hydration of Calciumaluminoferrite in the Presence of Calcium Carbonate”, Cement Science and Concrete Technology, Vol.53, 1999, pp.78-83

EFFECT OF RICE HUSK ASH ON THE FUNDAMENTAL PROPERTIES OF MORTAR ACCORDING TO THE CALCINATION ENVIRONMENT

Junho KIM
Department of Architecture Faculty of Science and Technology, Tokyo University of Science, 2641 Yamazaki, Noda City, Chiba Prefecture, 278-8510, Japan.

Hikaru FUMINO
National Institute of Technology (KOSEN) Oyama College, 771 Nakakuki, Oyama City, Tochigi Prefecture, 323-0806, Japan.

Manabu KANEMATSU
Department of Architecture Faculty of Science and Technology, Tokyo University of Science, 2641 Yamazaki, Noda City, Chiba Prefecture, 278-8510, Japan.

ABSTRACT:
Rice husk ashes are widely studied in the spectacle of effective recycling of resources. In particular, the study of concrete, it has been reported that the pozzolanic reaction with conventional Admixture of concrete containing silica as the main component, such as fly ash and silica fume is carried out. In the production of RHA (Rice Husk Ash), temperature setting, and smooth oxygen supply are essential factors in the calcination process. In addition, it has been reported that pre-treatment and post-treatment of RHA is an influencing factor. In this study, the grade of RHA according to calcination degree was evaluated based on the Luxan value, were conducted. As a result, the overall trend showed similar or better performance than that of the specimen using only cement. In addition, the Luxan value, the standard used in this study, tend to be proportional to the degree of compressive strength expression. However, it showed a tendency inversely proportional to the change in drying shrinkage.

Keywords: Rice Husk Ash, Fundamental Properties of Mortar, Luxan value, Treatment of RHA, Calcination method

1. INTRODUCTION

RHA (Rice Husk Ash) has about 90% silica, so it is a pozzolanic reaction material such as fly ash and silica fume, which are conventionally used concrete admixtures. According to previous studies, it has been shown that RHA contains a large amount of silica, and it has been reported that the use of RHA can induce a pozzolan reaction such as fly ash and silica fume. In addition, in the fire resistance test, the fire resistance performance was higher than that of ordinary concrete [1, 2]. As such, RHA is actively reviewing the possibility of using concrete to reduce the environmental load and recycle resources.

In addition, when RHA is substituted for cement in concrete, a positive effect is shown, and the effect according to the substitution rate is also considered. Regarding the use of RHA, the method of substituting for cement is generally performed, and different properties are shown depending on the substitution method. However, it is reported that the substitution amount of RHA is generally 10% to 20% [3~9]. The properties of RHA concrete have been reported to increase long-term compressive strength, decrease autogenous shrinkage, and durability have been reported [10~13]. In addition, experiments to confirm the effect of adjusting the particle size of RHA have been reported, and silica fume exhibits comparable mechanical properties according to the adjustment of the particle size [14].

There are two main factors that affect the production quality of RHA as an admixture in concrete. First, there are factors in the calcination process, and temperature and time are essential factors in the calcination process. Andres Salas et al. reported the effect of the change in the calcination method. RHA to which chemical and calcination treatment was applied had more amorphous properties and showed positive results in increasing the compressive strength of concrete [15]. Lingling Hu et al. performed hydrochloric acid treatment as a pretreatment method and experimented by changing the calcination temperature. In this study, after pretreatment with hydrochloric acid, calcined at 600 °C was used as RHA, and it was reported to show higher performance compared to other admixtures [16].

To summarize the factors, the higher the temperature, the higher the production of RHA from amorphous silica. In general, the firing temperature was 600°C to 700°C. Under the influence of chemical treatment and washing, this pretreatment removes impurities and K to obtain high-purity RHA.

In the above existing literature, there are many considerations on basic characteristics of RHA. In this study, RHA is classified based on the Luxan value, which is a simple measurement method, and the Luxan value is proposed as a standard for quality evaluation of RHA by

clarifying the relationship between Luxan value and concrete foundation characteristics.

2 Experimental programs

2.1 Mixture design

Table1 shows the formulation design. The same amount of RHA having different calcination levels was replaced by 15% with respect to the cement. Fig. 1 presents an overview of the RHA used in the experiments.

2.2 Calculation of Luxan

Value of Luxan, M.P. Luxan It was proposed by Luxan and is a simple method for measuring the pozzolanic reaction [17] and is known to be effective in measuring the amount of amorphous silica [18]. In general, it is known that the higher the Luxan value, the higher the active value.

After measuring the following two measurements, the result is derived by substituting it in Equation 1).

1) Measure the electrical conductivity before adding 40 ml of calcium hydroxide (Value a; mS/cm).

2) Add 1.0 g of RHA sample to calcium hydroxide mix and measure electrical conductivity for 2 minutes (Value b; mS/cm).

$$\text{Luxan} = \text{value a} - \text{value b} \qquad \text{Equation 1)}$$

For the saturated solution of calcium hydroxide used here, 0.64 g of calcium hydroxide reagent is added to 500 ml of pure water, and a saturated calcium hydroxide solution is prepared and used by mixing in an environment of 40 °C.

2.3 XRD

Measurements were performed using PANalytical Empyrean as the measuring device. The measurement was carried out using the sample powder. The measurement conditions are shown below. A 45kV tube voltage and 40mA tube current, increments are 0.02°, scan range of 2θ was 6° to 13° and 5° to 65°.

2.4 TG-DTA

The measurement was performed using Shimadzu DTG-60h as the measuring device. The measurement was performed using a sample powdered by the method described above. In this study, since the measurement is performed up to 1, 000 °C depending on the conditions, a platinum sample pan that can withstand up to 1, 000 °C was used instead of a platinum sample pan (sample container) that can withstand only 600 °C. The measurement conditions are shown below. The atmosphere in the furnace Nitrogen, Inflow of atmosphere in the furnace 50 ml/min, temperature rise is 30 °C/min, the temperature measurement range is 40 °C ~ 1, 000 °C.

3 Experimental results

In this study is to understand the effect of the Luxan value of RHA generated according to the change in the plastic environment. Compressive strength and drying shrinkage length change rate were measured as basic characteristics of mortar with 4 RHAs with different Luxan values. In addition, to understand the effect on the fundamental characteristics, chemical analysis was performed in parallel.

3.1 Compressive strength

Fig. 2 shows the results of measuring the compressive strength of the RHA specimen according to the change in Luxan value. The lower the Luxan value, the higher the intensity at the initial age, and the lower the long-term age. Conversely, specimens with high Luxan values showed low compressive strength at the beginning, but high compressive strength at long-term curing age. In particular, Specimen A showed the lowest strength at 7 days of curing age, but showed the same compressive strength as the Plain specimen at 28 days of age, and showed the highest compressive strength at 91 days of age. The improvement of long-term compressive strength with respect to RHA substitution showed the

Table 1. Mixture design

Sample [1)]	W/C(%)	Mixing ratio of RHA (%)	Water [g]	Cement [g]	RHA [g]	Sand [g]
Plain	50	0	225	450.0	0	1350
A:4.2		15		382.5	67.5	
B:2.85						
C:2.33						
D:1.97						

1): Numbering of Sample : Measured Luxan value.

Picture				
Value of Luxan	3.5~4.2	2.33	2.85	1.97
calcination condition	600℃	550℃	500℃	500℃

Fig. 1. RHA properties according to the change in calcination condition

same trend as in the previous study, and in the previous study, it is judged that the test specimen substituted with RHA 20% caused an appropriate pozzolan reaction [5]. In addition, it was reported that a higher increase rate of compressive strength at long-term curing age than at initial curing age showed the same trend as in the previous study [7, 14, 15, 20], and it was reported that the amount of voids and water absorption decreased in inverse proportion to the compressive strength [7, 9].

Other specimens substituted with RHA showed similar compressive strength to Plain specimen until 7 days of age, and similar strength to 91 days. Therefore, in the compressive strength, the higher the Luxan value, the lower the compressive strength at the early curing age, but the higher the compressive strength at the long-term curing age.

At the curing age of 28 days, the compressive strength of the specimen substituted with RHA decreased, similar to the results of other researchers' studies. This is considered to be the cause of the increase in the amount of voids according to the use of RHA [1, 6, 19]. Lingling Hu et al. substituted 15% of RHA in the same way as in this study and went through a pretreatment process with acid. Based on this consideration, it is judged that the pre-treatment process with acid has a great influence on the initial curing age [16]. Van Breugel, K., Ye, G. et al. reported that the curing reaction occurs in the pores of RHA, and it is thought that the reaction of RHA is a complex reaction caused by the pozzolan reaction and the curing reaction in the voids of RHA [10]. R. Zerbino et al. [13], Graciela Giaccio et al. [21] reported the characteristics of RHA with or without particle size adjustment. It was reported that strong bonding to the aggregate and cement matrix occurred when the two samples were substituted in an appropriate amount. Therefore, it is judged that it is possible to make the same tendency as OPC using only cement by adjusting the appropriate particle size.

3.2 Dry shrinkage

Fig. 3 shows the results of drying shrinkage measurement. Test specimen D substituted with RHA with a low Luxan value showed the lowest shrinkage at all curing ages. Conversely, specimen A substituted for RHA with the highest Luxan value showed high shrinkage at all curing ages. Specimen B with a Luxan value of 2.85 showed almost the same trend as plain specimen, and the dry shrinkage at 28 days of curing age was lower than that of Plain specimen. Therefore, in the results of the drying shrinkage, the higher the Luxan value, the higher the drying shrinkage tendency, and the lower the drying shrinkage rate, the lower Luxan value. In the previous study, RHA was substituted for calcined dolomite, and in that study, as the ratio of RHA increased, the dry shrinkage tended to decrease [4]. In this study, similar dry shrinkage results were shown similar to that of the plain specimens. Also, Jie WANG et al. [3] study showed that the amount of voids, which decreased with increasing curing age, tended to increase as the RHA substitution rate increased. If it is judged that the pores are filled by the hydration products generated by the pozzolan reaction, it is thought that the increase in curing age and the expression of compressive strength greater than that of the Plain specimen can be explained. In Van Breugel, K., Ye, G. et al. autogenous shrinkage experiment, it is reported that RHA with a particle size of 5.6 μm or more reduces the amount of autogenous shrinkage as the curing reaction occurs in the pores of RHA [10]. Therefore, it is judged that the appropriate particle size control will have a positive effect on drying shrinkage. In addition, in the study of Viet-Thien-An Van et al. [12], Gemma Rodriguez de Sensale et al. [22] reported that substitution of RHA affects the reduction of autogenous shrinkage. Zhi-hai He et al., creep decreased as the substitution rate of RHA increased. Although the experimental items are different, it is judged that similar results were obtained, and it was judged that the decrease in the amount of capillary voids had an effect as increased the substitution amount of RHA about particle size of 10 μm [8].

3.3 XRD result

Fig. 4 shows the result of XRD measurement according to the different calcination conditions. As the Luxan value increases, the peak of calcium hydroxide tends to decrease at the same curing age. On the contrary, the peak of calcium carbonate showed a tendency to increase with the increase of Luxan value. In addition, the peak of C-A-S-H showed a tendency to decrease as the Luxan value was higher. At 28 days of curing age, the compressive strength increased with the increase of the Luxan value, but the peak of calcium hydroxide in XRD showed the opposite trend. It is thought that the change of calcium hydroxide into calcium carbonate affected on

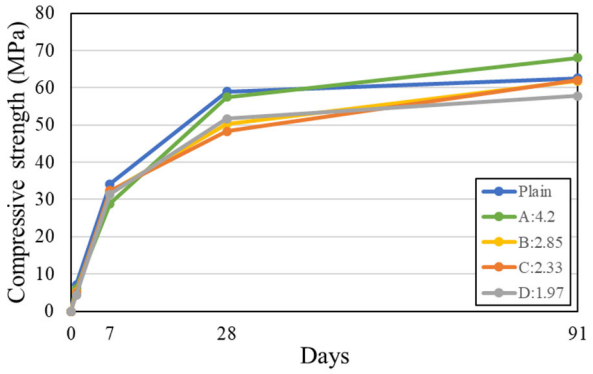

Fig. 2. Compressive strength of the mortar with different calcination condition.

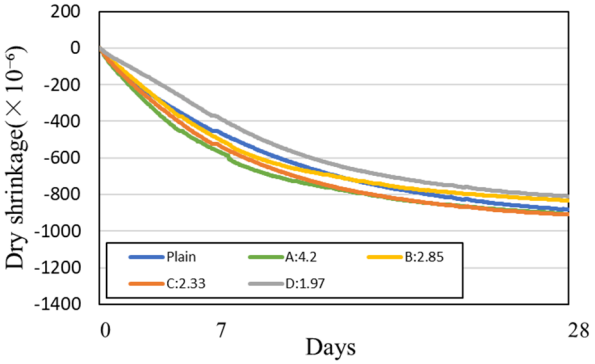

Fig. 3. Dry shrinkage of the mortar with different calcination condition.

the compressive strength.

Fig. 5 shows the result of focusing on the degree from 5 to 15 of the XRD. The peak of ettringite showed a tendency to increase with the increase of Luxan value. C4AF also exhibited the same trend.

3.4 TG-DTA result

Fig. 6 shows the weight reduction rate of the sample measured by differential thermal analysis. Specimen C showed the same tendency as the plain test specimen, and the other specimen showed a greater amount of weight loss.

Fig. 7 shows the measurement results of DTA according to the change in Luxan value. In the case of the RHA-substituted specimen, the amount of ettringite and C-S-H was more Significant than that of the plain, which was consistent with the trend of the peak size measured by XRD. The peak of calcium hydroxide also exhibited the same trend as that of XRD.

Fig. 8 shows the quantified measurement results of TG calcium hydroxide. The plain specimen showed the highest amount of calcium hydroxide, and in the case of the RHA specimen, the higher the Luxan value, the lower the amount of calcium hydroxide.

This trend is the same as in previous studies, and it is thought that calcium hydroxide is consumed when compressive strength is expressed by the pozzolan reaction [2, 9, 15, 16]. In addition, it was reported that a decrease in the amount of calcium hydroxide and a decrease in the amount of pores in the interfacial zone was associated with an increase in physical properties [9]. J.H.S. Rêgos et al. conducted an experiment by substituting 20% of RHA with a different amount of amorphous silica. As a result, the higher the amount of amorphous silica, the more active the pozzolan reaction was by consuming calcium hydroxide [11]. These results showed the same trend as in this study, and it is judged that there is a correlation with the Luxan value used in this study.

Nguyen Van Tuan et al., reported that the water absorbed from the porous structure of RHA increases the hydration reaction of cement, and as a result, the strength development is promoted. In addition, it is reported that calcium hydroxide and RHA have a pozzolan reaction, and it is considered that this effect is due to the decrease in the amount of calcium hydroxide and the increase of compressive strength at the same time in this study [2].

In the case of RHA with a high Luxan value, more calcium hydroxide was consumed, and higher compressive strength was expressed at a later age.

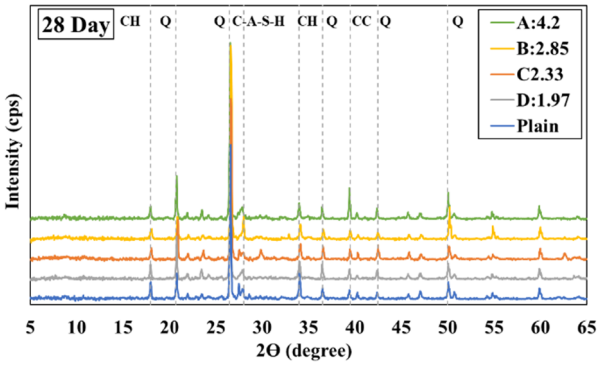

Fig. 4. XRD pattern of the mortar with different calcination condition.

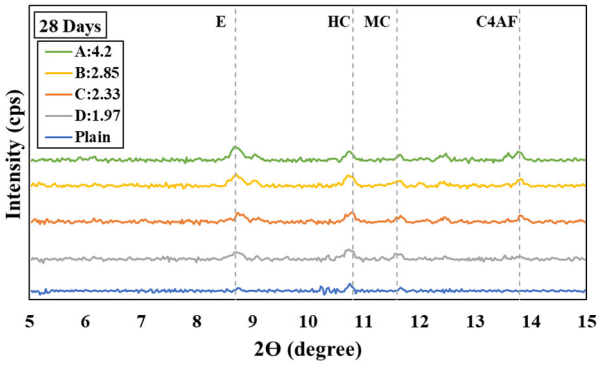

Fig. 5. XRD pattern of the mortar with different calcination condition.

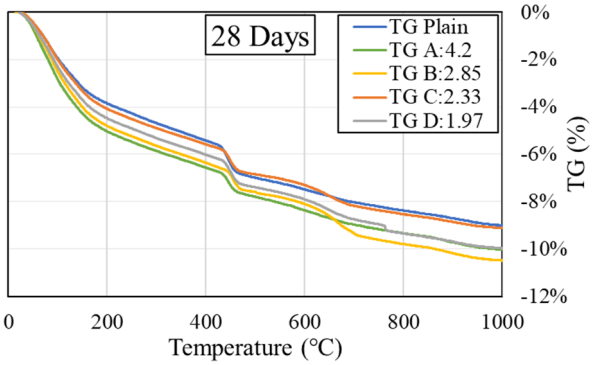

Fig. 6. DTG of the mortar with different calcination condition.

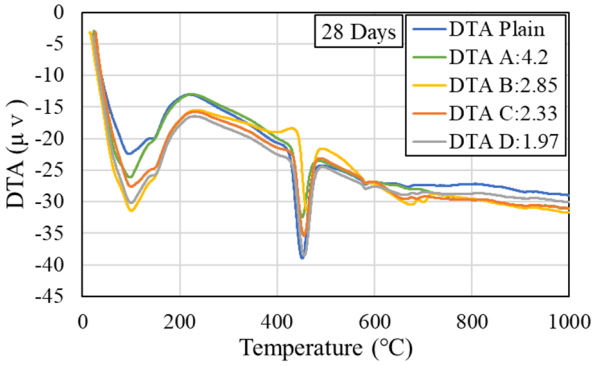

Fig. 7. DTA of the mortar with different calcination condition.

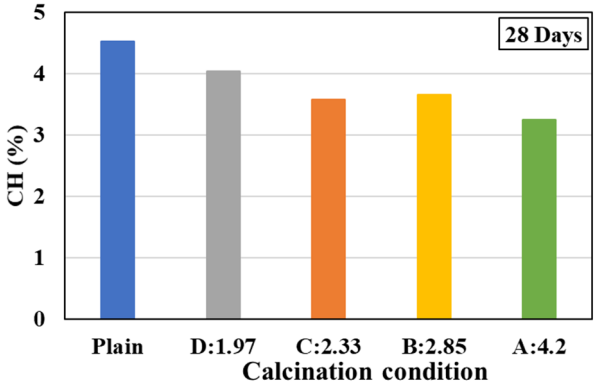

Fig. 8. CH amount of the mortar with different calcination condition.

Therefore, the Luxan value used in this study can be considered to have a proportional relationship with the amount of amorphous silica. On the other hand, according to the study of Viet-Thien-An Van et al. [12], in the mechanism of strength expression by RHA, water absorbed by the mesopores of RHA, rather than consuming calcium hydroxide, had the effect of lowering the W/B ratio of the formulation and It was judged to have an effect on the pozzolanic response of long-term age.

4 Conclusion

In this study, in order to use RHA as an admixture for concrete, the effect of the change of the firing method on the physical properties was investigated. In addition, the effect

of changes in plasticity on physical properties such as compressive strength and drying shrinkage was investigated, and the effect on physical properties was analyzed more closely using chemical and thermal analysis. The results obtained in this study are summarized as follows:

(1) In the case of the compressive strength based on the Luxan value, the specimen with a high Luxan value showed the same tendency as the pozzolan reaction material with a low initial compressive strength but high long-term compressive strength. On the other hand, the specimen with a low Luxan value showed overall low compressive strength.

(2) In the case of drying shrinkage based on the Luxan value, contrary to the result of compressive strength, the specimen with a high Luxan value showed higher drying shrinkage than the plain specimen. On the other hand, the specimens with low Luxan values showed lower drying shrinkage than the plain specimens overall.

(3) In the case of the thermal analysis result based on the Luxan value, the higher the Luxan value, the higher the decrease in calcium trioxide at 28 days of age. This tends to be inversely proportional to the increase in compressive strength, and is considered to be due to the pozzolanic reaction of RHA reported in previous studies.

references

1. Aleksandr Ketov, Larisa Rudakova, Iakov Vaisman, Iurii Ketov, Viktors Haritonovs, Genadijs Sahmenko, Recycling of rice husks ash for the preparation of resistant, lightweight and environment-friendly fired bricks, Construction and Building Materials, Volume 302, 4 October 2021, 124385, https://doi.org/10.1016/j.conbuildmat.2021. 124385.
2. Nguyen Van Tuan, Guang Ye, Klaas van Breugel, Oguzhan Copuroglu, Hydration and microstructure of ultra high performance concrete incorporating rice husk ash, Cement and Concrete Research 41 (2011) 1104-1111, https://doi.org/10.1016/j.cemconres.2011.06.009.
3. Jie WANG, Jianxin FU, Weidong SONG, Yongfang ZHANG, Effect of rice husk ash (RHA) dosage on pore structural and mechanical properties of cemented paste backfill, Journal of Materials Research and Technology Volume 17, March–April 2022, Pages 840-851, https://doi.org/10.1016/j.jmrt.2022.01.044.
4. Mostafa Shaaban, Properties of concrete with binary binder system of calcined dolomite powder and rice husk ash, Heliyon, Volume 7, Issue 2, February 2021, e06311, https://doi.org/10.1016/j.heliyon.2021.e06311.
5. Pokpong Rattanachu, Prajak Toolkasikorn, Weerachart Tangchirapat, Prinya Chindaprasirt, Chai Jaturapitakkul, Performance of recycled aggregate concrete with rice husk ash as cement binder, Cement and Concrete Composites, Volume 108, April 2020, 103533, https://doi.org/10.1016/j.cemconcomp.2020.103533.
6. Travis D.Garrett, Henry E.Cardenas, Joan G.Lynam, Sugarcane bagasse and rice husk ash pozzolans: Cement strength and corrosion effects when using saltwater, Current Research in Green and Sustainable Chemistry, Volumes 1–2, February–April 2020, Pages 7-13, https://doi.org/10.1016/j.crgsc.2020.04.003.
7. Rafat Siddique, Karambir Singh, Kunal, Malkit Singh, Valeria Corinaldesi, Anita Rajor, Properties of bacterial rice husk ash concrete, Construction and Building Materials 121 (2016) 112–119, https://dx.doi.org/10.1016/j.conbuildmat.2016.05.146.
8. Zhi-hai He, Long-yuan Li, Shi-gui Du, Creep analysis of concrete containing rice husk ash, Cement and Concrete Composites 80 (2017) 190-199, https://dx.doi.org/10.1016/j.cemconcomp.2017.03.014.
9. M.H. Zhang, R. Lastra, and V.M. Malhotra, rice-husk ash paste and concrete: some aspects of hydration and the microstructure of the interfacial zone between the aggregate and paste, Cement and Concrete Research, Vol. 26, No. 6, pp. 963-977, 1996. https://doi.org/10.1016/0008-8846(96)00061-0.
10. Klaas van Breugel, Guang Ye, Nguyen Van Tuan, Ultra High Performance Concrete made with Rice Husk Ash for reduced Autogenous Shrinkage, Proceedings of the 4th International FIB Congress, Mumbai, India, 10-14 February 2014; Authors version.
11. J.H.S. Rêgo, A.A. Nepomuceno, E.P. Figueiredo, N. P. Hasparyk, Microstructure of cement pastes with residual rice husk ash of low amorphous silica content, Construction and Building Materials 80 (2015) 56–68, https://doi.org/10.1016/j.conbuildmat.2014.12.059.
12. Viet-Thien-An Van, Christiane Robler, Danh-Dai Bui, Horst-Michael Ludwig, Rice husk ash as both pozzolanic admixture and internal curing agent in ultra-high performance concrete, Cement & Concrete Composites 53 (2014) 270-278, https://doi.org/10.1016/j.cemconcomp.2014.07.015.
13. R. Zerbino, G. Giaccio, G.C. Isaia, Concrete incorporating rice-husk ash without processing, Construction and Building Materials 25 (2011) 371–378, https://doi.org/10.1016/j.conbuildmat.2010.06.016.
14. Josephin Alex, J. Dhanalakshmi, B. Ambedkar, Experimental investigation on rice husk ash as cement replacement on concrete production, Construction and Building Materials 127 (2016) 353–362, https://dx.

doi.org/10.1016/j.conbuildmat.2016.09.150.
15. Andres Salas, Silvio Delvasto, Ruby Mejia de Gutierrez, David Lange, Comparison of two processes for treating rice husk ash for use in high performance concrete, Cement and Concrete Research 39 (2009) 773-778, https://doi.org/10.1016/j.cemconres.2009.05.006.
16. Lingling Hu, Zhen He, Shipeng Zhang, Sustainable use of rice husk ash in cement-based materials : Environmental evaluation and performance improvement, Journal of Cleaner Production 264 (2020) 121744, https://doi.org/10.1016/j.jclepro.2020.121744.
17. M.P. Luxan, F. Madruga and J. Saavedra, Rapid Evaluation of pozzolanic Activity of Natural Products by Conductivity Measurement, Cement and Concrete Research. Vol. 19, pp. 63-68, 1989, https://doi.org/10.1016/0008-8846(89)90066-5.
18. Shuichi SUGITA and Masami SHOYA, A Fundamental Study on the Effective use for Rice Husk Ash as a Pozzolanic Material, Japan Society of Civil Engineers, Vol. 526, pp.43-53. 1995, https://doi.org/10.2208/jscej.1995.526_43.
19. Shaik Numan Mahdi, Dushyanth V. Babu R, Shivakumar M, Mohd Mustafa Al Bakri Abdullah, Mitigation of environmental problems using brick kiln rice husk ash in geopolymer composites for sustainable development, Current Research in Green and Sustainable Chemistry 4 (2021) 100193, https://doi.org/10.1016/j.crgsc.2021.100193.
20. Nsesheye Susan Msinjili, Wolfram Schmidt, Andreas Rogge, Hans-Casrten Kuhne, Performance of rice husk ash blended cementitious systems with added superplasticizers, Cement and Concrete Composites 83 (2017) 202-208, https://doi.org/10.1016/j.cemconcomp.2017.07.014.
21. Graciela Giaccio, Gemma Rodriguez de Sensale, Raul Zerbino, Failure mechanism of normal and high-strength concrete with rice-husk ash, Cement & Concrete Composites 29 (2007) 566-574, https://doi.org/10.1016/j.cemconcomp.2007.04.005.
22. Gemma Rodriguez de Sensale, Antonio B. Ribeiro, Arlindo Gonc;alves, Effects of RHA on autogenous shrinkage of Portland cement pastes, Cement & Concrete Composites 30 (2008) 892-897, https://doi.org/10.1016/j.cemconcomp.2008.06.014.

ASSESSMENT OF RESIDUAL DEF POTENTIAL IN THE CONBINED DEF AND ASR EXPANSIVE SPECIMENS

Natsuki YOSHIDA
Specially appointed associate professor, Osaka University, Japan.

Yuto SHIBUI
Researcher, General Building Research Corporation of Japan, Japan.

ABSTRACT:
In the diagnosis of concrete structures, it is crucial to distinguish between delayed ettringite formation (DEF) and alkali-silica reaction (ASR), as DEF and ASR have similar macroscopic deterioration phenomena. This study employed electron probe micro analyzer (EPMA) to analyze the composition of the cement paste matrix to assess the potential for DEF. Before and after the residual expansion test, EPMA mapping analysis of CaO, Al_2O_3, and SO_3 was conducted on specimens with combined DEF and ASR potential. In DEF-expansive specimens, a distinct data group was observed, extending from the C-S-H composition towards the ettringite (Ett) composition. When plotted on a backscattered electron (BSE) image, this data group remained on the lighter C-S-H for specimens that continued to exhibit expansion. The lighter C-S-H, which appears bright on the BSE image, forms under high-temperature conditions and is considered to contribute to DEF expansion. For the specimens after the water immersion test, the amount of data groups overlapping the lighter C-S-H decreased. This decrease in data groups is consistent with the observed reduction in expansion. For specimens after NaOH immersion test, the amount of these data groups was found to be preserved. The formation of Ett is suppressed by alkali supply, maintaining the potential for DEF.
Keywords: DEF, ASR, Ettringite, Residual expansion test, EPMA, Mapping analysis, lighter C-S-H

1. INTRODUCTION

In the diagnosis of concrete deterioration, it is crucial to carefully distinguish between delayed ettringite formation (DEF) and alkali-silica reaction (ASR) due to their similar macroscopic appearances, such as mapping cracks and cracks parallel to the direction of restraint [1][2]. DEF is characterized by the formation of gaps around the aggregate [1], whereas ASR is characterized by several features such as cracks extending from the aggregate into the surrounding mortar matrix and the presence of ASR gels [3]. Therefore, it is of primary importance to differentiate between DEF and ASR under a microscopic observation. However, microscopy is not an easy method, as it requires skilled techniques.

On the other hand, a method has been proposed to distinguish between DEF and ASR using a residual expansion test of concrete cores [4][5]. This method evaluates the potential expansion of DEF and ASR by immersing cores in water and in a 1 mol/L NaOH solution, respectively. For the water immersion method, it has been reported that ettringite is more likely to form when the pH of the pore solution drops, and immersing the cores in water accelerates alkali leaching, resulting in expansion due to DEF [4]. The authors confirm the usefulness of the residual expansion test by conducting an interlaboratory test across four institutions [5].

A method has also been proposed to assess the potential of DEF using electron microscopy and elemental analysis of micro areas [6][7][8][9]. It has been reported that in DEF, subjected to high temperatures during the early stages of hydration, the density of internal C-S-H formed inside the cement particles increases, and the internal C-S-H appears brighter in backscattered electron (BSE) images [10]. This tissue is referred to as "lighter C-S-H" [10]. Furthermore, elemental analysis of lighter C-S-H has indicated DEF potential when the composition of the lighter C-S-H were distributed around the line connecting C-S-H and ettringite (Ett) compositions [6][7][8]. The authors have proposed a method of compositional analysis using electron probe micro analyzer (EPMA) equipped with wavelength dispersive spectroscopy (WDS) [9] and are investigating its applicability for DEF diagnosis.

When considering the complexity of diagnosing DEF, we would like to propose that it is essential to establish a reliable diagnostic method by combining microscopic observation, residual expansion test, and elemental analysis, rather than relying on a single method. Therefore, with the purpose of obtaining valuable insights for the diagnosis of DEF, this study reports the results of DEF potential analysis using EPMA mapping analysis. The specimens used in this study had combined DEF and ASR potential previously assessed in our past study [5] through residual expansion tests.

2. EXPERIMENTAL METHOD

2.1 PREPARATION OF CONCRETE SAMPLES

The concrete specimens used in this study consist of core specimens that were subjected to residual expansion tests in our previous study [5]. The materials used in this study included high-early-strength Portland cement, crushed stone (ASR-reactive andesite), crushed

limestone (non-ASR-reactive), and crushed limestone sand (non-ASR-reactive). To accelerate DEF and ASR, the reagents K_2SO_4 [11] and NaOH were added, respectively.

Three types of specimens were prepared for this study (Table 1): one specimen had only DEF potential with the addition of K_2SO_4 (referred to as DEF_K_2SO_4), and two specimens had combined DEF and ASR potential using ASR-reactive aggregate (referred to as D+A_K_2SO_4 and D+A_NaOH). The D+A_K_2SO_4 specimen was designed to enhance DEF potential by adding K_2SO_4, while the D+A_NaOH specimen was to enhance ASR by adding NaOH. After mixing the materials, the concrete was placed in a plastic container with internal dimensions of approximately 26 cm x 24 cm x 20 cm (Fig. 1 (1)).

For curing conditions, plastic containers were sealed with a plastic lid and pre-cured at 20°C for 4.5 hours. Subsequently, the specimens were placed in a thermostatic chamber with sealed conditions (Fig. 1 (2)). The temperature in the chamber was controlled to maintain the core temperature of the specimens at 80-90°C. To induce DEF potential, the temperature was maintained above 80°C for 12 hours. The thermostatic chamber was then turned off, allowing the specimens to cool naturally. They were kept sealed and cured in the containers at 20°C for up to 28 days. After this period, the specimens were removed from the containers and exposed to the outdoor field for 6 months (Fig. 1 (3)). After 6 months of field exposure, core samples 5 cm in diameter and 20 cm in length were extracted (Fig. 1 (4)). In this study, cores were subjected to two immersion tests: immersion in tap water at 20°C to promote DEF (referred to as "water immersion"), and immersion in 1 N NaOH solution at 80°C to promote ASR (referred to as "NaOH immersion"). Measurement bands or studs were placed to monitor length changes, with measurements taken at regular intervals. A contact gauge with a 50 mm length was used.

The length change measured in our laboratory for each specimen is shown in Fig. 2 and Fig. 3 [5]. The DEF_K_2SO_4 specimens exhibited significant expansion under water immersion, while expansion was very small under NaOH immersion. On the other hand, the D+A series showed expansion in both water and NaOH immersion. The D+A_K_2SO_4 specimens expanded larger in water immersion, and the D+A_NaOH specimens expanded slightly larger in NaOH immersion. These differences are attributed to the increased dosage of SO_3 in DEF_K_2SO_4 and the increased NaOH amounts in D+A_NaOH specimens, respectively.

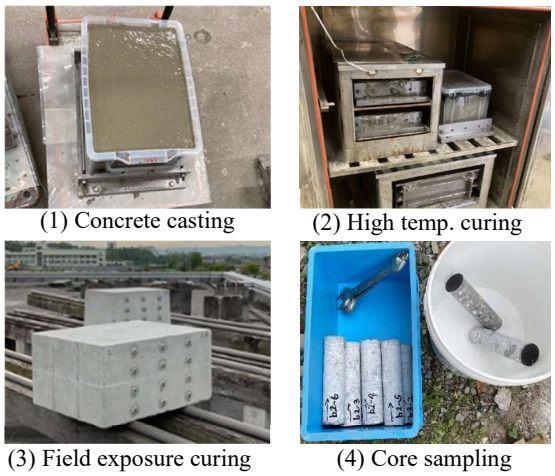

Fig. 1. Preparation of concrete specimens.

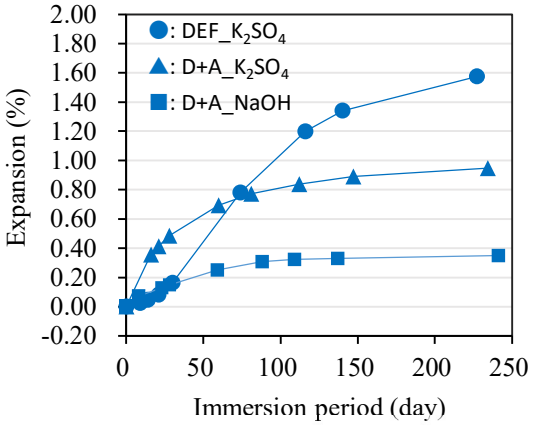

Fig. 2. Expansion of specimens in water immersion.

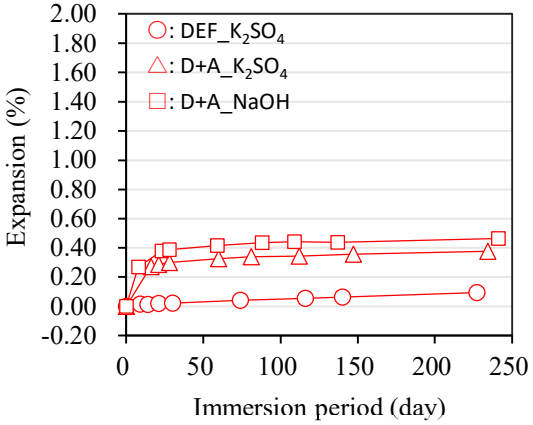

Fig. 3. Expansion of specimens in NaOH immersion.

Table 1. Mix proportions of the concrete specimens.

Name	Mix proportions (kg/m^3)							Na_2O_{eq} (kg/m^3)
	W	HPC	S	G_1	G_2	K_2SO_4	NaOH	
DEF_K_2SO_4	175	255	891	1076	-	10.33	-	5.12
D+A_K_2SO_4	175	255	891	753	323	10.33	-	5.12
D+A_NaOH	175	255	891	753	323	-	3.87	4.01

W: Water, HPC: High-early-strength Portland cement, S: Non-ASR-reactive limestone sand, G_1: Non-ASR-reactive limestone, G_2: ASR-reactive andesite

2.2 EPMA MAPPING ANALYSIS METHOD

Polished samples for EPMA analysis were prepared from each concrete specimen. In this study, the cement paste matrix was the focus of the analysis.

For the EPMA mapping analysis, we used an acceleration voltage of 15 kV, an probe current of 30 nA, and a measurement time of 15 msec/pixel. The analysis was conducted on a 0.5 μm pixel area, with a total area of 200 × 200 pixels (100 × 100 μm) being analyzed. The results for CaO, Al_2O_3, and SO_3 were plotted on a ternary diagram to determine the C-S-H composition. The distribution of data groups extending from the C-S-H composition to the Ett and monosulfate (Ms) compositions was visualized on the BSE image. Additionally, the composition of the internal C-S-H, referred to as lighter C-S-H, which appears brighter in the BSE image and is characteristic of DEF, was analyzed.

3. RESULTS AND DISCUSSION

3.1 MICROSCOPE OBSERVATION

Fig. 4 shows results of polarization microscope observation. Fig. 4 (1) shows gaps around the aggregate in DEF_K_2SO_4 specimen after water immersion, which are indicative of DEF characteristics. No expansion or DEF features were observed in the NaOH immersed specimens. In the water immersion of the D+A series (Fig.4 (2) and (4)), both DEF and ASR features were identified, suggesting that ASR occurred during the 6-month field exposure period and continued during subsequent immersion until DEF expansion was caused due to alkaline leaching.

During NaOH immersion of the D+A series (Fig. 4 (3) and (5)), only ASR features were observed, indicating that DEF expansion does not occur under NaOH immersion due to the alkali supply.

3.2 EPMA MAPPING ANALYSIS

(1) Procedure of data analysis

EPMA mapping analysis was conducted to investigate the potential for DEF. The specimens had been exposed to outdoor field for 6 months, and before and after immersion tests in water or NaOH were analyzed. The objective of this study was to assess the compositional features of specimens with higher potential and lower potential of DEF expansion.

First, using DEF_K_2SO_4 as an example, the data analysis procedure is described in Fig. 5. Electron images of the sample for analysis were observed using EPMA, and mapping analysis data (200 × 200 pixels) of CaO, Al_2O_3, and SO_3 were acquired from the portion of cement paste matrix. All 40,000 data points were plotted on a ternary diagram, and a 2D histogram was described. The compositional positions of Ett ($CaO:Al_2O_3:SO_3$=6:1:3) and Ms ($CaO:Al_2O_3:SO_3$=4:1:1) were indicated on the diagram. The histograms were generated by dividing the scatterplot into 400 × 400 squares. The data groups at the CaO apex consist of the composition of $Ca(OH)_2$, unreacted cement minerals (C_3S and β-C_2S), and limestone sand ($CaCO_3$) used as fine aggregate. The data groups distributed vicinity of the CaO apex were the composition of C-S-H, which accounts for the majority

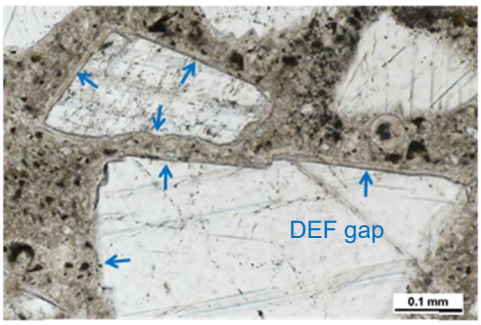

(1) DEF_K_2SO_4, Water immersion.

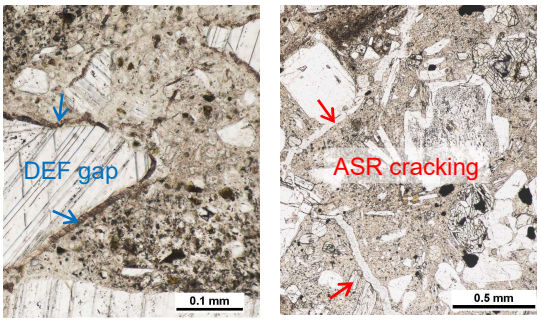

(2) D+A_K_2SO_4, Water immersion.

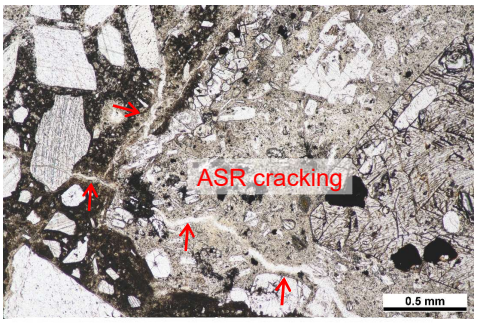

(3) D+A_K_2SO_4, NaOH immersion.

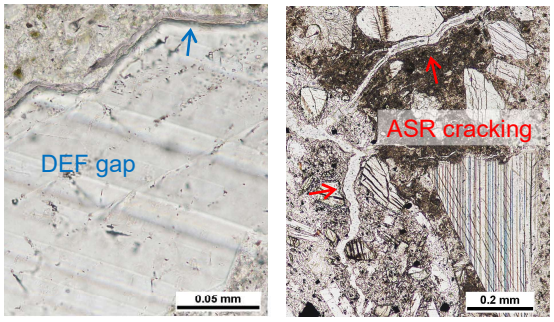

(4) D+A_NaOH, Water immersion.

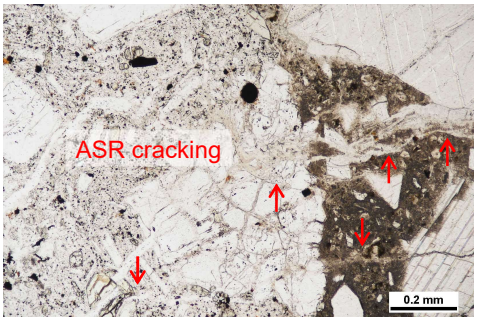

(5) D+A_NaOH, NaOH immersion.

Fig. 4. Results of microscopic observation.

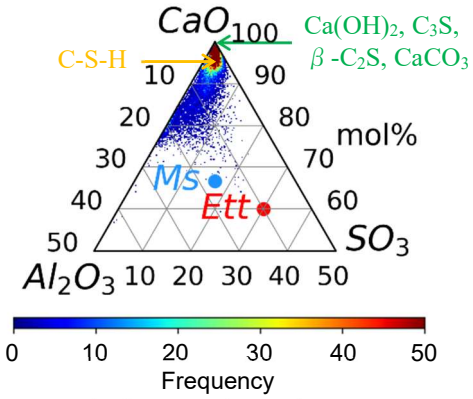

(1) A total of 40,000 data points were plotted on a ternary diagram.

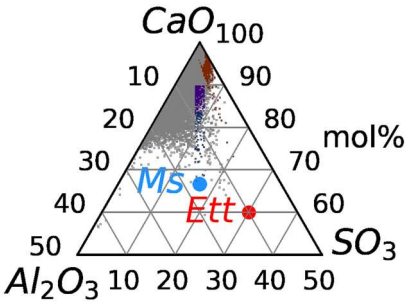

(2) Select a data group extending from C-S-H compositions to Ett and Ms compositions.

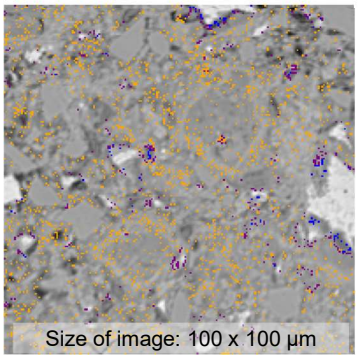

(3) The selected data group is plotted on the backscattered electron image.

Fig. 5. Procedure of data analysis (DEF_K_2SO_4, water immersion)

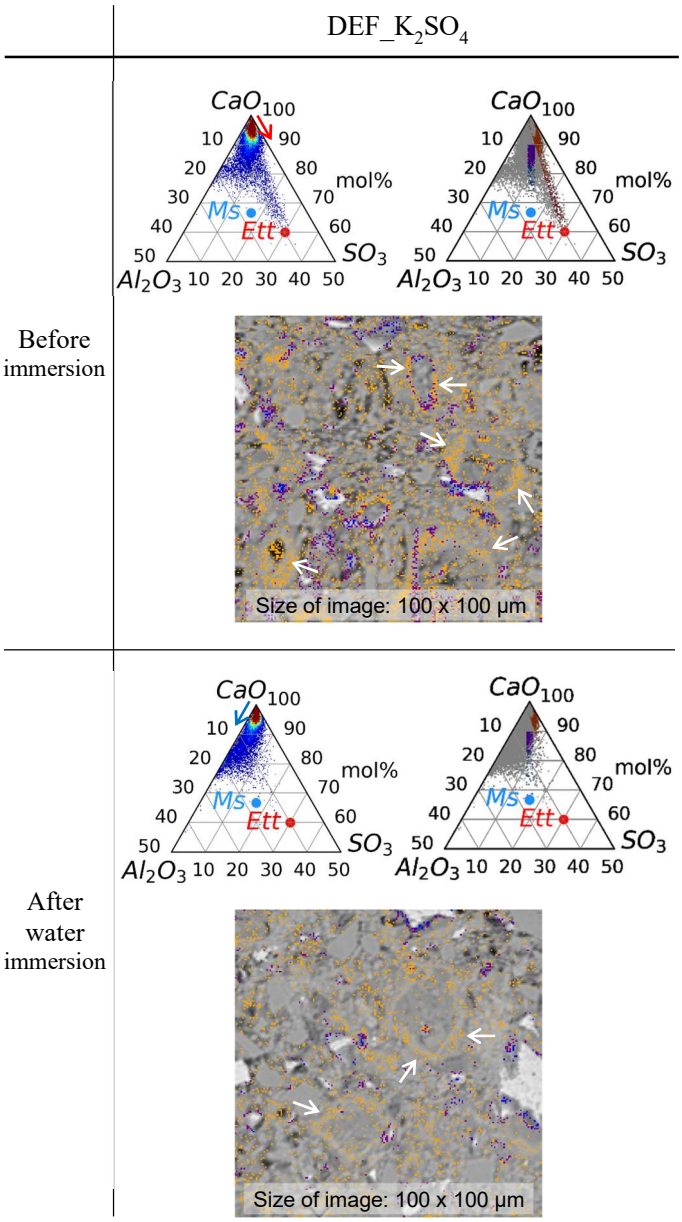

Fig. 6. Data analysis results of specimen (DEF_K_2SO_4)

of the cement hydrates.

Data groups extending from the C-S-H composition to the Ett (or Ms) composition were then extracted, and their distribution was depicted on the BSE image. These data groups are considered to be C-S-H pixel data that have absorbed sulfate and aluminate ions, approaching the composition of Ett (or Ms), or are mixed with super fine Ett (or Ms) crystals or gel-like products. To analyze data groups extending from the C-S-H composition to the Ett (or Ms) composition, C-S-H compositions with a frequency of 50 counts or less were targeted. These compositions were connected to the Ett (or Ms) composition, and a composition range of ±1% from that line was extracted. Data groups extending to Ett compositions were colored orange and red, while those extending to Ms compositions were colored purple and blue.

(2) Analysis results of EPMA mapping data

Fig. 6 and Fig. 7 show the analysis results of EPMA mapping data. For DEF_K_2SO_4, before the immersion test, the C-S-H compositions were distributed towards the Ett composition (Fig. 6), with the majority of these data groups overlapping with the lighter C-S-H. After water immersion test, the C-S-H composition shifted towards the Ms composition (Fig. 6), indicating a reduction in the Ett composition data set within the cement paste. However, as shown in the expansion test results (Fig. 2), DEF_K_2SO_4 still continued to expand at the end of the test, indicating that the data group of Ett composition overlapping the lighter C-S-H still

remained (Fig. 6).
Next, the results of D+A series shown in Fig. 7 are discussed. Regarding the analysis results before immersion test, the C-S-H composition of D+A_K_2SO_4 extends towards the Ett composition, which is not clear for D+A_NaOH. This may be due to the low dosage of

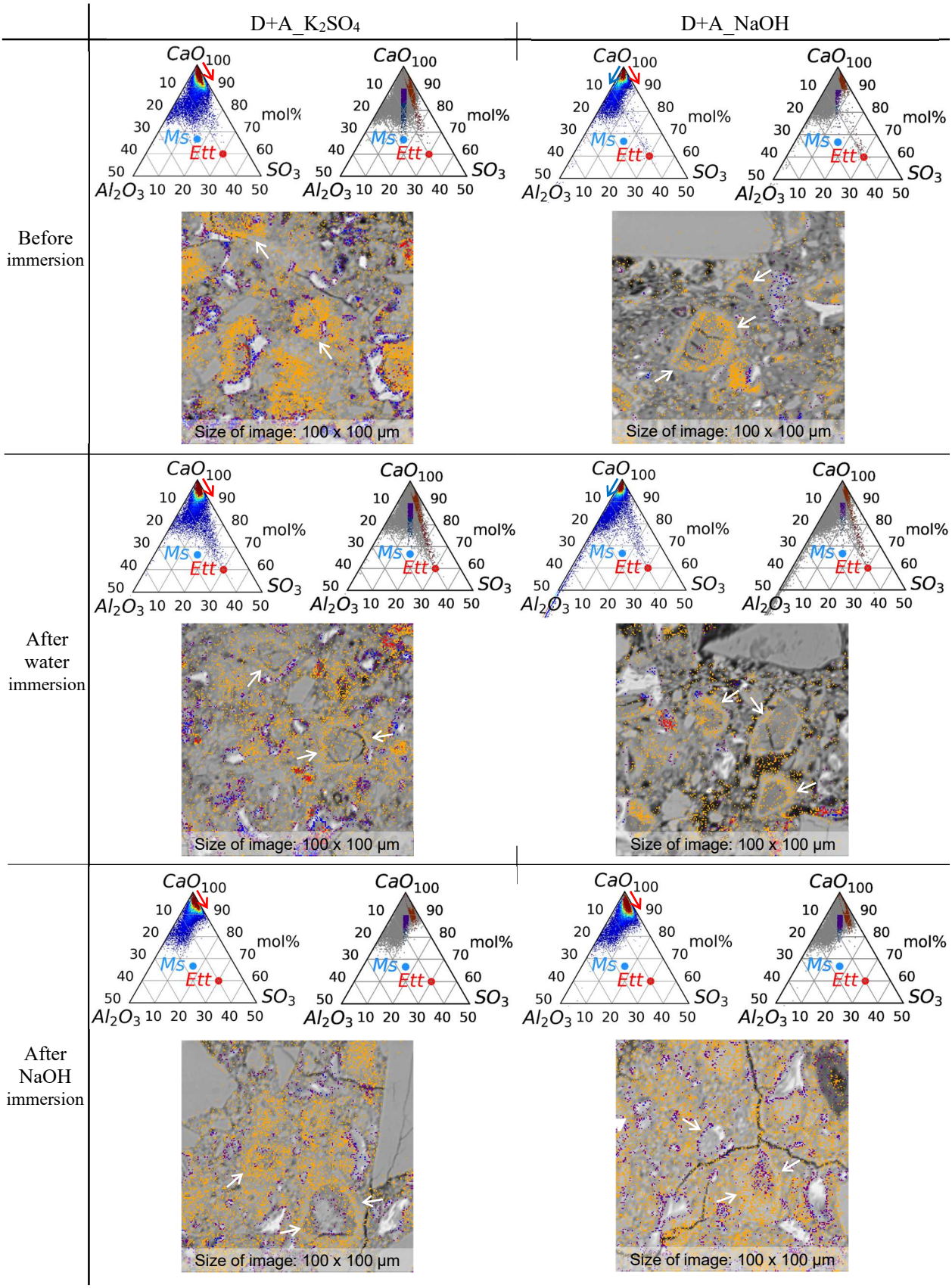

Fig. 7. Data analysis results of specimens (D+A series)

K_2SO_4 in D+A_NaOH, resulting in a relatively low SO_3 content in the specimen. However, the analysis results plotted on the BSE image show that a group of data extending to the Ett composition is distributed on the lighter C-S-H. This indicates the difficulty in determining DEF potential solely based on the ternary diagram analysis results.

For the analysis results after water immersion test, both D+A_K_2SO_4 and D+A_NaOH exhibit some distribution of data groups towards the Ett composition in lighter C-S-H, though there is a considerable reduction in these data groups. Considering the expansion test results in Fig. 2, the expansion has nearly ended, which is consistent with the analysis data. And it is assumed that the Ett produced by DEF is consumed by the Ostwald ripening of Ett in the cracks, air voids and pores.

Regarding the results of the analysis after NaOH immersion, both D+A_K_2SO_4 and D+A_NaOH show that the C-S-H composition extends towards the Ett composition. The formation of Ett is suppressed by the supply of the alkaline solution, preserving the potential for DEF. This also indicates that the expansion observed in Fig. 3 is clearly due to ASR.

The method of analyzing compositional data using EPMA is considered effective for diagnosing DEF. For accurate detection of DEF, it is essential to combine petrographic analysis, residual expansion tests, and microanalysis of the cement paste matrix.

4. CONCLUSIONS

In this study, concrete specimens with combined DEF and ASR potential were analyzed for detecting DEF potential by using EPMA analysis of the cement paste matrix before and after residual expansion tests. The conclusions obtained are presented below.

1) Plotting data groups extending from the C-S-H composition to the Ett composition on the BSE image for specimens before residual expansion test reveals that most of these data groups overlap with the lighter C-S-H, which is considered to contribute to DEF expansion.
2) For the specimens after the water immersion test, the amount of data groups overlapping the lighter C-S-H decreased. This decrease in data groups is consistent with the observed reduction in expansion, indicating that the expansion had nearly ended.
3) For specimens after NaOH immersion test, the amount of data groups overlapping with lighter C-S-H was found to be preserved. During NaOH immersion, the formation of Ett is suppressed by alkali supply, thereby maintaining the potential for DEF.

REFERENCES

1. Shimada, Y. et al. : Chemical path of ettringite formation in heat-cured mortar and its relationship to expansion: a literature review, Portland Cement Association, 2005
2. W.G. Hime et al.: Chemical and petrographic analyses and ASTM test procedures for the study of delayed ettringite formation, Cement, Concrete and Aggregates, Vol.22, No.2, 2000, pp.160-168.
3. Johansen, V., Thaulow, N. and Skalny, J.: Simultaneous Presence of Alkali-Silica Gel and Ettringite in Concrete, Advances in Cement Research, Vol. 5, No. 17, 1993, pp. 23-29.
4. Thomas, M. et al.: Diagnosing delayed ettringite formation in concrete structures, Cement and Concrete Research, Vol. 38, 2008, pp.841-847.
5. Yoshida, N. et al.: Expansion properties and microscopic features of DEF and ASR expansive specimens subjected to residual expansion tests, RILEM bookseries Proceedings of the 17th International Conference on Alkali-Aggregate Reaction in Concrete, 2024, pp. 217-225.
6. Lewis, M: Heat curing and delayed ettringite formation in concretes, Ph.D. thesis of Imperial College, Materials Department, London, UK, 1996
7. Scrivener, K.L. and Lewis, M.C.: Effect of heat curing on expansion of mortars and composition of calcium silicate hydrate gel, ACI SP-177, 1999, pp. 93-104.
8. Ramlochan, T., Thomas, M.D.A, Hooton, R.D.: The effect of pozzolans and slag on the expansion of mortars cured at elevated temperature Part II: Microstructural and microchemical investigations, Cement and Concrete Research, No. 34, 2004, pp. 1341-1356.
9. Yoshida, N.: Microanalysis of cement paste matrix deteriorated by delayed ettringite formation, Proceedings of 6th International Conference on Construction Materials, Performance, Innovations, and Structural Implications, 2020
10. Famy, C. et al.: Effects of an early or a late heat treatment on the microstructure and composition of inner C-S-H products of Portland cement mortars, Cement and Concrete Research, Vol.32, 2002, pp.269-278.
11. Kawabata, Y. et al.: The long-term suppression effects of fly ash and slag on the expansion of heat-cured mortar due to delayed ettringite formation, Construction and Building Materials, Vol. 310, 2021, 125235.

Strength performance of mortar using BFS and $CaCO_3$

Zhongli Wang
PhD candidate, Muroran institute of technology, 27-1 Mizumoto, Muroran, Japan

Kotaro Yamashita
Senior researcher, Konoike construction CO., LTD., 1-20-1 Sakura, Tsukuba, Japan

Yuki Kanazawa
Researcher, Konoike construction CO., LTD., 1-19-37 Nankokita, Suminoe-ku, Osaka, Japan

Yukio Hama
Professor, Muroran institute of technology, 27-1 Mizumoto, Muroran, Japan
Professor, Hokkaido University, Kita 8, Nishi 5, Kita-ku, Sapporo, Japan

ABSTRACT:
The production of cement emits a large amount of carbon dioxide. In this study, $CaCO_3$ is produced by absorbing CO_2 into $Ca(OH)_2$. After using $CaCO_3$ and BFS to replace part of the cement to prepare mortar samples, the compressive strength, pore volume, reaction products and microstructure of samples with different replacement rates were tested. The BFS replacement rate ranges from 0-80%, and the $CaCO_3$ replacement rate ranges from 0-75%. There are likely other optimal ratios, but within the range of ratios, the strength reaches the maximum when the $CaCO_3$ content is 25% and the BFS content is 40%. From the MIP results, at this ratio, there are fewer harmful pores. The reaction products were measured by XRD. After $CaCO_3$ is added, the main reaction products of $CaCO_3$ are hemicarbonate and monocarbonate. And it is found that the addition of $CaCO_3$ is beneficial to the densification of the mortar structure.

Keywords: $CaCO_3$, BFS, compressive strength, Carbon capture and utilization

1. INTRODUCTION

Many strategies have been proposed to reduce the 8% of the world's CO_2 emissions associated with cement production[1]. Using supplementary cementitious materials (SCM) to replace part of cement clinker is a common strategy currently. Based on the GCCA Roadmap data for the year 2020, the clinker-to-cement ratio on a global level was 72 %. With a total cement production of about 4200 Mio.t, this was equivalent to the use of around 1160 Mio.t of supplementary cementitious materials (SCM) substituting clinker[2]. Typical SCMs used in the cement industry are limestone and industrial by-products such as fly ash from coal-fired power plants, blast furnace slag (BFS) from iron production, and silica fume from ferrosilicon[3].

Limestone (LS) has been used in cement-based materials for many years. In 2000, the European standard (EN 197-1) defined different types of Portland cement blends containing LS, with the permitted substitution level increased to 35%[4]. In 2008, the Canadian standard (CSA A3001-08) also introduced Portland limestone cement with LS content less than 15% of the total cementitious material[5]. Subsequently, in CSA A3001-10, Portland limestone cement was designated as GUL (General Use Limestone Cement)[6]. In 2012, ASTM C595 also introduced Portland limestone cement with LS content up to 15%[7].

Limestone is one of the traditional raw materials to produce OPC. Therefore, cement manufacturers have sufficient access to limestone and can replace part of the cement with limestone in the production plant. Reduced calcination energy, good grindability and low transportation costs are the reasons why people are increasingly supporting the use of limestone as a substitute for cement[8]. The main chemical component of limestone is calcium carbonate ($CaCO_3$). Natural limestone is usually crushed and ground into powder before adding it to concrete[9]. Limestone powder plays a filling, nucleation, dilution and chemical role in concrete, and is affected by factors such as the particle size, dosage, crystal form of limestone powder, mineral composition of cement and supplementary cementitious materials[10].

Limestone can accelerate hydration and shorten setting time in cement-based materials, and can provide sufficient carbonate ions to participate in cement hydration reaction, thereby enhancing the reactivity of aluminate and forming (larger and possibly harder) carbonaluminate to replace sulfoaluminate, which can explain why adding a certain amount of limestone can improve strength[11]. Since carbonate ions in calcium carbonate react easily with aluminosilicates, the reactivity of limestone can be improved to some extent by co-replacing it with aluminosilicate-based SCMs. Blast furnace slag (BFS) is a by-product acquired in the production of pig iron in a blast furnace. It is developed in an igneous condition consecutively with iron in a blast furnace and is involving essentially of silicates and alumino-silicates of calcium and of other bases, with Al_2O_3 for approximately 10–20% of the BFS chemical composition[12,13].

Fig. 1 shows the strength isoresponse curves under

different BFS and limestone contents. Carrasco et al.[14] and Menéndez et al.[15] both concluded that there is a ternary blend of limestone, BFS and Portland cement that present an optimum strength, better than binary limestone or BFS cement and Portland cement. Limestone and BFS exhibit complementary behaviors: limestone improves early strength, while BFS improves later strength through its cementation reaction.

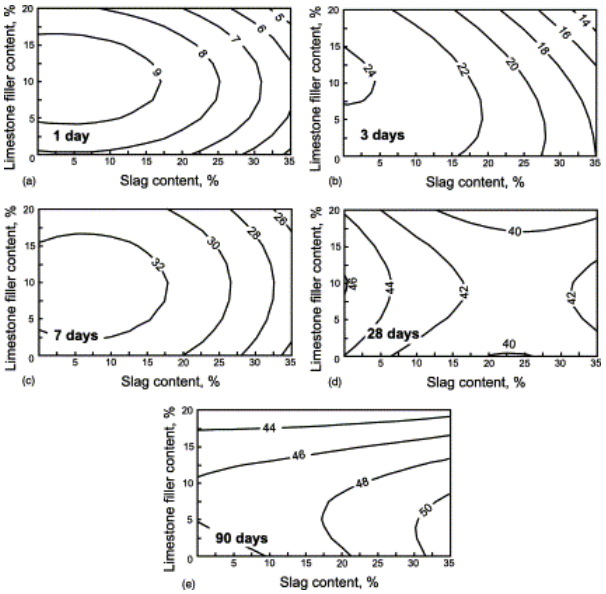

Fig. 1 Compressive strength (in MPa) isoresponse curves for the ternary system at different ages[15]

Zhang et al.[16] also found that if only BFS is added, the compressive strength decreases as the BFS replacement rate increases from 0 to 45%, but the addition of limestone powder can improve the strength of BFS mortar. To achieve the same strength as ordinary Portland cement, 4% limestone powder needs to be added. There are also studies on bending strength, Zhou et al.[17] studied the synergistic effect of BFS and limestone powder in fiber-reinforced concrete. It is found that as the limestone powder content increases, the flexural deflection capacity and the tensile strain capacity first increase and then decrease. With the same limestone powder content, as the cement replacement by BFS increases from 50 to 70%, the flexural deflection capacity and the tensile strain capacity increase.

Unlike previous studies that mostly used natural limestone, the light calcium carbonate (LCC) used in this study is produced by fixing the carbon dioxide in the boiler exhaust gas from the highly alkaline wastewater generated by the concrete product factory. At the same time, this process neutralizes the highly alkaline wastewater, which can reduce sulfuric acid usage. About 60% of the CO_2 in Portland cement production comes from the decarbonization of limestone in the clinker process. The remaining 40% comes from the fuel and electricity used for heating and grinding[8]. Therefore, using carbon dioxide produced by boiler combustion to prepare $CaCO_3$ and applying it to concrete production can further enhance the effect of reducing carbon dioxide emissions.

In this study, cement mortar samples with different $CaCO_3$ and BFS contents were prepared to explore the changing rules of mortar compressive strength, pore structure, reaction products and micromorphology under the condition of ultra-high SCM replacement rate. It is found that $CaCO_3$ and BFS have a synergistic effect, which can maintain a high strength while increasing the SCM replacement rate. Compared to previous studies, CO_2 emissions were further reduced due to the use of a new type of $CaCO_3$ that absorbs CO_2.

2. MATERIALS AND TEST METHODS

2.1 Materials and preparation methods

The properties of light calcium carbonate (LCC) used in this study are shown in Table 1. The chemical composition measured by X-ray fluorescence spectrometer is shown in Table 2. Fig. 2 is the SEM image of $CaCO_3$, which has an irregular shape and a rough surface. For the convenience of description, $CaCO_3$ is abbreviated as CC below.

Table 1 The properties of $CaCO_3$

Density (g/cm^3)	Blaine surface area (cm^2/g)	Purity (%)	Moisture (%)	Average size (μm)
2.54	2620	97	1.23	40.78

Table 2 The chemical composition of $CaCO_3$

$CaCO_3$	SiO_2	Al_2O_3	Fe_2O_3	MgO	SO_3
97.3%	0.08%	0.09%	0.04%	<0.01%	1.2%

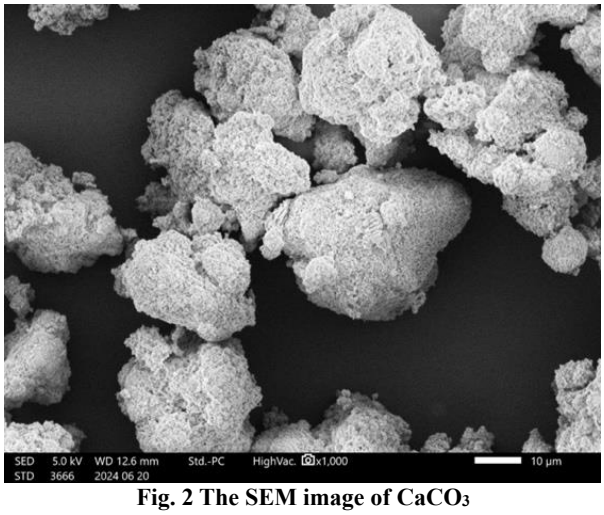

Fig. 2 The SEM image of $CaCO_3$

The basic properties of cement, BFS, sand, water and admixtures used in the experiment are shown in the Table 3. The material preparation process is as follows: stir OPC, BFS, $CaCO_3$ and sand for 30 seconds, add water and admixtures and continue stirring, and finally pour into the mold. After pouring, the concrete is sealed and cured in a constant temperature and humidity room (20℃, 60% RH) for 16 hours.

Table 3 The basic properties of raw materials

Raw materials	symbol	Basic info
Cement	C	Ordinary Portland cement density: 3.16g/cm3
Blast furnace slag	BFS	Specific surface area: 4000cm^2/g, density: 2.88 g/cm^3
Water	W	Tap water
Fine aggregate	S	Mountain sand, surface dry density: 2.56g/cm^3
Admixtures	SP	High-performance water reducing agent

After curing, the mortars were removed from the mold and cured underwater until it reaches the age (14 days). In this study, 9 samples with different CC and BFS replacement rates were prepared (Table 4). The mass ratio of water to powder of all samples is w/(C+BFS+$CaCO_3$)=39.8%. The mortar preparation ratio is shown in the Table 5.

Table 4 SCM replacement rate and sample number

Sample No.		$CaCO_3$ replacement rate		
		0%	25%	75%
BFS replacement rate	0%	1	7	14
	40%	3	9	16
	80%	5	11	18

Table 5 The mortar raw material mixing ratio

No	Mixture (kg/m^3)						
	w	c	BFS	$CaCO_3$	S1	S2	SP
①	288	725	0	0	806	361	0.40%
③	287	433	288	0	795	357	0.20%
⑤	285	143	574	0	784	352	0.10%
⑦	286	539	0	179.68	789	354	0.40%
⑨	285	322	215	178.97	781	350	0.40%
⑪	284	107	428	178.28	773	347	0.40%
⑭	281	177	0	530.34	756	339	2.50%
⑯	281	106	70.6	529.66	753	338	1.80%
⑱	281	35.3	141	528.98	751	337	2.40%

2.2 Test methods

2.2.1 Compressive strength

The compressive strength test was measured based on JIS R 5201 (physical test method for cement). The sample shape is φ50×100mm, and the age of material for compressive strength test is 14 days.

2.2.2 Mercury intrusion porosimetry (MIP)

Mercury intrusion porosimetry (MIP) is a widely used technique for characterizing the distribution of pore sizes in cement-based materials[18]. PoreMaster33 porometer was used to perform the MIP experiments. The size of the MIP specimen was approximately 5×5×5 mm cube, which was taken from the mortar specimen core. When calculating the pore size, we assumed that the mercury contact angle is 140°, the surface tension of mercury is 0.480 N/m and the density of mercury is 13.546 g/ml.

The relationship between the pressure and capillary diameter is described by Washburn[19] as

$$P = \frac{-4\gamma\cos\theta}{d}$$

where P =pressure, γ =surface tension of the liquid, θ=contact angle of the liquid, and d=diameter of the capillary.

2.2.3 XRD

The XRD results of samples were measured by Rigaku MiniFlex600, and the differences in the reaction products at different ratios of $CaCO_3$ and BFS were qualitatively analyzed. CuKα was used as the target, the tube voltage was 40 kV, the tube current was 15 mA, the 2θ scanning range was 5°–70°, and the step size was 0.01°. The scanning speed is 10°/min.

2.2.4 SEM

The scanning electron microscope (JCM-7000, JEOL) was used to observe the mortar microstructure. Before being observed, the surface of the sample was subjected to gold spraying for 60 seconds.

3. RESULTS AND DISCUSSION

3.1 Compressive strength

Fig. 3 shows the compressive strength of samples with different $CaCO_3$ and BFS ratios.

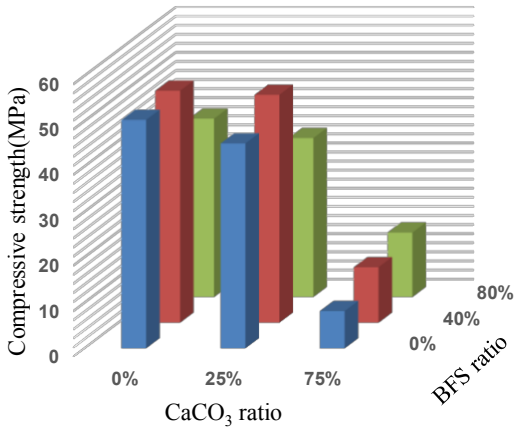

Fig. 3 The compressive strength of samples with different $CaCO_3$ and BFS ratios

For the convenience of comparison, the compressive strengths of all samples were converted into relative ratio to the strengths when the $CaCO_3$ ratio is 0% and the BFS ratio is 0% (Table 6). There are likely other optimal ratios, but within the range of ratios have been checked, No. 9 has the greatest strength. When the $CaCO_3$ content is 25%, as the BFS content increases, the strength first increases and then decreases; in the process of increasing

the $CaCO_3$ content from 0% to 25%, the strength decreases slightly, but after increasing to 75%, the strength is only about 20% of that when the $CaCO_3$ content is 0.

Table 6 Relative ratio of sample compressive strength

Relative ratio of sample compressive strength		$CaCO_3$ replacement rate		
		0%	25%	75%
BFS replacement rate	0%	1.00	0.90	0.16
	40%	1.02	1.00	0.24
	80%	0.78	0.70	0.28

The combination of limestone filler and blast-furnace slag is complementary, and the simultaneous addition of CC and BFS can increase the replacement rate of SCM while ensuring the compressive strength.

3.2 MIP

It is generally accepted that the strength of mortar is fundamentally a function of the form and distribution of void space and porosity within it[20–22]. Fig. 4 shows the incremental pore diameter distribution curves of the samples measured using MIP.

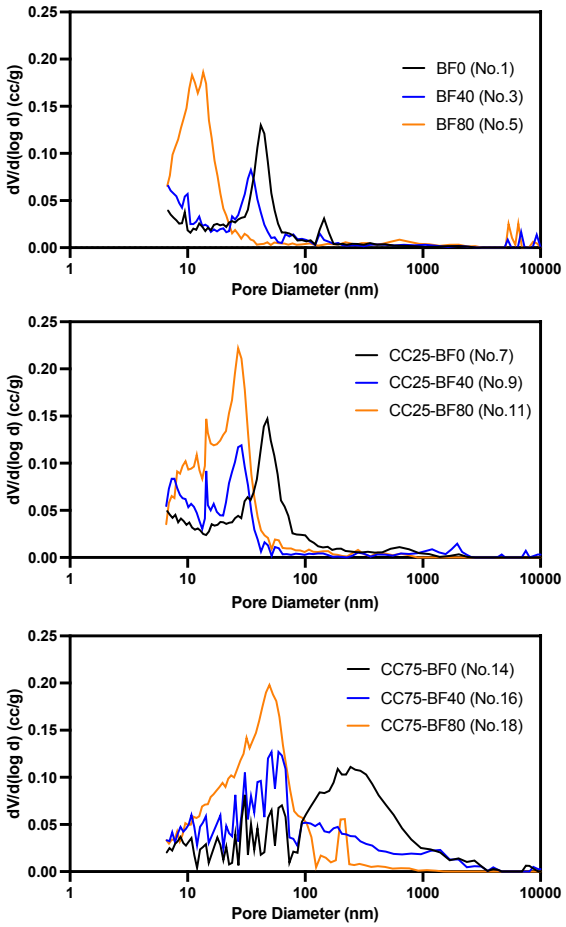

Fig. 4 The incremental pore diameter distribution curves of the samples

Fig. 5 shows the cumulative pore diameter distribution curves of the samples measured using MIP.

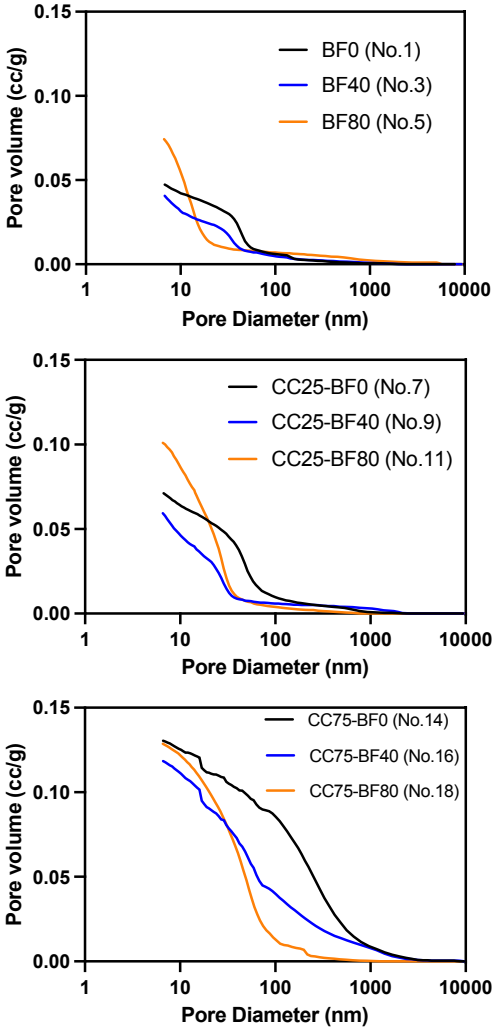

Fig. 5 The cumulative pore diameter distribution curves of the samples

The mainstream academic view is that the compressive strength is mainly affected by the incremental pore distribution rather than the total cumulative pore volume [23,24]. The effect of porosity at each pore grade on strength is different. According to the porosity at each pore grade in concrete and their influence coefficient, the pore diameter is finely divided into four categories, as follows: harmless pores ($d < 20$ nm), little harmful pores ($d = 20$ nm–50 nm), harmful pores ($d = 50$ nm–200 nm), and much harmful pores($d > 200$ nm)[25].

No. 9 has the highest strength due to its small harmful pore size and small pore volume. Under the same BFS content, as the calcium carbonate content increases, the pore volume increases. Under the same CC content, as the BFS content increases, the pore volume first decreases and then increases. BFS additive highly refined the pore size of cement containing CC. Zhang et al.[26] attributed this phenomenon of ternary cement to the optimal ratio matching and particle size matching.

3.3 XRD

For BFS cement compositions containing limestone, the remaining aluminates will react with CC to form a combination of monocarbonate and hemicarbonate (Mc at 11.7° 2θ and Hc at 10.8° 2θ). In this case ettringite

does not decompose in reaction with C_3A[27]:

$$C_3A + C\underline{C} + 11H \rightarrow C_4A\underline{C}H_{11}\ (M_C)$$

$$C_3A + 0.5C\underline{C} + 0.5CH + 11.5H \rightarrow C_4A\underline{C}_{0.5}H_{12}\ (H_C)$$

Fig. 6 is the XRD pattern of No.3, No.9, No.16. Consistent with previous reports[28], carboaluminate hydrates such as Mc and Hc were generated. After adding BFS, the amount of Hc generated was relatively large. As CC increases, the balance of chemical reactions between Hc and Mc changes, and the chemical reaction of Mc gradually becomes the dominant reaction. When CC is introduced into a BFS cement system, the main phase change is the transformation from Hc(280 cm^3/mol) to Mc(262cm^3/mol)[24]. $Ca(OH)_2$, abbreviated as CH, gradually decreases with the increase of calcium carbonate content. This is because, as the proportion of cement decreases, the amount of CH as a hydration product will also decrease accordingly.

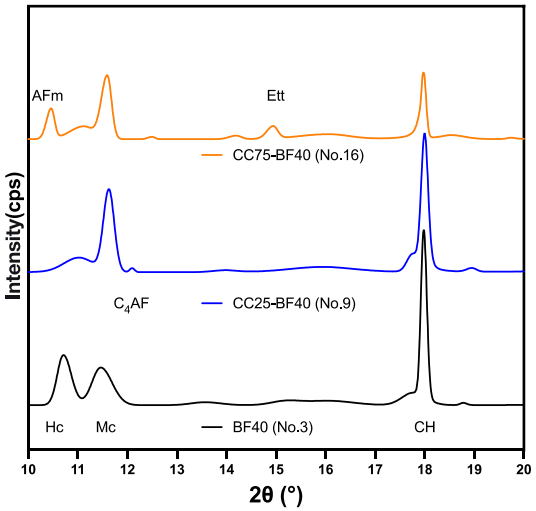

Fig. 6 The XRD pattern of No.3, No.9, No.16

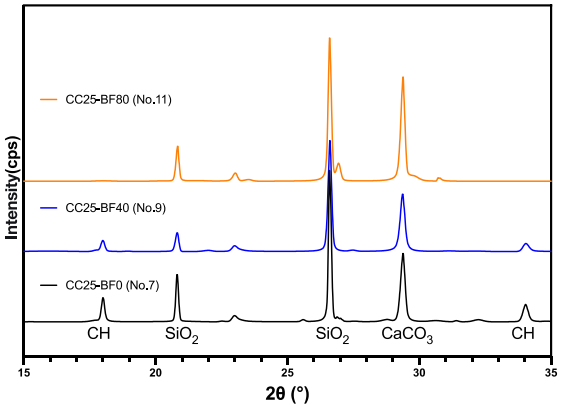

Fig. 7 The XRD pattern of No.7, No.9, No.11

Fig. 7 shows the XRD pattern of No.7, No.9, No.11. The three samples were prepared with the same amount of CC added. Comparing the CC peak intensities of the three samples, the CC peak of sample No. 9 is the lowest, suggesting that the most CC is involved in the chemical reaction. Therefore, it can be inferred that BFS can promote the chemical reactivity of CC and achieve the effect of refining the mortar structure. In fact, there may be more complex chemical reactions here, and the reaction direction and chemical equilibrium need further study.

3.4 SEM

Fig. 8 are the SEM image of No.7, No.9 and No.11. That is, when the CC ratio is 25%, the microscopic morphology images are when the BFS ratio is 0%, 40%, and 80%, respectively. Compared with No.7 and No.9, No.11 has obviously loose structure and increased porosity.

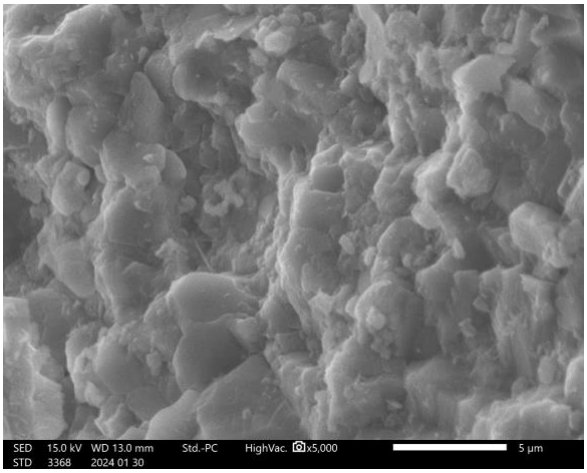

(a) No.7

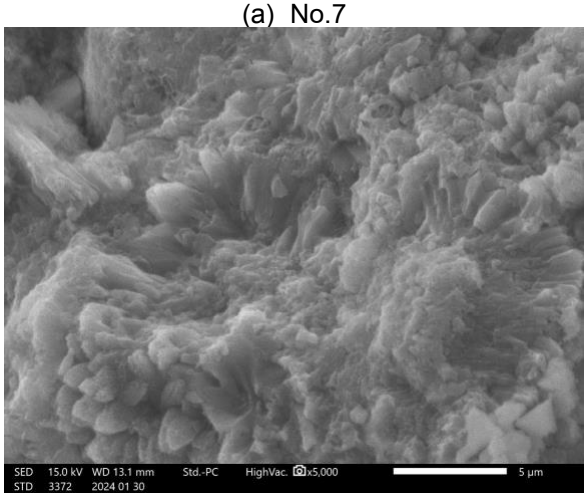

(b) No.9

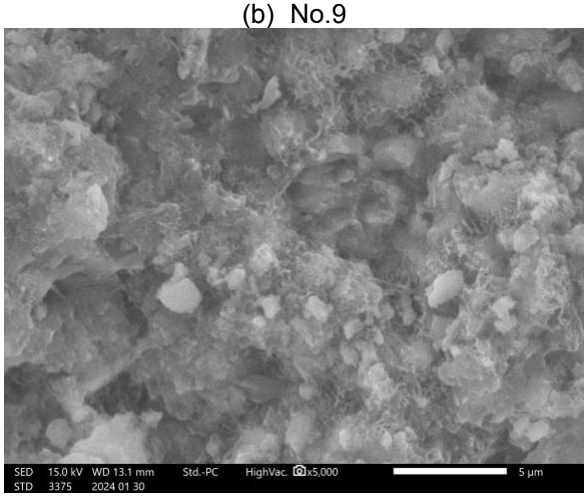

(c) No.11

Fig. 8 The SEM image of samples.

No.11 has fibrous hydration products that are not found in samples No.9 and No.7. The composition is generally considered to be C-S-H[29]. The loose hydration products lead to an increase in the amount of harmful pores, resulting in a sharp drop in compressive strength.

4. CONCLUSIONS

It is generally believed that $CaCO_3$ has two functions, one as an active participant in the hydration process, the other as an inert filler[30]. The performance of calcium carbonate cement is mainly determined by two aspects: the crystal form of calcium carbonate, particle size, specific surface area and particle size of cement, alumina of C_3A and C_4AF, and the proportion of blast furnace slag. Only one type of CC was tried in this study so far, so it is planned to prepare multiple CCs with different particle sizes and specific surface areas to test their effects on mortar strength in the future.

The MIP results show that under the same BFS content, as the calcium carbonate content increases, the pore volume increases. Under the same calcium carbonate content, as the BFS content increases, the pore volume first decreases and then increases. At present, the XRD result has preliminarily confirmed that the addition of CC and BFS will produce hydration products such as Hc and Mc. In the future, Rietveld and other methods will be used to quantify chemical products. The SEM results show that the addition of a certain amount of calcium carbonate and blast furnace slag is beneficial to the densification of cement pores, thereby improving the compressive strength. EDS and other methods will be used to determine the distribution of CC in mortar.

With a high SCM replacement rate and the use of $CaCO_3$ that has absorbed CO_2, this study has certain value in energy conservation, emission reduction and achieving carbon neutrality in the cement industry.

REFERENCES

[1] S.A. Miller, A. Horvath, P.J.M. Monteiro, Readily implementable techniques can cut annual CO2 emissions from the production of concrete by over 20%, Environ. Res. Lett. 11 (2016) 074029. https://doi.org/10.1088/1748-9326/11/7/074029.

[2] M. Schneider, V. Hoenig, J. Ruppert, J. Rickert, The cement plant of tomorrow, Cement and Concrete Research 173 (2023) 107290. https://doi.org/10.1016/j.cemconres.2023.107290.

[3] J. Skibsted, R. Snellings, Reactivity of supplementary cementitious materials (SCMs) in cement blends, Cement and Concrete Research 124 (2019) 105799. https://doi.org/10.1016/j.cemconres.2019.105799.

[4] European Committee For Standardisation, 197-1, Cement-Part 1: Composition, specifications and conformity criteria for common cements, (2011).

[5] Canadian Standards Association, CSA A3001-08, Cementitious materials for use in concrete, (2008).

[6] Canadian Standards Association, CSA A3001-10, Cementitious materials for use in concrete, (2010).

[7] ASTM International, West Conshohocken, PA, C595. Standard specification for blended hydraulic cements, (2003).

[8] Y. Dhandapani, M. Santhanam, G. Kaladharan, S. Ramanathan, Towards ternary binders involving limestone additions — A review, Cement and Concrete Research 143 (2021) 106396. https://doi.org/10.1016/j.cemconres.2021.106396.

[9] D. Wang, C. Shi, N. Farzadnia, Z. Shi, H. Jia, Z. Ou, A review on use of limestone powder in cement-based materials: Mechanism, hydration and microstructures, Construction and Building Materials 181 (2018) 659–672. https://doi.org/10.1016/j.conbuildmat.2018.06.075.

[10] D. Wang, C. Shi, N. Farzadnia, Z. Shi, H. Jia, A review on effects of limestone powder on the properties of concrete, Construction and Building Materials 192 (2018) 153–166. https://doi.org/10.1016/j.conbuildmat.2018.10.119.

[11] D.P. Bentz, A. Ardani, T. Barrett, S.Z. Jones, D. Lootens, M.A. Peltz, T. Sato, P.E. Stutzman, J. Tanesi, W.J. Weiss, Multi-scale investigation of the performance of limestone in concrete, Construction and Building Materials 75 (2015) 1–10. https://doi.org/10.1016/j.conbuildmat.2014.10.042.

[12] A.C.I. Committee, Cement and concrete terminology, in: American Concrete Institute, 1985.

[13] E. Özbay, M. Erdemir, H.İ. Durmuş, Utilization and efficiency of ground granulated blast furnace slag on concrete properties – A review, Construction and Building Materials 105 (2016) 423–434. https://doi.org/10.1016/j.conbuildmat.2015.12.153.

[14] M.F. Carrasco, G. Menéndez, V. Bonavetti, E.F. Irassar, Strength optimization of "tailor-made cement" with limestone filler and blast furnace slag, Cement and Concrete Research 35 (2005) 1324–1331. https://doi.org/10.1016/j.cemconres.2004.09.023.

[15] G. Menéndez, V. Bonavetti, E.F. Irassar, Strength development of ternary blended cement with limestone filler and blast-furnace slag, Cement and Concrete Composites 25 (2003) 61–67. https://doi.org/10.1016/S0958-9465(01)00056-7.

[16] W. Zhang, S. Na, J. Kim, H. Choi, Y. Hama, Evaluation of the combined deterioration by freeze–thaw and carbonation of mortar incorporating BFS, limestone powder and calcium sulfate, Mater Struct 50 (2017) 171. https://doi.org/10.1617/s11527-017-1039-1.

[17] J. Zhou, S. Qian, M.G. Sierra Beltran, G. Ye, K. van Breugel, V.C. Li, Development of engineered cementitious composites with limestone powder and blast furnace slag, Mater Struct 43 (2010) 803–814. https://doi.org/10.1617/s11527-009-

9549-0.
[18] A.B. Abell, K.L. Willis, D.A. Lange, Mercury Intrusion Porosimetry and Image Analysis of Cement-Based Materials, Journal of Colloid and Interface Science 211 (1999) 39–44. https://doi.org/10.1006/jcis.1998.5986.
[19] E.W. Washburn, The Dynamics of Capillary Flow, Phys. Rev. 17 (1921) 273–283. https://doi.org/10.1103/PhysRev.17.273.
[20] K. Kendall, A.J. Howard, J.D. Birchall, P.L. Pratt, B.A. Proctor, S.A. Jefferis, P.B. Hirsch, J.D. Birchall, D.D. Double, A. Kelly, G.K. Moir, C.D. Pomeroy, The relation between porosity, microstructure and strength, and the approach to advanced cement-based materials, Philosophical Transactions of the Royal Society of London. Series A, Mathematical and Physical Sciences 310 (1997) 139–153. https://doi.org/10.1098/rsta.1983.0073.
[21] J.L. Granju, J. Grandet, Relation between the hydration state and the compressive strength of hardened Portland cement pastes, Cement and Concrete Research 19 (1989) 579–585. https://doi.org/10.1016/0008-8846(89)90009-4.
[22] A.M. Neville, Properties of concrete, Longman London, 1995.
[23] J.D. Birchall, A.J. Howard, K. Kendall, Flexural strength and porosity of cements, Nature 289 (1981) 388–390. https://doi.org/10.1038/289388a0.
[24] H.F.W. Taylor, Cement chemistry, 2nd ed, T. Telford, London, 1997.
[25] X. Han, B. Wang, J. Feng, Relationship between fractal feature and compressive strength of concrete based on MIP, Construction and Building Materials 322 (2022) 126504. https://doi.org/10.1016/j.conbuildmat.2022.126504.
[26] Y. Zhang, G. Ye, Effect of Limestone Powder on Microstructure of Ternary Cementitious System, in: Sustainable Construction Materials 2012, American Society of Civil Engineers, Wuhan, China, 2012: pp. 225–234. https://doi.org/10.1061/9780784412671.0020.
[27] K. De Weerdt, M.B. Haha, G. Le Saout, K.O. Kjellsen, H. Justnes, B. Lothenbach, Hydration mechanisms of ternary Portland cements containing limestone powder and fly ash, Cement and Concrete Research 41 (2011) 279–291. https://doi.org/10.1016/j.cemconres.2010.11.014.
[28] S. Hoshino, K. Yamada, H. Hirao, XRD/Rietveld Analysis of the Hydration and Strength Development of Slag and Limestone Blended Cement, Journal of Advanced Concrete Technology 4 (2006) 357–367. https://doi.org/10.3151/jact.4.357.
[29] K. Scrivener, R. Snellings, B. Lothenbach, A Practical Guide to Microstructural Analysis of Cementitious Materials, CRC Press, 2018.
[30] T. Matschei, B. Lothenbach, F.P. Glasser, The role of calcium carbonate in cement hydration, Cement and Concrete Research 37 (2007) 551–558. https://doi.org/10.1016/j.cemconres.2006.10.013.

Preparation of Aramid Nanofibers (ANFs) by Recycling Aramid Fiber and Its Effects on Cement Hydration

Yan Wan
Master student, School of Civil Engineering, Harbin Institute of Technology, Harbin 150006, China.

Zhichao Xu
PhD student, School of Civil Engineering, Harbin Institute of Technology, Harbin 150006, China.

Yingzi Yang
Professor, School of Civil Engineering, Harbin Institute of Technology, Harbin 150006, China.

ABSTRACT:
Aramid nanofibers (ANFs) are one-dimensional materials of great interest in various applications due to their excellent strength, chemical stability, thermal stability, and high specific surface area. However, their application is hindered by the long preparation period (7 days), low preparation concentration (0.2 wt%), and extremely high production cost. In this paper, ANFs were prepared from waste aramid resources by using a modified deprotonation method and then to enhance the mechanical properties of cementitious materials. The results showed that the diameter of the prepared ANFs was around 15 nm. The results of the heat of hydration showed that it promoted the early-age hydration of cement. When the dosage was 0.03 wt%, the compressive strength was increased by 48.72% for 1 day and 23.39% for 3days. This study provides a short-time, low-cost and effective preparation method of ANFs and the potential application of ANFs in cementitious composites.

Keywords: aramid nanofibers, ANFs, early-age hydration, mechanical properties.

1. INTRODUCTION

As the most widely used building material, concrete has the advantages of high compressive strength, durability and low cost, but it is still expected to have better microstructure, mechanical performance and more diverse properties such as durability, heat resistance and fire resistance. It has become a common method to improve the hydration process and performance of concrete by adjusting the mix ratio, adding additives such as water-reducing agent and air-entraining agent, and adding appropriate mineral admixtures.

Nanomaterials refer to materials with at least one-dimensional scale within 100 nm or composed of them as basic units in three-dimensional space. Because of their special size, nanomaterials have different performance from larger materials in many aspects such as light, electricity, magnetism and mechanics. It is found that nanomaterials often have excellent strength and hardness, which can help to enhance the strength of composite materials, and can also realize functions such as conductivity and sensing. At the same time, some nanomaterials can be produced by waste recycling or renewable resources, which is environmentally friendly. Therefore, nanomaterials are introduced into different application fields.

In recent years, the incorporation of nanomaterials into concrete has become a hot topic in civil engineering materials. Studies have shown that nanomaterials can act as fillers to improve the accumulation of particles in concrete, thereby refining the pores of concrete, improving the microstructure of concrete, and improving its macroscopic properties [1]. Among them, there are a large number of experimental studies on nano-oxides, carbon nanotubes (CNT) and nanocellulose.

Nano-oxides can be used as additives in concrete to enhance its mechanical properties, improve the permeability and durability of concrete. Some nano-oxides also have photocatalytic properties, which can decompose pollutants under sunlight and achieve self-cleaning effect on the surface of concrete. It helps to maintain the beauty of the structure and reduce maintenance costs. Qing et al. [2] compared and analyzed the effects of silica fume and nano-silica on hardened cement paste by means of XRD and scanning electron microscopy. It was found that the addition of silica accelerated the hydration process of cement, and the improvement of compressive strength and bond strength by nano-materials was more significant, but the effect of nano-silica would be reduced when the content exceeded a certain amount (3%). Yu et al. [3] studied the effect of nano-silica on the hydration and microstructure of Ultra High Performance Concrete (UHPC) under the use of low cementitious materials, and found that nano-silica played a role in promoting nucleation, and increased the viscosity of UHPC to increase the air involved in mixing. The two effects compete with each other, so there is an optimal dosage to obtain UHPC with the lowest porosity. Adak et al. [4] studied the effect of nano-silica on the strength of low-calcium fly ash low-quality polymer mortar. It was found that the compressive, flexural and tensile strength were significantly improved at 6% content. Field emission scanning electron microscopy and XRD results showed that the addition of nano-materials promoted the crystallization of amorphous compounds. Hou et al. [5] believed that compared with silica fume, nano-silica reaction products have a denser gel structure and worse crystallinity. Nano-silica can promote the early hydration of cement, but due to the dense structure, hydration slows down with age. The effect of nano-silica obtained by Bede

et al. [6] on the hydration rate is also consistent. Wu et al. [7] introduced nano-alumina into reinforced concrete by electrokinetic treatment. The sampling results at different depths show that the introduction of nano-alumina can reduce the porosity. Ahmed [8] compared the behavior of concrete obtained by ordinary water and magnetized water with different nano-alumina content. The results show that the addition of nano-alumina can significantly improve the porosity of concrete. Li et al. [9] studied the effect of nano-alumina on the properties of low-temperature cured concrete, and found that the addition of nano-alumina can compensate for the loss of compressive strength caused by low temperature, but excessive addition will lead to a decrease in the compensation effect. In addition, there are also some studies on the performance of nano-titanium dioxide, zinc oxide and other nano-oxides and composite modified concrete [10–12].

Carbon nanotubes (CNTs) can be divided into single-walled and multi-walled according to the number of concentric tubes. The former has a size of less than 3 nm, and the latter can reach 100 nm. Due to its extremely high strength and stiffness, it is widely used to enhance polymer matrix composites (such as CFRP) [13,14]. In addition, carbon nanotubes have excellent electrical properties and are also used as basic materials for structural health monitoring sensors. They can be integrated into concrete as conductive elements to realize real-time monitoring of structural deformation and cracks and improve the safety and reliability of the structure.

Lim et al. [15] explored the relationship between the conductivity of CNTs cement composites and the crack width, and verified the possibility of incorporating CNTs as a concrete sensing material. Carriço et al. [16] found that different types of multi-walled carbon nanotubes have improved the mechanical properties of cement, and nanomaterials play a role in bridging cracks and promoting nucleation. Mohsen et al. [17] used ultrasound and batch mixing to prepare concrete with different CNTs content. Experiments showed that the addition of carbon nanotubes significantly improved its ductility, impermeability and flexural strength. Viana et al. [18] carried out the performance test of UHPC after fast and slow heat treatment, and found that the presence of CNTs can effectively reduce the occurrence of spalling and the oxygen permeability coefficient of concrete after slow heat treatment. Zhao et al. [19] carried out experiments on the early thermal cracking of panel concrete, and found that the incorporation of CNTs can effectively reduce the early thermal expansion coefficient and reduce the early cracking.

Nanocellulose is usually derived from renewable resources, such as plant fibers, and is environmentally friendly. Because of its high specific surface area and strength, it is used as a reinforcing agent for cement-based materials. Due to the different types, dosage and dispersion of cellulose, it has different effects on the hydration, shrinkage, microstructure and mechanical properties of concrete [20]. Cengiz et al. [21] found that the incorporation of 1 g of nanocellulose from Cladophora can increase the bending stress of concrete by 2.7 times, while the commercial cellulose has a lower bending stress due to uneven dispersion. Hisseine et al. [22] tested the effect of cellulose on the macroscopic properties and microstructure of concrete. It was found that the compressive strength, elastic modulus and flexural strength were improved, and the hydrophilicity and water retention of cellulose made the 28 d hydration degree significantly improved. Kamasamudram et al. [23] studied the effects of wood and delignification cellulose nanofibrils on the hydration, microstructure and mechanical properties of cement paste, and found that early cement hydration was promoted, two kinds of nanofibers reduced the production of ettringite and magnesium hydroxide, and the compressive and flexural strength were improved. Sun et al. [24] proposed to improve the rheological properties of the matrix by nanocellulose suspension to optimize the distribution of steel fibers in UHPC. The experimental results showed that the addition of nanocellulose improved the direction and settlement of steel fibers, and the cracking mode of UHPC also changed from single crack to multiple cracks. Zhang et al. [25] introduced modified bamboo cellulose nanofibers into autoclaved aerated concrete, and found that the flexural strength and compressive strength of the concrete were improved. The modified material reacted with cellulose to make cellulose overlap with the matrix.

Although there have been many studies on the entry of nanomaterials into concrete, there are still some challenges and problems, mainly related to material preparation, dispersion and compatibility with concrete matrix.

Aromatic polyamide fiber (aramid fiber) is based on rigid aromatic amide bonds. The hydrogen bonds between the chains have high directivity, which makes the material have high crystallization tendency and extremely high cohesive energy density. Therefore, it has the advantages of high strength, high temperature resistance and good chemical stability. It is not easy to dissolve in water and most organic solvents, and is resistant to weak acid and weak alkali corrosion. It is widely used to manufacture high-grade fabrics [26]. Poly-phenylene terephthalamide (PPTA) is a member of the aramid fiber family. It was developed in the 1960s. The repeating unit of the chemical formula is -[-CO-C6H4-CONH-C6H4-NH-]-, which is obtained by polycondensation of p-phenylenediamine (PPD) and terephthaloyl chloride (TPC). The amide group attached to the benzene ring is a para-position structure. It is a rod-like macromolecule with high strength, high hardness, heat resistance and solubility，and Kevlar is one of the most well-known brands in commercial PPTA. The addition of two Aramid nanofibers, as the name implies, are nano-scale materials with the same chemical composition as aramid fibers. There are four main preparation methods: electrospinning, mechanical crushing, polymerization-induced self-assembly and deprotonation. The electrospinning process uses high pressure to charge the spinning solution, and the electrostatic repulsion is used to overcome the surface tension to obtain the jet droplets, so as to realize the fiber-scale nanoscale. Yao et al. [27] dissolved PPTA in concentrated sulfuric acid to obtain solutions with different concentrations. Short fibers with a length of less than 100 nm were obtained from 7wt % solution at an applied voltage of 25 kV and a distance of 5 cm. The

mechanical treatment is to use the "scraping" of physical action to refine the fibers. Ifuku et al. [28] used 200 MPa high-pressure water jet circulating atomization to treat the aramid fiber pre-hydrolyzed in NaOH solution to obtain 10-200 nm ANFs.

Electrospinning and mechanical treatment are to obtain ANFs from molded fibers, and polymerization-induced self-assembly is to start with the synthesis of PPTA. In the process of PPTA synthesis, PPD and TPC undergo polycondensation reaction, and PPTA is continuously precipitated from the liquid phase with the increase of chain length. If the continuous growth of PPTA chain can be prevented, it is possible to obtain ANFs. Yan [29] et al. attempted to introduce methoxy polyethylene glycol (mPEG) into the PPTA synthesis process and continuously stirred it. It was found that the diameter of the obtained fiber decreased with the increase of the amount of mPEG. Monofilaments with a diameter of about 50 nm were synthesized at a dosage of 10 %. Further increasing the amount of mPEG cannot reduce the size of the obtained nanofibers but can improve their dispersibility.

Although the above three methods can prepare ANFs, they have problems such as high energy consumption, complicated operation, low product concentration and large diameter. As shown in Figure 1, the amide group of PPTA can be deprotonated by a strong base to form polyanion, which is soluble in a simple organic solvent dimethyl sulfoxide (DMSO). In 1990, Burch et al.in order to improve the solubility and processability of PPTA fibers, it was proved that proton donors (such as alcohol or water) can reduce the viscosity of PPTA polyanion solution in DMSO and increase the solution concentration of PPTA polyanion, and its solubility and solution viscosity depend on the cations of the base. Burch compared the three alkali cations of Na^+, Li^+ and K^+, and found that the use of K^+ can obtain a higher concentration of PPTA solution in the shortest time and has better fluidity [30]. In 2011, Yang et al. [31] added water to the PPTA/KOH/DMSO system at room temperature, and the red ANFs / DMSO dispersion was obtained after a week of magnetic stirring. In 2019, Yang et al. [32] studied the effect of the volume ratio of water to DMSO on the preparation time, and compared it with mechanical treatment and ultrasound-assisted deprotonation methods. It was found that proton donor-assisted deprotonation can obtain ANFs with smaller diameter and more uniform distribution in a shorter time. In addition, when the volume ratio of water to DMSO is 1:25, the preparation time of ANFs is shortened to 4h.

In contrast, ANFs can be obtained by using water as a proton donor, KOH and DMSO as a deprotonated base and solvent, which is a simple, time-consuming and low-cost preparation method. In this paper, ANFs will be prepared by deprotonation method and its effect on the early hydration of cement will be studied.

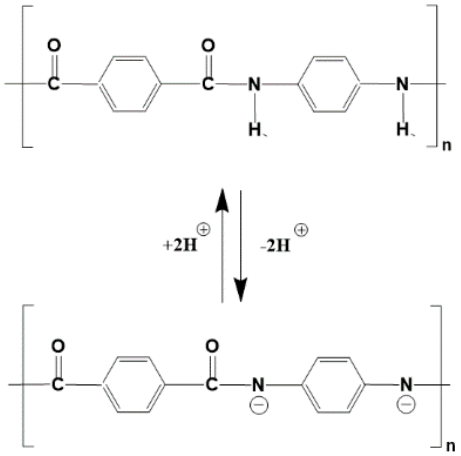

Fig.1. Schematic representation of the deprotonation process of PPTA.

2. EXPERIMENTAL SECTION

2.1. MATERIALS

The cement was provided by Fushun Cement Company. The mineral compositions of cement are shown in Table 1. As shown in Fig.2a, the aramid fiber (diameter: 0.7 mm) was obtained from Dongguan Shengxin Special Rope Co., Ltd, and made of Kevlar fiber from Dupont, the United States. KOH and dimethyl sulfoxide (DMSO) were obtained from Shanghai Macklin Biochemical Co., Ltd.

2.2. PREPARATION OF ANFs

First, the recovered aramid fiber was cut into 1-2 mm. Then the fiber was added to acetone for ultrasonic cleaning for 30 min to remove surface impurities. Afterward, the fiber was washed with ethanol for 2-3 times, rinsed with DI water for 2-3 times, and vacuum dried at 60 ℃ for 24 h. Subsequently, above fiber (0.6 g), KOH (0.9 g), DMSO (300 ml) and DI water (12 g) were mixed and stirred at 350 rpm for 4h to obtain red solution, as shown in Fig.2b. Add ethanol to wash 2-3 times to remove excess organic solvents. The obtained suspension was washed with DI water until the pH value reached approximately 7. Then the obtained suspension was prepared as 5 mg/ml solution (Fig.2c).

Table 1. Mineral composition of cement.

Mineral composition	C_3S	C_2S	C_3A	C_4AF
wt%	57.58	18.55	7.14	11.37

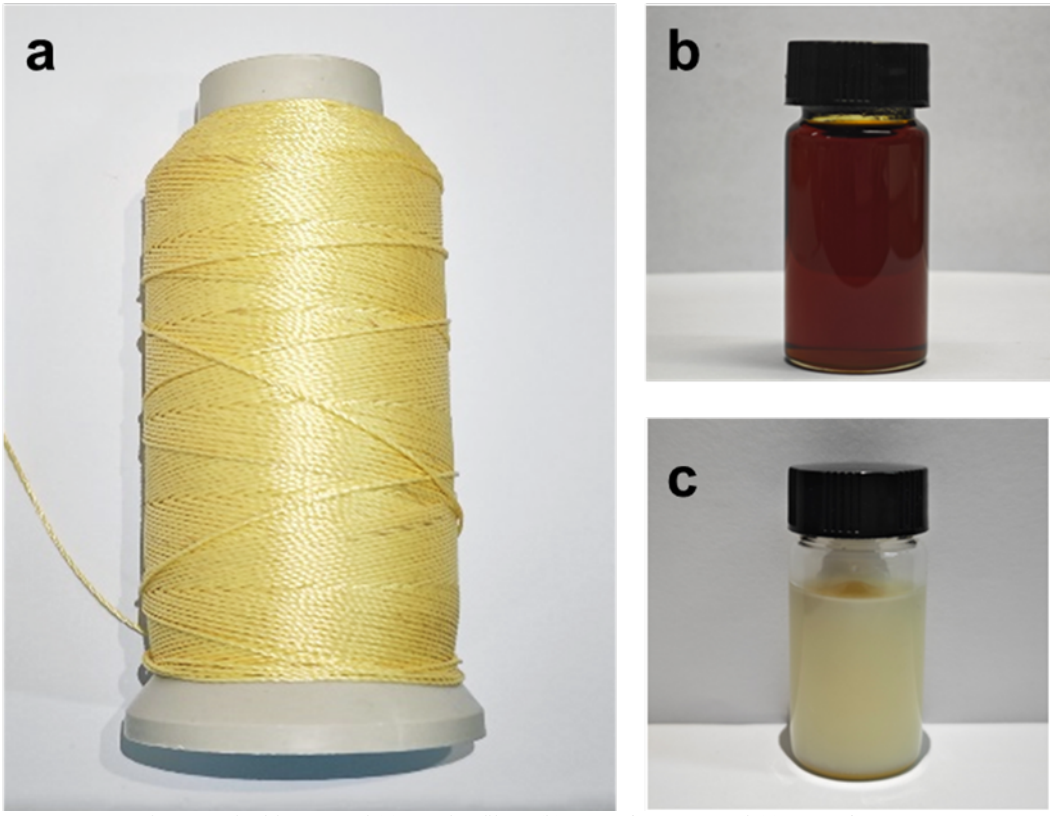

Fig.2. Optical images of (a) Kevlar fiber, (b) ANFs/DMSO, and (c) ANFs/water

2.3. PREPARATION OF SPECIMENS

Table 2 shows the mix proportions of cement paste. Specifically, ANFs solution was stirred (500 rpm) with DI water for 5 min. The mixture was added to the cement and stirred at a low-speed for 2 min, followed by 3 min high-speed stirring. The paste was then cast in models (20 mm × 20 mm × 20 mm). After 24 h at room temperature, all specimens were demolded and transferred to a standard curing room maintained at 20 ± 2 ℃ and 95% relative humidity for a curing period of 28 days.

2.4. CHARACTERIZATION

Transmission electron micrograph (TEM, FEI Tecnai G2 F30) was used to characterize the morphologies of ANFs. The chemical composition of aramid fiber and ANFs were characterized by Fourier transform infrared (FTIR; Nicolet is 50, Thermo Fisher). X-ray diffraction (XRD) patterns were recorded with a Panalytical X-ray powder diffractometer with Cu Kα radiation at 40 kV. The hydration heat evolution was analyzed by isothermal calorimeter (TAM AIR) under an isothermal condition of 20 ℃ for 72 h. The compressive strength was measured at 1 d, 3 d and 28 d (loading rate: 1 kN/s), then the specimens were immersed in anhydrous ethanol to terminate hydration, removed and stored at 40°C under vacuum drying conditions. The 1d and 3d samples were ground into powder, sieved at 150 mesh, and the diffraction patterns were recorded using the X-ray diffractometer (2theta: 5°-70°, step size: 0.0131303°). The XRD data were qualitatively analyzed for composition using JADE 6.5 and then quantitatively analyzed using GSAS-II. Thermogravimetric analysis (TGA) of 1 d and 3 d powders was performed using a Simultaneous SDT 650 manufactured by TAM Air, with a set temperature increase range of 10-1000 ℃ and a temperature increase rate of 10 ℃/min. The 28 d samples were cut into small cubes (3-5 mm) and lyophilized for 24 h and then analyzed for their pore structure by mercury-in-pressure (MIP) experiments.

3. RESULTS AND DISCUSSION

3.1. CHARACTERIZATION OF ANFs

As shown in Fig.3a, the ANFs aqueous dispersion has a Tyndall effect, indicating that ANFs has good dispersion. A small amount of ANFs was added to water and stirred

Table 2. Mix proportion of cement paste.

Mixture ID	Cement (%)	Water (%)	ANFs (%)
C/A-0	100	40	0
C/A-3	100	40	0.03

to obtain a semi-transparent liquid, as shown in Fig.3a, when laser light was transmitted through it, an obvious Tyndall effect was observed, which indicated that ANFs were dispersed in water to form a colloid. As shown in Fig.3b, 2 ml of ANFs was taken and filtered under reduced pressure to obtain a yellow film. Fig.3c shows the transmission electron micrograph of ANFs, and Fig.3d shows the statistical graph of the size distribution of ANFs, and the diameter of the produced ANFs is 13.70 ± 7.67 nm. Fig.4a shows the FTIR spectra of ANFs and aramid fibers, it can be observed that the N-H vibration at 3430 cm^{-1} and the C=O vibration at 1645 cm^{-1}, while the deprotonation treatment led to an increase of O-H in ANFs. Fig.4b shows the XRD patterns of the two, and the diffraction peaks at 20.5°, 22.9° , and 28.1° appeared in both the produced ANFs and aramid fibers, which are almost the same. Therefore, it is believed that the ANFs was obtained by KOH etching, and the molecular chain structure of the fiber itself was not damaged, and still retained the excellent properties of aramid fibers.

3.2. HEAT OF HYDRATION

Fig.5 shows the 72h cumulative heat flow and differential heat flow of two groups of pastes, the addition of ANFs increased the 3d cumulative heat of hydration by 3.52%, which promoted the cement hydration. ANFs can form hydrogen bonds with water molecules due to the presence of their functional groups, which possesses a certain degree of water absorption, and in the early stage of cement hydration (0-24 h), part of the water adsorption in the vicinity of ANFs, which delayed cement hydration, so the hydration differential curve was shifted to the right (Fig.5b). In the later stage, the adsorbed water was gradually released and participated in the hydration process, the hydration rate increased, and the cumulative hydration heat increased.

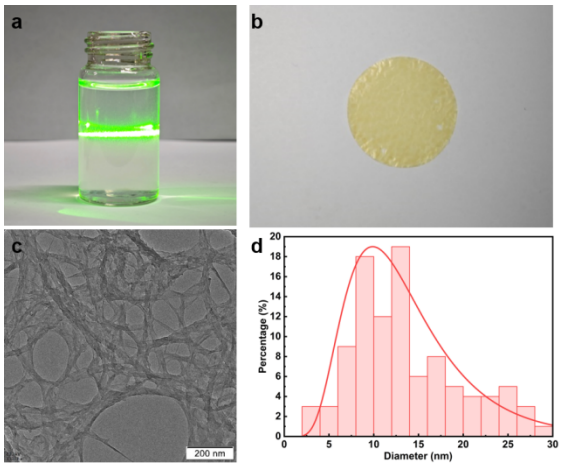

Fig.3. (a) Tyndall effect of ANFs. (b) Optical image of ANFs film. (c) TEM of ANFs. (d) Size distribution of ANFs.

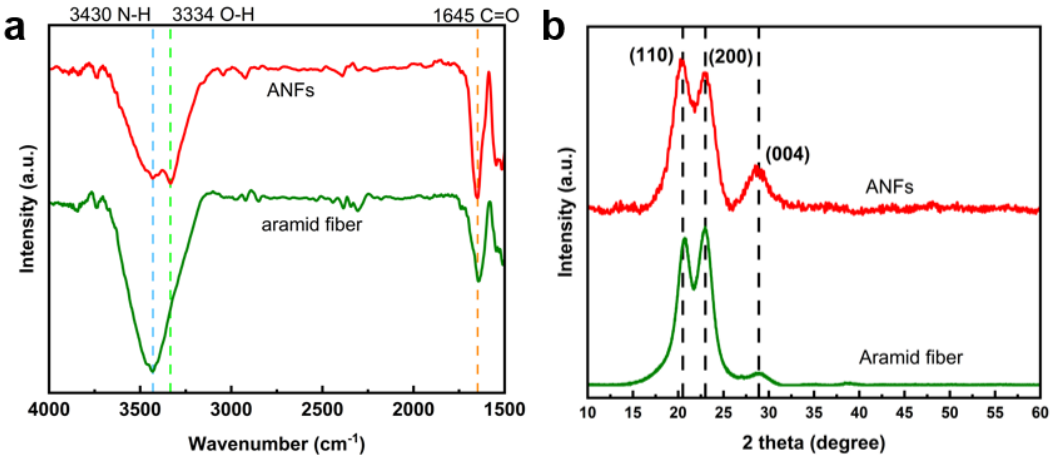

Fig.4. (a) FTIR spectra of aramid fiber and ANFs. (b) XRD curve of aramid ANFs.

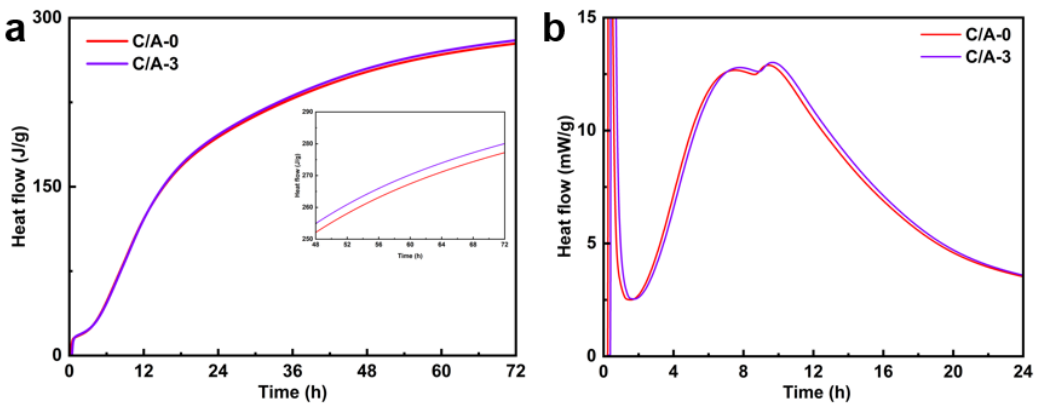

Fig.5. (a) Cumulative heat of hydration; (b) Differential heat of hydration

3.3. HYDRATION DEGREE

3.3.1. XRD-RIETVELD

Fig.6 shows the four sets of XRD diffraction results and their XRD-Rietveld fits. Table 3 shows the mineral composition of each group obtained from XRD-Rietveld analysis.

From the 1 d XRD data, it can be seen that the incorporation of 0.03 wt% ANFs slightly decreased the hydration of C_3S, C_2S and C_3A in the cement, with C_4AF consuming more and generating less $Ca(OH)_2$, which is consistent with the initial stage of the differential curve of the heat of hydration (0-24 h). Comparison of the 3 d XRD data revealed that the consumption of all four minerals increased when 0.03 wt% ANFs was incorporated, with C_3S and C_4AF increasing significantly and generating more $Ca(OH)_2$. The degree of hydration of each group was calculated from Eq.1:

$$\text{Hydration degree} = \left(1 - \frac{w_{C_3S}+w_{C_2S}+w_{C_3A}+w_{C4AF}}{w_{0C_3S}+w_{0C_2S}+w_{0C_3A}+w_{0C4AF}}\right) \times 100\% \quad (1)$$

where, w_X is the mass fraction of mineral X obtained by XRD-Rietveld; w_{0X} is the initial mass fraction of mineral X.

Fig.7 shows the calculated degree of hydration for each group. With the incorporation of 0.03 wt% ANFs, the degree of hydration at 1 d and 3 d increased by 3.04% and 10.94%, respectively, indicating that the addition of ANFs promotes the early hydration of the cement, and the promotion effect is higher at 3

Table 3. Mineral composition of four samples.

Mineral composition	0-1d	3-1d	0-3d	3-3d
C_3S (wt%)	28.54	28.16	18.44	13.17
C_2S (wt%)	9.01	9.11	9.16	8.83
C_3A (wt%)	1.82	1.93	0.67	0.54
C_4AF (wt%)	4.14	2.69	3.17	1.79

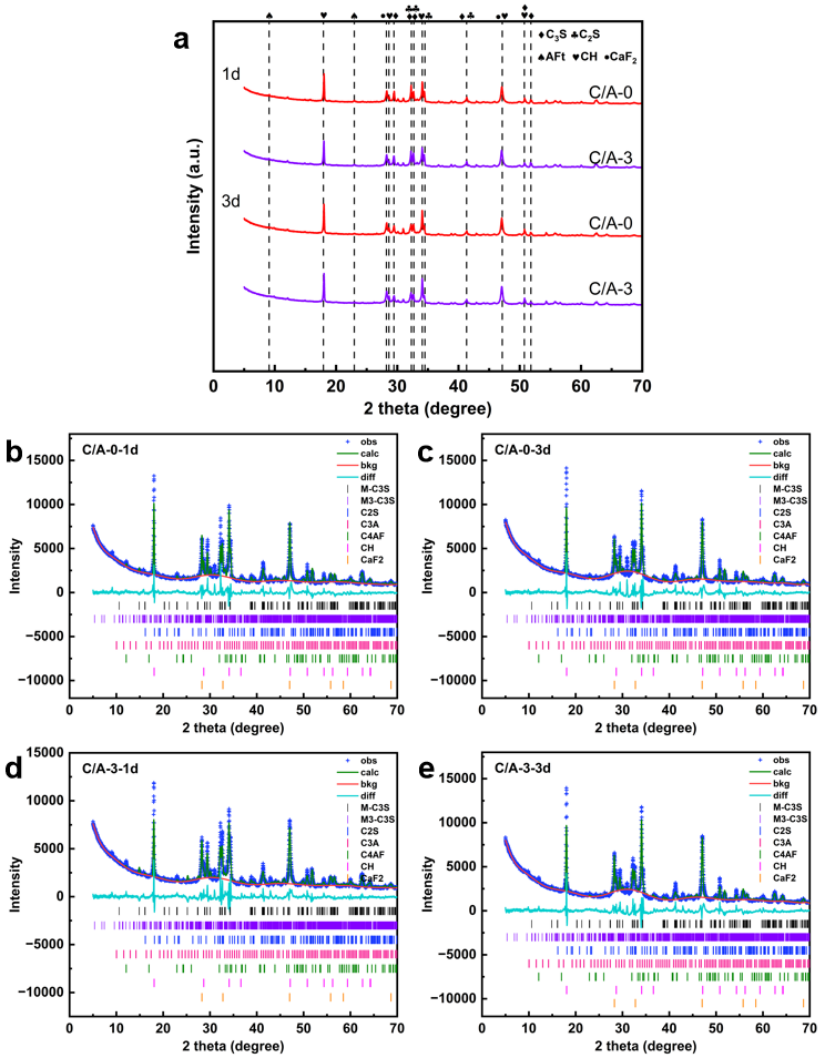

Fig.6. (a) XRD of four samples. (b) XRD of the sample without ANFs at 1 d. (c) XRD of the sample without ANFs at 3 d. (d) XRD of the sample with 0.03 wt% ANFs at 1 d. (e) XRD of the sample with 0.03 wt% ANFs at 3 d.

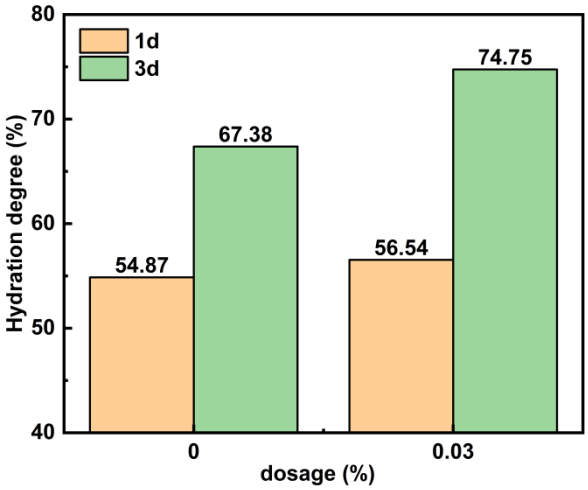

Fig.7. Hydration degree of four samples.

3.3.2 TG-DTG

The thermogravimetric analysis (TGA) curve is shown in Figure 8. The bound water content of the sample was calculated by Eq.2:

$$\text{Bound water} = \frac{w_{550℃} - w_{50℃}}{w_{50℃}} \times 100\% \quad (2)$$

where, $w_{50℃}$ and $w_{550℃}$ refer to the mass of the sample at 50 ℃ and 550 ℃, respectively.

Fig.9a shows the bound water content for each group. With the incorporation of 0.03wt% ANFs, the bound water contents of 1d and 3d were increased by 1.10% and 4.03%, respectively, indicating that the increase in the degree of hydration was consistent with the change in the degree of hydration calculated by XRD-Rietveld analysis. According to the thermogravimetric curve, the decomposition temperature range of $Ca(OH)_2$ is 375-550 °C in this paper. $m_{Ca(OH)2}$=7 4 g/mol, m_{H2O}= 18 g/mol, The content of $Ca(OH)_2$ was calculated by Eq.3:

$$w_{Ca(OH)_2} = \frac{w_{550℃} - w_{375℃}}{w_{550℃}} \times \frac{74}{18} \quad (3)$$

The content of $Ca(OH)_2$ is shown in Fig.9b, and the variation trend is consistent with the change of $Ca(OH)_2$ content calculated by XRD-Rietveld analysis.

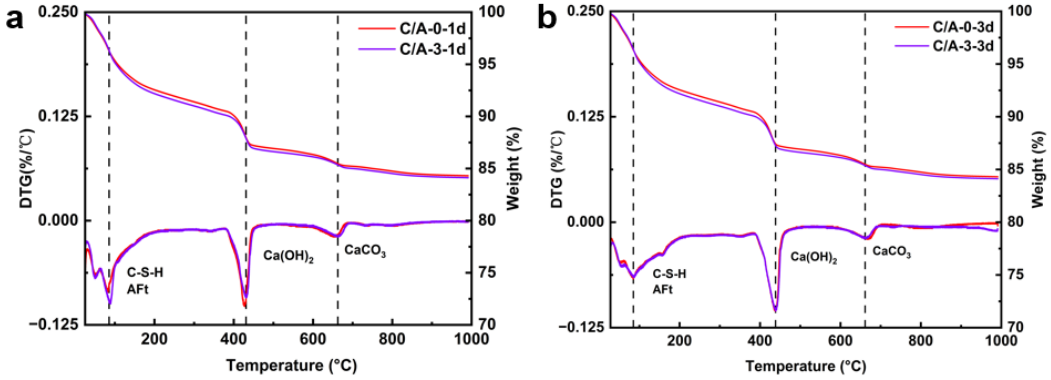

Fig.8. (a) TG/DTG of two samples at 1 d. (b) TG/DTG of two samples at 3 d.

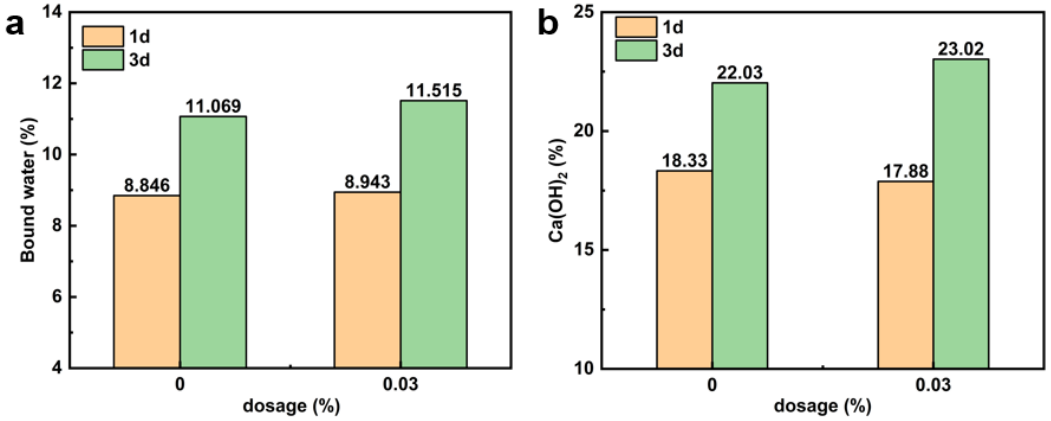

Fig.9. (a) Bound water of four samples. (b) Content of $Ca(OH)_2$ of four samples.

3.4. COMPRESSIVE STRENGTH ANG POROSITY

Fig.10 shows the results of compressive test and mercury intrusion. The 1 d compressive strength of the cement paste mixed with 0.03 wt% ANFs increased by 48.72% compared with the blank group, and the 3 d compressive strength and 28 d compressive strength increased by 23.39% and 16.50% respectively. According to the results of MIP, the porosity of the blank group was 26.48% at 28 d, and the porosity decreased to 22.68% at 28 d with 0.03wt% ANFs. The change of porosity is consistent with the change of compressive strength. According to the mercury intrusion differential curve, the addition of ANFs mainly reduced the proportion of 25-340 nm pores and 125-170 um pores, and increased the proportion of gel pores below 10 nm, indicating that the addition of ANFs can optimize the pore structure of cement paste, thereby improving its compressive strength.

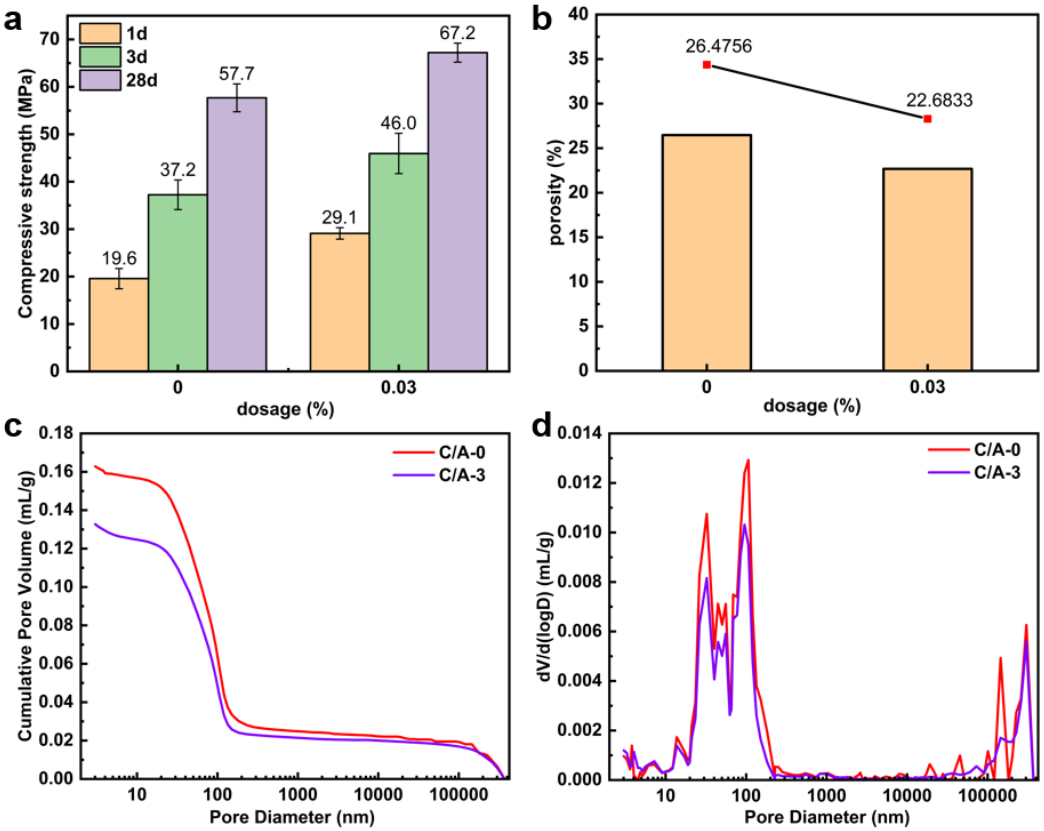

Fig.10. (a) Compressive strength at 1 d, 3 d and 28 d. (b) Porosity at 28 d. (c) Accumulated mercury curve at 28 d. (d) Differential mercury curve at 28 d.

4. CONCLUSION

In this study, ANFs was prepared in a short time by deprotonation and incorporated into cement paste to observe its effect on cement hydration. The main findings are as follows:

(1) The Kevlar fiber was etched into ANFs by adding water as a proton donor, which realized the preparation of nanomaterials with short time and low cost.

(2) The produced ANFs had a diameter of 13.70 ± 7.67 nm and could be well dispersed in water. The results of Fourier transform infrared spectroscopy and XRD scanning showed that the structure of ANFs was almost the same as that of its raw materials.

(3) ANFs can promote the early hydration of cement. When 0.03 wt% ANFs was added, the hydration heat of cement pastes in 3 d increased by 3.52% compared with the blank group, and the bound water content of 1d and 3d samples increased by 1.10% and 4.03% respectively. The content of four minerals was obtained by XRD-Rietveld analysis and the degree of hydration was calculated. The results showed that the degree of hydration of 1 d and 3 d samples increased by 3.04% and 10.94% respectively compared with the blank group.

(4) ANFs can optimize the pore structure of cement paste and improve its compressive strength. When 0.03 wt% ANFs was added, the 28 d porosity of cement paste decreased from 26.48% to 22.68%, in which the proportion of capillary pores and harmful macropores decreased and the proportion of gel pores increased. The strength of 1 d, 3 d and 28 d increased by 48.72%, 23.39% and 16.50 % respectively compared with the blank group.

ACKNOWLEDGMENTS

The financial support from the National Natural Science Foundation of China (No. 52178197) for current research are gratefully acknowledged.

REFERENCE

[1] M.S.M. Norhasri, M.S. Hamidah, A.M. Fadzil, Applications of using nano material in concrete: A

review, Constr. Build. Mater. 133 (2017) 91–97. https://doi.org/10.1016/j.conbuildmat.2016.12.005.

[2] Y. Qing, Z. Zenan, K. Deyu, C. Rongshen, Influence of nano-SiO2 addition on properties of hardened cement paste as compared with silica fume, Constr. Build. Mater. 21 (2007) 539–545. https://doi.org/10.1016/j.conbuildmat.2005.09.001.

[3] R. Yu, P. Spiesz, H.J.H. Brouwers, Effect of nano-silica on the hydration and microstructure development of Ultra-High Performance Concrete (UHPC) with a low binder amount, Constr. Build. Mater. 65 (2014) 140–150. https://doi.org/10.1016/j.conbuildmat.2014.04.063.

[4] D. Adak, M. Sarkar, S. Mandal, Effect of nano-silica on strength and durability of fly ash based geopolymer mortar, Constr. Build. Mater. 70 (2014) 453–459. https://doi.org/10.1016/j.conbuildmat.2014.07.093.

[5] P. Hou, J. Qian, X. Cheng, S.P. Shah, Effects of the pozzolanic reactivity of nanoSiO2 on cement-based materials, Cem. Concr. Compos. 55 (2015) 250–258. https://doi.org/10.1016/j.cemconcomp.2014.09.014.

[6] A. Bede, A. Pop, M. Moldovan, I. Ardelean, The influence of silanized nano-SiO2 on the hydration of cement paste: NMR investigations, AIP Conf. Proc. 1700 (2015) 060009. https://doi.org/10.1063/1.4938459.

[7] H. Wu, F. Torabian Isfahani, W. Jin, C. Xu, E. Redaelli, L. Bertolini, Modification of properties of reinforced concrete through nanoalumina electrokinetic treatment, Constr. Build. Mater. 126 (2016) 857–867. https://doi.org/10.1016/j.conbuildmat.2016.09.098.

[8] H.I. Ahmed, Behavior of magnetic concrete incorporated with Egyptian nano alumina, Constr. Build. Mater. 150 (2017) 404–408. https://doi.org/10.1016/j.conbuildmat.2017.06.022.

[9] C. Li, G. Li, Q. Du, X. Wu, F. Wang, J. Lin, J. Yue, H. Zhang, L. Tang, H. Jia, Effects of nano-alumina on Portland concrete at low temperatures (5 ℃), Case Stud. Constr. Mater. 20 (2024) e02922. https://doi.org/10.1016/j.cscm.2024.e02922.

[10] G. Rawat, S. Gandhi, Y.I. Murthy, Influence of nano-TiO2 on the chloride diffusivity of concrete, Emerg. Mater. Res. 11 (2022) 495–505. https://doi.org/10.1680/jemmr.22.00056.

[11] Z. Li, B. Han, X. Yu, S. Dong, L. Zhang, X. Dong, J. Ou, Effect of nano-titanium dioxide on mechanical and electrical properties and microstructure of reactive powder concrete, Mater. Res. Express 4 (2017) 095008. https://doi.org/10.1088/2053-1591/aa87db.

[12] F.E.-Z.M. Mostafa, P. Smarzewski, G.M.A. El Hafez, A.A. Farghali, W.M. Morsi, A.S. Faried, T.A. Tawfik, Analyzing the Effects of Nano-Titanium Dioxide and Nano-Zinc Oxide Nanoparticles on the Mechanical and Durability Properties of Self-Cleaning Concrete, Materials 16 (2023) 6909. https://doi.org/10.3390/ma16216909.

[13] Y. Ruan, B. Han, X. Yu, W. Zhang, D. Wang, Carbon nanotubes reinforced reactive powder concrete, Compos. Part Appl. Sci. Manuf. 112 (2018) 371–382. https://doi.org/10.1016/j.compositesa.2018.06.025.

[14] P.-C. Ma, N.A. Siddiqui, G. Marom, J.-K. Kim, Dispersion and functionalization of carbon nanotubes for polymer-based nanocomposites: A review, Compos. Part Appl. Sci. Manuf. 41 (2010) 1345–1367. https://doi.org/10.1016/j.compositesa.2010.07.003.

[15] M.-J. Lim, H.K. Lee, I.-W. Nam, H.-K. Kim, Carbon nanotube/cement composites for crack monitoring of concrete structures, Compos. Struct. 180 (2017) 741–750. https://doi.org/10.1016/j.compstruct.2017.08.042.

[16] A. Carriço, J.A. Bogas, A. Hawreen, M. Guedes, Durability of multi-walled carbon nanotube reinforced concrete, Constr. Build. Mater. 164 (2018) 121–133. https://doi.org/10.1016/j.conbuildmat.2017.12.221.

[17] M.O. Mohsen, M.S. Al Ansari, R. Taha, N. Al Nuaimi, A.A. Taqa, Carbon Nanotube Effect on the Ductility, Flexural Strength, and Permeability of Concrete, J. Nanomater. 2019 (2019) 6490984. https://doi.org/10.1155/2019/6490984.

[18] T.M. Viana, B.A. Bacelar, I.D. Coelho, P. Ludvig, W.J. Santos, Behaviour of ultra-high performance concretes incorporating carbon nanotubes under thermal load, Constr. Build. Mater. 263 (2020) 120556. https://doi.org/10.1016/j.conbuildmat.2020.120556.

[19] Z. Zhao, C. Xie, Y. Liu, Z. Zhao, Y. Ouyang, Y. Song, T. Shi, Early-age thermal cracking performance of carbon nanotube modified face slab concrete, Constr. Build. Mater. 433 (2024) 136666. https://doi.org/10.1016/j.conbuildmat.2024.136666.

[20] A. Guo, Z. Sun, N. Sathitsuksanoh, H. Feng, A Review on the Application of Nanocellulose in Cementitious Materials, Nanomaterials 10 (2020) 2476. https://doi.org/10.3390/nano10122476.

[21] A. Cengiz, M. Kaya, N. Pekel Bayramgil, Flexural stress enhancement of concrete by incorporation of algal cellulose nanofibers, Constr. Build. Mater. 149 (2017) 289–295. https://doi.org/10.1016/j.conbuildmat.2017.05.104.

[22] O.A. Hisseine, W. Wilson, L. Sorelli, B. Tolnai, A. Tagnit-Hamou, Nanocellulose for improved concrete performance: A macro-to-micro investigation for disclosing the effects of cellulose filaments on strength of cement systems, Constr. Build. Mater. 206 (2019) 84–96. https://doi.org/10.1016/j.conbuildmat.2019.02.042.

[23] K.S. Kamasamudram, W. Ashraf, E.N. Landis, R.I. Khan, Effects of ligno– and delignified– cellulose nanofibrils on the performance of cement-based materials, J. Mater. Res. Technol. 13 (2021) 321–335. https://doi.org/10.1016/j.jmrt.2021.04.090.

[24] H. Sun, Z. Que, H. Wei, A. Zhou, X. Peng, W. Cui, X. Wang, Tunning matrix rheology and mechanical performance of ultra-high performance concrete using cellulose nanofibers, Nanotechnol. Rev. 11 (2022) 1570–1582. https://doi.org/10.1515/ntrev-2022-0099.

[25] J. Zhang, F. Huang, Y. Wu, T. Fu, B. Huang, W. Liu, R. Qiu, Mechanical properties and interface improvement of bamboo cellulose nanofibers reinforced autoclaved aerated concrete, Cem. Concr. Compos. 134 (2022) 104760. https://doi.org/10.1016/j.cemconcomp.2022.104760.
[26] J.A. Reglero Ruiz, M. Trigo-López, F.C. García, J.M. García, Functional Aromatic Polyamides, Polymers 9 (2017) 414. https://doi.org/10.3390/polym9090414.
[27] J. Yao, J. Jin, E. Lepore, N.M. Pugno, C.W.M. Bastiaansen, T. Peijs, Electrospinning of p-Aramid Fibers, Macromol. Mater. Eng. 300 (2015) 1238–1245. https://doi.org/10.1002/mame.201500130.
[28] S. Ifuku, H. Maeta, H. Izawa, M. Morimoto, H. Saimoto, Facile preparation of aramid nanofibers from Twaron fibers by a downsizing process, RSC Adv. 4 (2014) 40377–40380. https://doi.org/10.1039/C4RA06924B.
[29] H. Yan, J. Li, W. Tian, L. He, X. Tuo, T. Qiu, A new approach to the preparation of poly(p-phenylene terephthalamide) nanofibers, RSC Adv. 6 (2016) 26599–26605. https://doi.org/10.1039/C6RA01602B.
[30] R.R. Burch, W. Sweeny, H.W. Schmidt, Y.H. Kim, Preparation of aromatic polyamide polyanions: a novel processing strategy for aromatic polyamides, Macromolecules 23 (1990) 1065–1072. https://doi.org/10.1021/ma00206a026.
[31] M. Yang, K. Cao, L. Sui, Y. Qi, J. Zhu, A. Waas, E.M. Arruda, J. Kieffer, M.D. Thouless, N.A. Kotov, Dispersions of Aramid Nanofibers: A New Nanoscale Building Block, ACS Nano 5 (2011) 6945–6954. https://doi.org/10.1021/nn2014003.
[32] B. Yang, L. Wang, M. Zhang, J. Luo, X. Ding, Timesaving, High-Efficiency Approaches To Fabricate Aramid Nanofibers, ACS Nano 13 (2019) 7886–7897. https://doi.org/10.1021/acsnano.9b02258.

STRENGTH IMPROVEMENT AND MECHANIZATION OF THERMAL STORAGE FUNCTIONALIZED LC^3 COMPOSITES

Chengwei Xu
Master student, School of Civil Engineering, Harbin Institute of Technology, Harbin, China

Yunshi Pan
Master student, School of Civil Engineering, Harbin Institute of Technology, Harbin, China

Yushi Liu*
Associate Professor, School of Civil Engineering, Harbin Institute of Technology, Harbin, China

Yingzi Yang*
Professor, School of Civil Engineering, Harbin Institute of Technology, Harbin, China

ABSTRACT:

Thermal storage functionalized LC^3 composites effectively achieve energy-saving and carbon reduction in buildings. However, the addition of phase change material (PCM) particles leads to a significant decrease in strength, which imposes higher requirements on early performance. To address this issue, this paper proposes the application of microwave curing to improve the strength and microstructure of thermal storage functionalized LC^3 composites. As a result of the experiment, microwave curing at a power of 320 W for 5 minutes increased the 3-day compressive strength of heat-stored LC^3 by 87.3%, without adverse effects on the later strength. The results of hydration product analysis showed that the enhancement of early strength by microwave curing was mainly attributed to the promotion of early hydration of clinker and the activation of pozzolanic reaction occurred calcined clay. The additional formation of C-(A)-S-H gel reduced the matrix porosity, improved overall integrity, and enhanced the microstructure.

Keywords: Limestone calcined clay cement, Phase change microcapsules, Microwave curing, Hydration mechanisms, Mechanical properties

1.INTRODUCTION

Limestone calcined clay cement (LC^3) has garnered significant attention because of its ability to substitute up to 45 wt% of cement clinker with SCMs[1–3]. By partially substituting cement clinker with calcined clay and limestone in the production process, it is possible to significantly reduce energy consumption and greenhouse gas emissions without compromising the mechanical properties and workability of the cementitious material[4,5]. The application of building materials with phase change microcapsule (PCM) can attain thermal comfort temperature inside the buildings and improve the buildings energy efficiency, due to the heat store

and release ability[6]. Currently, there is limited research on the combined use of PCMs with LC^3 cementitious materials. Introducing PCMs into LC^3 cementitious materials allows for the design of low-carbon gelling system with auxiliary temperature regulation capabilities[7]. Yu et al. have developed a novel functionalized green composite cementitious material called LC^3-based HSCM containing form-stable PCMs[8]. However, the introduction of PCM typically inhibits hydration reactions and introduces numerous weak interfaces, which have adverse effects on the hydration process and overall integrity of the matrix[9]. This leads to an increase in porosity and poorer mechanical performance of the sample in the early stages[10–13].

Microwave curing is a rapid curing method that utilizes the thermal effect generated by the interaction between the alternating magnetic field produced by electromagnetic waves within the frequency range of 300 MHz to 300 GHz and the polar molecules inside the material. This leads to an increase in curing temperature and promotes the rapid development of early strength. Compared to other curing methods, microwave curing offers advantages such as lower energy consumption and higher curing efficiency due to its ability to achieve more uniform heating. Currently, the effectiveness of microwave curing in enhancing the performance of cementitious materials has been confirmed, especially for systems containing a significant amount of active mineral admixtures, where microwave curing often exhibits a good improvement in early strength[14,15]. LC^3 replaces traditional clinker with calcined clay/metakaolin (CC/MK) and limestone powder (LSP)[16], which means microwave curing has a potential to enhance the early strength of the LC^3. However, there is limited research on the application of microwave curing to composite cementitious materials composed of multiple mineral admixtures, and the stimulating effect and mechanism of microwave curing on the early strength of LC^3 cementitious materials are not yet clear.

This study aims to optimize the early strength of heat-stored LC^3 using microwave curing methods and investigate the influence of different microwave powers on the development of early strength, hydration products, and microstructural evolution. Additionally, whether microwave curing not only enhances the early-stage performance of samples but also significantly impacts their long-term properties was investigated. This study aims to provide a theoretical foundation for expanding the functional applications of such green cementitious materials.

2. RAW MATERIALS, PREPARATION AND CHARACTERIZATION

2.1 RAW MATERIALS

The LC^3 cement system used in this study consists of cement clinker, calcined clay, limestone, and gypsum, the mineral composition of LC^3 cement is presented in Table 1. In order to achieve a dense packing effect, silica fume, an active mineral admixture, was added to the system. The median particle size of silica fume is 350 nm, with an average specific surface area of 21,000 m^2/kg. PCM was obtained from the Laboratory of Civil Engineering Materials, Harbin Institute of Technology, China. The average particle size of the PCM was 2.19μm, the standard deviation was 0.8μm and the particle size distribution was more concentrated and uniform, as shown in Fig. 1(a) and (b). The Polycarboxylate Superplasticizer(PCA) used in the experiments was produced by Shanghai Sanrui Chemical Co., Ltd., with a solid content of 50 wt%. The defoaming agent (DA) was obtained from Zhuben Oil and Fat (Suzhou) Co., Ltd. Its purpose is to reduce the adverse effects of air bubbles generated by the superplasticizer during the mixing and vibration processes on the

compactness of the matrix.

Table 1 The mineral composition of LC^3 cement (%).

	Cement clinker	Calcined clay	Limestone
CaO	64.26	0.23	55.51
SiO_2	20.78	54.55	0.2
Al_2O_3	5.08	42.68	0.11
MgO	2.30	0.06	0.3
Fe_2O_3	3.29	0.58	0.05
K_2O	-	0.13	-
TiO_2	-	1.77	-
SO_3	2.15	-	0.02
LOI	2.14	-	43.81

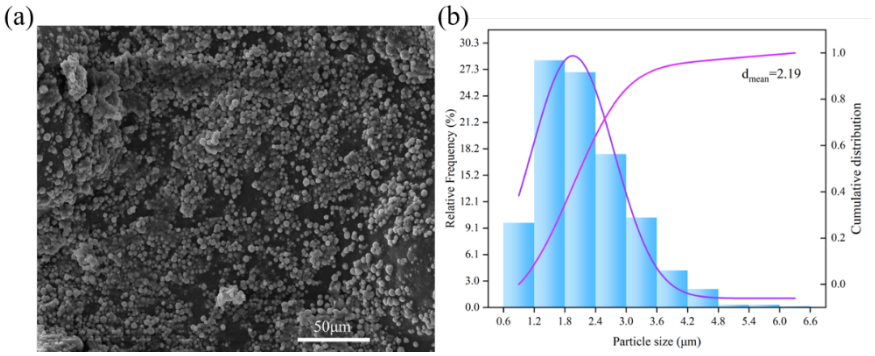

Fig.1 The fundamental properties of PCM: (a) for SEM; (b) for particle size distribution.

2.2 RAW MATERIALS, PREPARATION AND CHARACTERIZATION

2.2.1 RAW MATERIALS

The specific mix proportions are shown in Table 2. The LC^3 with PCM contains a 5% mass fraction of PCM. LC^3-HSC represents high-strength composites prepared using LC^3, while LC^3-MPCM-HSC represents high-strength composites prepared using LC^3 with phase change microcapsules. The mix proportions were calculated based on the theory of particle packing density.

The preparation process of LC^3-HSC and LC^3-MPCM-HSC is shown in Fig. 2. It is worth noting that prior to mixing, the PCM were pre-dispersed in a certain quantity of purified water using magnetic stirring.

Table 2 Mix ratio design (kg/m^3)

	LC^3-HSC	LC^3-MPCM-HSC
LC^3	920	-
LC^3 with PCM	-	920
Silica fume	212.5	212.5
Sand	1090	1090
PCA	21.87	21.87
DA	0.96	0.96
Water	228.12	228.12

w/b	0.2	0.2
w/c	0.25	0.25

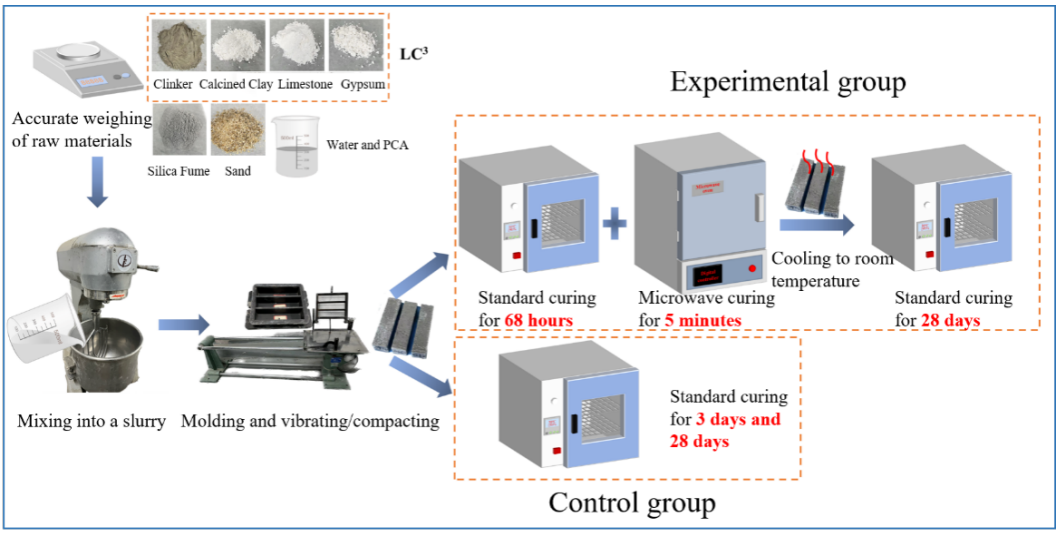

Fig.2 The preparation process of specimen.

2.2.2 CURING PROCEDURES

The microwave equipment is Microwave Muffle Furnace (MAKEWAVE, MKX-M1A) with the maximum microwave power of 1600 W. In order to investigate the influence of microwave power and energy on the early strength of specimens, experiments were conducted with a power gradient ranging from 80 W to 320 W. The microwave power and the corresponding output energy are shown in Table 3. After curing under standard conditions for 68 hours, all specimens in the experimental groups underwent 5 minutes of microwave curing at different powers and were then cooled to room temperature. Subsequent tests were conducted at the standard curing ages of 3 days and 28 days. The control group underwent standard curing after demolding until the designated curing age, where standard curing refers to placing the samples in a controlled curing room with a temperature of 20±1℃ and a relative humidity of at least 95% for further curing.

Table 3 Microwave curing procedures design.

Sample		Microwave power (W)	Energy (J)
LC^3-HSC / LC^3-MPCM-HSC	STC	-	-
	MC 80	80	24000
	MC 136	136	40800
	MC 200	200	60000
	MC 256	256	76800
	MC 320	320	96000

Note: STC stands for standard curing; MC x represents microwave curing with a power of x W.

2.3 CHARACTERIZATION METHODS

2.3.1 MECHANICAL PROPERTY

The mechanical properties of the specimens were characterized by compressive strength and flexural strength. According to the standard "GB/T17671-2021," the compressive strength and flexural strength of the samples were tested using a universal testing machine with a maximum load of 10 kN. The loading rate for compressive strength testing was 2.4 kN/s[17].

2.3.2 HYDRATION PRODUCT ANALYSIS

The hydration products of specimens at different microwave powers and curing ages were characterized using X-ray diffraction (XRD) with an X'pert PRO diffractometer and thermogravimetric-differential scanning calorimetry (TG-DSC) with an SDT650 instrument.

XRD analysis was performed using Cu Kα radiation with a testing voltage and current of 40 kV and 40 mA, respectively. The scan range was 5° to 60°, with a scan step of 0.013 and a dwell time of 70 seconds per step. CaF_2 was used as an internal standard. For TG-DSC testing, approximately 30 mg of each sample was taken. The temperature range was 25°C to 1000°C, with a heating rate of 10°C/min, and the entire heating process was conducted under a nitrogen atmosphere.

2.3.3 MICROSTRUCTURE ANALYSIS

The samples were observed using scanning electron microscopy (SEM) to examine their microstructure. Prior to observation, the samples were vacuum-dried and covered with a thin layer of gold foil by sputtering for 180 seconds at a current of 15 mA[18]. The hydration products and interface characteristics were analyzed using energy-dispersive X-ray spectroscopy (EDS). Mercury intrusion porosimetry (MIP) was employed to analyze the influence of microwave curing on the internal pore structure of the matrix[19]. The maximum pressure applied was 206.8 MPa, and the minimum measurable pore diameter was 2.13 nm. Before testing, all samples were cut into small particles with diameters ranging from 3 to 5 mm and freeze-dried under vacuum conditions for 24 hours.

3. RESULTS AND DISCUSSION

3.1 PHYSIC-MECHANICAL PROPERTIES

3.1.1 COMPRESSIVE STRENGTH

Under standard curing conditions, the compressive strengths of LC^3-HSC and LC^3-MPCM-HSC specimens at 3 days were 23.15 MPa and 20.72 MPa, respectively. Fig. 3(a) illustrates the compressive strengths of LC^3-HSC specimens after 68 hours of standard pre-curing and 5 minutes of microwave curing at different power levels. The compressive strengths of the specimens at 3 days were as follows: 27.98 MPa at 80W, 30.65 MPa at 136W, 33.21 MPa at 200W, 35.39 MPa at 256W, and 40.08 MPa at 320W. Compared to standard curing, the 3-day compressive strengths of LC^3-HSC specimens respectively increased by 20.82%, 32.38%, 43.42%, 52.85%, and 73.1% after 5 minutes of microwave curing at different power levels. This indicates a significant enhancement in the early strength of LC^3-HSC due to microwave curing, and the 3-day strength of LC^3-HSC is positively correlated with microwave power. Fig. 3(b) presents the 3-day compressive strengths of LC^3-MPCM-HSC specimens under different curing regimes. Under standard curing conditions, the 3-day strength of LC^3-MPCM-HSC was 10.5% lower than that of LC^3-HSC. However, after 5 minutes of microwave curing at 320W, the 3-day

compressive strength of LC^3-MPCM-HSC reached 38.79 MPa, which was a 67.6% improvement compared to LC^3-HSC under standard curing. Under microwave exposure, the early strength development of LC^3-MPCM-HSC followed a similar trend to that of conventional LC^3-HSC. The increase in compressive strength showed an approximately linear positive correlation with microwave power when the power was below 256W. However, there was a significant increase in compressive strength when the power was raised from 256W to 320W. Therefore, microwave curing also significantly enhances the early strength of LC^3-MPCM-HSC.

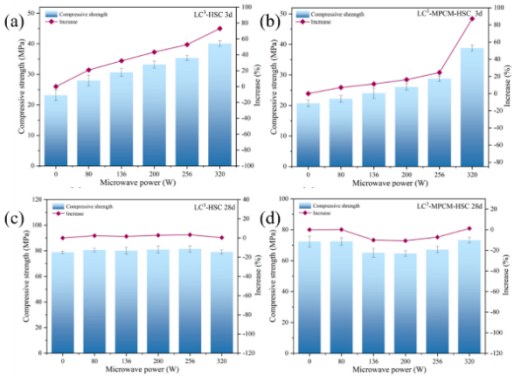

Fig.3 The compressive strength of LC^3-HSC at 3 days (a); 28 days (c) and LC^3-MPCM-HSC at 3 days (b) ; 28 days (d) with different microwave curing power.

After 5 minutes of microwave curing, the LC^3-HSC and LC^3-MPCM-HSC specimens were cooled to room temperature and continued standard curing for 28 days. The compressive strengths of the specimens are shown in Fig. 4(c) and (d). Under standard curing conditions, the 28-day compressive strengths of LC^3-HSC and LC^3-MPCM-HSC specimens were 78.77 MPa and 72.35 MPa, respectively. After 5 minutes of microwave curing at 320W, the 28-day compressive strengths of LC^3-HSC and LC^3-MPCM-HSC specimens were 79.05 MPa and 73.29 MPa, respectively. From the graph, it can be observed that there is only a slight difference in the 28-day compressive strengths between the specimens cured with different microwave powers and the specimens under standard curing. This difference does not seem to have a clear correlation with microwave power, and the differences in compressive strength between the specimens cured at all power levels and the standard curing control group are within ±5%. Therefore, it can be concluded that for both LC^3-HSC and LC^3-MPCM-HSC, microwave curing at various power levels does not have a significant negative impact on the later hydration and strength development. It does not lead to a severe loss of compressive strength in the later stages.

3.1.2 FLEXURAL STRENGTH

Under standard curing conditions, the flexural strengths of LC^3-HSC and LC^3-MPCM-HSC specimens at 3 days were measured at 6.68 MPa and 6.12 MPa, respectively. Fig. 4(a) shows the flexural strengths of LC^3-HSC specimens after pre-curing for 68 hours under standard conditions and then subjecting them to microwave curing for 5 minutes at different power levels. At microwave powers of 80 W, 136 W, 200 W, 256 W, and 320 W, the flexural strengths of the specimens at 3 days were 7.36 MPa, 7.92 MPa, 8.55 MPa, 7.94 MPa, and 10.12 MPa, respectively. Compared to standard curing, microwave curing at different power levels for 5 minutes increased the flexural strengths at 3 days by 10.18%, 18.67%, 28.01%, 18.97%, and 51.62%, respectively. Microwave curing also had a positive effect on the flexural strength of LC^3-MPCM-HSC specimens. Similar to the compressive strength trend, the flexural strength of LC^3-MPCM-HSC specimens increased with increasing microwave power. Fig. 4(b) illustrates the flexural strengths of LC^3-MPCM-HSC specimens. At microwave powers of 80 W, 136 W, 200 W, 256 W, and 320 W, the flexural strengths were 5.91 MPa, 6.43 MPa, 6.72 MPa, 6.81 MPa, and 7.41 MPa, respectively. At 80 W, the flexural strength of LC^3-MPCM-HSC decreased by 3.43%. However, as the microwave

power increased to 200 W and 256 W, the flexural strengths of LC^3-MPCM-HSC specimens improved by 9.81% and 11.39% compared to standard curing, respectively. When the microwave power reached 320 W, the flexural strength at 3 days increased by 21.14% compared to standard curing. The improvement in flexural strength through microwave curing primarily arises from the enhanced interface between the cementitious material and aggregates. Overall, suitable power levels of microwave curing have a significant positive impact on the early flexural strength of LC^3-MPCM-HSC.

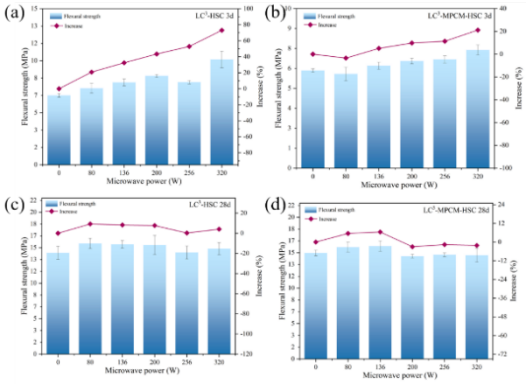

Fig.4 The flexural strength of LC^3-HSC at 3 days (a); 28 days (c) and LC^3-MPCM-HSC at 3 days (b) ; 28 days (d) with different microwave curing power.

After 5 minutes of microwave curing, the 28-day flexural strengths of LC^3-HSC and LC^3-MPCM-HSC specimens are shown in Fig. 4(c) and (d), respectively. Under standard curing conditions, the 28-day flexural strengths were measured at 14.28 MPa for LC^3-HSC and 14.96 MPa for LC^3-MPCM-HSC. However, after applying a microwave power of 320 W for 5 minutes, the 28-day flexural strengths was not significantly different from that of the control group. For all microwave power levels, the differences in flexural strengths between LC^3-HSC and LC^3-MPCM-HSC specimens and the standard curing control group were within ±6%. Therefore, in terms of flexural strength, microwave curing does not have a significant adverse impact on the later-stage strength development for the LC^3 system. In conclusion, short-duration microwave curing at moderate power levels can significantly improve the early mechanical performance of LC^3-HSC and LC^3-MPCM-HSC without compromising the later-stage strength.

3.1.3 RELATIONSHIP BETWEEN MECHANICAL PROPERTIES AND MICROWAVE ENERGY

Microwaves are electromagnetic waves generated by mutually orthogonal electric and magnetic fields. Under microwave radiation, the alternating electromagnetic waves interact with polar particles in the material, causing the polar ions in the material to rotate and oscillate, thereby generating thermal energy and increasing the temperature of the substance. Different types of cementitious materials exhibit varying absorption and response behaviors to microwave energy. In order to investigate the relationship between the degree of performance enhancement and microwave energy, the microwave energy output at a predetermined power level was taken as the independent variable. Regression analyses were conducted on the 3-day compressive strength and flexural strength of LC^3-HSC and LC^3-MPCM-HSC, respectively. The results are shown in Fig. 5. From the graph, it can be observed that both compressive strength and flexural strength of LC^3-HSC and LC^3-MPCM-HSC exhibit a nearly linear positive correlation with microwave energy.

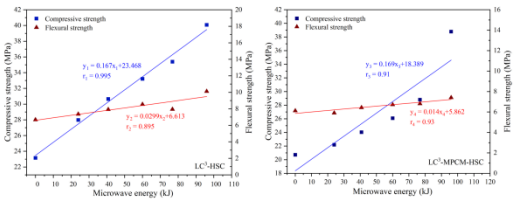

Fig.5 The relationship between early intensity and microwave energy.

Specifically, for LC^3-HSC, the linear correlation coefficients between 3-day compressive strength, flexural strength, and microwave energy are 0.995 and 0.895, respectively. The linear

relationship between compressive strength and microwave energy is more significant. At the same time, the slope of the fitted line for compressive strength and microwave energy is larger, indicating that compressive strength is more sensitive to changes in microwave energy. As for LC^3-MPCM-HSC, the linear correlation coefficient between flexural strength and microwave energy is 0.91 and the linear correlation coefficient between compressive strength and microwave energy is 0.93. The difference between the two coefficients is small, but the slope of the fitted line for compressive strength is still greater than that of flexural strength, demonstrating a stronger sensitivity. This behavior is similar to that observed in LC^3-HSC without PCM.

It is worth noting that the early compressive strength of LC^3-MPCM-HSC exhibits significant differences in sensitivity to microwave action at different power levels. This may be due to the trade-off relationship between the promoting effect of the thermal effect generated by microwave curing on the hydration of cementitious materials and the microstructural damage caused by the high-speed oscillation of polar molecules within the system during microwave radiation. Compared to ordinary LC^3-HSC, LC^3-MPCM-HSC has more pores and defects after 68 hours of pre-curing. When the microwave power is low, the rapid stimulation of hydration activity in the cementitious material is limited, and its beneficial effect is hindered by microstructural degradation, resulting in a reduced magnitude of early strength improvement. However, when the microwave power is further increased, the hydration activity of the cementitious material is significantly stimulated, and the increased production of gel-like hydration products compensates for the microstructural degradation without affecting the overall structure. Microwave curing dominates the promotion of hydration, leading to a significant increase in compressive strength.

In conclusion, regardless of the presence of PCM, the compressive strength of LC^3-HSC is more sensitive to changes in microwave energy, and increasing microwave energy has a more significant effect on improving compressive strength.

However, there are certain boundary conditions to the positive correlation between early mechanical performance and microwave energy, meaning that the early mechanical performance of specimens does not infinitely increase with the increase in microwave energy. In this study, as the microwave energy continued to increase to 400 W, both LC^3-HSC and LC^3-MPCM-HSC specimens experienced varying degrees of damage during the 5-minute microwave curing process, as shown in Fig. 6. When the internal stress generated by the oscillation of polar particles in the system under microwave action, as well as the thermal stress generated by the thermal effect, exceeded the restraining force provided by the matrix bond strength, internal microcracks rapidly expanded and propagated, eventually leading to specimen failure or even cracking. Therefore, the energy of microwave curing should be limited within a certain range, which allows for rapid improvement of early strength while avoiding specimen damage and failure.

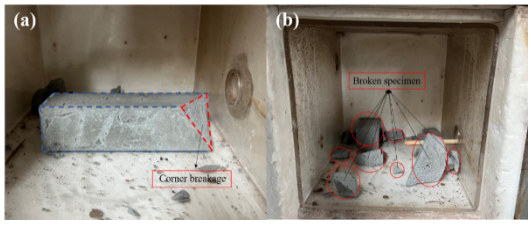

Fig.6 The photo of damaged specimen at 400W power: (a) for LC^3-HSC and (b) for LC^3-MPCM-HSC.

3.2 EFFECT OF MICROWAVE CURING ON HYDRATION PRODUCTS

3.2.1 X-RAY DIFFRACTION ANALYSIS

The XRD patterns of LC^3-HSC and LC^3-MPCM-

HSC specimens at the 3-day age are shown in Fig. 7(a) and (b), respectively. The main hydration products in the system include CH, AFt, AFm phases dominated by carbonated aluminate and monosulfate hydrate phases[20], and C-(A)-S-H gel, with the C-(A)-S-H gel primarily existing in an amorphous form. From the graph, it can be observed that microwave curing did not alter the types of main hydration products in the system. However, it can be observed that the diffraction peaks corresponding to AFt in the samples after microwave curing are weakened. This is due to the thermal effect generated during the microwave curing, which raises the temperature of the matrix. At around 50°C, AFt becomes unstable and transforms into AFm, and during the heating process, HC also becomes unstable and transforms into MC[21,22]. The internal temperature variation in the specimen under microwave radiation is the main reason for the transformation of hydration products in the samples after microwave curing. Moreover, diffraction peaks corresponding to hydrocalumite can be observed in the samples after microwave curing. Hydrocalumite is one of the representative products in the AFm system, and it exhibits high thermal stability. It is one of the typical products resulting from the pozzolanic reaction occurred in metakaolin, primarily occurring during the later stages of hydration [23,24]. Therefore, it can be inferred that microwave curing has a certain stimulating effect on the pozzolanic reactivity of palygorskite. The XRD patterns of LC^3-HSC and LC^3-MPCM-HSC samples under different curing conditions at the 28-day age are shown in Fig. 7(c) and (d), respectively. By comparison, it can be seen that microwave curing at different powers did not cause any changes in the types of hydration products at the 28-day age. The diffraction peak intensities of the major crystalline phases also showed minimal differences. This is consistent with the variation trend of compressive strength and the comprehensive thermal analysis results (see Section 3.2.2 for details).

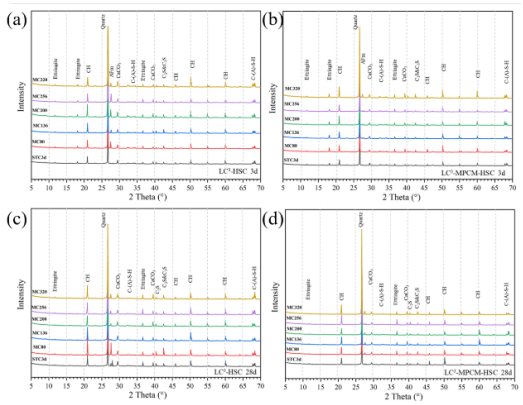

Fig.7 X-ray diffractograms of the LC^3-HSC cured at: a) 3 days; c) 28 days and the LC^3-MPCM-HSC cured at: b) 3 days; d) 28 days.

3.2.2 THERMOGRAVIMETRIC ANALYSIS

The TG/DTG curves of LC^3-HSC and LC^3-MPCM-HSC at the 3-day age are shown in Fig. 8. In the DTG curve, the weight loss peak around 100°C is attributed to the dehydration of AFt and C-(A)-S-H gel. The shoulder peak around 130°C is generated by the thermal instability of the AFm phase. The broad peak near 450°C represents the weight loss due to the decomposition of CH in the system. The narrow peak between 700°C and 800°C is caused by the decomposition of calcite.

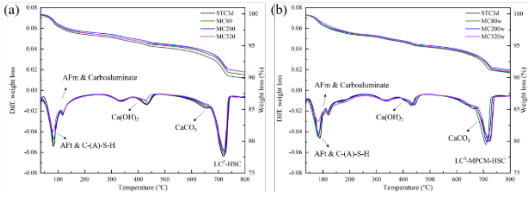

Fig.8 The TG/DTG curves of LC^3-HSC (a) and LC^3-MPCM-HSC (b) specimens at 3 days at different microwave curing power.

Upon comparison, it can be observed that there are no new weight loss peaks in the DTG curves of microwave-cured LC^3-HSC and LC^3-MPCM-HSC samples, indicating that microwave curing did not generate new hydration products in the system, which is consistent with the XRD analysis results. It is worth noting that at a microwave power of 320 W, a significant reduction in the area of the weight loss peak

corresponding to AFt was observed in both LC^3-HSC and LC^3-MPCM-HSC. This is due to the rapid temperature rise caused by higher microwave power, leading to the destabilization of AFt and its transformation into AFm starting at around 50°C. This further confirms that the thermal effect generated within the matrix due to microwave radiation may be the main factor influencing the formation and evolution of early hydration products.

The CH content in the samples at various microwave powers, as calculated from the thermogravimetric test results, is shown in Fig. 9. In both LC^3-HSC and LC^3-MPCM-HSC samples, a decreasing trend in CH content is observed with increasing microwave power. When the pozzolanic reaction process is accelerated by the activation of the pozzolanic activity of palygorskite in calcined clay, it consumes more CH generated by clinker hydration. The enhanced activity of pozzolanic reaction of palygorskite with increased microwave power may be one of the main reasons for the decrease in CH content. It is worth noting that the variation in CH content with different microwave curing powers in LC^3-HSC and LC^3-MPCM-HSC samples shows a high degree of consistency with the trend of compressive strength changes with power. This suggests that microwave curing has a significant effect on the early strength improvement of LC^3-HSC and LC^3-MPCM-HSC, largely due to the activation of pozzolanic reaction activity of palygorskite. When the pozzolanic reaction of palygorskite is promoted, more C-(A)-S-H gels are generated in the hydration products, which fills the pores and improves the microstructure, leading to a significant increase in the matrix strength.

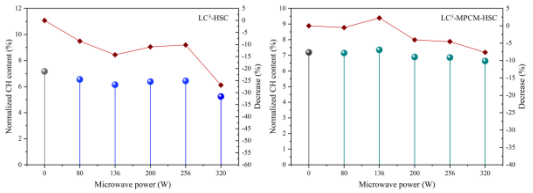

Fig.9 The CH content of LC^3-HSC and LC^3-MPCM-HSC samples at 3d

4. CONCLUSIONS

This study focuses on the effects of different microwave powers on the early and later strengths, hydration products, pore structure, and microstructure of thermal storage functionalized LC^3 composites. The main conclusions are as follows:

(1) Microwave curing can significantly improve the early strength of LC^3-HSC and LC^3-MPCM-HSC without compromising the later strength. With increasing microwave power, the enhancement of short-term microwave curing on early strength shows an increasing trend.

(2) Regardless of the presence of PCM, the compressive strength of LC3-HSC is more sensitive to changes in microwave energy, and increasing microwave energy has a more significant effect on improving compressive strength.

(3) Microwave curing promotes the hydration of LC3 cementitious materials mainly due to the thermal effect stimulating the pozzolanic reaction of calcined clay and the mutual transformation of AFm phases in the system during the temperature variation of the matrix.

ACKNOWLEDGEMENTS

The financial supports from the Harbin Manufacturing Technology Innovation Talents Project by Harbin Science and Technology Bureau of China (No. 2022HBRCGD001) and the National Natural Science Foundation of China (No. 52278254, No. 51902068).

REFERENCES

[1] M. Antoni, J. Rossen, F. Martirena, K. Scrivener, Cement substitution by a combination of metakaolin and limestone, Cement and Concrete Research 42 (2012) 1579–1589.

https://doi.org/10.1016/j.cemconres.2012.09.006.
[2] K. Scrivener, F. Martirena, S. Bishnoi, S. Maity, Calcined clay limestone cements (LC^3), Cement and Concrete Research 114 (2018) 49–56. https://doi.org/10.1016/j.cemconres.2017.08.017.
[3] K. Vance, M. Aguayo, T. Oey, G. Sant, N. Neithalath, Hydration and strength development in ternary portland cement blends containing limestone and fly ash or metakaolin, Cement and Concrete Composites 39 (2013) 93–103. https://doi.org/10.1016/j.cemconcomp.2013.03.028.
[4] M. Sharma, S. Bishnoi, F. Martirena, K. Scrivener, Limestone calcined clay cement and concrete: A state-of-the-art review, Cement and Concrete Research 149 (2021) 106564. https://doi.org/10.1016/j.cemconres.2021.106564.
[5] J. Wang, D. Shi, Y. Xia, M. Liu, X. Ma, K. Yu, Y. Zhao, J. Zhang, Stabilization/solidification of radioactive borate waste via low-carbon limestone calcined clay cement (LC^3), Journal of Environmental Chemical Engineering 12 (2024) 113129.
https://doi.org/10.1016/j.jece.2024.113129.
[6] K. Yu, M. Jia, W. Tian, Y. Yang, Y. Liu, Enhanced thermo-mechanical properties of cementitious composites via red mud-based microencapsulated phase change material: Towards energy conservation in building, Energy 290 (2024) 130301. https://doi.org/10.1016/j.energy.2024.130301.
[7] A. Marani, L. Zhang, M.L. Nehdi, LC^3 with microencapsulated phase change materials for reducing embodied and operational carbon, Cement and Concrete Research 172 (2023) 107234.
https://doi.org/10.1016/j.cemconres.2023.107234.
[8] K. Yu, C. Liu, L. Li, W. Tian, Y. Yang, Y. Liu, Carbon-negative heat-stored limestone calcined clay cement mortar containing form-stable phase change materials, Journal of Cleaner Production 437 (2024) 140703. https://doi.org/10.1016/j.jclepro.2024.140703.
[9] H. Abbasi Hattan, M. Madhkhan, A. Marani, Thermal and mechanical properties of building external walls plastered with cement mortar incorporating shape-stabilized phase change materials (SSPCMs), Construction and Building Materials 270 (2021) 121385. https://doi.org/10.1016/j.conbuildmat.2020.121385.
[10] V.D. Cao, S. Pilehvar, C. Salas-Bringas, A.M. Szczotok, L. Valentini, M. Carmona, J.F. Rodriguez, A.-L. Kjøniksen, Influence of microcapsule size and shell polarity on thermal and mechanical properties of thermoregulating geopolymer concrete for passive building applications, Energy Conversion and Management 164 (2018) 198–209. https://doi.org/10.1016/j.enconman.2018.02.076.
[11] V.D. Cao, S. Pilehvar, C. Salas-Bringas, A.M. Szczotok, J.F. Rodriguez, M. Carmona, N. Al-Manasir, A.-L. Kjøniksen, Microencapsulated phase change materials for enhancing the thermal performance of Portland cement concrete and geopolymer concrete for passive building applications, Energy Conversion and Management 133 (2017) 56–66. https://doi.org/10.1016/j.enconman.2016.11.061.
[12] M. Hunger, A.G. Entrop, I. Mandilaras, H.J.H. Brouwers, M. Founti, The behavior of self-compacting concrete containing micro-encapsulated Phase Change Materials, Cement and Concrete Composites 31 (2009) 731–743. https://doi.org/10.1016/j.cemconcomp.2009.08.002.
[13] M. Ren, X. Wen, X. Gao, Y. Liu, Thermal and mechanical properties of ultra-high performance concrete incorporated with microencapsulated phase change material, Construction and Building Materials 273 (2021) 121714.
https://doi.org/10.1016/j.conbuildmat.2020.121714.
[14] Y. Pan, Y. Zhang, S. Li, Effects of isothermal microwave curing on steel fibre-reinforced

reactive powder concrete: Strength, microstructure and hydration products, Construction and Building Materials 302 (2021) 124435. https://doi.org/10.1016/j.conbuildmat.2021.124435.

[15] S. Li, Y. Zhang, Y. Pan, X. Gao, Effects of isothermal microwave heating on the strength and microstructure of ultra-high performance concrete embedded with steel fibers, Journal of Materials Research and Technology 14 (2021) 1893–1902. https://doi.org/10.1016/j.jmrt.2021.07.092.

[16] M. Antoni, J. Rossen, F. Martirena, K. Scrivener, Cement substitution by a combination of metakaolin and limestone, Cement and Concrete Research 42 (2012) 1579–1589. https://doi.org/10.1016/j.cemconres.2012.09.006.

[17] D. Shi, Y. Xia, Y. Zhao, J. Wang, X. Ma, M. Liu, K. Yu, J. Zhang, W. Tian, Valorization of steel slag into sustainable high-performance radiation shielding concrete, Journal of Building Engineering 91 (2024) 109650. https://doi.org/10.1016/j.jobe.2024.109650.

[18] J. Wang, Y. Zhao, D. Shi, Y. Xia, M. Liu, X. Ma, K. Yu, Microstructure and radiation shielding properties of lead-fiber reinforced high-performance concrete, Ceramics International 50 (2024) 23656–23667. https://doi.org/10.1016/j.ceramint.2024.04.089.

[19] D. Shi, Y. Xia, Y. Zhao, X. Ma, J. Wang, M. Liu, K. Yu, Evaluation of technical and gamma radiation shielding properties of sustainable ultra-high performance geopolymer concrete, Construction and Building Materials 436 (2024) 137003. https://doi.org/10.1016/j.conbuildmat.2024.137003.

[20] S. Berger, C.C.D. Coumes, P. Le Bescop, D. Damidot, Influence of a thermal cycle at early age on the hydration of calcium sulphoaluminate cements with variable gypsum contents, Cement and Concrete Research 41 (2011) 149–160. https://doi.org/10.1016/j.cemconres.2010.10.001.

[21] D. Wang, C. Shi, N. Farzadnia, Z. Shi, H. Jia, Z. Ou, A review on use of limestone powder in cement-based materials: Mechanism, hydration and microstructures, Construction and Building Materials 181 (2018) 659–672. https://doi.org/10.1016/j.conbuildmat.2018.06.075.

[22] T. Matschei, B. Lothenbach, F.P. Glasser, Thermodynamic properties of Portland cement hydrates in the system CaO–Al2O3–SiO2–CaSO4–CaCO3–H2O, Cement and Concrete Research 37 (2007) 1379–1410. https://doi.org/10.1016/j.cemconres.2007.06.002.

[23] H.G. Midgley, P. Bhaskara Rao, Formation of stratlingite, 2CaO.SiO2.Al2O3.8H2O, in relation to the hydration of high alumina cement, Cement and Concrete Research 8 (1978) 169–172. https://doi.org/10.1016/0008-8846(78)90005-4.

[24] J. Ding, Y. Fu, J.J. Beaudoin, Strätlingite formation in high alumina cement - silica fume systems: Significance of sodium ions, Cement and Concrete Research 25 (1995) 1311–1319. https://doi.org/10.1016/0008-8846(95)00124-U.

[25] Y. Renhe, L. Baoyuan, W. Zhongwei, Study on the pore structure of hardened cement paste by SAXS, Cement and Concrete Research 20 (1990) 385–393. https://doi.org/10.1016/0008-8846(90)90028-V.

[26] Z.-L. Jiang, Y.-J. Pan, J.-F. Lu, Y.-C. Wang, Pore structure characterization of cement paste by different experimental methods and its influence on permeability evaluation, Cement and Concrete Research 159 (2022) 106892. https://doi.org/10.1016/j.cemconres.2022.106892.

Part2:

Structure/Construction

MACHINE LEARNING MODEL FOR RC BEAM SUBJECTED TO SEVERAL SEISMIC LOAD AND CRACK REPAIR

Miki Matsubahashi
Grad. Student, Division of Engineering, Muroran Institute of Technology, Muroran, Japan

Sota Sugawara and Mizuki Nakamura
Grad. Student, Division of Sustainable and Environ. Eng., Muroran Institute of Technology, Muroran, Japan.

Yuya Takase
Prof, College of Design and Manufacturing Technology, Muroran Institute of Technology, Muroran, Japan.

ABSTRACT:
Japan is prone to large earthquakes. Therefore, buildings may be subjected to multiple seismic loads. In this study, the RC cantilever specimens were subjected to shear loads three times. As the results of the test, as the number of loads increased, the crack width opened; and the stiffness decreased without repair. However, with crack repair, the crack width became small; and the stiffness recovered slightly. In addition, the machine learning model were constructed; and then it could reasonably estimate the envelope curves.
Keywords: crack repair, RC beam, machine learning, prediction accuracy

1. INTRODUCTION

In Japan, large earthquakes occur frequently, and many structures have been damaged by seismic load. Recently, the seismic design method has been improved, therefore buildings constructed according to the new seismic standards almost never collapse. However, while they may not collapse, there is an increasing number of buildings that have repairable damage such as cracking and spalling of the facing concrete. According to the guidelines published by the Architectural Institute of Japan, damage to reinforced concrete (hereinafter referred to as RC) buildings after an earthquake is classified into five levels, from damage level I to V[1]. Buildings classified as damage levels II and III can continue to be used after repairs.

As for crack repair methods, crack injection is used when the crack width is about 0.2 to 2 mm, and section repair is used when the crack width exceeds this range or spalling occurs. Focusing on the crack injection method, previous studies[2-4] have often verified the effectiveness of crack repair by applying force to RC specimens until they reach maximum load, then repairing the cracks and reloading the specimens. However, as mentioned above, in recent years there have been more cases where members corresponding to damage levels II to III are repaired, or where structures are re-exposed to large seismic motions after repair and the repair process is repeated. However, there are very few examples where the effectiveness of repairs in such cases has been verified.

To continuously and safely use buildings, it is essential to properly evaluate the performance of such structures. Generally, when analytically evaluating member performance, finite element analysis and other methods are used. However, it seems extremely difficult to analytically reproduce the performance of members that have undergone multiple loadings and repairs. On the other hand, in recent years, artificial intelligence (AI) has been utilized in various fields, and it is also being widely applied in the fields of architectural engineering and concrete engineering. By using machine learning, a subset of AI, it is possible to estimate maximum loads and envelope curves, which may also be applicable to the structures mentioned earlier.

In this study, load tests of RC cantilevers subjected to repeated horizontal loading and repair are conducted, and several machine learning models are constructed to verify whether the envelope curves of members subjected to repeated damage and repair can be predicted, and the effects of explanatory variables are discussed.

2. TEST PROCEDUE

2.1 TEST PRAMETER

Table 1 shows the specimen parameters, while **Tables 2** and **3** show the material properties of the concrete and the mechanical properties of the rebars, respectively. In this paper, we fabricated four specimens listed in **Table 1** and conducted loading tests. In order to achieve a state where crack repair is possible, the damage inflicted on the specimens was set to damage levels II and III. In addition, we prepared two types of specimens: one type was reloaded without crack repair after the damage was inflicted, and the other type was reloaded after the cracks were repaired. After the second loading, we also used the presence or absence of repair as a parameter and applied horizontal loading three times in total. The specimen names are composed of the symbol D-II or D-III

indicating the level of damage, followed by the symbols N (no repair) or R (repair).

For the repaired specimens, after the first loading (1st Load), the specimens were removed from the loading frame, then repaired, and allowed to cure before the second loading (2nd Load). Similarly, after the second load, the specimens were repaired again before the third load (3rd Load) was applied. As a result, the material properties of the concrete differed with each loading cycle, as shown in **Table 2**. For the unrepaired specimens, three loading cycles were applied consecutively, so only one type of material property was used.

Table 1 Test parameters.

ID	p_t (%)	p_w (%)	$B \times D$ (mm × mm)	Damage	Crack repair	
					Afte l[st] load	Afte 2[nd] load
D-II-N	1.44	0.20	210×300	II	–	–
D-II-R	〃	〃	〃	II	–	–
D-III-N	〃	〃	〃	III	✓	✓
D-III-R	〃	〃	〃	III	✓	✓

Table 2 Concrete properties.

ID	Load Cycle	f_c (N/mm^2)	f_t (N/mm^2)	E_c (N/mm^2)	Age
D-II-R, D-III-R	1st Load	23.7	1.95	20.1	47
	2nd Load	22.9	1.31	25.1	60
	3rd Load	23.3	1.55	19.7	69
D-II-N, D-III-N	All	23.3	1.55	19.7	69

f_c: compressive strength, f_t: tensile strength, E_c: Young's modulus, Age: age during test.

Table 3 Mechanical properties or rebar.

Rebar type	f_y (N/mm^2)	E_s (N/mm^2)	f_u (N/mm^2)	EL (%)
D6	488	250	584	15.2
D16 (Stub)	399	176	551	12.5
D16 (Beam)	393	187	568	22.9

f_y: yield strength, E_s: Young's modulus, f_u: ultimate strength, EL: elongation

2.2 DETAILS OF SPECIMEN

Fig. 1 shows the specimen specifications. The shape of the specimen is an RC cantilever beam with a section size of 210 mm × 300 mm, which is about half the size of a full-size beam. The rebars are mainly deformed bars with a bamboo-like pattern, but due to constraints related to the attachment of the specimen to the loading setup and the anchorage length of the main reinforcing bars, only threaded reinforcing bars were used for the main reinforcement. An H-shaped steel was installed at the ends of the beams to fix the bracing devices and provide mechanical anchorage for the main rebars.

In the test, we focus on beams that exhibit shear failure first. The tensile reinforcement ratio p_t is set to 1.44 %, the stirrup ratio p_w is 0.20%, and the shear span to depth ratio M/Qd is 1.91. The shear margin α, calculated by the following formula, is 0.79.

$$M_u = 0.9 \times a_t \times \sigma_y \times d \quad (1)$$

$$Q_{su} = \left\{ \frac{0.068 p_t^{0.23} (f_c + 18)}{M/Qd + 0.12} + 0.85\sqrt{\sigma_{wy} p_w} \right\} b \cdot j \quad (2)$$

$$\alpha = \frac{Q_{su}}{Q_{mu}} \quad (3)$$

where, σ_{wy} is the yield strength of stirrup (N/mm^2), b is the beam width (mm) and j is the stress center distance (mm).

2.3 LOADING SETUP

Figs. 2 and **3** show the loading setup and the loading cycle, respectively. Two 200 mm × 200 mm H-shaped steel beams were installed on both sides of the loading axis of the beam. These two H-shaped steel beams were fixed together with full-thread bolts, and a 500 kN actuator was attached to the H-shaped steel beam on the reaction wall side to apply positive and negative alternating cyclic loading. The horizontal displacement δ at the height center of the loaded H-shaped steel was measured by a high-sensitivity displacement meter with a capacity of 25 mm, which was fixed to a measuring frame attached to the stub. The deformation angle R was calculated by dividing δ by the loading height of 500 mm. Based on **Fig. 3**, for specimens D-II-N, D-II-R, D-III-N, and D-III-R, the results of the preliminary experiments were used to apply repeated load cycles twice, up to R = 1/100 rad and 1/75 rad to achieve damage levels II and III, respectively. The third load cycle was then applied.

2.4 CRACK REPAIR TECHNIQUE

Fig. 4 shows the crack repair. For the crack repair method, the epoxy injection method, which is widely used in practice and can fill cracks internally, was used. The repair process is shown in Figure 1. Cracks of 0.2 mm or wider were targeted for repair. After cleaning the surface of these cracks, washers were applied, and the crack surfaces were sealed with a fast-setting epoxy adhesive. After the adhesive cured, epoxy resin was injected with an injection device until the resin overflowed from the crack edges.

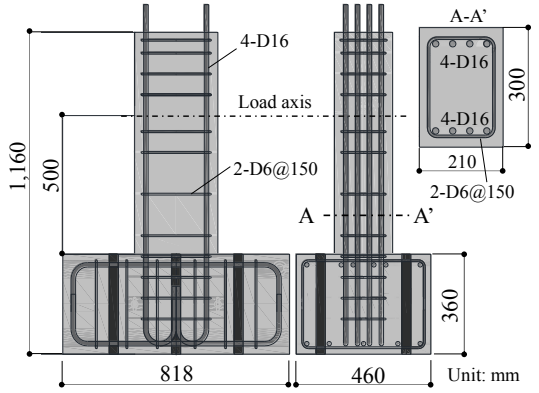

Fig. 1 Specimen dimension.

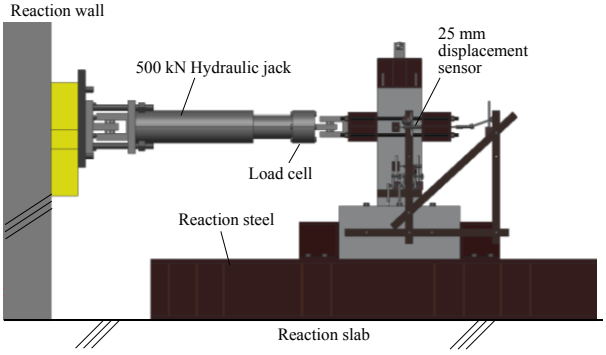

Fig. 2 Loading setup.

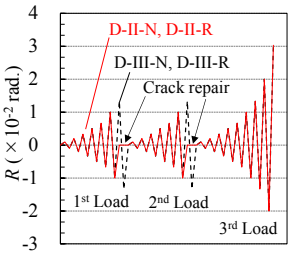

Fig. 3 Loading cycle.

Fig. 4 Crack repair.

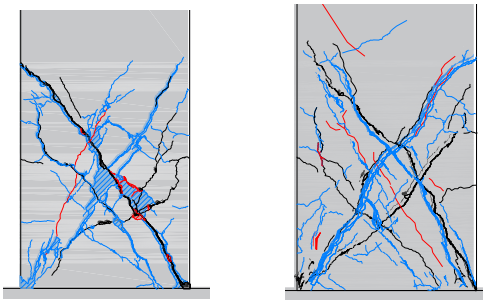

(a) D-III-N (b) D-III-R

Fig. 5 Crack pattern.

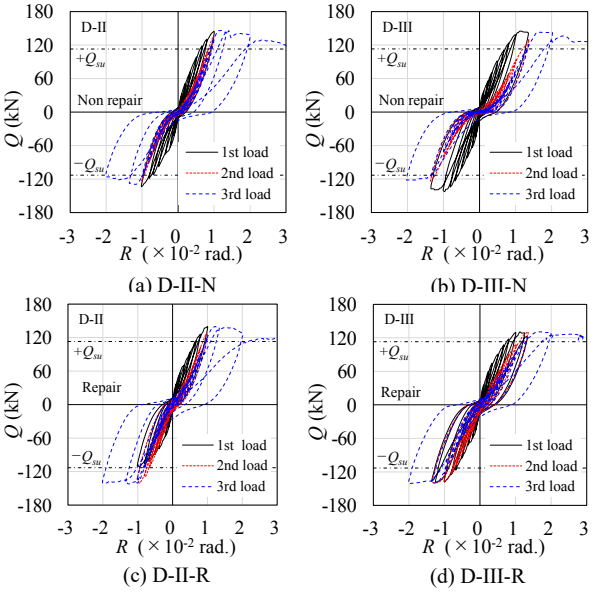

(a) D-II-N (b) D-III-N

(c) D-II-R (d) D-III-R

Fig. 6 Load-displacement (*Q* - *R*) curves.

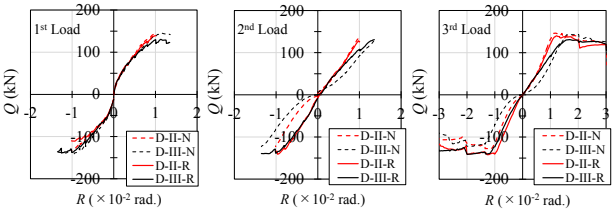

(a) 1st Load (b) 2nd Load (c) 3rd Load

Fig. 7 Comparison of envelope curves for each load cycle.

2.5 TEST RESULTS

Figs. 5 to **7** show the crack pattern, the load-deformation curves, and the envelope curves of each load cycle, respectively. Table 4 shows the maximum residual crack width.

Focusing on **Fig. 5**, the diagonal cracks were generated in all specimens, then the load reached at the peak. In D-II-N and D-III-N, which are referred to as non-repair specimens, the crack widths of crack generated at the 1st load were increased at the 2nd and 3rd loads. From **Table 4**, the crack width of 3rd load was larger than it of 2nd load. Meanwhile, for D-II-R and D-III-R, which are referred to as repair specimens, the crack widths of the crack generated at 2nd and 3rd loads were smaller than that of 1st load.

Subsequently, focusing on **Fig. 6**, it can be observed that for all specimens, the maximum load was reached at R = 1.00-1.33 × 10^{-2} rad. and then the load gradually decreased to about 80 % of the maximum load at R = 2.0-3.0 × 10^{-2} rad. From these results, it can be judged that the failure mode of these specimens was shear failure.

Observing **Fig. 7**, in the 1st load of **Fig. 7** (a), since all four specimens were under the same conditions, they exhibited almost the same behavior despite some variability. However, in the 2nd load of **Fig. 7** (b), while D-II-N and D-II-R showed almost the same behavior on the positive side, the stiffness of unrepaired D-II-N was smaller on the negative side. In D-III, the stiffness of the unrepaired specimen was also lower on the positive side, and when comparing D-II-N and D-III-N, the latter had lower stiffness. The same trend can be observed in the 3rd load. In other words, the damage in the first load was significant, and without repair, the stiffness in the second and third loads decreased greatly, but it could be recovered somewhat by repair. However, as shown in **Fig. 6**, the stiffness could not be restored to the level of the first load.

Table 4 Maximum residual crack width ω

ID	R (×10^{-2} rad.)	ω (mm) 1st Load	ω (mm) 2nd Load	ω (mm) 3rd Load
D-II-N	1.00 rad.	0.5	0.95	0.4
D-II-R	1.00 rad.	0.85	0.4	0.1
D-III-N	1.33 rad.	1.4	1.5	2.35
D-III-R	1.33 rad.	1.7	0.9	0.25

Therefore, to evaluate the performance of the members under multiple seismic motions and with or without repairs, it is considered important to adequately predict the envelope curves or energy absorption reflecting the presence or absence of repairs for each load cycle, not just the residual strength.

3. MACHINE LEARNING

3.1 LEARNING ALGORYTHM

Fig. 8 shows the machine learning algorithms used in this study. In this research, decision tree-based machine learning algorithms, namely LightGBM (hereafter referred to as LG), XGBoost (hereafter referred to as XG), and Random Forest[6] (hereafter referred to as RF), were used. These algorithms build a learning model while analyzing data in a tree-structured manner during training with teacher data. RF has a relatively long history in machine learning and has been used to predict test results such as the flow of high flow mortar[7]. XG introduces gradient boosting, where the errors of the previous decision tree are gradually improved as the next decision tree is constructed. LG also introduces a leaf-wise growth approach, which allows for more efficient and faster learning compared to XG.

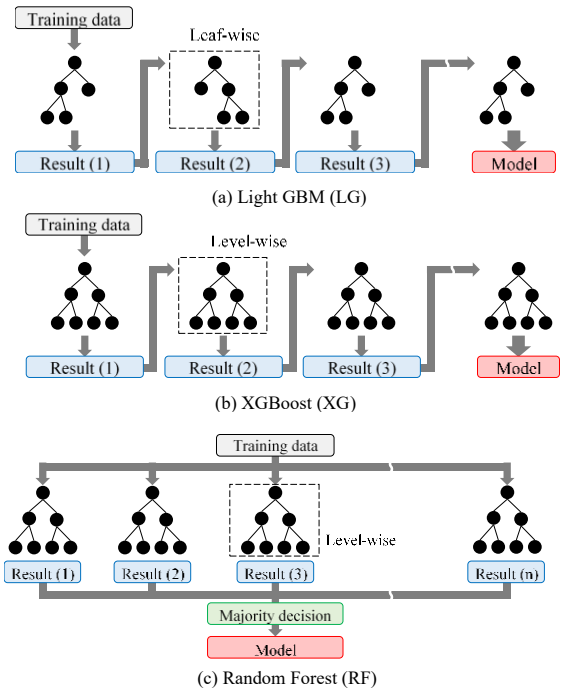

Fig. 8 Comparison of envelope curves[6].

Table 5 Learning models.

Type	ID	ω	Cyc 2	Cyc 3	D-II-N	D-II-R
M-1	M-1–ω	Non	✓	✓	✓	✓
	M-1+ω	✓	✓	✓	✓	✓
M-2	M-2–ω	Non	Non	✓	✓	✓
	M-2+ω	✓	Non	✓	✓	✓
M-3	M-3–ω	Non	✓	Non	✓	✓
	M-3+ω	✓	✓	Non	✓	✓
M-4	M-4–ω	Non	✓	✓	Non	✓
	M-4+ω	✓	✓	✓	Non	✓
M-5	M-5–ω	Non	✓	✓	✓	Non
	M-5+ω	✓	✓	✓	✓	Non

3.2 LEARNING TECHNIQUE

In the study, nine types of explanatory variables were used; thus, δ, p_w, positive/negative PN (+1 or -1), number of repairs (Rep), number of load cycles (Cyc), maximum displacement experienced up to that point (δ_{max}), f_c, f_t, and ω. In machine learning, only numerical data can be learned. Therefore, when learning the presence or absence of repairs, the states were coded as follows: 0 for no repair, 1 for the first repair after the first load, and 2 for the second repair after the second load. Similarly, the number of load cycles was coded as 1, 2, and 3 for the 1st, 2nd, and 3rd load, respectively. Although pw was common to all specimens in this study, it was adopted in consideration of future model expansion. The variables fc and ft reflected slightly different values depending on the number of load cycles and the presence or absence of repairs.

Table 5 shows the learning cases. In this paper, 10 types of learning models were constructed for each of the three algorithms. These were broadly divided into five cases from M-1 to M-5, with each case having models that include and exclude ω. For example, before an earthquake, ω cannot be determined before the survey, but sometimes it can be determined after the survey. Therefore, we tested whether taking ω into account improves the learning accuracy. In M-2 and M-3, the effect of the number of load cycles was investigated by excluding the 2nd and 3rd load cycles from all the samples. In M-4 and M-5, the effect of the presence or absence of repairs was examined by excluding D-II-N and D-II-R, respectively. The number of teacher data rows in M-1 was 4748.

4. DISCUSSION

4.1 FEATURE IMPORTANCE

Fig. 9 shows the density distribution of feature importance in M-1. Feature importance refers to the frequency of use of the explanatory variables during training. In both figures (a) and (b), δ has the highest importance, and when ω is included in the training, ω also becomes relatively important. In RF, PN has high importance, but it is hardly used in LG and XG. Conversely, δ_{max} and Rep, which have low importance in RF, have high importance in LG and XG. Thus, the explanatory variables considered important differ between the algorithms, and these differences are likely to affect the prediction accuracy and the characteristics of the prediction results.

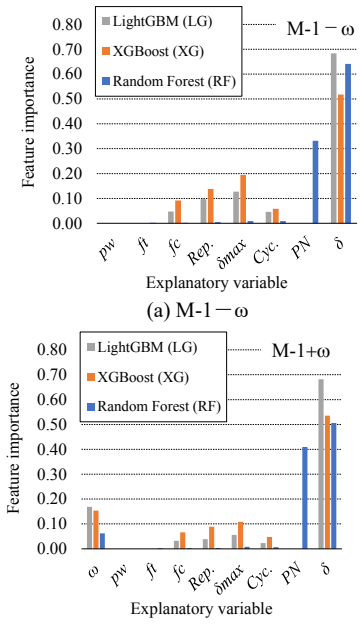

Fig. 9 Feature importance.

4.2 PREDICTION OF ENVELOPE CURVES

Fig. 10 shows examples of the predicted results of the envelope curves. In **Fig. 10**, the 1st, 2nd and 3rd loads are shown from left to right. Due to space limitations, not all prediction results can be shown, so only representative results focusing on D-III-R are shown. In **Fig. 10** (a) M-1, all three algorithms accurately predicted the experimental values because all specimens were included in the training. However, looking at **Fig. 10** (b) to (e), errors can be seen in the prediction results for untrained items, specifically the 2nd Load in M-2, the 3rd Load in M-3, D-II-N in M-4, and D-II-R in M-5. Since the 1st load is common to all items, the predictions were reasonably accurate, even for items not included in the training for M-4 and M-5.

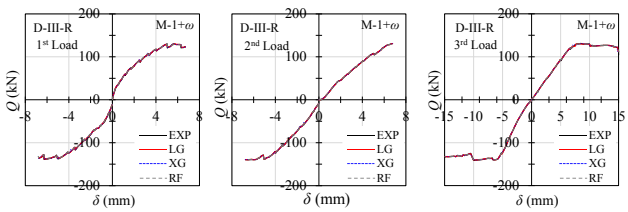

(a) M-1+ω/D-III-R

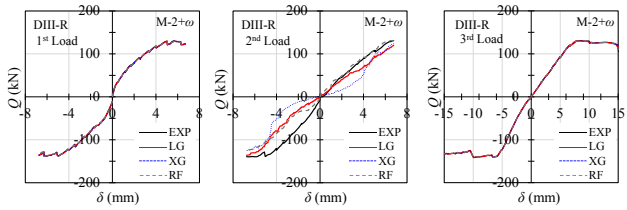

(b) M-2+ω/D-III-R

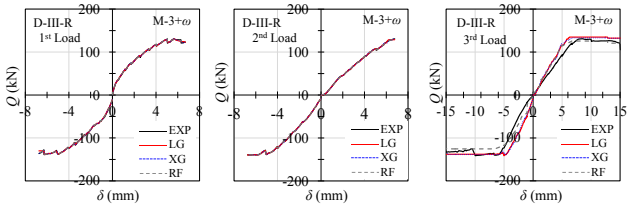

(c) M-3+ω/D-III-R

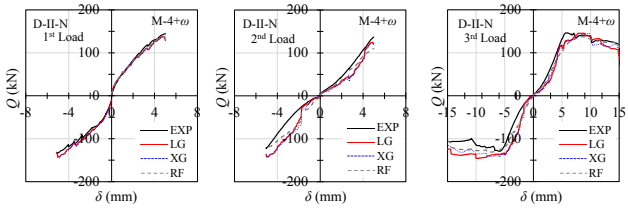

(d) M-4+ω/D-II-N

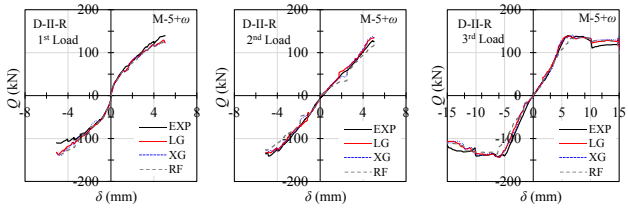

(e) M-5+ω/D-II-R

Fig. 10 Prediction results.

4.3 ROOT MEAN SQUARE ERROR (RMSE)

Fig. 11 shows the comparison of RMSE between test and predicted results. In this figure, the results of LG, XB and RF are shown from the left to right sides. For each result, the results of the 1st, 2nd and 3rd loads are shown. Moreover, the left and right sides are the result of the model without and with ω, respectively.

The RMSE can be calculated as follows.

$$RMSE = \sqrt{\frac{1}{n}\sum_{i=1}^{n}(y_i - \hat{y}_i)^2} \qquad (3)$$

where, n is the number of test data, y_i is test results, and $\hat{y}_i$ is predicted values.

(1) M-1

First, let's focus on the results of M-1 in **Fig. 11**(a), where all specimens were included in the training. The RMSE of the 1st load without ω is 0.52-2.54 kN, which is somewhat larger compared to 0.28-1.43 kN for the 2nd and 3rd loads. The reason for this is that, as mentioned earlier, the conditions for the 1st Load are the same for all specimens except for slight differences in FC, resulting in four sets of teacher data. In contrast, there are no other subjects with the same conditions for the 2nd and 3rd loads. In other words, when predicting the results of the 1st Load, there are four possibilities, leading to greater variability, whereas for the 2nd and 3rd Loads, there is only one possibility, leading to almost no error. Conversely, this implies that the RMSE for the 1st Load represents a common error. In addition, when focusing on the presence or absence of ω, it is generally better to include ω since the RMSE is smaller. Therefore, to accurately predict the load, it is desirable to include ω.

(2) EFFECT OF NUMBER OF LOADS

From **Figs. 11**(b) and (c), we can observe the results of M-2 and M-3, which exclude the 2nd and 3rd loads, respectively. Obviously, the RMSE for the 2nd and 3rd loads is large in M-2 and M-3, respectively. Especially in XG, the RMSE for D-II-R and D-III-R in (b) is larger than that of LG and RF, but it is slightly improved by including ω in the training. As shown in **Fig. 8**, the slightly higher importance of Cyc in XG suggests the possibility of overfitting, making LG or RF more desirable for predicting the results of this experiment. Comparing M-2 and M-3, the difference due to the algorithms is smaller in M-3. Therefore, to improve the prediction accuracy, it is important to collect more teacher data for the 2nd load.

(3) EFFECT OF REPAIR

From **Figs. 11**(d) and (e), we can observe the effect of the presence or absence of repairs on the prediction accuracy. Looking at D-II-N in **Fig. 10**(d), the RMSE for the 2nd load is large for all algorithms, but for the 3rd load, only LG has a significantly large RMSE that exceeds 16 kN. On the other hand, in M-5, although there is some variability, the RMSE for all models is smaller than in M-4, ranging from 2.18 to 8.32 kN. This indicates that repairs reduce the effect of previous damage on the envelope curve, whereas for unrepaired specimens, the degree of damage significantly affects the envelope curve.

Finally, regarding the effect of residual crack width ω, adding ω reduced the RMSE in M-1, but in M-2 to M-5 the results were case by case. This is probably because the complex experience of loading and repair made it difficult to observe qualitative trends in ω, suggesting the need for further investigation in the future.

5. CONCLUSIONS

In this study, loading experiments were performed on RC cantilevers subjected to three seismic motions, with the parameters of damage severity and the presence or absence of crack repairs. In addition, envelope curves were predicted using three machine learning algorithms based on decision trees. The results are presented below.

1) The results of this experiment showed that a higher degree of damage during the 1st load resulted in larger residual crack widths and stiffness reduction after the

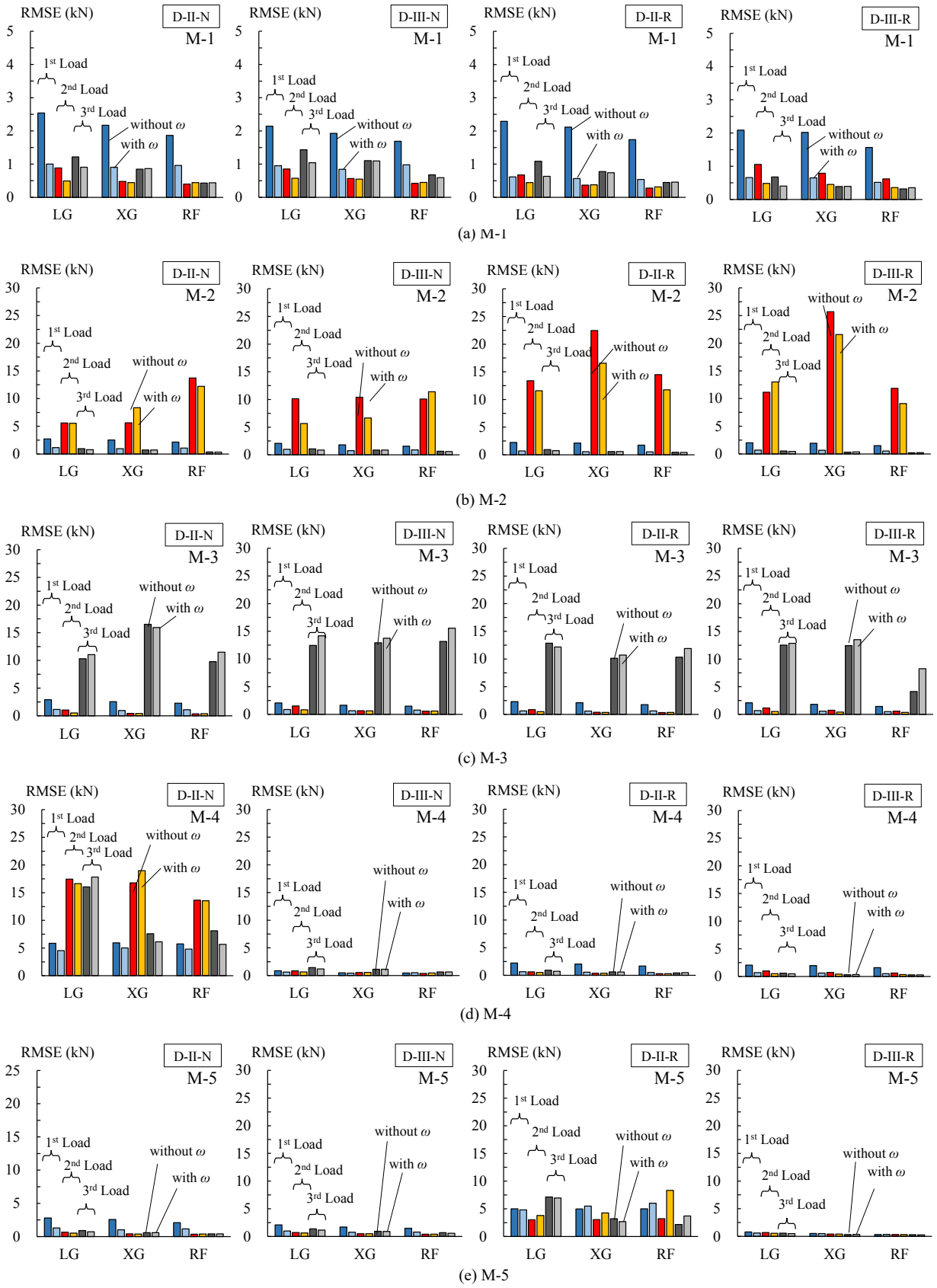

Fig. 11 Root mean square error between prediction and test results.

2nd load and beyond. However, it was found that crack repairs reduced the residual crack widths and restored some stiffness, although not to the level of the 1st load.

2) Among the learning models from M-1 to M-5, the XG model of M-2, which excluded the second load, had a large RMSE. On the other hand, the RMSE of LG and RF did not increase significantly, indicating that XG

is somewhat unsuitable for predicting the envelope curve in this experiment, and it is more desirable to use LG or RF.

3) Comparing M-4 and M-5, the RMSE of M-4 was larger. This means that when there is less teacher data for unrepaired samples, the prediction results tend to deteriorate. This is because for repaired specimens, the effect of damage level is reduced, while for unrepaired specimens, the envelope curve is strongly influenced by the experienced damage level.
4) Regarding the effect of residual crack width ω, in M-1, where all specimens were trained, adding ω as an explanatory variable reduced the RMSE. However, in other models where certain samples were excluded, no significant effect was observed. This is presumably because with repeated loading and varying repair experience, qualitative trends in ω became less noticeable.

This study demonstrated that the use of machine learning can effectively predict complex loading and repair experiences.

References

1. Architectural institute of Japan, Guidelines for performance evaluation of earthquake resistant reinforced concrete buildings(draft), 2004.
2. Furuuchi H. and Watanabe T.: Fatigue capacity of reinforced concrete beam repaired by crack injection, Proceedings of JCI, Vol.37, No.2, pp.1243-1248, 2015.
3. Yamaguchi M., Wang Y., Komiya R. and Dozono A.: Recovery effect of flexural performance of reinforced concrete beams by crack injection repair using ultra-loa viscosity epoxy resin and tensile behavior of rebars embedded in repaired concrete, Cement Science and Concrete Technology, Vol.77, pp.441-449, 2023.
4. Mikawa A., Akiya R., Nagai T., Shegay A., Miura K., Maeda M. and Sekimatsu T. : Evaluation of Recovery of Stiffness, Strength, and Hysteretic Damping by Repair Based on Database of Experimental Data of Reinforced Concrete Members Damaged by Earthquakes, Proceeding of the 17th annual meeting of Japan association for earthquake engineering, 2022.11.
5. KONISHI: Catalog, E206(SW), http://www.bond.co.jp/bond/catalog/pdf/ (accessed at 2024.7.26).
6. Suenaga D., Takase Y., Abe T., Orita G. and Ando S.: Prediction accuracy of Random Forest, XGBoost, LightGBM, and artificial neural network for shear resistance of post-installed anchors, Structures, Vol. 50, pp.1252-1263, 2023.4.
7. Higashifunamichi Y., Yamada Y., Namihira Y. and Hirano N. : Prediction of Flowability of High-Fluidity Concrete by Machine Learning Using Mortar Flowability, Materials Used, and Mixing (Formulation) and Analysis of Influence of Features, Proceedings of JCI, Vol.45, No.1, pp.784-789, 2023.6.

Estimation of the period of hot weather concreting in Republic of Korea introducing the caution periods.

Ji-Man CHUNG
Mr., of Architectural Engineering, Cheongju University, Republic of Korea.

Jun-Hui HAN
Dr., Dept. of Architectural Engineering, Cheongju University, Republic of Korea.

Seong-Jin BAEK
Mr., Dept. of Architectural Engineering, Cheongju University, Republic of Korea.

Gun-Su LIM
Mr., Dept. of Architectural Engineering, Cheongju University, Republic of Korea.

Jong KIM
Assistant Professor, Dept. of Architectural Engineering, Cheong-Ju University, Republic of Korea.

Min-Cheol HAN
Professor, Dept. of Architectural Engineering, Cheong-Ju University, Republic of Korea

ABSTRACT:

The purpose of the present study is to estimate the period of hot weather concreting in Republic of Korea by applying the average 10 years of daily temperature data from the Korea Meteorological Administration. The estimated data were compared with the actual hot weather concreting dates whether it satisfies the Korea Construction Standards (KCS) regulations, including the new temperature condition. In addition, the estimated period was compared with the period determined by the moving average method from JASS. Moreover, the caution period was presented which was evaluated by using the mean value and standard deviation. The results of this study indicated that the former method was more appropriate for KCS regulations with the additional temperature conditions than the other method. Furthermore, one or two days of hot weather concreting were expected per week during the caution periods.

Keywords: hot weather, concreting regulations, meteorological data, caution period

1. INTRODUCTION

Due to global warming, the peak temperature has been continuously increasing during summer seasons. Such hot weather conditions can adversely affect the quality of concrete construction if appropriate precautions are not taken during the summer. Therefore, measures to ensure concrete quality under these hot weather conditions should be prepared in advance. In addition, the proper guidelines or regulations are required to be clearly specified.

Recently, the Ministry of Land, Infrastructure, and Transport (MOLIT) of the Republic of Korea announced that the regulations of the Korea Construction Standards for hot weather concreting would be strengthened. A supplementary temperature condition stipulates that hot weather concreting is required if the daily maximum temperature exceeds 30℃. This proactive step aims to enhance the resilience and quality of concrete construction in response to rising temperatures caused by global warming.

The present study compared the predicted period of hot weather concreting by applying the regulations for hot weather concreting specified by the Korea Construction Standards (KCS) with the period of that estimated by the method provided by Japanese Architectural Standard Specification (JASS). Additionally, a caution period was introduced to enable site managers to promptly implement hot weather concreting procedures on-site when unexpected hot weather conditions arise during the summer.

2. RESEARCH ASSUMPTIONS

2.1 Assumptions

The data for the daily mean and maximum temperatures from the Korea Meteorological Administration (KMA) for 32 areas in South Korea over a 20-year period (2004~2023) was selected. The temperature increase due to global warming is negligible over a period of 10 years and the data samples follow normal distributions.

2.2 Justifications

According to the National Institute of Meteorological Sciences of the Republic of Korea, the annual mean temperature in South Korea has increased by 0.18°C per decade over a span of 106 years. In the recent 30 years (1988~2017), the daily mean and daily maximum temperatures have increased by 0.3°C per decade during the summer season. Therefore, it is acceptable to assume that the temperature increase over a decade has a little effects on the normality of the samples.

The Shapiro-Wilk test was also conducted on 270,100 samples collected from 74 different areas. The test was performed separately for the daily mean temperature and daily maximum temperature. For the daily mean temperature, 16,566 samples (6.1%) were rejected at the significance level α=0.05, and 4,041 samples (1.5%) were rejected at α=0.01. Similarly, for the daily maximum temperature, 16,003 samples (5.9%) were rejected at α=0.05, and 3,491 samples (1.3%) were rejected at α=0.01. Therefore, it is reasonable to assume that the samples follow a normal distribution. The number of rejected samples was slightly higher than expected. This could possibly be attributed to a small increase in temperatures due to global warming.

3. METHODOLOGY

The current hot weather concreting regulation states that hot weather concreting is required if the daily mean temperature exceeds 25°C. To estimate the period for hot weather concreting, the daily mean temperatures over 10 consecutive years were averaged. For instance, the daily mean temperature data from 2004 to 2013 were used to predict the hot weather concreting period for 2014. The earliest and latest dates were determined based on the mean temperatures when it exceeds 25°C.

The moving average method from JASS was applied for the comparative analysis. First, the daily mean temperatures over 10 years were averaged. Denote the first day of a year of the averaged value as $d_1^{(0)}$ and the last day as $d_{365}^{(0)}$ assuming that the year is not a leap year. Let

$$d_n^{(k)} = \frac{\left(d_{n-4}^{(k-1)}+d_{n-3}^{(k-1)}+\cdots+d_n^{(k-1)}+\cdots+d_{n+3}^{(k-1)}+d_{n+4}^{(k-1)}\right)}{9},$$

where n is the nth day of the year. Then, $d_n^{(3)}$ is the value explained in JASS. The earliest and latest dates for hot weather concreting were determined by identifying all the dates satisfying $d_n^{(3)}>25$.

The analysis proceeded by comparing the periods of hot weather concreting determined by the method 1 and 2 with the actual hot weather concreting days. For the new temperature condition where the daily maximum temperature exceeds 30°C, the same methodology was applied using the daily maximum temperatures averaged over a decade. The final hot weather concreting period was determined by combining the periods identified by both temperature conditions.

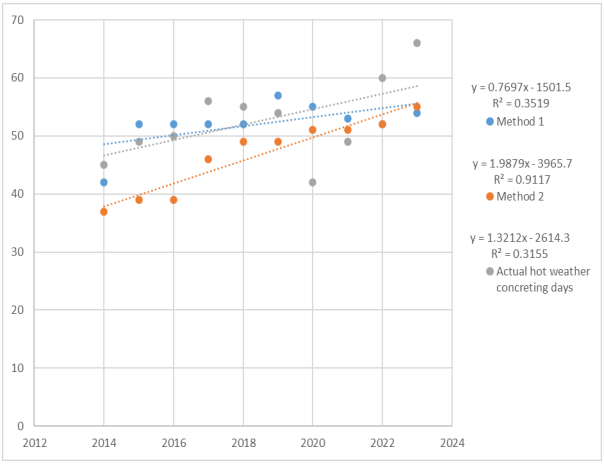

Figure 1. The number of hot weather concreting days in Seoul determined by the method 1, 2 and the actual hot weather concreting days

Finally, the caution periods for hot weather concreting by adding the mean value and standard deviation of the daily mean temperature and daily maximum temperature were suggested. The periods were determined when the added values exceeded 25°C and 30°C, respectively.

4. COMPARISON OF PERIOD OF HOT WEATHER CONCRETING IN SOUTH KOREA WITH RESPECT TO THE CURRENT KCS REGULATIONS

By comparing Table 1 and Table 2, in every region of South Korea except for Gwangju, the period predicted by the method 1 was longer than that determined by the method 2 from JASS. The two cities with the largest differences were Gumi and Pohang, both located in Gyeongbuk, with an average increase of 10 days. By adding the number of hot weather concreting days for every region in the same year, the total number of hot weather concreting days gradually increased as the years passed. For instance, Figure 1 shows the number of hot weather concreting days in Seoul using both methods. The R^2 value indicates that the moving average method provides a better fit for a linear graph because it effectively smooths out the data, whereas the method 1 and the actual hot weather concreting days have similar R^2 values. The gradient value of the method 2 indicates that the number of hot weather concreting days is increasing by 1.99 days per year, which presents a rapid increase. In contrast, the method 1 shows a small increase of 0.77 days per year. The gradient of the actual hot weather concreting days is 1.32, which falls between the gradients of the other two values but is slightly closer to the gradient of the method 1. Therefore, the trend observed in the Method 1 aligns more closely with the actual temperature data. This observation was insufficient to determine which method is acceptable. However both methods indicated that the number of hot weather concreting days was on the rise.

Let d be the actual number of hot weather concreting days and D_1 and D_2 be the number of hot weather

concreting days determined by the method 1 and 2, respectively. Additionally, let d_1 and d_2 denote the actual hot weather concreting days within the periods determined by the method 1 and 2, respectively. To determine which method was better, d_i/d and d_i/D_i values were crucial. As a point, we aim to maximize the number of hot weather concreting days within the period as well as minimize the number of days that are not hot weather concreting days in the period. In other words, the d_i/d value is sufficiently large to maximize hot weather concreting days within the period, while the d_i/D_i value is sufficiently large to minimize the number of days that are not hot weather concreting days within the period. If the period becomes shorter, the d_i/D_i value tends to increase while the d_i/d value decreases. Conversely, if the period becomes longer, the d_i/D_i value tends to decrease while the d_i/d value increases. Therefore, it needs to find the period such that both of the d_i/d and d_i/D_i values are sufficiently large. In Table 3, the d_1/d values for the major cities in South Korea are generally larger than the d_2/d values but the d_2/D_2 values are larger than d_1/D_1, which was due to the period determined by the method 1 being larger than period determined by the method 2. Both periods determined by the method 1 and 2 were good enough since the d_i/d, and d_i/D_i values were larger than 70%. Since the period determined by the method 1 was longer, it became more cautious regarding hot weather concreting.

Table 1. Period and number of days of hot weather concreting by KCS specifications in South Korea (2014~2023)

Table 3. Comparison between the data of method 1 and 2 for the current KCS regulations

[illegible]	[illegible]	[illegible]	[illegible]	[illegible]	[illegible]	[illegible]	[illegible]	[illegible]	[illegible]
[illegible]	[illegible]	[illegible]	[illegible]	[illegible]	[illegible]	[illegible]	[illegible]	[illegible]	[illegible]
[illegible]	[illegible]	[illegible]	[illegible]	[illegible]	[illegible]	[illegible]	[illegible]	[illegible]	[illegible]
[illegible]	[illegible]	[illegible]	[illegible]	[illegible]	[illegible]	[illegible]	[illegible]	[illegible]	[illegible]
[illegible]	[illegible]	[illegible]	[illegible]	[illegible]	[illegible]	[illegible]	[illegible]	[illegible]	[illegible]
[illegible]	[illegible]	[illegible]	[illegible]	[illegible]	[illegible]	[illegible]	[illegible]	[illegible]	[illegible]
[illegible]	[illegible]	[illegible]	[illegible]	[illegible]	[illegible]	[illegible]	[illegible]	[illegible]	[illegible]
[illegible]	[illegible]	[illegible]	[illegible]	[illegible]	[illegible]	[illegible]	[illegible]	[illegible]	[illegible]
[illegible]	[illegible]	[illegible]	[illegible]	[illegible]	[illegible]	[illegible]	[illegible]	[illegible]	[illegible]

Table 4. Period and number of days of hot weather concreting by future KCS specifications in South Korea (2014~2023)

[illegible]		[illegible]		[illegible]		[illegible]		[illegible]		[illegible]		[illegible]		[illegible]		[illegible]		[illegible]		[illegible]	
		[illegible]	[illegible]	[illegible]	[illegible]	[illegible]	[illegible]	[illegible]	[illegible]	[illegible]	[illegible]	[illegible]	[illegible]	[illegible]	[illegible]	[illegible]	[illegible]	[illegible]	[illegible]	[illegible]	[illegible]
[illegible]	[illegible]	[illegible]	[illegible]	[illegible]	[illegible]	[illegible]	[illegible]	[illegible]	[illegible]	[illegible]	[illegible]	[illegible]	[illegible]	[illegible]	[illegible]	[illegible]	[illegible]	[illegible]	[illegible]	[illegible]	[illegible]
	[illegible]	[illegible]	[illegible]	[illegible]	[illegible]	[illegible]	[illegible]	[illegible]	[illegible]	[illegible]	[illegible]	[illegible]	[illegible]	[illegible]	[illegible]	[illegible]	[illegible]	[illegible]	[illegible]	[illegible]	[illegible]
	[illegible]	[illegible]	[illegible]	[illegible]	[illegible]	[illegible]	[illegible]	[illegible]	[illegible]	[illegible]	[illegible]	[illegible]	[illegible]	[illegible]	[illegible]	[illegible]	[illegible]	[illegible]	[illegible]	[illegible]	[illegible]
	[illegible]	[illegible]	[illegible]	[illegible]	[illegible]	[illegible]	[illegible]	[illegible]	[illegible]	[illegible]	[illegible]	[illegible]	[illegible]	[illegible]	[illegible]	[illegible]	[illegible]	[illegible]	[illegible]	[illegible]	[illegible]
	[illegible]	[illegible]	[illegible]	[illegible]	[illegible]	[illegible]	[illegible]	[illegible]	[illegible]	[illegible]	[illegible]	[illegible]	[illegible]	[illegible]	[illegible]	[illegible]	[illegible]	[illegible]	[illegible]	[illegible]	[illegible]
	[illegible]	[illegible]	[illegible]	[illegible]	[illegible]	[illegible]	[illegible]	[illegible]	[illegible]	[illegible]	[illegible]	[illegible]	[illegible]	[illegible]	[illegible]	[illegible]	[illegible]	[illegible]	[illegible]	[illegible]	[illegible]
	[illegible]	[illegible]	[illegible]	[illegible]	[illegible]	[illegible]	[illegible]	[illegible]	[illegible]	[illegible]	[illegible]	[illegible]	[illegible]	[illegible]	[illegible]	[illegible]	[illegible]	[illegible]	[illegible]	[illegible]	[illegible]
[illegible]	[illegible]	[illegible]	[illegible]	[illegible]	[illegible]	[illegible]	[illegible]	[illegible]	[illegible]	[illegible]	[illegible]	[illegible]	[illegible]	[illegible]	[illegible]	[illegible]	[illegible]	[illegible]	[illegible]	[illegible]	[illegible]
	[illegible]	[illegible]	[illegible]	[illegible]	[illegible]	[illegible]	[illegible]	[illegible]	[illegible]	[illegible]	[illegible]	[illegible]	[illegible]	[illegible]	[illegible]	[illegible]	[illegible]	[illegible]	[illegible]	[illegible]	[illegible]
	[illegible]	[illegible]	[illegible]	[illegible]	[illegible]	[illegible]	[illegible]	[illegible]	[illegible]	[illegible]	[illegible]	[illegible]	[illegible]	[illegible]	[illegible]	[illegible]	[illegible]	[illegible]	[illegible]	[illegible]	[illegible]
[illegible]	[illegible]	[illegible]	[illegible]	[illegible]	[illegible]	[illegible]	[illegible]	[illegible]	[illegible]	[illegible]	[illegible]	[illegible]	[illegible]	[illegible]	[illegible]	[illegible]	[illegible]	[illegible]	[illegible]	[illegible]	[illegible]
	[illegible]	[illegible]	[illegible]	[illegible]	[illegible]	[illegible]	[illegible]	[illegible]	[illegible]	[illegible]	[illegible]	[illegible]	[illegible]	[illegible]	[illegible]	[illegible]	[illegible]	[illegible]	[illegible]	[illegible]	[illegible]
	[illegible]	[illegible]	[illegible]	[illegible]	[illegible]	[illegible]	[illegible]	[illegible]	[illegible]	[illegible]	[illegible]	[illegible]	[illegible]	[illegible]	[illegible]	[illegible]	[illegible]	[illegible]	[illegible]	[illegible]	[illegible]
[illegible]	[illegible]	[illegible]	[illegible]	[illegible]	[illegible]	[illegible]	[illegible]	[illegible]	[illegible]	[illegible]	[illegible]	[illegible]	[illegible]	[illegible]	[illegible]	[illegible]	[illegible]	[illegible]	[illegible]	[illegible]	[illegible]
	[illegible]	[illegible]	[illegible]	[illegible]	[illegible]	[illegible]	[illegible]	[illegible]	[illegible]	[illegible]	[illegible]	[illegible]	[illegible]	[illegible]	[illegible]	[illegible]	[illegible]	[illegible]	[illegible]	[illegible]	[illegible]
	[illegible]	[illegible]	[illegible]	[illegible]	[illegible]	[illegible]	[illegible]	[illegible]	[illegible]	[illegible]	[illegible]	[illegible]	[illegible]	[illegible]	[illegible]	[illegible]	[illegible]	[illegible]	[illegible]	[illegible]	[illegible]
[illegible]	[illegible]	[illegible]	[illegible]	[illegible]	[illegible]	[illegible]	[illegible]	[illegible]	[illegible]	[illegible]	[illegible]	[illegible]	[illegible]	[illegible]	[illegible]	[illegible]	[illegible]	[illegible]	[illegible]	[illegible]	[illegible]
	[illegible]	[illegible]	[illegible]	[illegible]	[illegible]	[illegible]	[illegible]	[illegible]	[illegible]	[illegible]	[illegible]	[illegible]	[illegible]	[illegible]	[illegible]	[illegible]	[illegible]	[illegible]	[illegible]	[illegible]	[illegible]
	[illegible]	[illegible]	[illegible]	[illegible]	[illegible]	[illegible]	[illegible]	[illegible]	[illegible]	[illegible]	[illegible]	[illegible]	[illegible]	[illegible]	[illegible]	[illegible]	[illegible]	[illegible]	[illegible]	[illegible]	[illegible]
[illegible]	[illegible]	[illegible]	[illegible]	[illegible]	[illegible]	[illegible]	[illegible]	[illegible]	[illegible]	[illegible]	[illegible]	[illegible]	[illegible]	[illegible]	[illegible]	[illegible]	[illegible]	[illegible]	[illegible]	[illegible]	[illegible]
	[illegible]	[illegible]	[illegible]	[illegible]	[illegible]	[illegible]	[illegible]	[illegible]	[illegible]	[illegible]	[illegible]	[illegible]	[illegible]	[illegible]	[illegible]	[illegible]	[illegible]	[illegible]	[illegible]	[illegible]	[illegible]
	[illegible]	[illegible]	[illegible]	[illegible]	[illegible]	[illegible]	[illegible]	[illegible]	[illegible]	[illegible]	[illegible]	[illegible]	[illegible]	[illegible]	[illegible]	[illegible]	[illegible]	[illegible]	[illegible]	[illegible]	[illegible]
[illegible]	[illegible]	[illegible]	[illegible]	[illegible]	[illegible]	[illegible]	[illegible]	[illegible]	[illegible]	[illegible]	[illegible]	[illegible]	[illegible]	[illegible]	[illegible]	[illegible]	[illegible]	[illegible]	[illegible]	[illegible]	[illegible]
	[illegible]	[illegible]	[illegible]	[illegible]	[illegible]	[illegible]	[illegible]	[illegible]	[illegible]	[illegible]	[illegible]	[illegible]	[illegible]	[illegible]	[illegible]	[illegible]	[illegible]	[illegible]	[illegible]	[illegible]	[illegible]
	[illegible]	[illegible]	[illegible]	[illegible]	[illegible]	[illegible]	[illegible]	[illegible]	[illegible]	[illegible]	[illegible]	[illegible]	[illegible]	[illegible]	[illegible]	[illegible]	[illegible]	[illegible]	[illegible]	[illegible]	[illegible]
[illegible]	[illegible]	[illegible]	[illegible]	[illegible]	[illegible]	[illegible]	[illegible]	[illegible]	[illegible]	[illegible]	[illegible]	[illegible]	[illegible]	[illegible]	[illegible]	[illegible]	[illegible]	[illegible]	[illegible]	[illegible]	[illegible]
	[illegible]	[illegible]	[illegible]	[illegible]	[illegible]	[illegible]	[illegible]	[illegible]	[illegible]	[illegible]	[illegible]	[illegible]	[illegible]	[illegible]	[illegible]	[illegible]	[illegible]	[illegible]	[illegible]	[illegible]	[illegible]
	[illegible]	[illegible]	[illegible]	[illegible]	[illegible]	[illegible]	[illegible]	[illegible]	[illegible]	[illegible]	[illegible]	[illegible]	[illegible]	[illegible]	[illegible]	[illegible]	[illegible]	[illegible]	[illegible]	[illegible]	[illegible]
[illegible]	[illegible]	[illegible]	[illegible]	[illegible]	[illegible]	[illegible]	[illegible]	[illegible]	[illegible]	[illegible]	[illegible]	[illegible]	[illegible]	[illegible]	[illegible]	[illegible]	[illegible]	[illegible]	[illegible]	[illegible]	[illegible]
	[illegible]	[illegible]	[illegible]	[illegible]	[illegible]	[illegible]	[illegible]	[illegible]	[illegible]	[illegible]	[illegible]	[illegible]	[illegible]	[illegible]	[illegible]	[illegible]	[illegible]	[illegible]	[illegible]	[illegible]	[illegible]
	[illegible]	[illegible]	[illegible]	[illegible]	[illegible]	[illegible]	[illegible]	[illegible]	[illegible]	[illegible]	[illegible]	[illegible]	[illegible]	[illegible]	[illegible]	[illegible]	[illegible]	[illegible]	[illegible]	[illegible]	[illegible]
[illegible]	[illegible]	[illegible]	[illegible]	[illegible]	[illegible]	[illegible]	[illegible]	[illegible]	[illegible]	[illegible]	[illegible]	[illegible]	[illegible]	[illegible]	[illegible]	[illegible]	[illegible]	[illegible]	[illegible]	[illegible]	[illegible]

Table 5. Period and number of days of hot weather concreting by moving average method from JASS with future KCS specifications in South Korea (2014~2023)

[illegible]		[illegible]		[illegible]		[illegible]		[illegible]		[illegible]		[illegible]		[illegible]		[illegible]		[illegible]		[illegible]	
		[illegible]	[illegible]	[illegible]	[illegible]	[illegible]	[illegible]	[illegible]	[illegible]	[illegible]	[illegible]	[illegible]	[illegible]	[illegible]	[illegible]	[illegible]	[illegible]	[illegible]	[illegible]	[illegible]	[illegible]
[illegible]	[illegible]	[illegible]	[illegible]	[illegible]	[illegible]	[illegible]	[illegible]	[illegible]	[illegible]	[illegible]	[illegible]	[illegible]	[illegible]	[illegible]	[illegible]	[illegible]	[illegible]	[illegible]	[illegible]	[illegible]	[illegible]
	[illegible]	[illegible]	[illegible]	[illegible]	[illegible]	[illegible]	[illegible]	[illegible]	[illegible]	[illegible]	[illegible]	[illegible]	[illegible]	[illegible]	[illegible]	[illegible]	[illegible]	[illegible]	[illegible]	[illegible]	[illegible]
	[illegible]	[illegible]	[illegible]	[illegible]	[illegible]	[illegible]	[illegible]	[illegible]	[illegible]	[illegible]	[illegible]	[illegible]	[illegible]	[illegible]	[illegible]	[illegible]	[illegible]	[illegible]	[illegible]	[illegible]	[illegible]
	[illegible]	[illegible]	[illegible]	[illegible]	[illegible]	[illegible]	[illegible]	[illegible]	[illegible]	[illegible]	[illegible]	[illegible]	[illegible]	[illegible]	[illegible]	[illegible]	[illegible]	[illegible]	[illegible]	[illegible]	[illegible]
	[illegible]	[illegible]	[illegible]	[illegible]	[illegible]	[illegible]	[illegible]	[illegible]	[illegible]	[illegible]	[illegible]	[illegible]	[illegible]	[illegible]	[illegible]	[illegible]	[illegible]	[illegible]	[illegible]	[illegible]	[illegible]
	[illegible]	[illegible]	[illegible]	[illegible]	[illegible]	[illegible]	[illegible]	[illegible]	[illegible]	[illegible]	[illegible]	[illegible]	[illegible]	[illegible]	[illegible]	[illegible]	[illegible]	[illegible]	[illegible]	[illegible]	[illegible]
	[illegible]	[illegible]	[illegible]	[illegible]	[illegible]	[illegible]	[illegible]	[illegible]	[illegible]	[illegible]	[illegible]	[illegible]	[illegible]	[illegible]	[illegible]	[illegible]	[illegible]	[illegible]	[illegible]	[illegible]	[illegible]
[illegible]	[illegible]	[illegible]	[illegible]	[illegible]	[illegible]	[illegible]	[illegible]	[illegible]	[illegible]	[illegible]	[illegible]	[illegible]	[illegible]	[illegible]	[illegible]	[illegible]	[illegible]	[illegible]	[illegible]	[illegible]	[illegible]
	[illegible]	[illegible]	[illegible]	[illegible]	[illegible]	[illegible]	[illegible]	[illegible]	[illegible]	[illegible]	[illegible]	[illegible]	[illegible]	[illegible]	[illegible]	[illegible]	[illegible]	[illegible]	[illegible]	[illegible]	[illegible]
	[illegible]	[illegible]	[illegible]	[illegible]	[illegible]	[illegible]	[illegible]	[illegible]	[illegible]	[illegible]	[illegible]	[illegible]	[illegible]	[illegible]	[illegible]	[illegible]	[illegible]	[illegible]	[illegible]	[illegible]	[illegible]
[illegible]	[illegible]	[illegible]	[illegible]	[illegible]	[illegible]	[illegible]	[illegible]	[illegible]	[illegible]	[illegible]	[illegible]	[illegible]	[illegible]	[illegible]	[illegible]	[illegible]	[illegible]	[illegible]	[illegible]	[illegible]	[illegible]
	[illegible]	[illegible]	[illegible]	[illegible]	[illegible]	[illegible]	[illegible]	[illegible]	[illegible]	[illegible]	[illegible]	[illegible]	[illegible]	[illegible]	[illegible]	[illegible]	[illegible]	[illegible]	[illegible]	[illegible]	[illegible]
	[illegible]	[illegible]	[illegible]	[illegible]	[illegible]	[illegible]	[illegible]	[illegible]	[illegible]	[illegible]	[illegible]	[illegible]	[illegible]	[illegible]	[illegible]	[illegible]	[illegible]	[illegible]	[illegible]	[illegible]	[illegible]
[illegible]	[illegible]	[illegible]	[illegible]	[illegible]	[illegible]	[illegible]	[illegible]	[illegible]	[illegible]	[illegible]	[illegible]	[illegible]	[illegible]	[illegible]	[illegible]	[illegible]	[illegible]	[illegible]	[illegible]	[illegible]	[illegible]
	[illegible]	[illegible]	[illegible]	[illegible]	[illegible]	[illegible]	[illegible]	[illegible]	[illegible]	[illegible]	[illegible]	[illegible]	[illegible]	[illegible]	[illegible]	[illegible]	[illegible]	[illegible]	[illegible]	[illegible]	[illegible]
	[illegible]	[illegible]	[illegible]	[illegible]	[illegible]	[illegible]	[illegible]	[illegible]	[illegible]	[illegible]	[illegible]	[illegible]	[illegible]	[illegible]	[illegible]	[illegible]	[illegible]	[illegible]	[illegible]	[illegible]	[illegible]
[illegible]	[illegible]	[illegible]	[illegible]	[illegible]	[illegible]	[illegible]	[illegible]	[illegible]	[illegible]	[illegible]	[illegible]	[illegible]	[illegible]	[illegible]	[illegible]	[illegible]	[illegible]	[illegible]	[illegible]	[illegible]	[illegible]
	[illegible]	[illegible]	[illegible]	[illegible]	[illegible]	[illegible]	[illegible]	[illegible]	[illegible]	[illegible]	[illegible]	[illegible]	[illegible]	[illegible]	[illegible]	[illegible]	[illegible]	[illegible]	[illegible]	[illegible]	[illegible]
	[illegible]	[illegible]	[illegible]	[illegible]	[illegible]	[illegible]	[illegible]	[illegible]	[illegible]	[illegible]	[illegible]	[illegible]	[illegible]	[illegible]	[illegible]	[illegible]	[illegible]	[illegible]	[illegible]	[illegible]	[illegible]
[illegible]	[illegible]	[illegible]	[illegible]	[illegible]	[illegible]	[illegible]	[illegible]	[illegible]	[illegible]	[illegible]	[illegible]	[illegible]	[illegible]	[illegible]	[illegible]	[illegible]	[illegible]	[illegible]	[illegible]	[illegible]	[illegible]
	[illegible]	[illegible]	[illegible]	[illegible]	[illegible]	[illegible]	[illegible]	[illegible]	[illegible]	[illegible]	[illegible]	[illegible]	[illegible]	[illegible]	[illegible]	[illegible]	[illegible]	[illegible]	[illegible]	[illegible]	[illegible]
	[illegible]	[illegible]	[illegible]	[illegible]	[illegible]	[illegible]	[illegible]	[illegible]	[illegible]	[illegible]	[illegible]	[illegible]	[illegible]	[illegible]	[illegible]	[illegible]	[illegible]	[illegible]	[illegible]	[illegible]	[illegible]
[illegible]	[illegible]	[illegible]	[illegible]	[illegible]	[illegible]	[illegible]	[illegible]	[illegible]	[illegible]	[illegible]	[illegible]	[illegible]	[illegible]	[illegible]	[illegible]	[illegible]	[illegible]	[illegible]	[illegible]	[illegible]	[illegible]
	[illegible]	[illegible]	[illegible]	[illegible]	[illegible]	[illegible]	[illegible]	[illegible]	[illegible]	[illegible]	[illegible]	[illegible]	[illegible]	[illegible]	[illegible]	[illegible]	[illegible]	[illegible]	[illegible]	[illegible]	[illegible]
	[illegible]	[illegible]	[illegible]	[illegible]	[illegible]	[illegible]	[illegible]	[illegible]	[illegible]	[illegible]	[illegible]	[illegible]	[illegible]	[illegible]	[illegible]	[illegible]	[illegible]	[illegible]	[illegible]	[illegible]	[illegible]
[illegible]	[illegible]	[illegible]	[illegible]	[illegible]	[illegible]	[illegible]	[illegible]	[illegible]	[illegible]	[illegible]	[illegible]	[illegible]	[illegible]	[illegible]	[illegible]	[illegible]	[illegible]	[illegible]	[illegible]	[illegible]	[illegible]
	[illegible]	[illegible]	[illegible]	[illegible]	[illegible]	[illegible]	[illegible]	[illegible]	[illegible]	[illegible]	[illegible]	[illegible]	[illegible]	[illegible]	[illegible]	[illegible]	[illegible]	[illegible]	[illegible]	[illegible]	[illegible]
	[illegible]	[illegible]	[illegible]	[illegible]	[illegible]	[illegible]	[illegible]	[illegible]	[illegible]	[illegible]	[illegible]	[illegible]	[illegible]	[illegible]	[illegible]	[illegible]	[illegible]	[illegible]	[illegible]	[illegible]	[illegible]
[illegible]	[illegible]	[illegible]	[illegible]	[illegible]	[illegible]	[illegible]	[illegible]	[illegible]	[illegible]	[illegible]	[illegible]	[illegible]	[illegible]	[illegible]	[illegible]	[illegible]	[illegible]	[illegible]	[illegible]	[illegible]	[illegible]
	[illegible]	[illegible]	[illegible]	[illegible]	[illegible]	[illegible]	[illegible]	[illegible]	[illegible]	[illegible]	[illegible]	[illegible]	[illegible]	[illegible]	[illegible]	[illegible]	[illegible]	[illegible]	[illegible]	[illegible]	[illegible]
	[illegible]	[illegible]	[illegible]	[illegible]	[illegible]	[illegible]	[illegible]	[illegible]	[illegible]	[illegible]	[illegible]	[illegible]	[illegible]	[illegible]	[illegible]	[illegible]	[illegible]	[illegible]	[illegible]	[illegible]	[illegible]
[illegible]	[illegible]	[illegible]	[illegible]	[illegible]	[illegible]	[illegible]	[illegible]	[illegible]	[illegible]	[illegible]	[illegible]	[illegible]	[illegible]	[illegible]	[illegible]	[illegible]	[illegible]	[illegible]	[illegible]	[illegible]	[illegible]

Table 6. The number of hot weather concreting days increased for each year in South Korea

[illegible]		[illegible]																			
		[illegible]		[illegible]		[illegible]		[illegible]		[illegible]		[illegible]		[illegible]		[illegible]		[illegible]		[illegible]	
[illegible]	[illegible]	[illegible]	[illegible]	[illegible]	[illegible]	[illegible]	[illegible]	[illegible]	[illegible]	[illegible]	[illegible]	[illegible]	[illegible]	[illegible]	[illegible]	[illegible]	[illegible]	[illegible]	[illegible]	[illegible]	[illegible]
	[illegible]	[illegible]	[illegible]	[illegible]	[illegible]	[illegible]	[illegible]	[illegible]	[illegible]	[illegible]	[illegible]	[illegible]	[illegible]	[illegible]	[illegible]	[illegible]	[illegible]	[illegible]	[illegible]	[illegible]	[illegible]
	[illegible]	[illegible]	[illegible]	[illegible]	[illegible]	[illegible]	[illegible]	[illegible]	[illegible]	[illegible]	[illegible]	[illegible]	[illegible]	[illegible]	[illegible]	[illegible]	[illegible]	[illegible]	[illegible]	[illegible]	[illegible]
	[illegible]	[illegible]	[illegible]	[illegible]	[illegible]	[illegible]	[illegible]	[illegible]	[illegible]	[illegible]	[illegible]	[illegible]	[illegible]	[illegible]	[illegible]	[illegible]	[illegible]	[illegible]	[illegible]	[illegible]	[illegible]
	[illegible]	[illegible]	[illegible]	[illegible]	[illegible]	[illegible]	[illegible]	[illegible]	[illegible]	[illegible]	[illegible]	[illegible]	[illegible]	[illegible]	[illegible]	[illegible]	[illegible]	[illegible]	[illegible]	[illegible]	[illegible]
	[illegible]	[illegible]	[illegible]	[illegible]	[illegible]	[illegible]	[illegible]	[illegible]	[illegible]	[illegible]	[illegible]	[illegible]	[illegible]	[illegible]	[illegible]	[illegible]	[illegible]	[illegible]	[illegible]	[illegible]	[illegible]
	[illegible]	[illegible]	[illegible]	[illegible]	[illegible]	[illegible]	[illegible]	[illegible]	[illegible]	[illegible]	[illegible]	[illegible]	[illegible]	[illegible]	[illegible]	[illegible]	[illegible]	[illegible]	[illegible]	[illegible]	[illegible]
[illegible]	[illegible]	[illegible]	[illegible]	[illegible]	[illegible]	[illegible]	[illegible]	[illegible]	[illegible]	[illegible]	[illegible]	[illegible]	[illegible]	[illegible]	[illegible]	[illegible]	[illegible]	[illegible]	[illegible]	[illegible]	[illegible]
	[illegible]	[illegible]	[illegible]	[illegible]	[illegible]	[illegible]	[illegible]	[illegible]	[illegible]	[illegible]	[illegible]	[illegible]	[illegible]	[illegible]	[illegible]	[illegible]	[illegible]	[illegible]	[illegible]	[illegible]	[illegible]
	[illegible]	[illegible]	[illegible]	[illegible]	[illegible]	[illegible]	[illegible]	[illegible]	[illegible]	[illegible]	[illegible]	[illegible]	[illegible]	[illegible]	[illegible]	[illegible]	[illegible]	[illegible]	[illegible]	[illegible]	[illegible]
[illegible]	[illegible]	[illegible]	[illegible]	[illegible]	[illegible]	[illegible]	[illegible]	[illegible]	[illegible]	[illegible]	[illegible]	[illegible]	[illegible]	[illegible]	[illegible]	[illegible]	[illegible]	[illegible]	[illegible]	[illegible]	[illegible]
	[illegible]	[illegible]	[illegible]	[illegible]	[illegible]	[illegible]	[illegible]	[illegible]	[illegible]	[illegible]	[illegible]	[illegible]	[illegible]	[illegible]	[illegible]	[illegible]	[illegible]	[illegible]	[illegible]	[illegible]	[illegible]
	[illegible]	[illegible]	[illegible]	[illegible]	[illegible]	[illegible]	[illegible]	[illegible]	[illegible]	[illegible]	[illegible]	[illegible]	[illegible]	[illegible]	[illegible]	[illegible]	[illegible]	[illegible]	[illegible]	[illegible]	[illegible]
[illegible]	[illegible]	[illegible]	[illegible]	[illegible]	[illegible]	[illegible]	[illegible]	[illegible]	[illegible]	[illegible]	[illegible]	[illegible]	[illegible]	[illegible]	[illegible]	[illegible]	[illegible]	[illegible]	[illegible]	[illegible]	[illegible]
	[illegible]	[illegible]	[illegible]	[illegible]	[illegible]	[illegible]	[illegible]	[illegible]	[illegible]	[illegible]	[illegible]	[illegible]	[illegible]	[illegible]	[illegible]	[illegible]	[illegible]	[illegible]	[illegible]	[illegible]	[illegible]
	[illegible]	[illegible]	[illegible]	[illegible]	[illegible]	[illegible]	[illegible]	[illegible]	[illegible]	[illegible]	[illegible]	[illegible]	[illegible]	[illegible]	[illegible]	[illegible]	[illegible]	[illegible]	[illegible]	[illegible]	[illegible]
[illegible]	[illegible]	[illegible]	[illegible]	[illegible]	[illegible]	[illegible]	[illegible]	[illegible]	[illegible]	[illegible]	[illegible]	[illegible]	[illegible]	[illegible]	[illegible]	[illegible]	[illegible]	[illegible]	[illegible]	[illegible]	[illegible]
	[illegible]	[illegible]	[illegible]	[illegible]	[illegible]	[illegible]	[illegible]	[illegible]	[illegible]	[illegible]	[illegible]	[illegible]	[illegible]	[illegible]	[illegible]	[illegible]	[illegible]	[illegible]	[illegible]	[illegible]	[illegible]
	[illegible]	[illegible]	[illegible]	[illegible]	[illegible]	[illegible]	[illegible]	[illegible]	[illegible]	[illegible]	[illegible]	[illegible]	[illegible]	[illegible]	[illegible]	[illegible]	[illegible]	[illegible]	[illegible]	[illegible]	[illegible]
[illegible]	[illegible]	[illegible]	[illegible]	[illegible]	[illegible]	[illegible]	[illegible]	[illegible]	[illegible]	[illegible]	[illegible]	[illegible]	[illegible]	[illegible]	[illegible]	[illegible]	[illegible]	[illegible]	[illegible]	[illegible]	[illegible]
	[illegible]	[illegible]	[illegible]	[illegible]	[illegible]	[illegible]	[illegible]	[illegible]	[illegible]	[illegible]	[illegible]	[illegible]	[illegible]	[illegible]	[illegible]	[illegible]	[illegible]	[illegible]	[illegible]	[illegible]	[illegible]
	[illegible]	[illegible]	[illegible]	[illegible]	[illegible]	[illegible]	[illegible]	[illegible]	[illegible]	[illegible]	[illegible]	[illegible]	[illegible]	[illegible]	[illegible]	[illegible]	[illegible]	[illegible]	[illegible]	[illegible]	[illegible]
[illegible]	[illegible]	[illegible]	[illegible]	[illegible]	[illegible]	[illegible]	[illegible]	[illegible]	[illegible]	[illegible]	[illegible]	[illegible]	[illegible]	[illegible]	[illegible]	[illegible]	[illegible]	[illegible]	[illegible]	[illegible]	[illegible]
	[illegible]	[illegible]	[illegible]	[illegible]	[illegible]	[illegible]	[illegible]	[illegible]	[illegible]	[illegible]	[illegible]	[illegible]	[illegible]	[illegible]	[illegible]	[illegible]	[illegible]	[illegible]	[illegible]	[illegible]	[illegible]
	[illegible]	[illegible]	[illegible]	[illegible]	[illegible]	[illegible]	[illegible]	[illegible]	[illegible]	[illegible]	[illegible]	[illegible]	[illegible]	[illegible]	[illegible]	[illegible]	[illegible]	[illegible]	[illegible]	[illegible]	[illegible]
[illegible]	[illegible]	[illegible]	[illegible]	[illegible]	[illegible]	[illegible]	[illegible]	[illegible]	[illegible]	[illegible]	[illegible]	[illegible]	[illegible]	[illegible]	[illegible]	[illegible]	[illegible]	[illegible]	[illegible]	[illegible]	[illegible]
	[illegible]	[illegible]	[illegible]	[illegible]	[illegible]	[illegible]	[illegible]	[illegible]	[illegible]	[illegible]	[illegible]	[illegible]	[illegible]	[illegible]	[illegible]	[illegible]	[illegible]	[illegible]	[illegible]	[illegible]	[illegible]
	[illegible]	[illegible]	[illegible]	[illegible]	[illegible]	[illegible]	[illegible]	[illegible]	[illegible]	[illegible]	[illegible]	[illegible]	[illegible]	[illegible]	[illegible]	[illegible]	[illegible]	[illegible]	[illegible]	[illegible]	[illegible]
[illegible]	[illegible]	[illegible]	[illegible]	[illegible]	[illegible]	[illegible]	[illegible]	[illegible]	[illegible]	[illegible]	[illegible]	[illegible]	[illegible]	[illegible]	[illegible]	[illegible]	[illegible]	[illegible]	[illegible]	[illegible]	[illegible]
	[illegible]	[illegible]	[illegible]	[illegible]	[illegible]	[illegible]	[illegible]	[illegible]	[illegible]	[illegible]	[illegible]	[illegible]	[illegible]	[illegible]	[illegible]	[illegible]	[illegible]	[illegible]	[illegible]	[illegible]	[illegible]
	[illegible]	[illegible]	[illegible]	[illegible]	[illegible]	[illegible]	[illegible]	[illegible]	[illegible]	[illegible]	[illegible]	[illegible]	[illegible]	[illegible]	[illegible]	[illegible]	[illegible]	[illegible]	[illegible]	[illegible]	[illegible]
[illegible]	[illegible]	[illegible]	[illegible]	[illegible]	[illegible]	[illegible]	[illegible]	[illegible]	[illegible]	[illegible]	[illegible]	[illegible]	[illegible]	[illegible]	[illegible]	[illegible]	[illegible]	[illegible]	[illegible]	[illegible]	[illegible]

Table 7. Comparison between the data of method 1 and 2 for future KCS regulations

[illegible]	[illegible]	[illegible]	[illegible]	[illegible]	[illegible]	[illegible]	[illegible]	[illegible]	[illegible]
[illegible]	[illegible]	[illegible]	[illegible]	[illegible]	[illegible]	[illegible]	[illegible]	[illegible]	[illegible]
[illegible]	[illegible]	[illegible]	[illegible]	[illegible]	[illegible]	[illegible]	[illegible]	[illegible]	[illegible]
[illegible]	[illegible]	[illegible]	[illegible]	[illegible]	[illegible]	[illegible]	[illegible]	[illegible]	[illegible]
[illegible]	[illegible]	[illegible]	[illegible]	[illegible]	[illegible]	[illegible]	[illegible]	[illegible]	[illegible]
[illegible]	[illegible]	[illegible]	[illegible]	[illegible]	[illegible]	[illegible]	[illegible]	[illegible]	[illegible]
[illegible]	[illegible]	[illegible]	[illegible]	[illegible]	[illegible]	[illegible]	[illegible]	[illegible]	[illegible]
[illegible]	[illegible]	[illegible]	[illegible]	[illegible]	[illegible]	[illegible]	[illegible]	[illegible]	[illegible]
[illegible]	[illegible]	[illegible]	[illegible]	[illegible]	[illegible]	[illegible]	[illegible]	[illegible]	[illegible]

5. COMPARISON OF PERIOD OF HOT WEATHER CONCRETING IN SOUTH KOREA WITH RESPECT TO THE FUTURE KCS REGULATIONS

By comparing the values in Table 1 with those in Table 4 with additional information of Table 6, it is observed that the number of hot weather concreting days determined by the method 1 has increased in 20 regions of South Korea, while little changes were observed in 12 regions. Figure 2 illustrates that the additional temperature conditions increased the period of hot weather concreting days in many major cities in South Korea. It can be seen that regions where there is a large difference between the daily minimum and maximum temperatures are likely to increase the number of hot weather concreting days. Especially, the average number of hot weather concreting days in Miryang from 2014 to 2023 was 27 days.

On the other hand, only 7 locations experienced an increase in the number of hot weather concreting days according to the method 2. Jecheon showed the largest increase for averaging 5 days, while other places showed an increase for 1 or 2 days. Therefore, it can be assumed that application of the moving average method for the additional temperature conditions may be insufficient. To be more specific, the same analysis was used in which the d_i/d, and d_i/D_i were applied. For the comparison of values in Table 3 and Table 6, the

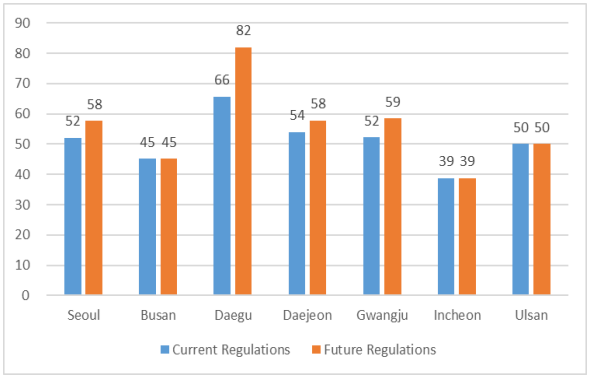

Figure 2. The average number of hot weather concreting days increased due to enhanced regulations with the method 1 in major cities of South Korea from 2014 to 2023

average value of d_1/d slightly decreased, while d_1/D_1 remained almost the same, with both values being greater than 70%. In contrast, the average value of d_2/D_2 slightly increased, but the total average of the d_2/d value drastically decreased to 64.5% from 73.7%. This indicates that there were significantly additional actual hot weather concreting days outside of the predicted period. This was obtained by the increase in the actual number of hot weather concreting days due to the new regulation, while the number of hot weather concreting days remained unchanged by the application of the moving average method. Therefore, it can be seen that the former method seemed to be preferable if the new regulation for hot weather concreting is implemented in the future.

6. INTRODUCTION OF THE CAUTION PERIODS FOR HOT WEATHER CONCRETING

In this section, the caution period for hot weather concreting is introduced in terms of the mean value and standard deviation. To be more specific, the standard deviation value to the mean value was added instead of the mean value of the daily mean temperature over 10 years. The earliest and latest dates were determined based on the added value which exceeds 25°C. Finally, the caution period was defined whether satisfy the above-mentioned conditions and which are not within the hot weather concreting period determined by the method 1. The purpose of the caution period was that there are 1 or more hot weather concreting days per week in this period assuming the sum of the mean value and standard deviation was exactly 25°C. Moreover, the temperature of that day next year follows a normal distribution, the probability of the temperature being greater than 25°C is 16% was assumed, which falls between 1/6 and 1/7. Therefore, at least one hot weather concreting day per week in this period can be expected. This process for the daily maximum temperatures with a condition of 30°C was repeated. In practice, the probability may be greater than 16% since the summed value may also be greater than 25°C in many cases and the actual daily temperatures tends to increase due to global warming. The caution period for hot weather concreting in South Korea in 2023 is shown in Table 8. The beginning and end dates of the caution periods were shown to be similar for many regions in contrast to the periods for hot weather concreting. Most of them began in May and ended in September.

As described in sections 4 and 5, a similar analysis was conducted for the major cities in South Korea. Let d be the actual total number of hot weather concreting days from 2014 to 2023. Let D_1 be the total number hot weather concreting days and D_2 be the total number of hot weather concreting days of the caution period. In addition, d_1 and d_2 as the actual number of hot weather concreting days within the hot weather concreting period and caution period were defined, respectively. It can be seen that the value of d_1/d, d_2/d and $(d_1+d_2)/d$ are 72.5%, 23.8% and 96.3% for the totals, respectively. The result implies that an arbitrary hot weather concreting day was either in the hot weather concreting period or the caution period with a probability of 96.3%. Moreover, the d_2/D_2 value of 24.2% indicated that there were approximately 1 or 2 days of hot weather concreting per week during the caution period.

Table 8. The caution periods and hot weather concreting periods in South Korea (2023)

Table 9. The relationship between the total number of hot weather concreting days, the days of hot weather concreting and the days of the caution period

7. CONCLUSION

This study focused on the comparison of different methods to determine the period and number of days suitable for hot weather concreting. In addition, one of the methods was utilized to propose and determine the caution periods for hot weather concreting. Based on the results of this study, the following conclusions can be drawn:

(1) For the current KCS regulations on hot weather concreting in major cities in South Korea, the periods for hot weather concreting were determined by the method of using the mean value and the method using the moving average method. 76.5% and 73.7% of the actual hot weather concreting days fell within these respective periods, suggesting that both periods were sufficiently long to cover most of the actual hot weather concreting days. For the accuracy of the periods, 72.9% and 77.2% of the days within the periods were the actual hot weather concreting days, respectively.
(2) Regarding the additional temperature condition, the hot weather concreting period determined by the method 1 increased in most regions of South Korea, while the period remained almost the same for the method 2. 72.5% of the actual hot weather concreting days were within the hot weather concreting period for the method 1. However, only 64.5% of the actual hot weather concreting days were within the period for the method 2. Also, 73.3% and 78.2% of the days within the periods were the actual hot weather concreting days, respectively. This can be seen that the method 1 is more appropriate when the new temperature condition is in effect.
(3) The caution periods for hot weather concreting were suggested when the sum of the mean value and the standard deviation is greater than 25°C for the daily mean temperature and greater than 30°C for the daily maximum temperature. 23.8% of the actual hot weather concreting days were within the caution periods. In other words, it is expected that there will be 1 or 2 hot weather concreting days per week during the caution periods. Moreover, 96.3% of the actual hot weather concreting days were covered either in the hot weather concreting period or the caution period.

REFERENCES

1. Ministry of Land, Infrastructure and Transport. “서중 콘크리트” [Hot weather concreting] Korea Construction Standards 14 20 41 :2021.
2. Architectural Institute of Japan, “暑中コンクリート工事” [Hot weather concreting], Japan Architectural Standard Specification 5: 2022, Section 13, pp. 475-500
3. National Institute of Meteorological Sciences 2018, “한반도 100 년의 기후변화” [Climate change in the Korean peninsula over 100 Years], GPRN 11-1360620-000132-01
4. Shapiro, S. S., & Wilk, M. B. (1965). “An Analysis of Variance Test for Normality (Complete Samples).” *Biometrika*, *52*(3/4), 591–611.
5. Royston, P. “Approximating the Shapiro-Wilk W-test for non-normality.” *Stat Comput* 2, 117–119 (1992).
6. Hanusz Z., Tarasinska J. (2011). “Tables for Shapiro-Wilk W statistic according to Royston approximation.” Colloquium Biometricum 41, 211–219.

Impact of Waste Clay Bricks on the Quality of Recycled Fine Aggregate

Dokyun KIM
Master course, Dept. of Architectural Engineering, Korea National University of Transportation, South Korea.

Jinseob KIM
Master course, Dept. of Architectural Engineering, Korea National University of Transportation, South Korea.

Geonwoo IM
Doctor course, Dept. of Architectural Engineering, Korea National University of Transportation, South Korea.

Youngmin KIM
Doctor course, Dept. of Architectural Engineering, Korea National University of Transportation, South Korea.

Guncheol LEE
Professor, Dept. of Architectural Engineering, Korea National University of Transportation, South Korea.

ABSTRACT
This study examined the impact of waste clay blocks, an inorganic foreign substance, on the quality of recycled fine aggregate. The cement mortar test was carried out with the replacement ratio of recycled fine aggregate to natural fine aggregate set at 0, 25, 50, 75 and 100%, and the mass ratio of waste clay bricks to natural fine aggregate set at 0, 1, 3 and 5 %. The flow value and unit volume mass were measured in fresh mortar, while the flexural strength, compressive strength and change in length due to drying shrinkage were measured in hardened mortar. The test found that the strength decreased as the recycled fine aggregate replacement ratio increased, and the strength decreased further as the content of waste clay bricks increased. The length change due to drying shrinkage was also found to increase as the incorporation ratio of recycled fine aggregate and waste clay bricks increased.

Keywords: Waste Clay Bricks, Inorganic Foreign Substances, Recycled Fine Aggregate

1. Introduction

In South Korea, the annual construction waste reaches around 80,000 tons, of which concrete waste accounts for about 65% of the total waste. At present, some of the concrete waste is used as recycled aggregate. However, most of the recycled aggregate is used for filling, covering, backfilling and subbase in roads, not as aggregate for concrete. However, in Japan, where construction recycling was implemented in 2000 to enable a wide range of applications, such as electrical utility-pipe conduit, boundary blocks, recycled crushed stone, drainage and crushed stone for sidewalks, it is recommended to expand the scope of recycled waste applications and to use recycled aggregate preferentially according to the purpose (JASS 5 2009).

Meanwhile, in South Korea, the quality of concrete aggregate has degraded due to the depletion of natural aggregate and restrictions on extraction, leading to a growing need to use recycled aggregate as concrete aggregate. However, since the volume of aggregate in concrete is relatively large, the quality of recycled aggregate can also have a significant impact the quality of concrete. Therefore, if the quality of recycled aggregate is not properly managed, a fatal problem may occur due to concrete degradation.

Recent research has reported that the low density and high-water absorption capacity of recycled aggregate have the greatest impact on the quality of concrete, and the inclusion of organic and inorganic foreign substances may adversely affect the quality of concrete. Accordingly, in South Korea, the content of organic and inorganic foreign substances is limited to less than 1%. Recently, however, as the number of demolished buildings made of clay bricks has increased, a large amount of inorganic foreign substances such as waste clay bricks have been included in recycled aggregate.

It is estimated that the inclusion of inorganic foreign substances such as waste clay bricks in recycled aggregate affects the quality of concrete even if high-quality recycled aggregate is used. However, there is still a lack of research on this subject.

Therefore, in this study, the mechanical and physical properties of cement mortar were evaluated using recycled fine aggregate incorporating waste clay bricks in order to examine the impact of inorganic

foreign substances such as waste clay bricks on the quality of recycled aggregate.

2. Experimental Design and Method

2.1 Experimental design

The experimental design of this study is shown in Table 1, and mix proportions are summarized in Table 2. The W/C ratio was 50%, and the replacement ratio of recycled fine aggregate was set at 5 levels: 0, 25, 50, 75 and 100% by mass of natural fine aggregate. The crushed waste concrete was used as recycled fine aggregate, and the incorporation ratio of waste clay bricks was set to 0, 1, 3, 5% as the mass ratio of recycled fine aggregate. The dimension of a specimen was 40×40×160 mm in accordance with KS L ISO 679. The table flow and unit volume mass were measured in fresh concrete. As the mechanical properties of hardened mortar, the flexural strength and compressive strength were measured at 3, 7 and 28 days of age. And, as the physical properties, the length change due to drying shrinkage was measured at up to 28 days of age, and the absorption rate was measured at 28-day age.

2.2 Properties of test materials

Three types of fine aggregates were used in the test: natural fine aggregate, recycled fine aggregate and waste clay bricks. To be specific, aggregate collected on land in the Chungju region was used as natural fine aggregate, and fine aggregate from waste concrete produced by domestic company D was used as recycled fine aggregate. Waste clay bricks were used after being crushed to have sizes ranging from 1.2 mm to 4.76 mm. The physical properties of the three fine aggregates are summarized in Table 2. Fig 1 shows the shape of materials used. Natural fine aggregate has a relatively spherical shape, while recycled fine aggregate and fine aggregate from waste clay bricks have a square shape due to the crushing process. And, close observation reveal that recycled fine aggregate and waste clay bricks have a relatively angular and rough grain shape. Fig. 2 shows the results of material observation using SEM. Recycled fine aggregate and fine aggregate from waste clay bricks have a rougher surface than natural fine aggregate, and some cracks are observed on the surface. It is adjudged that due to these cracks, recycled fine aggregate and fine aggregate from waste clay bricks have a higher absorption rate than natural fine aggregate, as shown in Table 3.

Table 1 Experimental Plan

Experimental factors		Experimental levels	
Mix proportions	W/C (%)	1	50
	Cement: Sand	1	1 : 3
	Fine aggregate type	2	Natural fine aggregate (NS), recycled fine aggregate (RS)
	Recycled fine aggregate replacement ratio (%) *	5	0, 25, 50, 75, 100
	Inorganic foreign substance type	1	Crushed waste clay bricks (CB)
	Inorganic foreign substance incorporation ratio (%) **	4	0, 1, 3, 5
Experimental items	Fresh mortar	2	- Table flow - Unit volume mass
	Hardened mortar	3	- Flexural/compressive strength (age 3,7 and 28 days) - Drying shrinkage (28-day age) - Absorption rate (28-day age)

* : Recycled aggregate is replaced by the mass ratio to natural fine aggregate, ** : Inorganic foreign substance is replaced by the mass ratio to recycled fine aggregate

Table 2 Mixing Table

Spec	W/B (%)	Binder (%)	Sand (%)		Waste clay brick (CB) (%)
		Cement	Natural fine aggregate (NS)	Recycled fine aggregate (RS)	
RS25	50	100	225	75	1, 3, 5
RS50			150	150	
RS75			75	225	
RS100			0	300	

Table 3 Properties of Test Materials

Items	Natural fine aggregate	Recycled fine aggregate	Waste clay bricks
Density(g/cm^3)	2.58	2.37	2.10
Absorption rate (%)	1.06	7.01	9.08
Fineness modulus (F.M)	2.64	2.93	-

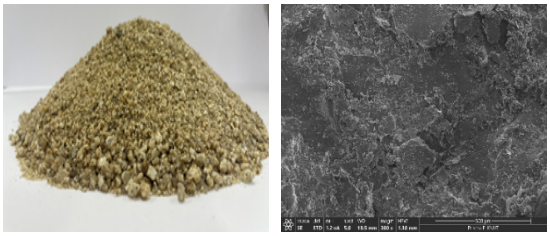

a) Fine aggregates used

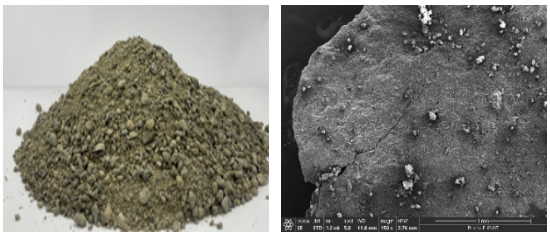

b) Recycled aggregates used

c) Waste clay brick used

Fig 1. Waste clay brick used
Fig 2. Surface conditions of materials used

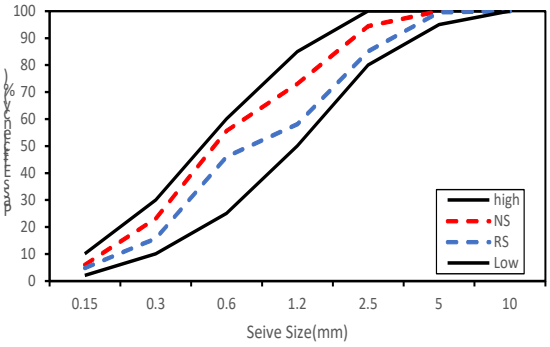

Fig 3. Particle size distribution curves of materials used

2.3 Experimental method

This experiment was intended to evaluate the basic properties of recycled fine aggregate mortar containing inorganic foreign substances such as waste clay bricks. In terms of the properties of fresh mortar, the fluidity was evaluated by measuring horizontal spread after 25 blows with the use of the flow table specified in KS L 5111(flow table for use in tests of hydraulic cement), and the unit volume mass was calculated by filling a 3-liter container with fresh mortar and dividing the measured mass by the volume. In relation to the mechanical properties of hardened mortar, after the fabrication of specimens with a dimension of 40×40×160mm in accordance with KS L ISO 679(testing method for compressive strength of cement mortar), the flexural strength was measured at 3, 7 and 28 days of age, and the compressive strength was measured on the split specimen. Regarding the change of length due to drying shrinkage, in accordance with KS F 2424(testing method for length change of mortar and concrete), a specimen with a dimension of 40×40×160mm was fabricated by inserting pins into both ends of the specimen and was cured in water at 20±2℃ for seven days. And it was then moved to a constant temperature and humidity test chamber with temperature and relative humidity maintained at 20℃ and 60%, respectively, and the length change was measured every seven days for up to 28 days. With respect to the absorption rate, after the specimen was completely dried out at 28 days of age, the mass was measured in a surface dry state with the surface water of the specimen saturated in water at 20±2℃ for one day removed.

3. Test Results and Analysis

3.1 Fresh mortar

Fig. 4 shows the properties of fresh mortar due to the incorporation of waste clay bricks. Overall, the flow value increased as the incorporation ratio of fine aggregate increased, but it decreased as the incorporation ratio of waste clay bricks increased. When the recycled fine aggregate incorporation ratio increased, the flow value increased by about 28%. On the other hand, when the incorporation ratio of waste clay bricks increased, the flow value decreased by about 34%. In general, it is expected that the fluidity will decrease as the incorporation ratio of angular recycled fine aggregate increases. However, it is adjudged that as a result of fineness modulus test shown in Fig 3, the fluidity of mortar increases as the recycled fine aggregate has a higher proportion of coarse particles and a relatively lower proportion of fine particles than natural fine aggregate. The unit volume mass decreased as the incorporation ratio of recycled fine aggregate and waste clay bricks increased. When the incorporation ratio of recycled fine aggregate increased, the unit volume mass showed a tendency to decrease by about 3.8 %. This is because the density of recycled fine aggregate is approximately 8.1% lower than that of natural fine aggregate.

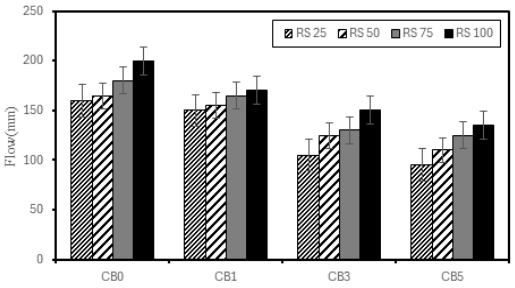

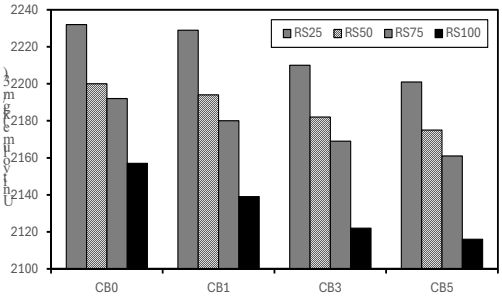

Fig 4 Physical properties of mortar due to the inclusion of waste clay bricks

3.2. Strength properties

Fig 5 show the strength properties of cement mortar due to an increase in the incorporation ratio of recycled fine aggregate and waste clay bricks. Overall, as the incorporation ratio of recycled fine aggregate and waste clay bricks increased, the strength decreased over the entire age. The compressive strength decreased by 3 to 8% in CB3 and 20 to 26% in CB5 compared to CB1 incorporated with 1% waste clay bricks at 3 days of age. The flexural strength showed a similar tendency to the compressive strength. The compressive strength at 28 days of age was reduced by 15 to 17% in CB3 and 19 to 25% in CB5 compared to CB1, and the flexural strength showed similar results to the compressive strength. The mechanical performance decreased as the incorporation ratio of recycled fine aggregate and waste clay bricks increased. This is because in the case of recycled fine aggregate, it has low density, and the aggregate strength itself is low due to the presence of cracks on the surface. And in the case of waste clay bricks, they are porous and have plate-shaped grains, showing a lower modulus of elasticity than natural fine aggregate.

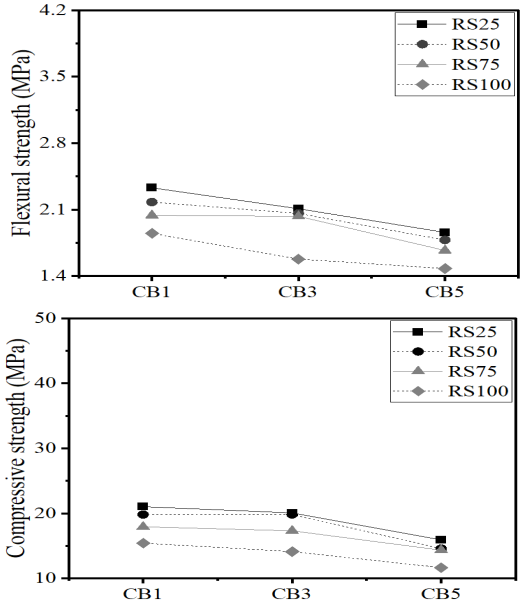

a) 3 days

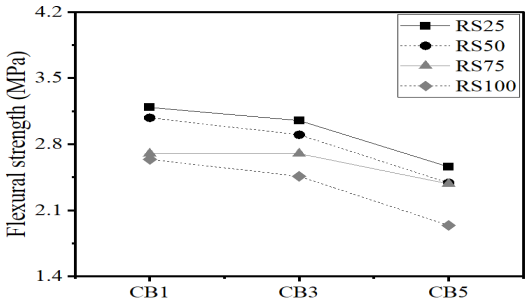

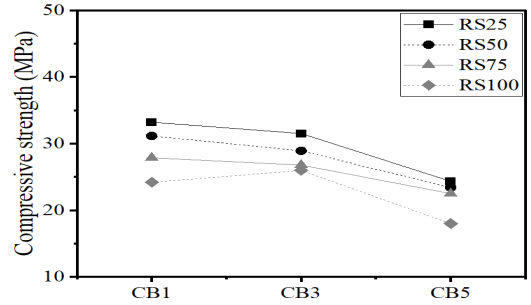

b) 7 days

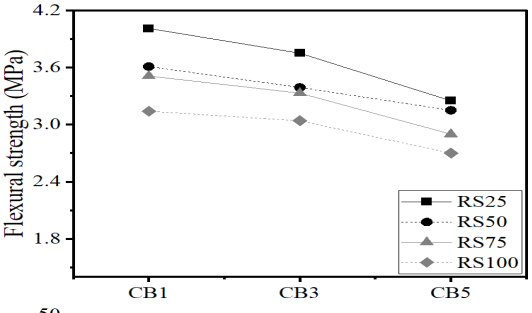

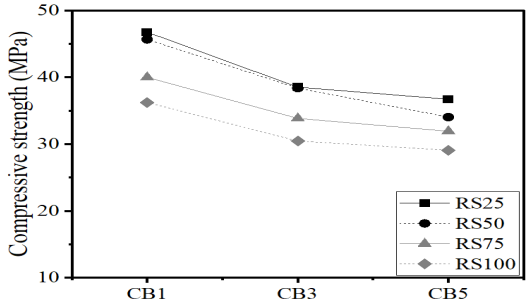

c) 28days

Fig 5 Flexural/compressive strength according to the incorporation ratio of waste clay bricks

3.3. Length change due to drying shrinkage

The drying shrinkage characteristics of the recycled fine aggregate mortar containing clay bricks as an inorganic foreign substance are shown in Fig 6, and the absorption rate of the hardened mortar is shown in Fig 7. The shrinkage rate tended to increase as the recycled fine aggregate incorporation ratio increased, and the shrinkage rate showed a tendency to increase rapidly until the 21st day. The length change was about 22 to 28% in CB1, 10 to 24% in CB3, and 14 to 37% in CB5. The increase of length change due to an increase in the incorporation ratio of waste clay bricks was not confirmed. However, the results of

absorption rate testing showed that the absorption rate tended to increase with the addition of waste clay bricks, and the absorption rate ranged from 14.3 to 32.24%. This is because capillary pores increase in size due to the porosity and high absorption rate of recycled fine aggregate and waste clay bricks.

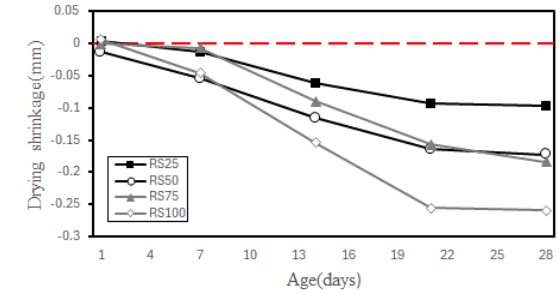

a) 1% incorporation ratio

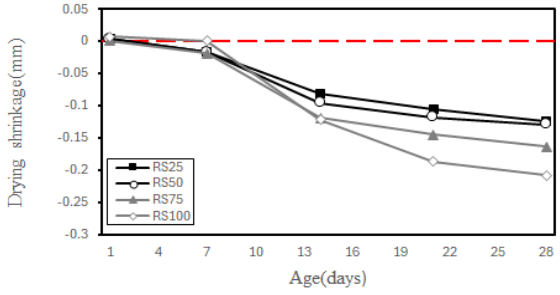

b) 3% incorporation ratio

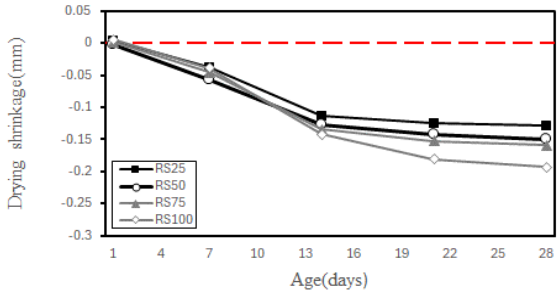

c) 5% incorporation ratio

Fig 6 Length change according to the incorporation ratio of waste clay bricks

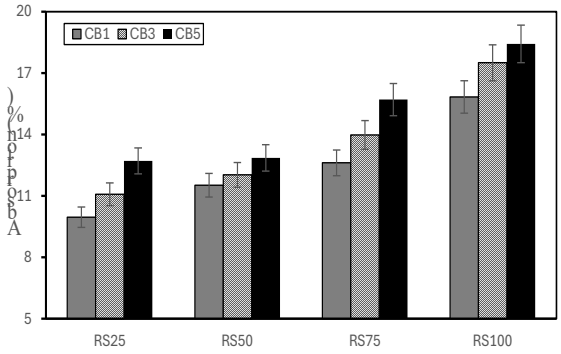

Fig 7 Absorption rates of hardened mortar specimens

4. Conclusion

This study sought to investigate the mechanical and physical properties of waste clay bricks when included in recycled fine aggregate as an inorganic foreign substance and to examine the impact of excessive incorporation of waste clay bricks among inorganic foreign substances. The results are summarized as follows.

1) As a result of the test on fresh mortar, the flow value tended to increase as the incorporation ratio of recycled fine aggregate and waste clay bricks increased. This is because the fluidity of mortar increases as the water absorption rate decreases because the recycled fine aggregate has a high proportion of coarse particles and a low proportion of fine particles.
2) The result of the strength test of hardened mortar revealed that the compressive strength and flexural strength showed a tendency to decrease as the incorporation ratio of recycled fine aggregate and waste clay bricks increased. This is because in the case of recycled fine aggregate, the density is lower as the attached mortar volume increases, and the porous properties affect the increase of capillary pores in size. And in the case of waste clay bricks, the elastic modulus is lower than that of natural aggregate due to the porosity of the material and the thin and pointed particle shape.
3) As a result of the test for drying shrinkage length change, the length changes increased as the incorporation ratio of recycled fine aggregate increased. The increase in length change due to an increase in the incorporation ratio of waste clay bricks was not confirmed. However, the result of the absorption rate testing confirmed that the absorption rate tended to increase due to the incorporation of waste clay bricks.

ACKNOWLEDGEMENT

This research was supported by the Mid-career Researcher Program through the National Research Foundation of Korea (NRF) funded by the Ministry of Education (Grant No. 2023R1A2C2006400).

5. References

1. Lee, Seung-Hoon, Park, Min-Su, & Kim, Young-Su (2014-10-23). A Study on Mechanical Properties of Concrete Using Waste Clay Bricks as Coarse Aggregate Replacement. Journal of the Korea Concrete Institute, Seoul

2. . On, Jae Hoon, Lee, Sun Kwan, & Kim, Young Su (2013-10-16). A Study on Mechanical Properties of Concrete Using Waste Clay Bricks as Coarse Aggregate Replacement

3. Park, Kyung Taek, Lim, Yong Ju, Hong, Ji Hoon, Baek, Hyun Soo, Seo, Ki Hwan, & Park, Min Yong (2016-11-02). Optimum Particle

Size Distribution and Physical Properties of Mortar depending on Particle Size of Crushed Fine Aggregates.

4. Won-Young Choi, Sang-Heon Kim, Sea-Hyun Lee, & Chan-Soo Jeon (2019). A Study on the Strength Properties and Life Cycle Assessment of Recycled Fine Aggregate Concrete. Journal of the Korean Recycled Construction Resources Institute, 7(2), 123-130.

5. Yu, Myeong Hwa, Park, Seung Wan, Cho, Hyun Dae, & Jaung, Jae Dong A Study on the Compressive Strength and Durability of Concrete by Mixing of Recycled Fine Aggregate.

6. Jeon, Esther, Yun, Hyun Do, Jang, Yong Heon, Choi, Ki Sun, Bae, Kee Sun, & Kim Keung Hwan Effect of Recycled Fine Aggregate Quality on Strength Properties of Concrete.

BOND STRENGTH OF ADHESIVE POST-INSTALLED ANCHOR FOR RC CANTILEVER BEAM DAMAGED BY SHEAR LOAD

Taito Shiokoshi
Graduate Student, College of Environmental Technology, Muroran Institute of Technology, Japan.

Atsuto Yasui
Graduate Student, College of Environmental Technology, Muroran Institute of Technology, Japan.

Yuya Takase
Professor, College of Design and Manufacturing Technology, Muroran Institute of Technology, Japan.

ABSTRACT:
Post-installed anchors are used to repair and reinforce existing concrete structures. While these are also applied to RC structures damaged by earthquakes. Therefore, in this study, we investigate the bond performance of the post-installed anchor bonded to the RC cantilever beam damaged by the shear load. As a result, the deformation drift during the shear loading test and the distance of the fixing position from the cross-section at the maximum moment M_{max} had a significant effect on the bond strength. In this study, the drifts were set to 1/100 to 1/75 rad., and the distance from the cross-section at M_{max} was about 0.3 to 1.0 times that of the beam, and the bond strength was reduced by up to 33%. On the other hand, the effect on bond strength by the width and number of cracks was small.
Keywords: Post-installed anchor, Post-installed reinforcing bar, Damage, Crack-Repair

1. INTRODUCTION

Fig.1 shows an example of the application of post-installed anchors and post-installed reinforcing bar [1] (both together called adhesive anchors). Adhesive anchors are commonly used to connect existing members to other members to strengthen reinforced concrete (RC) structures that have lost their seismic resistance and durability, to change the use of the building, and to shorten the construction period. In countries such as Japan, where large earthquakes frequently occur, adhesive anchors must also be bonded to RC members that have been damaged by earthquakes. Therefore, it is necessary to consider the damage to members such as cracks when anchoring adhesive anchors. In previous studies[2),3)], cracks were generated by wedges and anchors were bonded to confirm the effect of crack damage on bond properties. However, these studies did not consider seismic damage such as member deformation drifts. Thus, there have been few studies on members subjected to seismic loading, and bond properties have not been evaluated considering the damage.

In this study, RC cantilever beams were damaged by shear loading tests, and then adhesive anchors were bonded to the beams to conduct bond-slip tests to investigate the effect of earthquake damage on the bond properties of adhesive anchors.

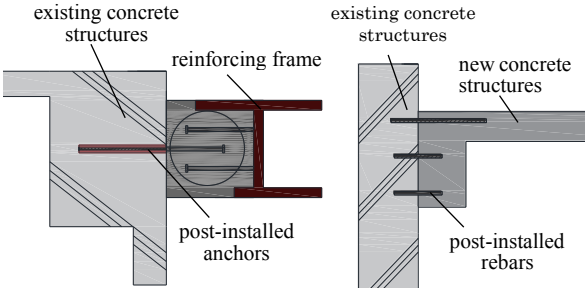

(a) Seismic rerofit (b) Renovation

Fig.1 Application of post-installation method.

Table1 Specimen parameters for shear loading tests.

Specimen name	$f_{c,s}$ (N/mm^2)	$E_{c,s}$ (kN/mm^2)	Damage[4)]	R(rad)	w_t(mm)
ND	23.8	20.2	I	—	—
DII-1			II	1/100	0.2~1.0
DII-2					
DIII-1			III	1/75	1.0~2.0
DIII-2					

$f_{c,s}$: Compressive strength of concrete, $E_{c,s}$: Young's modulus of concrete, R : Drift angle, w_t : Target crack width.

Table2 Mechanical property of rebar.

Rebar Type	Rebar Part	d	E_S	f_y	f_u	Elongation (%)
SD295	Beam and Stub	6	252	488	580	12.5
SD390	Stub	16	169	394	544	22.4
SD390	Beam	16	191	394	568	18.0

d : Diameter (mm), E_S : Young's modulus (kN/mm^2), f_y : Yield strength (N/mm^2), f_u : Ultimate strength (N/mm^2).

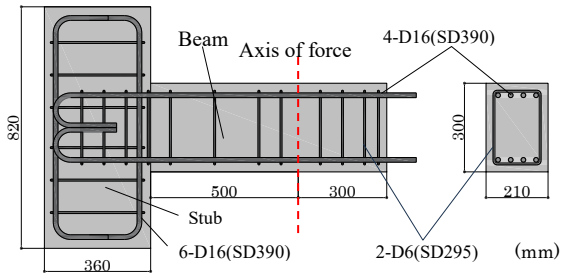

Fig.2 Details of specimen.

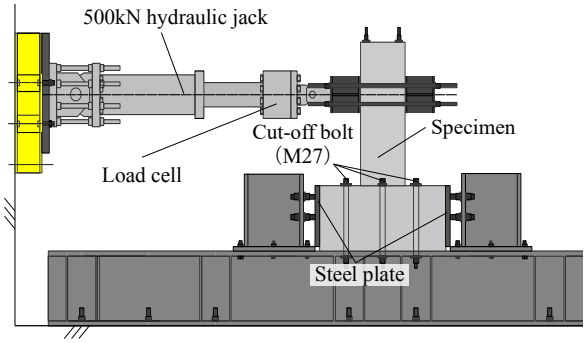

Fig.3 Setup for the shear loading tests.

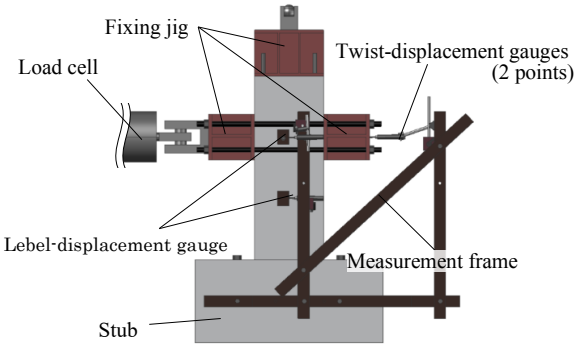

Fig.4 Displacement measurement method.

Table3 Shear loading tests results.

Specimen name	R(rad)	Q_{max}(kN) +	Q_{max}(kN) −	w_t(mm)	w(mm) front w_+	front w_-	back w_+	back w_-
ND	—	—	—	—	—	—	—	-
DII-1	1/100	134	-132	0.2~1.0	0.15	0.40	0.25	0.30
DII-2		135	-125		0.20	0.70	0.45	0.70
DIII-1	1/75	100	-129	1.0~2.0	2.00	1.60	2.00	0.90
DIII-2		130	-123		0.45	1.30	0.20	1.40

R : Drift angle, Q_{max} : Maximum shear load, w_t : Target crack width, w : Crack width.

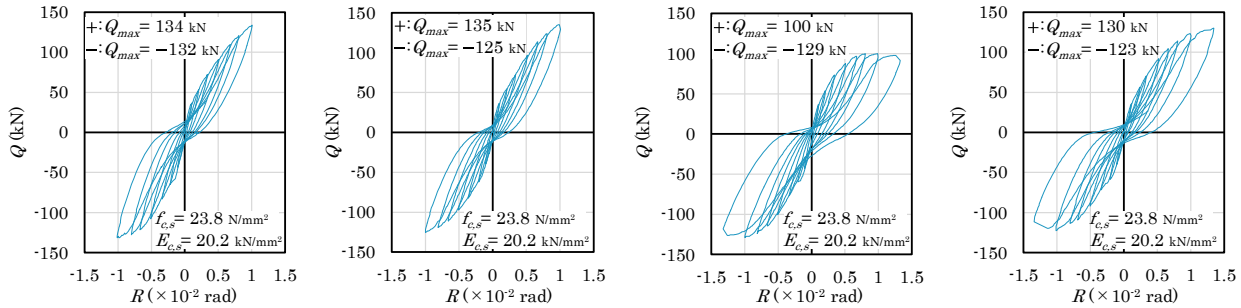

(a) DII-1 (b) DII-2 (c) DIII-1 (d) DIII-2

Fig.5 Load-drift angle relationship.

2. Shear Loading Tests on Beam Specimens

2.1 Outline of Shear Loading Tests

Table1 shows the test specimen parameters, **Table2** shows the concrete formulation, and **Fig.2** shows the specimen dimensions. The parameters were mainly the degree of damage, which is one of the five levels of damage specified in the seismic performance evaluation guidelines of the Architectural Institute of Japan (AIJ)[4]. The damage levels were I (ND) for no damage, II (DII) for target crack widths of 0.2 to 1.0 mm, and III (DIII) for crack widths of 1.0 to 2.0 mm. The specimen used in this study was a RC cantilever beam with a total length of 1,160 mm, a length of 500 mm from the top of the stub to the load shaft, a beam thickness of 300 mm, and a beam width of 210 mm, as shown in **Fig.2**. The main bars of the beam were D16 (SD390) threaded section rebars, D6 (SD295) deformed rebars were used for the ribs, and D16 (SD390) deformed rebars were used for the main bars of the stubs. The results of the acceptance tests of the concrete were 23.1 cm for the slump test and 2.4 % for the air content test. The shear margin, shear span ratio, tensile bar ratio, and rib ratio were set to 0.79, 1.91, 1.44 %, and 0.20 %, respectively. The beam specimens were designed so that shear failure would be preceded by cracking, which would easily damage the specimens. The cross-sectional size was assumed to be 1/2 the scale of the actual structure.

The beam specimen was subjected to cyclic positive and negative loading using a 500 kN actuator, and the loads were measured by a load cell. 6 inch-cut bolts (M27) and steel plates on both sides were used to secure the stubs. Horizontal displacement was measured at two locations: at the force axis and at the midpoint between the force axis and the stub. In addition, two horizontal displacement transducers were installed on the fixture to measure the torsion. The deformation drift R was calculated by dividing the horizontal displacement measured at the force shaft by 500 mm, the position of the force shaft. The cycles of loading were ±1/1000, ±1/500, ±1/300, ±1/200, ±1/150, ±1/125, ±1/100, and ±1/75 rad, respectively, and were repeated under manual control using a hydraulic actuator. The deformation drift at the end of loading was determined after a preliminary test of RC beams was conducted to determine the relationship between the deformation drift and the crack width of

Table4 Specimen parameters (bond-slip tests).

Specimen name	$f_{c,b}$	$E_{c,b}$	d_a	φ	l_e	adhesive type	Bonded beam	R	w_t	n_c	w		Anchorage position	
											w_1	w_2	x	y
ND-1	23.0	25.1	13	16	$4.5d_a$	Ep	ND(front)	—	—	—	—	—	0.51	0.27
ND-2							ND(front)						0.3	0.67
ND-3							ND(front)						0.67	1.00
DII-1c-1							DII-1(front)	1/100	0.2～1.0	1	0.30	—	0.43	0.99
DII-1c-2							DII-1(back)				0.30	—	0.67	1.01
DII-1c-3							DII-2(back)				0.35	—	0.59	0.59
DII-2c-1							DII-1(back)			2	0.30	0.25	0.51	0.40
DII-2c-2							DII-2(front)				0.70	0.20	0.54	0.47
DIII-Nc-1							DIII-1(back)	1/75	1.0～2.0	0	—	—	0.49	0.39
DIII-Nc2							DIII-2(back)				—	—	0.51	0.32
DIII-1c-1							DIII-1(back)			1	0.90	—	0.66	1.03
DIII-1c-2							DIII-1(front)				1.20	—	0.3	1.01
DIII-1c-3							DIII-2(back)				1.20	—	0.3	1.00
DIII-2c-1							DIII-1(front)			2	2.00	1.60	0.62	0.67
DIII-2c-2							DIII-2(back)				1.40	0.20	0.47	0.68
DIII-2c-3							DIII-2(front)				1.30	0.45	0.74	0.52

$f_{c,b}$: Compressive strength of concrete(N/mm^2), $E_{c,b}$: Young's modulus of concrete(kN/mm^2), d_a : Diameter of anchor(mm), φ : Diameter of the concrete coring hole(mm), l_e : Embedded length of anchor(mm), Ep : Epoxy resin, R : Deformation drift(rad), w_t : Target crack width(mm), n_c : Number of cracks, w : Crack width(mm), x : Direction of x(×D mm), y : Direction of y(×D mm), D : Beam diameter(mm).

the specimens used in this study. The loading was continued until the target deformation drift was reached. Cracks were measured with a crack scale at the peak of each cycle, Q = 0 kN, s = 0 mm. Shear loading tests were conducted on four specimens, two for each degree of damage.

2.2 Shear Loading Tests Results

Fig.5 shows the load-displacement relationship, **Fig.6** shows an example of crack initiation, and **Table 3** shows the results of the shear loading tests. In **Fig.6** and **Table3**, the maximum cracks that occurred under positive and negative loading are shown as residual crack widths w_+ and w_-, respectively. DIII was applied up to R= 1/75 rad, and the DIII-1 specimen had a Q_{max} of 2.00 mm at 129 kN (negative), and the DII-2 specimen had a Q_{max} of 1.30 mm at 130 kN (positive), indicating that all specimens were damaged to the target crack width. In DII, the loading was terminated before the peak load was observed, but in DIII-1 and DIII-2, the peak load was observed in the region exceeding 1/100 rad, but as can be seen from the crack initiation in **Fig.6**, large shear cracks were observed in the diagonal direction, suggesting that all specimens failed in shear. The shear failure is considered to have occurred in all specimens.

3. Bond-slip Tests of Anchor

3.1 Outline of Bond-slip Tests

Table4 shows the specimen parameters for the bond-slip tests, **Fig.7** shows the force apparatus for the bond-slip tests, and **Fig.8** shows the anchor bar anchorage locations. The parameters were the deformation drift of the member during the shear loading tests and the width and number of cracks at the anchorage. The cracks were classified into three types: no cracks (Nc), one crack (1c), and two cracks (2c). The diameter of the anchor bar was 13.0 mm, the anchorage length was 4.5 da, and the type of adhesive was organic epoxy resin (Ep). The compressive strength of the concrete during the bond-slip tests $f_{c,b}$ was 23.0 N/mm^2 , Young's modulus $E_{c,b}$ was 25.1 kN/mm^2 , cracking tensile strength $f_{t,b}$ was 1.31 N/mm^2 , yield strength of the anchor bar $f_{y,a}$ was 490 N/mm^2 , Young's modulus $E_{s,b}$ was 189 kN/mm^2 , compressive strength of the adhesive f_a was 155 N/mm^2, the cracking tensile strength f_{ta} was 38.6 N/mm^2, and Young's modulus E_a was 2.81 kN/mm^2.

The anchor bar anchorage procedure consisted of three steps: 1) damage by shear force testing, 2) drilling using a wet core drill, and 3) anchor bar anchorage by injecting adhesive. The effect of the drilling on the cracking was minimal, as it did not change before and after the drilling. The anchorage locations for 1c and 2c were selected above the cracks, and for Nc, the location close to the critical section where damage from the shear stress test was expected to be large. The anchorage points were selected from these areas at locations that did not interfere with the ribs and at locations that did not interfere with the stubs of the force application device. As shown in **Fig.7(a)**, the beam test specimen was inverted so that the anchor bars were pointing vertically upward, and the beam section was supported by a panther jack. As shown in **Fig.7(b)**, a 320 kN center hole jack was used to apply a vertical upward tensile force to the anchor bars, and a 500 kN load cell was used to measure the load. To prevent cone failure of the concrete, a reaction plate (250 mm × 150 mm × 20 mm, hole diameter: 25 mm) was installed at the bottom of the force application device. No. 7 silica sand was placed between the plates and the concrete to ensure that the stresses acted uniformly on the plates. Two vertical displacement gauges were installed to measure the displacement, and the average value of these gauges was used as the

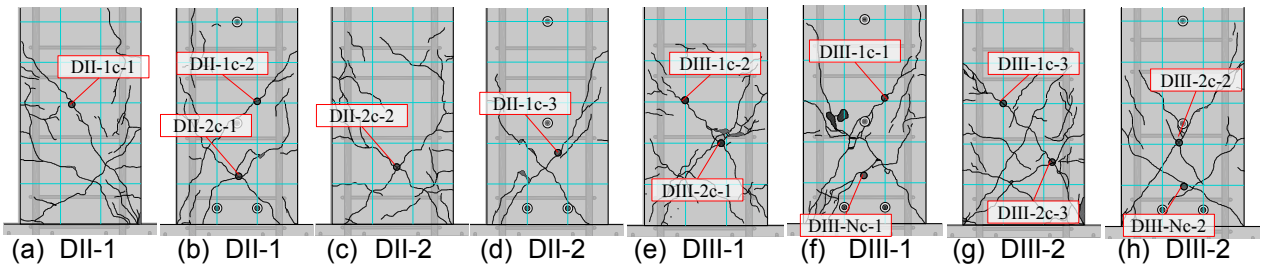

(a) DII-1 (front) (b) DII-1 (back) (c) DII-2 (front) (d) DII-2 (back) (e) DIII-1 (front) (f) DIII-1 (back) (g) DIII-2 (front) (h) DIII-2 (back)

Fig.7 Crack in beam specimens after shear loading tests.

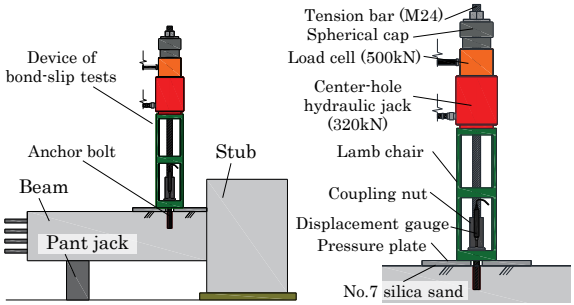

(a) Loading method (b) Loading set up

Fig.8 Setup for the bond-slip tests.

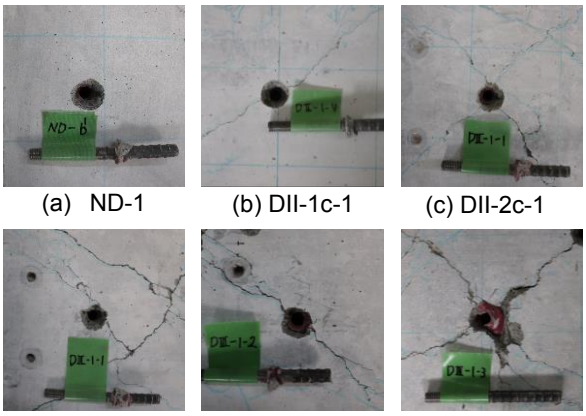

(a) ND-1 (b) DII-1c-1 (c) DII-2c-1

(d)DIII-Nc-1 (e) DIII-1c-1 (f) DIII-2c-1

Photo.1 Failure modes of the Bond-slip.

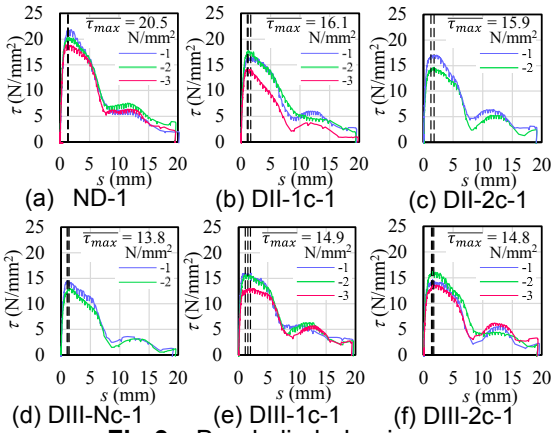

(a) ND-1 (b) DII-1c-1 (c) DII-2c-1

(d) DIII-Nc-1 (e) DIII-1c-1 (f) DIII-2c-1

Fig.9 Bond-slip behaviors.

amount of slip, s (mm). As shown in **Fig.8**, the anchor bars were bonded in the following locations: Nc in no cracks or cracks outside the damage range, 1c in a single crack, and 2c in the intersection of cracks. The anchorage positions were bonded at distances y from the critical section ranging from 0.32 to 0.39 D for Nc, 0.59 to 1.03 D for 1c, and 0.40 to 0.68 D for 2c (D = 300 mm).

3.2 Bond-slip Tests Results

Fig.9 shows the fracture conditions after the bond-slip tests. According to the Composite Structure Design Guidelines and Commentary 2010[5], the failure modes of adhesive anchors under tensile force are (1) yield and rupture of anchor bolts, (2) cone failure of concrete, (3) adhesion failure at the adhesive-concrete interface, and (4) adhesion failure at the steel bar-adhesive interface. adhesion failure at the adhesive-concrete interface, and (4) adhesion failure at the rebar-adhesive interface. As shown in **Fig.9**, although a small amount of concrete remained above the anchor bar in all specimens, cone failure did not occur, and only the anchor bar was pulled out. The fact that no adhesive remained in the anchor bar suggests that adhesion failure occurred at the rebar-adhesive interface.

Fig.10 shows the bond-slip behaviors for each parameter, and **Table5** lists the bond-slip tests results for the bond strength τ_{max} and displacement at bond strength s_{max} for each specimen. The average $\overline{\tau_{max}}$ of τ_{max} was 20.5 N/mm^2 for the ND specimen. The $\overline{\tau_{max}}$ of the other anchor bars decreased by 21 to 33 % compared to ND, with the greatest decrease in DIII-Nc. DIII-Nc, unlike the other parameters, showed the greatest decrease in τ_{max} despite the absence of cracks in the anchorage area. Compared with 1c and 2c, $\overline{\tau_{max}}$ did not change much for both DII and DIII, and the effect of the width and number of cracks was small. However, compared to DII and DIII, 1c and 2c decreased by 7.8 % and 6.4 %, respectively. s_{max} ranged from 1.05 to 2.03 mm for all specimens, and there was no significant variation among the parameters.

4. Evaluation of Bond-slip Tests Results

4.1 Effect of Parameters on the Bond Strength

Fig.11 shows the relationship between each parameter and the bond strength. The correlation coefficient of -0.43 indicates that the crack width has little influence on the bond strength, although it is expected to have a large influence. On the other hand, the correlation coefficient of -0.87 was strongly negative for the deformation drift R. The bond strength

tended to decrease as the deformation drift of the member increased. The τ_{max} tended to decrease as the deformation drift of the member increased. The tendency for τ_{max} to decrease with increasing deformation drift was also observed. These trends were compared with the bond strength using the distance of the anchorage point from the critical section and the moment obtained from the maximum load during the shear loading tests. The moment of the beam specimen at maximum load M_{max} was calculated and compared to the ratio of the moment to the yield moment M_u of the beam and the bond stress, and a correlation coefficient of -0.83 was found. However, since all the specimens used in this study were identical, additional tests will be conducted in the future using beam spans and cross-sections as parameters to verify whether a similar trend can be confirmed.

5. Conclusion

In this study, RC cantilever beams were damaged by shear forces and then bonded with adhesive anchors to conduct bond-slip tests to verify the effect of the degree of damage on the bond properties of adhesive anchors.

(1) Comparing the mean $\overline{\tau_{max}}$ for each parameter, the bond strength of the specimens bonded to the damaged beams was 21-33% lower than that of the ND specimens, with DIII-Nc being the parameter with the greatest reduction.

(2) Comparing each parameter to the bond stress, the crack width w, was expected to have a significant effect on the bond stress, but the correlation coefficient was -0.43, indicating that the effect was small.

(3) The correlation coefficient of the deformation drift R was -0.87, which is a strong negative correlation, and the bond strength tended to decrease as the deformation drift of the member increased.

(4) The moment of the beam specimen at maximum load M_{max} was calculated and compared to the ratio of the moment to the yield moment M_u of the beam and the bond stress, and the correlation coefficient was -0.83, which is a strong negative correlation like that of the deformation drift. The correlation coefficient was -0.83, which is a strong negative correlation as with the deformation drift of the member.

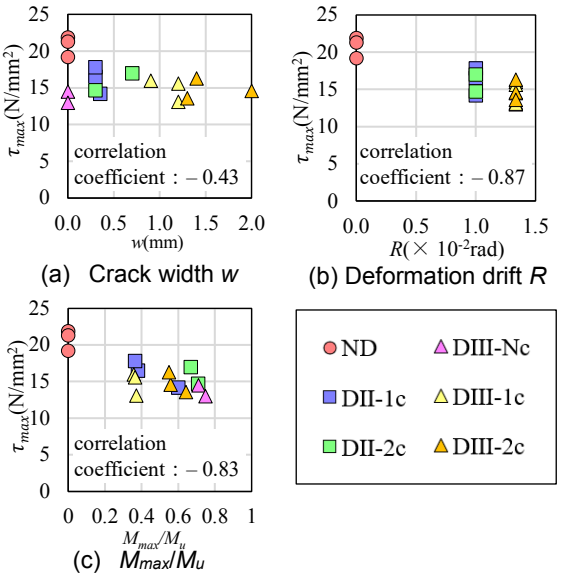

Fig.10 Relationship between parameters and τ_{max}.

REFERENCES

1. EOTA TR 029: Design of bonded anchors, European organization for technical approvals, 2010.9.
2. Hamazaki H., Aoyama Y., Watanabe K. and Satoh S. : Evaluation of Bond Strength and Deformation Properties of Adhesive Post-installed Anchors to Cracked Concrete, Proceedings of the Japan Concrete Institute, Vol.42, No.1, pp.1723-1728, 2017. (in Japanese)
3. Ishihara R., Kunieda M. and Takahashi M. : Development of test methods and experimental studies to evaluate the influence of concrete cracking on the mechanical performance of post-installed anchors, Proceedings of the Japan Concrete Institute, Vol.39, No.1, pp.1723-1728, 2017. (in Japanese)
4. Architectural Institute of Japan (AIJ): Guidelines for performance evaluation of earthquake resistant reinforced concrete buildings(draft), 2004. (in Japanese)
5. Architectural Institute of Japan (AIJ): Design recommendations for composite constructions 2023. (in Japanese)

A Bonding Performance Evaluation of Super Retarding Concrete for Cold Joint Integration under Hot Weather Conditions

Juntaek Jeong
Master student, Dept. of Architectural Engineering, Cheong-Ju University, Republic of Korea

Jaewoong Park
Master student, Dept. of Architectural Engineering, Cheong-Ju University, Republic of Korea.

Gunsu Lim
Doctoral student, Dept. of Architectural Engineering, Cheong-Ju University, Republic of Korea.

Jong Kim
Assistant Professor, Dept. of Architectural Engineering, Cheong-Ju University, Republic of Korea

Mincheol Han
Professor, Dept. of Architectural Engineering, Cheong-Ju University, Republic of Korea

Cheongoo Han
Chair Professor, Dept. of Architectural Engineering, Cheong-Ju University, Republic of Korea

Correspondence: jeaim0202@gmail.com

ABSTRACT:

Recently, the rapid growth of building construction industry for large buildings has led to a significant increase in the amount of pouring concrete over large areas in South Korea (Hereafter Korea). However, A regulation such as the 'Ready-Mixed Concrete 8.5 Policy' has limited the daily usage of concrete. It has created more joints causing inhibitions of structural integration. Therefore, this study aims to prevent cold joints for ensuring the structural integration under hot weather conditions by using super retarding agents. The bonding and integration performance were evaluated through the splitting tensile strength and direct shear tests. Test specimens were prepared with super retarding agents by mixing ratios of 0.1% and 0.2%, In addition, Air-entrained water-reducing retarders were used for comparison with conventional retarders. The specimens were cured at 35˚C to simulate hot weather conditions. As a result, the outcomes of the splitting tensile strength and direct shear tests indicated that the strength by using super retarding agents was higher than that by conventional retarders. Moreover, substantial integration performance was observed with a 0.2% super retarding agent mix.

….

Keywords: super retarding agent, integration, cold joint, hot weather, bonding performance

1. INTRODUCTION

In South Korea (Hereafter Korea), a trend for construction of high-rise and large-scale buildings is rapidly increasing. In accordance with the trend, the "8-5 Ready-Mixed Concrete (RMC) Policy" has been implemented to shorten the working hours of RMC workers from 8 am to 5 pm since 2016. Due to this policy change, the daily usage of concrete has been restricted. Moreover, traffic congestion in urban areas caused a delay in supplying the RMC to the construction sites. Under hot weather conditions when the outside air temperature exceeds 25°C, cold joints in the structure may occur although the concrete is poured within the 2-hour allowable time due to high temperatures. Consequently, more joints in the structure were created in that their integration in the structure was hindered as shown in Figure 1. Finally, it can harm the durability of the structures.

According to this issue, the research team in Cheongju University has developed super retarding agents (SRA)[1)2)3)] that can control the setting time for concrete. In addition, the team is currently developing a method to prevent cold joints for improving structural integration in a building by applying concrete mixed with the SRA to the existing concrete. The present study aims to evaluate the bonding performance between super retarding concrete and ordinary concrete according to the delay time and the SRA mixing ratio. This is analyzed through the splitting tensile strength and direct shear tests to assess the structural integration performance, which is the most suitable method for assessing compressive shear bonding performance by Kim et al.[4)].

Figure 1. Impediment to integration due to the occurrence of cold joints.

2. RESEARCH METHOD

2.1 EXPERIMENTAL PLAN

For the study, experiments were planned as shown in Table 1. To find out the proper mixing ratio of the SRA for the desired delay time, the mixing ratios of the SRA were set from 0% to 0.3% by increasing 0.1%. For a performance comparison between the SRA and conventional retarders, an Air-entraind water-reducing agent (AE retarder) was used.

The specimen was fabricated with three different parts (Figure 2). It included the existing concrete, super retarding concrete and newly poured concrete. The delay time between the pouring of super retarding concrete and the newly pouring concrete was set to 2 hours and 4 hours, which corresponded to the standard specified in the Korean Concrete Standard Specifications for outdoor temperatures exceeding 25°C. The curing and resting during the delay time was planned to be conducted at 35°C. During the measurements, the splitting tensile strength, the direct shear tests and the fracture mode on hardened concrete were performed.

Table 1. Experimental plan

Factors			Variables
Mixture	W/C(%)	1	45
	Binder (%)		OPC100
	Test specimens (mm)	3	Ø 100 cylinder mold Ø 150 cylinder mold 150X150X150
Variables	Cure temperature	1	35° C
	Retarders	2	AE water reducing retarder2) Super retarding agent
	SRA contents(%)	2	0.1, 0.2, 0.3
	Delay time (hr.)1)		2, 4
Experimental	Fresh concrete	4	Slump
	Hardened concrete		Air content Setting time
			Compressive strength 3)
			Tensile splitting strength 4)
			Direct shear test 4)
			Fracture mode

1) time between initial and subsequent pours
2) the same amount of water-reducing agent incorporated into the plain mix
3) 3, 7, 28 days
4) 7, 28 days

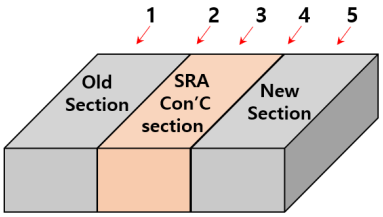

Figure 2. Specimen Representative Positions

2.2 SPECIMEN FABRICATION METHOD

The fabrication method for specimens to assess the splitting tensile strength is presented in Figure 3. First, a cylindrical mold with a diameter of 150mm was vertically halved as illustrated in Figure 3a. One half was filled with the super retarding concrete, AE retarder concrete, and normal concrete according to the variables. The remaining half was filled with normal concrete at different delay times as illustrated in Figure 3b.

a) b)

Figure 3. Fabrication of Splitting Tensile Strength Specimen

The fabrication method for specimens to evaluate the Direct shear is shown in Figure 4. First, a 150x150x150 mm mold was vertically divided into three parts as illustrated in Figure 4a. Two-thirds of the mold was filled with super retarding concrete, AE retarder concrete, and normal concrete according to the variables. The remaining one-third was filled with normal concrete at different delay times as illustrated in Figure 4b.

a) b)

Figure 4. Fabrication of Direct Shear Test Specimen

2.3 MATERIALS FOR MEASUREMENTS

(1) CEMENT

The cement used for these measurements was a Type 1 Portland Cement product from Company H in Korea. Its physical properties are listed in Table 2

Table 2. Physical properties of cement

density (g/cm3)	Blaine (cm2/g)	setting time(min.)		compressive strength (MPa)		
		Ini.	Fin.	3ds.	7ds,	28ds,
3.15	3 740	210	315	32.0	42.5	52.6

(2) AGGREGATES

The aggregates used in the experiments were crushed quarry aggregates that satisfy KS standards. Their physical properties are presented in Table 3.

Table 3. Physical properties of aggregates

Aggregates	density (g/cm3)	absorption ratio (%)	0.08 mm sieve passing (%)	F.M.
Crushed sand	2.59	1.92	4.98	2.96

(3) ADMIXTURE

The admixtures used in the experiments included domestically produced water-reducing agents, AE agents, and AE retarder agents, and their physical properties are shown in Table 4.

Table 4. Physical properties of chemical admixtures

Kinds	Main ingredient	Appearance	density (20℃)
plasticizer	poly carboxylic acid	dark brown, liquid	1.05
AE agent	Sodium lauryl sulfate	light yellow, liquid	1.04
AE retarder	gluconate	dark brown, liquid	1.18

(4) SUPER RETARDING AGENT

The super retarding agent used in the measurements was prepared through the method derived from previous studies (Figure 2). First, the sugar solution was prepared by mixing water and sugar at a ratio of 1:1. The thickener was prepared by mixing the thickener and water at a ratio of 4:996 (1:249). The AE agent was used in its original form. The super retarding agent was then prepared and used by mixing the sugar solution, Polyethylene Oxide (PEO) thickener, and AE agent at a ratio of 2:1:0.05. The physical properties of each material are shown in Table 5.

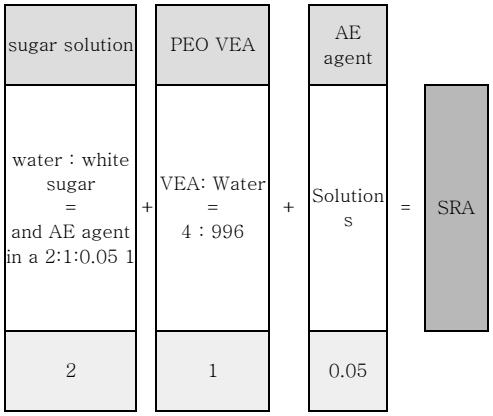

Figure 2. Method to mix each material for making SRA

Table 5. Physical properties of chemical admixtures in SRA

Type	Main ingredients	Appearance	density (20℃)
VEA	Polyethylene oxide	white, powder	1.00
Retarder	White sugar	White powder	1.59
AE agent	Sodium lauryl sulfate	Yellow bright Solution	1.04

2.3 EXPERIMENTAL METHOD

Slump, air content, and setting time for the compressive strength and splitting tensile strength tests were set according to KS standards, while the Direct shear test was performed with reference to the study by Dinis et al.[5)]

As shown in Figure 5, the fabricated specimens were positioned for the splitting tensile strength test ensuring that the joint was perpendicular to the loading surface. The tensile strength at the joint was measured for at 7th and 28th day according to KS F 2423.

The Direct shear test was conducted as illustrated in

Figure 6. A 50x50x150 mm steel plate was placed 50 mm from the left or right side of the upper interface of the specimen. A similar steel plate was placed at the left and right ends of the bottom. This allowed the application of compressive force indirectly to the bonding surface.

The fracture mode was observed and recorded after completing the Direct Shear Test to assess the degree of integration of the specimen.

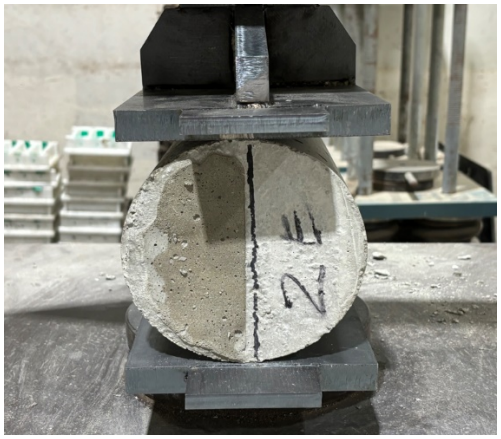

Figure 5. Splitting Tensile Strength Test Method

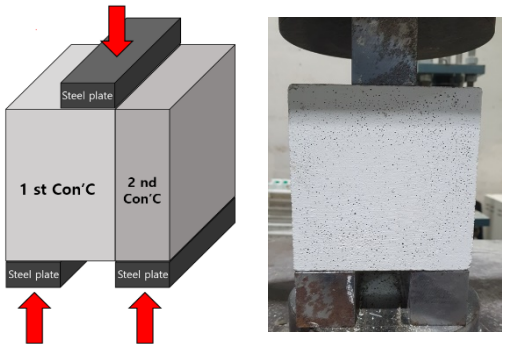

Figure 6. Direct Shear Test Method

3. RESULTS AND DISCUSSIONS

3.1 THE PROPERTIES OF FRESH CONCRETE

The slump and air content of fresh concrete in the experiments are shown in Figure 7. In addition, the penetration resistance over time is shown in Figure 8. As the mixing ratio of the super retarding agent increased, the slump slightly also increased within standard range values which showed a little impact. Similarly, it was observed that the AE retarder had little effect on the slump. Regarding air content, an increase in the SRA mixing ratio resulted in a slight increase in air content within the standard range. This implies that the SRA is a little impact on air content. A similar outcome was observed in the measurements with the AE retarder. It also had little impact on air content.

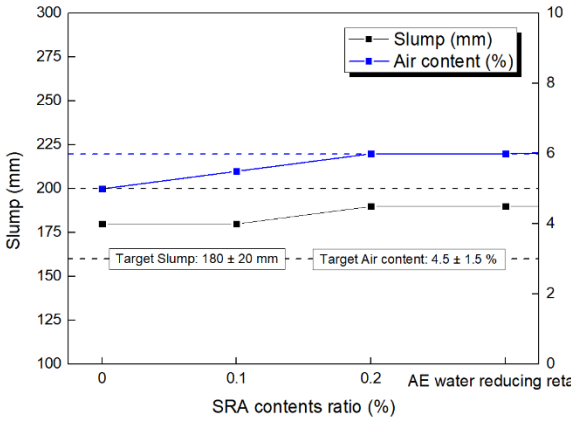

Figure 7. Air Content and Slump According to Super Retarding Agent Mixing Ratio and Admixture Changes

By the changes of the mixing ratio of super retarding agent and the admixtures, the penetration resistance over setting time was measured (Figure 8). The finale setting time of the plain mix was approximately 6 hours and 40 minutes. As the mixing ratio of the super retarding agent increased by 0.1%, the setting time incrementally increased by approximately 1 hour, 4 hours, and 12 hours. In the case of the AE retarder, the initial setting time was delayed compared to the 0.1% super retarding agent mix. After the initial set, it accelerated rapidly and resulted in the final setting time about 20 minutes faster than the 0.1% super retarding agent mix.

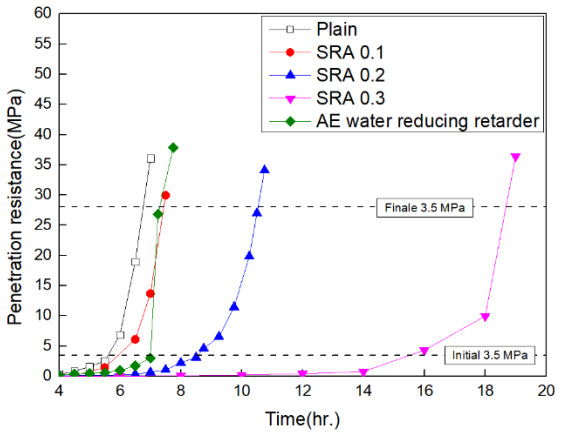

Figure 8. Penetration Resistance Over Time According to Super Retarding Agent Mixing Ratio and Admixture Changes

3.2 HARDENED PROPERTIES OF THE CONCRETE

The study on the properties of the hardened concrete was conducted by selecting the mixing ratio of the super retarding agent that satisfies the target setting delay time. The target setting delay time was approximately 10 hours, which is sufficient to avoid negative impact on the subsequent processes at the construction site. Therefore, the hardened concrete

experiments were conducted excluding the 0.3% mixing ratio of the super retarding agent, which had a finale setting time of approximately 19 hours.

3.2.1 COMPRESSIVE STRENGTH

Figure 9 shows the compressive strength according to the changes of the mixing ratio of the super retarding agent and admixtures. Overall, all mixes showed a decrease in the compressive strength compared to the plain mix at early ages. At later ages, it increased. According to Hyun et al.[6] when the solubility of cement increased, a large amount of ions was generated during the delayed hydration caused by the super retarding agent and retarders. Moreover, these ions diffused over a wide area. The diffused ions rapidly participated in the hydration reaction, resulting in an increase in the compressive strength, when the setting delay effect ends, .

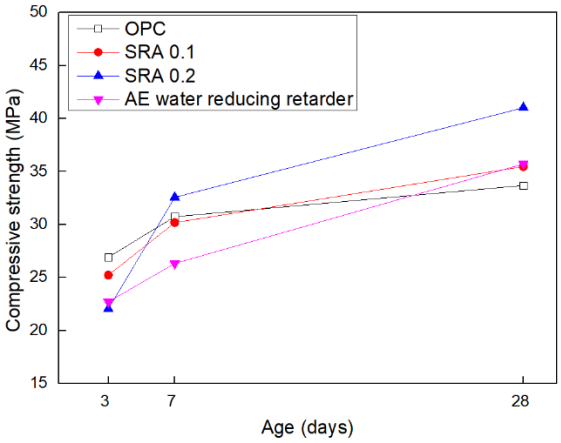

Figure 9. Compressive Strength at Different Ages According to Super Retarding Agent Mixing Ratio and Admixture Changes

3.2.2 SPLITTING TENSILE STRENGTH

Figures 10 and 11 show the splitting tensile strength values of Ø 150 specimens for 2-hour and 4-hour delays in placing according to the changes of the mixing ratio of the super retarding agent and admixtures. At 7 days of age, except for the case of a 2-hour delay with AE retarder, all mixes showed an increase in the strength compared to that by the separated placement. At 28 days of age, all mixes showed an increase in the strength compared to that by the separated placement, particularly the mix with 0.1% super retarding agent and a 4-hour delay, which exhibited approximately twice the strength.

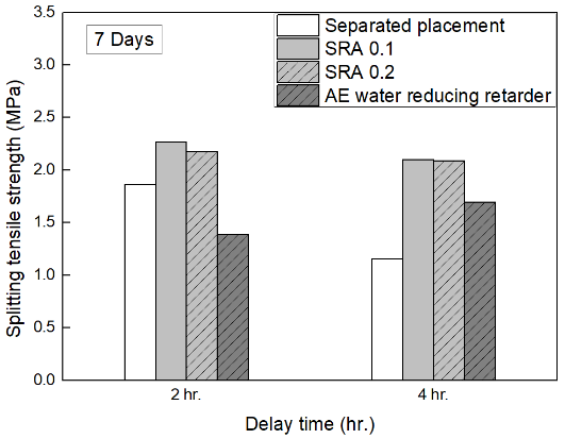

Figure 10. Splitting Tensile Strength at 7 Days for Different Delay Times with Varying Super Retarding Agent Ratios and Admixture Changes

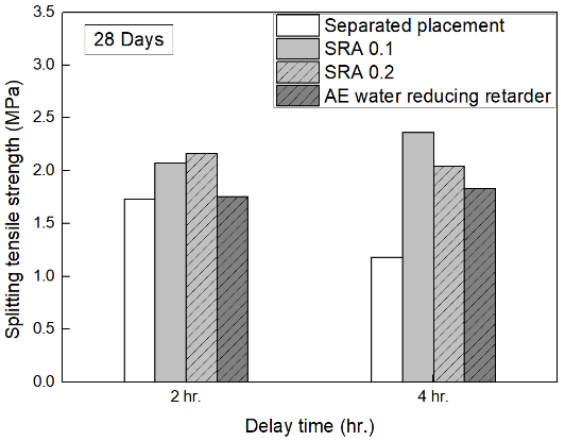

Figure 11. Splitting Tensile Strength at 28 Days for Different Delay Times with Varying Super Retarding Agent Ratios and Admixture Changes

3.2.3 DIRECT SHEAR TEST

Figures 12 and 13 show the compressive shear bond strength of 150x150x150 mm specimens for 2-hour and 4-hour delays according to the chagnes of the mixing ratio of the super retarding agent and admixtures. At 7 days of age, all delay times showed an increase in the compressive shear bond strength for the specimens with super retarding agent and AE retarder. Similarly, all mixes showed an increase in the strength at 28 days of age compared to that by the separated placement. In particular, the application of the super retarding agent with a 4-hour delay has resulted in more than twice the strengths at all ages.

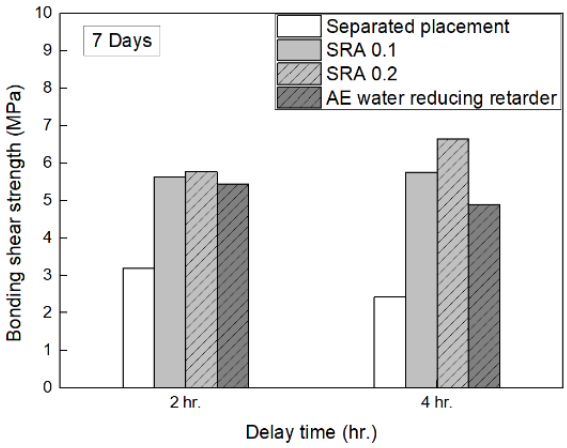

Figure 12. Direct Shear Test Results at 7 Days for Different Delay Times with Varying Super Retarding Agent Ratios and Admixture Changes

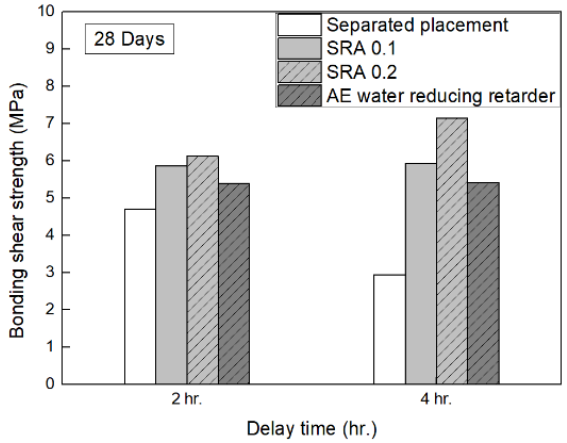

Figure 13. Direct Shear Test Results at 28 Days for Different Delay Times with Varying Super Retarding Agent Ratios and Admixture Changes

3.2.3 FRACTURE MODE AFTER DIRECT SHEAR TEST

Tables 6 and 7 show the fracture modes after the Direct Shear Test for different delay times in placing. The fracture modes were categorized into three types based on the fractured shapes. Type A denotes fractures at the bonding interface between the initial pour and subsequent pour concrete, Type B denotes fractures at non-interface areas, and Type C denotes simultaneous fractures at both the bonding interface and non-interface areas.

For a 2-hour delay in placing, as shown in Table 6, the separated placement without super retarding agent resulted in Type A fractures, indicating hindered integration between the initial and subsequent pours. In contrast, specimens with super retarding agent and AE retarder showed Type C fractures, suggesting good integration and uniform stress distribution.

For a 4-hour delay in placing, as shown in Table 7, Type A fractures were observed in specimens without super retarding agent and with AE retarder. However, specimens with super retarding agent exhibited Type C fractures at all mixing ratios, indicating that the inclusion of super retarding agent effectively enhanced integration performance compared to separated placement or AE retarder.

Table 6. Fracture Modes with 2-Hour Delay in Placing

	7 Days	28 Days
Seperate	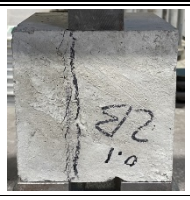	
	Type A	Type A
0.1		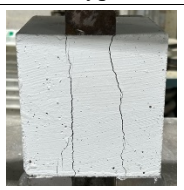
	Type C	Type C
0.2		
	Type C	Type C
AE retarder		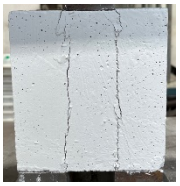
	Type C	Type C

Table 7. Fracture Modes with 4-Hour Delay in Placing

	7 Days	28 Days
Seperate	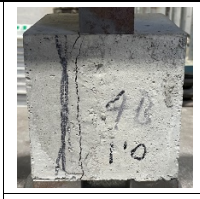	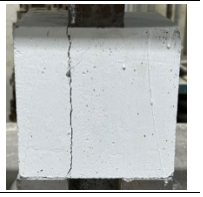
	Type A	Type A
0.1		
	Type C	Type C

0.2		
	Type C	Type C
AE retarder	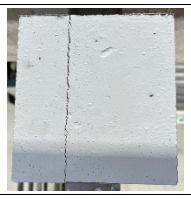	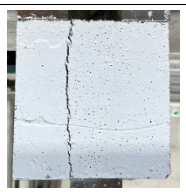
	Type C	Type C

4. CONCLUSION

This study aimed to develop a method to prevent cold joints for the structural integration by using super retarding agents (SRAs). A series of experiments were conducted to evaluate the bonding performance of concrete with SRAs or AE retarders under hot weather conditions with varying delay times. The summary of the results is as follows:

1) The compressive strength was measured at 3, 7, and 28 days. The application of both SRA and AE retarder showed a tendency for the reduced compressive strength compared to that by the plain mix at early ages. At later ages, it increased.

2) The bonding strength was evaluated through the splitting tensile strength at 7th day and 28th day. All mixes showed the increased strength compared to that by the separated placement. Notably, the mix with 0.1% SRA and a 4-hour delay exhibited approximately twice the strength at 28th day, demonstrating the excellent bonding performance.

3) The bonding strength was also evaluated through the Direct Shear tests at 7th day and 28th day. All mixes generally showed a increased strength compared to that by the separated placement. Specifically, the mix with SRA and a 4-hour delay showed more than twice the strength at all ages.

In conclusion, the application of SRAs is advantageous for the structural integration under hot weather conditions compared to AE retarders. To enhance integration performance, it requires to verify stability and effectiveness of the cement with SRAs at 0.2%.

REFERENCES

1. Sim BG, Yoo DS, Yoon CH, Han MC, Han CG. A fundmental study on the development of saccharic type super retarding agent. Architectural Institute Of Korea,21(1),309-312.

2. Han CG, Han MC, Yoon CH, Sim BG. Settingtime and mechanical properties of concrete using saccharic type super retarding agent. Korea concrete institute,14(4),589-596

3. Jeong YJ. Setting Time and Compressive Strength of the Cement Paste depending on Super Retarding Agent Types. master's thesisgraduate school cheongju university. 2022

4. Kim MS. Study on the Period of Cold joint occurrence effecting shear bond Performances of UHSCC. master's thesisgraduate school hanyang university. 2017

5. Dinis S., Pedro M.D., and Daniel D. (2012) Effect of surface preparation and bonding agent on the concrete-to-concrete interface strength, Construction and Building Materials, Vol. 37, pp. 102−110

6. Hyeon SY. Estimation of setting of super retarding concrete using maturity and settimeter. Doctoral dissertation graduate school cheongju university. 2022

EXPERIMENTAL STUDY ON STRUCTURAL PERFORMANCE OF HOT-DIP GALVANIZED REINFORCEMENT IN CONCRETE CONSIDERING BAR PLACEMENT

Hongbok CHOE
Assistant professor, College of Industrial Technology, Nihon University, Japan.

Tomohisa MUKAI
Head, Evaluation System Division, Building Dept., National Institute for Land and Infrastructure Management, Japan.

Hideyuki KINUGASA
Professor, Faculty of Science and Technology, Tokyo University of Science, Japan.

ABSTRACT:
In previous studies on the structural performance of RC beam specimens using hot-dip galvanized reinforcement (hereinafter, HDG rebar), the shear safety margin (the ratio of ultimate shear strength to ultimate bending strength) was used to evaluate failure modes such as bending failure, bond failure after main bar yielding, bond failure before main bar yielding, and shear failure. However, the differences between RC beams using HDG rebar and those using ordinary steel reinforcement (hereinafter, OS rebar) under the same design conditions, including concrete strength, rebar strength, and bar placement, have not been clearly identified. This study aims to clarify the differences in structural performance between HDG rebar and OS rebar in RC beam specimens. As a result, it was clearly confirmed that there are both similarities and differences between the two types of rebar with regard to the shear safety margin.
Keywords: hot-dip galvanized reinforcement, cut-off main bar, structural test, load-rotation angle curve, crack behavior, local bond stress

1. INTRODUCTION

In previous studies [1]-[5], the structural performance of RC beams using hot-dip galvanized reinforcement (hereafter, HDG rebar) have been evaluated based on shear safety margin (the ratio of ultimate shear strength to ultimate bending strength). Those evaluations have been conducted by RC beams with continuous reinforcement.

Previous studies have indicated that under conditions with insufficient shear and bond capacity, HDG rebar are more prone to bond splitting failures compared to ordinary steel reinforcement (hereafter, OS rebar) [1, 2]. However, differences between RC beams using HDG rebar and those using OS rebar under the same design conditions have not been clearly identified. Furthermore, there are no evaluation cases for cut-off HDG rebar (cut-off : reinforcement applied in the 2nd layer main bar), which requires higher bond performance than continuous reinforcement, and their application is not recognized in current guidelines [6].

Therefore, the aim of this study is to clarify the differences in structural performance between HDG rebar and OS rebar in RC beam specimens. This study considered the design conditions which are bending failure, bond splitting failure, and shear failure in the continuous bar (B9~B11 specimens), and bond failure in the cut-off bar (CO1 specimens).

2. EXPERIMENTAL

2.1 Specimen Outline

Figure 1 shows the outline of beam specimens. Firstly, the differences between B9 to B11 specimens are the spacing of the shear reinforcement in the test area (B9=87mm, B10=130mm, and B11=195mm). Those beams are reinforced with either HDG rebar (B9-HDG, B10-HDG, B11-HDG) or OS rebar (B9-OS, B10-OS, B11-HDG) by continuous bars. Secondly, CO1 specimens are beam specimens with cut-off bars in the 2nd layer main bar using either HDG rebar (CO1-HDG) or OS rebar (CO1-OS). A shear reinforcement spacing of 78 mm is embedded at both specimens. Including all, total numbers of beams are 8 specimens in this experiment.

Table 1 presents the material test results for the beam specimens in this experiment. For B9~B11 specimens, D16-SD295 for the main bar and D10-SD295 for the shear bar were used. For CO1 specimens, D13-SD295 for the main bar and D10- SD295 for the shear bar were used. For all specimens, a concrete with W/C=62.5% was used and placed together at the same day. σ_B is measured at the day when structural test was performed.

Table 2 provides a list of calculated values for the beam specimens in this experiment (based on material test results, referred to Table 1). About the reinforcement ratio, B9~B11 specimens are designed to have p_t = 1.15% (p_t : tensile reinforcement ratio) and p_w =

0.36~0.82% (p_w : shear reinforcement ratio). For CO1 specimens, p_t is 1.32%, and p_w is 0.95%. Next, the values of Q_{su} and Q_{mu} are calculated based on reference [7], and τ_{bu} and τ_f are calculated based on reference [8].

Figure 2 compares the shear safety margin (Q_{su}/Q_{mu}) and bond safety margin (τ_{bu}/τ_f) between the specimens in this experiment and that in the previous studies [1, 2]. From the left figure, it shows that B9 is designed for bending failure (above 1.2 of Q_{su}/Q_{mu}), B10 for bond splitting failure after bending yield (1.1~1.2 scope of Q_{su}/Q_{mu}), and B11 for shear failure after bending yield (1.0~1.1 scope of Q_{su}/Q_{mu}). These design conditions are based on the failure modes observed in previous studies [1, 2] for specimens B2 to B8 (B2: bending failure, B5: bond splitting failure, B6: bending failure, B7: bond splitting failure after bending yield, B8: shear failure after bending yield). From the right figure, No.11 and No.13 are HDG rebar-embedded specimens placed with 2nd layer continuous main bars [4]. Those specimens satisfied the design guideline [8, 9], with τ_{bu}/τ_f above 1.0 for both 1st and 2nd layer main bars. In contrast, For CO1 specimens, it was shown that the 1st layer main bar satisfied τ_{bu}/τ_f above 1.0, but the 2nd layer main bar did not. This was intended to induce bond splitting failure at the 2nd layer main bar and influence the 1st layer main bar.

2.2 Structural Test Outline

Figure 3 shows the structural test outline. The loading method is based on the Ohno method, which applies a reversed symmetric bending moment distribution to the test area through unidirectional loading. Strain gauges were applied to one side of the rebar at each location (B9 : 4 to 23 gauges, B10 : 4 to 20 gauges, B11 : 4 to 18 gauges, CO1 : 4 to 32 gauges as shown in Figure 1). The experiment was controlled by applying load to specific rotation angle (=R) and increasing the load up to R = 5%. R (%) is calculated by Eq.1.

$$R(\%)=\frac{\text{vertical displacement of test area (mm)}}{\text{test area length (780mm)}}\times 100 \quad (1)$$

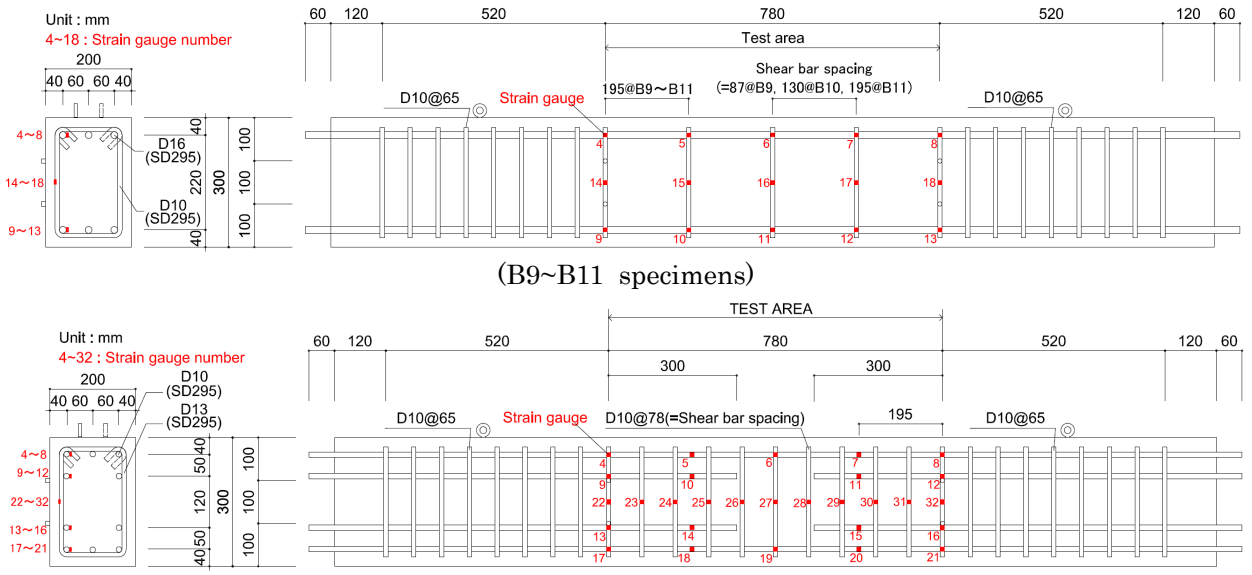

Figure1 Specimen outline

Table 1 Material test results

Specimen	Main bar			Shear bar			Concrete		
	σ_y (N/mm²)	ε_y (μ)	E_s (N/mm²)	σ_y (N/mm²)	ε_y (μ)	E_s (N/mm²)	W/C (%)	σ_B (N/mm²)	E_c (N/mm²)
B9-HDG	348	1859	189088	343	1777	193373	62.5	25.6	26800
B9-OS	336	1811	184882	340	1786	190421			
B10-HDG	348	1859	189088	343	1777	193373		25.6	26800
B10-OS	336	1811	184882	340	1786	190421			
B11-HDG	348	1859	189088	343	1777	193373		26.4	24900
B11-OS	336	1811	184882	340	1786	190421			
CO1-HDG	341	1834	186670	340	1786	190421		28.5	25500
CO1-OS	351	1890	186726	343	1777	193373			

σ_y : Yield strength of the rebar, ε_y : Yield strain of the rebar, E_s : Young's modulus of the rebar, W/C : Water-cement ratio of the concrete, σ_B : Compressive strength of the concrete, E_c :, , Young's modulus of the concrete

Table 2 Calculation results

Specimen	p_t (%)	p_w (%)	Q_{su} (kN)	Q_{mu} (kN)	τ_{bu} (N/mm^2)	τ_f (N/mm^2)	Q_{su}/Q_{mu}	τ_{bu}/τ_f
B9-HDG	1.15	0.82	151 (377.5)	125 (312.5)	3.87	6.12	1.21	0.63
B9-OS	1.15	0.82	150 (375)	120 (300)	3.87	5.91	1.25	0.65
B10-HDG	1.15	0.55	139 (347.5)	125 (312.5)	3.10	6.12	1.11	0.51
B10-OS	1.15	0.55	139 (347.5)	120 (300)	3.10	5.91	1.15	0.52
B11-HDG	1.15	0.36	131 (327.5)	125 (312.5)	2.60	6.12	1.05	0.43
B11-OS	1.15	0.36	131 (327.5)	120 (300)	2.60	5.91	1.08	0.44
CO1-HDG	1.32	0.95	146 (365)	123 (308)	5.47 [1L] 6.33 [2L]	4.75 [1L] 24.15 [2L]	1.18	1.15 [1L] 0.26 [2L]
CO1-OS	1.32	0.95	145 (362.5)	120 (300)	5.47 [1L] 6.33 [2L]	4.61 [1L] 23.46 [2L]	1.21	1.19 [1L] 0.27 [2L]

p_t : Tensile reinforcement ratio, p_w : Shear reinforcement ratio, Q_{su} : Ultimate shear strength by Arakawa mean formula, Q_{mu} : Ultimate bending strength by simplified formula, τ_{bu} : Bond reliability strength, τ_f : Design bond stress, Q_{su}/Q_{mu} : Shear safety margin, τ_{bu}/τ_f : Bond safety margin, [1L] : 1st layer main bar, [2L] : 2nd layer main bar, ( ): The values are $2.5Q_{mu}$ or $2.5Q_{su}$ for comparison with the experimental maximum load P_{max}.

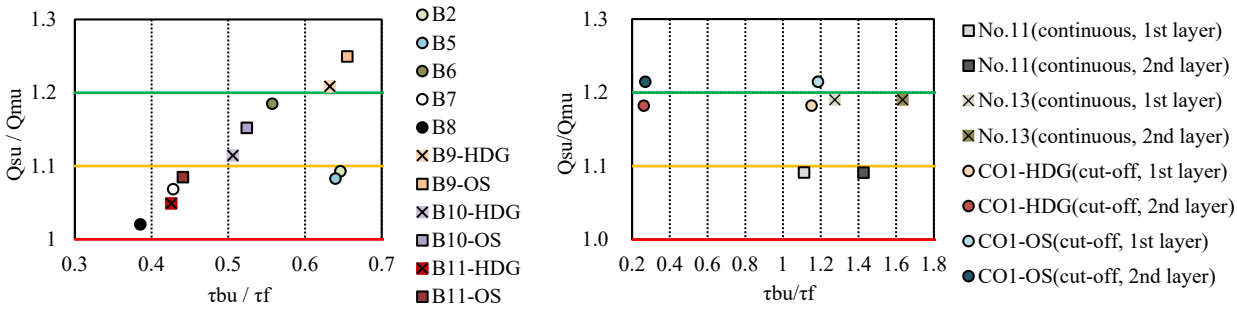

Figure 2 Comparison of calculation result (Left : B9~B11, Right : CO1) including previous studies [1, 2, 4]

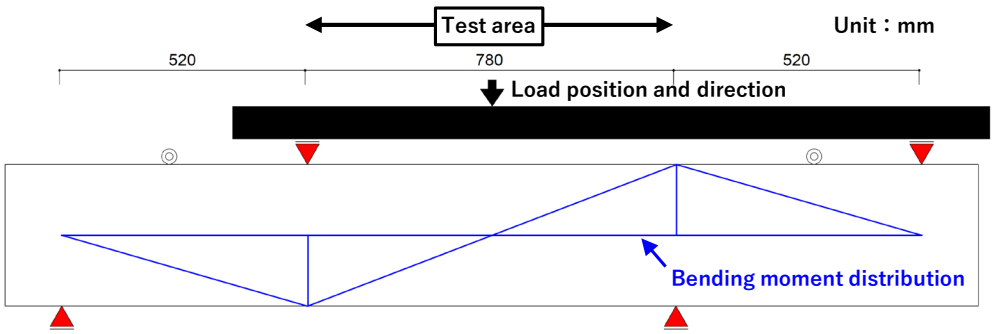

Figure 3 Structural test outline (same side as seen in Figure 1)

3. RESULT AND DISSCUSSION

3.1 Load-rotation angle, strain and Cracking Characteristics

Figure 4 shows the load-rotation angle relationship up to R = 3% for each specimen, including the yielding points of strain gauges (=SG) at the rebar, comparing with HDG and OS rebar. Table 3 presents the experimental maximum load (P_{max}), the calculated ultimate bending strength ($2.5Q_{mu}$) for comparison with P_{max}, and the ratio of P_{max} to $2.5Q_{mu}$ (P_{max} / $2.5Q_{mu}$). Figure 5 illustrates the cracking characteristics after the end of structural test.

From Figure 4, it is confirmed that the yield points of the main bar in B9-HDG and B10-HDG shows a delayed behavior compared to B9-OS and B9-OS, respectively. Despite this difference, the load-rotation angle relationships (Figure 4) and cracking characteristics (Figure 5) for B9 and B10 are generally consistent for both HDG and OS rebar. In addition, since the yield of the shear reinforcement did not affect the load reduction on both B9 and B10, it is confirmed that B9 experienced bending failure, and B10 experienced bond splitting failure after bending yield. Therefore, the structural performance of both types of rebar can be considered equivalent in the condition that a shear safety margin is 1.1 or more.

However, for B11 specimens, which a shear safety

margin is below 1.1, different load-rotation angle relationships and cracking behaviors were observed between the two types of rebar. B11-OS underwent shear failure, whilst B11-HDG experienced bond splitting failure after bending yield. This difference is believed to be due to the earlier yielding of SG16-OS at shear bar in B11-OS (Figure 4), which prevented the strain at the main bar ends (SG8, SG9) from reaching yield, causing a continuous reduction in strain after the yielding of SG16.

Next, about CO1 specimens in Figure 4, load-rotation angle relationship showed that the stiffness up to the first yield of the main reinforcement (SG8-HDG, SG8-OS) and the subsequent structural performance were generally similar between the two specimens (CO1-HDG, CO1-OS). Comparing both specimens up to around R=0.6%, CO1-HDG shows yielding at SG8, SG17, SG18, and SG13, while CO1-OS exhibits more yielding at SG7, SG8, SG12, SG13, SG17, and SG18.

However, in Figure 4, in the range of approximately R=0.5~1.4%, CO1-OS exhibited higher loads compared to CO1-HDG. The maximum load (P_{max}) for CO1-OS was 361.78kN (R=0.86%), which is larger than CO1-HDG (P_{max} was 341.9kN and R=1.29%). Figure 6 presents the strain distributions at the tension end of the 2nd layer main bar of CO1 specimens. From SG12 and SG13 (illustrated in Figure 5), CO1-OS strains significantly exceeding the yield strain after around R=0.5%, whereas CO1-HDG strains barely exceed or increase beyond the yield strain. In addition, this behavior difference in both specimens was similarly observed in SG8 (=tension end of the upper 1st layer main bar). It is suggested that slip at the tension end of the upper main bar in CO1-HDG might have led to reduced load increases compared to CO1-OS. Therefore, the difference in load within the specified range (R=0.5~1.4%) is attributed to the strain behavior at the tension end of the upper main bar.

Meanwhile, in Figure 4, a load decrease between R=0.88% and 2.0% was observed for CO1-OS, which was greater than that for CO1-HDG. Figure 7 presents the strain distributions at the shear bar. For SG24, strain increases gradually in CO1-HDG, while in CO1-OS, strain increases rapidly after exceeding the yield strain at R=0.84%. This rapid strain increase in CO1-OS is likely responsible for the greater load decrease observed between R=0.88% and 2.0% compared to CO1-HDG (refer to Figure 4). Meanwhile, red lines in Figure 5 indicate the reinforcement layout in the test area. Both specimens exhibited local large shear cracks at positions where the main bar tension ends yielded (SG17, SG18), followed by yielding at SG24 and SG25. Consequently, Though the load decrease was gradual, both specimens ultimately experienced shear failure after bending yield.

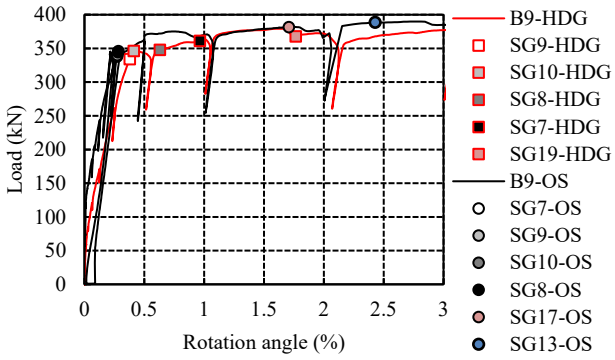

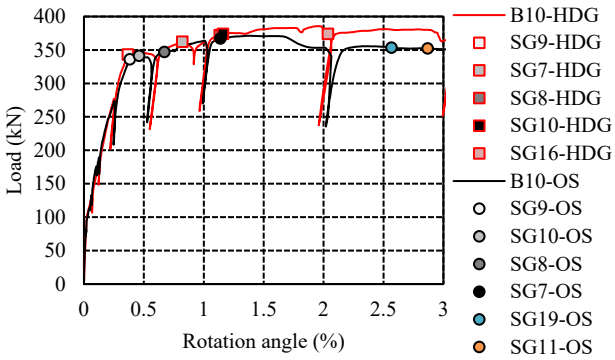

B9-HDG	Yield order	R (%)	P (kN)
Lower bar	SG9-HDG	0.38	333.99
Lower bar	SG10-HDG	0.41	346.11
Upper bar	SG8-HDG	0.63	347.95
Upper bar	SG7-HDG	0.96	361.17
Shear bar	SG19-HDG	1.77	367.78

B9-OS	Yield order	R (%)	P (kN)
Upper bar	SG7-OS	0.27	337.79
Lower bar	SG9-OS	0.27	339.99
Lower bar	SG10-OS	0.28	344.40
Upper bar	SG8-OS	0.28	345.99
Shear bar	SG17-OS	1.71	381.49
Lower bar	SG13-OS	2.43	388.59

B10-HDG	Yield order	R (%)	P (kN)
Lower bar	SG9-HDG	0.37	343.17
Upper bar	SG7-HDG	0.82	362.39
Upper bar	SG8-HDG	1.13	372.07
Lower bar	SG10-HDG	1.16	374.15
Shear bar	SG16-HDG	2.04	374.15

B10-OS	Yield order	R (%)	P (kN)
Lower bar	SG9-OS	0.38	336.07
Lower bar	SG10-OS	0.46	341.21
Upper bar	SG8-OS	0.67	347.09
Upper bar	SG7-OS	1.14	367.05
Shear bar	SG19-OS	2.57	353.46
Lower bar	SG11-OS	2.87	352.35

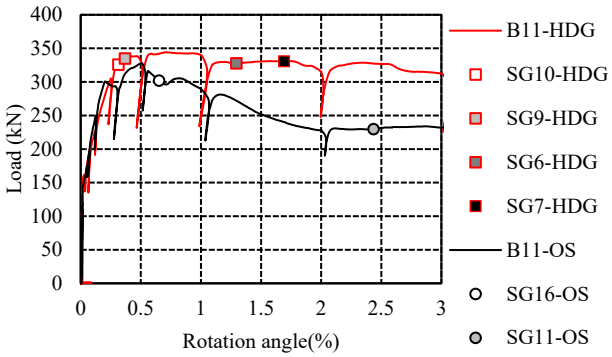

B11-HDG	Yield order	R (%)	P (kN)
Lower bar	SG10-HDG	0.31	325.66
Lower bar	SG9-HDG	0.37	334.72
Upper bar	SG6-HDG	1.29	327.62
Upper bar	SG7-HDG	1.69	330.81

B11-OS	Yield order	R (%)	P (kN)
Shear bar	SG16-OS	0.65	301.91
Lower bar	SG11-OS	2.43	229.80

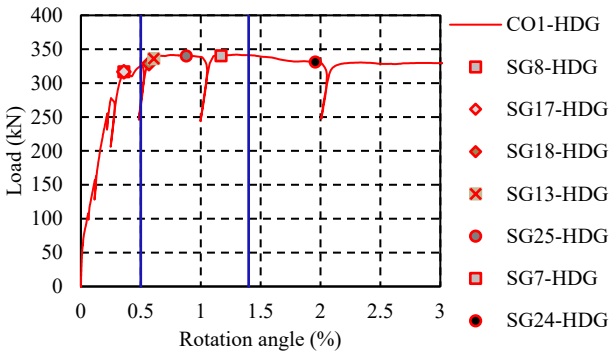

CO1-HDG	Yield order	R (%)	P (kN)
Upper bar [1L]	SG8-HDG	0.36	316.85
Lower bar [1L]	SG17-HDG	0.36	316.85
Lower bar [1L]	SG18-HDG	0.57	328.73
Lower bar [2L]	SG13-HDG	0.61	336.07
Shear bar	SG25-HDG	0.88	340.11
Upper bar [1L]	SG7-HDG	1.17	340.36
Shear bar	SG24-HDG	1.96	331.17

[1L] : 1st layer main bar
[2L] : 2nd layer main bar

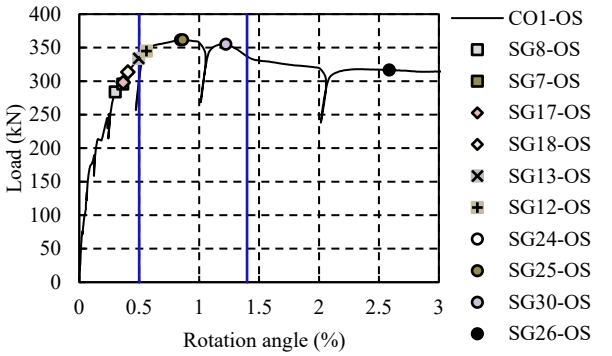

CO1-OS	Yield order	R (%)	P (kN)
Upper bar [1L]	SG8-OS	0.30	284.04
Upper bar [1L]	SG7-OS	0.36	295.67
Lower bar [1L]	SG17-OS	0.37	298.00
Lower bar [1L]	SG18-OS	0.41	313.67
Lower bar [2L]	SG13-OS	0.50	333.87
Upper bar [2L]	SG12-OS	0.56	344.89
Shear bar	SG24-OS	0.84	361.54
Shear bar	SG25-OS	0.86	361.78
Shear bar	SG30-OS	1.22	355.17
Shear bar	SG26-OS	2.58	316.73

[1L] : 1st layer main bar
[2L] : 2nd layer main bar

Figure 4 Load-Rotation angle (=R) curve and yielding event of main and shear bar until R=3%

Table 3 Comparison of experimental maximum load (P_{max}) and $2.5Q_{mu}$

(Unit:kN)	B9-HDG	B9-OS	B10-HDG	B10-OS	B11-HDG	B11-OS	CO1-HDG	CO1-OS
P_{max}	385.9	389.9	386.7	371.2	344.3	328.0	341.9	361.8
$2.5Q_{mu}$	301.0	311.8	301.0	311.8	301.0	311.8	365.0	362.5
$P_{max}/2.5Q_{mu}$	1.28	1.25	1.28	1.19	1.14	1.05	0.94	1.00

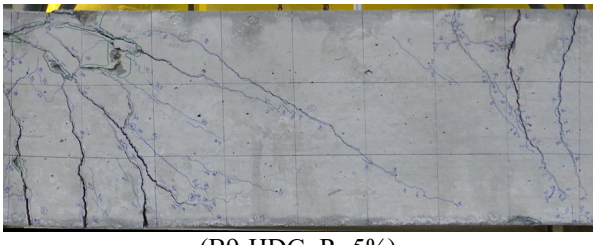
(B9-HDG, R=5%)

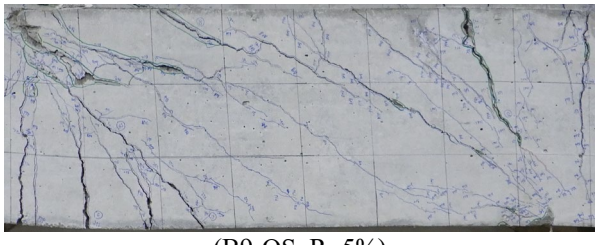
(B9-OS, R=5%)

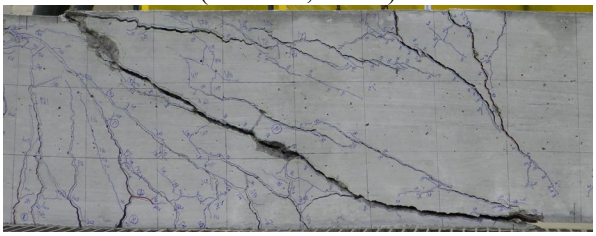
(B10-HDG, R=5%)

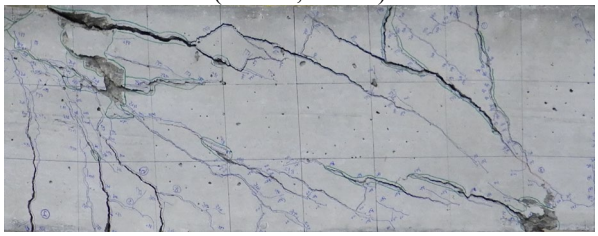
(B10-OS, R=5%)

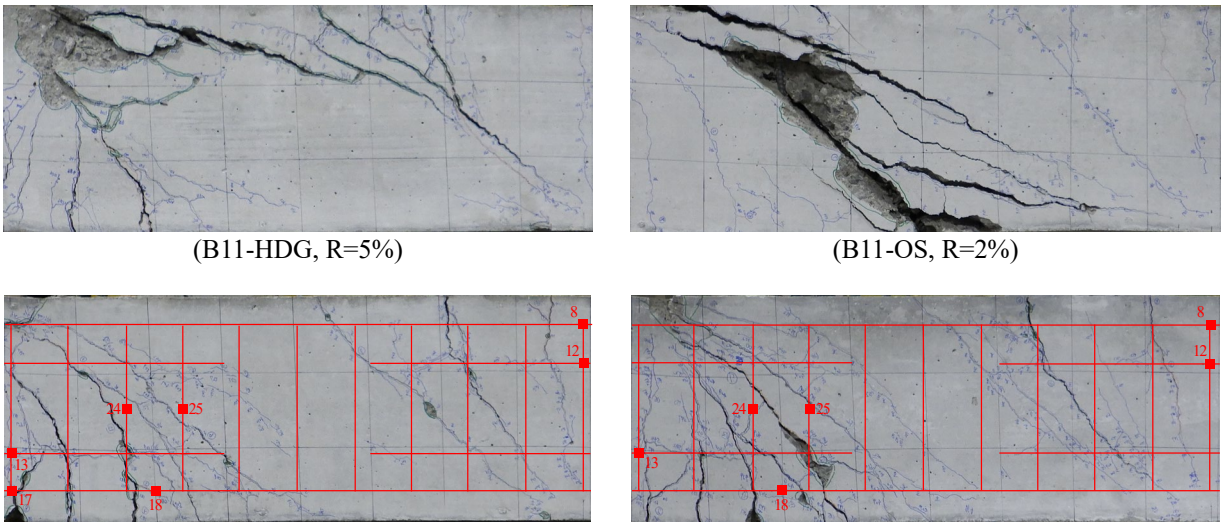

(B11-HDG, R=5%) (B11-OS, R=2%)

(CO1-HDG, R=5%) (CO1-OS, R=5%)

Figure 5 Crack behavior of test area after the test (same side as seen in Figure 1 and 3)(■: SG position)

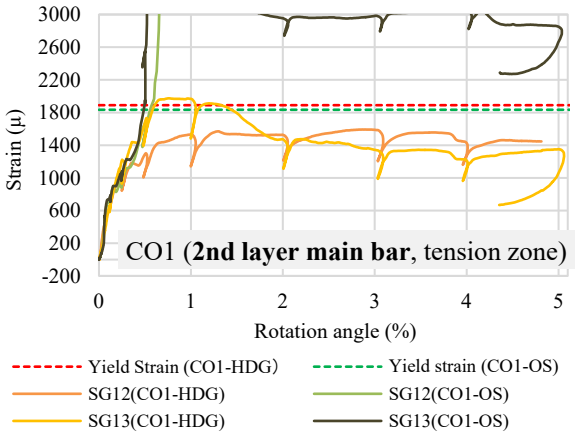

Figure 6 Strain behavior at tension end of 2nd layer main bar

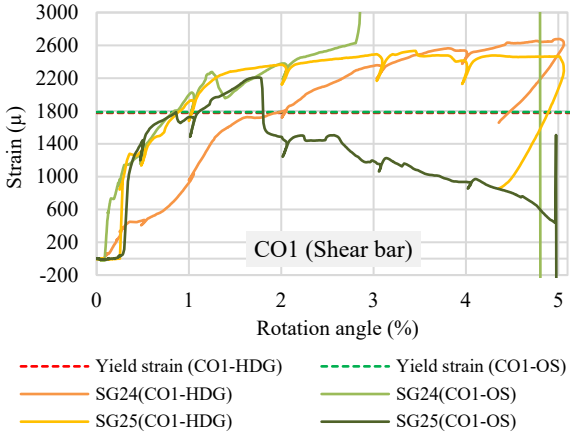

Figure 7 Strain behavior at shear bar

3.2 Bond Stress in Local Sections of Main Bars

Figure 8 shows the bond stress (τ) in specimen B11, where significant differences between HDG and OS rebars were observed in load-rotation angle relationship. The legend indicates $\tau_{i\text{-}i\pm1}$ (i: strain gauge number), which represents the bond stress in local sections between two adjacent gauges on the main bar. The results show that the maximum bond stress values in the central part of the beam specimen ($\tau_{6\text{-}5}$, $\tau_{7\text{-}6}$, $\tau_{10\text{-}11}$, $\tau_{11\text{-}12}$) for HDG rebar are mainly higher compared to OS rebar (indicated by red dotted circles), and similar results were confirmed for B9 and B10 as well. This indicates that, in terms of bond behavior of the main bars in the B9~B11 specimens, the bond stress in local sections is more concentrated for HDG rebar compared to OS rebar. Future work will focus on detailed analysis of the relationship between load-rotation angle and bond stress.

Figure 9 shows the local bond stress (τ) at the tension end of the main bar for CO1-HDG and CO1-OS. It is observed that the bond stress at the tension end of the 1st layer main bar ($\tau_{8\text{-}7}$, $\tau_{17\text{-}18}$) for both specimens decreases nearly to zero by the effects of tension shift [9]. However, the bond stress at the tension end of the 2nd layer main bar ($\tau_{12\text{-}11}$, $\tau_{13\text{-}14}$) shows an increasing trend in both specimens, demonstrating similar behavior. As indicated by the green and red solid line in Figure 6, SG12 and SG13 in CO1-HDG maintain values near the yield strain after R=0.5%. Furthermore, since the local bond stress was calculated with the yield strain as an upper limit, $\tau_{12\text{-}11}$ and $\tau_{13\text{-}14}$ for both specimens exhibit similar behavior. Also, similarly to the B9~B11 specimens, $\tau_{12\text{-}11}$ and $\tau_{13\text{-}14}$ showed more concentrated bond stress in HDG rebar, despite being at the tension end of the 2nd layer main bar. Through the results, this study confirmed that it is necessary to investigate in future work the differences and roles of bond stress at the tension end, central part, and compression end of main bar including 1st and 2nd layer. In addition, it needs to be compared to continuous bar-embedded specimens.

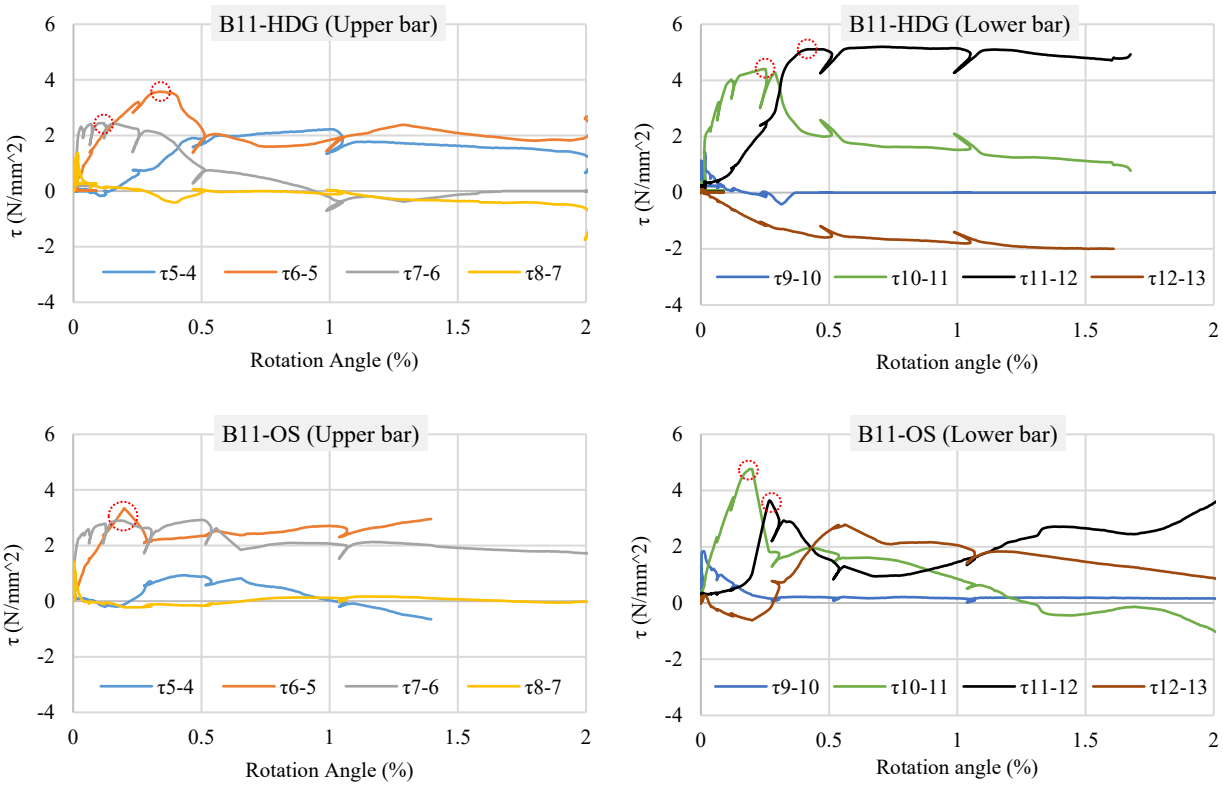

Figure 8 Local bond stress (τ) at B11 until R=2%

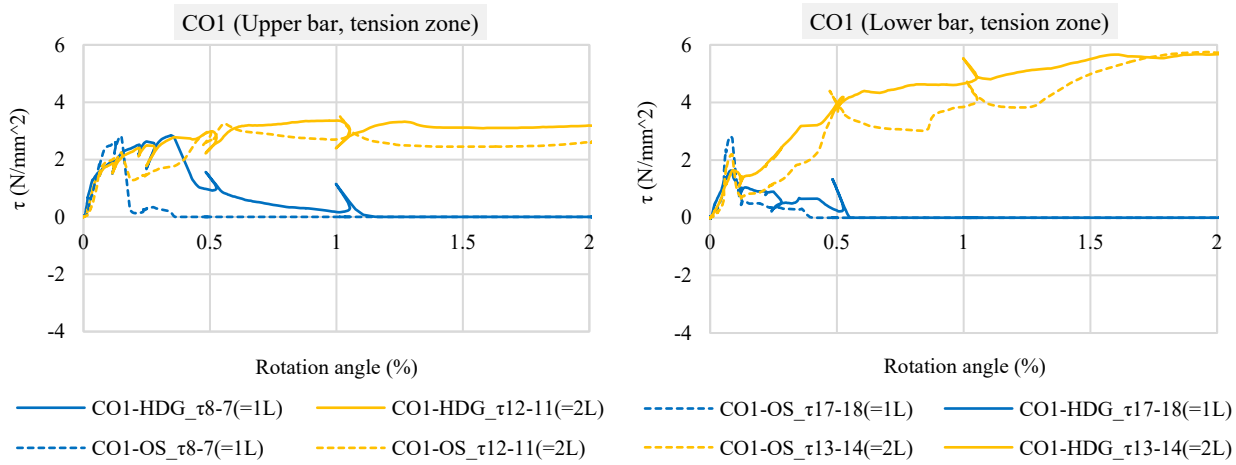

Figure 9 Local bond stress (τ) at CO1 until R=2%

4. CONCLUSION

This study aimed to clarify the differences in structural performance between HDG rebar and OS rebar in RC beam specimens.

In B9~B11 specimens which applied 1st layered placement of continuous bar, the structural performance of HDG rebar was found to be equivalent to OS rebar when the shear margin was above 1.1. However, when the shear margin was below 1.1, distinct differences were observed between HDG and OS rebars in terms of both reinforcement yield behavior and failure modes.

In CO1 specimens which applied 2nd layered placement with cut-off bar, the stiffness up to the yield point of the main bar was almost identical between HDG and OS rebar. Although strain behavior which expects the potential of bond slip was observed in the upper main bar of the HDG rebar, there was no significant difference in the overall load-rotation angle relationship. Therefore, the structural performance of RC beams with HDG rebar is comparable to those with OS rebar in the cut-off condition.

REFERENCES

1. Hongbok C., Tomohisa M., Akihiro N. and Hideyuki K., "An Experimental Study on Failure Behavior of RC Beam Which Embedded Hot-dip Galvanized Steel Rebar", Proceedings of AIJ Hokkaido Architectural Research Conference, No.96, 2023, pp.69-74.
2. Hongbok C., Tomohisa M., Hideyuki K., "An Experimental Study on Failure Behavior of RC Beam Using Hot-dip Galvanized Steel Rebar", 18th World Conference on Earthquake Engineering (WCEE), 2023, 12p.
3. Hongbok C., Tomohisa M., Riku K., Manabu K., Takafumi N. and Hideyuki K., "An Evaluation on Bond Behavior of Hot-dip Galvanized Steel Reinforcement under disadvantaged Bond Condition of RC beam", Summaries of Technical Papers of Annual Meeting, Architectural Institute of Japan, 2021, pp.297-298.
4. Hongbok C., Tomohisa M., Riku K., Yuhei N., Manabu K. and Takafumi N. "Experimental Test for Structural Performance Evaluation of RC Beam with Hot-dip Galvanized Reinforcement", Summaries of Technical Papers of Annual Meeting, Architectural Institute of Japan, 2020, pp.207-208.
5. Hongbok C., Tomohisa M., Masanobu S. and Manabu K., "Structural Performance for R/C Beam with Hot-dip Galvanized Steel Reinforcement with/without its Corrosion", AIJ Journal of Technology and Design, Vol. 26, No.62, 2020, pp.7-12.
6. Architectural Institute of Japan, "Guidance for Design and Construction of Reinforced Concrete Buildings Using Hot-dipped Galvanized Rebars", Architectural Institute of Japan, 2022.
7. National Institute for Land and Infrastructure Management, "Commentary on structural regulations of the building standard law of Japan", Information Center for Building Administration, 2020.
8. Architectural Institute of Japan, "Design Guidelines for Earthquake Resistant Reinforced Concrete Buildings Based on Inelastic Displacement Concept", Architectural Institute of Japan, 1999.
9. Architectural Institute of Japan, "AIJ Standard for Structural Calculation of Reinforced Concrete Structures", Architectural Institute of Japan, 2018.

ACKNOWLEDGEMENT

This research was funded by the Ministry of Land, Infrastructure, Transport and Tourism of Japan (MLIT). Additionally, this work was supported by the Japan Mining Promotive Foundation. The authors also appreciate the members of the full committee of the project funded by MLIT for their valuable suggestions and discussions.

Influence of Flow Distance and Compaction of Plasticized Concrete Controlled by Slump Flow on Structure Quality

Gota KISHIMOTO
Researcher, TOYO CONSTRUCTION CO.,LTD. TECHNICAL INSTITUTE, Ibaraki, Japan.

Hiroshi HAMAI
DAISUE CONSTRUCTION CO., LTD., Tokyo, Japan.

Masayuki YASUDA
Department Head, TOYO CONSTRUCTION CO.,LTD. TECHNICAL INSTITUTE, Ibaraki, Japan.

Yukio HAMA
Prof, Dr. Eng., Muroran Institute of Technology, Muroran, Japan.

ABSTRACT:
This study evaluated the influence of flow distance and compaction on the structural quality of column wall specimens made of plasticized concrete controlled by SF. The results showed that the strength of the structure satisfied the nominal strength of the base concrete regardless of the flow distance of the plasticized concrete and whether it was compacted or not. The large specimens of the full-scale model had generally good strength development, carbonation resistance, and permeability regardless of the flow distance and compaction. The coarse aggregate area ratio around the core was measured. When plasticized concrete is used, the nominal strength of the concrete to be ordered relative to the design base strength be the same as the base concrete.

Keywords: plasticized concrete, high fluidity concrete flow distance, compaction, structure quality

1. INTRODUCTION

It is expected to expand using high fluidity concrete of normal strength (27-45MPa) from the viewpoint of improving productivity at construction sites [1]. However, there are still few ready-mixed concrete plants in Japan that have obtained "Japan Industrial Standards" (JIS) certification and standardized the use of normal-strength high-fluidity concrete, and the reality is that normal-strength high-fluidity concrete cannot be used universally at construction sites.

Against this background, the "High-Fluidity Guidelines" [2] revised in 2021 and "JASS5" [3] revised in 2022 newly include plasticized concrete controlled by slump flow (SF), and it is expected the method of plasticizing JIS product concrete on site and using high fluidity concrete. When the slump (SL) controlled concrete of JIS product is plasticized, the amount of coarse aggregate is higher than that of the high fluidity concrete produced at ready-mix plants, and there are concerns about the influence on flowability, pore passage, and resistance to material segregation. Since high fluidity concrete of normal strength includes SFs in the range of 45-50 cm, it is assumed that mild compaction may be required for concrete placement, and the influence of compaction on material segregation is also a concern.

We have been evaluating the quality of plasticized concrete controlled by SF through laboratory tests and experiments on actual equipment [4], [5]. In this paper, construction tests were conducted on a full-scale model using this plasticized concrete, and the effects of flow distance and compaction of the fluidized concrete on the quality of the structure were investigated.

2. EXPERIMENTAL SUMMARY

2.1 EXPERIMENT CASE

Table-1 shows concretes used in this experiment. The experiments were conducted on three types of concrete with nominal strengths of 30, 36, and 42 then add superplasticizer containing a viscosity agent to the concrete with a SL 18cm or 21cm (base concrete) to plasticize it within the target SF range. The target values of SF were 50 ± 7.5 cm for nominal strength 30, 55 ± 7.5 cm for nominal strength 36, and 60 ± 10 cm for nominal strength 42, and the target value of air volume was 4.5 ± 1.5% for all concretes.

2.2 MATERIALS USED AND MIX PROPORTIONS OF CONCRETE

Table-2 shows the materials used for concretes and Table-3 shows the concrete mix proportions. The superplasticizer was from the same bland as the base concrete admixtures. The base concrete was a JIS

Table-1 Concretes used in the experiment

Symbol	Nominal strength	Target SL of base concrete (cm)	Target SF of plasticized concrete (cm)
30-18→50	30	18±2.5	50±7.5
36-21→55	36	21±2.0	55±7.5
42-21→60	42		60±10

product usually manufactured from the ready mixed concrete plant, and the addition ratio of the superplasticizer was determined by test mixing in advance.

2.3 CONCRETE MANUFACTURING

The concrete was mixed in two batches of 2.0 m^3 using a 3.0 m^3 capacity forced twin-shaft mixer, and a total of 4.0 m^3 was loaded onto an agitator truck and transported to the experiment site. Transportation time was approximately 30 minutes. After arriving at the experimental site, quality tests were conducted, and after confirming that quality tests results were within the control values, plasticization was conducted. For the plasticization method of concrete, the drum was rotated at high speed for about 2 minutes after superplasticizer was added then the drum was rotated at low speed for about 5 minutes.

2.4 SPECIMEN OVERVIEW AND PLACING METHOD OF CONCRETE

Fig.1 and 2 show an overview of the specimens, and Table-4 shows the combinations of using concrete and specimens. The large specimen consisted of columns 600 x 600 mm, wall thickness = 200 mm, distance between columns 10 m, and height 2.2 m. The large specimen consisted of columns 600 x 600 mm, wall thickness = 200 mm, distance between columns 10 m, and height 2.2m. The columns were reinforced with 8-D22 main bars and D13@200 band bars, and the walls were double reinforced with D13@200 in both vertical and horizontal directions. The small specimen was 200 mm thick and 3.6m long, with double reinforcement of D13@200 in both horizontal and vertical directions. The reinforcement cover thickness was 50 mm for columns and 30 mm for walls. Concrete of nominal strength 36 was used for the large specimens, and concrete of nominal strength 30 and 42 was used for the small specimens, and two levels of specimens were prepared with and without compaction, respectively. Plywood was used as the formwork material, but one side of the wall of the large specimen was made of acrylic transparent formwork so that the flow condition could be observed.

Concrete was poured from one side of the column for the large specimens and from the end of the wall for the small specimens. For the large specimens, concrete was placed in four layers, and for the small specimens, concrete was placed in three layers, and the large specimens were compacted for 5 seconds at 1 m intervals for each layer using a φ40 vibrator with a frequency of 200 to 240 Hz. The large specimens were placed on a simple trestle so that the tip of the hose could be placed horizontally (Photo-1). Two agitator trucks were used to place the large specimens, and the second truck was placed after the first truck was finished.

2.5 TEST ITEMS AND METHODS

Table-5 shows the test items and methods. SL, SF, air content, and concrete temperature were measured as acceptance tests of the base concrete, and SF, air volume, and concrete temperature were measured as quality control tests after plasticization.

Table-2 The materials used for concretes

Materials/Symbol		Kinds/Physical property/Chemical composition
Cement (C)		Ordinary Portland cement, density 3.16g/cm^3
Fine aggregate 1 (S1)		Sand, density 2.59 g/cm^3,f.m.2.30
Fine aggregate 2 (S2)		Crushed sand, density 2.63 g/cm^3,f.m.3.30
Coarse aggregate (G)		Crushed stone , maximum size 20mm, density 2.68 g/cm^3, solid content 60.0%
Water(W)		Underground water
Admixture (Ad)	AE	Air-entraining and water-reducing admixture standard type(brand B) Main ingredient: Lignin sulfonates and oxycarboxylates
	SP	Air-entraining and high range water-reducing Admixture standard type(brand B) Main ingredient: Polycarboxylic acid compounds
	VSP-F	Superplasticizer containing viscosity modifying agent(brand B) Main ingredient: Composite of polycarboxylic acid compounds and surfactant-based special viscosity agent

Table-3 Mix proportions of base concrete

Symbol	W/C (%)	s/a (%)	SL (cm)	quantity of material per unit volume of concrete(kg/m^3)					
				W	C	S1	S2	G	Ad
30-18→50	49.0	44.9	18	183	374	531	232	965	AE:3.74
36-21→55	44.0	49.0	21	172	391	586	256	901	SP:3.52
42-21→60	39.0	47.4	21	174	447	549	240	901	SP:4.02

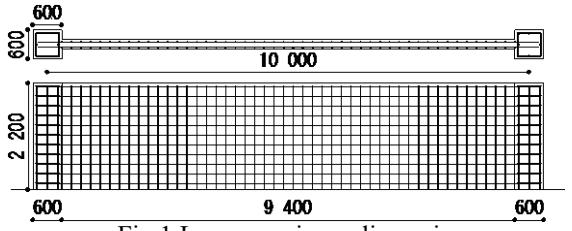

Fig.1 Large specimen dimensions

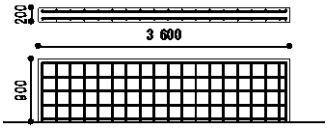

Fig.2 Small specimen dimensions

Pic.1 Placing point

Table-4 the combinations of using concrete and specimens

Using concrete	Large specimen		Small specimen	
	no compacted	compacted	no compacted	compacted
36-21→55	○	○	—	—
30-18→50	—	—	○	○
42-21→60	—	—	○	○

Table-5 Test items and methods

Test item	Test method	Base concrete	Plasticized concrete	Core
Slump	JIS A 1101	○	—	—
SF	JIS A 1150	○	○	—
Air content	JIS A 1128	○	○	—
Concrete Temperature	JIS A 1156	○	○	—
J ring flow	JIS A 1159	—	○	—
Coarse Aggregate Residual Ratio	JSCE-F 702-2022	—	○	—
Plastic viscosity Yield value	Two-Point	—	○	—
Compressive strength	JIS A 1108	○	○	○
Coarse aggregate area ratio	Image processing	—	—	○
Carbonation resistance	JIS A 1153 reference	—	—	○※
Permeability	Torrent metho	—	—	○(wall)※

The J-ring flow test was used to evaluate the pore passage of plasticized concrete, and the coarse aggregate volume ratio [6] and apparent plastic viscosity were measured to evaluate the resistance to material segregation. Apparent plastic viscosity was calculated from the relationship between the number of rotations and torque of a rotary blade viscometer according to the Two-Point method [7]. The rotational speed was increased in the order of 0, 5, 10, 20, 40, and 60 rpm, and then decreased at the same rotational speed intervals as the increase. The value obtained during the descending phase was used to calculate the apparent plastic viscosity.

Cores of large specimens were sampled at flow distances of 0, 1, 2, 4, 7.5, and 10 m for compressive strength measurements and tested at 91 days of age.

Coarse aggregate area ratio was calculated by marking the coarse aggregate around the sampled cores and counting the number of pixels using image processing software.

Carbonation rate coefficients were evaluated using cores taken at flow distances of 3, 6, and 9m. The depth of carbonation was measured at 91 days of age, followed by accelerated carbonation at 20°C, 60%RH, and 5% CO2 concentration, and the depth of carbonation was measured at 4 and 13 weeks of accelerated period.

Permeability was measured on the plywood formwork side at flow distances of 3, 6, and 9 m using the torrent method on the wall members after at least one year of age. The moisture content at the time of the permeability measurements ranged from 4.9 to 5.2%. The specimens were demolded at 6 days of age and exposed to the open air after demolding.

3. RESULATS OF EXPERIMENTS

3.1 BASIC PROPERTIES, PORE PASSAGE AND MATERIAL SEGREGTION OF CONCRETE

Table-6 shows the basic properties of the base concrete and plasticized concrete. The slump, air volume, and concrete temperature of the base concrete for all mixes satisfied the control values, and the target control values were also satisfied after plasticized concrete. The condition of the plasticized concrete after the SF test was visually confirmed, and no material segregation was observed.

The compressive strength of both the base concrete and plasticized concrete at the standard curing age of 28 days satisfied the nominal strength. The compressive strength of the plasticized concrete tended to be higher than that of the base concrete due to the decrease in air volume after plasticization.

Fig.3 shows the relationship between SF and PJ values in the J-ring flow test. The PJ values satisfied the evaluation criteria of JIS A 1160. According to the classification by PJ value in the High Fluidity Concrete Guideline [2], the plasticized concrete used in this study is classified as category C, which requires placing with compaction when the open space between reinforcing bars is about 40 mm.

Fig.4 shows the coarse aggregate content ratio and apparent plastic viscosity. The concrete used in this experiment showed a coarse aggregate ratio of approximately 60% or more at all levels during 5 second compaction. The JSCE guidelines[5] define a coarse aggregate ratio of 40% for 10 second compaction as a value for good resistance to material segregation.

The apparent plastic viscosity was relatively high for the mix with a nominal strength of 42, which has a high unit cement content, and relatively low for the mix with a nominal strength of 30, which has a low unit cement content.

Table-6 The basic properties of the base concrete and plasticized concrete

symbol	Base concrete					Plasticized concrete				
	SL (cm)	SF (cm)	Air (%)	CT (℃)	σ 28 Compressive strength (MPa)	VSP-F (C×wt. %)	SF (cm)	Air (%)	CT (℃)	σ 28 Compressive strength (MPa)
36-21→55① (self compacted)	21.0	36.5	4.6	25	43.9	0.275	61.0	3.5	25	46.5
36-21→55② (self compacted)	21.0	35.0	5.4	24	42.2	0.250	54.5	3.9	24	45.5
36-21→55③ (mild compaction)	22.5	45.0	5.1	21	44.7	0.150	60.0	4.0	21	47.6
36-21→55④ (mild compaction)	22.0	36.5	5.9	22	41.9	0.250	59.0	4.3	21	48.3
30-18→50	18.5	31.0	4.0	24	32.9	0.350	49.5	3.8	24	31.6
42-21→60	22.0	39.5	6.0	22	53.2	0.200	62.5	4.0	22	58.9

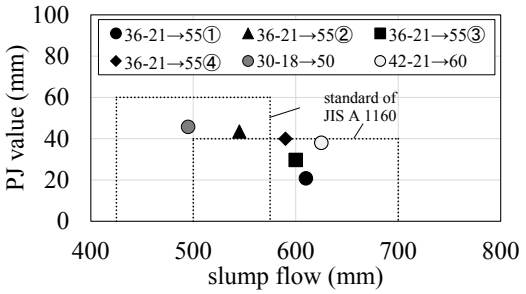

Fig.3 The relationship between SF and PJ value

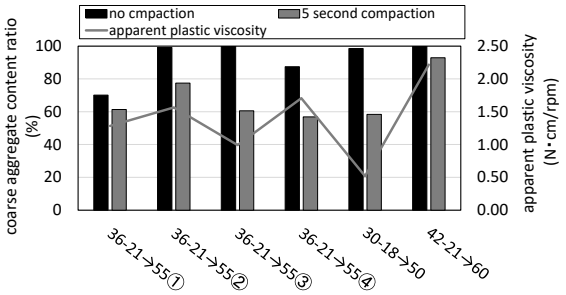

Fig.4 The coarse aggregate content ratio and apparent plastic viscosity

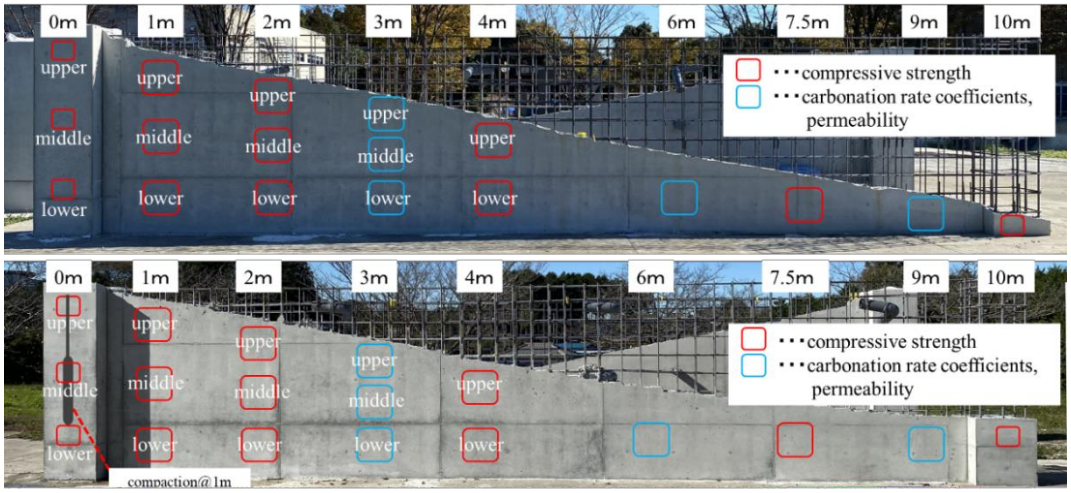

Pic.2 The appearance of large specimens （upper：no compacted, lower：compacted）

3.2 FLOW GRADIENT AND APPEARANCE OF THE SPECIMENS

Fig.5 shows the flow gradient of a large specimen, Pic.2 and 3 show the appearance of large specimens and small specimens respectively. Each of the pictures also shows the location of the cores taken. The flow gradient is that of a no compacted specimen. The SF of the pomp tip before placing was 61.5cm, and the placement speed was low, averaging about 15m^3/h then flow gradient was about 11°. In a previous study [8] on full-scale construction of high-fluidity concrete, the SF was about 65cm, and the flow gradient was about 7°, which was smaller than that in this experiment. This may be since the SF of the plasticized concrete in this experiment was slightly smaller than in the previous study, and the unit coarse aggregate bulk volume was 0.56m^3/m^3, which was larger than the 0.50m^3/m^3 in the previous study [8], resulting in slightly inferior pore passage, although the reinforcement conditions were the same.

The flow gradient of the small specimen with nominal strength 30 was about 9° at 52.5cm SF at the pump tip, and that of the specimen with nominal strength 42 was about 5° at 57.0cm SF at the pump tip, resulting in a smaller flow gradient than that of the large specimen, although the SF at the pump tip was smaller. The small specimen was placed from the wall, while the large specimen was placed from the column, and the amount of reinforcement through which the concrete passed and the number of collisions of the coarse aggregate increased due to flow from large to small cross section members [9]. However, it is not clear in this experiment.

The appearance of the compacted specimens was not significantly different from that of the no compacting specimens overall, although the columns on the opposite side were driven up to approximately 700mm. On the other hand, the top edge of the small specimen was generally level after compaction.

The reason why the large specimens showed less flow by compaction may be that the large specimens had a larger volume of concrete than the small specimens and therefore had a greater self-weight, or that it took more time to place the large specimens, resulting in a decrease in SF and stiffness [10].

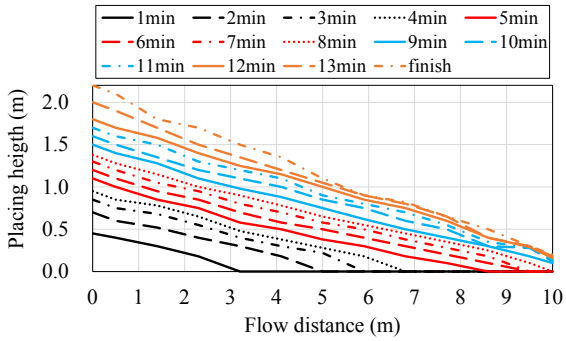

Fig.5 The flow gradient of large specimen

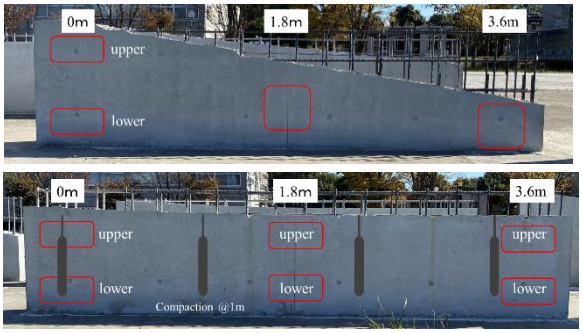

Pic.3 The appearance of small specimens
（upper：no compacted, lower：compacted）

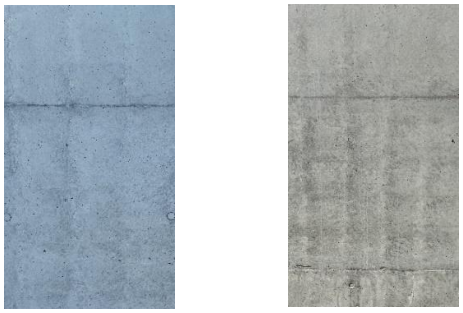

a) no compacted （Surface Fill Rate :99.7%）　b) compacted （Surface Fill Rate :99.8%）

Pic.4 The surface of specimens

The surface of the specimen is shown in Picture-4. The surface filling ratio shown in the lower part of the photo is defined as the percentage of the filled area excluding surface bubbles larger than about 3mm and was

calculated by image processing. The filling condition of the specimens was good regardless of whether they were compacted or not, and there was no lack of filling in any of the specimens.

3.3 COMPRESSIVE STRENGTH AND COARSE AGGREGATE AREA RATIO OF LARGE SPECIMENS

Fig.6 shows the core compressive strength of the large specimens and the standard deviation σ, which represents the variation of each core compressive strength. Fig.7 shows the coarse aggregate area ratio.

The nominal strength of 36MPa was satisfied at all sampling locations. In the no compacted specimens, the compressive strength of the columns at a flow distance of 10m was relatively small, and in the compacted specimens, the compressive strength of the columns at the placing position was relatively small.

Although the coarse aggregate area ratio of the columns at a flow distance of 10m in the self-compacting specimens was small and the mortar content was high, resulting in concrete with a tendency of material segregation, previous studies [11] have reported that the influence of the segregation of coarse aggregate and mortar on compressive strength is small.

In addition, a study [12] that investigated the quality of structural concrete by taking cores from actual RC buildings reported that the standard deviation of the distribution of compressive strength (σ), ranged from about 3 to 7.5MPa, and the difference in compressive strength in this experiment was within the range of variation in structural strength. However, since the Young's modulus and drying shrinkage may differ significantly due to the segregation of the coarse aggregate and mortar [11], care should be taken during construction.

In terms of the area ratio of coarse aggregate for each section, the area ratio of coarse aggregate in the column section of the specimen with compaction was larger than that of the column section in the vertical direction. This is because the columns have a larger cross section and lower reinforcement density than the walls, which facilitates the downward movement of the coarse aggregate due to compaction.

3.4 CARBONATION RATE COEFFICIENT AND PERMEABILITY OF LARGE SPECIMENS

Fig.8 shows the carbonation rate coefficients and permeability of the large specimens. Although the coefficient of neutralization rate tended to be slightly smaller for the specimens with compaction, there was no significant difference between the no compacted specimens. The permeability also tends to be slightly lower for the compacted specimens but is not significantly different from that of the no compacted specimens. There was almost no difference in the carbonation rate coefficient and the permeability coefficient depending on the flow distance. Therefore, it can be said that the influence of compaction and flow distance on carbonation resistance and permeability were small under the conditions of this experiment.

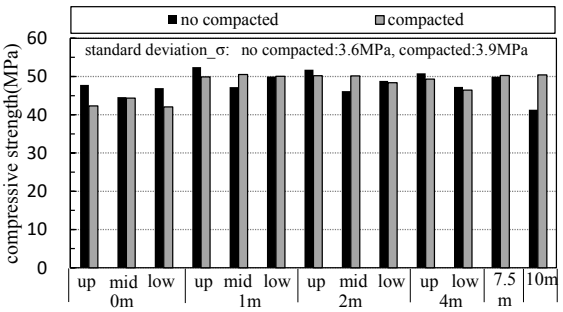

Fig.6 Compressive strength of large specimen

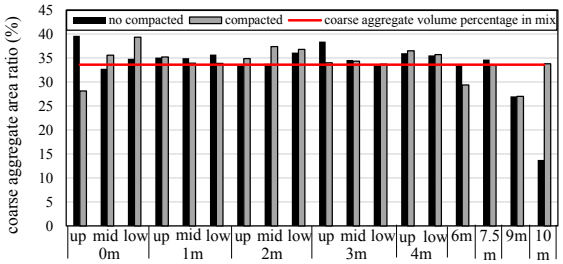

Fig.7 Coarse aggregate area ratio of large specimen

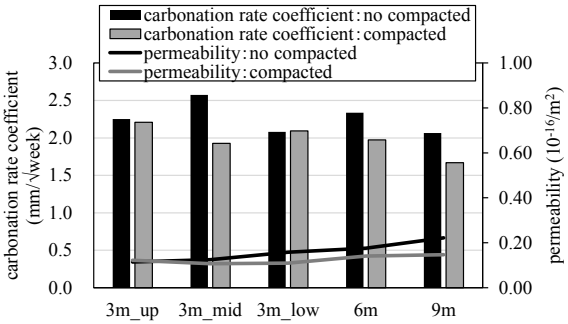

Fig.8 Carbonation rate coefficient and permeability

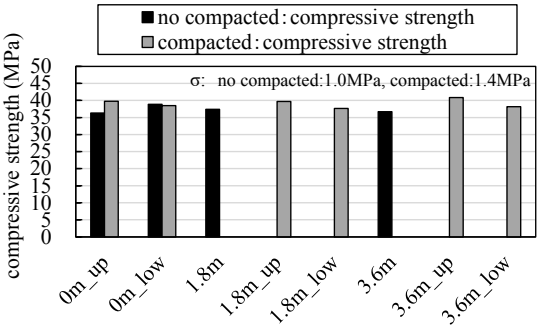

Fig.9 Compressive strength of small specimen (nominal strength 30)

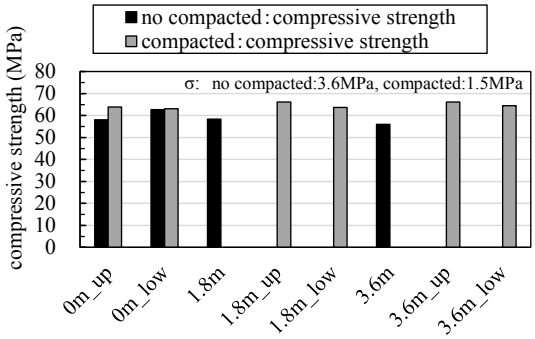

Fig.10 Compressive strength of small specimen (nominal strength 42)

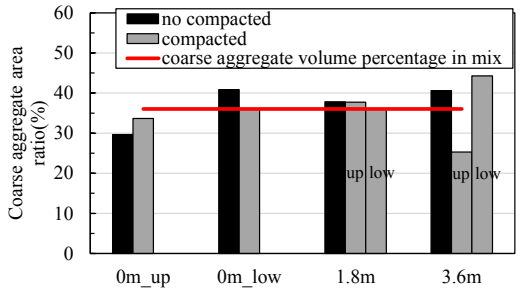

Fig.11 Coarse aggregate area ratio of large specimen (nominal strength 30)

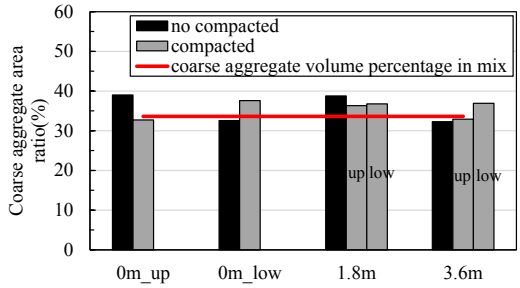

Fig.12 Coarse aggregate area ratio of large specimen (nominal strength 42)

3.5 COMPRESSIVE STRENGTH AND COARSE AGGREGATE AREA RATIO OF SMALL SPECIMENS

Fig.9 and Fig.10 show the core compressive strength of small specimens using concrete of nominal strength 30 and 42. While there was no consistent trend of compaction on compressive strength for the large specimens, the small specimens showed a trend of increased compressive strength due to compaction. However, considering the variation in compressive strength within the specimens, it is difficult to say that the difference is significant, and it is considered that there was no significant influence of compaction on the compressive strength. No significant difference in compressive strength was observed with flow distance.

Figures 11 and 12 show the coarse aggregate area ratio of small specimens using concrete of nominal strength 30 and 42, respectively. The difference in coarse aggregate area ratio in the vertical direction at a flow distance of 3.6 m for the nominal strength 30 was large due to compaction, but there was no significant difference between the other location with and without compaction. No significant difference in coarse aggregate area ratio was observed at all locations for the nominal strength 42. The coarse aggregate settlement due to compaction is relatively small for the nominal strength of 42 because of its high unit cement content and high viscosity, but for the low unit cement content such as mix of nominal strength 30, it is necessary to pay attention to the compaction time.

4. CONCLUSION

1) The compressive strength of the structure satisfied the nominal strength of the base concrete regardless of the flow distance of the plasticized concrete and whether it was compacted or not.
2) The variation in compressive strength of plasticized concrete structures is considered to be comparable to that of normal concrete.
3) In this experiment, the influence of flow distance and compaction on compressive strength, carbonation resistance, and permeability were small.

REFERENCES

1. Koshiro Y., et.al, “QUESTIONARY SURVEY ON HIGH-FLUIDITY CONCRETE FOR CONSTRUCTOR”, AIJ Journal of Technology and Design. Vol. 26, No.64, pp.822-826, 2020
2. Architectural Institute of Japan., “Recommendations for Mix Design and Construction Practice of High Fluidity Concrete “, 2021.12
3. Architectural Institute of Japan., “Japanese Architectural Standard Specification for Reinforced Concrete Work JASS5”, 2022
4. Kishimoto G., Hamai H., Takabuchi T. and Yasuda M., “Study on Plasticized Concrete using Superplasticizer containing Viscosity Modifying Agent”, Proceeding of the Japan Concrete Institute, Vol.43, No.1, pp.814-819, 2021
5. Kishimoto G., Hamai H., Hama Y. and Yasuda M., “Basic properties of plasticized concrete managed by SF”, Proceeding of the Japan Concrete Institute, Vol.44, No.1, pp.814-819, 2022
6. Japan Society of Civil Engineers, “Recommendations for Mix Design and Construction of Mechanically-compacting Flowable Concrete”, 2023.2.
7. Tattersal G.H., et al : ”The Rheology of Fresh Concrete”, PITMAN, 1983
8. Kokubo M., et al,” Experimental Study on the Real-size Model Execution of High Fluidity Concrete (Part 5 Flowing Gradient)”, Architectural Institute of Japan Summaries of Technical Papers of Annual Meeting, pp.327-328, 1995.
9. Hashimoto C., et al,” EVALUATION OF DEFORMABILITY OF FRESH CONCRETE FLOWING IN BEND PIPES OR TAPERED PIPES” , Japanese Journal of JSCE, Vol.15, No.433, pp.91-100, 1991
10. Nemoto K., et al,” Experimental Study of the Influence of Fresh Concrete Stiffness on Construction Performance” , Proceeding of the Japan Concrete Institute, Vol.41, No.1, pp.1079-1084, 2019
11. Teranishi K. and Niwa D.,”EFFECTS OF SEGREGATION ON VARIOUS PROPERTIES OF CONCRETE IN STRUCTURES” , Journal of Structural and Construction Engineering (Transactions of AIJ), Vol.83, No.749, pp.923-933, 2018
12. Masuda Y., Tomosawa F. and Yajima Y.,” CONCRETE-QUALITY IN EXISTING REINFORCED CONCRETE BUILDING -Part 1 Compressive Strength in Each Building-” Journal of the Architectural Institute of Japan, Vol.311, pp.153-162, 1982

Part3:
Durability

Study on the effect of suppressing frost damage deterioration of concrete with hydrophobic compounds

Reiko YASUDA
Flowric Co.,Ltd., Tsukuba, Japan
Muroran Institute of Technology, Muroran, Japan

Hironobu NISHI
Flowric Co.,Ltd., Tsukuba, Japan

Yukio HAMA
Muroran Institute of Technology, Muroran, Japan
Hokkaido University, Sapporo, Japan

ABSTRACT:
Hydrophobic compounds consisting of oil-based substance and emulsifiers are materials that are expected to suppress frost damage deterioration. Hydrophobic compounds may be able to inhibit the movement of unfrozen water during freezing, and reduce the expansion pressure during ice crystal growth. In this study, we investigated the effect of the type and ratio of emulsifiers on the formation of hydrophobic compounds and the frost resistance of concrete. Regarding the frost resistance of non-AE concrete using hydrophobic compounds, hydrophobic compound D showed the best performance, but it was lower than that of AE concrete. It is considered that the frost resistance of concrete containing hydrophobic compounds cannot be evaluated by the air-void system, and may be influenced by the dispersion state of hydrophobic compounds in the liquid phase.

Keywords: hydrophobic compounds, dispersion state, frost resistance, air-void system, concrete

1. INTRODUCTION

Concrete structures in cold regions are subject to freezing and thawing, which can cause destruction of the concrete structure. It is known that the entrainment of fine air void is effective in suppressing the migration of unfrozen water accompanying the formation of ice crystals in order to improve the resistance of concrete to the freeze-thaw action. However, depending on used materials, mix proportion, environmental conditions, and construction conditions, it can be difficult to ensure a stable air content. There is also concern that the increase of air content result in decreasing compressive strength in concrete.

Given the above background, researches are being conducted into improving the frost resistance of concrete by using alternative materials of air-void. Nishi et al.[1)] have proposed a technology to suppress frost damage in concrete by introducing a hydrophobic compound to block the continuity of capillary pore, and relieving pressure in the same way as entrained air during freezing. Ushiro et al.[2)] studied the frost resistant of concrete using acrylonitrile-based hollow microspheres with an average diameter of 80 μm. They inferred that the hollow microspheres reduce pressure during the freezing process in the same way as entrained air, thereby improving the frost resistance of concrete. In addition, Okada et al.[3)] have focused on Nishi et al.'s theory[1)] and developed a technology to improve frost resistance in concrete using special paraffin. They reported that the water absorption rate is reduced and the expansion behavior during freezing is suppressed by mixing an emulsion containing paraffin particles with an average diameter of 0.5μm in concrete.

In this study, we focused on the technique proposed by Nishi et al.[1)] to prevent frost damage in concrete using hydrophobic compounds, and observed the morphology of hydrophobic compounds in the alkaline liquid phase depending on the type and amount of emulsifier. In addition, the effect of these hydrophobic compounds in inhibiting frost damage deterioration was evaluated for non-AE and AE concrete.

2. EXPERIMENTS

2.1 EXAMINATION OF DISPERSION STATE OF HYDROPHOBIC COMPOUNDS

In order to confirm the dispersion state of hydrophobic compounds in alkaline liquid phase depending on the type and amount of emulsifier, a method was used based on Nishi et al.[1)] and hydrophobic compounds were added to the liquid phase filtrated from cement paste with W/C=2000% using ordinary Portland cement. Table 2.1.1 shows the composition of

hydrophobic compounds. The oil-based substance was a hydrocarbon compound, and two types of emulsifiers were used. The hydrophobic compounds was adjusted by changing the ratio of oil-based substance to emulsifier. The hydrophobic compounds was adjusted to the concentration shown in Table 2.1.2, assuming a cement paste with W/C=55%. The solution was stirred at 750 rpm for 1 minute using a magnetic stirrer, and then observed under the optical microscope at magnifications of 12 and 160x.

2.2 CONCRETE EXPERIMENTS

2.2.1 MIX DESIGN

Table 2.2.1 shows used materials and mix proportion in concrete. The cement was ordinary Portland cement, the fine aggregate was mountain sand from Kakegawa city, Shizuoka prefecture, and the coarse aggregate was crushed hard sandstone from Oume city, Tokyo prefecture. The chemical admixtures were AE water-reducing admixtures whose main components were lignin sulfonates and oxycarboxylates, and another AE water-reducing admixture that contained polycarboxylic acid compounds in addition to these components. These were adjusted to give a slump of about 15-18cm. To adjust air content in concrete, air-entraining (AE) agent containing a resin acid salt surfactant as its main component was used.

Table 2.1.1 Composition of hydrophobic compounds

symbol	Composition		
	Oil-based substance	Emulsifier α	Emulsifier β
A	Hydrocarbon compound	high	-
B		low	-
C		-	-
D		-	low

Table 2.1.2 Concentration of hydrophobic compounds

symbol	Dosage of hydrophobic compounds in cement paste of W/C=55% [%/C]	Concentration of hydrophobic compounds in cement paste of W/C=55% [%]
Blank	0.0	0
A1	1.0	1.79
A2	2.0	3.51
A4	4.0	6.78
B1	1.0	1.79
C1	1.0	1.79
D1	1.0	1.79

The water-to-cement ratio (W/C) was 55% and the unit water content=173 kg/m^3, and the concrete was mixed in 20°C environment by revolving-paddle mixer. Hydrophobic compounds were added externally to the amount of water. Regarding the mixing method, first, the fine aggregate and cement were mixed for 10 seconds. Next, water and chemical admixtures were added, followed by another 60 seconds of mixing after which scraping was done to ensure all cement was mixed. Then, the coarse aggregate was added and mixed for 90 seconds. Finally, the hydrophobic compound was added and mixed for an additional 60 seconds.

Table 2.2.2 shows experimental program of concrete consists of 13 experiment standards. The air content in non-AE concrete was adjusted to 3.0% or less. The air content in AE concrete was set to 2.5±0.5% and 4.5±1.0% for the standards without hydrophobic compounds, and 4.5±1.0% for the standards with hydrophobic compounds.

2.2.2 Experimental method

Fresh properties of concrete of slump, air content, and temperature were measured according to JIS A 1101, JIS A 1128, and JIS A 1156. Hardened properties including compressive strength and underwater freeze-thaw were measured according to JIS A 1108 and JIS A 1148. Air content, air-void spacing factor, and air-void size distribution in hardened concrete were assessed via image observation with an optical microscope (Keyence) at 40x magnification, with binarization performed using the supplied software.

Table 2.2.2 Experimental program of concrete

Symbol	kind	Air content [%]	hydrophobic compounds	
			kind	Dosage [%/C]
Blank	Non-AE	0.0-3.0	-	-
Non-A-1			A	1.0
Non-A-2				2.0
Non-A-4				4.0
Non-B-1			B	1.0
Non-C-1			C	1.0
Non-D-1			D	1.0
AE2.5	AE	2.0-3.0	-	-
AE4.5		3.5-5.5	-	-
AE-A-1			A	1.0
AE-B-1			B	1.0
AE-C-1			C	1.0
AE-D-1			D	1.0

Table 2.2.1 Used materials and mix proportion of concrete

W/C [%]	s/a [%]	Design air content [%]	Unit content [kg/m^3]			
			W	C	S	G
55	46	4.5	173	315	807	975

【Used materials】

W: Tap water, density 1.00g/cm^3

C: Ordinary portland cement, density 3.16g/cm^3

S: Mountain sand, density (saturated surface-dry) 2.57g/cm^3, water absorption rate 1.97%, F.M.; 2.69

G: Crushed graywacke sandstone, density (saturated surface-dry) 2.65g/cm^3, water absorption rate 0.62%, solid content 59.0%

Ad1: AE water-reducing admixture, main component ; Lignosulfonates and hydroxycarboxylates

Ad2: AE water-reducing admixture,
main component ; Lignosulfonates, hydroxycarboxylates and polycarboxylic acid compounds

AE: Air-entrained agent, main component ; Resin acid salt surfactants

3. RESULTS AND DISCUSSION

3.1 DISPERSION STATE OF HYDROPHOBIC COMPOUNDS

Table 3.1 shows the dispersion state of hydrophobic compounds A, and table 3.2 shows the dispersion state of hydrophobic compounds B, C and D. At a magnification of 12x, the liquid phase containing hydrophobic compound A was more cloudy than that of

Table 3.1 Dispersion state of hydrophobic compounds A

Hydrophobic compounds	magnification	
	12	160
Blank	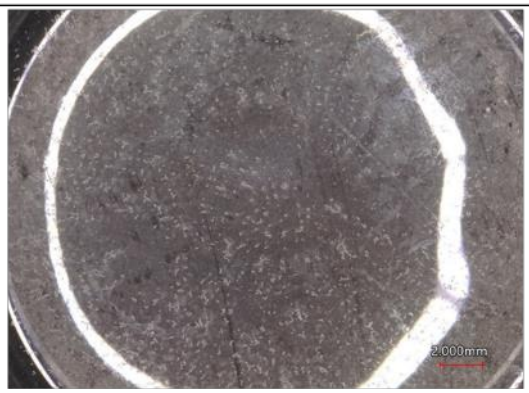	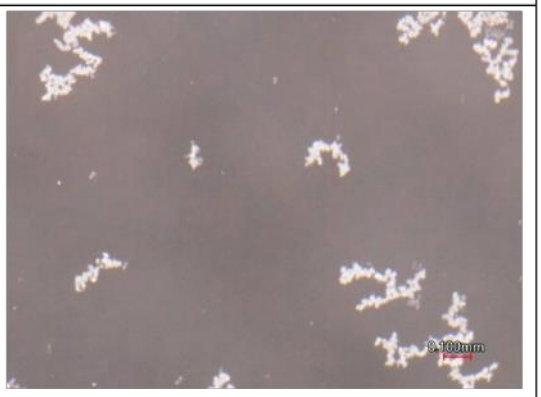
A1	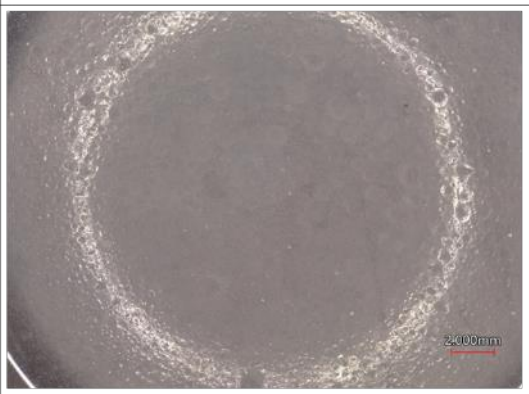	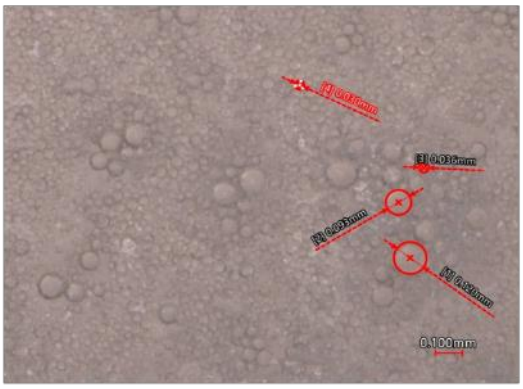
A2	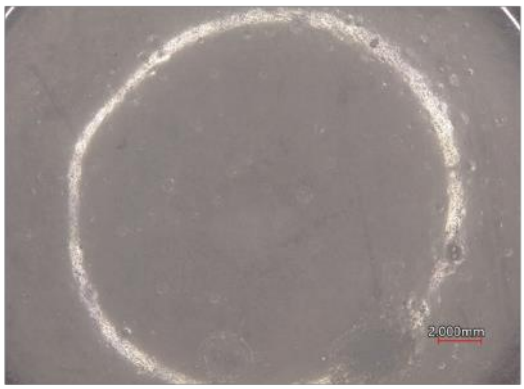	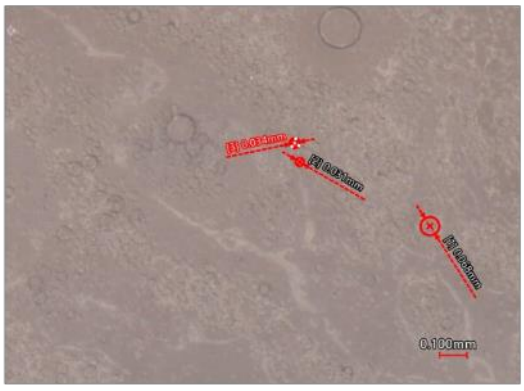
A4	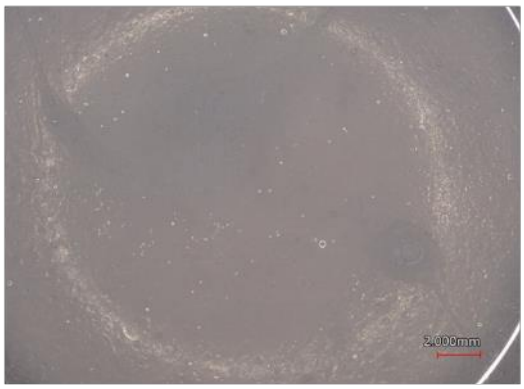	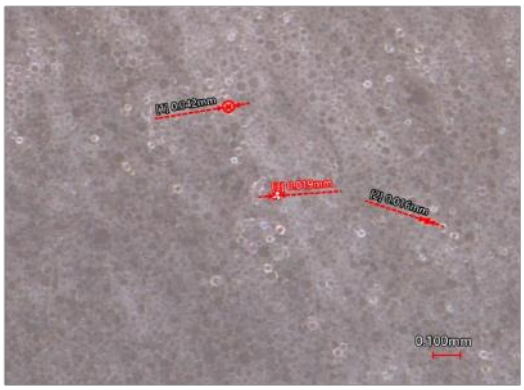

Table 3.2 Dispersion state of hydrophobic compounds B, C and D

Hydrophobic compounds	magnification	
	12	160
B1	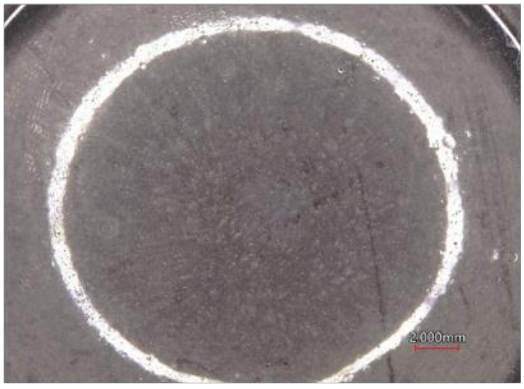	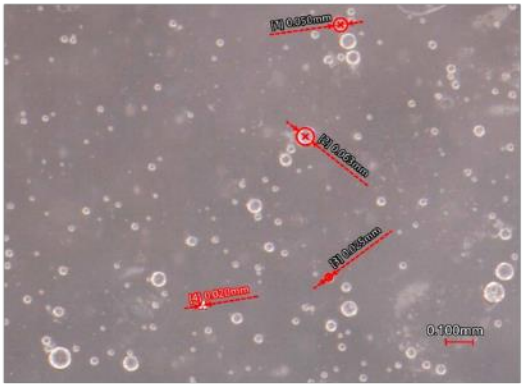
C1	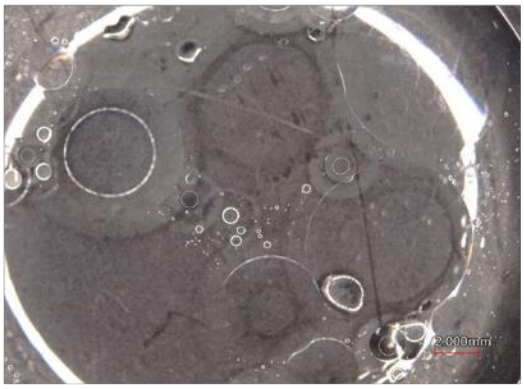	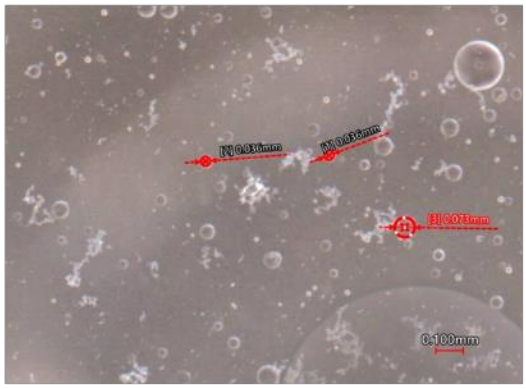
D1	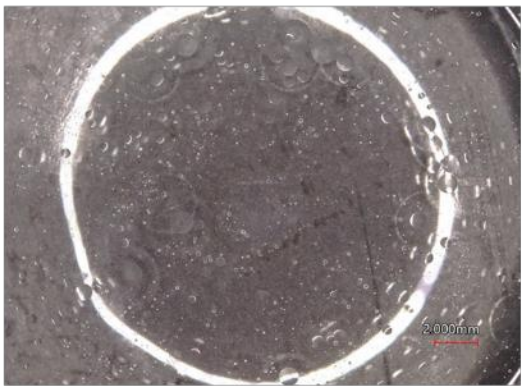	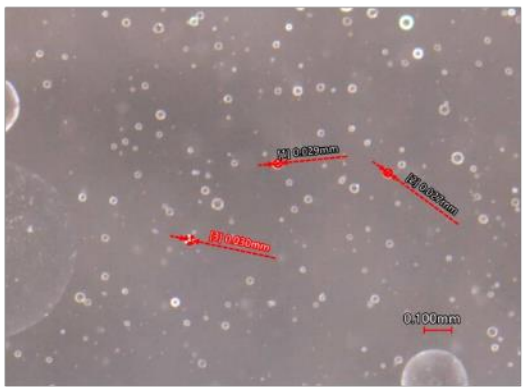

the other hydrophobic compounds at all dosage. Additionally, the solution became cloudier as the dosage of hydrophobic compound A increased. At a magnification of 160x, many fine oil droplets were observed, confirming the presence of aggregated oil droplets.

Hydrophobic compound B was less cloudy than A1, and it was confirmed that the oil droplets were dispersed independently and fewer oil droplets were observed. These results confirmed that the formation of oil droplets varied significantly with the ratio of emulsifier α. Additionally, increasing the dosage of the hydrophobic compound resulted in finer and more dispersed oil droplets.

Since hydrophobic compound C did not contain any emulsifier, the liquid phase was not cloudy and showed the largest oil droplet size compared to the other hydrophobic compounds. Moreover, compared to hydrophobic compound A, independent oil droplets were present and the oil droplets size tended to be larger than that of hydrophobic compound B.

The liquid phase of hydrophobic compound D, prepared with emulsifier β, was significantly clearer compared to those of hydrophobic compounds A and B. Additionally, the oil droplets in compound D were larger than those in compounds A and B, but smaller than those in compound C..

It was confirmed that the size and dispersion of oil droplets in the alkaline liquid phase vary significantly with the type of emulsifier. Specifically, as the emulsifier ratio increases, the liquid phase tends to become cloudier and the oil droplets tend to become smaller.

Table 3.3 Result of the fresh properties of concrete

Symbol	Chemical admixture	AE		Hydrophobic compounds		Slump	Air coent	Concrete temperature
	kind	dosage [%/C]	dosage [%/C]	kind	dosage [%/C]	[cm]	[%]	[°C]
Blank	Ad1	1.5	-	-	-	17.8	1.4	19
Non-A-1	Ad2	1.3	-	A	1.0	16.0	1.2	20
Non-A-2	Ad2	1.5	-	A	2.0	18.2	0.9	20
Non-A-4	Ad2	1.5	-	A	4.0	18.0	1.5	20
Non-B-1	Ad2	1.3	-	B	1.0	16.6	1.3	20
Non-C-1	Ad2	1.4	-	C	1.0	18.1	1.4	20
Non-D-1	Ad2	1.4	-	D	1.0	18.1	2.0	20
AE2.5	Ad1	1.3	0.002	-	-	17.1	2.5	20
AE4.5	Ad1	1.1	0.007	-	-	15.6	4.7	20
AE-A-1	Ad2	1.2	0.015	A	1.0	18.6	4.2	20
AE-B-1	Ad2	1.3	0.042	B	1.0	17.8	4.0	20
AE-C-1	Ad2	1.4	0.024	C	1.0	18.1	4.2	20
AE-D-1	Ad2	1.3	0.015	D	1.0	18.1	5.4	20

3.2 CONCRETE EXPERIMENT

3.2.1 FRESH PROPERTIES

Table 3.3 shows the result of the fresh properties of concrete, and figure 3.1 shows the relationship between the dosage of AE agent and the air content of concrete (dosage of hydrophobic compound: 1.0%/C). Compared to concrete without hydrophobic compounds, air entrainment performance decreased when using hydrophobic compounds. Among compounds using emulsifier α, hydrophobic compound B, with a lower emulsifier ratio, showed reduced air entrainment compared to compound A. In addition, the air entrainment performance decreased in the order of D, C, and B, where D and B contain same emulsifier amount and C does not contain emulsifier.

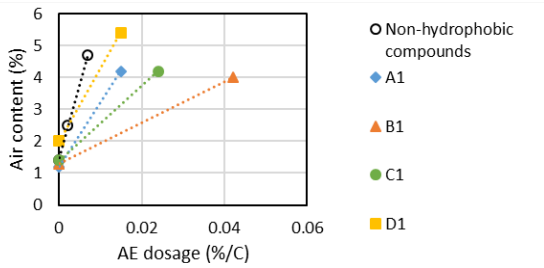

Figure 3.1 Relationship between dosage of AE agent and air content

3.2.2 COMPRESSIVE STRENGTH

Figure 3.2 shows the result of compressive strength in concrete. In non-AE concrete, the compressive strength of concrete regardless of a type of hydrophobic compound was equal to or greater than that of blank. The compressive strength of AE concrete using hydrophobic compounds was almost the same as that of AE4.5. Therefore, it is considered that the type of hydrophobic compound has little effect on the compressive strength of concrete.

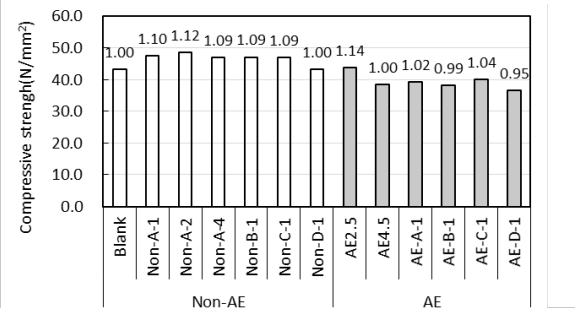

*In Non-AE, the value above the bar: Compressive strength ratio to Blank
In AE, the value above the bar: Compressive strength ratio to AE4.5

Figure 3.2 Result of compressive strength

3.2.3 FROST RESISTANCE

Figure 3.3 shows the result of relative dynamic modulus of elasticity (RDM) in concrete, and figure 3.4 shows the result of mass loss in concrete. In non-AE concrete, the RDM of concrete using hydrophobic compounds A, B and C were reduced similarly to that of the blank. The RDM of concrete using hydrophobic compound D was higher than that of Blank, but lower than that of AE2.5 and AE4.5. The mass of concrete using hydrophobic compounds A and B with emulsifier α increased early, resulting in a significantly lower effect of inhibiting frost resistance. The mass loss of concrete using hydrophobic compound C was similar to that of AE2.5, but RDM of concrete using hydrophobic compound C was reduced. The mass loss of concrete using hydrophobic compound D, which uses emulsifier β, is slightly higher than that of AE2.5, but scaling is suppressed more than that of Blank. Therefore,

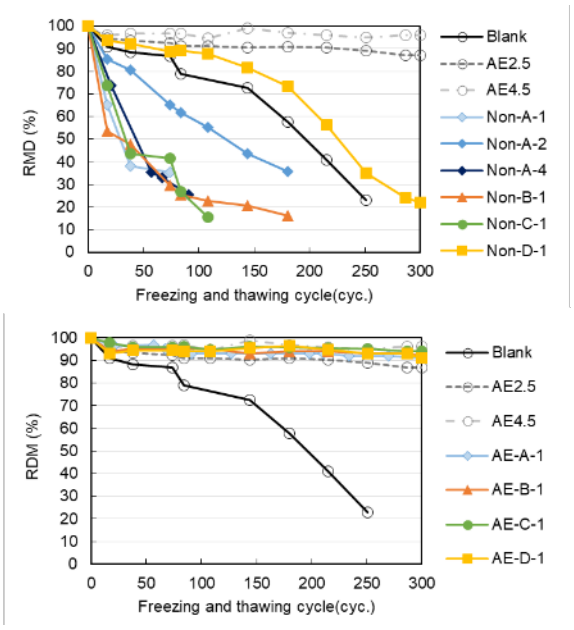

Figure 3.3 Result of RDM

hydrophobic compound D showed a slightly greater inhibitory effect on frost damage deterioration compared to the blank.

In AE concrete, regardless of the type of hydrophobic compounds, the RDM of concrete resulted equivalent to AE4.5. The mass loss of hydrophobic compounds A, B, and C were lower than that of AE2.5, but higher than that of AE4.5. The mass loss rate of hydrophobic compound D was similar to that of AE4.5. These results indicate that hydrophobic compounds A, B, and C reduce frost resistance, whereas hydrophobic compound D may help inhibit frost damage deterioration.

3.2.4 AIR-VOID SYSTEM

Table 3.4 shows the result of air-void system of concrete, and figure 3.5 shows the relationship between air content of fresh concrete and air content of hardened concrete. In non-AE concrete, compared to concrete without hydrophobic compounds, the air content of hardened concrete using hydrophobic compounds is higher than that of fresh concrete. This may be due to the hydrophobic compounds being measured as apparent air void. However, no similar tendency was observed in AE concrete. In non-AE concrete, when hydrophobic compound A was used, air-void spacing factor tended to decrease as dosage of hydrophobic compound A increased. In addition, compared to hydrophobic compound A, hydrophobic compound B, which contains a lower ratio of emulsifier α, had a smaller air-void spacing factor. The air-void spacing factor of hydrophobic compound C, which does not use an emulsifier, and hydrophobic compound D, which uses emulsifier β, was larger than the others. In the AE concrete, the air content of the concrete using hydrophobic compounds was 4% or more regardless of the type of hydrophobic compound, but the air-void spacing factor was larger than that of AE4.5.

Figure 3.6 shows the result of air content with arbitrary air void chord length. In non-AE concrete, using hydrophobic compound A at dosage of 1%/C, the air content with air-void chord length 50-150μm was greater than that of blank, at dosage of 2%/C, the content with air-void chord length 150μm or less was greater than that of blank, and at dosage of 4%/C, the air content with air-void chord length 100μm or less was greater than that of blank. In addition, the air content with small air-void increased with increasing dosage of hydrophobic compound A. When hydrophobic compound B was used, the air content with air-void chord length 150μm or less was greater than that of Blank, and compared to the dosage of hydrophobic compound A at 1%/C, there was a tendency for the air content with air-void chord length 100μm or less to increase. When hydrophobic compound C was used, the air content with air-void chord length 50-100μm was greater than that of Blank, and the air content with air-void chord length with 50μm or less was lower than others. When hydrophobic compound D was used, the air content with air-void chord length 100μm or less was greater than that of Blank. In addition, compared to hydrophobic compound B, which used a different type of emulsifier, the air content at larger air-void increased.

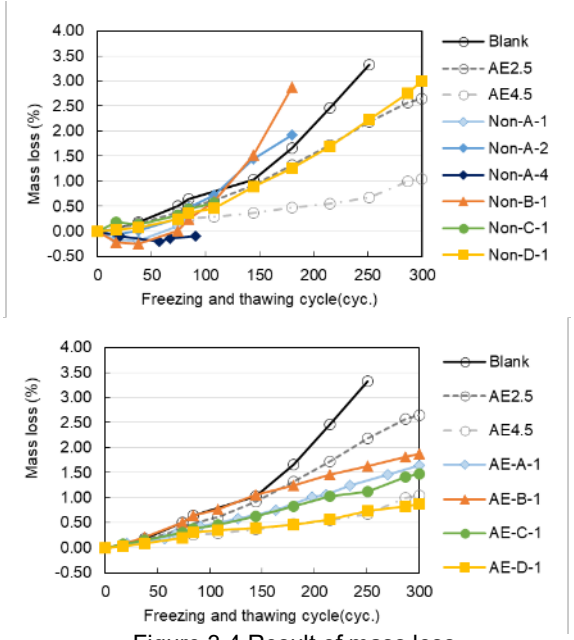

Figure 3.4 Result of mass loss

Table 3.4 Result of air-void system

symbol	Air content (%)		Air-void spacing factor	Durability factor
	Fresh	hardened	(μm)	
Blank	1.4	1.5	307	35
AE2.5	2.5	2.6	226	87
AE4.5	4.7	5.4	146	96
Non-A-1	1.2	1.8	309	4
Non-A-2	0.9	2.3	281	18
Non-A-4	1.5	2.0	166	7
Non-B-1	1.3	1.8	276	3
Non-C-1	1.4	1.9	390	5
Non-D-1	2.0	2.4	384	41
AE-A-1	4.2	4.8	172	91
AE-B-1	4.0	5.1	193	92
AE-C-1	4.2	5.2	225	94
AE-D-1	5.4	5.3	218	91

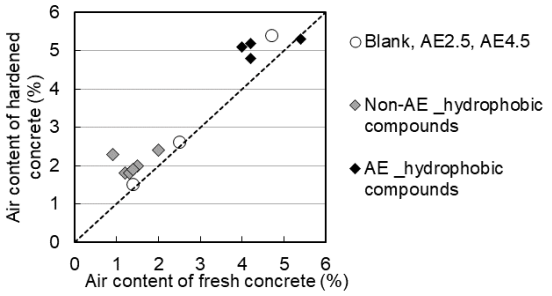

Figure3.5 Relationship between air content of fresh concrete and air content of hardened concrete

In AE concrete, the air content with air-void chord length 100μm or less of concrete using hydrophobic compound A and B, which used emulsifier α, was similar to that of AE4.5. When hydrophobic compound A and B used, the air content with air-void chord length 100-200μm was lower than that of AE4.5. The air content with air-void chord length 200μm or less of concrete using hydrophobic compound C without emulsifier was lower and the air content at larger air-void was greater than that of AE4.5. The air content with air-void chord

length 150μm or less of concrete using hydrophobic compound D, which used emulsifier β, was lower and the air content over air-void chord length 500μm was greater than that of AE4.5.

3.2.5 RELATIONSHIP BETWEEN FROST RESISTANCE AND AIR-VOID SYSTEM

Figure 3.7 shows the relationship between air content of hardened concrete and durability factor of concrete, figure 3.8 shows the relationship between air-void spacing factor and durability factor of concrete. In non-AE concrete, the durability factor decreased significantly when hydrophobic compounds A and B using emulsifier α were used, even though the air content was equal to or greater than that of blank. In addition, Powers[4] reported that air-void spacing factor of 250μm or less is effective in terms of frost resistance of concrete, but in the case of hydrophobic compound A, even though the air-void spacing factor was 200μm or less, the durability factor was lower than that of blank. Therefore, when emulsifier α was used, no effect on suppressing frost damage could be expected, regardless of the emulsifier ratio. As shown in Table 3.1, the emulsifying effect is so strong that round oil droplets-like air void are not formed, or the oil droplets become so small that they cannot be detected by optical microscopes, and therefore may not contribute to relieving water pressure during freezing.

In the case of hydrophobic compound C, the air content was slightly greater than in the blank, but the air -void spacing factor was large and the durability factor was low. As shown in Table 3.2, because no emulsifiers were used, the oil-based substance do not form round oil droplets like air void, or they become large oil droplets, which are unable to play the same role as air void.

In the case of hydrophobic compound D, the air content was greater than that of Blank and similar to that of AE2.5, but the air-void spacing factor was very large and the durability factor was slightly higher than that of Blank and lower than that of AE2.5. As shown in Table 3.1, emulsifier β has a weaker emulsifying effect than emulsifier α, and the size of oil droplets formed are larger. Alternatively, as shown in Figure 3.6, the air content with air-void chord length 200μm or less in concrete using hydrophobic compound D was lower than that of AE2.5, but was slightly higher than that of blank. This suggests that while hydrophobic compound D did not have a greater frost damage inhibition effect than air-entraining agents, it may be possible for it to improve frost damage resistance compared to blank.

On the other hand, in AE concrete, regardless of the type of hydrophobic compounds, the air content was similar to that of AE4.5, but the air-void spacing factor was larger than that of AE4.5, and the durability factor was 90 or higher. From these results, when AE agent was used, no effect was observed on the frost resistance of concrete, regardless of the ratio of emulsifier or dosage of hydrophobic compound.

Previous study[5] has shown that frost resistance in concrete is effective when the air content with air-void diameter of 300μm or less is 1.8% or more. Figure 3.9 shows the relationship between the air content with air-

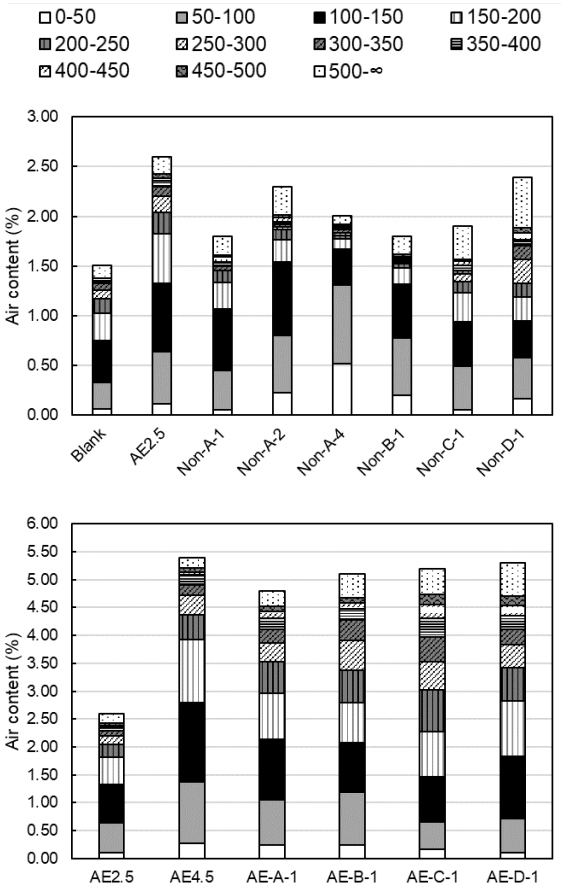

Figure 3.6 Result of air content with arbitrary air-void chord length

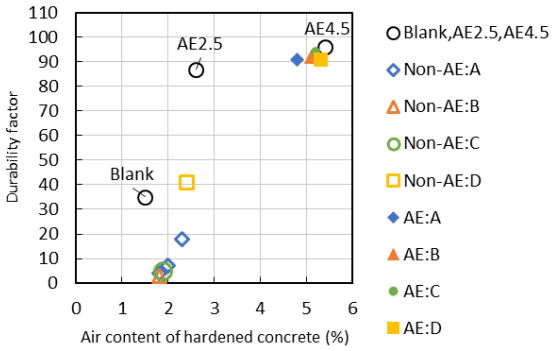

Figure 3.7 Relationship between the air content of hardened concrete and durability factor

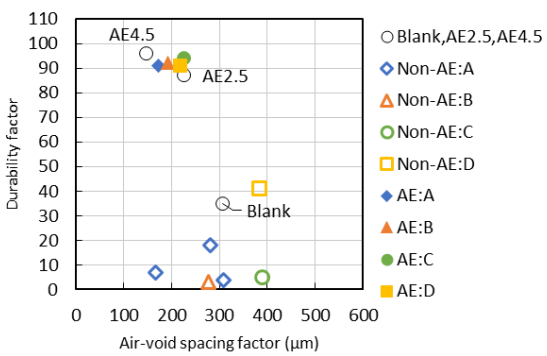

Figure 3.8 Relationship between the air-void spacing factor of concrete and durability factor

void chord length 300μm or less and the durability factor. When hydrophobic compounds were not used, the trends were similar to those observed in previous studies. In non-AE concrete, the durability factor differs greatly depending on the type of hydrophobic compound, even though the air content with air-void chord lengths of 300μm or less is similar. Therefore, it is difficult to evaluate frost resistance of concrete using hydrophobic compounds based on the air-void system. It is necessary to consider the factors caused by the type and ratio of emulsifier to reduce the frost resistance of concrete in the future.

In recent years, in order to realize a carbon-neutral society, many researches have been conducted on concrete that uses industrial by-products, such as fly ash and blast furnace slag, etc., and developed concrete using materials that absorb and fix carbon dioxide (Carbon Capture and Utilization materials). When fly ash which contains a lot of unburned carbon is used in concrete, it is difficult to entrain air by AE agents. Similarly, new materials being developed as concrete materials may make it difficult to ensure a sufficient air content in concrete. In this study, the hydrophobic compound was not able to sufficiently ensure the frost resistance of non-AE concrete, but if the hydrophobic compounds can ensure the frost resistance of non-AE concrete, it could become a very useful material. In the future, we would like to clarify the mechanism to suppress frost damage deterioration of concrete using hydrophobic compounds, and aim to establish the technology as a method of preventing frost damage in concrete.

4. CONCLUSION

We investigated the effect of using hydrophobic compounds to suppress frost damage deterioration of concrete. The findings are as follows:

1) In the case of hydrophobic compounds using emulsifier α, it was revealed that the oil droplets in the liquid phase became finer as the dosage of hydrophobic compound increased. In addition, the dispersion state of the oil droplets differed greatly depending on the emulsifier ratio.

2) The hydrophobic compounds without emulsifiers formed larger oil droplets than the others.

3) It was confirmed that the emulsifying effect of hydrophobic compounds using emulsifier β was weaker than that of emulsifier α, and oil droplets of various sizes were present.

4) In non-AE concrete, hydrophobic compounds without emulsifiers and hydrophobic compounds using emulsifier α cannot be expected to inhibit frost damage deterioration, but hydrophobic compounds using emulsifier β may be able to improve frost damage resistance.

5) In AE concrete, the durability factor was high regardless of the type of hydrophobic compound, but it was confirmed that hydrophobic compounds using emulsifier β tended to have the least scaling.

6) The frost resistance of concrete containing hydrophobic compounds is difficult to evaluate based on the air-void system.

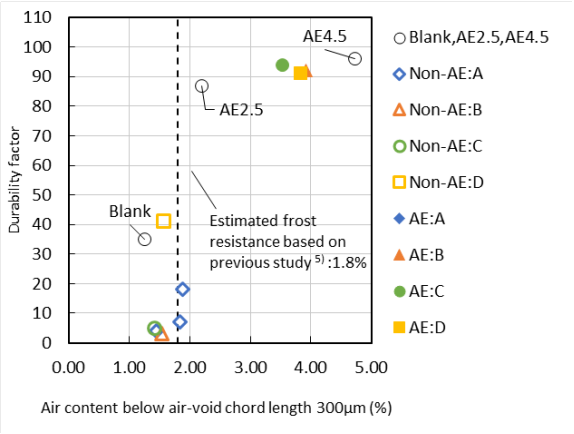

Figure 3.9 Relationship between the air content with air-void chord length 300μm or less and durability factor

REFERENCES

1. Hironobu NISHI, Toyoharu NAWA, “STUDY ON FROST DAMAGE DEGRATION IN HYDRATED CEMENT USING HYDROPHOBIC COMPOUND”, J. Struct. Constr. Eng., AIJ, Vol.79, No.704, 2014.10, pp.1415-1424.

2. Masataka USHIRO, Takayuki HIGUCHI, Minoru MORIOKA, Toshiharu KISHI, “THE MECHANISM OF IMPROVING THE FROST RESISTANCE BY ADDING MICROSPHERES”, Cement Science and Concrete Technology, Vol.69, 2015, pp.490-495.

3. A. OKADA, H. MARUTA, H. NAKAMURA, T. HAYAKAWA, “Frost Damage Restraing Technology with Special Paraffin Emulsion”, Concrete Journal, Vol.60, No.10, 2022.10, pp.902-908.

4. Powers, T. C., “The air requirement frost resistance concrete, Proceedings of the Highway Research Board, 29, 1949, pp.184-211.

5. J. Stark, B. Wicht, (Translation) T. OTA, S.SHIMOBAYASHI, N. SAEKI, “Durability of concrete”, Japan Cement Association, Vol.2, 2003.

C-S-H Seeds Used as Accelerator for Cold Weather Concreting

Yingzi Yang
Professor, School of Civil Engineering, Harbin Institute of Technology, Harbin 150006, China.

Sile Hu
Master student, School of Civil Engineering, Harbin Institute of Technology, Harbin 150006, China.

Yi Jiang
PhD student, School of Civil Engineering, Harbin Institute of Technology, Harbin 150006, China.

ABSTRACT

In this study, the effects of C-S-H seeds on the mechanical properties and hydration of cement paste at subzero temperatures were studied. The results show that at 0 ℃ and -5 ℃, the addition of C-S-H seeds can reduce the freezing point of the cement paste, and accelerate the cement hydration, so as to significantly improve the compressive strength of the cement paste and prevent freezing damage. At -10 ℃, the addition of C-S-H seeds cannot avoid the freezing damage of cement paste. In addition, LT-DSC and XRD tests help to reveal the mechanism of C-S-H seeds at low temperatures. Furthermore, the combination of C-S-H seeds and pre-curing several hours can make the early-age cement paste have frost resistance in cold weather concreting.

Keywords: C-S-H seeds; compressive strength; freezing point; hydration degree;

1. INTRODUCTION

As a chemical admixture, accelerator can improve the hydration rate of hydraulic cement, thereby shortening the setting time, increasing the strength development rate, or both [1]. The main applications of accelerator for normal concrete are to allow workers to remove the formwork earlier, finish the concrete surface earlier, and sometimes even apply loads earlier, such as early opening up to traffic when repairing road. In addition, accelerator also helps concrete constructed in winter to reach the expected strength as soon as possible to avoid freezing damage [2]. Accelerators are mainly inorganic compounds, such as soluble chlorides, carbonates, silicates, fluorosilicates, nitrates, nitrites, thiocyanates, formates and some organic compounds, such as triethanolamine. However, high dosages of accelerators are particularly harmful for late strength and durability [3–12]. .

At present, an alternative to traditional accelerator is Calcium-silicate-hydrate (C-S-H) seeds [13,14]. C-S-H seeds have an excellent acceleration effect because of their large specific surface area and similar chemical composition to cement hydration products [14]. It can provide nucleation sites for hydration products and improve the microstructure of cement paste [13], thus accelerating the early hydration of the cement. Many studies have shown that C-S-H seeds can significantly improve the early strength of cement without sacrificing the late strength [15–19], which makes it have better application prospects than traditional accelerators.

This work attempts to characterize the effects of C-S-H seeds on the properties of cement paste at low temperature. C-S-H seeds were incorporated into Portland cement as an accelerator/antifreezer, and their effects on the compressive strength, freezing point and freezing water content of cement paste were investigated. The effects of C-S-H seeds on the hydration of Portland cement were studied by quantitative XRD analysis.

2. EXPERIMENTAL

2.1 RAW MATERIALS

The nano-sized C-S-H seeds used were prepared from RHA and CS by the co-precipitation method, and the average particle size of C-S-H seeds were 316.4 nm, and the main components were C-S-H gel, PCE, and $NaNO_3$[20]. The mass of the C-S-H gel in the C-S-H seeds can be roughly calculated by subtracting the mass of PCE and NaNO3 from the total mass of the dried C-S-H seeds. The mass ratio of these three components was calculated to be approximately C-S-H gel: PCE: $NaNO_3$=39: 20: 41.

2.2 MIX DESIGN

C-S-H seeds are added to cement paste to investigate their effects on the early hydration and mechanical properties of cement. The mixture proportion of cement paste is shown in Table 1. The water/cement ratio was 0.35. The control is named PC. When the solid content of C-S-H seeds is 0.5% and 1% of cement mass, it is named CSH-0.5 and CSH-1,

respectively. Considering the PCE in C-S-H seeds, 0.2% PCE was added to cement paste to disclose the effect of PCE and named PCE-0.2. PCE-0.2 has the same PCE content as CSH-0.5.

Table 1 Mix proportion of cement paste.

Code	Cement (g)	Water (g)	PCE (g)	C-S-H seeds (wt%)
PC	100	35	0	0
PCE-0.2	100	35	0.2	0
CSH-0.5	100	31.5	0	0.5
CSH-1	100	28	0	1

2.3 CURING SYSTEMS

In order to study the effect of C-S-H seeds on the properties of cement paste at subzero temperature, three temperatures of 0 ℃, -5 ℃ and -10 ℃ were designed. Fresh cement paste was cast in steel mold (20 × 20 × 20 mm) and the specimens were put into the low-temperature test chamber at the specified temperatures (0 ℃, -5 ℃, and -10 ℃) immediately after molding, and when the specimens were cured for 7 d in the negative temperature, they were transferred to the standard curing room (the temperature was controlled at 20 ± 1 ℃, and relative humidity was not less than 95 %) for curing for 28 d. One pre-curing times were designed, and after the specimens were molded, they were put into the standard curing room to the specified pre-curing times of 12 h, and then they were put into the low-temperature test chamber, and after being cured for 7 d under the negative temperature, they were transferred to the standard curing room to be cured for 28 d.

3. RESULTS AND DISCUSSION

3.1 COMPRESSIVE STRENGTH

Fig.1 shows the compressive strength of immediately frozen samples at 0 ℃. At 0 ℃, the compressive strength of the PC develops more slowly, and there is almost no strength at -1 d, only 0.6 MPa, which indicates that the decrease in temperature will significantly inhibit the hydration of cement. When the specimens were transferred to room temperature curing, the PC had a good strength growth, but both showed a slight decrease in strength compared to the normal temperature curing for 28 d, which indicated that even at 0 ℃, the cement paste would undergo a slight frost damage.The strength of the PCE-0.2 was very close to that of the PC, which indicated that the addition of PCE had almost no effect on the hydration of the cement at 0 ℃.The strength development of cement paste at 0 ℃ was significantly promoted by the addition of C-S-H seeds, and the promotion effect increased with the increase of the dosage of C-S-H seeds. The compressive strengths of CSH-1 at -1 d, -3 d, -7 d, and -7+28 d were 3.7 MPa, 25.6 MPa, 45.7 MPa, and 68.2 MPa, respectively, which were improved by 580.0 %, 102.9 %, 41.5 % and 23.4 % compared with that of PC, respectively, which is also attributed to the lower compressive strength of the PC at 0 ℃. In addition, the strengths of CSH-0.5 and CSH-1 at -7+28 d were 67.6 MPa and 68.2 MPa, respectively, which were higher than that of 60.7 MPa for the PC group at 28 d of normal temperature curing, which indicated that the C-S-H seeds not only promoted the hydration of the cement at 0 ℃, but also successfully avoided the freezing damage of the cement paste.

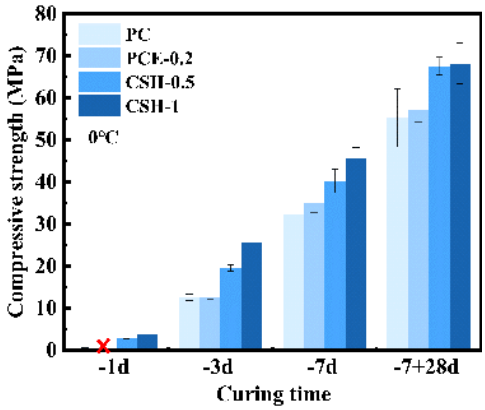

Fig.1 Compressive strength of cement paste at 0 ℃

Fig.2 shows the compressive strength of immediately frozen samples at -5 ℃. Compared with 0 ℃, the strength development of all samples at -5 ℃ is much more slow, and at -1 d, the strength of all samples is lower than 1 MPa. With the increase of the age of negative temperature curing, the compressive strength of the PC grows extremely slowly, which is only 13.51 MPa at -7 d. Even if it is transferred to the positive temperature curing, the strength of -7+28 d is only 45.1 MPa, which is 24.7 % lower compared with that of the positive temperature curing of 28 d. This indicates that serious frost damage occurs to the cement paste at -5 ℃. The strength of PCE-0.2 was significantly lower than that of PC at the early age, which indicated that PCE was detrimental to the frost resistance of cement at -5 ° C. The addition of C-S-H seeds promoted the development of compressive strength of cement at -5 ° C, but unlike that at 0 ° C, the lower dosage of C-S-H seeds (0.5 %) at -5 ℃ has a very limited improvement in the compressive strength of cement. The strengths of CSH-0.5 at -3 d, -7 d, and -7+28 d are 7.8 MPa, 20.4 MPa, and 49.4 MPa, respectively, which are not ideal for the CSH-0.5 group, although they are improved by 94.1%, 51.3%, and 9.3%, respectively, with respect to the PC. In addition, the strength of CSH-0.5 at -7+28 d decreased by 18.6 % compared to the PC group cured at positive temperature for 28 d. This indicates that the lower dosage of CSH seeds at -5 ℃ does not enable the cement paste to resist frost damage. When the dosage of C-S-H seeds was increased to 1 %, the strength of cement paste at -5 ℃ had a better development, and the strength of CSH-1 at -3 d, -7 d, and -7+28 d reached 11.4 MPa, 33.2 MPa, and 65.7 MPa, which were 185.3 %, 145.9 %, and 45.3 % higher than that of PC, and the strength of CSH-1 at -7+28 d increased by 185.3 %, 145.9 %, and 45.3 % compared with that of PC. A

increase of 8.2 % was compared with the PC group cured at positive temperature for 28 d. This indicates that the higher dosage of C-S-H seeds (1 %) can effectively avoid the frost damage of the cement paste at -5 ℃.

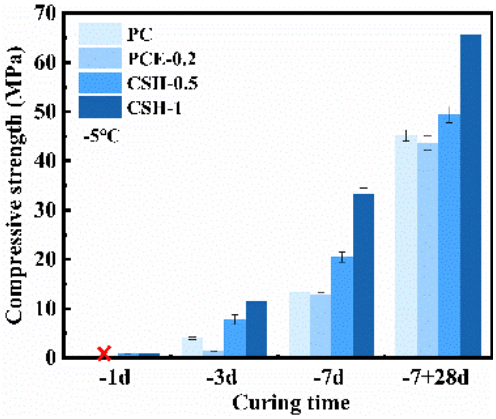

Fig.2 Compressive strength of cement paste at -5 ℃

Fig.3 shows the compressive strength of the immediately frozen samples at -10 ℃. It can be found that there is almost no strength development in the cement paste regardless of the addition of CSH seeds, all the samples have no strength at -1 d and -3 d, and even at -7 d the strengths are lower than 3 MPa, which indicates that the cement is almost unable to hydrate at -10 ℃. Even when transferred to normal temperature curing for 28 d, the strength of all samples at -7+28 d was only about 40 MPa, which indicated that serious frost damage occurred in the cement at -10 ℃. Even if the C-S-H seeds were added, it was not possible to prevent the frost damage, which was probably due to the low temperature leading to the freezing of a large amount of water in the cement paste and an extremely low rate of hydration reaction.

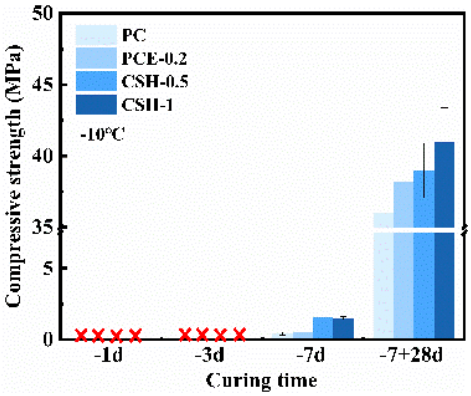

Fig.3 Compressive strength of cement paste at -10 ℃

Fig. 4 shows the compressive strength of cement paste at 28 d versus -7+28 d at different temperatures. It can be found that the strength of all samples at -7+28 d under negative temperature is lower than that of the corresponding group of samples cured at positive temperature for 28 d, which indicates that some samples suffered from frost damage at negative temperature. At 0 ℃, the strengths of all samples at -7+28 d are smaller than those of the corresponding group of samples cured at positive temperature for 28 d, which indicates that the cement paste does not suffer from serious frost damage at 0 ℃, and the samples with the addition of C-S-H crystalline species even have better strengths in the later period. However, at -5 ℃, only the CSH-1 group has a better strength in the late stage without serious frost damage, which indicates that when the temperature drops to -5 ℃, the control group and the samples with low dosage of crystalline species can no longer resist the early frost damage. When the temperature drops to -10 ℃, no matter whether the crystal seed is added or not, the cement will have serious frost damage.

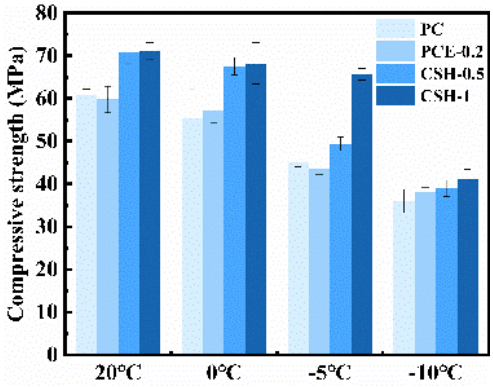

Figure 4 Compressive strength of cement paste at 28 d vs. -7+28 d under different temperature conditions

3.2 FREEZING POINT AND FREEZABLE WATER CONTENT

In the range of -30 ℃~25 ℃, only the liquid phase inside the cement paste can undergo phase transition, so the phase transition temperature of the cement paste is equivalent to the phase transition temperature of the liquid phase. Although the phase transition temperature of the liquid phase inside the cement paste is somewhat different from its freezing point when it is warmed up, the effect of C-S-H seeds on the freezing point of the cement paste can be expressed under the same conditions, and the value of the phase transition temperature of the samples is the temperature corresponding to the intersection of the tangent line of the epitaxial extension of its LT-DSC curve.

Fig. 5 show the LT-DSC plots of the aqueous solution, H2O is deionized water, and CSH-1aq is the mixed solution of deionized water and C-S-H seeds with 1 % of cement mass in the preparation of CSH-1. It can be seen that the addition of C-S-H seeds can reduce the phase transition temperature of water from 0 ℃ to -2.2 ℃, and this phenomenon can be attributed to the large amount of ions such as Ca_2^+, SiO_3^{2-}, NO_3^-, and Na^+ in the C-S-H seeds, and the increase in the ionic concentration will reduce the freezing point of the aqueous solution, and this is one of the reasons for the increase in the freezing resistance of the cement by C-S-H seeds.

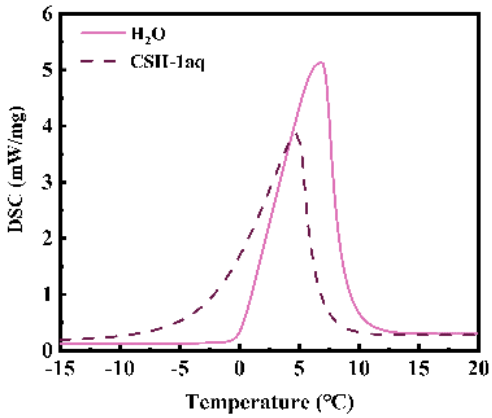

Figure 5 LT-DSC plot of C-S-H aqueous solution

Table 2 shows the phase transition temperatures of cement pastes W or W/O CSH seeds under the precuring times of 0 h or 12 h, and it can be found that for the immediately frozen samples, the phase transition temperature point of PC is -2.5 ℃, and for the cement pastes, a certain amount of ions will be dissolved when the cement is mixed with the water, which will make the freezing point of the cement pastes less than 0 ℃.The addition of the C-S-H seeds can make the phase transition temperatures of the immediately frozen cement pastes decrease to -3.6 ℃, which is related to the ions in the C-S-H seeds, and the decrease in freezing point can allow the cement paste to continue hydration at a lower temperature, thus improving the frost resistance of the cement paste, which can explain the better negative temperature strength development and less severe frost damage of the CSH-1 group compared with the PC group at 0 ℃ and -5 ℃ in Section 3.1. After 12 h of pre-curing, the freezing point of PC decreased from -2.5 °C to -3.9 °C, but that of the cement paste with added C-S-H seeds decreased from -3.6 °C to -10.2 °C. This suggests that CSH-1 develops good strength at -10 °C with the addition of a longer pre-curing period.

Table 2 Freezing point, enthalpy of melting and freezable water content of cement paste.

Code	Freezing point （℃）	Enthalpy of melting （J/g）	Freezable water content (%)
PC	-2.5	71.42	85.5
CSH-1	-3.6	61.16	73.2
PC+12h	-3.9	47.33	56.6
CSH-1+12h	-10.2	13.96	16.7

In order to quantify the change in the freezable water content of a cement paste during hydration, the concept of free water index (FWI) proposed by Damasscen et al [21] was used. The free water index is the ratio of free water to initial free water content at moment t. In cement pastes, the measured free water can be equated to the internal freezable water, so the free water index is used in this paper to represent the freezable water content of cement pastes. The formula for the free water index is shown in Equation 1.

$$FWI_t = \frac{\Delta H_{exp}}{w_e \Delta H_{init}} \quad (1)$$

Where: we is the average mass fraction of water in the cement paste, the water-cement ratio of the cement paste in this paper is 0.35, so the value of we is 0.259; ΔHexp is the enthalpy change of melting measured in the test, and the heat of melting of the sample is the peak area of its LD-DSC curve; ΔHinit is the theoretical value of the specific enthalpy of melting of water at 0 ℃; and the beginning of the hydration of the cement paste is FWIt=1.

As showed in Table 2, the freezable water content of both PC and CSH-1 decreased with the increase of precuring time, which was due to the water consumption by the hydration reaction of the cement paste during this period. Due to the faster hydration rate of CSH-1 in the early stage, the freezable water content of CSH-1 was lower than that of PC for the same precuring time. The effect of precuring on the freezable water content of CSH-1 was more obvious than that of PC. When the precuring time was increased from 0 h to 12 h, the freezable water content of PC decreased from 85.5 % to 56.6 %, and that of CSH-1 decreased from 73.2 % to 16.7 %. In summary, the combination of C-S-H seeds with pre-curing can significantly reduce the freezable water content of cement paste and reduce its risk of frost damage.

3.3 QUANTITATIVE XRD ANALYSIS

Fig. 6 show the XRD patterns of the cement pastes immediately frozen at 0 °C and -5 °C. The peaks of clinker minerals C_3S and C_2S can be clearly observed, and the main hydration products of all samples are $Ca(OH)_2$ and AFt. This indicates that the negative temperature curing and the PCE and C-S-H seeds do not change the main hydration products of the cement paste. It can be found that the peaks of C_3S and C_2S of all samples decreased with the increase of age, which indicates that the cement paste can be hydrated normally at 0 ℃ and -5 ℃. In order to further analyse the effect of C-S-H seeds on the hydration degree of immediately frozen samples at negative temperatures, the clinker content and hydration degree of immediately frozen samples at -3 d, -7 d, and -7+28 d were quantitatively analysed by XRD-Rietveld.

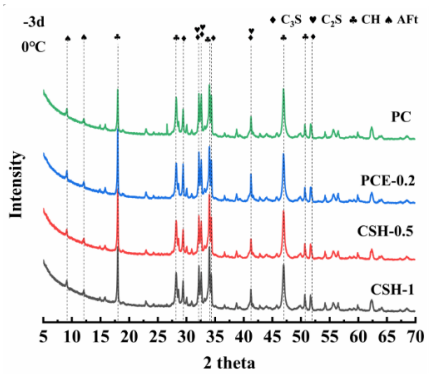

(a) 0℃ -3d

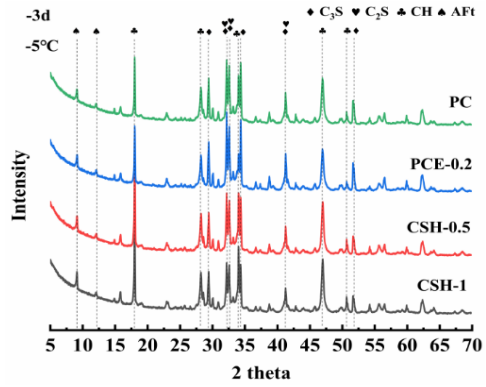

(b) -5℃ -3d

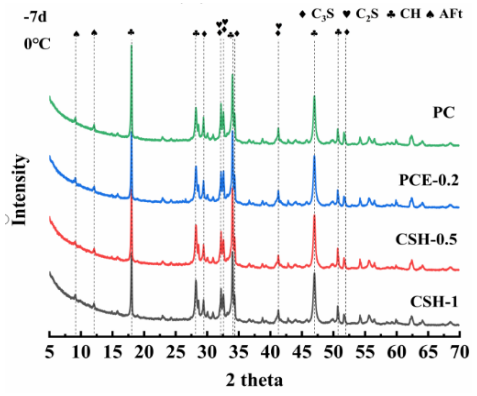

(c) 0℃ -7d

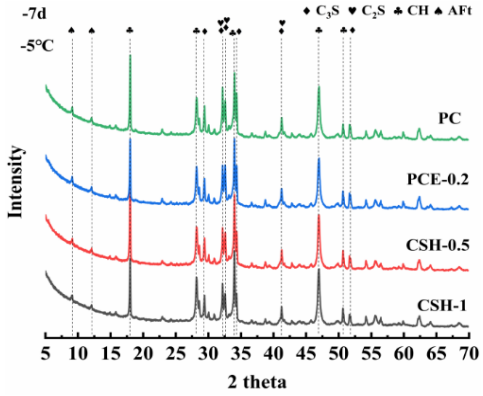

(d) -5℃ -7d

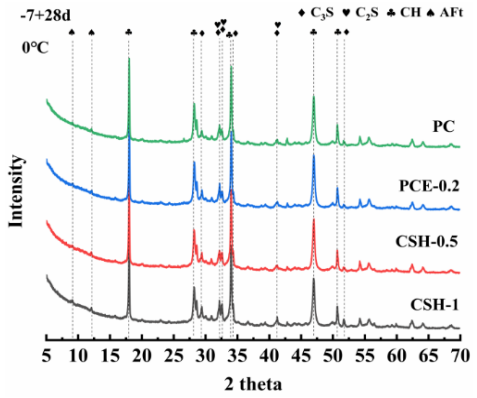

(e) 0℃ -7+28d

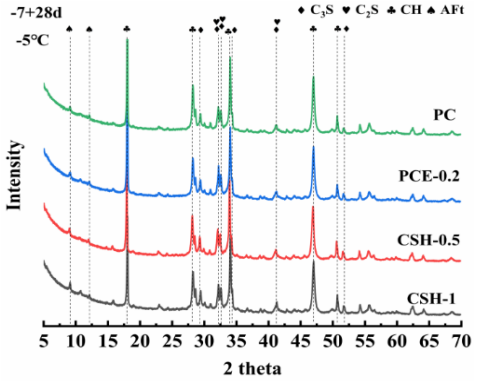

(f) -5℃ -7+28d

Fig. 6 XRD diffractograms of cement paste at 0 °C and -5 °C

Fig. 7 shows the hydration degree of cement paste at 0 ℃ and -5 ℃. It can be seen that the hydration degree of cement at each age under negative temperature is much lower than that under positive temperature. the hydration degree of PC group at 0 ℃ and -5 ℃ for -3 d is 35.5 % and 15.5 % respectively, which is lower than that of PC group at room temperature for 1 d (37.2 %), indicating that the negative temperature greatly slows down the rate of hydration reaction of the cement paste. The hydration degree of PC group at 0 ℃ and -5 ℃ for -7 + 28 d is only 65.4% and 61.5%, which are lower than that of positive temperature for 28 d (68.5 %), which indicates that frost damage occurs in cement under negative temperature environment. The hydration degree of the PCE-0.2 group was similar to that of the PC group at -7+28 d, which indicated that the addition of PCE would not change the degree of freezing damage of the cement paste. The hydration degree of the CSH-0.5 and CSH-1 was higher than that of the PC group at 0 ℃ and -5 ℃ for all the age periods. In addition, the hydration degree of CSH-0.5 and CSH-1 at -7+28 d at 0 ℃ is 69.16 % and 69.88 %, which is higher than that of the PC group at 68.5 % for the 28 d of positive temperature curing. The hydration degree of the CSH-1 group at -5 ℃ is higher than that of control PC(68.5 %) , which indicates that the addition of C-S-H seeds not only accelerates the hydration of cement paste at negative temperature, but also prevents the occurrence of frost damage of cement paste. Therefore when the temperature is lower (-5 ℃), the higher dosage of C-S-H crystalline species is needed to resist the frost damage. The results of the degree of hydration can correspond well with the results of the compressive strength in section 3.1, so that the increase in the negative temperature strength of the cement can be attributed to the increase in the degree of hydration of the cement by the C-S-H seeds.

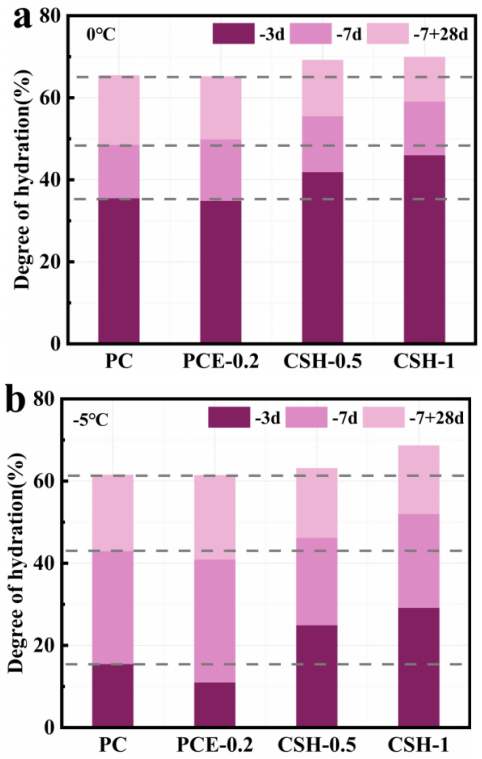

Fig. 7 Degree of hydration of cement paste at -3 d, -7 d and -7+28 d: (a) 0 °C (b) -5 °C

Fig.7 shows a schematic of the hydration of a cement paste W/ and WO C-S-H seeds at negative temperature. As shown in Fig. 7(a), the hydration of the PC samples at negative temperatures is extremely slow and does not allow for the formation of a denser structure. The low ion concentration in the pore solution results in a higher freezing point of the pore solution. At negative temperatures, the pore solution freezes in large quantities, preventing the cement from hydrating properly and causing frost damage. The lower the temperature, the more severe the freezing of the pore solution and the more severe the frost damage. The slow hydration rate at negative temperatures combined with frost damage results in a very low compressive strength of the cement paste immediately frozen at negative temperatures and an irreparable loss of strength when the temperature is changed to positive.

As shown in Fig. 7(b), after the addition of C-S-H seeds, due to the nucleation effect of C-S-H seeds, a large number of hydration products will be produced in cement paste during the pre-curing period, generating a more dense microstructure compared with the PC, which drastically reduces the freezing point of the pore solution. When the pre-curing time is prolonged, the freezing point of the pore solution can even be reduced to below the freezing temperature, thus completely eliminating frost damage. Meanwhile the rapid hydration reaction during pre-curing period consumes a large amount of water, which significantly reduces the freezable water content of the cement paste. In addition, the addition of C-S-H seeds further accelerated the hydration of the cement paste at negative temperatures, resulting in a certain degree of strength development under the harsher negative temperature environment. In summary, the rapid hydration of the C-S-H seeds during the pre-curing period and the promotion of hydration after the transition to negative temperatures together result in a relatively good compressive strength of the cement paste even at the more severe negative temperatures. The combination of C-S-H crystals and precuring at negative temperatures is much better than their use alone, which indicates a very good synergy between C-S-H seeds and pre-curing.

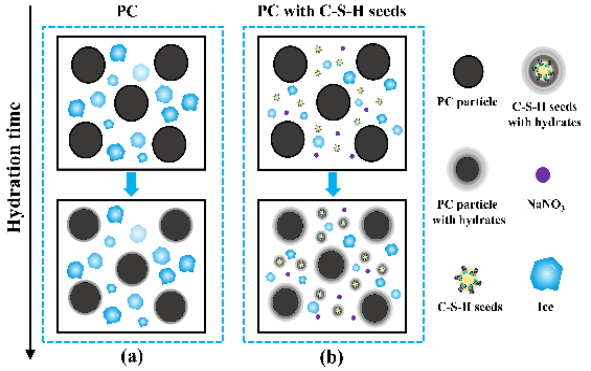

Fig. 7 Schematic of the hydration of PC and CSH-1 at negative temperature

4 CONCLUSIONS

At 0 ℃ and -5 ℃, the addition of C-S-H seeds can greatly improve the compressive strength and reduce frost damage of cement paste. 1 % of C-S-H seeds can increase the compressive strength of cement paste at 0 °C and -5 °C by 102.9 % and 145.9 % at -3 d, respectively, and their strength at -7+28 d are not lower than that at 28 d of normal temperature curing. Compared with the 0 ℃, the -5 ℃ condition requires a higher dosage of C-S-H to resist the frost damage. At -10 °C, there was almost no strength development in the cement paste with or without the addition of C-S-H seeds.

The addition of C-S-H seeds can lower the freezing point of the liquid phase of the cement paste by increasing the ionic concentration, and 1 % of C-S-H seeds can reduce the freezing point of the cement paste from -2.5 ℃ to -3.6 ℃ as well as the amount of freezable water from 85.5 % to 73.6 %.

The XRD results indicate that the C-S-H seeds can promote the hydration of the cement paste at 0 ℃ and -5 ℃, which leads to a higher degree of hydration and strength of the cement paste after the negative temperature to positive temperature curing.

The freezing point of the cement paste has been reduced to -10.2 °C due to the 12-hour pre-curing and the C-S-H seeds. Therefore, the combination of pre-curing time and C-S-H seeds can provide a new way of winterising cementitious materials at -10 °C and below.

ACKNOWLEDGMENTS

The financial support from the National Natural Science Foundation of China (No. 52178197) for current research are gratefully acknowledged.

REFERENCES

[1] Q. Yuan, D. Zhou, H. Huang, J. Peng, H. Yao, Structural build-up, hydration and strength development of cement-based materials with accelerators, Constr. Build. Mater. 259 (2020) 119775.
[2] G. Zhang, Y. Yang, H. Li, Calcium-silicate-hydrate seeds as an accelerator for saving energy in cold weather concreting, Constr. Build. Mater. 264 (2020) 120191.
[3] Z. Wu, J. Liu, G. Zhang, Y. Wang, Y. Wang, Effect of aluminum sulfate alkali-free liquid accelerator with compound alkanol lamine on the hydration processes of Portland cement, Constr. Build. Mater. 308 (2021) 125101.
[4] U. Rattanasak, K. Pankhet, P. Chindaprasirt, Effect of chemical admixtures on properties of high-calcium fly ash geopolymer, Int. J. Miner. Metall. Mater. 18 (2011) 364–369.
[5] S. Aggoun, M. Cheikh-Zouaoui, N. Chikh, R. Duval, Effect of some admixtures on the setting time and strength evolution of cement pastes at early ages, Constr. Build. Mater. 22 (2008) 106–110.
[6] T. Lee, J. Lee, Y. Kim, Effects of admixtures and accelerators on the development of concrete strength for horizontal form removal upon curing at 10 °C, Constr. Build. Mater. 237 (2020) 117652.
[7] J. Khan, S.K. G., Influence of binary antifreeze admixtures on strength performance of concrete under cold weather conditions, J. Build. Eng. 34 (2021) 102055.
[8] H. Huang, X. Shen, Influence of low-dose chemicals on the early strength of Portland cement: statistical and calorimetric evidence, Adv. Cem. Res. 29 (2017) 155–165.
[9] W. Li, S. Ma, Y. Hu, X. Shen, The mechanochemical process and properties of Portland cement with the addition of new alkanolamines, Powder Technol. 286 (2015) 750–756.
[10] Y. Wang, L. Lei, J. Liu, Y. Ma, Y. Liu, Z. Xiao, C. Shi, Accelerators for normal concrete: A critical review on hydration, microstructure and properties of cement-based materials, Cem. Concr. Compos. 134 (2022) 104762.
[11] C.Y. Lee, H.K. Lee, K.M. Lee, Strength and microstructural characteristics of chemically activated fly ash–cement systems, Cem. Concr. Res. 33 (2003) 425–431.
[12] J. Qian, C. Shi, Z. Wang, Activation of blended cements containing fly ash, Cem. Concr. Res. 31 (2001) 1121–1127.
[13] S.C. Paul, A.S. van Rooyen, G.P.A.G. van Zijl, L.F. Petrik, Properties of cement-based composites using nanoparticles: A comprehensive review, Constr. Build. Mater. 189 (2018) 1019–1034.
[14] E. John, T. Matschei, D. Stephan, Nucleation seeding with calcium silicate hydrate – A review, Cem. Concr. Res. 113 (2018) 74–85.
[15] M. Theobald, J. Plank, C–S–H–Polycondensate nanocomposites as effective seeding materials for Portland composite cements, Cem. Concr. Compos. 125 (2022) 104278.
[16] V. Kanchanason, J. Plank, Effectiveness of a calcium silicate hydrate – Polycarboxylate ether (C-S-H–PCE) nanocomposite on early strength development of fly ash cement, Constr. Build. Mater. 169 (2018) 20–27.
[17] X. Li, J. Bizzozero, C. Hesse, Impact of C-S-H seeding on hydration and strength of slag blended cement, Cem. Concr. Res. 161 (2022) 106935.
[18] J. Sun, H. Dong, J. Wu, J. Jiang, W. Li, X. Shen, G. Hou, Properties evolution of cement-metakaolin system with C-S-H/PCE nanocomposites, Constr. Build. Mater. 282 (2021) 122707.
[19] G. Land, D. Stephan, The effect of synthesis conditions on the efficiency of C-S-H seeds to accelerate cement hydration, Cem. Concr. Compos. 87 (2018) 73–78.
[20] Sile Hu,Zhichao Xu,Yingzi Yang, Preparation of C-S-H seeds from solid waste and its application as Portland cement accelerator, Constr. Build. Mater. 93 (2024).
[21] L. Nicoleau, Accelerated growth of calcium silicate hydrates: Experiments and simulations, Cem. Concr. Res. 41 (2011) 1339–1348.

A proposal for the mass concrete hydration heat reduction by applying proper mixing time and mixing methods

Seong-Jin, Baek
Ph.D. student, Dept. of Architectural Engineering, Cheong-ju University, *Republic of Korea*

Gun-su Lim
Doctoral student, Dept. of Architectural Engineering, Cheong-Ju University, Republic of Korea

Jun-Hui, Han
Ph.D, Dept. of Architectural Engineering, Cheong-ju University, Republic of Korea

Jong Kim
Assistant Professor, Dept. of Architectural Engineering, Cheong-Ju University, Republic of Korea

Mincheol Han
Professor, Dept. of Architectural Engineering, Cheong-Ju University, Republic of Korea

Correspondence: psj970616@gmail.com

ABSTRACT:

The purpose of the present study was to evaluate the various physical properties, Evaluation Index for Segregation of Normal Strength Concrete (EISN), and compressive strength of concrete based on different mixing methods and mixing time for ensuring homogeneous mixing and optimal performance of a 3-component low-heat mix in mass concrete applications. As a result, Pre-Mixed Cement (Pre-C) showed superior material segregation resistance compared to conventional mixed cement (Conv.C) for all mixing times with Pre-C's EISN for all time variables. In a case of compressive strength, Conv.C showed decreased variability after 120 seconds, whereas Pre-C had minimal variability for mixing times of 60 seconds or more. Thus, Pre-C was considered an effective mixing method for maintaining high concrete quality as well as enhancing ready-mix concrete productivity when using it with a mixing time of 60 seconds or more.

Keywords: Pre-Mixed Cement, Mass concrete, Material segregation resistance, Repeated Measures ANOVA

1. INTRODUCTION

In the Republic of Korea (Hereafter, Korea), the foundations of large-scale buildings are commonly constructed using mat foundation mass concrete. This type of concrete generates a high heat of hydration in its thick sections, which can cause cracking. Therefore, it is essential to apply proper methods to reduce the heat of hydration.

Currently, the methods to reduce the heat of hydration include the use of low-heat binders, pre-cooling of raw materials, reduction of heat generation, the use of super retarding agents, the temperature reinforcement, and pipe cooling.

Particularly, in an aspect of materials, the use of low-heat binders is crucial to reduce the heat of hydration. The combination of types and replacement rates of the materials plays a significant role in concrete performance. However, recent combinations of materials for low-heat binders used in mass concrete have evolved to include 3 to 4-component systems. Due to differences in density and fineness among the materials, it challenges to achieve efficient and homogeneous mixing of these binders in the batching plants of ready-mix concrete plants. Additionally, manufacturers may shorten the mixing time for raw materials of concrete to meet the construction demand due to regulation such as the 52-hour workweek system and the "8-5 system" for ready-mix concrete (starting at 8 AM and ending at 5 PM) in Korea. This can lead to concrete quality issues such as reduced fluidity, segregation, and insufficient strength development.

Therefore, the present study aims to propose appropriate mixing methods and mixing time to ensure homogeneous mixing and performance of a 3-component low-heat mix in mass concrete applications. Specifically, the study will evaluate the various physical properties of concrete, resistance to material segregation (Evaluation Index for Segregation of Normal Strength Concrete, EISN), and compressive strength.

2. RESEARCH METHOD

2.1 EXPERIMENTAL PLAN

The experiment plan and the mix proportions are shown in Table 1 and 2, respectively. The mix factor was a W/B ratio of 50%. In addition, the binder composition ratio was set to OPC : GGBFS = 4:4:2 for the low-heat mix. The types of cement according to the

mixing method were conventional mixed cement (Conv.C) and pre-mixed cement (Pre-C) from the company S. The mix was designed to achieve a target slump of 180±25mm with a mixing time of 180 seconds for both methods used to all levels. In the case of aggregates, both coarse and fine aggregates were used, which consisted of well-graded crushed aggregate produced in a quarry. The experimental items for fresh concrete included slump and slump flow. The EISN was used to assess segregation in ordinary concrete. In addition, compressive strength analysis was conducted with 30 repeated measurements of 28-day compressive strength for hardened concrete followed by Repeated Measures ANOVA (RM ANOVA) for statistical analysis.

Table 1. Experimental plan

Factors		Variables	
Mix Proportions	W/B (%)	1	50
	Target Slump (mm)		180 ± 25
	Target Air content (%)		4.5 ± 1.5
	Binder Composition		OPC:BFS:FA = 4:4:2
	Mixed Methods Cement		Conv.C
			Pre-C
	Coarse Aggregate		aggregate
	Fine Aggregate		crushed Fine Aggregate
	Mixing Time		10, 30, 60, 120, 180[1)], 360
Experimental Items	Fresh Concrete		Slump
			Slump Flow
			Air content
	Hardened concrete	2	Compressive strength
Analysis Methods	Segregation Analysis	1	EISN
	Strength Analysis		RM ANOVA

1) Plain

Table 2. Mix proportions of the concrete

Factors		Conv.c	Pre-c
W/C (%)		50	
S/a (%)		50	
Mix Proportions	W	175	
	C	140	350[1)]
	BFS	140	0
	FA	70	0
	CG	845	845
	CS	861	861
AE×C (%)		0.050	0.025
SP×C (%)		0.60	0.60

Pre-C: The binder composition rations of 4:4:2 (The Company S)

2.2 Experimental methods

2.2.1 Concrete mixing

The concrete mixing was carried out by using a twin-shaft mixer following the sequence shown in Figure 1. To simulate a ready-mix concrete batching plant (BP), aggregates, binder, water, and chemical agents were added simultaneously and mixed according to the mixing time variable before being discharged.

RPM	60						
Mixing Materials	fine Aggregate+Aggregate+ cement+water+chemical agent						Discharge
Mixing time (s)	10	30	60	120	180	360	

Fig 1 Concrete mixing

2.2.2 EISN

The method for deriving the EISN is based on the findings of Han et al. (2015) and Figure 2 shows the calculation procedure. This method evaluates the material segregation index by taking the ratio of the maximum to the minimum values of the slump flow of the slumped concrete. Using an EISN threshold of 1.09, the calcuated value above the threshold indicates the material segregation, while it below was considered satisfactory. In sum, the performance grades for segregation prevention are assigned as follows: 1.06 to 1.09 is classified as Grade III, 1.03 to 1.06 as Grade II, and 1.00 to 1.03 as Grade I.

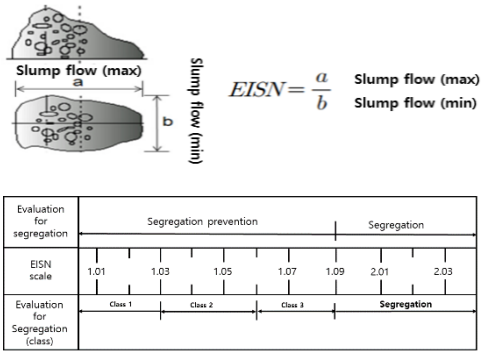

Fig 2 The calculation procefure for the EISN

2.2.3 RM ANOVA

To verify the significance of the standard deviation of compressive strength according to the mixing method and mixing time, a Repeated Measures ANOVA was conducted. The data processing was performed by using JAMOVI Ver 2.3.0.

Repeated Measures ANOVA is a statistical analysis technique to analyze the results of dependent variables measured for three or more independent variables on the same population, or for repeated measurements of dependent variable changes over time for one or more groups under the same independent variables.

After verifying the sphericity of the Repeated Measures ANOVA, the F-value was derived. If Mauchly's test of sphericity had a P-value less than 0.05, the Greenhouse-Geisser method was used to

correct the within-subject effects and present the F-value. Post hoc tests involved multiple comparisons, using the Bonferroni method for adjustment.

3. Results

3.1 The characteristics of fresh concrete

3.1.1 Flowability

Figure 3 shows the slump and slump flow over time according to the mixing method and cement types. Initially, the slump met the target range of 180 seconds plain mixing time regardless of the cement mixing method. For Conv.C), the flowability decreased from a maximum of 220mm to 155mm between 10 and 60 seconds of the mixing time, then increased within the target range from 120 to 360 seconds. However, these results were attributed to the dispersion state of the cement powder and the mixed materials. As observed in Table 3, a visual inspection of the slump during the 10 to 60 seconds mixing time showed that segregation was occurred in the concrete using Conv.C.

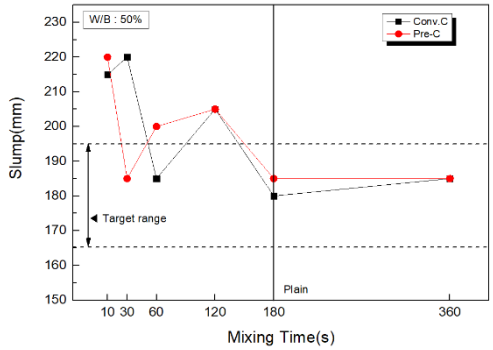

a) The concrete slump

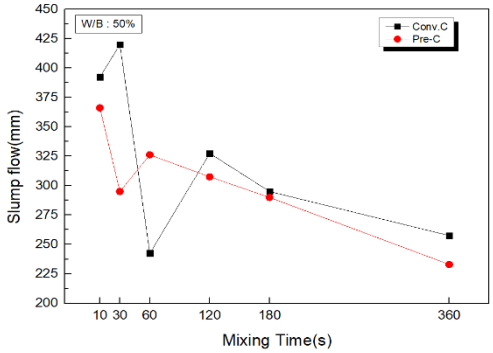

b) The concrete slump flow

Fig 3 The concrete slump and flow by the mixing methods and mixing time

3.1.2 Air conten t

Figure 4 shows the air content over time according to the mixing method and cement types. The results indicate that the target air content range was achieved for mixing time of 60 seconds or more regardless of the cement mixing method. However, the target air content was not met even with the same amount of air-entraining agent as in the plain mix for Conv.C. when the mixing time was 30 seconds or less, It can be caused by the insufficient dispersion of the chemical agent within the short mixing time in that it led to quality variations in the concrete samples for air content testing.

In contrast, the target air content was achieved within 30 seconds of mixing time for Pre-C (Pre-Mixed Cement) although the mixing time was short (10 seconds). This proved that the Pre-C minimizes the quality variations in the concrete.

Table 3 Visual inspections for segregation by the mixing methods and mixing time

	The concrete mixing methods	
Mixing Time (s)	CONv-C	Pre-C
10		
30	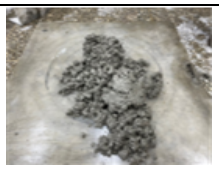	
60		
120		
180		
360		

3.1.3 EISN

Figure 5 shows the EISN according to the mixing method and mixing time. Overall, no segregation was occurred for mixing times of 120 seconds or more regardless of the mixing method. Specifically, the

EISN exceeding 1.09 at 10 and 30 seconds for Conv.C, indicated the segregation. This was caused by the decreased dispersion of cement and mixed materials in that it led to a collapse of the concrete slump and a large deviation between the maximum and minimum slump flow values as shown in Table 3. In contrast, the use of the Pre-C showed the EISN of 1.09 or below across all mixing times except for 10 seconds performing excellent segregation resistance. This can be seen that the use of the Pre-C enhances the dispersion of concrete mixing materials within a shorter mixing time achieving sufficient viscosity and better quality in terms of segregation resistance compared to Conv.C.

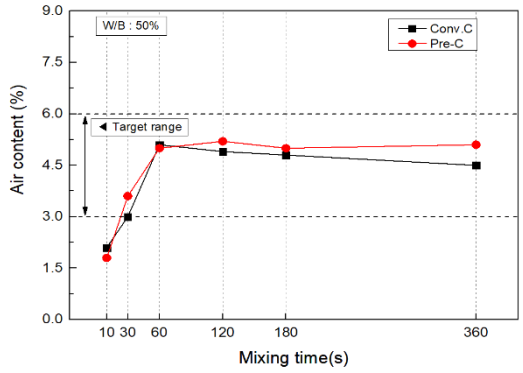

Fig 4. Air content by the mixing methods and mixing time

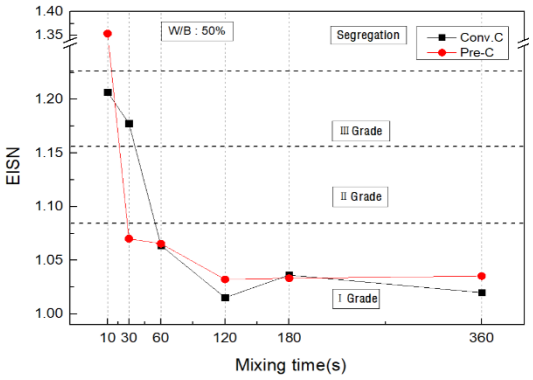

Fig 5. EISN with W/B of 50% by the mixing methods and mixing time

3.2 The characteristics of hardened concrete

3.2.1 The analysis result of RM ANOVA by the mixing methods and mixing time

(1) The analysis result of RM ANOVA

The results of the RM ANOVA are shown in Table 4. Figure 6 presents the box plots of the compressive strength according to the cement mixing method and mixing time.

First, both Conv.C and Pre-C showed a decrease in compressive strength at a 10-second mixing time compared to the plain mixing time. As shown in Figure 6a, compressive strength was increased with longer mixing times for Conv.C. However, the post hoc multiple comparisons using 120 seconds as a reference showed that there was little change in the estimated mean compressive strength, while there wa slight variability in the strength distribution, In contrast, the mixing time of 60 seconds or more showed a slight change in compressive strength over time when conducting post hoc multiple comparisons using 60 seconds as a reference for Pre-C (Figure 6b). The data for compressive strength measured at 10 and 30 seconds had a little variation compared to Conv.C. Although there were slight differences in the estimated mean compressive strength for mixing time over 60 seconds, the post hoc test results indicated little differences in strength ($p > .05$) for multiple comparisons except at 10 and 30 seconds, as shown in Table 3. Thus, a set of the mixing time of 60 seconds or more can ensure sufficient dispersion of concrete materials as well ass achieve good quality in terms of compressive strength for Pre-C.

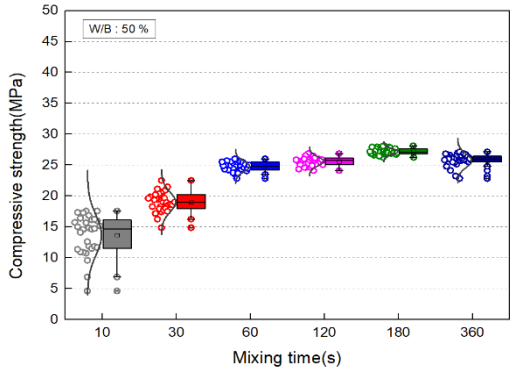

a) Pre-C

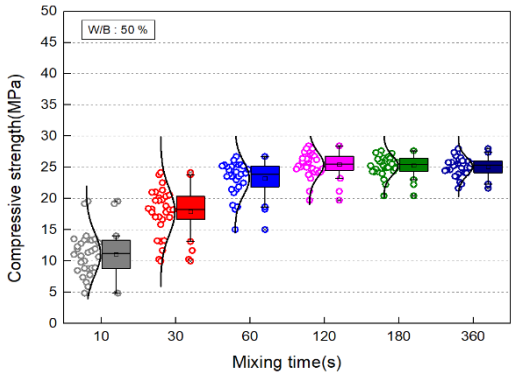

b) Conv. C

Fig 6 The box plots of compressive strength for Pre-C and Conv.C by different the mixing time

Table 4. The result of RM ANOVA by the mixing methods and mixing time

W/B (%)	Mixing Method	Mixing time (s)	N	M±SE*	Min	Max	95% Confidence Interval		F-1)	p-2)	Bonferroni
							Lower Bound	Upper Bound			
50	Conv.C	10	30	13.1±0.611	6.85	21.6	11.9	14.3	287****	<.001	<.001
		30		25.6±0.67	17.7	31.9	24.3	26.9			<.001
		60		30.9±0.488	22.7	34.4	30	31.9			<.001
		120		31.2±0.357	25.4	34.2	30.5	31.9			<.05
		180		34.6±0.40	26.8	37.4	33.8	35.4			>.05
		360		35.0±0.325	31.5	41.1	34.4	35.7			>.05
	Pre-C	10	30	13.7±0.586	4.64	17.6	12.5	14.8	283****	<.001	<.001
		30		18.0±0.295	13.9	21.5	17.4	18.6			<.001
		60		23.8±0.154	21.8	25.0	23.5	24.1			>.05
		120		24.6±0.131	23.1	25.9	24.4	24.9			>.05
		180		26.2±0.092	25.2	27.1	26.0	26.4			>.05
		360		24.7±0.203	21.8	26.1	24.3	25.1			>.05

1) F-value: The result of Repeated Measures ANOVA, indicating whether the difference between group means is significant. A larger F-value suggests a greater difference between groups.
2) p-value: Represents the level of statistical significance. A p-value less than 0.05 indicates that the result is statistically significant.
3) Estimated marginal means ± Standard error, p < .05, p < .01,* **p < .001

(2) Normal distribution

Figure 7 shows the normal distribution of compressive strength for 30 samples at 28 days of age according to the mixing method and time. In addition, Table 5 provides the statistical data. The normal distribution indicates that the standard deviation was 3.34, for Conv.C, while it was 3.21 for Pre-C. It shows a similar distribution of strength data each other. This suggests that there is a large variability in the compressive strength values at a mixing time of 10 seconds regardless of the mixing method. This variability has resulted in a wider spread of the data due to outliers in the strength measurements.

(3) Standard deviation and variance

Figures 8 and 9 show the standard deviation and variance of the compressive strength data according to mixing method and mixing time. Overall, the standard deviation tends to decrease as the mixing time increases. Specifically, both Conv.C and Pre-C showed significant variability in the data at a mixing time of 10 seconds. However, the variability decreased at a mixing time of 30 seconds for Pre-C. When an arbitrary coefficient of variation of 5 MPa was set, the variability of Pre-C at a 30-second mixing time was equivalent to that of Conv.C at a mixing time of 60 seconds or more for a W/B ratio of 50%.

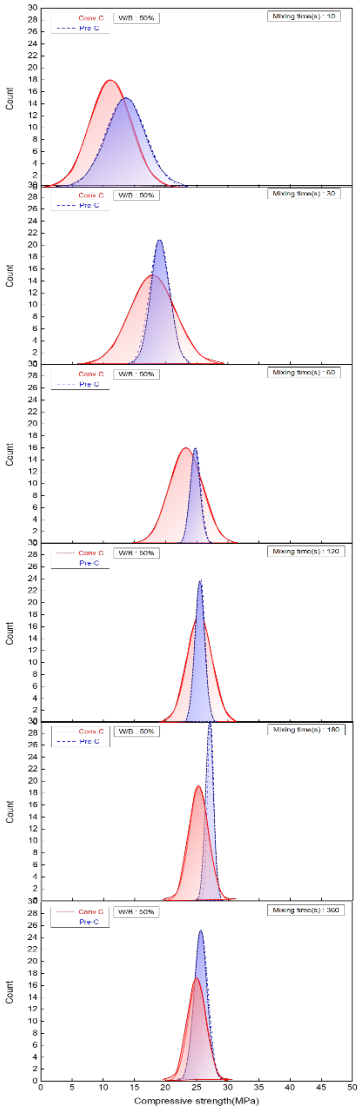

Fig 6 The box plots of compressive strength for Pre-C and Conv.C by different the mixing time

Table 5 Statistical data by the mixing methods and mixing time

W/B (%)	Mixing Method	Mixing time (s)	Sapmle (Count)	Mean (MPa)	Standard Deviation (MPa)	Variance (MPa)	Min (MPa)	Max (MPa)
50	Conv.C	10	30	11.13	3.34	11.2	4.85	19.59
		30		17.91	3.67	13.5	9.99	24.17
		60		23.25	2.67	7.1	15.04	26.73
		120		25.45	1.96	3.8	19.74	28.45
		180		25.31	1.56	2.4	20.44	27.68
		360		25.12	1.47	2.2	21.65	28
	Pre-C	10	30	13.68	3.21	10.3	4.64	17.58
		30		19.02	1.62	2.6	14.86	22.52
		60		24.8	0.84	0.7	22.85	26.02
		120		25.61	0.72	0.5	24.11	26.86
		180		27.18	0.5	0.3	26.24	28.12
		360		25.72	1.11	1.2	22.83	27.14

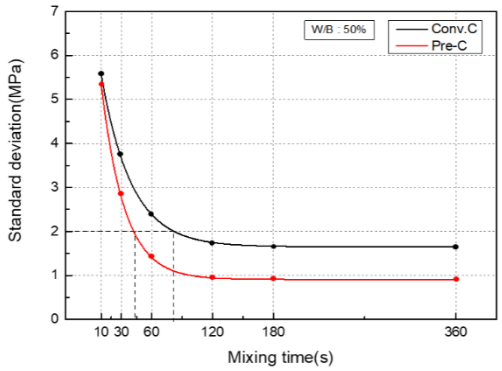

Fig 8 Standard deviation by the mixing methods and mixng time

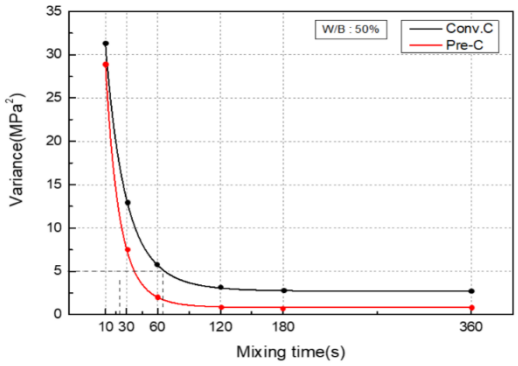

Fig 9 Variance by the mixing methods and mixng time

4. Conclusion

In this study, the various physical properties, EISN, and compressive strength of concrete were evaluated by applying the different mixing methods and mixing time to ensure homogeneous mixing and performance of a 3-component low-heat to reduce mass concrete hydration heat. The results are as follows:

1) Pre-C showed superior material segregation resistance compared to Conv.C for all mixing time except for 10 seconds. This was attributed to the uniform dispersion of particles due to pre-mixing forming a stable concrete mixture.

2) The EISN for Pre-C was 1.09 or below for all time variables except for 10 seconds. This showed excellent resistance to material segregation.

3) The compressive strength variability for Conv.C, decreased after 120 seconds, while Pre-C showed the minimal strength variability for mixing times of 60 seconds or more. This can be seen that the pre-mixed method can ensure the consistent quality of concrete by enhancing productivity and dispersion of powder materials.

In summary, the use of Pre-C with a mixing time of 60 seconds or more can provide the minimal strength variability, superior flowability and material segregation resistance. Thus, Pre-C can be considered as a useful mixing method for maintaining the high-quality concrete, while increasing the productivity of ready-mix concrete.

REFERENCES

1. Kim, Jong (2019). Effect of Various Partial Replacements of Cement with Blast Furnace Slag and Different Placing Times on Thermal Properties of Mass Concrete and Modeling Work. JOURNAL OF THE ARCHITECTURAL INSTITUTE OF KOREA Structure & Construction, 35(10), 207-215..

2. Kim, Jin-Keun, Noh, Jae-Ho, Park, Yon-Dong, Han, Jung-Ho, Kim, Hoon (1995). Hydration Heat Characteristics of Cement and Concrete. Journal of the Korea Concrete Institute, 7(3), 211-219.

3. Ji, Sangkyu, Jang, Seokjoon, Kim, Jihyeon, Park, Wanshin, and Yun, Hyundo(2017) Hydration Heat Characteristics of Mass Concrete Using Phase Change Material J Korean Soc Hazard Mitig 2017; 17(6): 1-10

4. Han, Cheon-Goo, & Lee, Hae-Ill (2009). Physical Analysis of High Strength Concrete According to Mixing Methods of Binders for Application Analysis of Pre-Mix Cement. JOURNAL OF THE KOREA INSTITUTE OF BUILDING CONSTRUCTION, 9(5), 127-133.

5. Han, C. (2008). Quality Control of Ready-Mixed Concrete (I). Gimundang.

6. Min-Ho Kim, & Cheon-Goo Han (2016). Method of Decreasing Cracking Index by Different Mix Conditions for Separated Placement and its Field Application. Journal of the Korean Recycled Construction Resources Institute, 4(3), 292-298.

7. Korea Concrete Institute. Temperature Crack Control in Mass Concrete. Concrete.

8. Korea Concrete Institute. (2015). Practical Manual KCI PM204.1-10. Gimundang.

9. Han, Cheon-Goo, and In-Deok Han. “Proposal on the Evaluation Method of Segregation Resistance of Normal Strength Concrete.” Journal of the Architectural Institute of Korea Structure & Construction Vol.31, No.7. 2015.

10. Taylor HFW. Chemistry of cements. 2nd ed. London(UK): ICE Publishing. 01, 1997.

Microstructural changes in blast-furnace cements with different replacement ratios under repeated drying and wetting cycles

Xi LUO
Graduate Student, Division of Sustainable and Environmental Engineering, Muroran Institute of Technology, 27-1 Mizumoto, Muroran 050-8585, Japan

Jhoon KIM
Assistant Professor, College of Design and Manufacturing Technology, Muroran Institute of Technology, 27-1 Mizumoto, Muroran 050-8585, Japan

Yukio HAMA
Professor, College of Design and Manufacturing Technology, Muroran Institute of Technology, 27-1 Mizumoto, Muroran 050-8585, Japan
Professor, Graduate School of Engineering, Hokkaido University, Nishi-8chome, Kita-13-jyo, Kita, Sapporo, 060-8628, Japan

ABSTRACT:
In this study, the effects of dry and wet cycles of blast-furnace cements with different replacement ratios on the microstructural changes were investigated by solid-state NMR and MIP, testing frost resistance by RILEM-CIF method. As a result, it was confirmed that the cumulative pore size increased after repeated dry and wet, and that the increase became smaller as the replacement ratio of BFS increased.^{27}Al MAS NMR results showed that after repeated dry and wet curing, and that Al[IV] and the increase in Al content in the interlayer, it is inferred that AlO_4 bonds to C–S–H and C–A–S–H is formed, which maintains the width of the C-S-H interlayer and reduces the pore structure change. Finally, the frost resistance of blast furnace slag mortar samples with different replacement ratios was tested, and the results showed that mortars with high blast furnace slag replacement ratios had higher frost resistance than those made of Ordinary Portland Cement after wet and dry cycling.

Keywords: Blast furnace slag cement, Repeated dry and wet, C-S-H, Microstructure, Pore structure, MAS NMR, Frost resistance

1. INTRODUCTION

C–S–H (calcium silicate hydrate) is sensitive to temperature and humidity, and these changes cause significant structural changes in the concrete. In real environments, repeated dry–wet cycles cause a deterioration in concrete structures. Creep, drying shrinkage, and aging are attributed to changes in the state of water in the C–S–H interlayer. Moreover, even if the moisture in C–S–H dissipates due to drying, regardless of the different drying conditions, the moisture content can be recovered by the re-adsorption of water vapor. To study the microstructural changes and durability of concrete, it is necessary to conduct laboratory experiments under realistic conditions with repeated drying and drying cycles.

Kamada et al. [1] studied the effect of pore structure on the frost resistance of concrete and found that the diameter of the pores affecting frost damage was in the range of 40–2000 nm. Aono et al. [2] reported that when hardened cement pastes are subjected to drying and dry–wet cycles at 50 °C, the pore size distribution in the diameter range of 50–100 nm obtained using mercury injection porosimetry (MIP) increases and that the microstructure becomes coarser, resulting in a decrease in the frost damage resistance. However, Kurosawa et al. [3] showed that the structural changes in C–S–H due to drying and repeated wetting and drying may be attributed to the condensation polymerization of silicate anion by dehydration caused by the drying and subsequent coarsening of the pores due to the densification of the globule interlayer. Other studies [4,5,6] conducted on drying-induced pore structure changes have reported coarsening of the capillary pores and a decrease in the gel porosity when subjected to drying and dry–wet cycles. Moreover, hydration due to sustained drying is paused, and when moisture is supplied again, the hydration resumes, and there is densification [7,8].

The cement industry is estimated to account for approximately 8% of the global CO_2 emissions. One ton of ordinary Portland cement (OPC) as a raw material emits approximately 800 kg of CO_2 during the manufacturing process [9]. Cement usage must be reduced to alleviate its environmental impact. In this context, the use of blended cement, in which a part of the cement is replaced by an industrial by-product, such as blast-furnace slag (BFS) or fly ash (FA), is being

promoted. In this paper, we expound on the use of blast-furnace cement, which is a cement mixed with slag collected from a blast furnace. Owing to the increase in the slag content, the presence of C–S–H appears to decrease the Ca/Si ratio, increase the Al/Ca ratio, and fill the spaces with more finely distributed voids[10].

Kojima et al. [11] studied the microstructural changes in ordinary cement and blast-furnace cement with different C–S–H compositions under repeated dry and wet cycles and found that the accumulated pore volume in the blast-furnace cement with a 45% blast-furnace slag fine powder was lower than that in the ordinary cement, though a large proportion of Al was present in the cement. In addition, the changes in the gel voids and moisture content in the interlayer due to drying were lower in the blast-furnace cement than in the ordinary cement, suggesting that the presence of more amounts of Al in the interlayer helps maintain the width of the C–S–H layer following dehydration due to drying and repeated drying and wetting, and that compaction is less likely to occur. This can lead to differences in the C–S–H structure in mixed cements, which may affect the microstructure of the hardened material due to the severe thermal drying and dry–wet cycling.

To overcome these challenges, this study employed solid-state NMR (^{29}Si MAS NMR and ^{27}Al MAS NMR) and MIP to understand the effect of drying and dry–wet cycles on the microstructural changes of blast-furnace cements with different replacement rates. The study objective was also to investigate the effect of the high content of Al_2O_3 in the BFS on microstructural changes caused by repeated drying and wetting. To investigate the effect of differential constitutive changes in blast furnace slag with different replacement ratios under dry and wet cycles on the actual frost resistance, mortar samples were used, and the frost resistance of mortar samples by RILEM-CIF.

2. EXPERIMENTS

2.1 EXPRIMENTAL DESIGN

In this study, white Portland cement (wPC) with low Fe_2O_3 content was used as the ordinary cement to measure solid-state NMR. Table1 shows the physical properties and chemical composition of the wPC and BFS used in this experiment and table 2 shows the experimental design. For the paste and mortar specimens, the BFS replacement ratio was determined based on accordance with the JIS R 5211 “Portland blast-furnace cement” [12]. The replacement ratios of BFS were 15%, 45%, and 65%, assuming blast furnace cement classes A, class B and class C. A water-binder ratio (W/B) of 0.5 and a binder sand ratio of 1:2 for the mortar specimens were prepared. The paste specimens were hand-mixed for 3 min and kneaded back every 30 min until approximately 5 h 30 min had elapsed from the start of kneading to reduce the effect of bleeding water. For the mortar specimens, wPC and BFS and fine aggregate were added using a mortar mixer and kneaded at low speed for 30 seconds. Ion-exchange water was then added and kneaded for 60 s, followed by scraping off for 30 s and then kneading at high speed for 120 s. Casting was carried out in a 40 mm × 40 mm × 160 mm steel formwork.

Each specimen was sealed and cured at 20°C for 24 hours immediately after casting. The specimens were demolded 24 hours after casting and cured in water at 20°C for up to four weeks (Pre curing for 4 weeks:4w) of age before being used for dry–wet cycles. The temperature and humidity of the dry state in the dry and wet repetitions are cured in air at 50°C and 11%RH, assuming severe drying. In addition to the level of drying in air curing at 50°C and 11%RH for four weeks (Dry50°C: D50), the dry/wet cycle was repeated four times (Dry 50°C + Wet20°C: D50W20) for a total of four weeks, and measurements were taken 4 and 8 weeks before and after applying the repeated dry and wet conditions. The experimental flow is shown in Fig.1.

Table 1 Physical properties and Chemical composition of wPC and BFS

type	Density (g/cm^3)	Surface area (cm^2/g)	Chemical composition(%)							
			CaO	SiO_2	Al_2O_3	MgO	SO_3	Na_2O	Fe_2O_3	K_2O
wPC	3.05	3440	64.87	22.82	4.55	1.13	2.87	0.06	0.19	0.07
BFS	2.91	3930	43.36	34.03	14.36	6.51	-	0.18	0.83	0.31

Table 2 Experimental plan

Sample	Binder(%)		W/B	Pre curing	Dry and wet conditions	Measurement
	wPC	BFS				
N	100	0	0.5	Water curing at 20 ℃ for 4weeks:(4w)	1. Air curing at 50℃ 11%RH 4weeks: (D50) 2. Air curing at 50 ℃ 11%RH for 5days after water curing at 20 ℃ for 2days: (D50W20)	^{29}Si MAS NMR ^{27}Al MAS NMR MIP RILEM-CIF
B15	85	15				
B45	55	45				
B65	35	65				

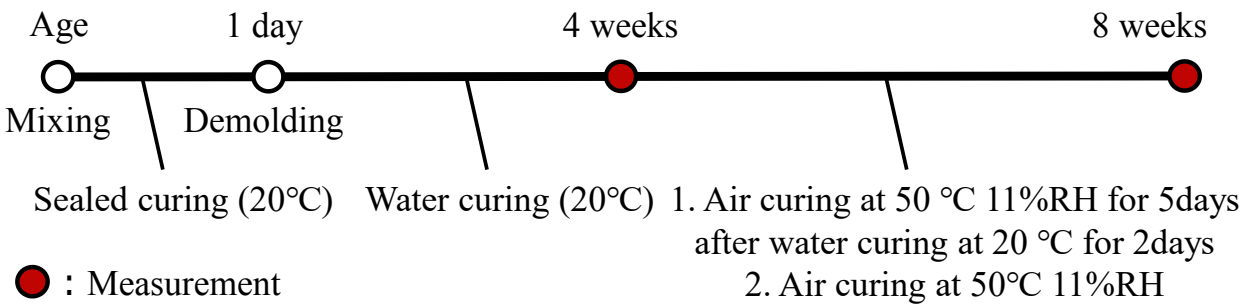

Fig. 1. Experimental flow.

2.2 MEASUREMENT

(1) Solid-state Nuclear Magnetic Resonance

A JEOL ECA-500 (11.75T) was used with a 3.2 mm φ probe was used for solid-state NMR. The measurement conditions for ^{29}Si MAS NMR were a spinning speed of 10 kHz, relaxation delay of 15 s, scans of 2048, ^{27}Al MAS NMR, spinning speed 20 kHz, relaxation delay 0.5 s, scans 1280.The test specimens used for the measurements were paste specimens of diameter 6 mm × 5 mm used for MIP. They were crushed, repeatedly dried and wetted, and then dried after 24 h of acetone displacement.

(2) Mercury Intrusion Prosimetry (MIP)

Specimens molded to diameter 6 mm × 5 mm were used for the measurements. Hydration was stopped by 24 h acetone displacement, followed by 24 h vacuum freeze-drying, after which the specimens were used for measurement.

(3) Frost Resistance Test

The frost resistance test was carried out according to the RILEM CIF method, which uses prismatic specimens with dimensions of 40 × 40 × 160 mm to assess the effect of dissolution by freezing on one side in water. The sides of the specimen are covered with waterproof aluminum tape to prevent water absorption from the sides. The test procedure consisted of immersing the specimens in ion exchange, ensuring that the solution level was 10 mm from the bottom, for a period of seven days. After the immersion phase,56 cycles of freeze-thaw testing were initiated. Each cycle consisted of an eight-hour freezing process and a 4-hour thawing process. Measurements were taken every four cycles during the test to assess relative dynamic modulus of elasticity (RDME).

3. RESULTS

3.1 ^{29}Si MAS NMR

Fig.2 shows the ^{29}Si MAS NMR results before and repeated dry and wet cycles. Each peak was measured in the range of Q^0: -66 to -78ppm, Q^1: -78ppm, Q^2(1Al): 81ppm, and Q^2: -85ppm based on previous studies[13], and the relative area fraction of each peak is shown in Fig.3.

At 4w, where only pre-curing was performed, it was observed that in the samples ranging from N to B65, as listed in Table 2, with the increase in the replacement rate of the BFS, no significant difference in Q^0, which is an unhydrated material, was noted. Owing to the high replacement rate of the blast-furnace cement, the hydration reaction could not proceed sufficiently because of the 28-day curing in water. In the samples ranging from N to B45, an increase in Q^1 was observed (N→B15→B45: 9.7%→13.8%→16.6%). In B65, the Q^1 content was lower; however, the corresponding Q^0 content was higher than that in hardened cements with lower replacement rates. Moreover, in N to B65, with the increase in the substitution rate, the Q^2(1Al) content increased. Al content in the slag is higher than that in ordinary cement. However, the Q^2(1Al) content was lower. In N to B45, the hydration product Q^2 decreased with the increase in the substitution rate. In B65, small amounts of Q^3 were also formed.

In D50W20, the Q^0 and Q^1 contents decreased, whereas the Q^2(1Al) and Q^2 contents increased in N to B65. This can be attributed to the resupply of water and the accelerated hydration reaction under the action of repeated dry–wet cycles. In N to B45, the Q^0 and Q^1 contents were reduced by half as unreacted material because of the dry–wet cycles, whereas in B65, more amount of unreacted material from the previous period remained, indicating that a greater amount of unreacted hydration material remained after four dry–wet cycles.

In D50, when only drying was performed, in N to B65, the Q^0, Q^2(1Al), and Q^2 contents increased whereas the Q^1 content decreased. However, the extent of each change was lower than that in D50W20. This may be due to the inability of water to replenish the cement due to low-humidity drying, which prevents the hydration reaction from progressing compared with that under repeated dry–wet cycles, and due to the possibility of a pause in the hydration reaction under continuous drying at lower ages, according to previous studies [9,10]

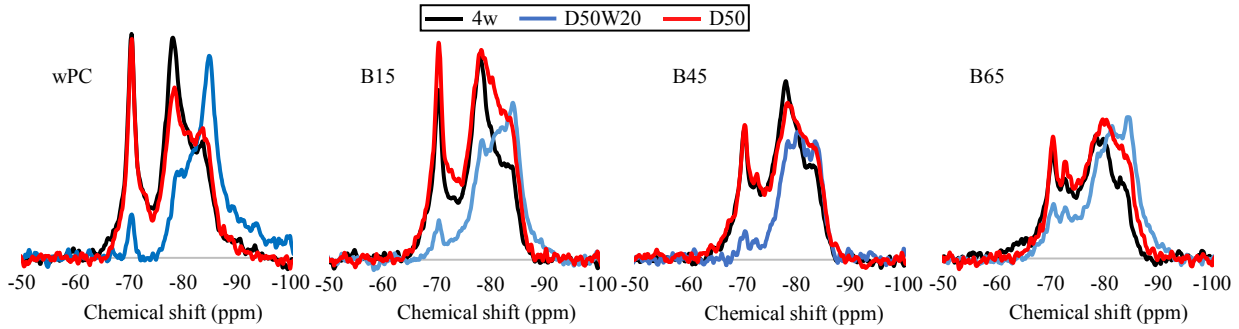

Fig.2 Change in ^{29}Si MAS NMR peak with dry/wet repetitions

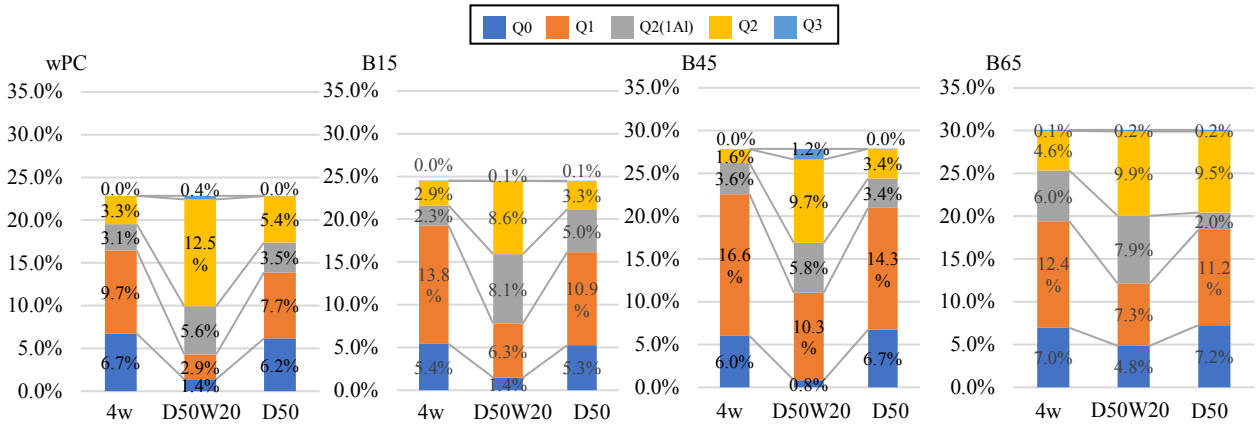

Fig.3 ^{29}Si MAS NMR relative peak area ratio of each specimen

3.2 ^{27}Al MAS NMR

Fig. 4 shows the ^{27}Al MAS NMR measurement before and after the dry–wet cycles. Fig. 5 shows the relative area fractions of each peak. With reference to previous studies [13] 50–100 ppm was identified as tetrahedral (Al[IV]) with four Al coordinations, 30–40 ppm as pentahedral (Al[V]) with five Al coordinations, and −10–20 ppm as octahedral (Al[VI]) with six Al coordinations. The identification was also performed. In this study, the relative area fractions of each peak were obtained by referring to previous studies to identify the range [14], 73 ppm: C–A–S–H, 60–68 ppm; a peak overlapping unreacted materials, such as unreacted slag and C–A–S–H, 35 ppm: Al present within the interlayer, 13 ppm: ettringite, 9 ppm: monosulfate and 5 ppm: third aluminate hydrate (TAH).

At 4 w, in Al[VI], which accounts for more than half of the total, higher contents of unreacted substances, such as C–A–S–H and unreacted slag, could be found with the increase in the replacement rate of the blast-furnace slag fines. In contrast, the contents of ettringite, monosulfate, and third aluminate hydrate (TAH) decreased with increasing substitution rates. The ettringite content was zero in B45 and B65. This could be attributed to a decrease in the amount of Al[VI] produced in B45 and B65 due to the relative decrease in the amount of wPC given the greater substitution of the BFS. According to previous studies, the pozzolanic reaction of the blast-furnace slag fines was delayed after 28 d of curing in water [15]. In addition, because no gypsum was present in the blast-furnace slag fines used in this study, previous studies [16,17] have shown that a higher slag content increases the leaching of Al, which reacts with gypsum to significantly increase ettringite formation. This in turn leads to a reduction in the amount of ettringite formed in the cement without gypsum. The amount of ettringite formed in blast-furnace cement may decrease with the increase in the replacement rate of the slag fines.

The results of the dry and wet cycling showed a significant increase in the contents of unreacted substances, such as C–A–S–H and unreacted slag, in the Al[IV] range from 4w. The extent of the increase in N and B15 was greater that in B45 and B65. A decrease in the ettringite content and increase in the monosulfate and TAH contents were observed. The total peak area fractions of Al [IV] and Al[V] in N, B15, and B65 were also greater than that during 4w. This is believed to be due to the increase in the Al content with the increase in the replacement ratio of the blast-furnace slag fines.

At D50, the degree of change was lower than that at D50W20, as in the ^{29}Si MAS NMR results, and was

Al [IV] range from 4w. The extent of the increase in N and B15 was greater that in B45 and B65. A decrease in the ettringite content and increase in the monosulfate and TAH contents were observed. The total peak area fractions of Al [IV] and Al[V] in N, B15, and B65 were also greater than that during 4w. This is believed to be due to the increase in the Al content with the increase in the replacement ratio of the blast-furnace slag fines.

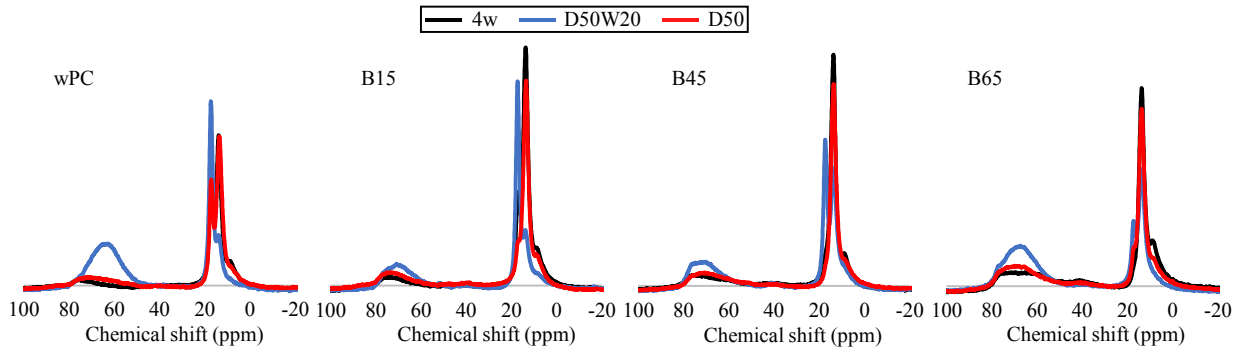

Fig.4 Change in ^{27}Al MAS NMR peaks with dry/wet repetitions

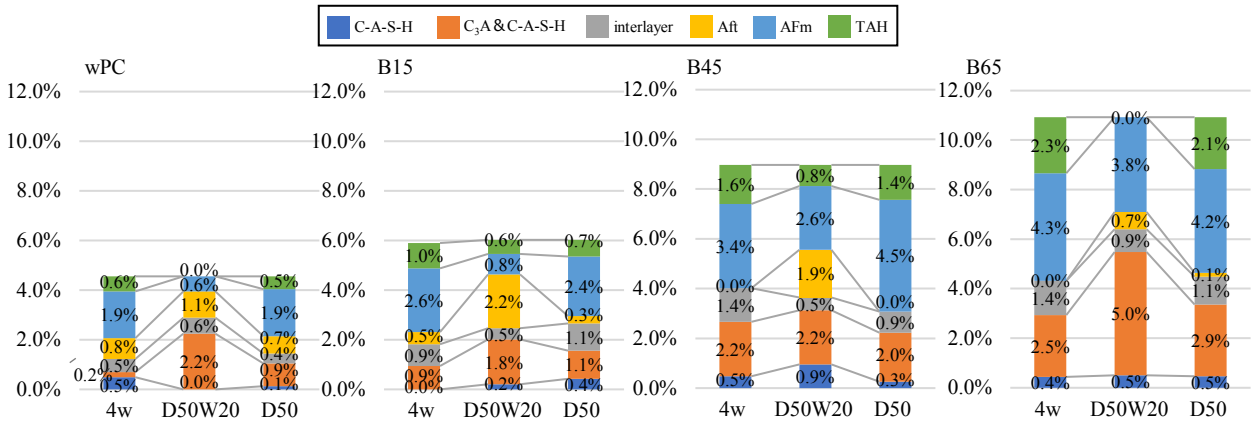

Fig.5 ^{27}Al MAS NMR relative peak area ratio of each specimen

3.3 MIP

Figs. 6–7 show the MIP measurement results of the samples N to B65. Overall, the pore volume increased with the number of dry–wet cycles. A small difference can be observed between N and B15. This is attributed to the lower amount of slag powder added to B15 compared to that added to N, which resulted in less change.

At 4w, a distribution centered at 37 nm for N and 35 nm for B15 was observed, whereas a distribution centered at pores smaller than 14 nm was observed for B45 and B65. Previous studies [11] have confirmed that blast-furnace cement has a finer pore distribution than ordinary cement. Thus, differences in the pore distribution were observed between ordinary cement and blast-furnace cement due to the differences in the composition of the products. Moreover, the pore-size distribution decreased with increasing replacement ratio.

For D50W20, the pore distributions for the samples N, B15, B45, and B65 were centered at 49, 60, 25, and 15 nm, respectively. In this regime, the pores coarsened because of the dry and wet cycles. The degree of coarsening was slightly greater in B15 than in N but it was lower in B45 and B65 than in N. The degree of pore coarsening due to dry and wet cycles decreased when the amount of blast-furnace slag fine powder added was more than 45%.

For D50, the pore distributions for the samples N and B15 are centered at 72 and 77 nm, respectively. However, from the pore size distributions of the samples B45 and B65, a slight increase in the number of pores could be observed not only at a size of 46 nm but also at 20 nm in B45, and an increase in the number of pores with sizes of 18 nm and 41 nm was observed in B65. The same trend was observed under dry and wet cycles. The same trend as in the case of the dry and wet cycles was observed in B15, where the degree of coarsening was greater than that in N. However, the degree of coarsening due to drying reduced when the mixture contained more than 45% blast-furnace slag fine powder.

Fig. 8 shows that the cumulative volume of the pores in the diameter range of 40–2000 nm increases because of repeated drying and wetting. Moreover, the dry–wet cycles had a smaller effect on the pore structural change than drying alone.

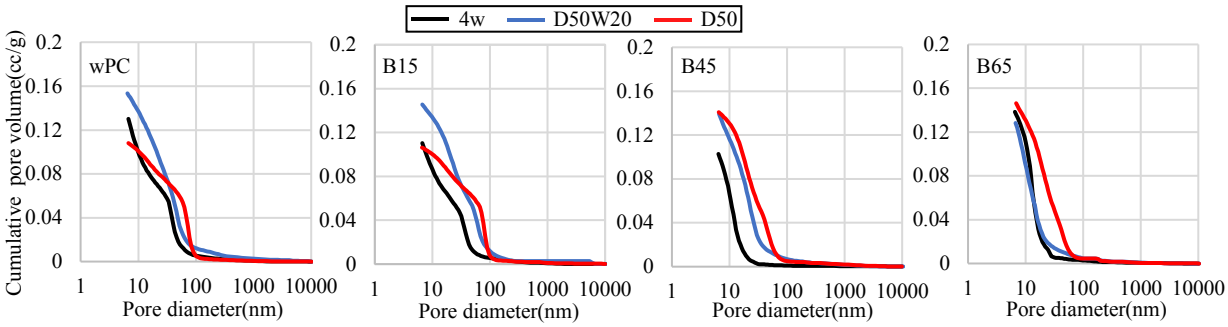

Fig.6 Measurement results of MIP of differentia pore volume

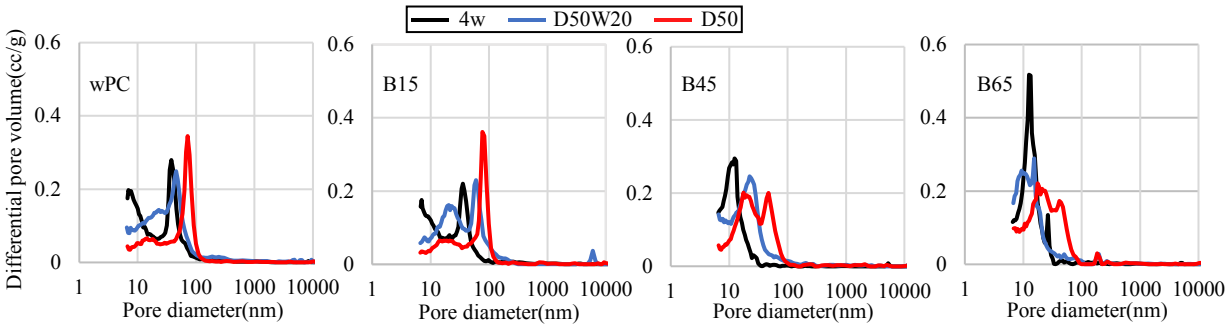

Fig.7 Measurement results of MIP of cumulative pore volume

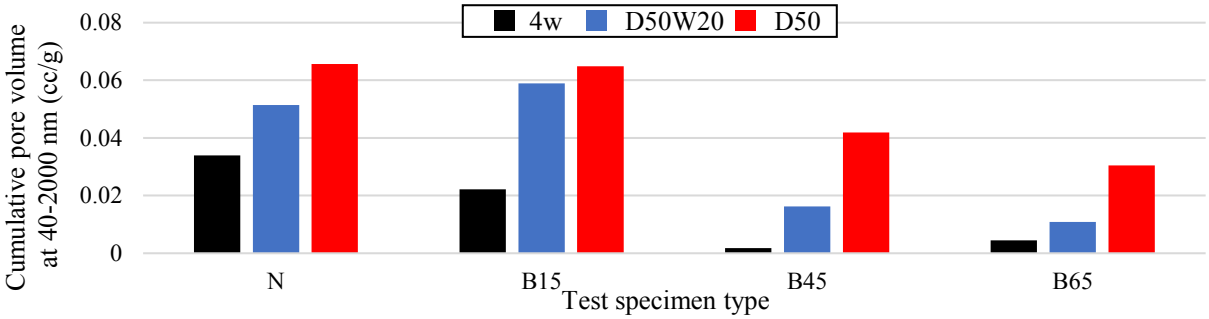

Fig. 8 Cumulative volume (cc/g) of the pores in the diameter range of 40–2000 nm

3.4 Relationship between ^{27}Al MAS NMR and MIP

Fig. 9 shows the relationship between the cumulative pore size range of 40–2000 nm measured by the MIP and the total peak area fractions of Al [IV] and Al[V].

At 4 w, the Al contents of Al [IV] and Al[V] were present at similar levels in N and B15, whereas the Al content of Al [IV] increased more than that of Al[V] in B45 and B65. This was confirmed by 4 weeks of curing in water, which resulted in an increase in the formation of unreacted materials in B45 and B65 blast-furnace cements with large amounts of replaced blast-furnace cement slag fines compared with blast-furnace cements with low replacement rates.

The results of the dry and dry–wet cycles were the same as that for 4 w, confirming that the Al content of Al [IV] increased more than that of Al[V]. The Al content increased significantly under the dry–wet cycles compared with that under the dry cycles. This is believed to be due to the hydration reaction being accelerated by the resupply of water, which is similar to the results of the ^{29}Si MAS NMR. During drying, the Al content was less distinct from that observed at 4 w, as the material was stored in a high-temperature and low-humidity environment for a long period after curing in water, which may have paused the hydration reaction [7,8].

In B15, the cumulative pore size decreased with dry–wet cycles compared with that in N, whereas the Al fraction also decreased slightly. Drying also resulted in a slight decrease in the pore volume compared with that of N. The Al fraction increased 1.9 times more than the N fraction owing to the addition of the slag. The Al content in B45 increased 1.3 times more than that in N and in B65 2.2 times more than in N after repeated dry–wet cycles, whereas the Al content in B45 increased 2.1 times more than in N and in B65 3.1 times more than N after drying. The cumulative pore volume decreased with increasing slag replacement rate.

This suggests that increasing the replacement rate of the BFS increases the Al content within the hardened cement and reduces pore structural changes.

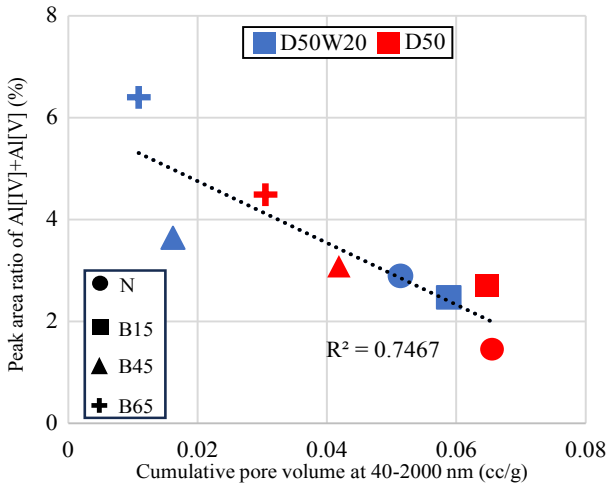

Fig. 9 Relationship between Al [IV] and Al[V] and cumulative pore size range (40–2000 nm)

3.5 FREEZING-THAWING TEST

Fig.10 shows the change in the relative dynamic modulus of elasticity in the RILEM CDF test. Fig.11 shows the relationship between durability factor and BFS replacement ratio.

The relative dynamic modulus of elasticity of the specimens cured in water for only 4w was found to decrease and the decrease increased with increasing BFS substitution rate. It was therefore hypothesized that a pre-curing period of only 28 days may not allow the water-sum reaction of a high replacement rate blast furnace slag blended cement to proceed adequately.

Furthermore, in terms of the effect of repeated dry and wet curing after 28 days of pre-curing, a decrease in the frost resistance of the specimens was observed, where n with no replacement of blast furnace slag(N) and sample B15 with only 15% replacement were significantly displayed.

In comparison，the decrease in frost resistance of B45 and B65 was moderated compared to N and B15.

Comparatively, the freezing resistance of N and B15 still declined in the pre-cure followed by 28 days of continuous high temperature and low humidity (D50), but to a lesser extent than in the wet and dry cycles, and the degree of resistance to freezing damage increased with the increase in blast furnace slag micropower. For B65, it was confirmed that the relative dynamic modulus of elasticity of the specimens after drying was less than after pre-curing. This is assumed to be since after 28 days of continuous drying, the test specimens contained less water.

Therefore, even in the case of repeated freeze-dissolution, less water is required to participate in the actual freeze-dissolution test.

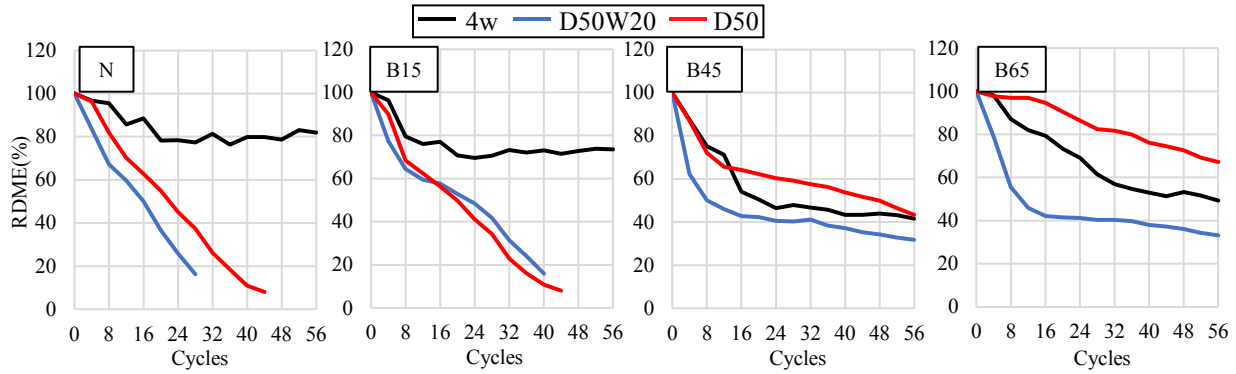

Fig. 10 RDME in the RILEM CDF test

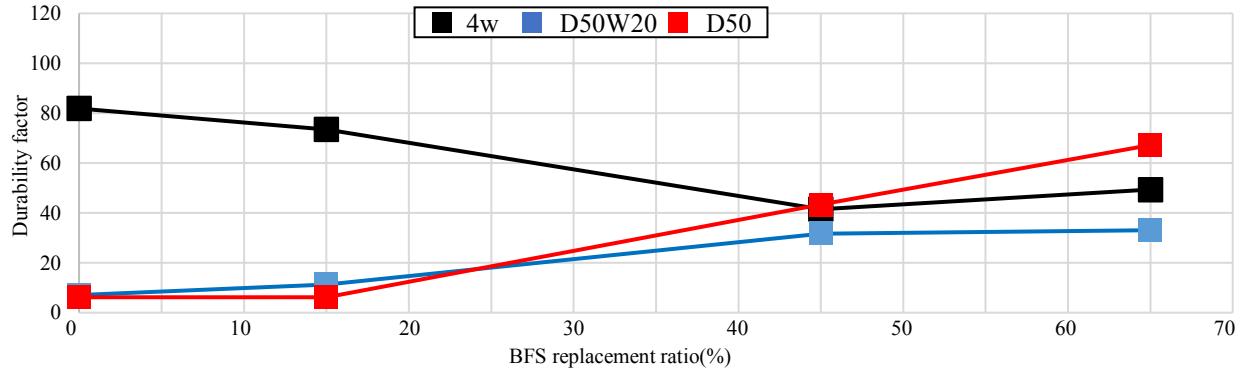

Fig. 11 Relationship between durability factor and BFS replacement ratio

CONCLUSIONS

In this study, the effect of microstructural changes in the C–S–H compositional structure of blast-furnace cements with different substitution rates on the Al content due to repeated drying and wetting under severe temperature and humidity conditions was investigated.

(1) The MIP results of the sample under drying and wetting cycles showed that in the samples N to B65, the cumulative pore volume in the size range of 40–2000 nm increased with the increase in the number of drying and wetting cycles compared to that at 4w, and the extent of this increase decreased with increasing substitution ratio.

(2) The ^{27}Al MAS NMR results showed that the dry and wetting cycles increased the Al/Si content of the samples N to B65, and the Al/Si content of the sample N-B65 decreased with the number of dry–wet cycles. The Al/Si ratio increased, and the Al content in the Al [IV] and interlayer increased. This led to the bonding of AlO_4 to C–S–H and the formation of C–A–S–H, which maintained the width of the C–S–H interlayer and reduced the change in the pore structure at sizes ranging from 40 to 2000 nm. This suggests that blast-furnace cements with higher replacement rates are less prone to freeze-damage resistance degradation than ordinary cements.

(3) It was observed that as the BFS replacement rate increased, the freeze-thaw resistance of each specimen under repeated dry and wet cycles increased.

REFERENCES

1. E. Kamada, O. Senbu, M. Tabata, H. Tanaka, Statistical investigation concerning the effects of pore structure on the frost resistance of concrete, J. Struct. Constr. Eng. AIJ. No. 487 (1996) 1–9, in Japanese
2. Y. Aono, F. Matsushita, S. Shibata, Y. Hama, Nano-structural changes of c-s-h in hardened cement paste during drying at 50℃, J. Adv. Concr. Technol. 5 (3) (2007) 313–323.
3. K. Kurosawa, D. Minato, R. Hattori, T. Nawa, Nano-structural changes of C-S-H in hardened cement paste under drying-wetting action, Cement Sci. Concr. Technol. No.65 (2011) 146–152, in Japanese.
4. K. Fukushima, M. Ishimori, K. Kurumisawa, T. Nawa, Behavior of cement paste in dry and wet cycle, Cement Sci. Concr. Technol. No.64 (2010) 74–81, in Japanese.
5. M. Miyazono, T. Kishi, The influence of repetition of dry-wet cycles on concrete pore structure and freeze-thaw resistance, Cement Sci. Concr. Technol. 73 (2019) 251–258, in Japanese.
6. I. Maruyama et al.：Microstructural and bulk property changes in hardened cement paste during the first drying process, Cement and Concrete Research, 50, pp.20-34 (2014)
7. T. Ishirota, K. Uomoto, Effect of drying at young age on the internal microstructure of hardened cement. Proceedings of Japan Society of Civil Engineers (Materials and Concrete Structures), Vol.59, No.732, pp.17-26 (2003) (in Japanese).
8. T. Ishirota, K. Uomoto, Effect of moisture history at young age on the formation of internal microstructure and physical properties of hardened cement on the formation of internal microstructure and physical properties of hardened cement, Concrete research and technology.15 (2004) 25–34
9. Robbie M. Andrew：Global CO2 emissions from cement production, Earth Syst. Sci. Data, 10, pp. 195–217 (2018)
10. I. G. RICHARDSON et al.：Microstructure and microanalysis of hardened cement pastes involving ground granulated blast-furnace slag.
11. K. Kojima：Study of microstructural changes in blast-furnace cement hardened by repeated dry and wet curing at high temperatures, Construction and Building Materials, 403, (2023)
12. Japanese Industrial Standards, Portland blast-furnace cement, JIS R 5211, Tokyo, Japan, Japanese Standards Association, 2009.
13. M. D. Andersen, et al, Characterization of white Portland cement hydration and the C-S-H structure in the presence of sodium aluminate by 27Al and 29Si MAS NMR spectroscopy, Cement and Concrete Research, 34(5), pp.857-868 (2004)
14. Schneider, J., Cincotto, M. A., Panepucci, H., "^{29}Si and ^{27}Al high-resolution NMR characterization of calcium silicate hydrate phases in activated blast-furnace slag pastes", Cement and Concrete Research, Vol.31, 2001, pp.993-1001
15. S. Koyanagi, Y. Takahashi, T. Ishida, Material properties of cement hardened body mixed with blast furnace slag fine powder and fly ash - Study on the change of salt penetration properties with time, Proceedings of the Japan Concrete Institute.37 (2015) 109–114, in Japanese.
16. Y. Suda, I. Kono, T. Saito, T. Saeki, Study on influence of Al substitution for relation between composition and specific surface area of C-S-H, Cement Sci. Concr. Technol. 69 (2015) 37–44, in Japanese.
17. Y. Suda, T. Saeki, T. Saito, Effect of chemical composition of C-S-H on volume and pore size distribution of gel pore, Proceedings of Japan Society of Civil Engineers E2 (Materials and Concrete Structures), Vol. 70, No. 2, pp. 134–152 (2014) (in Japanese).

EFFECT OF CARBONATION CURING ON THE LOW TEMPERATURE SULFATE ATTACK PERFORMANCE OF CEMENT PASTE ADDED WITH AUTOCLAVED AERATED CONCRETE POWDER

Ling Qin
Associate Professor, Qingdao University of Technology, China.

ABSTRACT:
This study explored effect of CO_2 curing on low temperature sulfate resistance of Portland cement (PC) samples added with autoclaved aerated concrete powder (WAAC). Performance metrics—compressive strength, mass/volume changes, and microstructure—were assessed using QXRD, MIP, and SEM-EDS. Findings revealed that PC-WAAC paste strength diminished post-sulfate attack, yet CO_2 curing mitigated this decline. After 6 months' sulfate exposure, CO_2-cured samples with 0-20% WAAC exhibited 3.93-18.31% higher strength than uncarbonated, non-immersed controls. Notably, the 6-month strength loss of carbonated samples (9.31-46.15%) was significantly lower than uncarbonated ones (15.55-61.97%). Furthermore, CO_2 curing reduced porosity, optimized pore structure, and hindered volume expansion due to sulfate. It enhanced PC-WAAC's resistance to low-temperature sulfate attack, preventing thaumasite formation. Thus, WAAC recycling coupled with CO_2 curing yields eco-friendly cementitious materials with superior long-term durability in sulfate-prone environments.

Keywords: carbonation curing, Portland cement, waste autoclaved aerated concrete, low-temperature sulfate attack, compressive strength, Microstructure

1. INTRODUCTION

Since the 1990s, industrialization and economic growth have spiked greenhouse gas concentrations, notably CO2, causing significant global warming and its consequences like sea-level rise, extreme weather, and drought expansion. Addressing the environmental-economic development paradox is imperative. Cement concrete, a ubiquitous building material, is a major CO2 emitter, especially in China, which produces over 60% of the world's Portland cement annually. Cement production emits CO2 through limestone decomposition, coal combustion, and power consumption, contributing 58%, 35%, and 7% respectively. This accounts for about 9% of global anthropogenic CO2 emissions, with each ton of cement releasing 0.9-1 ton of CO2. Thus, mitigating cement's carbon footprint is crucial. Additionally, construction rebuilds and renovations generate vast waste, posing risks like water/soil pollution, farmland loss, and landscape degradation. Managing construction waste sustainably is urgent. Notably, WAAC, a prevalent Chinese construction waste, remains understudied in recycling efforts.

To enhance PC's compressive strength while integrating WAAC and minimizing its carbon footprint, our prior study [17] introduced a novel carbonation curing method. This approach not only boosts PC-WAAC blend strength, mitigating WAAC's negative impact, but also sequesters 11.23-19.02% CO2. Distinct from weathering, where CO2 degrades cement hydrates, here, CO2 serves as a reactant, forming calcium carbonate and silica gel with unhydrated clinker (C3S, C2S) and hydration products (Ca(OH)2, C-S-H) [18-20]. Carbonation curing enhances strength, durability, and CO2 capture [21-24]. Our previous research on PC-WAAC blends found that adding 10-20% WAAC after carbonation still surpassed pure PC paste in strength, with reduced drying shrinkage [17]. For practical applications, durability—a material's resistance to environmental stressors—is crucial. Cement durability in sulfate-rich environments like groundwater, seawater, and saline-alkali soils faces ESA risks [27-28]. We ever studied the ESA performance of carbonation curing cement and found the carbonation curing could improve the sulfate resistance of cement [29].

Besides ESA, during the sulfate attack process at humidity and low temperature condition (below 15℃, especially between 0~5℃), thaumasite (CaSiO3· CaCO3· CaSO4· 15H2O) can be produced in cement concrete when containing limestone powder, which is called thaumasite sulfate attack (TSA) [30-32]. The chemical reaction is as follows [31]:

$$(CaO)x\cdot(SiO2)n\cdot(H2O)x+2n+CaSO4\cdot2H2O+CaCO3+y\ H2O\rightarrow CaSiO3\cdot CaCO3\cdot CaSO4\cdot15H2O \quad (1)$$

Calcium hydroxide reacts with atmospheric or aqueous CO2 to produce calcium carbonate, a crucial carbonate source [33]. Thaumasite formation, due to its insolubility, persists until cement hydrates like calcium hydroxide and C-S-H are depleted [34], causing C-S-H gel decomposition but less macro-damage than ESA [35-37]. Carbonation curing generates calcium carbonate, densifying concrete but also potentially triggering TSA. Thus, understanding TSA resistance in carbonated PC-WAAC under sulfate exposure is vital, especially given the scarcity of research on this topic. This paper explores the compressive strength, mass/volume changes, phase composition, pore structure, and morphology of carbonated PC-WAAC paste under low-temperature sulfate immersion, elucidating the microscopic

mechanisms involved.

2. MATERIALS AND METHODS

2.1 RAW MATERIALS

WAAC sourced from Heilongjiang Province is pulverized into powder, comprising tobermorite, calcite, gypsum, and quartz as primary minerals (Fig. 1). Portland Cement (PC), grade 42.5, sourced from Dalian Cement Group, exhibits a distinct particle size distribution from WAAC, as depicted in Fig. 2. Chemical compositions of both materials are listed in Table 1. For erosion testing, a 5% magnesium sulfate (MgSO4•7H2O) solution is employed.

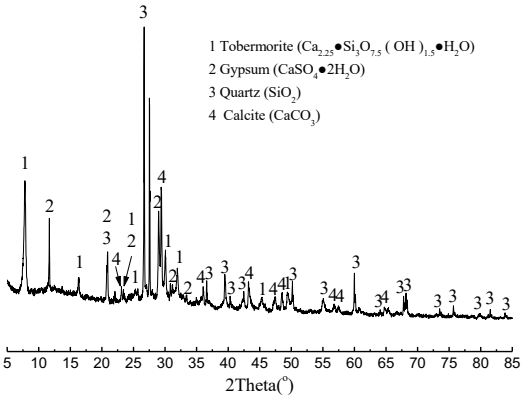

Fig. 1. XRD pattern of WAAC.

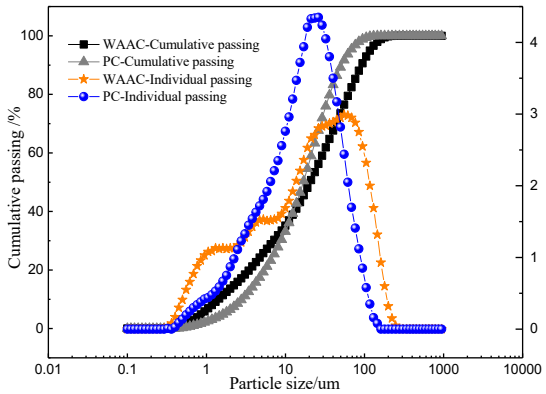

Fig. 2. Particle size distribution of PC and WAAC.

Table 1 Chemical composition of PC and WAAC (wt %).

Component	CaO	SiO_2	SO_3	Fe_2O_3	Al_2O_3	MgO	K_2O	Ignition loss
PC	61.60	20.38	4.52	3.99	3.27	2.62	0.65	2.97
WAAC	33.44	48.96	4.20	1.81	5.57	2.35	1.41	2.26

2.2 SPECIMEN PREPARATION

The WAAC qualities contribute 0% to 50% of total binder qualities in PC-WAAC blends (water-binder ratio 0.4), without sand or fillers. Compressive strength and deformation specimens measured 20x20x20mm³ and 25x25x280mm³, respectively. Excess water hinders CO_2 diffusion, inhibiting carbonation [38]. Pre-curing involved 24-hour exposure at room conditions before demolding, followed by 4 hours of carbonation (20% CO_2, 20±3℃, 60±5% RH). Carbonated samples then cured under standard conditions (20±1℃, RH>90%) for varying test ages. Uncarbonated controls were immediately placed in standard curing conditions.

2.3 MEASUREMENT

28-day-old standard and carbonated samples were immersed in 5% $MgSO_4$•$7H_2O$ solution at 5℃, with monthly solution replacement to maintain pH ≤ 8.5. Upon saturated surface drying, tests for volumetric deformation, mass change, and compressive strength were conducted. Phase composition and microstructure were analyzed on 3mm slices, 2mm from the surface, using isopropyl alcohol to halt hydration.

2.3.1 Compressive Strength

Compressive strength of control and carbonated samples was tested monthly for 6 months per GB/T17671-1999, averaging 6 samples per batch.

2.3.2 Volume Deformation:

Initial length of 28-day cured samples was recorded, with changes measured every half-month to 6 months. Final result is the average of 3 samples per batch.

2.3.3 Mass Change

To assess degradation, mass changes of samples were monitored every half-month to 6 months using a 0.001g scale. Final result is the average of 6 samples.

2.3.4 Phase Composition & Microstructure

XRD patterns (5°-65°, 0.02°/s) were collected using Cu-Kα radiation. Pore structure was analyzed with IV 9510 MIP (0-60,000 psi). Microstructure observed via SEM & EDS (30 kV). Experimental details in references [17-18, 23].

3. RESULTS AND DISCUSSION

3.1 COMPRESSIVE STRENGTH

Figure 3 illustrates the changes in PC-WAAC paste's compressive strength post low-temp sulfate immersion. Accelerated carbonation enhanced the 28-day pre-soak strength as anticipated. Following one month of sulfate soaking, all samples' strength rose 3.37%-7.77% due to cement hydration, subsequently declining with prolonged soaking. Notably, after 6 months, strength decreased by 9.31%-61.97%, yet carbonated samples with 0%-20% WAAC additions retained 3.93%-18.31% higher strength than their uncarbonated counterparts pre-immersion.

For uncarbonated controls, 10%-50% WAAC additions significantly reduced 6-month strength (15.55% vs. 20.16%-61.97% drop). However, carbonated PC-WAAC with 30% WAAC surpassed uncarbonated pure cement's pre-immersion strength even after 4 months. Importantly,

carbonated samples' 6-month strength decline (9.31%-46.15%) was substantially lower than that of uncarbonated controls (15.55%-61.97%), indicating carbonation curing mitigates sulfate-induced strength loss and enhances sulfate resistance

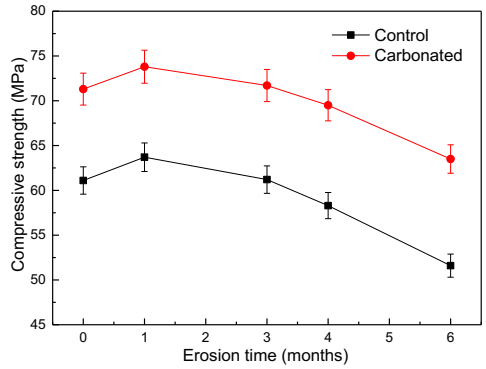

(a) 0% WAAC content

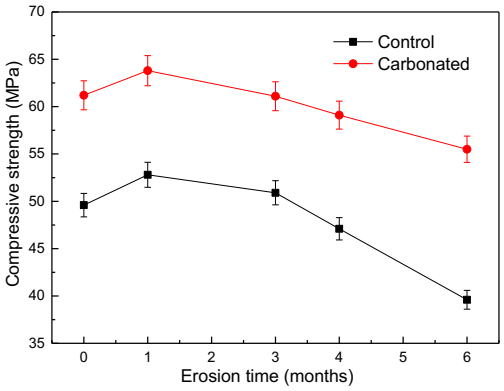

(b) 10% WAAC content

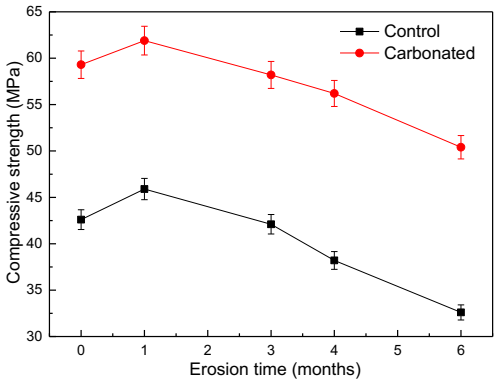

(c) 20% WAAC content

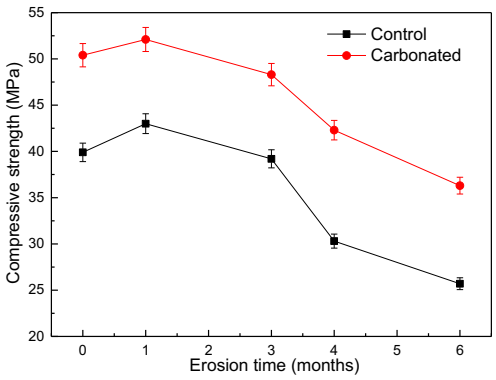

(b) 30% WAAC content

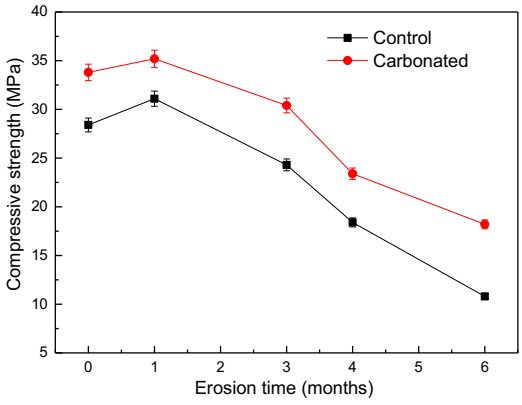

(e) 50% WAAC content

Fig. 3. Compressive strength of PC-WAAC pastes.

Fig. 4 displays the 6-month sulfate-exposed samples. Fig. 4(a) shows severe damage, including edge cracking and mushroom-like spalling, in uncarbonated cement paste due to C-S-H gel decomposition and sulfate formation [39]. The 50% WAAC control sample in Fig. 4(c) exhibits cracks due to gypsum and ettringite [40-41]. In contrast, carbonated specimens in Fig. 4(b) and (d) remain intact, attributed to microstructural and permeability enhancements from accelerated carbonation [17].

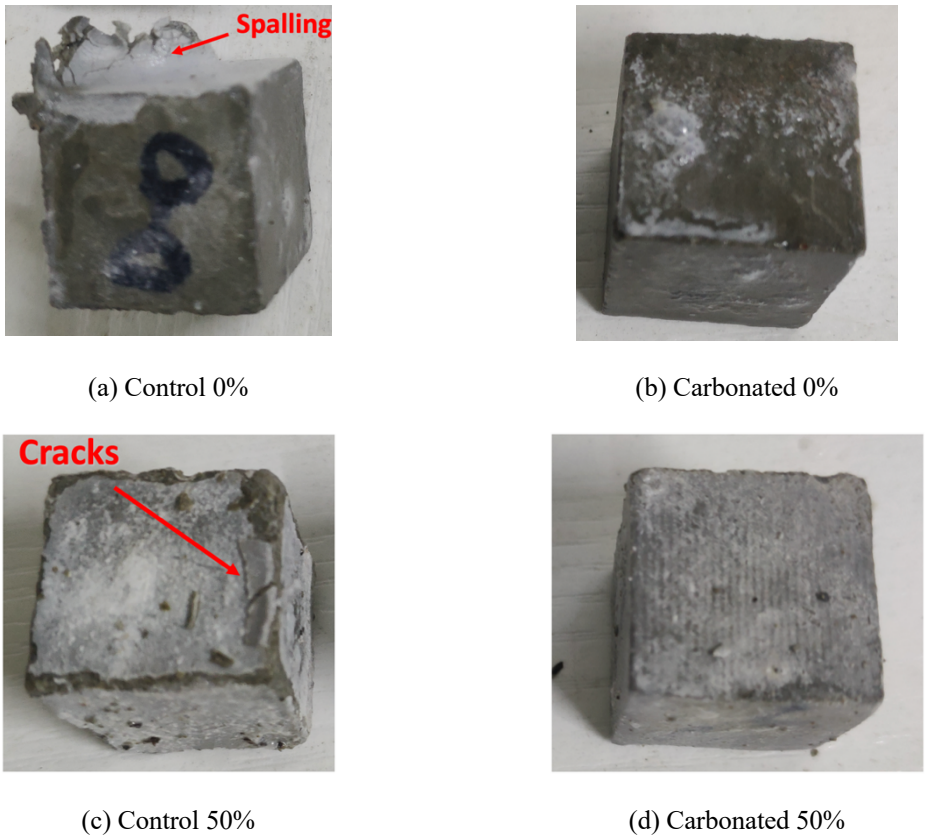

(a) Control 0% (b) Carbonated 0%

(c) Control 50% (d) Carbonated 50%

Fig. 4. Appearance of PC-WAAC pastes.

3.2 VOLUME DEFORMATION

Fig. 5 depicts the volume deformation of PC-WAAC specimens post low-temp sulfate attack. All samples expanded due to gypsum and ettringite formation in sulfate solution [42]. Notably, WAAC addition accelerated expansion, attributed to increased porosity facilitating corrosive agent infiltration and precipitate formation. Accelerated carbonation mitigated this effect, reducing expansion rates by 2.08%-6.04% (carbonated) compared to 3.00%-8.75% (uncarbonated), reinforcing the improvement in sulfate resistance.

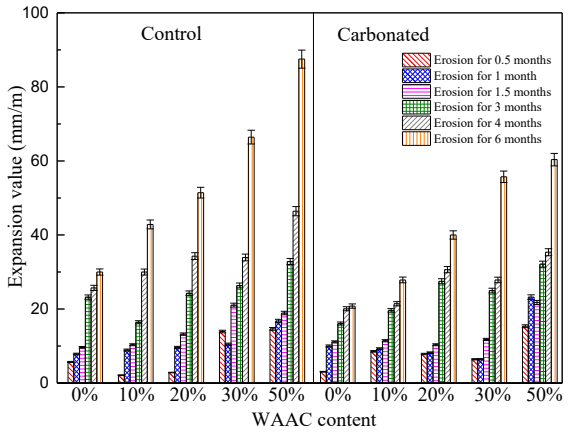

Fig. 5. Volume deformation of PC-WAAC pastes.

3.3 MASS CHANGE

Figure 6 illustrates the mass variations of PC-WAAC pastes subjected to low-temp sulfate attack over 6 months. All samples exhibited weight gain due to sulfate absorption [43], except for the control sample which lost weight significantly from 4 to 6 months, mirroring the spalling observed in Fig. 4. Accelerated carbonation mitigated weight gain, enhancing permeability resistance and sulfate durability [44-45]. After 6 months, all specimens gained 2.03% to 3.54% mass, highlighting the need for further long-term studies on low-temp sulfate resistance, given the early-stage weight loss insensitivity.

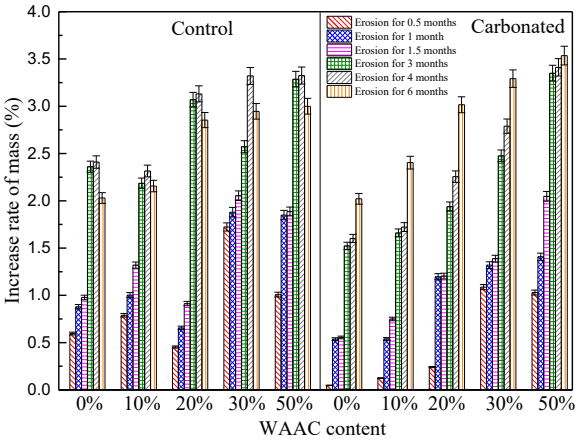

Fig. 6. Mass change of PC-WAAC pastes.

3.4 XRD ANALYSIS

XRD tests revealed the phase composition of specimens in Fig. 7. Uncarbonated samples exhibited peaks for alite, belite, Ca(OH)2, CaCO3 (from atmospheric carbonation), SiO2 (from WAAC), and sulfate products excluding Mg(OH)2 due to low content. Carbonated samples showed reduced Ca(OH)2 and enhanced CaCO3 peaks, confirming carbonation. Initial immersion reduced C3S/C2S peaks due to hydration, enhancing early strength. Prolonged sulfate exposure intensified gypsum and ettringite peaks, initially strengthening but later causing swelling, cracking, and strength decline. Carbonated samples exhibited lower gypsum and ettringite peaks after 6 months, indicating mitigated expansion. this evidence suggests that carbonation curing can inhibit the formation of sulfate products in cement and thus can improve the resistance of cement to low-temperature sulfate erosion.

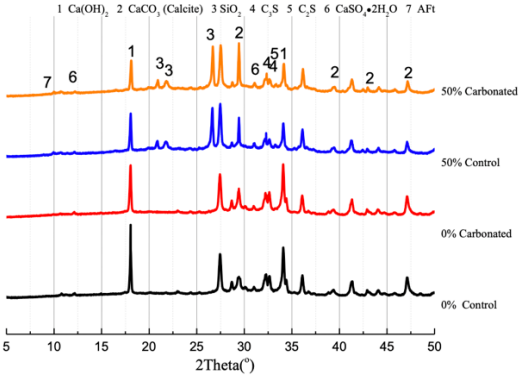

(a) 28d

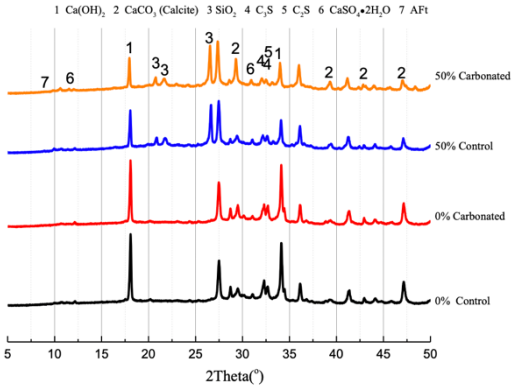

(b) Immersion for 1 month

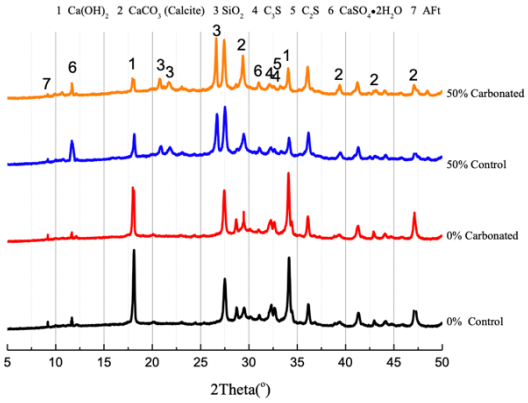

(c) Immersion for 6 months

Fig. 7. XRD patterns of PC-WAAC pastes.

3.5 PORE STRUCTURE

Fig. 8 displays MIP results of PC-WAAC specimens after 6 months of low-temp sulfate immersion, with pore parameters in Table 2. WAAC addition initially raised porosity, but carbonation curing refined pore structure by filling with calcium carbonate [17, 44-45, 48]. After 6 months, low-temp immersion coarsened PC-WAAC pores, increasing >1000 nm pores and porosity by 17.94%-36.65%, due to excessive Aft and CaSO4.2H2O formation causing expansion/cracking. Carbonated PC-WAAC samples showed 4.76%-7.77% lower porosity than uncarbonated controls, indicating improved sulfate resistance.

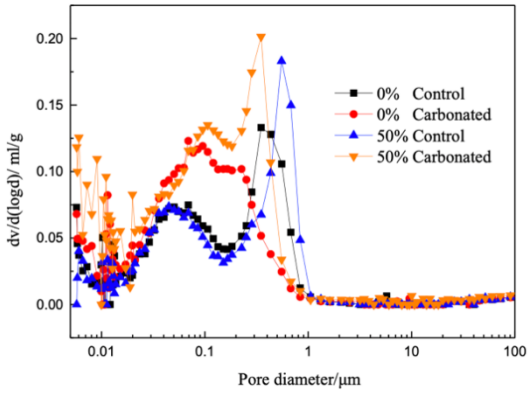

(a) Differential porosity curve-28d

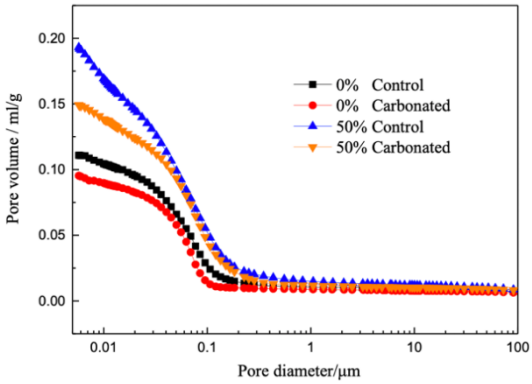

(b) Cumulative porosity curve-28d

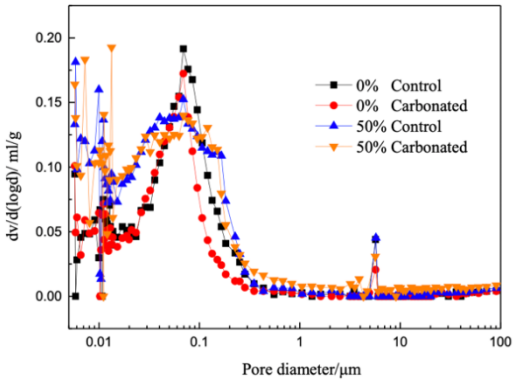

(c) Differential porosity curve- immersion for 6 months

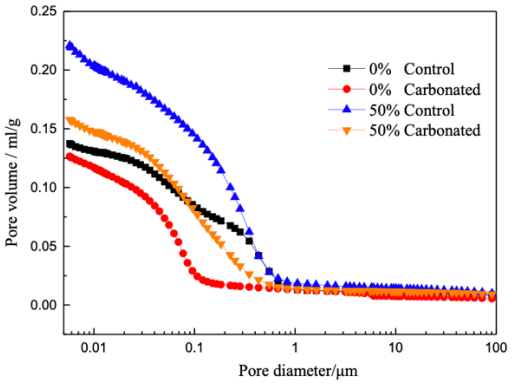

(d) Cumulative porosity curve- immersion for 6 months

Fig. 8. Pore structure of PC-WAAC pastes.

Table 2 Pore structure parameters of PC-WAAC pastes.

Curing days	Group		Porosity (%)	Pore size distribution (%)				
				<20nm	20～50nm	50～100nm	100～1000nm	>1000nm
28d	Control	0	18.0	18.6	17.0	23.2	30.8	10.4
		50%	26.2	17.5	12.6	18.5	41.4	10.0
	Carbonated	0	16.1	27.2	20.1	19.4	22.1	11.2
		50%	21.8	16.7	19.1	19.9	36.2	8.1
6 months immersion	Control	0	23.1	17.5	23.3	25.5	15.0	18.7
		50%	30.9	17.2	19.6	21.2	25.7	16.3
	Carbonated	0	22.0	24.1	30.6	27.9	5.9	11.5
		50%	28.5	20.1	32.3	15.1	19.1	13.4

3.6 SEM OBSERVATION

Fig. 9 depicts SEM images of PC-WAAC samples with EDS-verified mineral composition. Pre-immersion, hexagonal Ca(OH)2 and AFt needles were present. Post-carbonation, Ca(OH)2 disappeared, replaced by irregular CaCO3 particles filling pores and refining microstructure [49]. This modified shell reduces dissolution erosion by enhancing structural density and lowering solubility compared to Ca(OH)2. After 6 months of low-temp sulfate immersion, AFt formation in uncarbonated samples swelled pores, causing microcracks and strength loss (Fig. 9e,g). Conversely, carbonated PC-WAAC showed minimal deterioration due to improved sulfate resistance (Fig. 9f,h).

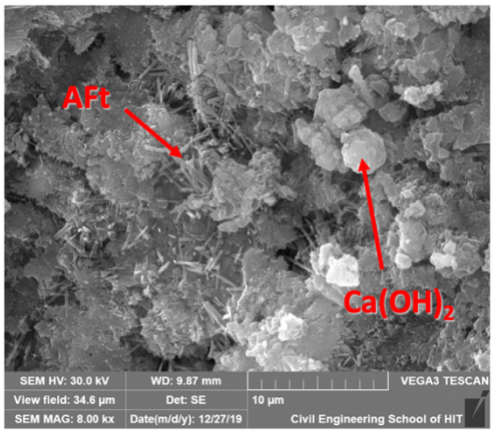

(a) 0% Control-28d (×8000)

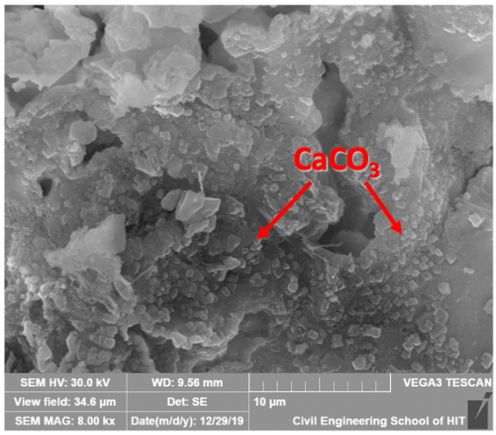

(b) 0% Carbonated-28d (×8000)

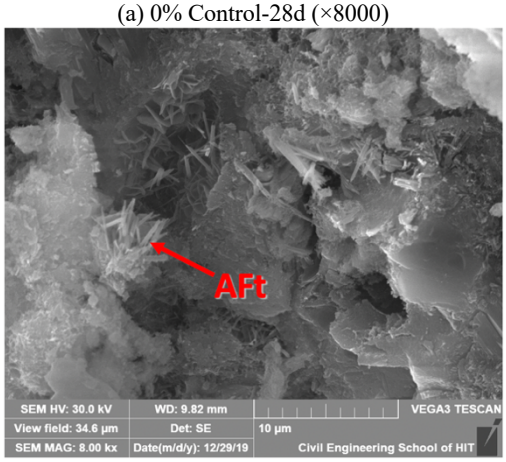

(c) 50% Control-28d (×8000)

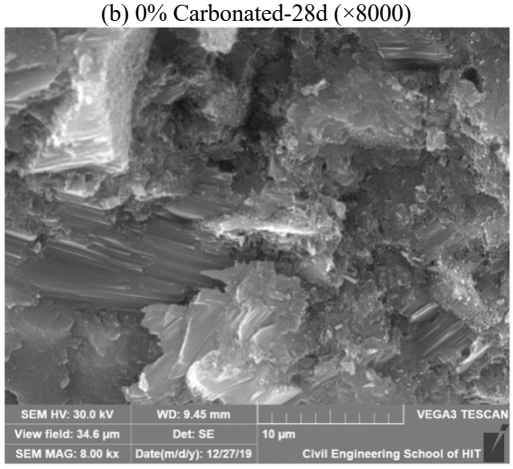

(d) 50% Carbonated-28d (×8000)

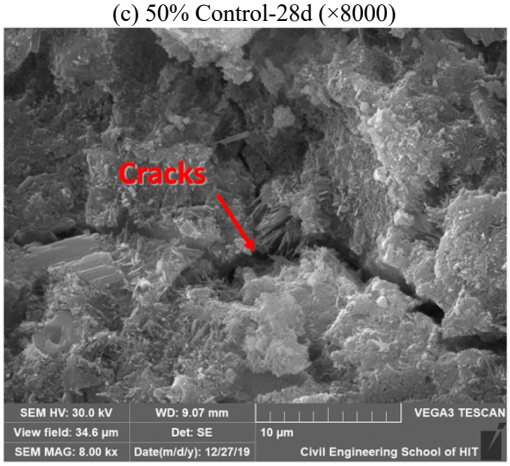

(e) 0% Control- immersion for 6 months (×8000)

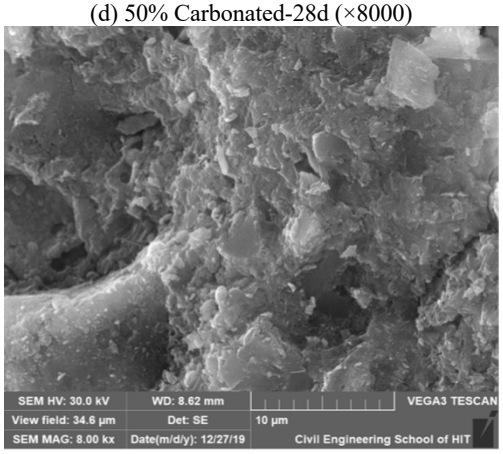

(f) 0% Carbonated- immersion for 6 months (×8000)

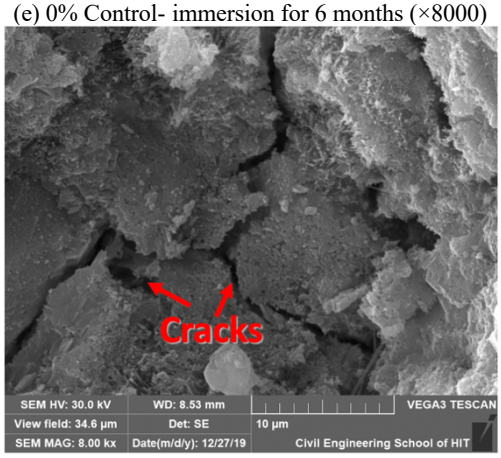

(g) 50% Control- immersion for 6 months (×8000)

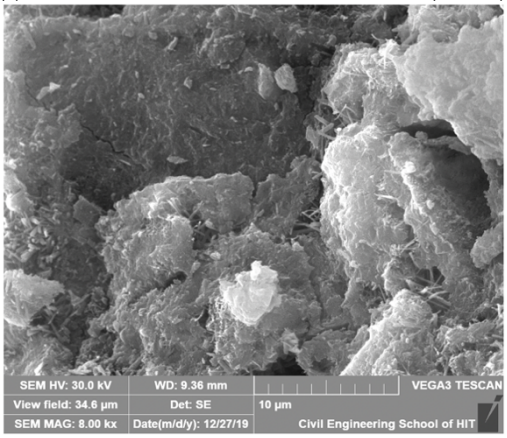

(h) 50% Carbonated- immersion for 6 months (×8000)

Fig. 9. SEM images of PC-WAAC pastes.

4. CONCLUSIONS

According to the above experimental results, the conclusions can be obtained as follows.
(1) The samples compressive strength increased by 3.37%~7.77% after 1 month of low-temperature sulfate immersion due to the continuous hydration reaction and the filling effect of moderate amount of CaSO4.2H2O and AFt. However, because of the excessive formation of CaSO4.2H2O and AFt, the 6-month immersion compressive strength decreased by 9.31%~61.97%.
(2) Accelerated carbonation reduced the decreasing effect of low-temperature sulfate immersion on the compressive strength. The 6-month immersion compressive strength of the carbonated specimens with 0%, 10%, 20% WAAC were still higher than those of the corresponding uncarbonated specimens before immersion.
(3) The longer the PC-WAAC specimens were immersed in the low-temperature sulfate solution, the greater the volume expansion. Nevertheless, the volume expansion can be suppressed by carbonation curing.
(4) All specimens increased in mass by 2.03%~3.54% after 6 months of low-temperature immersion. Therefore, mass loss is not a valid indicator of early damage deterioration by low-temperature sulfate erosion.
(5) The typical TSA production thaumasite wasn't observed in the carbonation curing specimens after low-temperature sulfate immersion. Accelerated carbonation improved the resistance of PC-WAAC pastes to low-temperature sulfate attack mainly due to the decreased porosity and improved pore structure.

References

[1] L.M. Haselbach, J.N. Thomle, An alternative mechanism for accelerated carbon sequestration in concrete, Sustain. Cities Soc. 12 (2014) 25-30. https://doi.org /10.1016/j.scs.2014.01.001
[2] L.F. Lepre, A.V. Gautier, M.C. Gomes, Ionic liquids can enable the recycling of fluorinated greenhouse gases, ACS Sustain. Chem. Eng. 7 (2019) 16900-16906. https://doi.org/10.1021/acssuschemeng . 9b04214.
[3] B. Zhan, C. Poon, C. Shi, CO2 curing for improving the properties of concrete blocks containing recycled aggregates, Cem. Concr. Compos. 42 (2013) 1–8. https://doi.org/10.1016/j.cemconcomp.2013.04. 013.
[4] J.J. Biernacki, J.W. Bullard, G. Sant, K. Brown, F.P. Glasser, S. Jones, Cements in the 21st century: challenges, perspectives, and opportunities, J. Am. Ceram. Soc. 100 (2017) 2746–2773. https://doi.org/10.1111/jace.14948.
[5] C.Shi, A.F. Jiménez, A. Palomo, New cements for the 21st century: the pursuit of an alternative to Portland cement, Cem. Concr. Res. 41 (2011) 750–763. https://doi.org/10.1016/j.cemconres.2011.03.016.
[6] M. Schneide, M. Romer, M. Tschudin, H. Bolio, Sustainable cement production-present and future, Cem. Concr. Res. 41 (2011) 642-650. https://doi.org/10.1016/j.cemconres.2011.03.019.
[7] Z. Wei, B. Wang, G. Falzone, M.U. Okoronkwo, Z. She, Clinkering-free cementation by fly ash carbonation, J. CO2. Util. 23 (2018) 117-127. https://doi.org/10.1016/j.jcou.2017.11.005.
[8] R.M. Andrew, Global CO2 emissions from cement production, Earth. Syst. Sci. Data. 10 (2018) 1-52. https://doi.org/10.5194/essd-2018-90.
[9] Z. Giergiczny, K. Wandoch, Performance of concrete with low CO2 emission, Energies. 13 (2020) 4328. https://doi.org/10.3390/en13174328.
[10] H. Huang, X. Gao, K.H. Khayat, Influence of fiber alignment and length on flexural properties of UHPC, Constr. Build. Mater. 290 (2021) 122863. https://doi.org/10.1016/j.conbuildmat.2021.122863.
[11] K. Vance, G. Falzone, I. Pignatelli, M. Bauchy, M. Balonis, G. Sant, Direct carbonation of Ca(OH)2 using liquid and supercritical CO2: implications for carbon-neutral cementation, Ind. Eng. Chem. Res. 54 (2015) 8908–8918. https://doi.org/10.1021/acs.iecr.5b02356.
[12] B. Bajzelj, J.M. Allwood, J.M. Cullen, Designing climate change mitigation plans that add up, Env. Sci.Tec. 47 (2013) 8062-8069. https://doi.org/10.1021/es400399h.
[13] S.A. Miller, V.M. John, S.A. Pacca, A. Horvath, Carbon dioxide reduction potential in the global cement industry by 2050, Cem. Concr. Res. 114 (2017) 115-124. https://doi.org/10.1016/j.cemconres.2017.08.026.
[14] R. Pachauri, A. Reisinger, Climate change 2014: synthesis report. Contribution of working groups I, II and III to the fifth assessment report of the intergovernmental panel on climate change, J. Romanc. Stud. 4 (2014) 85-88. https://doi.org/10013/epic.45156.
[15] C. Llatas, N. Bizcocho, B. Soust-Verdaguer, M.V. Montes, An lca-based model for assessing prevention versus non-prevention of construction waste in buildings, Waste. Manage.126 (2021) 608-622. https://doi.org/10.1016/j.wasman.2021.03.047.
[16] A. Rh, C.A. Ke, A. Wc, B. Qw, A. Hl, Estimation of construction waste generation based on an improved on-site measurement and svm-based prediction model: a case of commercial buildings in china, Waste. Manage. 126 (2021) 791-799. https://doi.org/10.1016/j.wasman.2021.04.012.
[17] L. Qin, X. Gao, Recycling of waste autoclaved aerated concrete powder in Portland cement by accelerated carbonation, Waste. Manage. 89 (2019) 254-264. https://doi.org/10.1016/j.wasman.2019.04.018.
[18] L. Qin, X. Gao, Q. Li, Upcycling carbon dioxide

to improve mechanical strength of Portland cement, J. Clean. Prod. 196 (2018) 726-738. https://doi.org/10.1016/j.jclepro.2018.06.120.

[19] D. Sharma, S. Goyal, Accelerated carbonation curing of cement mortars containing cement kiln dust: An effective way of CO2 sequestration and carbon footprint reduction, J. Clean. Prod. 192 (2018) 844-854. https://doi.org/10.1016/j.jclepro.2018.05.027.

[20] K. Watanabe, K. Yokozeki, R. Ashizawa, High durability cementitious material with mineral admixtures and carbonation curing, Waste. Manage. 26 (2006) 752-757. https://doi.org/10.1016/j.wasman.2006.01.030.

[21] A. Ebrahimi, M. Saffari, D. Milani, A. Montoya, M. Valix, A. Abbas, Sustainable transformation of fly ash industrial waste into a construction cement blend via CO2 carbonation, J. Clean. Prod. 156 (2017) 660-669. https://doi.org/10.1016/j.jclepro.2017.04.037.

[22] R. Hay, K. Celik, Accelerated carbonation of reactive magnesium oxide cement (RMC)-based composite with supercritical carbon dioxide (scCO2), J. Clean. Prod. 248 (2020) 119282. https://doi.org/10.1016/j.jclepro.2019.119282.

[23] L. Qin, X. Gao, Properties of coal gangue-Portland cement mixture with carbonation, Fuel. 245 (2019) 1–12. https://doi.org/10.1016/j.fuel.2019.02.067.

[24] D. Xuan, B. Zhan, C.S. Poon, Development of a new generation of eco-friendly concrete blocks by accelerated mineral carbonation, J. Clean. Prod. 133 (2016) 1235-1241. https://doi.org/10.1016/j.jclepro.2016.06.062.

[25] P. Zhang, F.H. Wittmann, M. Vogel, H.S. Müller, T. Zhao, Influence of freeze-thaw cycles on capillary absorption and chloride penetration into concrete, Cem. Concr. Res. 100 (2017) 60-67. https://doi.org/10.1016/j.cemconres.2017.05.018.

[26] P. Wang, Y. Jia, T. Li, D. Hou, Q. Zheng, Molecular dynamics study on ions and water confined in the nanometer channel of Friedel's salt: structure, dynamics and interfacial interaction, Phys. Chem. Chem. Phys. 20 (2018) 27049-27058. https://doi.org/10.1039/C8CP02450B.

[27] H.N. Atahan, K.M. Arslan, Improved durability of cement mortars exposed to external sulfate attack: the role of nano and micro additives, Sustain. Cities Soc. 22 (2016) 40-48. https://10.1016/j.scs.2016.01.008.

[28] G.J. Yin, X.B. Zuo, X.H. Sun, Y.J. Tang, Macro-microscopically numerical analysis on expansion response of hardened cement paste under external sulfate attack, Constr. Build. Mater. 207 (2019) 600-615. https://doi.org/10.1016/j.conbuildmat.2019.02.159.

[29] L. Qin, X. Gao, A. Su, Q. Li, Effect of carbonation curing on sulfate resistance of cement-coal gangue paste, J. Clean. Prod. 278 (2020) 123897. https://doi.org/10.1016/j.jclepro.2020.123897.

[30] J. Bensted, Thaumasite-background and nature in deterioration mortars and concretes, Cem. Concr. Compos. 21 (1999) 117–121, https://doi.org/10.1016/S0958–9465(97)00076-0.

[31] P.M. Carmona-Quiroga, M.T. Blanco-Varela, Resistance to thaumasite sulfate attack in BaCO3-bearing cement pastes and mortars, Cem. Concr. Res. 132 (2020) 106052. https://doi.org/10.1016/j.cemconres.2020.106052.

[32] K. Sotiriadis, P. Mácová, A.S. Mazur, A. Viani, S. Tsivilis, Long-term thaumasite sulfate attack on Portland-limestone cement concrete: a multi-technique analytical approach for assessing phase assemblage, Cem. Concr. Res. 130 (2020) 105995. https://doi.org/10.1016/j.cemconres.2020.105995.

[33] K. Sotiriadis, E. Nikolopoulou, S. Tsivilis, Sulfate resistance of limestone cement concrete exposed to combined chloride and sulfate environment at low temperature, Cem. Concr. Res. 34 (2012) 903-910. https://doi.org/10.1016/j.cemconcomp.2012.05.006.

[34] A. Skaropoulou, K. Sotiriadis, G. Kakali, S. Tsivilis, Use of mineral admixtures to improve the resistance of limestone cement concrete against thaumasite form of sulfate attack, Cem. Concr. Compos. 37 (2013) 267-275. https://doi.org/10.1016/j.cemconcomp.2013.01.007.

[35] R. Brueckner, S.J. Williamson, L.A. Clark, The effects of the thaumasite form of sulfate attack on skin friction at the concrete/clay interface, Cem. Concr. Res. 42 (2012) 424-430. https://doi.org/10.1016/j.cemconres.2011.11.009.

[36] D.D. Higgins, N.J. Crammond, Resistance of concrete containing ggbs to the thaumasite form of sulfate attack, Cem. Concr. Compos. 25 (2003) 921-929. https://doi.org/10.1016/S0958–9465(03)00149-5.

[37] E.F. Irassar, Sulfate attack on cementitious materials containing limestone filler-A review, Cem. Concr. Res. 39 (2009) 241-254. https://doi.org/10.1016/j.cemconres.2008.11.007.

[38] D. Zhang, Z. Ghouleh, Y. Shao, Review on carbonation curing of cement-based materials, J. CO2. Util. 21 (2017) 119-131. https://doi.org/10.1016/j.jcou.2017.07.003.

[39] S.M. Torres, C.A. Kirk, C.J. Lynsdale, R.N. Swamy, J.H. Sharp, Thaumasite-ettringite solid solutions in degraded mortars, Cem. Concr. Res. 34 (2004) 1297-1305. https://doi.org/10.1016/j.cemconres.2003.09.016.

[40] Y. Huang, C. Xu, H. Li, Z. Jiang, Z. Gong, X. Yang, Q. Chen, Utilization of the black tea powder as multifunctional admixture for the hemihydrate gypsum, J. Clean. Prod. 210 (2019) 231-237. https://doi.org/10.1016/j.jclepro.2018.10. 304.

[41] B. Tian, M.D. Cohen, Does gypsum formation during sulfate attack on concrete lead to expansion?, Cem. Concr. Res. 30 (2000) 117-123. https://doi.org/10.1016/S0008-8846(99)00211-2.

[42] M. Santhanam, M.D. Cohen, J. Olek, Effects of gypsum formation on the performance of cement mortars during external sulfate attack, Cem. Concr. Res. 33 (2003) 325-332. https://doi.org/10.1016/S0008-8846(02)00955-9.

[43] Y. Gu, R.P. Martin, O.O. Metalssi, T. Fen-Chong, P. Dangla, Pore size analyses of cement paste exposed to external sulfate attack and delayed ettringite formation, Cem. Concr. Res. 123 (2019) 105766. https://doi.org/10.1016/j.cemconres.2019.05.011.

[44] A. Hidalgo, C. Domingo, C. Garcia, S. Petit, C. Andrade, C. Alonso, Microstructural changes induced in Portland cement-based materials due to natural and supercritical carbonation, J. Mater. Sci. 43 (2008) 3101-3111. https://doi.org/10.1007/s10853–008–2521-5.

[45] Y. Shao, V. Rostami, Z. He, A.J. Boyd, Accelerated carbonation of Portland limestone cement, J. Mater. Civ. Eng. 26 (2014) 117-124. https://doi.org/10.1061/(ASCE)MT.1943-5533.0000773.

[46] Z. Guo, Y. Wang, P. Hou, Y. Shao, X. Zuo, X. Cheng, Comparison study on the sulfate attack resistivity of cement-based materials modified with nanoSiO2 and conventional SCMs: mechanical strength and volume stability, Construct. Build. Mater. 211 (2019) 556e570. https://doi.org/10.1016/j.conbuildmat.2019.03.235.

[47] Y. Wang, Y. Cao, L. Cui, Z. Si, H. Wang, Effect of external sulfate attack on the mechanical behavior of cemented paste backfill, Constr. Build. Mater. 263 (2020) 120968. https://doi.org/10.1016/j.conbuildmat.2020.120968.

[48] N. Li, N. Farzadnia, C. Shi, Microstructural changes in alkali-activated slag mortars induced by accelerated carbonation, Cem. Concr. Res. 100 (2017) 214-226. https://doi.Org/10.1016/j.cemconres.2017.07.008.

[49] L. Mo, F. Zhang, M. Deng, Mechanical performance and microstructure of the calcium carbonate binders produced by carbonating steel slag paste under CO2 curing, Cem. Concr. Res. 88 (2016) 217-226. https://doi.org/10.1016/j.cemconres.2016.05.013.

STRENGTH DEVELOPMENT PROPERTIES OF VARIOUS TYPES OF CONCRETE THAT FREEZE AT THE FINAL SETTING TIME

Kotaro YAMASHITA
Senior Researcher, Building Structual Engineering Group, TSUKUBA R&D Center, Research Institute of Technology, KONOIKE CONSTRUCTION CO.,LTD., 1-20-1 Sakura Tsukuba 305-003, Japan.

Yukio HAMA
Professor, Muroran Institute of Technology, 27-1 Mizumoto, Muroran 050-8585, Japan.
Professor, Hokkaido University, Kita 8, Nishi 5, Kita-ku, Sapporo, Japan

ABSTRACT:
In previous studies, the authors investigated the stagnation of strength gain due to freezing of cement pastes and mortars at the initial age of the materials. We reported that the hydration reactivity of cement paste did not change before and after freezing, and that for mortar, freezing before the final setting time resulted in a greater effect of damage. However, the effect of freezing at the final setting time on the strengthening of concrete is unknown. Therefore, this study investigated the effect of freezing at the final setting time on the strength gain of different types of concrete. The results showed that the increase in strength of concrete without air introduced by admixture stagnated due to freezing at final setting time.
Keywords: early-age frost damage, setting time, curing methods, compressive strength, air volume, chemical admixtures

1. INTRODUCTION

The most important aspects of concreting in cold weather are prevention of early-age frost damage and delay in strength development [1]. Early-age frost damage includes stagnation of strength development caused by freezing of water in concrete between the freshly poured stage and early-setting stage. It is differentiated from frost damage caused by repeated freezing and thawing of fully set concrete. Because low temperatures dramatically slow strength development, the required compressive strength for the specified age might not be attained. This leads to problems with process management during construction [1]

Generally, to prevent early-age frost damage, concrete should not be frozen during the initial setting until a compressive strength of 5.0 N/mm^2 is achieved [1]. To that end, heat curing is often used where heated protective enclosures and sheds are built to cover the structures. Meanwhile, the use of air-entraining agents, air-entraining water-reducing admixtures, and cold resistance accelerators is known to be effective for preventing frost damage to concrete materials and mixtures. Introducing air bubbles using air-entraining agents and air-entraining water-reducing admixtures has been shown to be effective when concrete has frozen after 1 d at a temperature of 10 °C [2]. Cold resistance accelerators not only reduce the freezing temperature of concrete but also promote the hydration reaction of cement to quickly secure a compressive strength of 5.0 N/mm^2 required to prevent early-age frost damage [3].

Early-age frost damage is usually assessed by determining whether the strength is recovered by curing after freezing and thawing. However, the correspondence between the strength recovery and the level of damage is unclear. Although thorough anti-freezing measures are implemented during midwinter, concrete that has been waterproofed, thin slabs and concrete parapets often develop defects when constituent surfaces freeze owing to unexpected cold snaps and deficiencies in curing management.

Previously, we studied how early-age freezing stagnates the strength development of cement paste and mortar and reported that the hydration reactivity of cement paste did not change after freezing [4]. In an experiment using mortar, we reported that the curing conditions after freezing had a notable impact on the level of mortar damage, meaning freezing before and after the final setting time determined the extent of damage [5]. However, the impact of freezing before and after the final setting time on the strength development of concrete with coarse aggregate is unknown. The impact of chemical admixtures also needs to be examined.

Therefore, in this study, we aimed to confirm the impact of freezing at the final setting time on the strength development of concrete using different types of chemical admixtures. We must note, however, that this study aimed to confirm the basic properties of test specimens and was not intended to determine the conditions under which damages would not occur, even without the compressive strength required to prevent early-age frost damage (5.0 N/mm^2).

2. EXPERIMENT

2.1 Materials and Preparation

Table 1 shows the materials used for the concrete. For the cement, we used the same amount of ordinary Portland cement from three different manufacturers specified under Section 6.2.1, materials used for the tests, of JIS A 6204 (chemical admixtures for concrete). We used tap water. For the aggregates, we used materials that met the quality specified under Section 6.2.1, materials used for tests, of JIS A 6204 (chemical admixtures for concrete). We used the following chemical admixtures: air-entraining agents, air-entraining water-reducing admixtures (normal), air-entraining water-reducing admixtures (delayed), high-range air-entraining water-reducing admixtures (normal), high-range air-entraining water-reducing admixtures (delayed), and high-range water-reducing agents.

Table 2 shows the composition of the concrete mixtures. The unit cement volumes were 300 kg/m^3 and 350 kg/m^3. The target slumps were 8 cm and 18 cm. The unit water volume was set so that the slump at the end of preparation would be within ±1.0 cm of the target slump. We followed the recommendations from manufacturers for the amount of chemical admixtures.

To prepare the concrete, we used a forced-action two-shaft mixer in a 20 °C laboratory and mixed the materials for 1.5 min.

2.2 Freezing, Thawing, and Curing Conditions

Table 3 shows the freezing, thawing, and curing conditions. The symbol N means the specimens were not frozen, while Ffin means freezing occurred at the final setting time. F6h indicates that freezing began at the age of 6 h, which was performed for the specimens No. 5, No. 6, and No. 9. S7d→W indicates that sealed curing was performed to the age of 7 d, which was followed by water curing. Specimen No. 5 was cured to confirm the impact of the water-curing start time. In this experiment, we performed sealed curing at 20 °C until freezing began. We performed a total of three cycles, where one cycle consisted of 12 h of freezing at –20 °C and 12 h of thawing at 5 °C.

Table 1. Materials used in the experiments.

Items	Symbol	Summary
Cement	C	Ordinary Portland cement, density: 3.16 g/cm^3
Water	W	Tap water
Fine aggregate	S	Land sand from Kamisu City, Ibaraki Prefecture, surface-dry density: 2.59 g/cm^3, F.M.: 2.30
Coarse aggregate	G	Crushed rocks from Ome City, Tokyo, surface-dry density: 2.65 g/cm^3, Solid content: 60.1%, Maximum dimensions: 20 mm
Chemical admixtures	Ad	Air-entraining agents Air-entraining water-reducing admixtures (normal) Air-entraining water-reducing admixtures (delayed) High-range air-entraining water-reducing admixtures (normal) High-range air-entraining water-reducing admixtures (delayed) High-range water-reducing agents

Table 2. Breakdown of concrete mixture.

No.	Chemical admixtures	W/C	s/a	Unit volume(kg/m^3)					Fresh		
		(%)	(%)	W	C	S	G	Ad	Sl(cm)	Air(%)	C.T.(℃)
1	Plain	61.0	47.0	183	300	860	1011	-	8.5	1.1	19.5
2	Air-entraining agents	56.7	45.0	170	300	804	1024	7	10.0	4.6	20.5
3	Air-entraining water-reducing admixtures (normal)	51.7	45.0	155	300	821	1047	15	7.5	4.0	20.5
4	Air-entraining water-reducing admixtures (delayed)	51.7	45.0	155	300	821	1047	15	7.5	3.9	20.0
5	Plain	58.0	47.0	203	350	817	960	-	18.5	1.0	20.0
6	High-range air-entraining water-reducing admixtures (normal)	46.6	47.0	163	350	829	974	20	19.5	3.2	20.0
7	High-range air-entraining water-reducing admixtures (delayed)	46.6	47.0	163	350	829	974	20	18.5	4.3	20.0
8	Plain	53.7	46.0	188	350	817	1000	-	8.5	1.6	20.0
9	High-range water-reducing agents	45.7	45.0	160	350	832	1060	15	7.0	1.7	20.0

Table 3. Freezing, thawing, and curing conditions.

Symbols	C [kg/m^3]	Slump [cm]	Freezing and thawing conditions			Curing Conditions	Test material age
			Start Time	Temperature [℃]	Number of cycles		
N	300 350	8 18	No freezing			20 ℃ In water	7 28 91
Ffin			At the final setting time	–20 ℃ 12 h ⇅ 5 ℃ 12 h	3		
F6h			6h				
Ffin-S7d→W	350	18	At the final setting time			7 d of sealed curing at 20 ℃ → water curing at 20 ℃	
F6h-S7d→W			6h				

Table 4. Measurement items and test methods.

Subjects	Measurement items	Test methods
Fresh Concrete	Slump	JIS A 1101
	Air volume	JIS A 1128
	Concrete temperature	JIS A 1156
Mortar (Wet-screening)	Setting time	JIS A 1147
	Total porosity	Archimedes' principle
Hardened concrete	Compressive strength	JIS A 1108
	Static modulus of elasticity	JIS A 1149
	Salt penetration depth	JIS K 5600-7-9
	Carbonation depth	JIS A 1152

2.3 Experimental Methods

Table 4 shows the measured items and test methods. We measured the slump, air volume, and concrete temperature for fresh concrete. We measured the setting time for mortar sampled through wet-screening. We measured the total porosity for N, F6h, and Ffin of No. 6 with hardened mortar. The total porosity was calculated using Archimedes's principle, with a 5 × 5 × 5 mm^3 sample collected from a specimen having a φ value of 50 × 100 mm^2. The compressive strength test was performed under all conditions, with specimen dimensions of φ = 100 × 200 mm^2. The compressive strength was evaluated using the average of three specimens. The age of the measured specimens were 7, 28, and 91 d. The static modulus of elasticity was measured during the compressive strength test at an age of 28 d.

Salt penetration depth was examined in specimen No. 6, where the mixture used high-range air-entraining water-reducing admixtures (normal). The test used specimens with a φ value of 100 × 200 mm^2. The specimens were cured in air for four weeks at a temperature of 20 ℃ and a relative humidity (RH) of 60%. With 2 h of saltwater spray (35 ± 1 ℃), 4 h of drying (20–30 %RH), and 2 h of wetting (RH of 95% or higher) as one cycle, we sprayed 5 ± 1% saltwater according to cycle A of JIS K 5600-7-9 (cyclic corrosion test methods). We measured salt penetration depth at the end of 225 cycles, which is equivalent to five years of exposure in Okinawa Prefecture. We measured the salt penetration depth using the silver nitrate solution spraying method [6]. We split the specimen vertically, sprayed 0.1 mol/L silver nitrate solution on the split surface to color the chloride ions, and measured the distance from the concrete surface to the boundary of white discoloration at 10 points. We used the average of these measurements as the test result.

We performed an accelerated carbonation test on specimens with dimensions of 100 × 100 × 400 mm^3 for N, Ffin, and F6h of No. 6 according to JIS A 1153 (accelerated carbonation test method for concrete). The depth of carbonation was measured according to JIS A 1152 (carbonation depth measurement method for concrete).

3. RESULTS

3.1 Fresh Concrete Test Result

Table 2 shows the result of the test on fresh concrete. The slump was 8 ± 1.0 cm for No. 1–4 and 8 and 18 ± 1.0 cm for No. 5–7.

The air volume was 1.0–1.6% for plain specimens (No. 1, 5, and 8) and 1.7% for No. 9, which used a high-range water-reducing agent. The air volume was in the range of 3.2 to 4.6% for No. 2–4, 6, and 7.

3.2 Strength Development Properties

Fig. 1 shows the result of the setting-time test. The figure also shows the start time for freezing. For all conditions, we considered the end of setting to be the start of freezing. No. 5, 6, and 9 began freezing at the age of 6 h; thus, No. 6 and 9 began freezing before setting started.

Fig. 2 shows the result of the compressive strength test performed on No. 1–4 (concrete with a unit cement volume of 300 kg/m^3 and target slump of 8 cm). When No. 1 (plain) froze at the final setting time (Ffin), the strength was notably reduced. On the other hand, the Ffin for No. 2 (air-entraining concrete) did not cause any stagnation in strength development. Air-entraining water-reducing admixtures No. 3 (normal) and No. 4 (delayed) did not experience any stagnation of strength

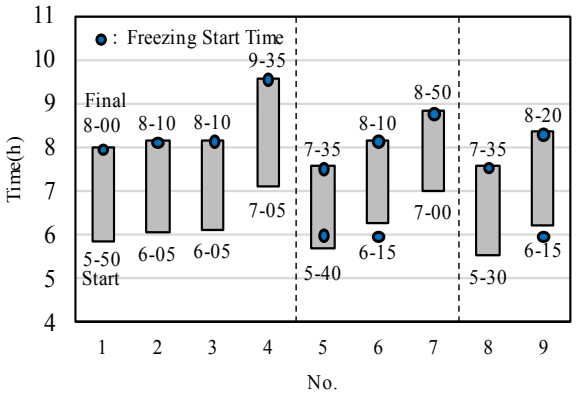

Fig. 1. Setting time test results.

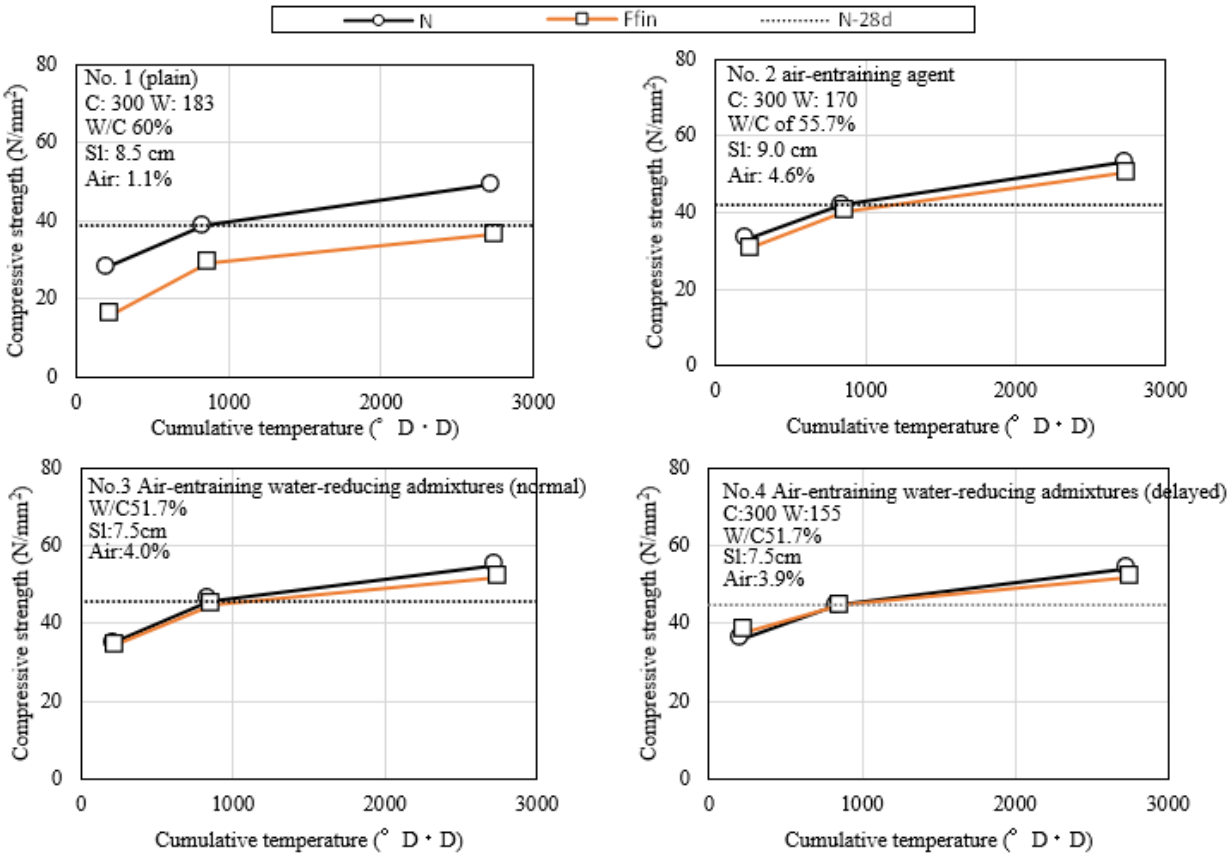

Fig. 2. Results of compressive strength tests No. 1–4 (C: 300 kg/m^3; target Sl: 8 cm).

development by Ffin and displayed similar strength-development properties.

Fig. 3 shows the result of the compressive strength test performed on No. 5–7 (concrete with a unit cement volume of 350 kg/m^3 and target slump of 18 cm). The compressive strength of No. 5 (plain) was reduced for every condition in which freezing occurred. Furthermore, Ffin-S7d→W and F6h-S7d→W with a delayed start for water curing experienced stagnated strength development. Neither No. 6 (high-range air-entraining water-reducing admixtures – normal) or No. 7 (high-

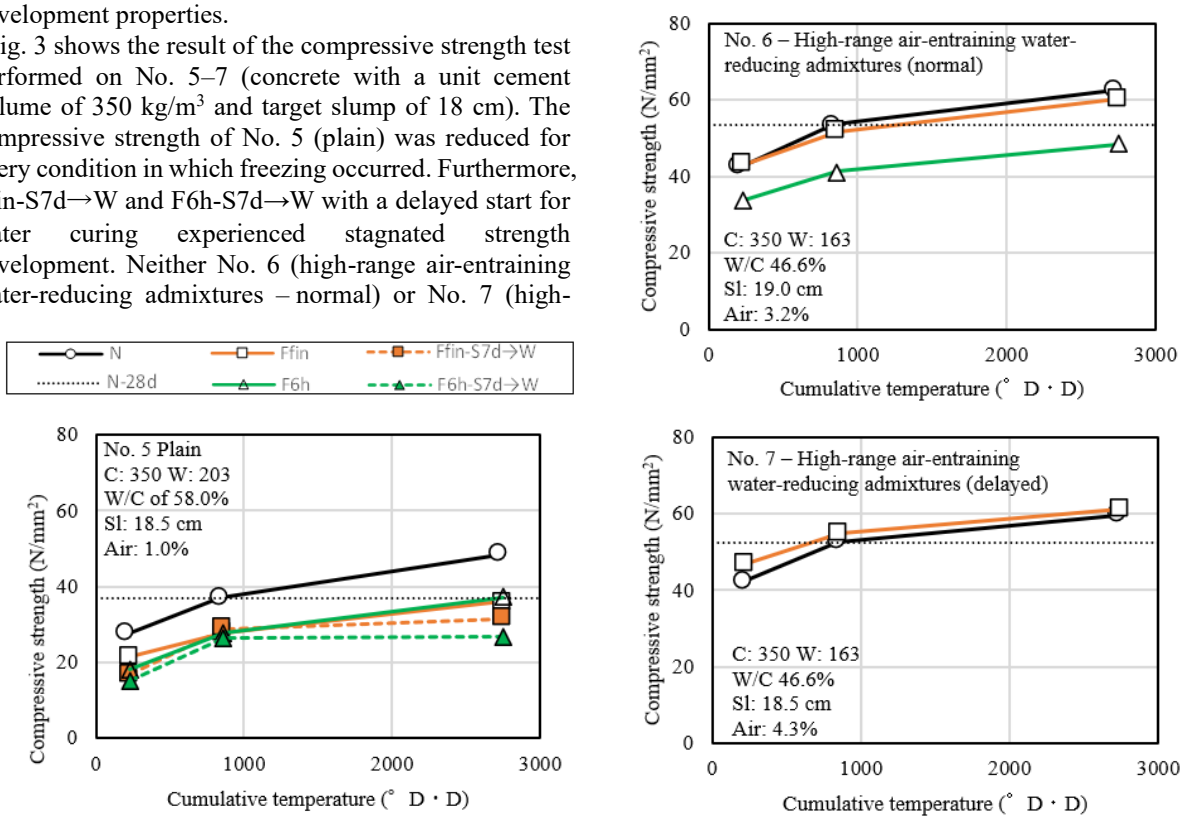

Fig. 3. Results of compressive strength tests No. 5–7.(C: 350 kg/m^3; target Sl: 18cm).

range air-entraining water-reducing admixtures – delayed) exhibited stagnated strength development by Ffin and had similar strength-development properties.

Fig. 4 shows the result of the compressive strength test performed on No. 8 and 9 (concrete with unit cement volume of 350 kg/m^3 and target slump of 8 cm). With Ffin, both No. 8 and No. 9 decreased in strength compared with N. No. 9 with Ffin decreased in strength despite having the same unit cement volume and water volume as No. 6. A previous study showed that air volume helps prevent early-age frost damage[2]; thus, its low air volume likely caused the strength decrease. In an experiment that used existing mortar[5] (non-air-entraining and W/C of 55%), if freezing occurred after the final setting time, strength development did not stagnate. However, in the present study, No. 1, 5, and 8 concrete (non-air-entraining; W/C of 60, 58, and 53.7%, respectively) experienced a stagnation in strength development owing to Ffin.

3.3 Relationship Between Compressive Strength and Other Factors

The relationship between compressive strength and static modulus of elasticity is shown in Fig. 5. All measurements of static modulus of elasticity satisfied at least 80% of the estimated value.

Fig. 6 shows the relationship between air volume and strength compared with N28d. The strength remained 90% or higher for Ffin when an air volume of 4.5% was maintained. On the other hand, the strength was lower at 75–90% of N28d for Ffin with an air volume of 1.0%. A higher air volume corresponds with a higher strength ratio to N28d. The plot shows that the increase in strength of concrete without air introduced by admixture stagnated due to freezing at final setting time.

3.4 Durability Test Result

Fig. 7 shows the relationship between compressive strength and carbonation rate coefficient. The F6h specimens had a large carbonation coefficient. Those with a drop in strength had a large carbonation coefficient, as reported in a previous study [7]. Ffin specimens had the same result as N in terms of both compressive strength and carbonation coefficient. One previous study reported low carbonation resistance despite the lack of any sign of early-age frost damage [8]. Therefore, it is necessary to examine the impact of early-

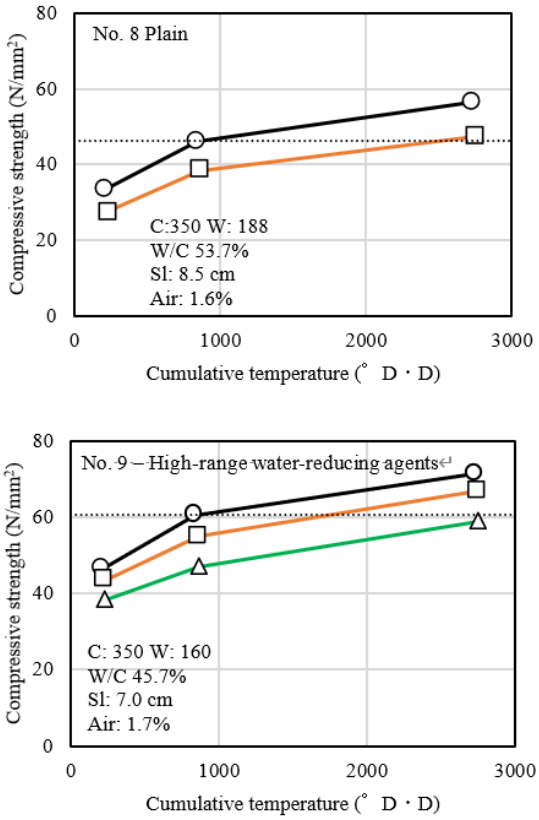

Fig. 4. Results of compressive strength tests No. 8 and 9.

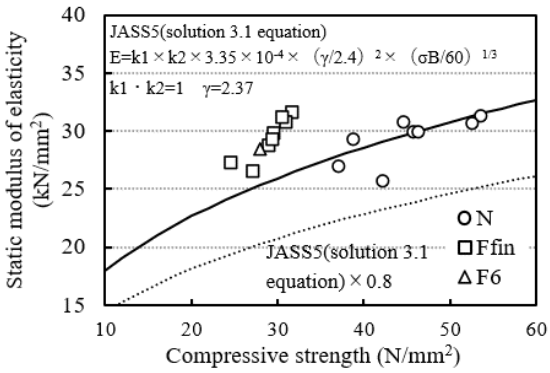

Fig. 5. Relationship between compressive strength and static modulus of elasticity (31 days of aging).

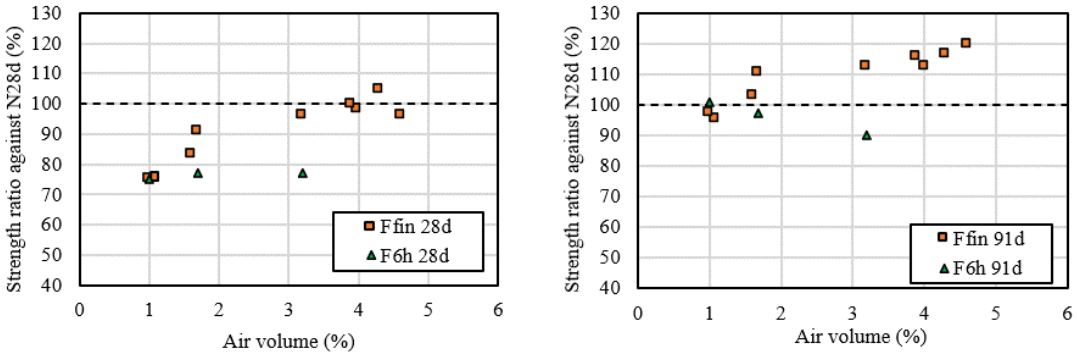

Fig. 6. Relationship between air volume and compressive strength ratio

age frost on the durability of concrete using a large number of experimental data.

The relationship between compressive strength and salt penetration depth is shown in Fig. 8. Salt penetrated deeply in F6h specimens, but as the compressive strength increased, the depth of salt penetration decreased. As the compressive strength increased in Ffin specimens, the salt penetration depth approached that of the unfrozen samples.

Fig. 9 shows the relationship between compressive strength and total porosity. Total porosity was high in F6h specimens, but as the compressive strength increased, total porosity decreased. As the compressive strength increased in Ffin specimens, the total porosity approached that of the unfrozen samples.

Within the limits of the experiment, as long as the compressive strength of the specimens after Ffin was identical to that of the unfrozen specimens, carbonation resistance and salt penetration resistance did not change notably.

4. CONCLUSIONS

The main conclusions can be summarized as follows:

(1) When no air is entrained by chemical admixtures, strength development stagnated owing to freezing at the final setting time.

(2) Air volume was effective in strengthening concrete frozen at the final setting time.

(3) For both air-entraining water-reducing admixtures and high-range air-entraining water-reducing admixtures, there was no difference in the impact of normal and delayed types on the strength development.

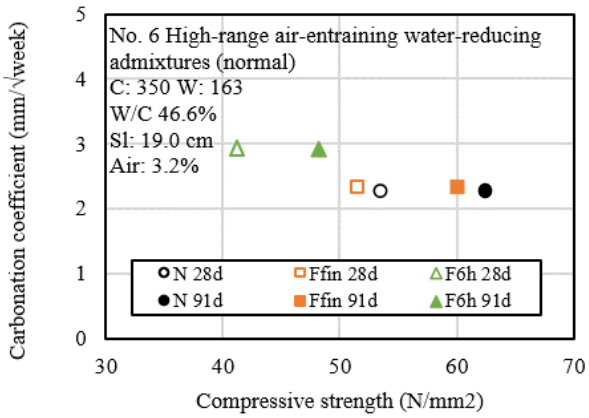

Fig. 7. Relationship between compressive strength and carbonation coefficient (No. 6).

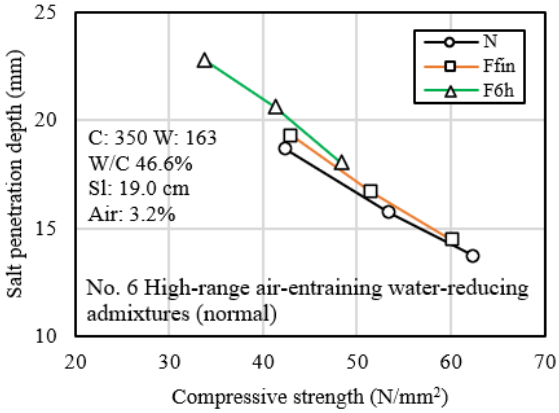

Fig. 8. Relationship between compressive strength and salt penetration depth (No. 6).

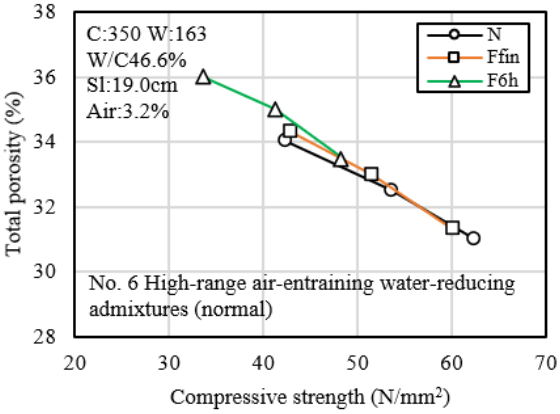

Fig. 9. Relationship between compressive strength and total porosity (No. 6).

REFERENCES

1) The Architectural Institute of Japan: The Architectural Institute of Japan, “Guidelines and Explanations for Concreting in Cold Weather” 2010, pp.19–25.

2) Moohan, K., Yokoyama, T., Tabata, M., Yoshiro, K., and Kamada, E., “An Experimental Study on the Effect of Air Entrainment for Frost Resistance of Concrete at an Early Age: Part I In the Case of Normal Weight Aggregate Concrete”, Transactions of the Architectural Institute of Japan, Vol. 265, March 1978, pp.1–10.

3) Hama, Y. and Kamada, E., “Strength Development Under Freezing Conditions and Freezing Behavior of Water in Concrete with Accelerators for Freeze Protection”, Concrete Research and Technology, Vol. 8, No. 2, July 1997, pp.73–80.

4) Furudate, M., Shimakage, R., Yamashita, K., and Hama, Y., “Study on Strength Development Stagnation Mechanism by Freezing at Early Age of Concrete”, Proceedings of the Concrete Structure Scenarios, JSMS 18, October 2018, pp. 443–448.

5) Yamashita, K., Furudate, M., Johoon, K., and Hama, Y., “The Impact of Early-Age Frost on Hardening Properties of Concrete and Mortar”, Proceedings of the Japan Concrete Institute, Vol. 41, No.1, 2019, pp.497–502.

6) Aoki, Y., Shimano, K., Miyoshi, Y., and Suzuki, M., “Estimation of Chloride Ion Penetration to Hardened Concrete by AgN03 Solution Spray Method”, Proceedings of the Japan Concrete Institute, Vol. 30, No.1, 2008, pp.759–764.

7) Shimakage, R., Kunisaki, M., Heesup, C., and Hama, Y., “The Impact of Early-Age Frost on Damage on and Durability of Concrete”, The Architectural Institute of Japan Summaries of Technical Papers of Annual Meeting, August 2016, pp. 689–690.

8) Kunisaki, M., Hama, Y., Heesup, C., and Honma, Y., “Influence of Early Age Frost Damage on Frost Resistance and Carbonation Resistance of Concrete”, Reports on Research by the Hokkaido Branch of The Architectural Institute of Japan (88), June 2015, pp. 9–12.

SUPPORTED BY

一般社団法人
ALC協会

〒101-0047 東京都千代田区内神田 3-24-4　9 STAGE kanda
TEL：03-5256-0432
URL：https://www.alc-a.or.jp/

●会員会社（3 社）

旭化成建材株式会社
〒101-8101 東京都千代田区神田神保町 1-105 神保町三井ビルディング
TEL：03-3296-3500
URL：https://www.asahikasei-kenzai.com/akk/alc/index.html

クリオン株式会社
〒135-0044 東京都江東区越中島 1-2-21 ヤマタネビル
TEL：03-6458-5400
URL：https://www.clion.co.jp

住友金属鉱山シポレックス株式会社
〒105-0012 東京都港区芝大門 2-2-11 泉芝大門ビル
TEL：03-3435-4660
URL：https://www.sumitomo-siporex.co.jp

本協会は、高温高圧蒸気養生された軽量気泡コンクリート製品（ＡＬＣパネル）の生産、販売及びその関連事業の健全なる発展と施工スキル及びマネジメント能力の増進を図り、わが国産業の発展に寄与することを目的しております。

日本製紙グループ
株式会社フローリック
本社:〒170-0013 東京都豊島区東池袋1-10-1
TEL.03-5960-6911 FAX.03-5960-6915
◎ 北海道・東北・東京・北関東・中部・関西・四国・中国・九州
◎ 出張所:長野・北陸・静岡・高松・岡山・鹿児島
◎ コンクリート研究所(つくば)・東日本技術センター(東松山)

コンクリート用化学混和剤はフローリック
フローリック 検索
https://www.flowric.co.jp

コンクリート用化学混和剤

時代を見据え、より高く、より強くありたい―
見つめる先は、コンクリート用化学混和剤の未来です。


Blue
Carbon
Green
Carbon
White
Carbon
脱炭素社会に向けて
いま私たちが出来ること
あしたのものがたりへ
安藤ハザマ
HAZAMA ANDO CORPORATION

当社は道路、河川、防災、電源開発、地質、環境、エネルギー、建築、実験・解析・研究などの専門技術者が集まる「総合建設コンサルタント」です。業務を通じて、人と自然が調和した社会づくりを目指しています。

総合建設コンサルタント

北電総合設計株式会社

建設コンサルタント登録　測量業　ISO9001・ISO14001 認証登録
一級建築士事務所　地質調査業　計量証明事業登録

2024 健康経営優良法人 Health and productivity

WORK-LIFE BALANCE+ 札幌市ワーク・ライフ・バランス plus

ほくでんグループ

〒060-0031　札幌市中央区北１条東３丁目１番地１ 北電興業ビル
TEL：(011) 222-4420　FAX：(011) 222-4426
E-mail：h-sogo.sekkei@hokuss.co.jp

http://www.hokuss.co.jp/

岩田地崎建設株式会社

〒060-8630 札幌市中央区北2条東17丁目2番地
TEL.011-221-2221 FAX.011-222-7682 https://www.iwatachizaki.jp/

現場で選ばれる水分計の新定番。

6 種類の専用目盛搭載

- ●コンクリート●モルタル●ＡＬＣ
- ●人口軽量骨材コンクリート (ALA)
- ●石膏ボード●ケイ酸カルシウム板

コンクリート・モルタル水分計HI-520-2

Kett 株式会社ケツト科学研究所

東京本社　〒143 -8507　東京都大田区南馬込1 -8 -1
西日本支店／北海道営業所／東北営業所／東海営業所／九州営業所
URL : https://www.kett.co.jp　E-mail:sales@kett.co.jp

まじめに、まっすぐ

KONOIKE

鴻池組

鴻池組は、強みの環境分野を中心に価値ある技術で社会から選ばれる企業をめざします。

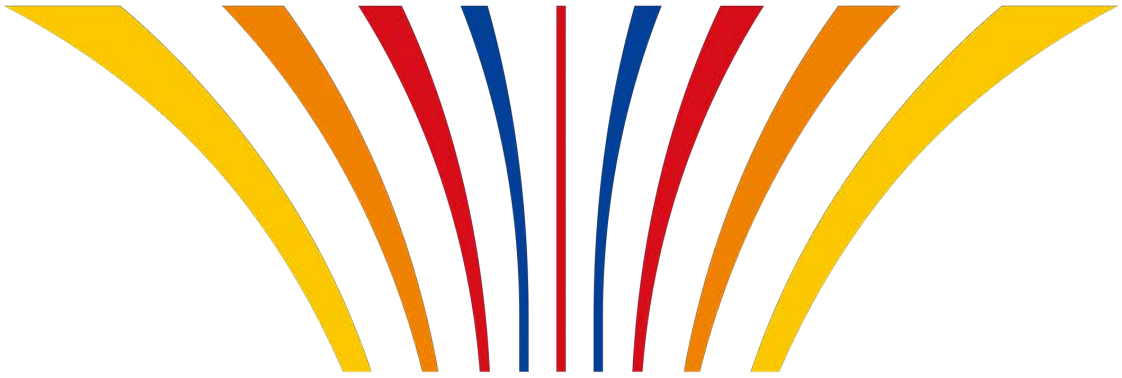

Minami-Gumi Co., Ltd.
株式会社 南組
技術と共に前へ

Our New Technology

Permanent Formwork Method
（永久型枠工法）

This is a method of repairing deteriorated and damaged parts of harbor and fishing port concrete structures such as breakwaters and quays using high-strength, high-durability mortar secondary products (panels, bolts and nuts) and shape-adjustable frames. Compared to conventional methods, this method is easier to work with and requires fewer construction days, which reduces costs and allows for early start of use.

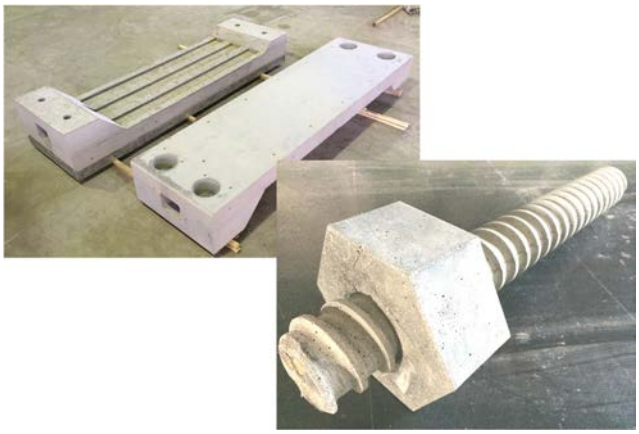

Working Movies ▶

Minami-Gumi Co., Ltd.

Head Office : 5 Sakaemachi, Samani, Samani-gun, Hokkaido 058-0023, JAPAN
Phone: +81-146-36-2311 / Fax: +81-146-36-4878
Sapporo Branch: 17-3-75 Tsukisamu 2-jo, Toyohira-ku, Sapporo, Hokkaido 062-0052, JAPAN
Phone: +81-11-595-7085 / Fax: +81-11-853-0220
Tokyo Office : 3 Chome-2-11 Kitazawa, Setagaya-ku, Tokyo 155-0031, JAPAN
Phone: +81-3-3481-9177

つくろう、セメントの未来。

セメントはインフラになくてはならないもの。
私たちは廃棄物・副産物からセメントを作ることにより
「循環型社会の構築」の一翼を担うと共に、
セメントの安定的な供給を通じて
これからも社会の持続的発展に貢献していきます。

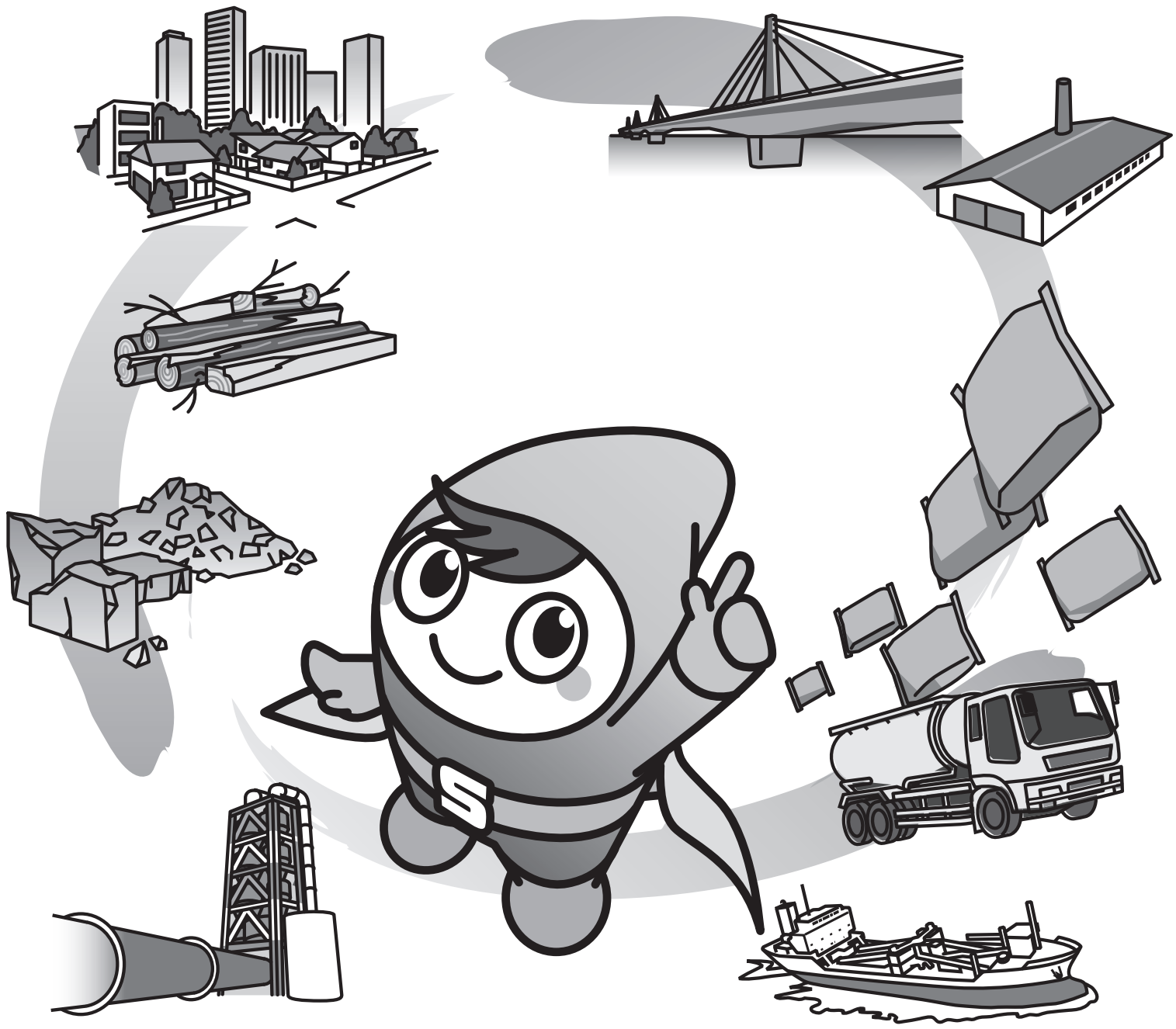

住友大阪セメント株式会社
〒105-8641 東京都港区東新橋1-9-2 汐留住友ビル20階　https://www.soc.co.jp/

■A4（260×180mm）

環境のことを、資源のことを。

まえむきに考えて、ひたむきに実行。

頭の上も足の下も

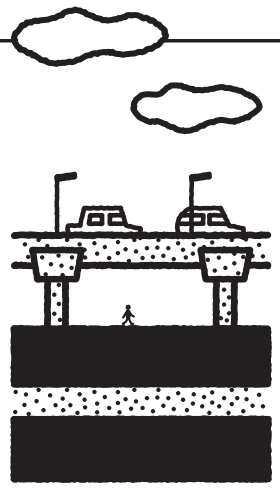

たとえば一般道路の上を走る高速道路。
地下に張り巡らされた下水道。
社会と暮らしをしっかり支えるインフラづくりに、
セメントは欠かせません。

太平洋セメント www.taiheiyo-cement.co.jp

世界で地産地消

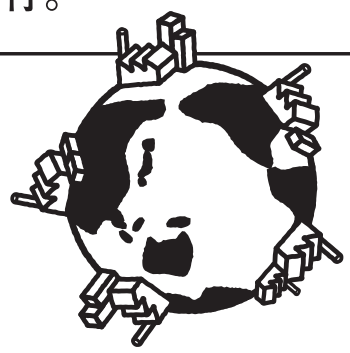

セメントはインフラづくりに
欠かせない基礎資材です。
環太平洋に配した
私たちのセメント工場が
各国・各地の発展と成長を
お手伝いしています。

太平洋セメント www.taiheiyo-cement.co.jp

私たちの資源置場

捨てればごみ、使えば資源。
家庭用のごみ置場も
私たちにすれば
大切な資源置場です。
しっかり回収し
新しい生命を与えます。

太平洋セメント www.taiheiyo-cement.co.jp

国産の白いダイヤ

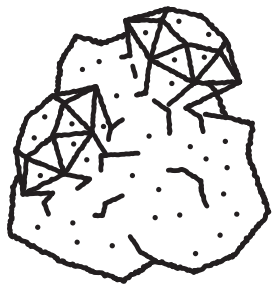

自給率100%の資源が石灰石。
海外にも輸出されるほど高品質。
食品・製鉄・紙類など幅広く用いられます。
白いダイヤと呼んでほしい人気者です。

太平洋セメント www.taiheiyo-cement.co.jp

コンクリート百貨店

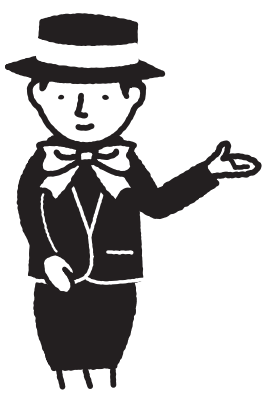

草花が生えてくるもの、
鉄に負けないぐらい強いもの、
水に浮かぶもの。
常識を一変させる
コンクリートを発明する。
私たちの仕事です。

太平洋セメント www.taiheiyo-cement.co.jp

「ゼロエミッション」を支えます

さまざまな産業が排出する廃棄物。
セメント工場が受け入れて廃棄物→原料という流れを作ります。
循環型社会をめざし私たちは努力しています。

太平洋セメント www.taiheiyo-cement.co.jp

夢から感動へ―ハートテクノロジー

東洋建設

〒101-0051　東京都千代田区神田神保町 1-105
TEL.03-6361-5450

https://www.toyo-const.co.jp/

Proceedings of 17th International Symposium on Performance Improvement of Concrete for Long life span Structure

---

Publication August 22, 2024

Publisher Muroran Institute of Technology

27-1, Mizumoto, Muroran, Hokkaido, Japan, 0508585

ISBN 978-4-9900489-6-9 (August 7, 2024)